Properties of E and S0 Galaxies in the Clusters Hydral and Coma

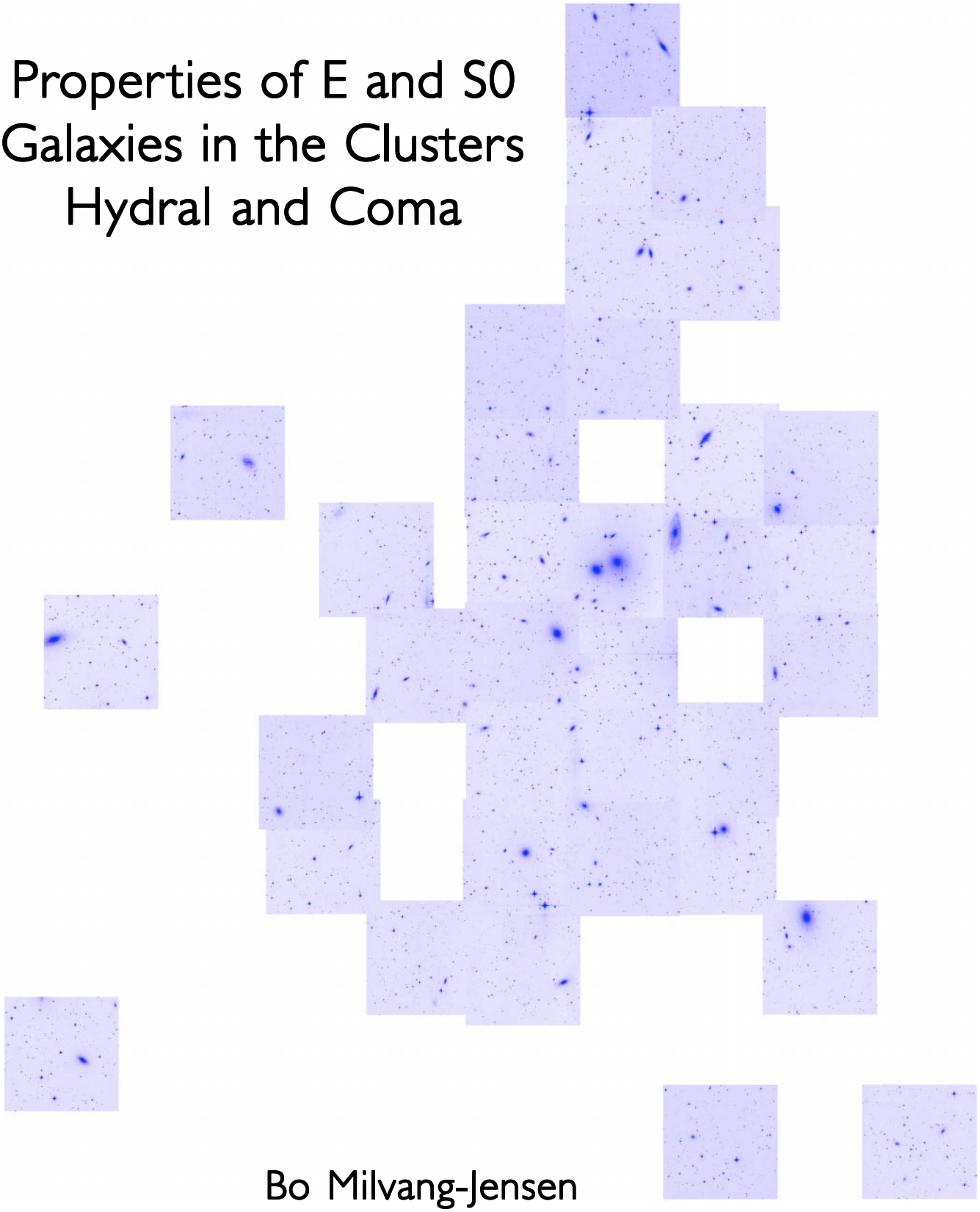

Bo Milvang-Jensen

July, 1997

Master's Thesis

University of Copenhagen

Contents

Abstract

We have investigated properties of E and S0 galaxies in the central parts of the clusters HydraI (Abell 1060) and Coma (Abell 1656) using large magnitude limited samples. The investigations serve the following main purposes: (1) They add pieces to our knowledge about galaxy formation and evolution, including the formation and evolution of the stellar populations of the galaxies. (2) They help establish a good reference point at $z \approx 0$ needed for the similar studies of high redshift galaxies. (3) They help identify possible limitations in the use of the Fundamental Plane (FP) as a distance determinator.

Surface photometry and global photometric parameters are presented for 64 E and S0 galaxies in HydraI. The observations were made with the Danish 1.5 meter telescope at La Silla, equipped with the DFOSC instrument. Combined with data from the literature and data yet to be published, photometry and spectroscopy are available for 45 E and S0 galaxies in HydraI and 114 in Coma.

The FP in Gunn r is not significantly different for the HydraI and Coma samples, although differences in the $\log\sigma$ coefficient on the 10% level cannot be ruled out. For the combined sample, we find the FP to be $\log r_{\rm e} = 1.35\log\sigma - 0.83\log <I>_{\rm e} + \gamma$. The distribution within the FP is not significantly different for the two samples. The FP has an intrinsic scatter of 0.087 in $\log r_{\rm e}$. For the HydraI sample we find that the intrinsic scatter is not significantly different in Gunn r, Johnson B, and Johnson U. This implies that the scatter cannot be caused by variations in only the age or only the metallicity. Changes in the age must be balanced to some extent by changes in the metallicity. This is compatible with the age–metallicity–sigma relation that we find.

From the mass-to-light ratios and the line indices $\rm Mg_2$ and $<$ Fe $>$, we have derived estimates of [Mg/H], [Fe/H], [Mg/Fe], and ages using stellar population models. The derived abundance ratio [Mg/Fe] increases with the velocity dispersion. This is mainly due to an increase in [Mg/H], with [Fe/H] being constant or slightly decreasing. For high velocity dispersion galaxies [Mg/Fe] is larger than solar and can reach values of 0.3 dex or more. This can be explained by an increase in the fraction of type II supernovae over type Ia supernovae with velocity dispersion. This could for example be caused by a variation in IMF slope or in the time scale for star formation. Both [Mg/H], [Fe/H], [Mg/Fe], and age show a much smaller scatter for galaxies brighter than $M_{\rm r_T} \approx -23\overset{\rm m}{.}1$ than for galaxies fainter than this magnitude. The galaxies are found to follow a tight age–metallicity–sigma relation, $[{\rm Mg/H}] = 1.15\log\sigma - 0.78\log{\rm age} + c$. This relation allows for a large variation in age and metallicity while still keeping the FP and the $\rm Mg_2$–σ relation thin.

The FP residuals are strongly correlated with [Mg/H], [Fe/H], and age, but are not correlated with [Mg/Fe]. Therefore, age or metallicity differences can cause systematic errors in the distances determined by the FP. A weaker correlation with the local cluster density is also found.

For none of the relations studied do we find any significant differences between HydraI and Coma. This is despite the fact that Coma is 2–3 times more massive than HydraI and has a smaller fraction of spiral galaxies. This suggests that the environmental differences between rich and less rich clusters have only a small effect on the properties of the E and S0 galaxies found in clusters as rich as HydraI and Coma.

Sammenfatning på dansk

Vi har undersøgt egenskaber ved E og S0 galakser i de centrale dele af hobene HydraI (Abell 1060) og Coma (Abell 1656) ved hjælp af store størrelsesklassebegrænsede samples. Undersøgelserne tjener følgende hovedformål: (1) De tilføjer brikker til vores viden om galaksedannelse og -udvikling, inklusive dannelsen og udviklingen af galaksernes stjernepopulationer. (2) De hjælper med til at etablere et godt referencepunkt ved $z \approx 0$ til brug for lignende studier af højrødforskydningsgalakser. (3) De hjælper med til at identificere mulige begrænsninger i brugen af Fundamentalplanet (FP) til afstandsbestemmelse.

Overfladefotometri og globale fotometriske parametre præsenteres for 64 E og S0 galakser i HydraI. Observationerne blev foretaget med det danske 1.5 meter teleskop på La Silla, udstyret med DFOSC instrumentet. Kombineret med data fra litteraturen og data der endnu ikke er publiceret er der fotometri og spektroskopi til rådighed for 45 E og S0 galakser i HydraI og 114 i Coma.

FP i Gunn r er ikke signifikant forskellig for vore HydraI og Coma samples, men forskelle i $\log\sigma$-koefficienten på 10% niveau kan ikke udelukkes. For det kombinerede sample finder vi at FP er givet ved $\log r_{\rm e} = 1.35\log\sigma - 0.83\log <I>_{\rm e} + \gamma$. Fordelingen indenfor FP er ikke signifikant forskellig for de to samples. FP har en indre spredning på 0.087 i $\log r_{\rm e}$. For vores HydraI sample finder vi at den indre spredning ikke er signifikant forskellig i Gunn r, Johnson B, og Johnson U. Dette medfører, at spredningen ikke kan være forårsaget af variationer i alder alene eller metalindhold alene. Ændringer i alder må i et vist omfang være afbalanceret af ændringer i metalindhold. Dette er foreneligt med den alder–metalindhold–sigma relation som vi finder.

Fra masse-lysstyrkeforholdene og de to linieindices $\rm Mg_2$ og $<\rm Fe>$ har vi afledt estimater af [Mg/H], [Fe/H], [Mg/Fe] og aldre ved hjælp af stjernepopulationsmodeller. Det afledte elementforhold [Mg/Fe] stiger med hastighedsdispersionen. Dette skyldes hovedsageligt at [Mg/H] stiger, mens [Fe/H] er konstant eller svagt faldende. For galakser med høje hastighedsdispersioner er [Mg/Fe] større end solværdien og kan nå 0.3 dex eller mere. Dette kan forklares med en stigning i brøkdelen af type II supernovae i forhold til type Ia supernovae med hastighedsdispersionen. Dette kunne for eksempel være forårsaget af en variation i IMF-hældningen eller i tidskalaen for stjernedannelse. Både [Mg/H], [Fe/H], [Mg/Fe] og alder viser en meget mindre spredning for galakser klarere end $M_{\rm rT} \approx -23\overset{\rm m}{.}1$ end for galakser svagere end denne størrelsesklasse. Vi finder at galakserne følger en snæver alder–metalindhold–sigma relation, $[\rm Mg/H] = 1.15\log\sigma - 0.78\log\,\text{alder} + c$. Denne relation tillader store variationer i alder og metalindhold samtidigt med at spredningen i FP og $\rm Mg_2$–σ relationen holdes lav.

FP-residuerne er stærkt korrelerede med [Mg/H], [Fe/H] og alder, men er ikke korrelerede med [Mg/Fe]. Dette betyder, at forskelle i alder eller metalindhold kan forårsage systematiske fejl i afstande bestemt ved hjælp af FP. Vi finder også en svagere korrelation med den lokale hobtæthed.

Vi finder ikke nogen signifikante forskelle mellem HydraI og Coma for nogen af de relationer som vi har studeret. Dette er til trods for, at Coma er 2–3 gange mere massiv end HydraI og har en mindre brøkdel af spiralgalakser. Dette antyder, at de miljømæssige forskelle mellem rige og mindre rige hobe kun har en lille effekt på egenskaberne for de E og S0 galakser man finder i hobe så rige som HydraI og Coma.

Chapter 1

Introduction

Preface

This is the Master's Thesis (Danish: *speciale*) for Bo Milvang-Jensen, presented to The University of Copenhagen as partial fulfillment of the requirements for obtaining the Master's Degree (Danish: *cand. scient.*) in astronomy. The thesis has been written under the supervision of Inger Jørgensen, McDonald Observatory & Department of Astronomy, The University of Texas at Austin. Formal supervisor at The University of Copenhagen has been Leif Hansen.

Introduction

A key issue in astronomy is to understand galaxy formation and evolution, including the formation and evolution of the stellar population of the galaxies. Another key issue is distance determination. The Fundamental Plane (Djorgovski & Davis 1987, Dressler et al. 1987b) for E and S0 galaxies provides valuable insight into both problems. The Fundamental Plane (FP) is the relation $\log r_{\rm e} = \alpha \log \sigma + \beta \log <I>_{\rm e} + \gamma$, where $r_{\rm e}$ is the effective (i.e. half-light) radius, $<I>_{\rm e}$ is the mean surface brightness within $r_{\rm e}$, and σ is the central velocity dispersion.

The existence of the FP, the low scatter in it, as well as its slope are properties that a successful theory of galaxy formation and evolution should be able to explain. (Different theories for the interpretation of the FP are briefly reviewed in Sect. 2.2.) This also goes for other relations between global parameters for E and S0 galaxies, such as the Mg_2–σ relation.

The $D_{\rm n}$–σ relation (which is closely related to the FP, as explained in Sect. 2.2) has been used to determine distances and deviations from the pure Hubble expansion of the Universe for a large number of galaxies by the '7 Samurai' group (Dressler et al. 1987a, Lynden-Bell et al. 1988, Faber et al. 1989). These authors found systematic deviations from the pure Hubble expansion, with the galaxies streaming towards the Hydra-Centaurus region. This streaming motion was interpreted as originating from a huge mass concentration ($\sim 5 \times 10^{16} M_{\odot}$, Lynden-Bell et al. 1988) coined the 'Great Attractor' (see also Faber & Burstein 1988).

However, the reality of the Great Attractor was not agreed upon. This dispute was one of the main reasons for Jørgensen and collaborators to undertake their observing program to study E and S0 galaxies. The group has presented surface photometry in Jørgensen, Franx, & Kjærgaard (1992, hereafter JFK92), Jørgensen and Franx (1994, hereafter JF94), and Jørgensen, Franx, & Kjærgaard (1995a, hereafter JFK95a). Spectroscopy has been presented in Jørgensen, Franx, & Kjærgaard (1995b, hereafter JFK95b) and Jørgensen (1997a, hereafter J97). Analysis of the data has been presented in Jørgensen, Franx, & Kjærgaard (1993, hereafter JFK93), JF94, Jørgensen, Franx, & Kjærgaard (1996, hereafter JFK96), and J97.

A new direction in the work started by Jørgensen and collaborators is to study the properties of E and S0 galaxies using large and complete magnitude limited samples. Only for complete samples it is possible to draw reliable conclusions about the physical properties of the galaxies, regarding e.g. the distribution of metallicities, abundance ratios, ages, and relative disk luminosities. With the new spectroscopy on galaxies in Coma to be published in Jørgensen (1997b, in prep.), a large and highly complete magnitude limited sample is available. This Coma sample is used in the analysis presented in this work. Likewise, the HydraI data presented in this work are part of magnitude limited sample of high completeness.

It should be noted that I did the basic reductions, most of the surface photometry, and the derivation of the global photometric parameters for the HydraI data. Inger Jørgensen did the HydraI spectroscopy reductions. The Coma data were taken from the literature and from work not yet published (Jørgensen 1997b, in prep.).

Document Overview

The main text (pp. 3–132) is organized as follows. The current chapter (Chapter 1) gives a general introduction to the thesis. Chapter 2 gives background information necessary for the subsequent chapters. The topics covered include the Fundamental Plane and stellar population synthesis models. Chapter 3 describes the sample selection and basic reductions for the HydraI photometry. Chapter 4 describes the HydraI surface photometry and the standard calibration. Chapter 5 describes the derivation of the global photometric parameters for the HydraI data. Chapter 6 describes the HydraI spectroscopy. Chapter 7 starts with a summary of the HydraI data and a presentation of the Coma data. Then the analysis is presented. Finally, in Chapter 8 the conclusions are given.

The appendices (pp. 133–267) are organized as follows. Appendix A gives details of the basic reductions of the photometry. Appendix B gives details of the surface photometry. Appendix C describes the standard calibration of the photometry. Appendix D lists the Coma data. Appendix E shows images of the 35 fields on the sky in which the galaxies in the HydraI surface photometry sample are located. Finally, Appendix F shows the HydraI surface photometry profiles (e.g. μ, ε and c_4 as function of radius).

Readers not interested in the data *details* can profitably read Chapter 2, skip Chapter 3–6, and read Chapter 7–8. The data used in the analysis will still be introduced in Sect. 7.1.

Acknowledgements

First and foremost I would like to thank my thesis advisor Inger Jørgensen, who has shown a large and consistent interest in my project during the times. Our numerous scientific discussions and her many constructive comments have greatly improved this work. She is also thanked for letting me use her Coma data not yet published (Jørgensen 1997b, in prep.).

Part of the thesis work was done while I was visiting scholar at The University of Texas at Austin. It is a pleasure to thank the Astronomy Department and McDonald Observatory for their hospitality. I am also indebted to the many people in Austin in and outside the Astronomy Department who made my stay in Austin a very pleasant one. The Fulbright Commission and Observator Julie Marie Vinter Hansens Rejselegat are acknowledged for their kind financial assistance, which in part funded my stay in Austin.

It has been a pleasure to study at the Observatory in Copenhagen during the years. My fellow students are cordially thanked for their friendship. Also my friends and family outside astronomy are thanked for their good company and support.

Lars Lindberg Christensen and Sune Hermit are thanked for helpful comments on the manuscript.

Leif Hansen, Henning Jørgensen, and Per Kjærgaard are acknowledged for their help in obtaining funding for my participation in the ESO/VLT workshop on Galaxy Scaling Relations in Garching, November 1996. Leif is also thanked for various assistance during my thesis work.

Last but not least I would like to acknowledge Åke Nordlund for his large responsibility for the outstanding computer facilities we have in Copenhagen, and for his stimulating courses on computer related topics.

Notation and Terminology

"log" is the base ten logarithm, and "ln" is the base e logarithm. The pronoun *we* is used instead of *I* to refer to the author of this thesis, as is customary for single author papers in the literature. However, where it would seem awkward or cause confusion, *I* is used. American-English spelling is attempted. Papers with three authors are referenced by all three author names at the first occurrence, and by the first author name at all subsequent occurrences.

Chapter 2

Background

This chapter gives background information necessary for the subsequent chapters. Section 2.1 introduces the observable quantities which are derived from the data in Chapter 4–6, and on which the analysis (Chapter 7) is based. Section 2.2 introduces the Fundamental Plane (FP), and explores the physics underlying the relation. Section 2.3 describes stellar population synthesis models. These models predict observable quantities like the mass-to-light ratios and line strengths, and can be used to infer mean ages and metallicities from the observations. They can also be used to interpret the found relations between the observable quantities in terms of variations in mean age or metallicity.

2.1 Observable Quantities of E and S0 Galaxies

The observations we normally have at hand of E and S0 galaxies are direct images and longslit spectroscopy along the major axis. Only for very nearby galaxies and with superb instrumentation (e.g. with the Hubble Space Telescope) it is possible to resolve the galaxy into individual stars; in all other cases only the *integrated light* of the stellar population of the galaxy can be observed.

For each galaxy, we want to determine a characteristic size and surface brightness, and the luminosity (or the total magnitude). This is in the following done by first fitting ellipses to the images of the galaxies. The resulting *surface photometry* yields among other things the local surface brightness $\mu(r)$ as function of projected radius r (in arcsec). μ is expressed in units of magnitudes per square arc second ($^{\rm m}/{\rm arcsec}^2$), and r is calculated as $r = \sqrt{ab}$, where a and b are the semi-major and semi-minor axes of the elliptical isophote, respectively. The surface photometry for the HydraI galaxies is described in Chapter 4.

Elliptical galaxies are in general well described by the $r^{1/4}$ law (de Vaucouleurs 1948),

$$\mu(r) = \mu_{\rm e} + 8.3268 \left[\left(\frac{r}{r_{\rm e}} \right)^{1/4} - 1 \right] \quad , \tag{2.1}$$

where $r_{\rm e}$ is the *effective radius* and $\mu_{\rm e} = \mu(r_{\rm e})$ is the local surface brightness at $r_{\rm e}$. An example is the nearby ($\sim$10 Mpc) 'standard' E1 galaxy NGC3379, for which the residuals from the $r^{1/4}$ fit are less than 0.08 mag over a 10-mag range in μ (de Vaucouleurs & Capaccioli 1979, Capaccioli et al. 1990). Small systematic deviations from the $r^{1/4}$ law have been found by e.g. Caon, Capaccioli, & D'Onofrio (1993). Makino, Akiyama, & Sugimote (1990) found from dynamical arguments that the $r^{1/4}$ law bared little physical significance. They also found that the $r^{1/4}$ law provided the best fit, but that generalized $r^{1/m}$ laws with $m = 3$–10 gave almost as good fits for a range in r of about 100. Here, we will by that token use the $r^{1/4}$ law as a good fitting function to derive a characteristic galaxy size $r_{\rm e}$. It is worth noting, that for studies of the FP, the $r^{1/4}$ parameters are well suited,

even though some E and S0 galaxies show deviations from the $r^{1/4}$ profile. This is due to the fact that the *combination* of r_e and $<I>_e$ enters the FP is rather insensitive to these deviations. The above-mentioned combination is "FP" $= \log r_e + 0.82 \log <I>_e$. Jørgensen (1997c) compared "FP" based on asymptotic magnitudes (the least model dependent parameters) with "FP" based on (1) fit with an $r^{1/m}$ profile, (2) fit with an $r^{1/4}$ profile, (3) fit with an $r^{1/4}$ + exponential disk profile, and (4) the Petrosian (1976) parameters. The differences Δ"FP" showed a small and comparable rms scatter for the four methods (rms = 0.04, 0.06, 0.07, and 0.05, respectively, based on a sample of 31 galaxies). Thus, "FP" is well-determined for several choices of parameters, including the $r^{1/4}$ parameters. Small systematic offsets ($\lesssim 0.02$) in "FP" between determinations from different methods were found. Therefore, parameters based on different methods should not be mixed.

The constant in Eq. (2.1) has been chosen so that half the light of the galaxy is inclosed within r_e. When r_e has been determined, the *mean* surface brightness within r_e, denoted $<\mu>_e$, can be calculated. From r_e and $<\mu>_e$ the total magnitude can be calculated as $m_T = <\mu>_e - 2.5 \log(2\pi {r_e}^2)$, since $\pi {r_e}^2$ is the surface within which half the light is found. The derivation of global photometric parameters for the HydraI galaxies is described in Chapter 5.

The surface brightness can be expressed in $L_\odot/\mathrm{pc}^2$ instead of $^{\mathrm{m}}/\mathrm{arcsec}^2$, where $L_\odot$ is the luminosity of the Sun in the given passband (e.g. Gunn r). This is done as

$$\log <I>_e = -0.4(<\mu>_e - k) \ , \tag{2.2}$$

where the constant k is given by

$$k = M_\odot + 5 \log \left(\frac{206265 \, \mathrm{pc}}{10 \, \mathrm{pc}} \right) = \begin{cases} 26.4 & \text{for Gunn r} & (M_\odot = 4\overset{\mathrm{m}}{.}83) \\ 27.0 & \text{for Johnson B} & (M_\odot = 5\overset{\mathrm{m}}{.}43) \\ 27.15 & \text{for Johnson U} & (M_\odot = 5\overset{\mathrm{m}}{.}58) \end{cases} \ . \tag{2.3}$$

k corresponds to the apparent magnitude of the Sun if placed at the distance where 1 pc subtends an angle of 1 arcsec. The values given are those from JFK96. The values of $M_\odot$ given in parentheses are calculated from k, and are correct to within $0\overset{\mathrm{m}}{.}05$.

From the spectroscopy we can obtain a measure of the kinetic energy of the galaxy, namely the line-of-sight velocity dispersion of the stars in the galaxy, σ.

We determine the strength of different individual absorption lines from the spectroscopy. Due to moderate spectral resolution and velocity broadening it is not possible to determine accurate equivalent widths as in high resolution spectroscopy of single stars. Instead, a so-called *line index* is calculated from the flux within an index passband centered on the spectral feature relative to the level defined by a pseudocontinuum passband on each side of the line. We use the Lick/IDS line index system (Faber et al. 1985, Worthey et al. 1994), of which examples are Mg_2 and $< Fe >$. These indices will usually depend strongly on the abundance of the element that gives rise to the absorption feature on which they are centered. But in addition, lines from other elements present in either the index passband or in the pseudocontinuum passbands will also have an effect. In a few cases the indices will respond in very unexpected ways to abundances changes. For example, Tripicco & Bell (1995) found the Fe4668 index to be very sensitive to the carbon abundance, but almost *insensitive* to the iron abundance! This index has later been renamed to C4668 or $C_2$4668. The indices we use in this study are more 'well-behaved', cf. Sect. 2.3.3. In addition to element abundances the line indices are also sensitive to the mean age of the stellar population. For the indices used in this study, namely Mg_2 and $< Fe >$, older ages give stronger absorption lines, cf. Sect. 2.3.1. Note, that this is not the case for the H_β index. We do not have H_β indices for our samples.

This project is based on *central* spectroscopical values. Because of the cost in observing time to get spatial information in the the spectra there is a trade off between either having large samples

of galaxies with centrally measured parameters or having much smaller samples with spatial information in the spectra. Further, this allows for the use of fiber-fed spectrographs. Several studies have found tight correlations between central quantities and more global quantities. For example, Burstein et al. (1988) and Bender, Burstein, & Faber (1993) found a tight correlation between central Mg_2 and global $(B-V)$ color. Here 'global' means within an aperture of 25 times larger diameter of that used for the central values. These authors concluded from this that variations in radial gradients in colors and line indices from galaxy to galaxy are small. However, if the size of the gradient is correlated with the central value, this conclusion does not necessarily hold. We do not study radial gradients in colors and line indices in this work.

From the spectroscopy the redshift z is determined. The observations are usually transformed from the observer's frame to some standard frame. In this work we will use two frames: (1) The heliocentric frame, in which the Sun is at rest. (2) The CMB frame, which is the frame that is at rest relative to the cosmic microwave (CMB) radiation, i.e. the frame in which the CMB radiation is isotropic. Redshifts in these two frames will be denoted $z_{\rm hel}$ and $z_{\rm CMB}$, respectively.

The spectroscopy for the HydraI galaxies is described in Chapter 6.

2.2 The Fundamental Plane

2.2.1 The Original Findings

The Fundamental Plane (FP) was discovered independently and simultaneously by Djorgovski & Davis (1987) and Dressler et al. (1987b). It is a relation between $r_{\rm e}$, σ, and $<I>_{\rm e}$, and is linear in logarithmic space. Since $L = 2\pi <I>_{\rm e} {r_{\rm e}}^2$, the FP can also be expressed as a relation between L, σ, and $<I>_{\rm e}$, or between $r_{\rm e}$, σ, and L.

Djorgovski & Davis (1987) found a tight correlation for elliptical galaxies between either a radius or the luminosity on the one hand, and a linear combination of velocity dispersion and mean surface brightness on the other hand. They dubbed this relation *the fundamental plane*. They found the best-fitting relation involving a radius to be

$$\log a_{\rm e} = 1.39 \log \sigma - 0.90 \log <I>_{\rm e} + \text{constant} \tag{2.4}$$

in the $r_{\rm G}$ passband (Djorgovski 1985), with the radius $a_{\rm e}$ being the effective semimajor axis from a fit to an $r^{1/4}$ profile. $a_{\rm e}$ is related to $r_{\rm e}$ through $r_{\rm e} = \sqrt{a_{\rm e} b_{\rm e}} = a_{\rm e}\sqrt{1-\varepsilon}$. They found, that the morphological shape parameters (ellipticity, ellipticity gradient, isophotal twist rate, and slope of the surface brightness profile) did *not* correlate with the residuals from the FP. Djorgovski & Davis found the thickness of the FP to be given by the measurement errors, and that the *intrinsic scatter* therefore had to be very small, a few percent or less. Their main sample only consisted of E galaxies, but they reported preliminary results that a fundamental plane also existed for S0 galaxies, and that it even might be identical to that for E galaxies.

Dressler et al. (1987b), also known as the *7 Samurai*, found the same result, namely that elliptical galaxies describe a plane in the 3-space of $(\log L, \log <I>_{\rm e}, \log \sigma)$ or $(\log r_{\rm e}, \log <I>_{\rm e}, \log \sigma)$. They found the plane to be given by

$$\log r_{\rm e} = 1.325 \log \sigma - 0.825 \log <I>_{\rm e} + \text{constant} \tag{2.5}$$

in the Johnson B passband.

Dressler et al. also introduced a new photometric diameter $D_{\rm n}$, the diameter within which the mean surface brightness is $20.75^{\rm m}/\text{arcsec}^2$, in Johnson B. They found $\log D_{\rm n}$ to correlate as well with $\log \sigma$ as any linear combination of $\log r_{\rm e}$ and $\log <I>_{\rm e}$, and they where thus able to reformulate the FP as the $D_{\rm n}$–σ relation, $\log D_{\rm n} = 1.333 \log \sigma + \text{constant}$. However, they noted that the correlation between $D_{\rm n}$ and a combination of $r_{\rm e}$ and $<I>_{\rm e}$, namely $D_{\rm n} \propto r_{\rm e} {<I>_{\rm e}}^{0.8}$, had a small residual curvature. Phillipps (1988) demonstrated theoretically that the relation $D_{\rm n} \propto r_{\rm e} {<I>_{\rm e}}^{0.8}$ is expected for galaxies with $r^{1/4}$ profiles and $<\mu>_{\rm e}$ around $21.8\,^{\rm m}/\text{arcsec}^2$ in Johnson B. He also showed, that for the range in $<\mu>_{\rm e}$ actually spanned by (giant) ellipticals, the FP will be seen as a *curved* line in the $\log D_{\rm n}$ versus $\log \sigma$ plot. Lucey, Bower, & Ellis (1991a) were the first to demonstrate that the residuals from the $D_{\rm n}$–σ relation were correlated with $<\mu>_{\rm e}$. They corrected for this by simply adding a linear term in $<\mu>_{\rm e}$ to the $D_{\rm n}$–σ relation. JFK93 found for a sample of galaxies in the Coma cluster that the $D_{\rm n}$–σ residuals showed the dependence on $<\mu>_{\rm e}$ that was predicted by Phillipps (1988), a dependence that has a quadratic term. They concluded that the FP is a true improvement of the $D_{\rm n}$–σ relation. In accordance with this, they found the scatter of the $D_{\rm n}$–σ relation to be larger than for the FP, namely 17% versus 11% for their sample.

In the following, we will mainly consider the FP, not the $D_{\rm n}$–σ relation.

2.2.2 Is the FP Universal?

To discuss whether the FP is universal, we will first need to make a point about $r_{\rm e}$ clear. What can be observed is *an angle*, measured in e.g. arcsec. To calculate the corresponding *length*, in e.g.

kpc, the distance $d_{\rm A}$ needs to be known, i.e.

$$r_{\rm e,kpc} = d_{\rm A} \cdot \frac{r_{\rm e,arcsec}}{206265\,{\rm arcsec/rad}} \quad . \tag{2.6}$$

The subscript "A" on the distance indicates that it is a so-called angular diameter distance; this will be explained later. We can write the FP using both versions of $r_{\rm e}$, i.e.

$$\log r_{\rm e,arcsec} = \alpha \log \sigma + \beta \log <I>_{\rm e} + \gamma_{\rm cl} \tag{2.7}$$

$$\log r_{\rm e,kpc} = \alpha \log \sigma + \beta \log <I>_{\rm e} + \Gamma \tag{2.8}$$

For $r_{\rm e}$ in arcsec, the zero point $\gamma_{\rm cl}$ for the given cluster depends on the distance (in kpc) as

$$\gamma_{\rm cl} = \Gamma - \log d_{\rm A} + \log 206265 \quad . \tag{2.9}$$

In the following we will not explicitly denote whether $r_{\rm e}$ is an angle or a length, unless there is reason for confusion.

The question about universality can now be phrased as: a) are the FP coefficients (α and β) universal? b) is the FP zero point (Γ) universal? JFK96 addressed both questions. Based on data for 226 E and S0 galaxies in 10 nearby clusters, they determined α, β, and $\gamma_{\rm cl}$ for each cluster. They found that α and β were not significantly different from cluster to cluster, although variations of α of the order 10% could not be ruled out. Furthermore, they did not find α and β to correlate with the distance to the cluster (more precisely $cz_{\rm CMB}$), the velocity dispersion of the cluster, or the intracluster gas temperature. This is remarkable, especially since their clusters spanned a large range in these cluster properties. JFK96 also found E and S0 galaxies to follow the same FP. The JFK96 values $\alpha = 1.24 \pm 0.07$ and $\beta = -0.82 \pm 0.02$ agree reasonably well with those from other studies in the literature of cluster E (and S0) galaxies. Different fitting methods and sample selection criteria make it difficult to compare FP coefficients from different studies in detail.

The universality of Γ is harder to assess when the distances to the clusters are not known. JFK96 found that under the assumption that Γ is constant, the derived peculiar velocities were small, mostly $< 1000\,{\rm km\,s^{-1}}$. This means that Γ can not be *very* different from cluster to cluster.

It is interesting to note, that some studies find that elliptical galaxies in the field are systematically different from elliptical galaxies in rich clusters. For example, de Carvalho & Djorgovski (1992) found that field ellipticals compared with cluster ellipticals had a larger value of the FP zero point, a larger intrinsic scatter in the FP, and perhaps also a different value of the FP slope. The larger value of the FP zero point for the field can also be phrased as a larger surface brightness (i.e. $<I>_{\rm e,field} > <I>_{\rm e,cluster}$) and/or a lower velocity dispersion at a given radius (cf. Eq. 2.8; remember that $\beta < 0$). de Carvalho & Djorgovski further found, that at a fixed radius (or luminosity) the field ellipticals were more blue and had a lower $\rm Mg_2$ value. A possible interpretation is that the field galaxies have experienced merger-induced star formation.

Along those lines, Schweizer et al. (1990) found for a sample of 36 mostly field ellipticals that various line indices (such as $\rm Mg_2$) were correlated with morphological *fine-structure* (ripples, jets, boxyness, and so-called X-structure). They found that the most probable interpretation was a variation in mean age with morphological fine-structure. This could be explained by merger-induced star formation. Gregg (1992) found that the peculiar velocities derived from the $D_{\rm n}$–σ relation for the galaxies in the Schweizer et al. sample were correlated with the morphological fine-structure. It was concluded, that these differences in stellar population induced spurious peculiar velocities. Note, that in these studies a distance is determined for *each field galaxy*, as opposed to determining the distance to a *cluster* using many galaxies in the given cluster.

The findings of de Carvalho & Djorgovski (1992) could lead to the suspicion that there might be differences between rich and poor clusters, and between the central and outer regions of clusters. JFK96 tested this by plotting the residuals from the FP versus the projected cluster surface density. They did not find any correlation. The found stability of the zero point of the FP corresponds to $3 \pm 3\%$ if the FP is used for distance determinations. Lucey et al. (1991b) tested the stability of the zero point of the $D_{\rm n}$–σ relation and found the derived distances to vary by only $6 \pm 9\%$. Their sample of galaxies in the Coma cluster spanned a range of over 150 in projected cluster surface density. JFK96 found that the FP zero point for the Lucey et al. sample had a comparable stability to that of the JFK96 sample, i.e. $3 \pm 3\%$.

2.2.3 The Physics Underlying the FP

To interpret the empirical FP relation, we need to relate the observable quantities to the physical quantities. The observable quantities are a radius $R_{\rm obs}$, a velocity $V_{\rm obs}$, and a mean surface brightness $\langle I \rangle_{\rm obs}$. One particular choice of observables is $R_{\rm obs} = r_{\rm e}$, $V_{\rm obs} = \sigma$, and $\langle I \rangle_{\rm obs} = <I>_{\rm e}$. Other choices could be used, for example $R_{\rm obs}$ could be taken as the core radius in a King model fit. The following considerations are inspired by Djorgovski, de Carvalho, & Han (1988).

For a bound system, such as a galaxy, the sum of the kinetic and potential energy must be less than zero. This can be written as

$$-E_{\rm pot} = k_{\rm E} E_{\rm kin}, \quad k_{\rm E} > 1 \ . \tag{2.10}$$

For a virialized system $k_{\rm E}$ has the value 2. We define $\langle R \rangle$ and $\langle V^2 \rangle$ as the mean radius and mean square velocity that enters the expressions for the potential and kinetic energy, respectively, i.e.

$$\frac{GM}{\langle R \rangle} M = -E_{\rm pot} \quad \text{and} \quad \frac{\langle V^2 \rangle}{2} M = E_{\rm kin} \ . \tag{2.11}$$

We can now write the energy equation (2.10) as

$$\frac{GM}{\langle R \rangle} = k_{\rm E} \frac{\langle V^2 \rangle}{2} \ . \tag{2.12}$$

We relate the observable quantities $R_{\rm obs}$, $V_{\rm obs}$, and $\langle I \rangle_{\rm obs}$ to the physical quantities $\langle R \rangle$, $\langle V \rangle$, and luminosity L through

$$R_{\rm obs} = k_{\rm R} \langle R \rangle \tag{2.13}$$

$$V_{\rm obs}^2 = k_{\rm V} \langle V^2 \rangle \tag{2.14}$$

$$L = k_{\rm L} \langle I \rangle_{\rm obs} R_{\rm obs}^2 \tag{2.15}$$

The parameters $k_{\rm R}$, $k_{\rm V}$, and $k_{\rm L}$ reflect the density structure, kinematical structure, and luminosity structure of the given galaxy. Obviously, they depend on the choice of observables (e.g. whether the $r^{1/4}$ half-light radius $r_{\rm e}$ or the King core radius $r_{\rm c}$ is used for $R_{\rm obs}$). From the energy equation (2.12) we can find the mass M as

$$M = \frac{k_{\rm E}}{2 G k_{\rm V} k_{\rm R}} V_{\rm obs}^2 R_{\rm obs} \ . \tag{2.16}$$

We can now find a relation for $R_{\rm obs}$, and compare it with the the FP

$$\begin{aligned} &\text{Theory} &: \quad R_{\rm obs} = k_{\rm S} k_{\rm E} (M/L)^{-1} \ V_{\rm obs}^2 \ \langle I \rangle_{\rm obs}^{-1} \\ &\text{Observations (FP)} &: \quad R_{\rm obs} = \quad \text{const} \quad V_{\rm obs}^{\alpha} \ \langle I \rangle_{\rm obs}^{\beta} \end{aligned} \tag{2.17}$$

where we have collected the three structural parameters in $k_{\rm S}$ as

$$k_{\rm S} = \frac{1}{2Gk_{\rm R}k_{\rm L}k_{\rm V}} \ . \tag{2.18}$$

Since the observations give $\alpha \approx 1.3$ and $\beta \approx -0.8$, it follows from Eq. (2.17) that $k_{\rm S}k_{\rm E}(M/L)^{-1}$ can *not* be constant, but has to be the following power law function of $V_{\rm obs}$ and $\langle I\rangle_{\rm obs}$

$$k_{\rm S}k_{\rm E}(M/L)^{-1} \propto V_{\rm obs}^{\alpha-2}\langle I\rangle_{\rm obs}^{\beta+1} \ . \tag{2.19}$$

In other words, either the structure $k_{\rm S}$ (and $k_{\rm E}$) or the mass-to-light ratio (M/L) (or both) need to vary in a systematic way to produce the observed FP slope. To explore the possibility of an (M/L) variation further, we first find an expression for $V_{\rm obs}$ as function of L from the first line of Eq. (2.17) and Eq. (2.15)

$$V_{\rm obs} = k_{\rm SR}^{-1/2}k_{\rm L}^{-1/4}L^{1/4}\,(M/L)^{1/2}\,\langle I\rangle_{\rm obs}^{1/4} \ , \tag{2.20}$$

where we have defined $k_{\rm SR} = k_{\rm S}k_{\rm E}$. We can now eliminate $V_{\rm obs}$ from Eq. (2.19) and instead get an expression involving L

$$(M/L) \propto k_{\rm SRL}L^{1/\alpha-1/2}\langle I\rangle_{\rm obs}^{-1/2-2\beta/\alpha-1/\alpha}, \quad k_{\rm SRL} \equiv k_{\rm SR}k_{\rm L}^{1/2-\alpha} \ . \tag{2.21}$$

For $\langle I\rangle_{\rm obs} = <I>_{\rm e}$, the exponent for $<I>_{\rm e}$ in the above equation turns out to be non-significantly different from zero. This is the case for the JFK96 values of α and β, where the $<I>_{\rm e}$ exponent is 0.02 ± 0.04, and this is also the case for the FPs studied by e.g. Faber et al. (1987). Also Prugniel & Simien (1996) found the $<I>_{\rm e}$ exponent to be non-significant. Therefore it can be stated, that the scalar virial theorem ($k_{\rm E} = 2$) and structural homology ($k_{\rm S}$ = constant) implies that the mass-to-light ratio varies with luminosity, or equivalently with mass, as

$$(M/L) \propto L^{\xi}\,, \quad \xi = 1/\alpha - 1/2\,; \qquad (M/L) \propto M^{b}\,, \quad b = \frac{\xi}{\xi+1} = \frac{2-\alpha}{2+\alpha} \ . \tag{2.22}$$

For the value of α that we find in this study (in Gunn r), $\alpha = 1.35 \pm 0.07$, the result is

$$(M/L_{\rm r}) \propto L^{0.24\pm0.04}\,; \qquad (M/L_{\rm r}) \propto M^{0.19\pm0.04} \ . \tag{2.23}$$

To actually calculate (M/L) from the data (under the above assumptions), we need to know the value of $k_{\rm R}$, $k_{\rm V}$, $k_{\rm L}$. For our choice of observables, $k_{\rm L}$ is simply 2π, i.e.

$$L = 2\pi<I>_{\rm e}{r_{\rm e}}^2 \cdot 10^6\,{\rm pc}^2/{\rm kpc}^2 \ , \tag{2.24}$$

where the identity $1 \equiv 10^6\,{\rm pc}^2/{\rm kpc}^2$ is inserted to denote that we in this study have $<I>_{\rm e}$ in units of $L_\odot/{\rm pc}^2$ and $r_{\rm e}$ in units of kpc.

Modeling is needed to calculate the constant in the equation for M, Eq. (2.16). We will here write this equation as $M = c_2\sigma^2 r_{\rm e}$. Note, that this *dynamical* determination of M gives the total mass $M_{\rm total}$, which includes luminous matter (stars) and dark matter. Bender, Burstein, & Faber (1992) calculated c_2 using models with King profiles and isotropic velocity dispersions. Assuming $M_{\rm total} = 10M_{\rm luminous}$ they found

$$M_{\rm luminous} = 5.0\,\sigma^2 r_{\rm e}/G, \quad G = 4.30 \cdot 10^{-6}\,({\rm km/s})^{-2}\,{\rm kpc}\,M_\odot^{-1} \ . \tag{2.25}$$

This is for $r_{\rm t}/r_{\rm c} = 100$, with $r_{\rm t}$ and $r_{\rm c}$ being the tidal and core radii in the King model, respectively. For $r_{\rm t}/r_{\rm c} = 300$, c_2 would be $4.0/G$, since c_2 turns out not to be quite constant in their models.

The ratio r_t/r_c is about 100–300 for giant ellipticals (Bender et al. 1992). Equation (2.25) and (2.24) combine into

$$\log(M_{\rm luminous}/L) = 2\log\sigma - \log <I>_e - \log r_e - 0.733 \ . \tag{2.26}$$

If we want to compare $\log(M_{\rm luminous}/L)$ for several passbands with for example prediction from stellar population synthesis models, the above equation cannot be used for all the passbands. This is because r_e varies with wavelength, which is also to say that E and S0 galaxies have radial color gradients. The Bender et al. model does not take this into account. Instead, r_e in a common passband "X" should be used to calculate the mass, and r_e in the given passband "Y" to calculate the luminosity, i.e.

$$\log(M_{\rm luminous}/L) = 2\log\sigma - \log <I>_e + \log r_{e,X} - 2\log r_{e,Y} - 0.733 \ . \tag{2.27}$$

Both equations are independent of the Hubble constant H_0, but since both M and L depend on r_e in kpc, which depends on the distance (cf. Eq. 2.6), which depends on H_0 if the distance is calculated from the redshift, $\log(M/L)$ becomes proportional to $\log H_0$.

2.2.4 Variation of (M/L) with L (or M)

A physical interpretation of the FP should not only be able to account for the observed slope, but also for the small scatter of the FP, a scatter which is more or less constant along the FP (JFK96 found a scatter in $\log r_e$ of 0.125 and 0.073 for galaxies with $\log\sigma$ below and above 2.0, respectively, and expected larger measurement errors for galaxies with $\log\sigma < 2.0$ to explain some of the difference). In this subsection we will consider the scenario of structural homology and a variation of (M/L) with L (or M). In the next subsection we will consider the opposite scenario.

First we will summarize evidence that there actually is a variation of (M/L) with L. van der Marel (1991) used a dynamical model to predict the kinematics of an elliptical galaxy on the basis of observed surface photometry. The predictions were compared with actual kinematical data along both the major and the minor axes of 37 bright E galaxies. From this, accurate mass-to-light ratios were derived that were corrected for the effects of rotation and radial anisotropy. Note, that these mass-to-light ratios were *not* based on the assumption of structural homology. van der Marel found, that the mass-to-light ratio correlated with luminosity as $(M/L_B) \propto L_B^{0.35\pm0.05}$.

Second we note, that part of the FP slope is due to a metallicity effect. Higher luminosity galaxies have higher metallicity than fainter galaxies, and because of the line-blanketing effect, brighter galaxies will emit more of their light at longer wavelengths than fainter galaxies. Therefore, the bolometric mass-to-light ratio could be constant with bolometric luminosity, while at the same time the blue mass-to-light ratio could increase with blue luminosity. Djorgovski & Santiago (1993) found the FP coefficient α to increase monotonically with the effective wavelength of the bandpass, from $\alpha \approx 0.95$ at U ($\lambda_{\rm eff} \approx 0.35\mu$m) to $\alpha \approx 1.5$ at K ($\lambda_{\rm eff} \approx 2.2\mu$m). β remained constant at $\beta \approx -0.8$. The increase in α with wavelength is indeed a sign of line blanketing, since it implies a decrease in ξ, the coefficient in $(M/L) \propto L^{\xi}$. However, at 2.2μm line blanketing should be negligible, and still Djorgovski & Santiago find $(M/L_K) \propto L_K^{0.17}$. Recillas-Cruz et al. (1990) found the same trend, namely $\alpha = 1.36 \pm 0.11$ at B, $\alpha = 1.48 \pm 0.13$ at V, and $\alpha = 1.69 \pm 0.11$ at K. At K this implies $(M/L_K) \propto L_K^{0.09\pm0.04}$. Dressler et al. (1987b) found that the metallicity effect only explains a minor part of the FP slope. They found $(M/L_B) \propto L_B^{0.25}$, and after applying bolometric correction, the dependence on L was only reduced to $(M/L_{\rm bol}) \propto L_{\rm bol}^{0.18}$.

Renzini & Ciotti (1993) explored whether a systematic variation in either the IMF slope below $0.3M_\odot$ or the minimum stellar mass could produce the FP slope. They found that a major change

of either of these parameters along the FP was required to reproduce the tilt. At the same time, an extremely small dispersion was required to reproduce the small constant thickness of the FP. In other words, *fine tuning* was needed, making this explanation unattractive.

Another possible explanation could be that the dark matter fraction $R \equiv M_{\rm dark}/M_{\rm luminous}$ increased with luminosity, while $(M_{\rm luminous}/L)$ remained constant. This was explored by Renzini & Ciotti (1993) and Ciotti, Lanzoni, & Renzini (1996), and also here it was found that a fine tuning was needed.

Part of the FP slope could also be due to a systematic variation of mean age along the FP (Faber et al. 1995), with the stellar populations of high luminosity galaxies having higher mean ages than for low luminosity galaxies.

2.2.5 Deviations from Homology

Observational evidence of systematic deviations from homology includes the following. Burkert (1993) found that E galaxies in general were well fitted by the $r^{1/4}$ profile, but that they nevertheless showed a small change of slope at some point $x_{\rm cut}$ in the profile (with $x_{\rm cut} \approx 0.8$–$0.9 r_{\rm e}$). This change of slope was quantified by the parameter δb. It was found, that δb was correlated with luminosity. Caon et al. (1993) fitted $r^{1/n}$ profiles and found n to correlate with $r_{\rm e}$ or L. The values of n spanned a large range, from $n = 0.5$ at $r_{\rm e} = 0.3$ kpc to $n = 16$ at $r_{\rm e} = 25$ kpc. Note, that none of these two studies explicitly take into account whether the galaxy has a disk. This is important since many E and S0 galaxies have disks (e.g. JF94).

Hjorth & Madsen (1995) used a model based on statistical mechanics of violent relaxation to give a possible explanation of the result from Burkert (1993). The one free parameter in their model is the dimensionless central potential ψ. They found δb to vary with ψ. They also found that the FP tilt could be explained by a variation of ψ with L, while keeping (M/L) constant, and that the result from Burkert (i.e. that δb varied with L) supported this. They did not address the question whether a fine tuning of the ψ–L relation was needed to reproduce the small and constant thickness of the FP. Note, that their model does not include any disk component.

The effect of a trend in the shape of the surface brightness profile was also studied by Ciotti et al. (1996). It was found that the FP slope could be explained in this way, but that a fine tuning was needed.

Renzini & Ciotti (1993) and Ciotti et al. (1996) also explored the effect of a trend in the relative distribution within the galaxy of luminous and dark matter. They parametrized this by the parameter $\beta' \equiv r_{\rm dark}/r_{\rm luminous}$, with r being the half mass radius of the given component. They found, that a decrease in β' could produce the FP tilt, but that still fine tuning was needed. Note, that a variation in β' implies a variation in $k_{\rm R}$ (Eq. 2.13), and thereby non-homology.

Djorgovski (1995) found that an FP also existed for globular clusters. When using the core parameters, the FP coefficients $\alpha = 2.2 \pm 0.15$ and $\beta = -1.1 \pm 0.1$ were found, indicating structural homology and a constant (M/L) ratio. When using half-light parameters, the FP coefficients $\alpha = 1.45 \pm 0.2$ and $\beta = -0.85 \pm 0.1$ were found, similar to what is found for elliptical galaxies. Also Nieto et al. (1990) and Burstein et al. (1997) found globular clusters to have similar FP coefficients to those of giant elliptical galaxies when using half-light parameters. Djorgovski argued, that for globular clusters this almost certainly implies non-homology, and that this suggests that a similar explanation may be at work for the elliptical galaxies. The argumentation for the latter statement seems somewhat dubious. Along those lines, Djorgovski later warns against assuming that the similar half-light FPs for globular clusters and elliptical galaxies reflect entirely the same physics.

Finally we mention, that Prugniel & Simien (1996) found that about half of the FP tilt was due to a trend in the global stellar population (age and/or metallicity), and that the other half

could be accounted for by partly a trend in the amount of rotational support and partly a trend in spatial structure (as seen by Caon et al. 1993).

2.2.6 The FP as a Distance Indicator

If the FP is universal (or the deviations from universality are known to be within certain limits), it can be used to determine distances.

If the FP is established for a given cluster of galaxies and in addition the distance to the cluster is known from some other method, the intrinsic FP zero point Γ can be calculated, cf. Eq. (2.9). A recent example of this is Hjorth & Tanvir (1997), who calibrated the intrinsic FP zero point using the observed FP zero point for 5 E and S0 galaxies in the Leo-I group and the HST cepheid distance to the Leo-I galaxy M96.

Without knowing the intrinsic FP zero point Γ, the FP can be used to determine *relative* distances. For example, if we have two clusters HydraI and Coma, it follows from Eq. (2.9) that their relative distance is related to their observed FP zero point difference as

$$\frac{d_{\rm A,Coma}}{d_{\rm A,HydraI}} = 10^{\Delta\gamma}, \quad \Delta\gamma \equiv \gamma_{\rm HydraI} - \gamma_{\rm Coma} \ . \tag{2.28}$$

In order to compare different zero points $\gamma_{\rm cl}$, i.e. to calculate a meaningful $\Delta\gamma$, the same values of α and β should be used, since $\gamma_{\rm cl}$ is very sensitive to the choice of α and β. This follows from the fact that $\gamma_{\rm cl}$ is the intersection of the fundamental plane with the $\log r_{\rm e}$ axis (cf. Eq. 2.7), and that the galaxies are not symmetrically distributed around this axis, but rather displaced somewhat to the side. The zero point *differences* $\Delta\gamma_{\rm cl}$, on the other hand, are quite stable for somewhat different values of α and β, so the only requirement is to use common values of α and β when comparing $\gamma_{\rm cl}$ for different clusters. However, for some values of α and β, the residuals from the FP are correlated with absolute magnitude, which will cause systematic errors on the derived distances if the different clusters have different limiting absolute magnitudes (cf. JFK96 and Sect. 7.6).

The subscript "A" on the distances d in Eq. (2.28) indicates that they are so-called angular diameter distances, cf. Weinberg (1972). $d_{\rm A}$ is defined as $d_{\rm A} \equiv D/\delta$, where D is the linear diameter and δ is the angular diameter of the object. Another distance is the luminosity distance $d_{\rm L}$, which is defined as $d_{\rm L} \equiv [L/(4\pi l)]^{1/2}$, where L is the (intrinsic) luminosity and l is the apparent luminosity of the object. In Euclidian geometry the two distances agree with each other and with the true distance. In an expanding universe (here given by the Robertson-Walker metric), this is not the case. Rather, $d_{\rm A}$ and $d_{\rm L}$ are related through the redshift z as

$$d_{\rm A} = d_{\rm L}(1+z)^{-2} \tag{2.29}$$

(Weinberg 1972). The luminosity distance is needed to calculate the distance modulus,

$$(m-M) = 5\log(d_{\rm L}/10\,{\rm pc}) \ . \tag{2.30}$$

In the absence of peculiar motions (i.e. deviations from the pure Hubble expansion), $d_{\rm L}$ can be calculated from the redshift z as

$$d_{\rm L} \approx \frac{c}{H_0}\left[z + 0.5(1-q_0)z^2\right] \tag{2.31}$$

(Weinberg 1972), neglecting terms of higher than second order in z. The approximation is very good at the redshift of Coma, with a relative error of less than 0.01%.

Later (in Sect. 7.1) we will determine the distance to Coma and HydraI in the following way. The distance to Coma will be derived from the redshift, assuming Coma to be at rest in the

CMB frame. The distance modulus can then be found from Eq. (2.31) and (2.30). The distance to HydraI relative to Coma will be calculated from the observed FP zero point difference. By combining Eq. (2.28), (2.29), and (2.31), we get the following equation for z_{HydraI}

$$\frac{\left[z_{\mathrm{Coma}} + 0.5(1-q_0)z_{\mathrm{Coma}}^2\right](1+z_{\mathrm{Coma}})^{-2}}{\left[z_{\mathrm{HydraI}} + 0.5(1-q_0)z_{\mathrm{HydraI}}^2\right](1+z_{\mathrm{HydraI}})^{-2}} = 10^{\Delta\gamma} \quad , \tag{2.32}$$

where z_{HydraI} is the CMB redshift for HydraI if HydraI has zero peculiar velocity. Equation (2.32) can be solved numerically. The distance modulus can then be found from Eq. (2.31) and (2.30). In the same framework, the conversion of r_{e} from arcsec to kpc becomes

$$\begin{aligned} \log r_{\mathrm{e,kpc}} &= \log r_{\mathrm{e,arcsec}} - \log(206265\,\mathrm{arcsec/rad}) + \log(10^3\,\mathrm{kpc/Mpc}) \\ &+ \log\left(\frac{c}{H_0}\left[z_{\mathrm{Coma}} + 0.5(1-q_0)z_{\mathrm{Coma}}^2\right](1+z_{\mathrm{Coma}})^{-2}\right) - \begin{cases} 0 & \text{for Coma} \\ \Delta\gamma & \text{for HydraI} \end{cases} \end{aligned} \tag{2.33}$$

using Eq. (2.6), (2.29), and (2.31), and for HydraI in addition Eq. (2.28). The identity $1 \equiv 10^3\,\mathrm{kpc/Mpc}$ enables us to insert H_0 in units of $\mathrm{km\,s^{-1}\,Mpc^{-1}}$ and get r_{e} in units of kpc. c needs to be in units of $\mathrm{km\,s^{-1}}$.

2.3 Stellar Population Synthesis Models

Stellar population synthesis models are tools for interpreting the integrated light (colors, line indices, and mass-to-light ratios) that we observe from the galaxies. Ideally, we want to determine what mix of stars give rise to the observations. This problem is underconstrained, however, so it is needed to make some assumptions about how the number of different types of stars are related. Here we will consider so-called single-age single-metallicity models. In these, all the stars are formed at the same time, with distribution in mass given by the chosen initial mass function (IMF), and with identical chemical composition. More advanced models take evolutionary processes into account, e.g. enrichment of the interstellar medium, differential loss of various element by galactic winds, time-dependent IMF, to mention a few. However, these processes are not well understood, and no consensus has yet been reached on these matters.

Model predictions from single-age single-metallicity models are obtained as follows. First it is needed to have theoretical stellar isochrones, i.e. loci in the theoretical HR-diagram $(\log T_{\rm eff}, \log L)$ for a stellar population of a given age and chemical composition. Depending on the model, the chemical composition can be specified either as just (X, Y, Z) (mass fraction of hydrogen, helium, and metals) with the *abundance ratios* of the metals being solar, or the abundances of individual metals can be taken explicitly into account. Besides the input parameters of age and chemical composition, to calculate an isochrone it is also necessary to have all the physics of stellar evolution specified, which includes opacities and how to treat convection.

Second it is needed to transform the theoretical quantities $\log T_{\rm eff}$, $\log L$, and $\log g$ (with g being the stellar surface gravity) to the observable quantities, i.e. colors, line indices, and mass-to-light ratios. This can be done on either empirical or theoretical grounds, as will be exemplified below by the Vazdekis et al. (1996) models and the Tripicco & Bell (1995) models.

Third, by integrating along the isochrone weighting by the IMF and the flux, the final values are obtained.

At this point it is warranted to define what we mean by the IMF. Following Scalo (1986), we define the (initial) *mass spectrum* $f(M)$ as the fraction or number of stars born per unit mass interval $\mathrm{d}M$, and the (initial) *mass function* $F(M)$ as the fraction or number of stars born per unit logarithmic (base ten) mass interval $\mathrm{d}\log M$. f and F are related through $F(M) = (\ln 10) M f(M)$. The logarithmic slopes of f and F evaluated at M are denoted γ and Γ, respectively. They are related through $\gamma = \Gamma - 1$. For power laws, γ and Γ are independent of M. As an example, Salpeter (1955) found the IMF for stars in the solar neighborhood to be reasonably well approximated by the power law $F(M) \propto M^{-1.35}$, which has slope $\Gamma = -1.35$. Vazdekis et al. (1996) say that the Salpeter IMF slope is $\mu = 1.35$. Worthey (1994) says that it is $x = 2.35$, but the expression he refers to is the mass spectrum in the above language. We will adopt the nomenclature of Vazdekis et al.

In the following, we consider some specific models.

2.3.1 Vazdekis et al. (1996)

The isochrones of the Padova group (Bertelli et al. 1994) is used. The conversion to observable quantities is based on empirical studies. For the line indices the conversion is done by the fitting functions of Worthey et al. (1994), a study based on field and cluster stars. Several IMFs are offered. The *unimodal* IMF is a plain power law with slope μ (with $\mu = -\Gamma$ in the above notation). The *bimodal* IMF is a constant below 0.2 $M_\odot$, a power law with slope μ above 0.6 $M_\odot$, and a spline in the interval 0.2–0.6 $M_\odot$. The metal abundance ratios are solar, e.g. [Mg/Fe] = 0. Predictions are given for 3 values of the total metallicity Z in the range 0.008–0.05, and 15 values of the age in the

range 1–17 Gyr. We prefer to use the total metal abundance relative to solar $[\mathrm{M/H}] \equiv \log(Z/Z_\odot)$ (with $Z_\odot = 0.02$) instead of Z, since the observable quantities vary almost linearly in [M/H]. For the same reason, we usually use log age instead of age.

Vazdekis et al. show that the bimodal IMF with high mass slope $\mu = 1.35$ gives a reasonable fit to data from Scalo (1986). This is the model we will be using as our basic model. Predictions from this model for the four observables Mg_2, $\log < \mathrm{Fe} >$, $\log(M/L_\mathrm{r})$, and $(B-r)$ are shown on Fig. 2.1. The general trend is, that all these four quantities increase with both age and metallicity.

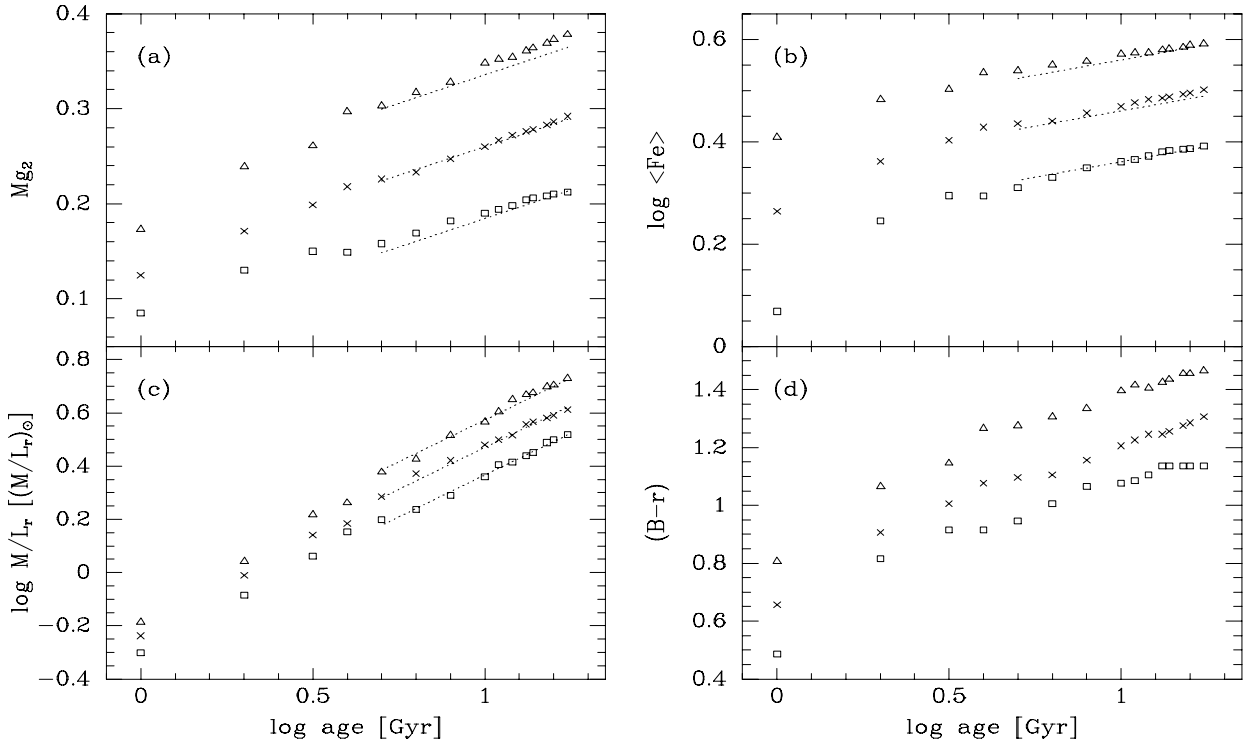

Figure 2.1: Predictions from the Vazdekis et al. (1996) model. This model has a bimodal IMF with high mass slope $\mu = 1.35$. Boxes, crosses, and triangles denote [M/H] = −0.4, 0.0, and 0.4, respectively, corresponding to $Z = 0.008$, 0.02, and 0.05. The ages are approximately 1, 2, 3, 4, 5, 6, 8, 10, 11, 12, 13, 14, 15, 16, and 17 Gyr. The overplotted relations are Eq. (2.34)–(2.36).

J97 found that the predictions from this model could be well approximated by the following analytical expressions for ages of 5 Gyr or larger

$$\mathrm{Mg}_2 \approx 0.12 \log \mathrm{age} + 0.19\,[\mathrm{M/H}] + 0.14 \tag{2.34}$$

$$\log < \mathrm{Fe} > \approx 0.12 \log \mathrm{age} + 0.25\,[\mathrm{M/H}] + 0.34 \tag{2.35}$$

$$\log(M/L_\mathrm{r}) \approx 0.63 \log \mathrm{age} + 0.26\,[\mathrm{M/H}] - 0.16 \tag{2.36}$$

These relations are overplotted in Fig. 2.1.

Vazdekis et al. give colors involving Kron-Cousins R. These were transformed to Gunn r using the constant offset $(r-R) = 0\overset{\mathrm{m}}{.}354$ from Jørgensen (1994). Vazdekis et al. only list the mass-to-light ratio in Johnson V, but the mass-to-light ratio in e.g. Gunn r is readily calculated as

$$\frac{(M/L_\mathrm{r})}{(M/L_\mathrm{r})_\odot} = \frac{(M/L_\mathrm{V})}{(M/L_\mathrm{V})_\odot} \cdot 10^{-0.4\left[(V-r)-(M_{\mathrm{V},\odot}-M_{\mathrm{r},\odot})\right]} \quad . \tag{2.37}$$

We used the following solar absolute magnitudes: $M_{V,\odot} = 4\overset{m}{.}84$, $M_{R,\odot} = 4\overset{m}{.}48$ (i.e. $M_{r,\odot} = 4\overset{m}{.}834$), $M_{B,\odot} = 5\overset{m}{.}41$, and $M_{U,\odot} = 5\overset{m}{.}60$. All are from Worthey (1994), except $M_{B,\odot}$, which is from Gonzáles (1993).

2.3.2 Weiss, Peletier, & Matteucci (1995)

Weiss et al. (1995) present models based on isochrones with non-solar abundance ratios. Specifically, these authors enhance the α-elements (O, Mg, Si, etc.) relative to Fe, and compute models with [Mg/Fe] = 0, 0.45, and 0.62, and total metallicities Z in the range 0.02–0.07.

The conversion to observable quantities is empirical and based on the galactic bulge stars from Rich (1988). For these stars, the line indices Mg_2 and $< Fe >$ are fitted as function of $(V - K)$ (the temperature indicator) and [M/H] $\equiv \log(Z/Z_\odot)$. In order to study the effect of non-solar abundance ratios, they simply replace [M/H] in the Mg_2 equation by [Mg/H], and [M/H] in the $< Fe >$ equation by [Fe/H]. In other words they assume, that Mg_2 only depends on the magnesium abundance, and that $< Fe >$ only depends on the iron abundance. They present evidence that the stars of Rich (1988) have [Mg/Fe] ≈ 0, which is a necessary condition for doing the above. We note, that the metallicity and the abundance ratios for the stars in the galactic bulge is not a settled issue. For example, Idiart, de Freitas Pacheco, & Costa (1996) found a mean abundance ratio [Mg/Fe] = 0.45.

The Salpeter (1955) IMF is used. Only ages of 12, 15 and 18 Gyr are given.

One of the results from Weiss et al. is, that the effect *on the isochrone* of changing [Mg/Fe] while keeping the total metallicity [M/H] constant is small compared with changing [M/H] by the same amount and keeping [Mg/Fe] constant. However, the changes in the former case are not totally negligible. This is shown by model 7 and 7H of Weiss et al. Model 7 has $Z = 0.04$ and [Mg/Fe] = 0.45, and is calculated in the way described above. Model 7H is a hybrid model, calculated as follows. First an isochrone is calculated for $Z = 0.04$ and [Mg/Fe] = 0. The resulting values of L and $T_{\rm eff}$ are used to calculate Mg_2 and $< Fe >$, but instead of inserting [Mg/Fe] = 0 in the equations for Mg_2 and $< Fe >$, the value [Mg/Fe] = 0.45 is used. The offsets ("7"−"7H") are $\Delta(Mg_2, \log < Fe >) = (-0.020, -0.005)$, $(-0.032, -0.004)$, and $(-0.017, -0.002)$ for ages of 12, 15, and 18 Gyr, respectively. We make the following two points: (1) That these offsets are small is another way of saying that the effect on the isochrones of abundance changes is small. This implies that the effect on (M/L) is small (Weiss et al. do not list the changes in L, only in Mg_2 and $< Fe >$). We use this fact in our analysis (Sect. 7.5) to derive [Mg/H] (and ages) from the Mg_2–$\log(M/L)$ diagram, and [Fe/H] (and ages) from the $\log < Fe >$–$\log(M/L)$ diagram, both using the Vazdekis et al. (1996) models which have [Mg/Fe] = 0. To strictly do this, it is necessary that (M/L) is not affected by non-solar abundance ratios. In addition, it is necessary that Mg_2 depends only on the magnesium abundance, and that $< Fe >$ depends only on the iron abundance. This is supported in part by the work of Tripicco & Bell (1995), cf. below. (2) Since these offsets are nevertheless both non-zero and varying with age and probably also with Z and the change in [Mg/Fe] (the latter two possibilities were not tested by Weiss et al.), the above-mentioned assumptions that we make in our analysis are only valid as a first approximation.

The effect of changing [Mg/Fe] while keeping [M/H] constant on Mg_2 and $< Fe >$ is large. This is not a surprise, especially since Weiss et al. assume that Mg_2 depends only on the magnesium abundance, and that $< Fe >$ depends only on the iron abundance. For $Z = 0.02$, the differences between [Mg/Fe] = 0.45 (model 5) and [Mg/Fe] = 0 (model 1) are $\Delta(Mg_2, \log < Fe >)$ $= (+0.036, -0.033)$, $(+0.047, -0.047)$, and $(+0.041, -0.063)$ for ages of 12, 15, and 18 Gyr, respectively, with the differences calculated as "5"−"1".

We want to compare the large grid of models from Vazdekis et al., which have [Mg/Fe] = 0,

with the somewhat smaller grid of models from Weiss et al. with [Mg/Fe] > 0 to illustrate the effect of [Mg/Fe] > 0. It turns out that the Weiss et al. models with [Mg/Fe] $= 0$ do not give quite the same values of Mg_2 and $\log <\mathrm{Fe}>$ as those from Vazdekis et al. If we define $\Delta \equiv$ (Vazdekis et al.) $-$ (Weiss et al.), we find $\Delta(\mathrm{Mg}_2) = -0.003$ and $\Delta(\log <\mathrm{Fe}>) = -0.050$ for $Z = 0.02$ and age $= 15$ Gyr, and $\Delta(\mathrm{Mg}_2) = -0.052$ and $\Delta(\log <\mathrm{Fe}>) = -0.065$ for $Z = 0.05$ and age $= 15$ Gyr. Weiss et al. do not have $Z = 0.05$, so we have calculated the above values by a linear interpolation between their $Z = 0.04$ and $Z = 0.07$ values. For the Vazdekis et al. models we used the bimodal $\mu = 1.35$ IMF. However, using the Salpeter IMF instead has very little impact on the offsets. Thus, they must be caused by a difference in the theoretical isochrones and/or the conversion to the observable quantities. We add the found offsets to the Weiss et al. predictions (also for their [Mg/Fe] > 0 models) when we compare with Vazdekis et al. We use the same offset for all the three ages given by Weiss et al. This was done in the same way by J97.

2.3.3 Tripicco & Bell (1995)

Tripicco & Bell (1995) present *theoretically calculated* line indices for *single stars* (not entire populations). The line indices are measured from synthetic spectra based on model atmospheres. This is done for $(T_{\rm eff}, \log g)$ points along a 5 Gyr solar abundance isochrone. The microturbulence is calculated from the luminosity.

The dependence of each index on the abundances of individual elements is determined in the following way. The abundance of a single metal (C, N, O, Mg, Fe, Ca, Na, Si, Cr, and Ti) is increased from 0.0 to 0.3 dex, while keeping the other metals at 0.0 dex. Then the line indices are calculated as described above, still for points along the said *solar abundance* isochrone. As found by Weiss et al. (1995), the error made by using a solar abundance isochrone instead of an isochrone calculated for the appropriate non-solar abundance ratios is probably small. Tripicco & Bell also try increasing *all* the metals from 0.0 to 0.3 dex.

Table 2.1 lists their results for the indices Mg_2 and $\log <\mathrm{Fe}>$ for increasing the abundances of C, Mg, and Fe, and the total metallicity. The elements not listed (N, O, Ca, Na, Si, Cr, and Ti) have smaller effects than the above. Note that the table show the result for two *individual* stars, and not for an entire single-age single-metallicity population. The two types of stars shown, a turnoff star and a cool giant, are expected to be the dominant sources of light in a typical E and S0 galaxy.

It is seen, that Mg_2 depends mostly on the magnesium abundance, but that it is also sensitive to the carbon abundance as well as the total metallicity. $\log <\mathrm{Fe}>$ depends just as much on the total metallicity as on the iron abundance.

Also shown in the table is $\widehat{\mathrm{Mg}_2}$, which is calculated from Mgb as $\widehat{\mathrm{Mg}_2} = 0.638 \log \mathrm{Mgb} - 0.133$. The relation $\widehat{\mathrm{Mg}_2} = \mathrm{Mg}_2$ was established by J97, based on 161 E and S0 galaxies. We use $\widehat{\mathrm{Mg}_2}$ as a substitute for Mg_2 for the spectra where Mgb but not Mg_2 could be measured, cf. Sect. 6.4. It is seen, that for these models the two values do not quite agree, and the the dependence on abundance changes is not always the same. However, since J97 found the above relation to have no significant intrinsic scatter, either (a) the differences cancel out when an entire population is considered; (b) they become smaller for the abundance ratios and metallicities actually found in E and S0 galaxies; or (c) the model is somewhat off. It is worth noting that the Mg_2 values of J97 are in the range 0.13–0.34, so the turnoff star with $\mathrm{Mg}_2 = 0.07$ and the cool giant with $\mathrm{Mg}_2 = 0.36$ are both outside this range. On the other hand, the $\widehat{\mathrm{Mg}_2}$ values are in *both* cases lower by the same large amount. This indicates, that even for a composite stellar population, the model $\widehat{\mathrm{Mg}_2}$ values will be lower than the model Mg_2 values. This is actually the case for e.g. the Vazdekis et al. (1996) models, although the discrepancy is smaller. For the bimodal $\mu = 1.35$ IMF model, $(\mathrm{Mg}_2 - \widehat{\mathrm{Mg}_2})$

is in the range 0.00–0.09, and typically 0.02.

Table 2.1: Spectral Line Index Response to Abundance Changes

Turnoff star ($T_{\rm eff} = 6200\,{\rm K}, \log g = 4.1$)

Index	Value	C	Mg	Fe	[M/H]
$\rm Mg_2$	0.07	0.01	0.02	−0.00	0.01
$\widehat{\rm Mg_2}$	−0.07	−0.03	0.10	−0.02	0.02
$\log <$ Fe $>$	0.05	0.01	−0.02	0.08	0.09

Cool giant ($T_{\rm eff} = 4255\,{\rm K}, \log g = 1.9$)

Index	Value	C	Mg	Fe	[M/H]
$\rm Mg_2$	0.36	0.04	0.08	−0.02	0.05
$\widehat{\rm Mg_2}$	0.23	−0.07	0.09	−0.02	0.02
$\log <$ Fe $>$	0.60	0.01	−0.02	0.06	0.05

Notes: $\widehat{\rm Mg_2} = 0.638 \log {\rm Mgb} - 0.133$ (J97). $<$ Fe $> =$ (Fe5270 + Fe5335)/2. The column 'Value' lists the value of the given index for a model with solar abundances. The columns 'C', 'Mg', 'Fe', and '[M/H]' list the absolute amount the given index changes when the abundance of C, Mg, Fe, and all metals are increased from 0.0 to 0.3 dex, respectively. From Tripicco & Bell (1995).

Chapter 3

Photometric Data and Basic Reductions

3.1 Instrumental Setup for the DFOSC April 1994 Observing Run

Table 3.1 below describes the instrumental setup for the April 1994 observing run with the Danish 1.5 meter telescope, La Silla, equipped with the DFOSC instrument. The data from this observing run will be referred to as *the DFOSC data*, or just *DFOSC*. The entire HydraI photometry sample used in this work is based on the DFOSC data, cf. the remaining sections of this chapter and Chapter 4–5. Part of the HydraI spectroscopy sample used in this work is also based on the DFOSC data, cf. Chapter 6.

Note that the Coma sample also used in the analysis (Chapter 7) is not introduced until Sect. 7.1.

Table 3.1: Instrumental Setup for the DFOSC April 1994 Observing Run

General information

Dates	April 7-8 to April 21-22, 1994 (night 0–14)
Observer	Inger Jørgensen
Observatory	ESO, La Silla, Chile
Telescope	Danish 1.5 m
Instrument	DFOSC
CCD	ESO #17
CCD size	1024 pixels × 1024 pixels
Pixel size	0.5073 arcsec/pixel
Read-out-noise	4.39 e^-
Conversion factor	1.95 e^-/ADU
CCD temperature	129 K (night 0–5), 139.5 K (night 6–14)
Dark current	10.9 e^-/h (night 0–5), 33.7 e^-/h (night 6–14)

Information specific to the photometry

Field size	$8.7' \times 8.7'$
Passbands for the galaxy photometry[a]	Gunn r, Johnson B, and Johnson U
Number of HydraI fields observed	43[b] (see Fig. 3.1, p. 25)

Information specific to the spectroscopy

Wavelength range	4954.2–5612.5 Å
Slitwidth	2.5 arcsec
Instrumental dispersion (σ)[c]	1.36 Å, 79 km/s
Grism	#13 + order sorter filter
CCD Readout window	401 pixels (spatial) × 1024 pixels (λ)
Binning	1×1
Number of HydraI E and S0 galaxies observed	21[d]

Notes:
[a] In addition Johnson V was used for standard star observations.
[b] In Johnson U only 5 HydraI fields were observed.
[c] The instrumental dispersion is determined as sigma in a Gaussian fit to the 5577 Å sky emission line. The equivalent dispersion in km/s is determined at 5177 Å.
[d] In total 35 E and S0 galaxies were observed: 21 in HydraI, 9 in Abell 3574, and 5 in the field. All the galaxies were used in the comparison with the literature, cf. Sect. 6.4.

3.2 Photometric Observations and Sample Selection

3.2.1 Photometric Observations

43 fields of size $8.7' \times 8.7'$ were observed in the HydraI area, see Figure 3.1. The fields were selected with the intention to cover all E and S0 galaxies brighter than $V_{25} = 15\overset{\text{m}}{.}5$ within 1.5° from the cluster center. V_{25} is the Johnson V magnitude within the $25^{\text{m}}/\text{arcsec}^2$ isophote, as listed in the HydraI catalog of Richter (1989).

37 fields form a contiguous area centered on the cluster center. This area has maximum dimensions of approximately $46' \times 76'$, with an area of approximately 0.63 square degrees. The two holes are fields that could not be observed due to the presence of very bright stars. An additional 6 outlying fields were observed in order to meet the above goal.

All 43 fields were observed in Gunn r and Johnson B. The 5 very central fields (00, 13, 14, 15, & 18) were also observed in Johnson U. The typical exposure times were 300 seconds in Gunn r, 900 seconds in Johnson B, and 1800 seconds in Johnson U.

Note, that we will occasionally (e.g. where space is limited) abbreviate Gunn r, Johnson B, and Johnson U as GR, JB, and JU, respectively.

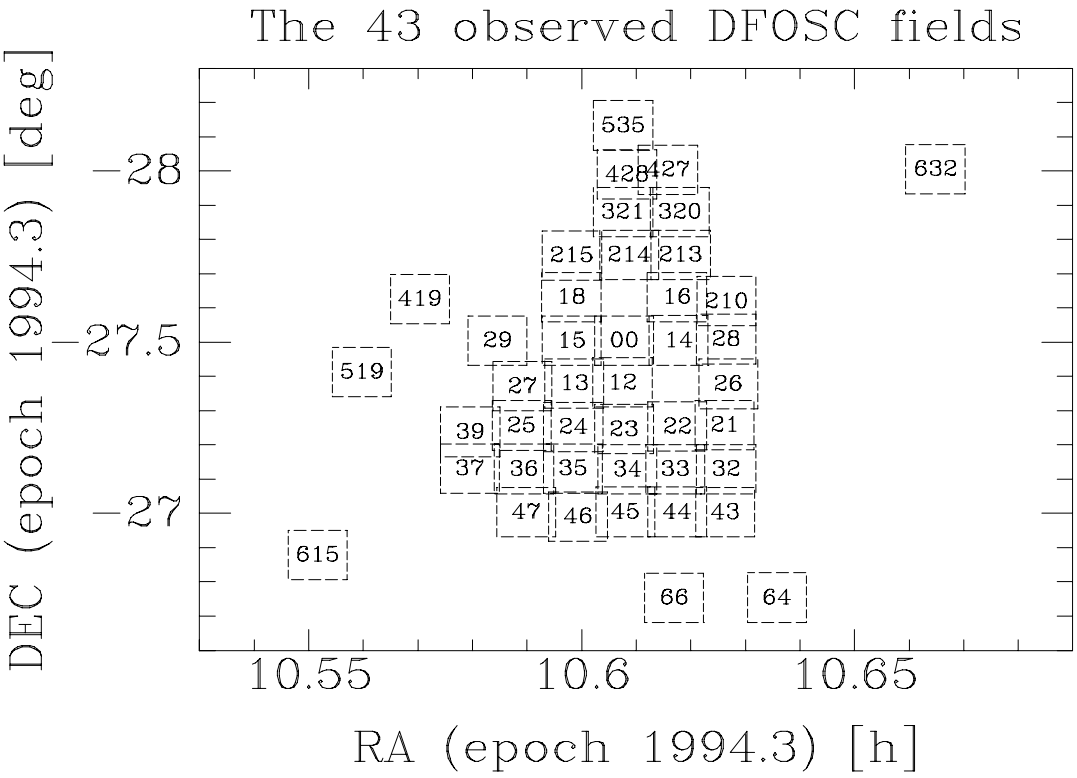

Figure 3.1: The 43 observed HydraI fields shown in a rectangular projection. North is down and east is to the right, which is the orientation that the CCD images have. The size of the individual fields is $8.7' \times 8.7'$. Field 00 is centered on $(\alpha, \delta)_{1950.0} = (10^{\text{h}}34^{\text{m}}21\overset{\text{s}}{.}6, -27^{\text{d}}16^{\text{m}}04^{\text{s}})$, the position of R269 (NGC3311), which is taken to be the cluster center.

3.2.2 Selection of the Photometric Sample

The HydraI photometric sample was selected from the catalog of Richter (1989). The catalog lists for each galaxy a number (throughout this thesis referred to with an 'R' prepended, e.g. R269), V_{25} (from Smyth 1980), a morphological type, and the heliocentric velocity ($cz_{\rm hel}$) where known. The catalog is supposedly complete to $V_{25} = 16\overset{\rm m}{.}65$ within a radius of 2° from the cluster center, i.e. covering all our observed fields.
The sample selection procedure was as follows:

1. All galaxies with $V_{25} \leq 16\overset{\rm m}{.}5$ in our 43 DFOSC fields were selected. This was 87 galaxies.

2. All galaxies with classifications of E, Ep, E/S0, S0p, S0/a, SB0, SB0p, and SB0/a were selected. The classifications listed by Richter (1989) were used. This left 70 galaxies.

3. All galaxies known to be cluster members from the spectroscopy or galaxies without spectroscopy were selected. Since HydraI is clearly isolated in redshift space, cf. Fig. 3.2 (p. 29), membership determination is straightforward. Redshifts were compiled as follows. Heliocentric velocities were compiled from 5 sources: Richter (1989), JFK95b, DFOSC, Lucey & Carter (1988), and Stein (1996)[1]. In addition, an error-weighted mean of JFK95b and DFOSC was formed. An "adopted" value was chosen as the value from JFK95b+DFOSC, Lucey & Carter, Stein, and Richter, in that order of preference. The data are listed in Table 3.2.

   Of the 70 galaxies, 62 had a measured redshift from one of the 5 sources. The redshift histogram is shown in Figure 3.2. HydraI is clearly isolated in redshift space. All galaxies with $cz_{\rm hel} > 7000$ km/s were taken to be in the background. That was 6 galaxies, leaving 64 galaxies in the sample, of which 56 are spectroscopically confirmed cluster members. These 64 galaxies are listed in Table 3.3.

The magnitude limit $V_{25} = 16\overset{\rm m}{.}5$ was chosen since for galaxies fainter than this reliable surface photometric profiles could not be derived. This limit corresponds *on the average* to $m_{\rm r_T} = 15\overset{\rm m}{.}75$, where $m_{\rm r_T}$ is fully corrected total Gunn r magnitude. This is based on the relation

$$m_{\rm r_T} = V_{25} - 0.75\,; \quad \text{rms} = 0.32 \ , \tag{3.1}$$

which is established for the 64 galaxies in the photometric sample. The above magnitude limit corresponds to $M_{\rm r_T} = -18\overset{\rm m}{.}85$ (for $H_0 = 50\,{\rm km\,s^{-1}\,Mpc^{-1}}$, cf. Sect. 7.1.1, p. 85).

[1]Stein (1996) only identifies the galaxies by his own sequential ID numbers and the position $(\alpha, \delta)_{1950.0}$. Cross-identification with the Richter (1989) 'R' ID numbers for the 70 galaxies selected as described above was made by forming all possible (Stein,Richter) galaxy pairs. For each pair the coordinate distance between the two galaxies in the pair was computed, and the pairs were then sorted after coordinate distance. 37 pairs had a distance of less than 4″. The following pairs had distances of 5.3″, 6.0″, 13.3″, and 24.5″. The first 3 were clear matches, since the heliocentric velocity from Stein differed by at most 2% from that of Richter. The fourth was a clear mismatch, since that Stein ID had already been matched to a Richter ID further up the list. Thus 40 galaxies from the Stein catalog were also in the above subset of the Richter catalog. The established cross-identification for these 40 galaxies can be seen in Table 3.2

Table 3.2: HydraI Redshift Data from Five Sources

ID	Name	Seq	$cz_{\rm hel}$ [km/s]							
			Richter	JFK95b	DFOSC	JFK95b+DFOSC	LC88	Stein	Adopted	Ref.
R112	E501G13	–	3504	3520	–	3520	–	–	3520	JFK95b+DFOSC
R120	–	–	–	–	–	–	–	–	–	–
R129	–	–	3371	–	–	–	–	–	3371	Richter
R138	–	–	3768	–	–	–	–	–	3768	Richter
R166	E501G20	–	4306	–	4353	4353	–	–	4353	JFK95b+DFOSC
R185	–	–	–	–	–	–	–	–	–	–
R188	E501G21	–	4554	–	4575	4575	4592	–	4575	JFK95b+DFOSC
R193	E501G26	–	–	–	–	–	–	–	–	–
R194	–	–	4424	–	–	–	–	–	4424	Richter
R202	–	–	2453	–	–	–	–	–	2453	Richter
R209	–	4	–	–	–	–	–	4155	4155	Stein
R211	–	7	–	–	–	–	–	3707	3707	Stein
R212	E501G27	8	3204	3230	–	3230	3207	3175	3230	JFK95b+DFOSC
R213	–	–	3610	3583	–	3583	3562	–	3583	JFK95b+DFOSC
R214	–	9	–	–	–	–	–	4069	4069	Stein
R216	A1033-27	–	2378	2286	–	2286	2277	–	2286	JFK95b+DFOSC
R217	–	–	4875	4895	–	4895	4890	–	4895	JFK95b+DFOSC
R218	N3305	11	3978	3976	3976	3976	3975	3927	3976	JFK95b+DFOSC
R219	–	12	4377	4188	–	4188	4196	4179	4188	JFK95b+DFOSC
R224	N3307	16	3897	3764	3762	3762	–	3808	3762	JFK95b+DFOSC
R225	–	17	3732	3522	–	3522	3551	3581	3522	JFK95b+DFOSC
R226	–	–	–	–	–	–	–	–	–	–
R228	–	18	–	–	–	–	–	28629	28629	Stein
R231	–	19	3619	3685	–	3685	3687	3633	3685	JFK95b+DFOSC
R234	N3308	21	3598	3568	3540	3547	3545	3532	3547	JFK95b+DFOSC
R237	–	24	2895	3006	–	3006	3004	2973	3006	JFK95b+DFOSC
R238	E501G35	25	4156	4181	4191	4190	–	4177	4190	JFK95b+DFOSC
R239	I629	26	2742	2822	2793	2796	2816	2781	2796	JFK95b+DFOSC
R241	–	–	–	–	–	–	–	–	–	–
R243	–	27	3297	3441	3342	3357	3379	3300	3357	JFK95b+DFOSC
R245	–	–	4756	4789	4782	4783	4776	–	4783	JFK95b+DFOSC
R246	–	29	11650	–	–	–	–	11647	11647	Stein
R249	–	31	10716	–	–	–	–	10647	10647	Stein
R250	E437G08	–	4333	–	4392	4392	–	–	4392	JFK95b+DFOSC
R252	E437G09	–	3807	–	3681	3681	–	–	3681	JFK95b+DFOSC
R253	–	32	4782	4686	–	4686	–	4682	4686	JFK95b+DFOSC
R254	–	33	4659	4662	–	4662	–	4640	4662	JFK95b+DFOSC
R255	–	34	8529*	–	–	–	3193	3154	3193	LC88
R256	N3309	35	4079	4094	4084	4086	4079	4055	4086	JFK95b+DFOSC
R258	–	36	–	–	–	–	–	10427	10427	Stein
R261	–	38	–	3807	–	3807	–	3834	3807	JFK95b+DFOSC
R266	A1034-27A	–	4698	4739	4760	4759	4768	–	4759	JFK95b+DFOSC
R268	–	43	–	–	–	–	–	3640	3640	Stein
R269	N3311	–	3725	3868	–	3868	3833	–	3868	JFK95b+DFOSC
R273	–	44	2772	2687	2749	2731	2703	2745	2731	JFK95b+DFOSC
R278	–	46	4450	–	–	–	4478	4462	4478	LC88
R283	E437G11	48	4745	4938	4871	4897	–	4831	4897	JFK95b+DFOSC
R286	–	50	–	–	–	–	–	5626	5626	Stein
R288	E437G13	52	3610	3499	3571	3561	–	3534	3561	JFK95b+DFOSC
R290	–	55	–	–	–	–	–	11689	11689	Stein
R293	–	56	–	4482	–	4482	–	4439	4482	JFK95b+DFOSC
R295	E437G15	–	2743	–	2725	2725	–	–	2725	JFK95b+DFOSC
R305	–	58	4048	–	4033	4033	–	3983	4033	JFK95b+DFOSC
R307	–	–	3924	–	–	–	–	–	3924	Richter
R308	–	60	4084	4103	–	4103	4115	4105	4103	JFK95b+DFOSC
R316	E501G47	63	4841	4838	–	4838	4820	4805	4838	JFK95b+DFOSC
R317	N3315	64	3840	3793	3776	3779	3785	3754	3779	JFK95b+DFOSC
R319	–	65	–	4460	–	4460	4412	4387	4460	JFK95b+DFOSC
R322	E501G49	66	4112	4063	–	4063	4014	4028	4063	JFK95b+DFOSC
R327	–	67	4302	4213	–	4213	–	4191	4213	JFK95b+DFOSC
R334	E501G52	–	–	–	–	–	–	–	–	–
R336	N3316	68	3979	3876	3975	3962	3940	3937	3962	JFK95b+DFOSC
R337	–	–	–	–	–	–	–	–	–	–
R338	–	–	4203*	3075	–	3075	–	–	3075	JFK95b+DFOSC
R340	–	–	–	–	–	–	–	–	–	–
R343	–	69	3045*	4372	–	4372	–	4361	4372	JFK95b+DFOSC
R347	I2597	–	3014	2971	2985	2983	–	–	2983	JFK95b+DFOSC
R359	–	–	5157	–	–	–	5247	–	5247	LC88
R389	–	–	3432	–	–	–	–	–	3432	Richter
R445	–	–	10637	–	–	–	–	–	10637	Richter

Notes: References: Richter = Richter (1989); LC88 = Lucey & Carter (1988); Stein = Stein (1996). "ID" is the number listed by Richter. "Seq" is the sequential ID listed by Stein. "Ref." is the reference for the adopted $cz_{\rm hel}$ value. A "*" denotes a value which is probably in error – this concerns the Richter values for R255, R338, and R343. Note, that the values given in the JFK95b paper for R338 and R343 should be switched, as done here (I. Jørgensen and P. Stein, private communication, 1996).

Table 3.3: The HydraI Surface Photometry Sample

ID	Name	RA (1950)	DEC (1950)	V_{25} [mag]	Type	$cz_{\rm hel}$ [km/s]	Ref.
R112	E501G13	10:31:08.9	-26:38:20	13.19	S0(4)	3520	JFK95b+DFOSC
R120	–	10:31:20.0	-26:42:28	16.01	S0/a	–	–
R129	–	10:31:38.8	-27:11:35	14.72	S0(5)	3371	Richter
R138	–	10:31:53.6	-27:24:01	14.81	S0(5)	3768	Richter
R166	E501G20	10:32:26.6	-26:57:19	13.92	SB0(2)	4353	JFK95b+DFOSC
R185	–	10:32:50.9	-26:54:37	15.27	S0	–	–
R188	E501G21	10:32:59.4	-27:06:09	13.81	S0(6)pec	4575	JFK95b+DFOSC
R193	E501G26	10:33:03.7	-27:13:22	14.53	S0(6)	–	–
R194	–	10:33:09.9	-27:07:17	15.22	S0/a(r)	4424	Richter
R202	–	10:33:23.3	-26:44:26	15.02	S0	2453	Richter
R209	–	10:33:32.7	-27:06:47	15.83	E3/S0(3)	4155	Stein
R211	–	10:33:34.4	-26:58:39	16.09	S0	3707	Stein
R212	E501G27	10:33:36.6	-27:03:35	14.61	E6/S0	3230	JFK95b+DFOSC
R213	–	10:33:37.1	-27:18:10	14.71	S0(6)	3583	JFK95b+DFOSC
R214	–	10:33:40.9	-27:25:32	16.13	S0	4069	Stein
R216	A1033-27	10:33:43.2	-27:14:58	14.47	E2	2286	JFK95b+DFOSC
R217	–	10:33:49.9	-27:11:41	14.90	S0(6)	4895	JFK95b+DFOSC
R218	N3305	10:33:50.4	-26:54:10	12.91	E1	3976	JFK95b+DFOSC
R219	–	10:33:52.0	-27:25:43	14.67	S0(4)	4188	JFK95b+DFOSC
R224	N3307	10:33:56.2	-27:16:12	14.27	S0(5)/a(rs)	3762	JFK95b+DFOSC
R225	–	10:33:58.0	-27:27:43	15.03	SB(r)0(1)	3522	JFK95b+DFOSC
R226	–	10:33:58.3	-27:13:13	16.21	E	–	–
R231	–	10:33:59.6	-26:54:24	15.71	S0	3685	JFK95b+DFOSC
R234	N3308	10:34:01.3	-27:10:43	12.13	SB0(2)	3547	JFK95b+DFOSC
R237	–	10:34:01.8	-27:05:41	14.41	S0(3)	3006	JFK95b+DFOSC
R238	E501G35	10:34:03.5	-26:44:23	13.46	S0(6)/a	4190	JFK95b+DFOSC
R239	I629	10:34:03.9	-27:19:19	14.16	E2/S0	2796	JFK95b+DFOSC
R241	–	10:34:05.5	-27:07:50	16.20	S0	–	–
R243	–	10:34:06.3	-27:03:33	14.16	S0(4)	3357	JFK95b+DFOSC
R245	–	10:34:08.0	-27:13:28	14.01	SB(rs)0(0)	4783	JFK95b+DFOSC
R250	E437G08	10:34:11.5	-27:48:10	13.92	S0(6)	4392	JFK95b+DFOSC
R252	E437G09	10:34:13.8	-27:57:16	14.03	E4/S0	3681	JFK95b+DFOSC
R253	–	10:34:13.9	-27:13:09	14.36	S(rs)0(1)	4686	JFK95b+DFOSC
R254	–	10:34:14.2	-26:53:21	15.47	E3	4662	JFK95b+DFOSC
R255	–	10:34:14.4	-27:12:38	15.46	E3	3193	LC88
R256	N3309	10:34:14.7	-27:15:29	11.50	E1	4086	JFK95b+DFOSC
R261	–	10:34:16.5	-27:27:27	15.07	S0	3807	JFK95b+DFOSC
R266	A1034-27A	10:34:20.0	-27:18:04	13.61	E7/S0	4759	JFK95b+DFOSC
R268	–	10:34:21.6	-27:19:33	16.05	S0	3640	Stein
R269	N3311	10:34:21.6	-27:16:04	10.65	S0(2)	3868	JFK95b+DFOSC
R273	–	10:34:23.9	-27:12:33	13.99	E1	2731	JFK95b+DFOSC
R278	–	10:34:27.7	-27:07:44	15.76	E1	4478	LC88
R283	E437G11	10:34:29.6	-27:39:35	13.41	S0(4)	4897	JFK95b+DFOSC
R286	–	10:34:31.3	-27:16:40	16.25	E	5626	Stein
R288	E437G13	10:34:33.0	-27:39:28	13.69	S0(5)pec	3561	JFK95b+DFOSC
R293	–	10:34:35.8	-27:18:29	15.98	E2	4482	JFK95b+DFOSC
R295	E437G15	10:34:37.2	-27:54:57	13.05	S0(7)	2725	JFK95b+DFOSC
R305	–	10:34:44.2	-27:43:30	14.07	SB(r)0(1)	4033	JFK95b+DFOSC
R307	–	10:34:47.0	-26:31:37	15.45	E2	3924	Richter
R308	–	10:34:48.5	-27:23:51	15.32	E3/S0	4103	JFK95b+DFOSC
R316	E501G47	10:34:55.7	-27:12:32	13.58	S0(5)	4838	JFK95b+DFOSC
R317	N3315	10:34:57.7	-26:55:54	12.93	SB0(0)	3779	JFK95b+DFOSC
R319	–	10:34:58.1	-27:00:48	15.40	S0	4460	JFK95b+DFOSC
R322	E501G49	10:34:59.2	-27:17:48	14.28	SB(s)0(6)	4063	JFK95b+DFOSC
R327	–	10:35:03.6	-27:36:50	14.82	SB(r)0(3)	4213	JFK95b+DFOSC
R334	E501G52	10:35:15.4	-27:07:36	13.95	S0(5)/a	–	–
R336	N3316	10:35:16.1	-27:20:02	12.85	SB0(1)	3962	JFK95b+DFOSC
R337	–	10:35:16.9	-27:20:24	16.00	E/S0	–	–
R338	–	10:35:18.9	-26:47:51	14.65	S0(5)	3075	JFK95b+DFOSC
R340	–	10:35:19.4	-27:14:11	16.17	E	–	–
R343	–	10:35:20.0	-26:47:02	15.11	S0(2)	4372	JFK95b+DFOSC
R347	I2597	10:35:25.7	-26:49:16	11.83	E3/S0	2983	JFK95b+DFOSC
R359	–	10:35:39.7	-27:11:27	15.19	SB(r)0(5)	5247	LC88
R389	–	10:36:11.4	-26:32:01	15.14	S0(5)	3432	Richter

Notes: All data are from Richter (1989), except for cz_{hel}, which is from "Ref." (cf. the caption to Table 3.2).

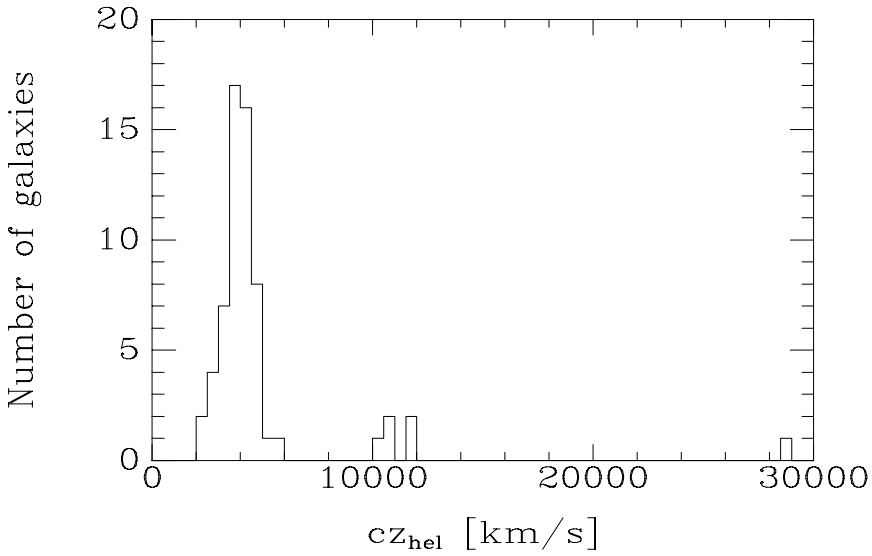

Figure 3.2: Redshift histogram for the 62 early-type galaxies brighter than $V_{25} = 16\overset{\text{m}}{.}5$ in the 43 observed DFOSC fields with a measured redshift. The redshift data are the "adopted" values from Table 3.2. Note that HydraI with a mean velocity of $cz_{\rm hel} = 3718$ km/s (Zabludoff, Huchra, & Geller 1990) is clearly isolated in redshift space.

3.2.3 The Individual Observations

The 64 program galaxies are distributed in 35 of the 43 fields (the 8 fields without program galaxies are the fields 21, 25, 32, 36, 44, 45, 213, and 632). The best seeing Gunn r images of these 35 fields are shown is Appendix E (p. 213) with the 64 program galaxies marked. All 64 galaxies have been observed in Gunn r and Johnson B. 22 galaxies have also been observed in Johnson U. Some of the galaxies have been observed more than once due to field reobservations or due to being located in the overlap region between two fields. A detailed break-down of this is found in Table 3.4. The entire list of observations is given in Table 3.5.

Table 3.4: Number of Galaxies and Observations

Filter	#galaxies	#observations	#galaxies observed i times			
			$i=1$	$i=2$	$i=3$	$i=4$
GR	64	104	35	20	7	2
JB	64	99	35	24	4	1
JU	22	24	20	2		
Total	-	227	-	-	-	-

Table 3.5: Chronological List of Observations

Night	fwhm (GR) [arcsec]	fwhm (JB) [arcsec]	Field	Notes	Program galaxies
1	1.7	1.7	00		R245, R253, R255, R256, R266, R268, R269, R273, R286, R293
1	1.6	1.7	16		R308
1	1.6	1.7	13		R209, R217, R234, R237, R241
1	1.3	1.4	25		–
1	1.3	1.4	37		R166, R185
1	1.3	1.6	18		R214, R219, R225
1	1.4	1.7	12		R255, R273, R278
1	1.8	2.1	21		–
1	1.7	1.9	33		R317
1	1.9	2.2	45		–
2	1.1	1.4	214		R261
2	1.2	1.4	320		R327
2	1.1	1.4	428		R250
2	1.2	1.3	632		–
2	1.1	1.3	29		R193
2	1.1	1.2	419		R138
2	1.3	1.7	519		R129
2	1.7	1.8	15		R213, R216, R224, R226, R239, R245
3	0.8	0.8	00	a	R245, R253, R255, R256, R266, R268, R269, R273, R286, R293
3	0.9	0.8	14		R316, R322
3	0.8	0.9	15	a	R213, R216, R224, R226, R239, R245
3	0.9	0.9	13	a, b	R209, R217, R234, R237, R241
3	0.9	0.8	27		R188, R194, R209
3	0.9	0.9	23		R243
3	0.9	0.9	43		R338, R343, R347
3	0.9	1.1	18	a	R214, R219, R225
3	0.9	1.1	321		R283, R288
3	1.0	1.2	535		R252, R295
3	1.2	1.3	35		R218, R231
4	0.8	0.9	46		R238
4	0.8	0.9	47		R202
4	0.8	0.9	34		R254
4	0.9	1.0	22		R319
4	0.9	0.9	26		R334, R359
4	1.0	1.0	24		R211, R212, R243
4	0.9	1.1	210		R336, R337
4	1.1	1.2	427		R305
4	1.0	1.2	215		R225
4	1.0	1.1	28		R336, R337, R340
4	1.1	1.3	33	a	R317
6	1.3	1.3	213		–
6	1.1	1.4	39		R166
6	1.1	1.0	36		–
6	0.9	1.0	44		–
6	0.9	1.0	45		–
6	0.9	0.9	32		–
6	1.0	1.1	64		R389
6	0.9	1.2	66		R307
6	1.3	1.3	615		R112, R120
6	1.1	1.3	16	a	R308
6	1.1	1.5	21		–
	fwhm (JU) [arcsec]				
9	1.1		00	c	R239, R245, R253, R255, R256, R266, R268, R269, R273, R286, R293
9	1.0		14		R316, R322
9	1.2		15	d	R213, R216, R224, (R226), R239, R245
9	1.4		13	e, f	R217, R234, R237, (R241)
9	1.6		18		R214, R219, R225

Notes: The seeing ('fwhm') is determined to better than the 1 decimal place shown here. [a] Reobservation of a field containing program galaxies. [b] Observed twice in GR. [c] Offset so that R239 is included. [d] R226 too faint for two-dim. photometry. [e] Offset so that R209 is excluded and R255 is included – the latter was not fitted, however. [f] R241 too faint for two-dim. photometry.

3.3 The Basic Reductions of the Photometry

The full description of the basic reductions for the direct images is given in Appendix A (p. 133). A summary is given below.

Removal of overscan area. The readout window for the photometry was the full CCD frame of [1:1060,1:1028]. The section [19:1042,3:1026] was extracted to remove the overscan area. The resulting images had dimensions 1024 pixels × 1024 pixels.

Subtraction of bias. Cf. Sect. A.1 (p. 133). A bias image was constructed from 55 individual bias images. The mean bias level was 124 ADU, with a small (0.5 ADU) gradient in the y-direction. Small night-to-night variations (±0.5 ADU) in level and gradient was seen. It was necessary to use an actual bias image (as opposed to a bias constant), since there was low amplitude structure (0.5 ADU) in the bias images which was also present in the uncorrected science images.

Correction for fat zero. Cf. Sect. A.5 (p. 143). 20 of the 1024 CCD columns were affected more or less severely by *fat zero*, which is a non-linear response in the CCD output signal to the incoming photon flux. The determination of fat zero behavior for the 20 affected columns was done from a large number of dome flats spanning levels all the way from 1 to 58000 ADU. In these images, the levels in the fat zero columns were mapped as function of the levels in the unaffected neighboring columns. The dome flats used were obtained *after* the CCD temperature change that happened between night 5 and 6, cf. Table 3.1 (p. 24). To determine the fat zero effect for the nights *before* the CCD temperature change, an extra correction had to be determined from the galaxy images themselves, since no low-level flats were available from this period. This was of course somewhat complicated due to the large number of objects (galaxies, stars, and cosmic-ray-events) present in these images. The fat zero effect was in all cases below 100 ADU.

To apply the fat zero correction, we need to know the level that *would* have been in the given pixel had it not been affected by fat zero. This level was taken as the mean level in two unaffected neighboring columns on both sides and within a running box of height 21 pixels. The fat zero correction worked well in most cases.

Subtraction of dark current. Cf. Sect. A.2 (p. 135). Two dark images were constructed, one for each CCD temperature. The dark current was 10.9 e^-/hour and 33.7 e^-/hour, respectively. It was necessary to use an actual image and not a constant since the images contained significant structure. Each final dark image was based on 3 individual dark images of 1 hour exposure time. 16 additional dark images had to be discarded, since it was discovered that there had been a light leak in the camera.

Shutter correction. Cf. Sect. A.3 (p. 138). The time that the CCD is actually exposed to light is not equal to the exposure time that the observer asks the controller to use. The difference δ between the latter and the former was determined from 48 dome flats. The value $\delta = 0.41 \pm 0.02$ seconds was found. It was also found that δ was constant across the CCD, so a scalar value could be used instead of an actual image. The shutter correction is applied by multiplying the image levels by $t/(t+\delta)$, where t is the requested exposure time and $(t+\delta)$ is the actual exposure time. See also Stetson (1989).

Flat field correction. Cf. Sect. A.6 (p. 147). Sky flats were obtained in Gunn r on night 1, 2, and 7, and in Johnson B and Johnson U on night 1, 2, 6, and 7. It was found that there was

a difference between the night 1 flats on the one hand and the night 2, (6), and 7 flats on the other hand. Therefore, for each passband, two flats were made, one for night 1, and one (supposedly) for night 2–14. The night 2–14 final images were based on about 12 individual images. The night 1 final images would have been based on only 2–3 individual images had they been made in the same way, which would have given insufficient signal-to-noise. Instead, the pixel-to-pixel variations from the night 2–14 final images were used to construct the night 1 final images, taking only the low frequency variations from the combined night 1 images.

In Gunn r and Johnson B an *illumination correction* was determined. This correction basically makes the background in the science images flat, which the above sky flats themselves fail to do. The reason for this failure is the different color of the night sky (i.e. the background in the galaxy images) and the morning twilight sky (where the flats were taken). The problem might be accentuated by a red leak in the Gunn r filter (cf. Stetson 1989). The illumination correction was determined from science images containing few galaxies. The so-called empty fields that had been observed did not prove useful. No illumination correction for Johnson U could be determined, since the background level in the galaxy images was too low and since all 5 images contained many galaxies.

The relative uncertainties on the final flat field images (based on photon statistics and read-out noise), and limits on possible remaining low spatial-frequency variations are listed in Table 3.6.

Table 3.6: Summary of Flat Field Accuracy

Passband	Relative uncertainty	Possible low frequency variations
Gunn r	0.35%	$\leq 0.2\%$
Johnson B	0.31%	$< 0.1\%$
Johnson U	0.31%	$< 0.1\%$

Removal of signal from remanence and overflow. Cf. Sect. A.7 (p. 153). Overflow is when a very bright and saturated star causes a stripe from the star to the edge of the image in the given image. Remanence is when these signals are seen in subsequent images in the same columns without the presence of a saturated star. The used CCD was *severely* affected by both phenomena, with remanence being visible in $\sim$ 20–30 exposures after the one that had caused it! The images were quite successfully corrected for both effects using a labor-intensive method.

Removal of signal from the spectroscopy calibration lamp. Cf. Sect. A.8 (p. 154). In a few cases, the spectroscopy calibration lamp was accidentally on when direct images were obtained. The imprint of the lamp was successfully modeled and subtracted.

Stacking of images. In the cases where a very bright star in the field made it necessary to take several shorter exposures, these were stacked, i.e. offset to match and then added. This concerned field 33, 35, and 535.

In addition, the following was performed.

Linearity test. Cf. Sect. A.4.2 (p. 141). Using dome flats with levels from 1 to 58000 ADU it was found that the CCD was linear within 0.7%.

Determination of conversion factor and read-out noise. Cf. Sect. A.4.1 (p. 140). `findgain` was used to determine the conversion factor (CF) and read-out noise (RON) for all the dome flats used in the linearity test. `findgain` reported that the CF increased with level. However, since the linearity test showed the CCD to be linear, the CF *had* to be constant. We concluded that it was the RON that was level-dependent, probably caused by a malfunction in the read-out electronics.

The variation in the CF reported by `findgain` was mainly at levels below 1000 ADU. For levels above 1000 ADU, the mean of the 15 determinations of the CF was 1.95 e^-/ADU with an rms scatter of 0.04; this value was adopted. The standard deviation in raw bias images was 2.25 ADU, and this (constant) value was adopted as the RON, corresponding to 4.39 e^-. The effect on the error estimates on the flat fields of using a constant RON instead of a level-dependent one is non-significant.

Seeing determination. By seeing we mean the full width at half maximum (FWHM) of the point spread function (PSF). For all the galaxy images, the seeing was determined using a script written by I. Jørgensen. It works as follows. All objects in the image is found using `daofind`. A Gaussian of user specified FWHM is fitted to all objects using `imexamine`. Based on a number of criteria, only bright but not saturated stars are attempted kept. The median FWHM for these objects is taken to be the first guess on the seeing. The above procedure is then repeated, this time using the first guess on the seeing as parameter for the Gaussian. The output median FWHM of the selected objects is taken as the seeing. The seeing determination is semi-automatic only, since the user has to experiment to find appropriate values for the parameters used for the object selection. It was found that different values were needed for different passbands and exposure times. For 8 out of the 123 galaxy images a manual determination of the seeing was done, and it was found that the two methods agreed well.

For the Gunn r and Johnson B images, the automatic seeing determination was based on about 45 stars, whereas for the Johnson U images it was based on about 5 stars only. The seeing values are shown in Table 3.5 (p. 30). They are in the range $0.77''$–$1.88''$. When given each of the 227 galaxy observations equal weight, the mean seeing values are $1.1''$, $1.2''$, and $1.2''$ for Gunn r, Johnson B, and Johnson U, respectively. At the distance of HydraI, this corresponds to about 0.5 kpc (for $H_0 = 50\,\mathrm{km\,s^{-1}\,Mpc^{-1}}$; cf. Sect. 7.1.1, p. 85). The range in seeing values in pixels is 1.52–3.70 pixels. Thus, in the best seeing conditions (seeing $<$ 2 pixels $\approx 1''$), the resolution is determined by the CCD pixel size, not the seeing. This is not a big problem, since the resolution obtained in any case is good and sufficient, especially since HydraI is such a nearby cluster. The used CCD scale of 0.5073 arcsec/pixel was found by doing astrometry, see Sect. A.9 (p. 156).

The ellipticities of the PSF were in the range 0.03–0.13 with a mean value of 0.06. The PSF was thus quite round, which is important, since an elongated PSF can introduce systematic errors in the ellipticities and position angles determined from the surface photometry; see Franx, Illingworth, & Heckman (1989b), and Peletier et al. (1990).

Chapter 4

Surface Photometry and Standard Calibration

4.1 Surface Photometry

We performed surface photometry by fitting ellipses to the galaxy images. This yielded the *radial profiles* of a number of quantities such as the (local) surface brightness $\mu(r)$, the ellipticity $\varepsilon(r)$, and the deviations from elliptical isophotes parametrized by the Fourier coefficients, e.g. $c_4(r)$. These radial profiles are shown in Appendix F (p. 251).

From these radial profiles *global parameters* can be derived, e.g. the effective radius $r_{\rm e}$, the effective mean surface brightness $<\mu>_{\rm e}$, and the mean $c_4(r)$ coefficient $<c_4>$. Global here means "one number per galaxy", in the sense that an entire radial profile is condensed into a single characteristic number.

The surface photometry is the subject of the present chapter. The determination of global photometric parameters is described in Chapter 5.

The ellipses fit was done using the GALPHOT program package. GALPHOT was written by Marijn Franx and later developed further by Inger Jørgensen. See Franx et al. (1989b), and JFK92.

It should be noted, that I (BMJ) fitted about 60% of the 227 galaxy observations, including the central field galaxies. The remaining 40% were fitted by Inger Jørgensen.

4.1.1 Finding and Classifying Objects

The first problem to address is what to do with all the pixels in the image that are contaminated by signal from other 'objects', such as other galaxies, stars, cosmic-ray-events, and remanence or overflow stripes that could not be removed. In our scheme, all such pixels are simply not used in the fit, with the exception of severely overlapping galaxies, cf. below.

The problem is then how to determine which pixels should be flagged (i.e. omitted from the fit). We do this as follows. First we attempt to automatically find all objects in the image using `daofind` called with suitable parameters. Based on the output from `daofind` (peak value, roundness and sharpness) and on the seeing value and the CCD saturation level we then classify the found objects as either 'stars' or cosmic-ray-events. The star category includes all objects that extend over several pixels and are 'unsharp', i.e. stars and galaxies. The star objects are assigned a flagging radius based on their estimated extend. The cosmic-ray-event objects are assigned a flagging radius of 1 pixel. In the fits, pixels within a circle centered on each object and with the corresponding radius are omitted.

The total number of objects found is in the range 400–1000 per image. This number depends on the exposure time (since the number of cosmic-ray-event grows linearly with exposure time), the fields looked at (how many stars and galaxies there actually are in the image), and the seeing (since whether objects with small angular separation can be separated depends on the seeing). The point here is just that the number is so high that an automated procedure is clearly needed. However, the algorithm that assigns radii to the 'stars' sometimes fails, especially for 'stars' located close to the center of the galaxy we want to fit where the background is not flat. The user can then intervene and manually change the radii.

4.1.2 Fitting of Ellipses

The fitting of ellipses to the galaxy images is done in a three step procedure. First a harmonic expansion along concentric circles is performed. Second the residuals from this expansion are used to flag additional pixels. Third the actual ellipse fit is performed, using another harmonic expansion to calculate an initial guess.

The harmonic expansion is done as follows. The user manually determines the coordinates of the center of the galaxy. Along concentric circles with this center a 6 term harmonic series is fitted to the intensities I. The series is given by

$$I(r,\varphi) = I_0^{(\mathrm{c})}(r) + \sum_{n=1}^{6} \left[A_n^{(\mathrm{c})}(r)\sin(n\varphi) + B_n^{(\mathrm{c})}(r)\cos(n\varphi) \right] \quad , \tag{4.1}$$

where r is the radius and φ is the position angle (measured from the CCD x-axis counterclockwise), and where the superscript c denotes that we are fitting along circles. Actually, discrete radii r_i are used; they are calculated as $r_i = r_{\min} \cdot s^{i-1}$, $i = 1, \ldots, N_{\max}$. In this way, the radii are equally spaced in $\log r$. $r_{\min}$ was set to 0.3 pixels, and the scaling factor s was usually set to 1.1, giving the radius sequence 0.3 pixels, 0.33 pixels, 0.363 pixels, ... $r_{\min}$ has to be as small as 0.3 pixels in order to get a good fit of the central pixels of the galaxy. The maximum radius number $N_{\max}$ is basically determined from the condition that 60% of the circle needs to be within the image. For the pixels outside the maximum radius only the intensity is fitted. The pixels contaminated by other objects are excluded from the fit, cf. above.

A residual image is calculated by simply subtracting the fit from the original image. This residual image will normally be flat, since the only thing left is what the harmonical terms of order higher than 6 would account for. In the cases where the galaxy has a very strong disk, some residual can be seen, though.

This residual image is used in the second step to flag all pixels that deviate by more than 5 sigma. This gives an additional list of pixels to exclude from future fits. The pixels flagged in this process could be due to cosmic-ray-events that extend over several pixels, unremoved remanence or overflow stripes, and a very strong disk in the galaxy. Of course one wants to *keep* the disk pixels, so in these cases it is necessary to specify a region where the 5 sigma flagging should *not* be done.

In the third step, the above harmonic expansion along concentric circles is done again, this time also excluding the additional pixels found in the above second step. From the resulting Fourier coefficients initial guesses on the center of the ellipses $x_{\mathrm{c}}(r), y_{\mathrm{c}}(r)$, the ellipticity $\varepsilon(r)$, and the position angle $\mathrm{PA}(r)$ are calculated. Then at each equivalent radius $r_i = \sqrt{a_i b_i}$ an ellipse is fitted to the image. The same values of r_i as above are used. For the pixels outside the maximum radius, the mean of the last three ellipses is used to define the center and shape of the ellipses with larger radii, and only the intensity is fitted. The fit is iterated 20 times. In each iteration step there is a limit on how much the center, ellipticity, and position angle can change from the values they had in the previous step. These limits are imposed to safeguard the iteration from running wild,

and most of the time they work fine. However, if the galaxy has a large change of for example center position (such as R269) or position angle (also known as *isophote twist*), the user will need to increase these limits.

A residual image is calculated by subtracting the ellipse fit from the original image. The structure seen in this image is per definition how the galaxy deviates from elliptical isophotes. This is quantified by fitting a 6 term harmonic series *along the fitted ellipses*,

$$I(r,\varphi) = I_0^{(\mathrm{e})}(r) + \sum_{n=1}^{6} \left[A_n^{(\mathrm{e})}(r)\sin(n\varphi) + B_n^{(\mathrm{e})}(r)\cos(n\varphi) \right] \ . \tag{4.2}$$

From $A_n^{(\mathrm{e})}(r)$ and $B_n^{(\mathrm{e})}(r)$ we calculate 'normalized' coefficients $s_n(r)$ and $c_n(r)$ as

$$s_n(r) = \frac{A_n^{(\mathrm{e})}(r)}{r \cdot \frac{dI(r)}{dr}} \ , \quad c_n(r) = \frac{B_n^{(\mathrm{e})}(r)}{r \cdot \frac{dI(r)}{dr}} \ , \quad n = 1, \ldots, 6 \ . \tag{4.3}$$

$s_n(r)$ and $c_n(r)$ have the advantage of measuring the *relative* radial deviation of the isophotes from ellipses. The names of $s_n(r)$ and $c_n(r)$ reflects the relation to the sine and cosine terms of the Fourier expansion, respectively. One of the most interesting of these coefficients is $c_4(r)$, since it is an indicator of whether the galaxy is disky ($c_4(r) > 0$) or boxy ($c_4(r) < 0$) (Carter 1987; Bender et al. 1989; Peletier et al. 1990). The first and second order coefficients will in general be zero since the expansion is done in the residual image where the best fitting ellipses have been subtracted.

In the ellipse fit we keep the center ($x_\mathrm{c}(r)$ and $y_\mathrm{c}(r)$) and the shape ($\varepsilon(r)$ and PA(r)) as free parameters, since these quantities are not constant with radius in real galaxies. However, at some point in the profile the signal-to-noise becomes too low to keep the center and the shape as free parameters. The last radius where the center is free, $r_{\mathrm{free-center}}$, is determined as the point where the uncertainty on the first order Fourier coefficients from the harmonic expansion along concentric circles is below 0.02 for Gunn r and Johnson B, and 0.04 for Johnson U. Likewise, $r_{\mathrm{free-shape}}$ is determined using the uncertainty on the *second* order coefficients. The condition $r_{\mathrm{free-center}} \leq r_{\mathrm{free-shape}}$ is imposed, since otherwise one could easily get overlapping ellipses. In general, however, one gets $r_{\mathrm{free-center}} = r_{\mathrm{free-shape}}$, and one can therefore speak of just one radius, r_{free}. Beyond the last free radius, the parameters are fixed at the mean value of the last three free radii.

The actual fitting of ellipses is done as described above by starting with suitable default values for the different parameters that control the fit. The residual image from the ellipse fit is then inspected as well as the text output from the fitting task (it might for example report overlapping ellipses at some radii). The parameters and the object flagging is then 'tuned' until a good fit is obtained. This is described in more detail in Sect. B.1 (p. 161).

The method of simply excluding from the fit the pixels that are contaminated by signal from other objects does not work if too large a fraction of a given radius is excluded by this. This is for example the case where a neighbor galaxy is sufficiently close to the galaxy we want to fit. In these cases we fitted the two galaxies iteratively, cf. Sect. B.1. An example is the central field (field 00, see the image on p. 215), where the two bright galaxies R256 and R269 were fitted iteratively. When these two galaxies had been successfully fitted, models of the two were subtracted from the original image, and the remaining 8 program galaxies in the central field were fitted in the normal way using this image. The same models of the R256 and R269 were subtracted from the neighboring fields. In this way, the galaxies in the overlap region between field 00 and a neighboring field were in any case fitted to an image where models of R256 and R269 had been subtracted. An example of this is R255 and R273, which are located both in field 00 and in field 12 (see image on p. 216).

Note, that the paper reproduction of the field 00 image (p. 215) might not convey the impression that there is signal from R256 and especially the cD galaxy R269 all over the image. However, that is easily seen when one views the image on screen, and that is also seen in the derived surface photometry. Another example of galaxies that needed this kind of iterative fitting is R336/R337 (p. 227 or 239).

The above method of iteratively fitting ellipses to two objects was also used when a bright star was close to the center of the program galaxy in question. It worked well. In the cases where this method was used, the separation between the centers of the star and the galaxy was typically 20 pixels ($10''$). An example is the galaxy R194 which has a star 21 pixels ($11''$) from the center – see the image on p. 226. In our images, the star had a peak intensity of about four times larger that of the galaxy. Another example is R308 (p. 220).

The output from the ellipse fit is the radial profiles of intensity (in ADU) $I_0^{(e)}(r)$, center $x_c(r), y_c(r)$, ellipticity $\varepsilon(r)$, position angle PA(r), and the normalized Fourier coefficient $s_n(r)$ and $c_n(r)$ $(n = 1, \ldots, 6)$; as well as the corresponding uncertainties, also as function of radius. The position angles are afterwards transformed so they are measured exactly as north through east, which is the standard. In addition the PA-profiles that cross 0° or 180° are made look 'continuous' by adding or subtracting 180° at certain points in the profile. These corrections to the PA-profiles are described in Sect. B.2 (p. 164).

4.2 Determination of Magnitudes

We want to determine aperture magnitudes as well as surface brightnesses for the galaxies. To do this, we first need to determine the sky background level.

4.2.1 Determination of the Sky Background Level

One method to determine the sky background level is to identify so-called empty regions of the image and measure the level in these. However, that is quite subjective, and sometimes there is even significant signal from the galaxies *everywhere* in the image. Instead, we used a less subjective method to determine the sky background level. The method does not use the image in question directly, but is based on the intensity profile $I_0^{(e)}(r)$ determined from the ellipse fit. To the outer parts of this profile a suitable function is fitted, and the asymptotic value for $r \to \infty$ is taken to be the sky background level.

Specifically, for normal E and S0 galaxies (here meaning non-cD galaxies) we fitted the following two functions

$$I(r) = \text{sky} + \frac{I_0}{r^\alpha},\ \alpha = 2, 3 \quad \text{(for non-cD galaxies)} \tag{4.4}$$

to the outermost points in the intensity profile, and the sky background level 'sky' was taken to be the mean of the two determinations (i.e. $\alpha = 2$ and $\alpha = 3$). The 'outermost points' are defined as the points where the intensity from the galaxy is less than 0.2 times the sky background level. The uncertainty on the sky background level is taken to be half the difference between the two determinations, unless this is less than a specified minimum value, in which case that is used instead. This is done in order to take systematic effects into account, like how well one can do flat fielding. The minimum relative uncertainty was set to 1% for Gunn r, and 0.5% for Johnson B and U. In all cases but for the cD galaxy R269, the uncertainty was calculated from the minimum value.

cD galaxies have per definition a more shallow profile than normal E and S0 galaxies, and are therefore better fitted by the two functions

$$I(r) = \text{sky} + \frac{I_0}{r^\alpha},\ \alpha = 1, 2 \quad \text{(for cD galaxies)}\ . \tag{4.5}$$

We used these for the galaxy R269, only.

For both set of functions, to obtain a good fit we sometimes excluded a few of the outer points from the fit.

4.2.2 Determination of Magnitudes

For each galaxy we construct a *cleaned image* from the original image by substituting the pixels contaminated by signal from other objects with the model values from the ellipse fit. From the cleaned images we determine the following four magnitude quantities

- $m_{\text{ell}}(r)$: the magnitude within the fitted ellipse with equivalent radius r
- $m_{\text{circ}}(r)$: the magnitude within a circle with radius r
- $\mu(r)$: the surface brightness at the fitted ellipse with equivalent radius r
- $<\mu>(r)$: the mean surface brightness within the fitted ellipse with equivalent radius r

The intensities in ADU are transformed to magnitudes using the sky level, the exposure time and an arbitrary zero point of 22. The surface brightnesses are transformed to $^{\text{m}}/\text{arcsec}^2$ using the CCD scale determined from the astrometry (Sect. A.9, p. 156).

4.3 Non-photometric Corrections and Standard Calibration

A few of the galaxy images were obtained in non-photometric conditions. For these, we determined the offsets needed to bring them to the system of the photometric images. This is described in Sect. B.3 (p. 166). The derived offsets are listed in Table B.2 (p. 172). In summary, two Gunn r and two Johnson B images were found to be non-photometric, with needed offsets in the range $-0\overset{\mathrm{m}}{.}01$ to $-0\overset{\mathrm{m}}{.}11$. The five Johnson U images were brought to an internally consistent system with offsets in the range $+0\overset{\mathrm{m}}{.}03$ to $-0\overset{\mathrm{m}}{.}06$. The offsets were added to $m_{\mathrm{ell}}(r)$, $m_{\mathrm{circ}}(r)$, $\mu(r)$, and $<\mu>(r)$.

The standard calibration is described in Appendix C (p. 179). A summary is given here. Three standard star fields were observed: PG1633+099 (5 stars), SA110 (8 stars), and M67 (23 stars). Since the M67 stars are very bright, they were observed with the telescope defocused in order to avoid very short exposure times. Standard star observations were made in Gunn r and Johnson V, B, and U on all the nights where the HydraI Gunn r and Johnson B galaxy images were taken, i.e. night 1, 2, 3, 4, and 6. In addition, standard star observations were made on night 7. No standard star observations were made on night 9 where the HydraI Johnson U galaxy images were taken. Aperture photometry was performed on the standard stars, and the magnitudes were corrected for the finite size of the aperture. The aperture corrected stellar magnitudes are denoted m_{raw}.

The field SA110 was observed twice each night, at low and high airmass (typically $X = 1.15$ and 1.65, respectively), to determine the extinction coefficients for the four passbands. No significant color dependence was found for for the extinction coefficients. The derived extinction coefficients for night 4 and 6 were significantly larger than those for the other nights. It was decided to use the mean value of night 1, 2, 3, and 7 as extinction coefficient for all nights. See Table C.8 (p. 198).

After the observed stellar magnitudes had been corrected for extinction, the magnitudes still showed night-to-night variations at the level of $0\overset{\mathrm{m}}{.}01$–$0\overset{\mathrm{m}}{.}04$ (depending on passband). These relative offsets (so-called night coefficients) were used to bring the different nights to an internally consistent system. The night coefficients are given in Table C.9 (p. 198).

Instrumental magnitudes were then calculated from the raw magnitudes as

$$m_{\mathrm{inst}} = m_{\mathrm{raw}} - kX + n \ , \tag{4.6}$$

where $-kX$ is the extinction correction and $+n$ is the night shift.

Standard star magnitudes were taken from Landolt (1992), Jørgensen (1994), and Montgomery, Marschall, & Janes (1993). Ten of the M67 stars did not have magnitudes in Johnson U, giving a total number of 26 stars in this passband instead of the 36 stars available in the other passbands.

We determined the following transformations

$$\begin{aligned}
r_{\mathrm{std}} &= r_{\mathrm{inst}} + \underset{\pm 0.005}{0.772} + \underset{\pm 0.003}{0.124}\ (B-r)_{\mathrm{inst}} \qquad \sigma_{\mathrm{fit}} = 0.019 \\
B_{\mathrm{std}} &= B_{\mathrm{inst}} - \underset{\pm 0.006}{0.052} + \underset{\pm 0.003}{0.125}\ (B-r)_{\mathrm{inst}} \qquad \sigma_{\mathrm{fit}} = 0.022 \\
U_{\mathrm{std}} &= U_{\mathrm{inst}} - \underset{\pm 0.017}{2.237} + \underset{\pm 0.006}{0.019}\ (U-B)_{\mathrm{inst}} \qquad \sigma_{\mathrm{fit}} = 0.039
\end{aligned} \tag{4.7}$$

σ_{fit} is the rms scatter. 3–7 stars were excluded from the fits, either because they had extreme colors outside the range needed, or because they deviated systematically; cf. Sect. C.5 (p. 201).

The raw galaxy magnitudes (as determined in Sect. 4.2) were then standard calibrated using Eq. (4.6) and (4.7). The Gunn r and Johnson B observations were made in pairs (cf. Table 3.5, p. 30), and were standard calibrated in this way. The Johnson U observations were paired with the best seeing Johnson B observations. A night coefficient of zero was assumed for night 9.

4.4 Internal Comparison of Photometry

Since almost half of the galaxies have been observed more than once in Gunn r and Johnson B (cf. Table 3.4, p. 29), we have ample opportunity to determine the internal accuracy of the data. For the photometry, we first compare aperture magnitudes, and then the entire surface brightness profiles.

4.4.1 Comparison of Aperture Magnitudes

For the galaxies observed more than once, all possible pairs of observations were formed. Within each pair, the two observations were ordered chronologically. For each pair, the aperture magnitude differences within circular apertures of radii $6''$ and $10''$ were calculated.

The results are plotted in Figure 4.1, and the statistics are listed in Table 4.1. The first thing to note is the small scatter of about $0\overset{\mathrm{m}}{.}011$, which gives a typical internal uncertainty of only $0\overset{\mathrm{m}}{.}008$ (i.e. $0\overset{\mathrm{m}}{.}011/\sqrt{2}$).

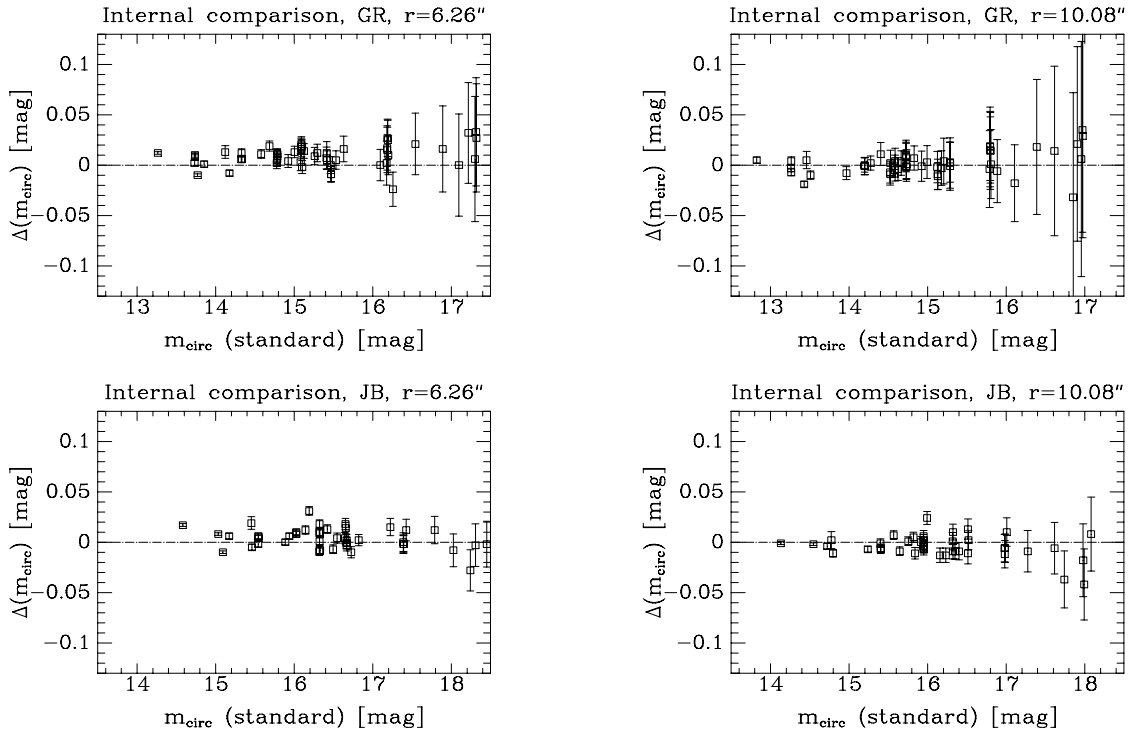

Figure 4.1: Internal comparison of aperture magnitudes. The top panels show Gunn r, and the bottom panels Johnson B. The left panels are for an aperture of $6.26''$, and the right panels are for an aperture of $10.08''$.

A small systematic offset is seen for the $6''$ aperture. This is most likely a seeing effect. A large fraction of the multiple observations originate from fields that were observed on night 1 or 2 in bad seeing, and then reobserved on night 3 in good seeing (cf. Table 3.5, p. 30). Since the observations within each pair are in chronological order, the seeing differences are in most cases larger than zero. In Fig. 4.2 we plot the aperture magnitude difference $\Delta(m_{\mathrm{circ}})$ versus the seeing difference Δ(seeing). At least for the Gunn r $6''$ aperture there is a significant correlation. A Spearman rank order test gives a probability that there is *no* correlation of less than 0.01%. The correlation has the right sign for a seeing effect.

Table 4.1: Statistics of the Internal Comparison of Aperture Magnitudes

Aperture	Filter	N	mean	rms
$6.26''$	GR	53	0.009 ± 0.001	0.011
$6.26''$	JB	42	0.004 ± 0.002	0.011
$6.26''$	JU	2	0.022 ± 0.001	0.001
$10.08''$	GR	53	0.002 ± 0.002	0.012
$10.08''$	JB	42	-0.004 ± 0.002	0.011
$10.08''$	JU	2	0.002 ± 0.002	0.004

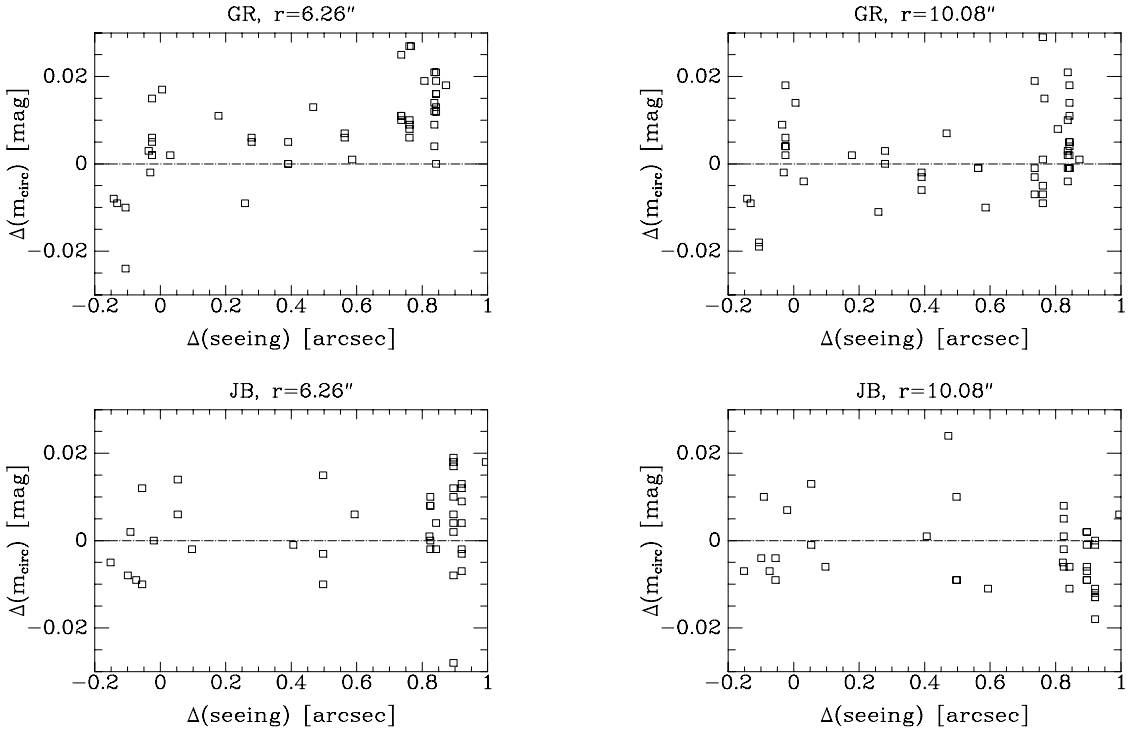

Figure 4.2: Seeing dependence for galaxy magnitude differences. From top to bottom the filters are GR and JB. The left two panels are for an aperture of $6.26''$, the right two panels are for an aperture of $10.08''$.

4.4.2 Comparison of Surface Brightness Profiles

For all the 97 possible pairs of galaxies observed more than once in the same filter, we calculated the difference of the surface brightness profiles, $\Delta\mu(r) = \mu_{\mathrm{obs.\,a}}(r) - \mu_{\mathrm{obs.\,b}}(r)$, and examined the plots of $\Delta\mu(r)$ vs. $\log r$. Nine of these plots are shown in Fig. 4.3 to exemplify characteristic features seen in these comparisons.

The most prominent feature in the 97 $\Delta\mu(r)$ plots is the seeing effect. A typical example is panel (a), where the first observations has worse seeing than the second (cf. Table 4.2). The same effect is also seen in panel (d) and (g); and also in panel (f) and (i) with the opposite sign, since Δseeing is negative here. The shown comparisons of R256 (panel d), R269 (panel e), and R273 (panel c) are all from the same pair of images, and yet the seeing effect is very different for the

three galaxies. This is because their profiles are quite different. R256 has a 'normal' profile, R269 has a flat or even decreasing profile towards the center due to dust, and R273 has a very steep profile towards the center (it has a central cusp). Panel (b) shows R234, which due to the problems with the spectral calibration lamp (cf. Sect. A.8, p. 154) was observed twice just after each other. The seeing is almost the same for the two images, and sure enough, the two profiles match very well even at very small radii.

A few of the plots show systematic differences at large radii. The worst example is R336, panel (f) and (i). A possible explanation could be a wrong sky determination. For R336 our sky determinations need to be off by 2.5 ADU (2.2%) and 8 ADU (2.7%) for Johnson B and Gunn r, respectively. (The number quoted for the given filter is the amount that needs to be added to the sky level used for the first observation, or equivalently the amount that needs to be subtracted from the sky level used for the second observation.) A manual sky determination (the median value in empty regions of the image) indicates that the used sky levels are off by 0.3 ADU and 3 ADU, respectively. Thus a wrong sky determination can only explain a minor part of the observed discrepancy. It seems likely that the discrepancy could originate from the iterative fit. R336 was fitted iteratively with R337 (see the images on p. 227 and 239). An additional complication is that R336 is located close to the edge of both images it is in, with a distance to the edges of $\log(r/\mathrm{arcsec}) = 1.7$–$1.8$, and with different sides being outside the image in the two observations. R256 and R269 also show systematic differences at large radii, but these are not significant within the estimated errors. These two galaxies were also fitted iteratively.

Anyway, in all cases the quantities we are mostly interested in, such as r_e and $<\mu>_\mathrm{e}$, are only moderately affected, cf. Table 4.2. The derivation of these parameters takes the seeing into account, as described in Sect. 5.1 (p. 53). Further, due to the correlation between the errors in r_e and $<\mu>_\mathrm{e}$ (cf. Sect. 5.4, p. 56), the combination of the two that enters the fundamental plane, approximately $\log r_\mathrm{e} - 0.328<\mu>_\mathrm{e}$, does not vary by more than typically 0.01.

Table 4.2: Internal Comparison of Surface Brightness Profiles – Info

Panel	ID	Filt.	Night a	Night b	Δseeing	$\Delta m(10'')$	$\Delta \log r_\mathrm{e}$	$\Delta<\mu>_\mathrm{e}$	Δ"FP"
(a)	R234	GR	1	3 (#2)	$0.74''$	-0.003	0.00	0.02	-0.007
(b)	R234	GR	3 (#1)	3 (#2)	$-0.03''$	0.004	-0.01	-0.03	-0.000
(c)	R273	GR	1	3	$0.84''$	-0.001	0.01	0.07	-0.013
(d)	R256	GR	1	3	$0.84''$	0.005	-0.02	-0.07	0.003
(e)	R269	GR	1	3	$0.84''$	0.005	0.04	0.12	0.001
(f)	R336	GR	4 (#1)	4 (#2)	$-0.11''$	-0.019	0.03	0.10	-0.003
(g)	R256	JB	1	3	$0.90''$	-0.001	-0.03	-0.13	0.013
(h)	R269	JB	1	3	$0.90''$	0.002	0.07	0.19	0.008
(i)	R336	JB	4 (#1)	4 (#2)	$-0.06''$	-0.004	0.04	0.16	-0.012

Notes: See caption to Fig. 4.3. The two observations, 'obs. a' and 'obs. b', are identified by the night number. For galaxies observed twice on the same night, the two observations are denoted '(#1)' and '(#2)', still in chronological order.
Δseeing should be compared with the shape of the $\Delta\mu(r)$ vs. $\log r$ plots in Fig. 4.3. The derivation of $\log r_\mathrm{e}$ and $<\mu>_\mathrm{e}$ takes the seeing into account, as described in Sect. 5.1 (p. 53). The other differences listed quantify the effect of the differences in $\mu(r)$. "FP" is the combination of $\log r_\mathrm{e}$ and $<\mu>_\mathrm{e}$ that enters the fundamental plane, and is defined by "FP" $= \log r_\mathrm{e} - 0.328<\mu>_\mathrm{e}$.

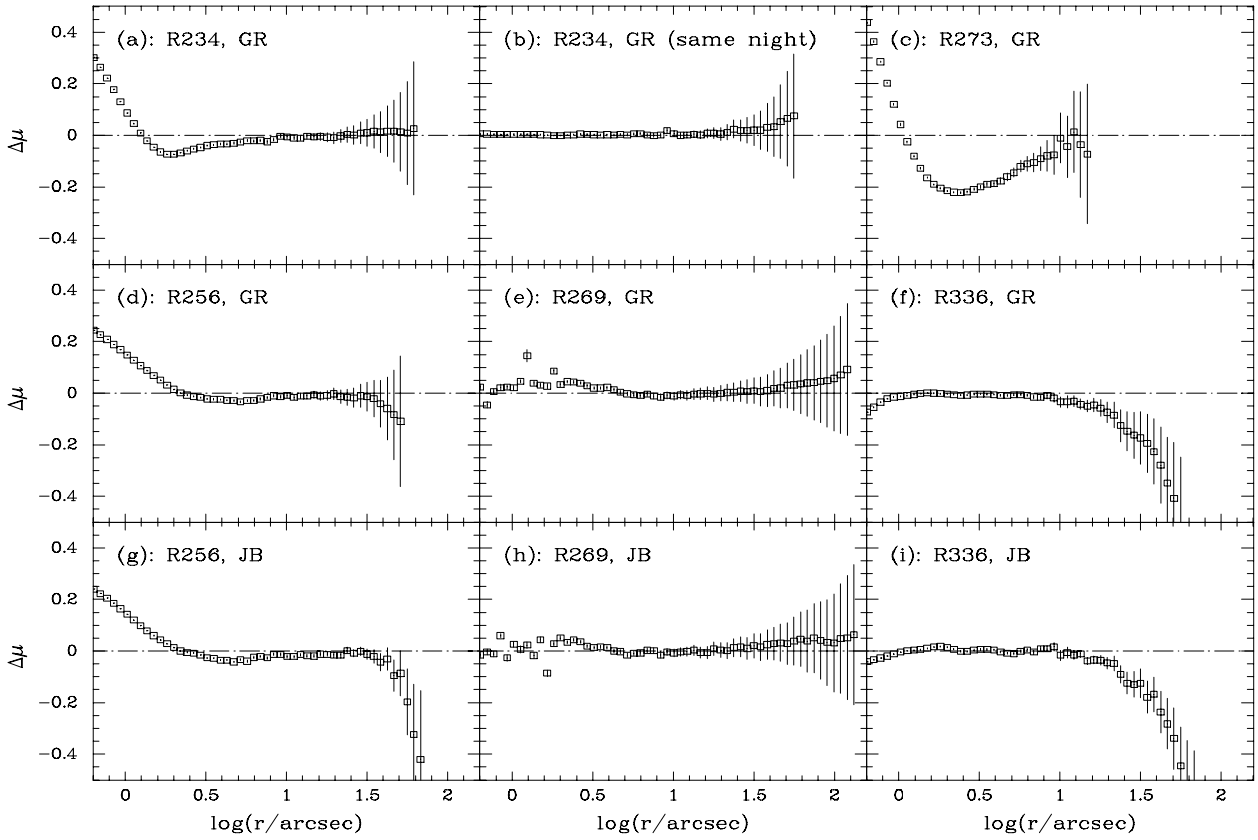

Figure 4.3: Internal comparison of surface brightness profiles. This figure shows 9 of the 97 possible internal comparisons of surface brightness profiles. On each panel is shown $\Delta\mu(r) = \mu_{\mathrm{obs.\,a}}(r) - \mu_{\mathrm{obs.\,b}}(r)$, where 'obs. a' and 'obs. b' are two observations of the same galaxy in the same filter, in chronological order. The observations can be uniquely identified through Table 4.2. Only points with an uncertainty on $\Delta\mu(r)$ less than $\sqrt{2}\cdot 0.2$ are plotted. The plotted range in $\log r$ corresponds to a range in r of $0.63''$–$158''$.

4.5 External Comparison of Photometry

We also compared our photometry with other studies in the literature. In this way we get an estimate of the *total* uncertainty, including systematic differences that could arise from e.g. the standard calibration. As for the internal comparison of the photometry, we both compare aperture magnitudes and entire surface brightness profiles. The main point of the comparison of aperture magnitudes is to test the zero point in the calibration to the standard system.

4.5.1 Comparison of Aperture Magnitudes

Our $m_{\rm circ}(r)$ profiles were interpolated to give $m_{\rm circ}$ (hereafter just m) at the radii which the given literature source had used. The interpolation was done by fitting a quadratic function to the profile. In the cases of JFK92 and JFK95a, for which we had access to their $m(r)$ profiles, the opposite was done: their magnitudes were interpolated to two of our apertures: $6.26''$ and $10.08''$.

Where we had observed a given galaxy more than once, a mean of our values was calculated before calculating the difference with the given literature source.

Note, that throughout this thesis, *aperture* refers to the *radius* of the aperture, *not* the diameter.

We compared with the following sources:

- JFK92: CCD photometry in Gunn r and Johnson B. Magnitudes cleaned for foreground stars and other galaxies. 3 galaxies in common: R218, R234, and R269. Two (synthetic) apertures: $6.26''$ and $10.08''$.

- JFK95a: CCD photometry in Gunn r. Magnitudes cleaned for foreground stars and other galaxies. 14 galaxies in common: R112, R216, R218, R234, R237, R243, R256, R266, R269, R283, R288, R338, R343, and R347. Two (synthetic) apertures: $6.26''$ and $10.08''$.

- Poulain & Nieto (1994): Photoelectric photometry in Kron-Cousins $R_{\rm C}$, Johnson B, and Johnson U. The expected offset between Gunn r and Kron-Cousins $R_{\rm C}$ is $(r - R_{\rm C}) = 0\overset{\rm m}{.}354$ (Jørgensen 1994). Magnitudes cleaned for foreground stars[1]. Magnitudes probably not cleaned for other galaxies. 2 galaxies in common: R256 and R347. 5 apertures: $11.4''$, $15.7''$, $21.7''$, $30.7''$, and $43.4''$. For Johnson U, R347 and the $15.7''$ aperture are not available.

- Burstein et al. (1987): Photoelectric photometry in Johnson B. Magnitudes cleaned for foreground stars[2]. Magnitudes probably not cleaned for other galaxies. 4 galaxies in common: R234, R256, R269, and R347. 3 apertures: $16.9''$, $30.7''$, and $45.4''$.

- Sandage (1975): Photoelectric photometry in Johnson U. Magnitudes cleaned for foreground stars[3]. Magnitudes probably not cleaned for other galaxies. 2 galaxies in common: R234 and R269. 1 aperture: $27.2''$.

[1] Poulain & Nieto (1994) write: "Foreground stars, when visible through the eye-piece, were measured through the smallest aperture available (10.9 arcsec [in diameter /BMJ]) and their contribution subtracted at a later stage." In their Table 1a, they note whether the given galaxy had one or more stars subtracted. The two galaxies in common with our study had no stars subtracted.

[2] Burstein et al. (1987) write: "Separate observations of contaminating stars are noted [in their Table 2 /BMJ] by asterisks in the columns headed by "Run" and "N" (notes); star observations always refer to the immediately preceding galaxy observation." One of the four galaxies in common with our study, R256, had one star subtracted.

[3] Sandage (1975) writes: "Contaminating stars were were present in some of the apertures as notes in Table 1. Measurements of the stars alone, using smaller apertures, are listed where appropriate. Contamination-free colors and magnitudes were calculated for the final reduction." One of the two galaxies in common with our study, R256, had one star subtracted.

- van den Bergh (1977): Photoelectric photometry (although this is not explicitly stated) in Johnson U. Magnitudes probably not cleaned cleaned for foreground stars and other galaxies (no information is given about this). 3 galaxies in common: R234, R256, and R269. 1–4 apertures: 2.5″, 5.0″, 7.5″, and 10.0″.
- Weedman (1976): Photoelectric photometry in Johnson U. Magnitudes probably not cleaned for foreground stars and other galaxies, but the used aperture is also quite small. 3 galaxies in common: R234, R256, and R269. 1 aperture: 8.25″.

The result of the external comparisons is given in Table 4.3 and Figure 4.4.

Table 4.3: External Comparison of Aperture Magnitudes

Gunn r

Source	$N_{\rm gal}$	$N_{\rm ap}$	N	mean	rms
JFK92, 6″	3	1	3	0.026 ± 0.001	0.002
JFK92, 10″	3	1	3	0.025 ± 0.004	0.007
JFK95a, 6″	14	1	14	0.010 ± 0.005	0.018
JFK95a, 10″	14	1	14	0.017 ± 0.004	0.015
Poulain & Nieto (1994)	2	5	10	$0.018^{\rm b} \pm 0.014$	0.045
Poulain & Nieto (1994)[a]	2	4–5	9	$0.007^{\rm b} \pm 0.010$	0.031

Johnson B

Source	$N_{\rm gal}$	$N_{\rm ap}$	N	mean	rms
Burstein et al. (1987)	4	3	12	-0.052 ± 0.020	0.071
Burstein et al. (1987)[a]	4	2–3	11	-0.067 ± 0.017	0.052
JFK92, 6″	3	1	3	-0.015 ± 0.001	0.003
JFK92, 10″	3	1	3	-0.022 ± 0.008	0.015
Poulain & Nieto (1994)	2	5	10	0.016 ± 0.014	0.045
Poulain & Nieto (1994)[a]	2	4–5	9	0.005 ± 0.009	0.027

Johnson U

Source	$N_{\rm gal}$	$N_{\rm ap}$	N	mean	rms
Poulain & Nieto (1994)	1	4	4	0.07 ± 0.05	0.09
Poulain & Nieto (1994)[a]	1	3	3	0.02 ± 0.01	0.02
Sandage (1975)	2	1	2	-0.19 ± 0.03	0.04
van den Bergh (1977)[c]	3	1–4	7	-0.06 ± 0.07	0.18
Weedman (1976)	3	1	3	0.01 ± 0.01	0.01

Notes: $N_{\rm gal}$ is the number of galaxies in common with the given source in the given filter. $N_{\rm ap}$ is the number of apertures pr. galaxy. N is the total number of data points. 'rms' is the root mean square standard deviation. The uncertainty on the mean has been calculated as $\mathrm{rms}/\sqrt{N}$. The differences have been calculated as "our"–"literature".
[a] Outermost aperture of R256, which may have contamination from R269, omitted. [b] The expected offset between Gunn r and Kron-Cousins R of $0\overset{\rm m}{.}354$ (Jørgensen 1994) has been subtracted. [c] The one data value marked ":" in van den Bergh (1977) was omitted.

Regarding tablenote 'a': The following support the conclusion that the magnitude for R256 for the largest aperture of Poulain & Nieto (1994) and Burstein et al. (1987) is significantly contaminated by signal from R269. Their largest aperture is approximately 45″, and the separation

between R256 and R269 is approximately 101″. At $r \approx 56''$ our data give a Johnson B surface brightness of $\mu(56'') = 23.6^{\rm m}/{\rm arcsec}^2$ for R269, and $\mu(56'') = 25.8^{\rm m}/{\rm arcsec}^2$ for R256.

The rms scatter of $0\overset{\rm m}{.}18$ for the Johnson U comparison with van den Bergh (1977) is mostly due to the R269 magnitude within the 2.5″ aperture, where the difference is $+0\overset{\rm m}{.}34$. This can be explained by the following. The galaxy has dust in the center, which can be seen in our images (which have good seeing). The dust causes problems in finding the appropriate center to use for the aperture photometry. Even if we and van den Bergh (1977) have used the same center, a positive magnitude difference will show up if we have better seeing than van den Bergh. Besides, we had overlapping ellipses out to $r = 2.7''$ when fitting this galaxy, and it is not clear what the impact is on $m_{\rm circ}(r)$.

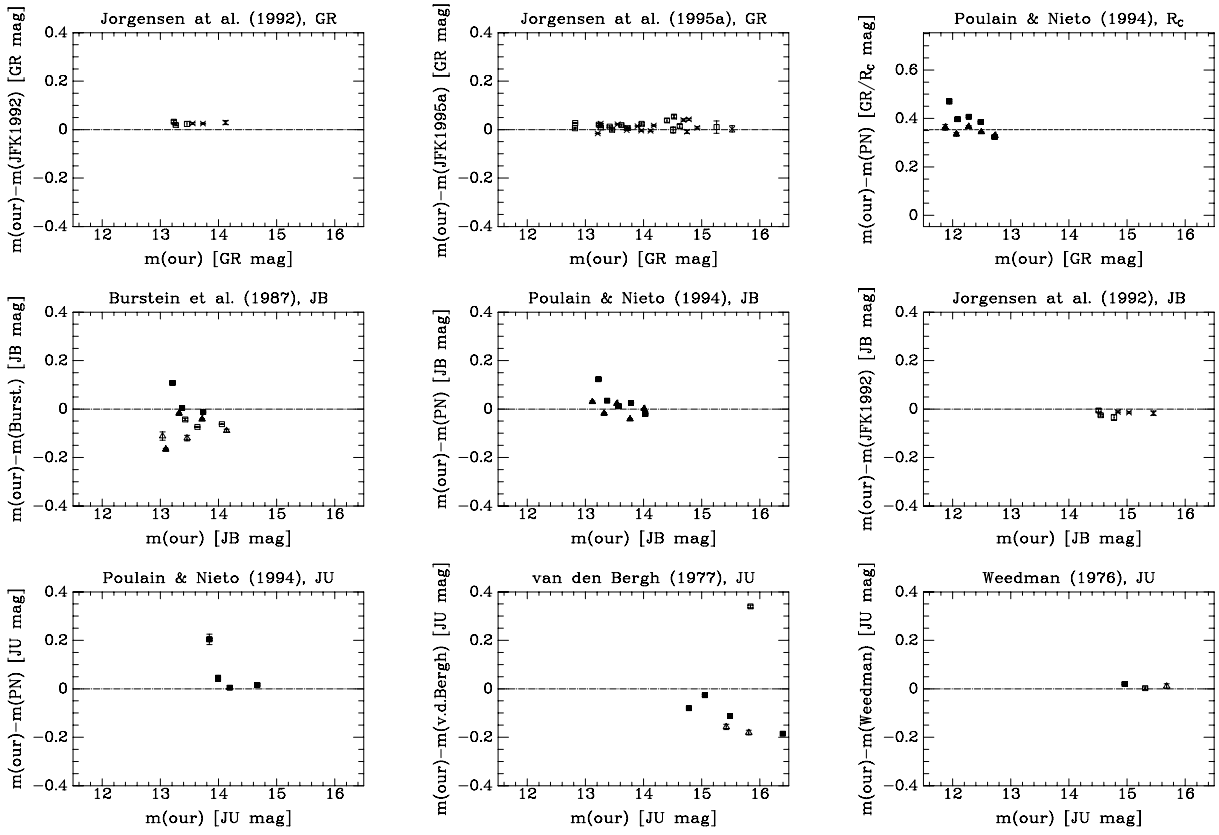

Figure 4.4: External comparison of aperture magnitudes. All the comparisons listed in Table 4.3 are shown in the figure, expect the one with Sandage (1975), which only has two data points. Data symbols for JFK plots: Boxes – 10″ aperture; crosses – 6″ aperture. Data symbols for other plots: Open box – R234; filled box – R256; open triangle – R269; filled triangle – R347.

From the above comparison we conclude that the magnitude zero point is consistent with literature data within $0\overset{\rm m}{.}02 \pm 0\overset{\rm m}{.}01$ for Gunn r, $-0\overset{\rm m}{.}02 \pm 0\overset{\rm m}{.}03$ for Johnson B, and $0\overset{\rm m}{.}00 \pm 0\overset{\rm m}{.}05$ for Johnson U.

4.5.2 Comparison of Surface Brightness Profiles

We compared surface brightness profiles with JFK92, JFK95a, and Jedrzejewski (1987). The plots of $\Delta\mu = \mu_{\rm our} - \mu_{\rm literature}$ vs. $\log(r/{\rm arcsec})$ are shown in Figure 4.5–4.9.

There is a good agreement with JFK92 and JFK95a. The only discrepancy is for R269. This discrepancy could not be fully explained by the hypothesis that we estimated the sky background level too *low*, since we can not move our sky level above the level found in the galaxy profile. We found, that the discrepancy could be fully explained by the hypothesis that JFK92 and JFK95a estimated the sky background level too *high* by 5%–9%, see Fig. 4.10. This is likely since they had a smaller field of view than we did, and since R269 is a very extended galaxy.

The comparisons with Jedrzejewski (1987) shows problems with the sky determination. This has been seen in other studies that has compared with Jedrzejewski, e.g. JFK95a.

Jedrzejewski (1987) obtained photometry in Johnson R ($R_{\rm J}$). We calculate the expected offset with Gunn r (r) as follows. Jørgensen (1994) found

$$r - R_{\rm C} = 0.354 \ , \tag{4.8}$$

where $R_{\rm C}$ is Kron-Cousins R. Davis et al. (1985) found

$$R_J = R_{\rm C} - 0.12(B - R_{\rm C}) - 0.07 \ . \tag{4.9}$$

Combining these two yields

$$r - R_{\rm J} = 0.12(B - r) + 0.47 \ . \tag{4.10}$$

Inserting a typical galaxy color of $(B-r) = 1\overset{\rm m}{.}15$ gives a typical offset between Gunn r and Johnson R of $(r - R_{\rm J}) = 0\overset{\rm m}{.}60$. This has been used in Fig. 4.7.

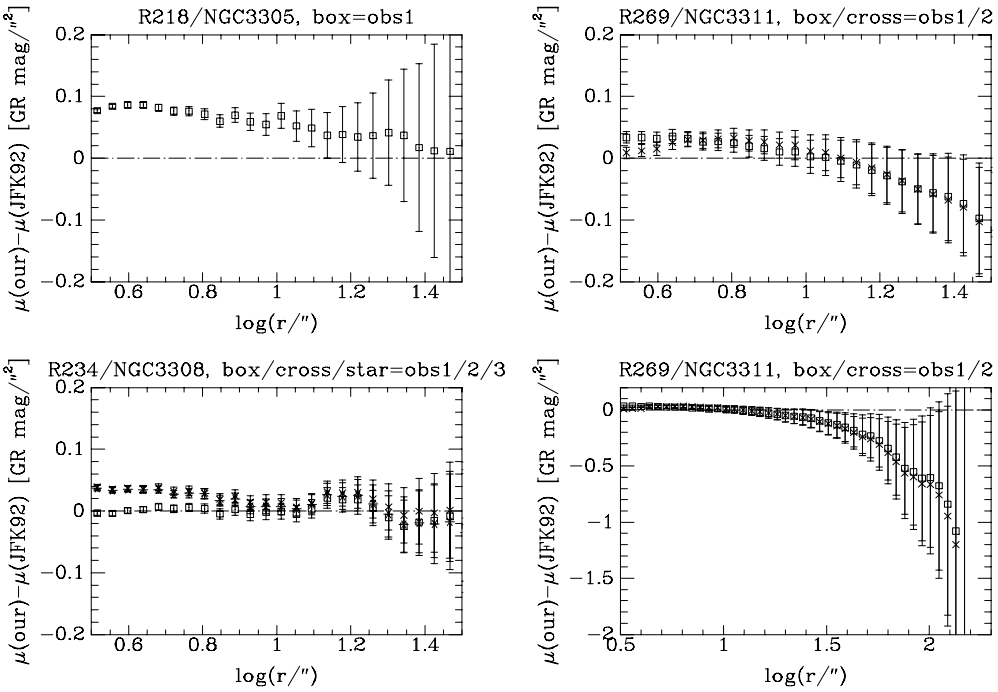

Figure 4.5: Comparison with JFK92, Gunn r. Note, that R269 appears twice, with different scales.

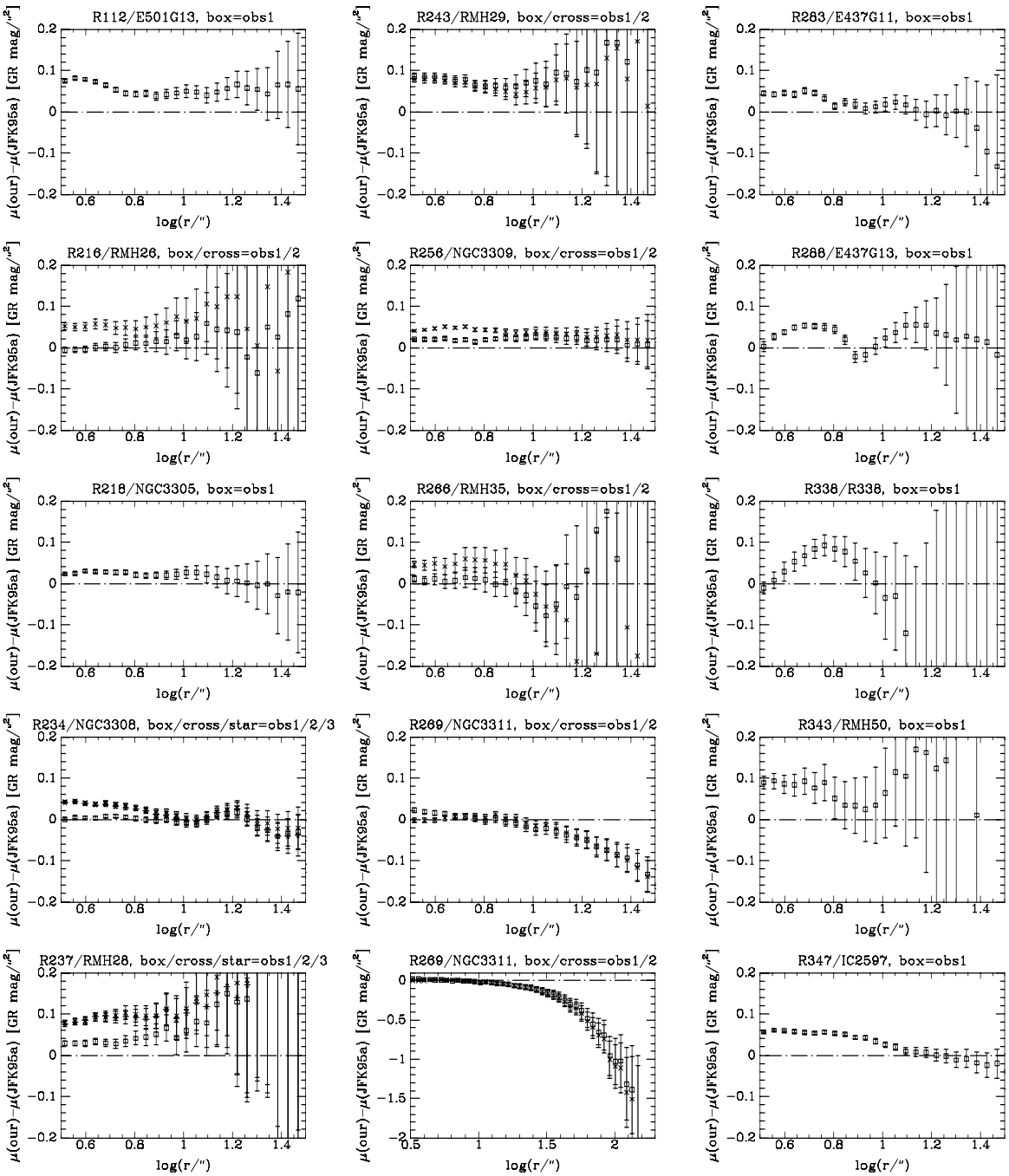

Figure 4.6: Comparison with JFK95a, Gunn r. Note, that R269 appears twice, with different scales.

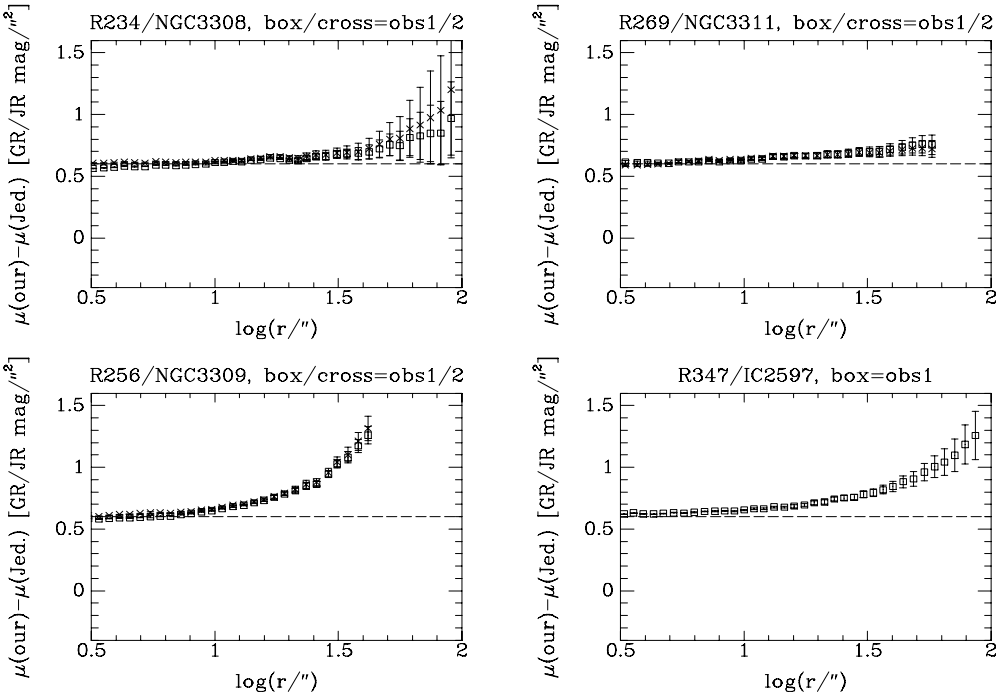

Figure 4.7: Comparison with Jedrzejewski (1987), Johnson R. The expected offset between Gunn r and Johnson R is 0.60 mag (see text).

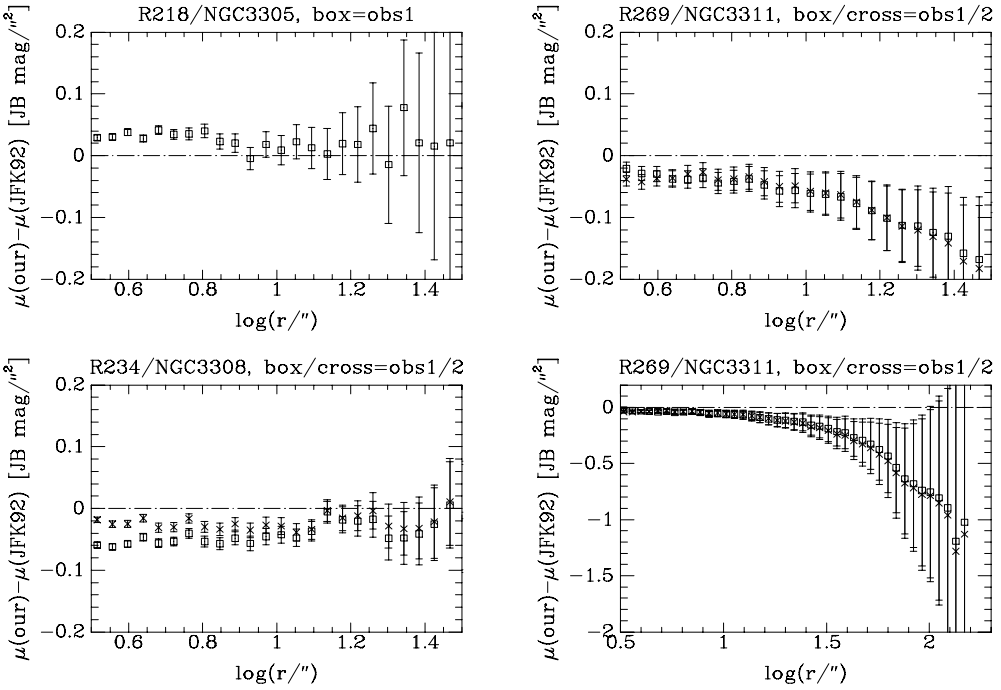

Figure 4.8: Comparison with JFK92, Johnson B. Note, that R269 appears twice, with different scales.

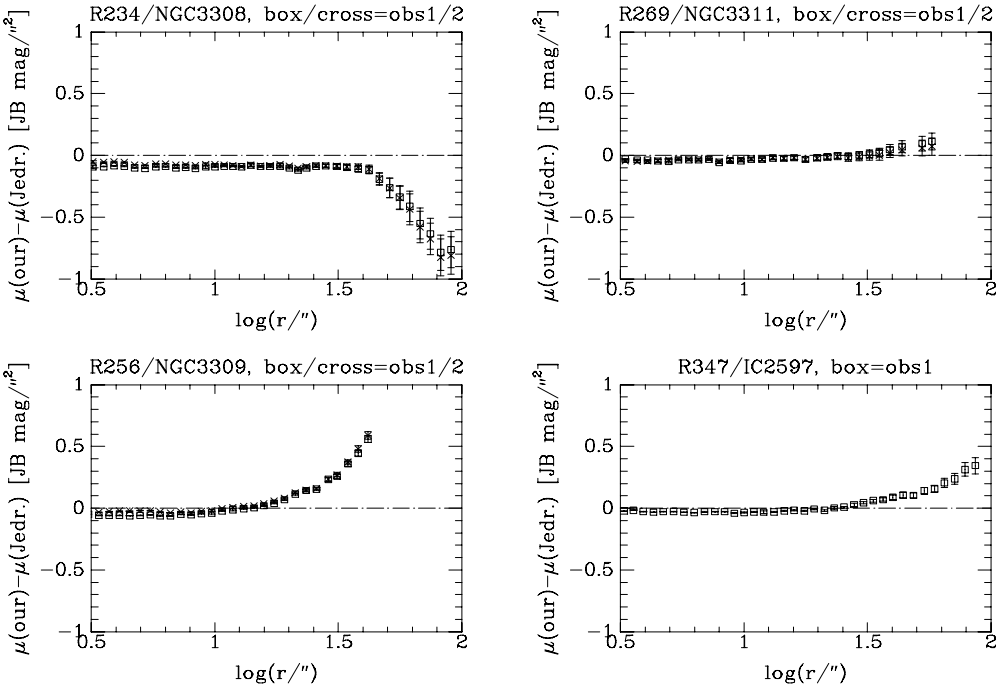

Figure 4.9: Comparison with Jedrzejewski (1987), Johnson B.

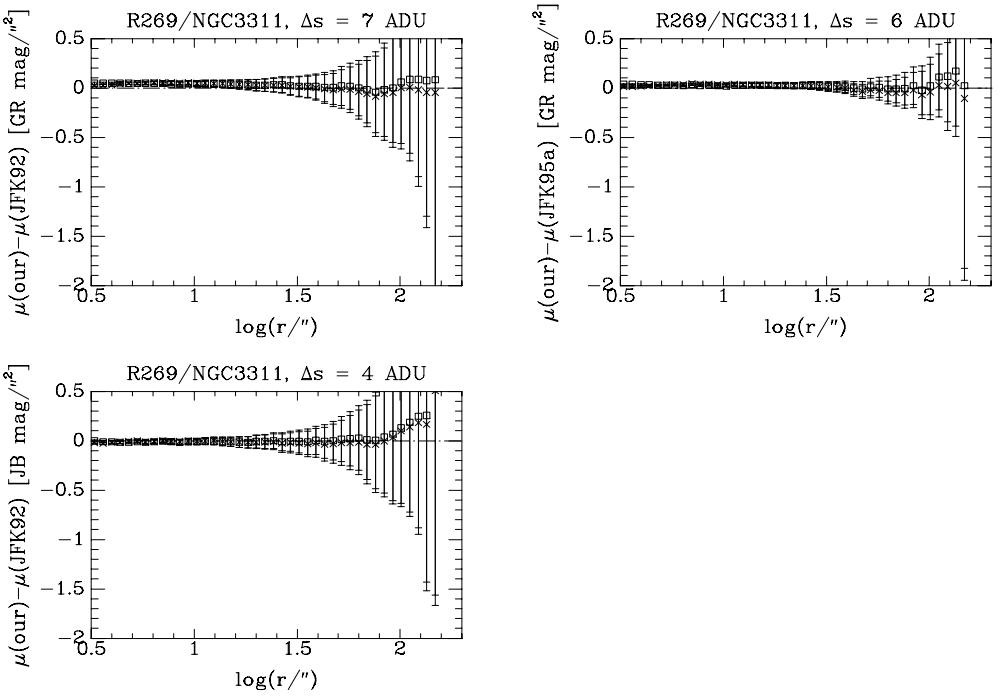

Figure 4.10: The effect of sky change for JFK92 and JFK95a. In these plots we have changed the sky background level that went into the calculation of the surface brightnesses of JFK92 and JFK95a by the amount Δs to achieve $\mu \approx 0$ at large radii. The 3 values of Δs needed were 7, 4, and 6 ADU, corresponding to relative changes of 5%, 9%, and 8%, respectively. In other words, the discrepancies for R269 seen in Figure 4.5, 4.6, and 4.8 can be explained by the hypothesis that JFK92 and JFK95a estimated the sky background level too high by 5%–9%.

Chapter 5

Global Photometric Parameters

5.1 Effective Parameters

For each of the 227 observations, we derived effective radius, $r_{\rm e}$, and mean surface brightness within this radius, $<\mu>_{\rm e}$, by fitting an $r^{1/4}$ growth curve to the observed aperture magnitudes, $m_{\rm ell}(r)$. Only radii in the interval from $3\cdot$FWHM to the radius where the uncertainty on $m_{\rm ell}$ exceeded $0\overset{\rm m}{.}15$ were used for the fit. (FWHM is the seeing, cf. Sect. 3.3.) This applies to 215 of the observations. For 10 observations the minimum radius was decreased to $2.5\cdot$FWHM, and for 2 observation also the maximum allowed uncertainty on $m_{\rm ell}$ was increased to $0\overset{\rm m}{.}2$. In this way, there was always at least 6 data points available for the fit.

It is important to take the seeing into account when deriving $r_{\rm e}$ and $<\mu>_{\rm e}$ (Saglia et al. 1993; see also JFK95a). We do this following JFK95a. First an initial guess on $r_{\rm e}$ is obtained from a fit that does not take the seeing into account. From the resulting $r_{\rm e}$ and the seeing of the data an intelligent guess on the real (i.e. seeing deconvolved) $r_{\rm e}$ is calculated. An $r^{1/4}$ growth curve corresponding to this $r_{\rm e}$ is then convolved with a model PSF that is scaled to the seeing of the data. This growth curve is fitted to the data, giving a new estimate of $r_{\rm e}$. The process is iterated until $\log r_{\rm e}$ is stable to within 0.005. Then $<\mu>_{\rm e}$ is calculated. Since the seeing convolved growth curve depends on $r_{\rm e}$ it is important to have a good guess on $r_{\rm e}$ to start with, which is why we calculate the above 'intelligent guess'. The model PSF is taken to be the Fourier transform of $\exp[-(kb)^{5/3}]$ (cf. Wolf 1982; Saglia et al. 1993), which is the theoretical prediction for seeing caused by atmospheric turbulence. b is a scale factor that is proportional to the FWHM.

From the definition of $r_{\rm e}$ and $<\mu>_{\rm e}$ it follows that the total magnitude $m_{\rm T}$ is given by $m_{\rm T} = <\mu>_{\rm e} - 5\log r_{\rm e} - 2.5\log 2\pi$.

At the effective radius in Gunn r the ellipticity $\varepsilon_{\rm e}$ and position angle $\rm PA_e$ were determined.

We determined effective colors $(B-r)_{\rm e}$ and $(U-r)_{\rm e}$ as

$$(B-r)_{\rm e} \equiv [B_{\rm ell}(r_{\rm e,Gunn\,r}) - r_{\rm ell}(r_{\rm e,Gunn\,r})] \quad (5.1)$$

$$(U-r)_{\rm e} \equiv [U_{\rm ell}(r_{\rm e,Gunn\,r}) - r_{\rm ell}(r_{\rm e,Gunn\,r})] \quad (5.2)$$

where $r_{\rm ell}$, $B_{\rm ell}$, and $U_{\rm ell}$ simply are $m_{\rm ell}$ in Gunn r, Johnson B, and Johnson U, respectively. $r_{\rm e,Gunn\,r}$ is the effective radius in Gunn r, and for galaxies observed more than once in Gunn r the mean value was used. $m_{\rm ell}$ in the three filters were interpolated using a quadratic function to give the values at $r_{\rm e,Gunn\,r}$. Note that the elliptical apertures in the different filters are not forced to be the same, but will of course be almost the same. Had we used circular apertures instead of elliptical ones the colors would remain almost the same – the typical difference for $(B-r)_{\rm e}$ would be only $0\overset{\rm m}{.}004$.

5.2 Isophotal Parameters

At the $\mu = 21.85^{\rm m}/{\rm arcsec}^2$ isophote in Gunn r we determined the ellipticity, $\varepsilon_{21.85}$. JF94 found that $\varepsilon_{21.85}$ was better determined than $\varepsilon_{\rm e}$ for their data and therefore used $\varepsilon_{21.85}$ in their analysis. They also found that $\varepsilon_{21.85}$ was close to the maximum ellipticity for disky galaxies for their Coma sample. For disky galaxies, the ellipticity varies substantially with radius, see e.g. the $\varepsilon(r)$ profile for R266 on p. 261. In Fig. 5.1 we compare $\varepsilon_{21.85}$ with $\varepsilon_{\rm e}$ for the 64 HydraI galaxies in our sample. It is seen that the two ellipticities in most cases agree well, although there is significant intrinsic scatter in the relation. For the analysis of our HydraI data, it will not be important whether we use $\varepsilon_{\rm e}$ or $\varepsilon_{21.85}$ as measure of the ellipticity. The two very deviating galaxies at $\varepsilon_{\rm e} \approx 0.1$ and $\varepsilon_{21.85} \approx 0.35$ are R225 and R327, both SB0 galaxies with an ellipticity that varies rapidly with radius. This can be seen from the $\varepsilon(r)$ profiles on p. 257 and p. 265 – the two galaxies both have $\log r_{\rm e} \approx 1.0$ and $\log r_{21.85} \approx 0.8$ (with r in arcsec).

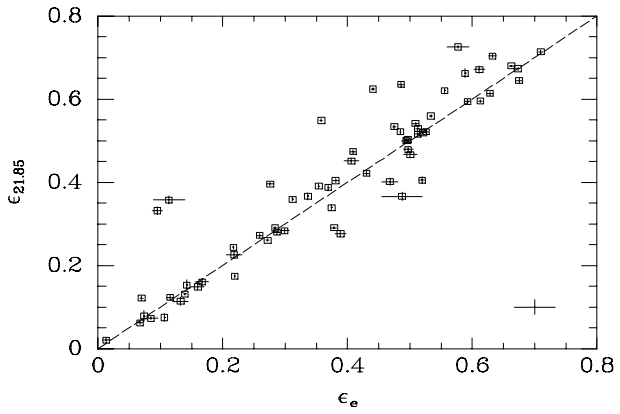

Figure 5.1: Comparison of $\varepsilon_{21.85}$, the ellipticity at the $\mu = 21.85^{\rm m}/{\rm arcsec}^2$ isophote, and $\varepsilon_{\rm e}$, the ellipticity at the effective radius. Both quantities refer to Gunn r. The dashed line marks the one to one correspondence. For galaxies observed several times, the mean values are used. The individual internal error bars are shown, and in the lower right corner the typical error bars based on the internal comparison (i.e. rms/$\sqrt{2}$ from Table 5.1, p. 56) are shown.

5.3 Parameters Quantifying the Global Deviations From Ellipses

We determined parameters that quantify the *global* deviations from elliptical isophotes in Gunn r. From the Fourier coefficient profiles $s_n(r)$ and $c_n(r)$ we determined intensity-weighted mean Fourier coefficients $<s_n>$ and $<c_n>$ as

$$<s_n> = \frac{\int_{r_{\rm min}}^{r_{\rm max}} I(r) \cdot s_n(r)\,{\rm d}r}{\int_{r_{\rm min}}^{r_{\rm max}} I(r)\,{\rm d}r}\,, \quad <c_n> = \frac{\int_{r_{\rm min}}^{r_{\rm max}} I(r) \cdot c_n(r)\,{\rm d}r}{\int_{r_{\rm min}}^{r_{\rm max}} I(r)\,{\rm d}r}\,, \quad n = 1, \ldots, 6\ . \tag{5.3}$$

Uncertainties are calculated on basis of min-max variations in $s_n(r)$ and $c_n(r)$, respectively. Following JF94, we used $r_{\rm min} = 2 \cdot {\rm FWHM}$ and $r_{\rm max}$ as the radius where $\mu = 23.35^{\rm m}/{\rm arcsec}^2$. This ensures that seeing effects are small and that the signal-to-noise is sufficient.

We determined a characteristic value of $c_4(r)$, denoted c_4, as the mean value of the three points around the extremum of $c_4(r)$. In case of no well-defined extremum, the mean value of the three points around the effective radius was used. This is the definition used by JF94 and JFK95a. We only looked for an extremum in the radius interval from $2 \cdot {\rm FWHM}$ to the radius where the uncertainty on μ exceeded $0.5^{\rm m}/{\rm arcsec}^2$. We calculated the uncertainty on c_4 as half the min-max variation of the 3 points. A few of the galaxies had a minimum and a maximum in the $c_4(r)$-profile of comparable amplitude. In these cases we still calculated c_4 at the extremum with the largest amplitude, and if a tie, at the most regular one. Examples are R194 (p. 254; $c_4 = -0.043$) and R238 (p. 258; $c_4 = -0.029$). Both galaxies are boxy at low radii, and disky further out. For 4 of the 64 galaxies we did not determine c_4, since it would be too uncertain ($\sigma_{c_4} > 0.05$). These galaxies had no extrema and $r_{\rm e}$ at or beyond the maximum radius used for the c_4 determination.

In Figure 5.2 we compare c_4 with $<c_4>$. The relation between them is $<c_4> = 0.33 \cdot c_4$ (dashed line). JF94 found $<c_4> = 0.6 \cdot c_4$ (dotted line). The discrepancy is likely due to the poorer spatial resolution of JF94, which affects c_4 but not $<c_4>$; see also Sect. 5.4. That $|<c_4>|$ per se is smaller than $|c_4|$ is because $<c_4>$ is integrated over a larger range in r than just the 3 points around the extremum as c_4 is. Some of the galaxies have quite different values of c_4 and $<c_4>$. For example, R188 (p. 253) and R250 (p. 259) have $c_4 \approx 0.07$ and $<c_4> \approx 0.01$, cf. Fig. 5.2(b). These two galaxies have a small $c_4(r)$ minimum at low radii and a large $c_4(r)$ maximum at large radii. Since $<c_4>$ is an *intensity-weighted* mean, $<c_4>$ is small for these galaxies, while c_4 is large.

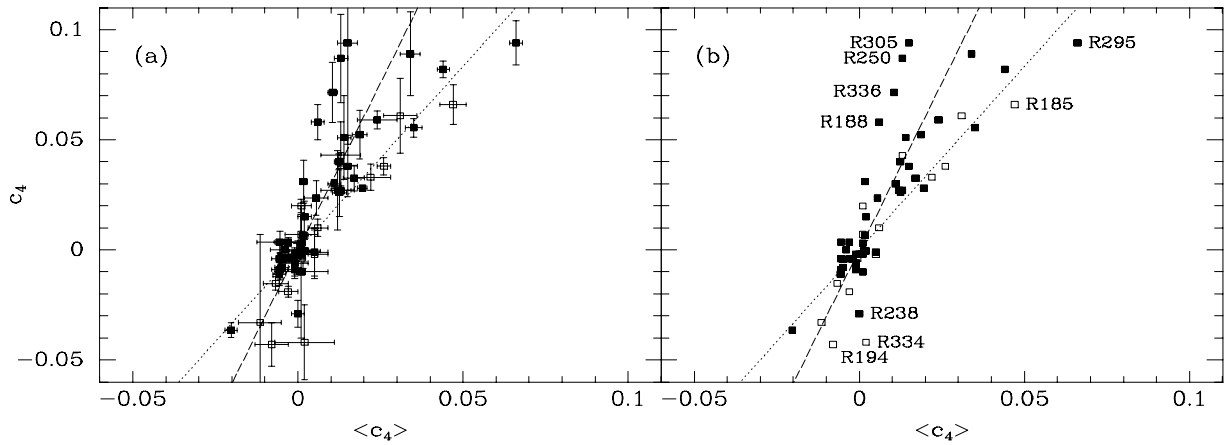

Figure 5.2: c_4 vs. $<c_4>$. Dashed line: $<c_4> = 0.33 \cdot c_4$ (our data). Dotted line: $<c_4> = 0.6 \cdot c_4$ (JF94). Filled/open boxes – galaxies with/without spectroscopy. (a): Individual error bars shown. (b): Galaxies that deviate from the median relation marked; see the $c_4(r)$-profiles in Ap. F (p. 251).

5.4 Internal Comparison of Global Photometric Parameters

We performed an internal comparison of the global photometric parameters. The result is shown in Table 5.1. The comparisons are also shown in Fig. 5.3–5.11. The data symbols are as follows: boxes – Gunn r; triangles – Johnson B; crosses – Johnson U. Each figure has two panels. In the left panel we plot the difference versus the first observation value. In the right panel we plot the difference versus the seeing difference, in order to check for seeing dependence. $\Delta \log r_{\rm e}$, $\Delta<\mu>_{\rm e}$, and $\Delta m_{\rm T}$ are correlated with Δ(seeing), see the right panels of Fig. 5.3, 5.4, and 5.7. Our $r^{1/4}$ fits did take the seeing into account, so perhaps the real PSF of our data has larger wings than the model PSF that we used. As a result, the individual error estimates for $\log r_{\rm e}$, $<\mu>_{\rm e}$, and $\varepsilon_{\rm e}$ are too low. This can be seen in the left panels of Fig. 5.3, 5.4, and 5.7 – the scatter is larger than what the individual error bars can account for.

The errors in $\log r_{\rm e}$ and $<\mu>_{\rm e}$ are highly correlated, cf. Fig. 5.12, with a linear correlation coefficient of $r = 0.99$. This is because $<\mu>_{\rm e}$ is the mean surface brightness within $r_{\rm e}$, so if $r_{\rm e}$ due to random errors is determined too large, $<\mu>_{\rm e}$ will correspondingly become too faint. This has the effect that the combination of $\log r_{\rm e}$ and $<\mu>_{\rm e}$ that enters the fundamental plane, approximately $\log r_{\rm e} - 0.328<\mu>_{\rm e}$, has a much lower uncertainty than $\log r_{\rm e}$ and $<\mu>_{\rm e}$ individually, cf. Table 5.1 and Fig. 5.5. The rms scatter for this combination is 0.012 in Gunn r, implying a typical internal uncertainty of only 0.008.

c_4 is also seeing dependent, in the expected sense that larger seeing makes $|c_4|$ smaller. See Fig. 5.9. Recall that $|c_4|$ is the *amplitude* of the observed extremum in the $c_4(r)$-profile. We found $<c_4>$ and $<c_6>$ *not* to be seeing dependent.

Table 5.1: Internal Comparison of Global Photometric Parameters

Gunn r

Parameter	N	mean	rms
$\log r_{\rm e}$	53	-0.037 ± 0.007	0.051
$<\mu>_{\rm e}$	53	-0.128 ± 0.023	0.170
"FP"	53	0.005 ± 0.002	0.012
$m_{\rm T}$	53	0.058 ± 0.013	0.095
$\varepsilon_{\rm e}$	53	-0.016 ± 0.006	0.047
$\varepsilon_{21.85}$	53	-0.015 ± 0.003	0.025
c_4	47	$(-3.2 \pm 12) \cdot 10^{-4}$	0.008
$\lvert c_4\rvert$	47	$(-28 \pm 11) \cdot 10^{-4}$	0.007
$<c_4>$	53	$(7.9 \pm 8.3) \cdot 10^{-4}$	0.006
$<c_6>$	53	$(4.9 \pm 5.5) \cdot 10^{-4}$	0.004

Johnson B

Parameter	N	mean	rms
$\log r_{\rm e}$	42	-0.053 ± 0.009	0.061
$<\mu>_{\rm e}$	42	-0.199 ± 0.033	0.214
"FP"	42	0.012 ± 0.002	0.014
$m_{\rm T}$	42	0.061 ± 0.016	0.102
$\varepsilon_{\rm e}$	42	-0.011 ± 0.008	0.050

Notes: "FP" $= \log r_{\rm e} - 0.328<\mu>_{\rm e}$.

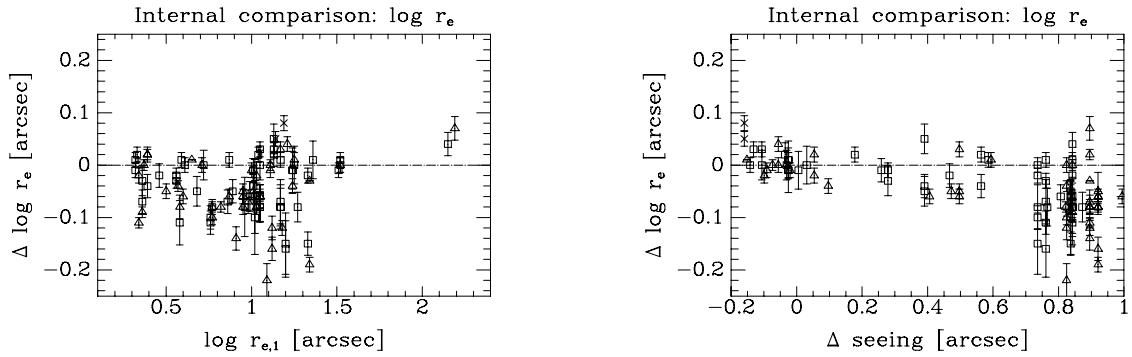

Figure 5.3: Internal comparison, $\log r_{\rm e}$

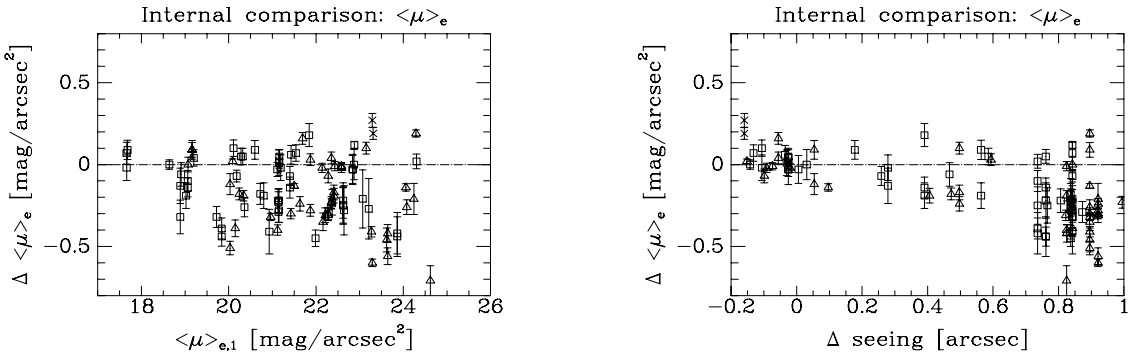

Figure 5.4: Internal comparison, $<\mu>_{\rm e}$

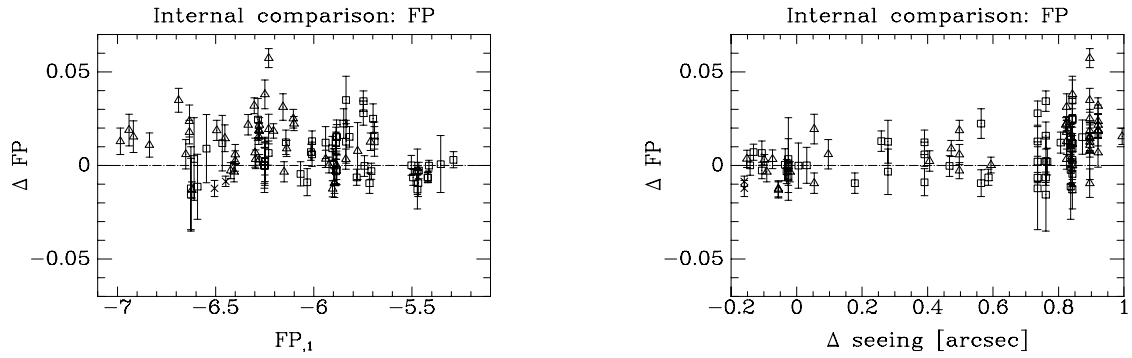

Figure 5.5: Internal comparison, "FP" $= \log r_{\rm e} - 0.328<\mu>_{\rm e}$

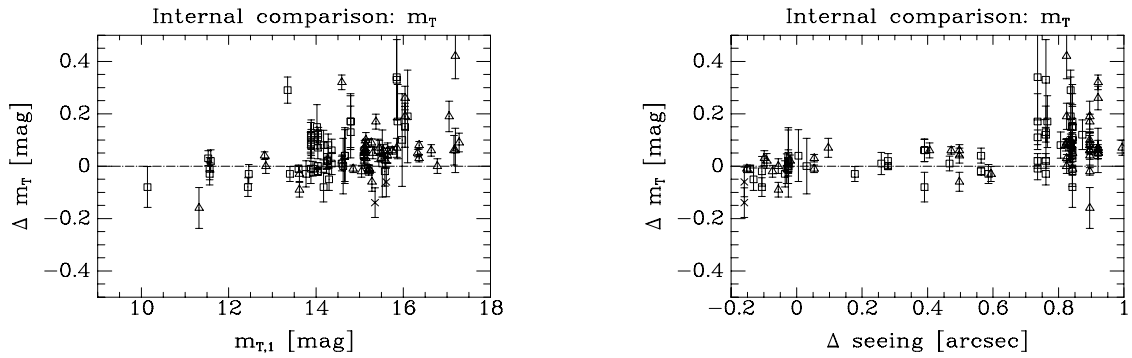

Figure 5.6: Internal comparison, $m_{\rm T}$

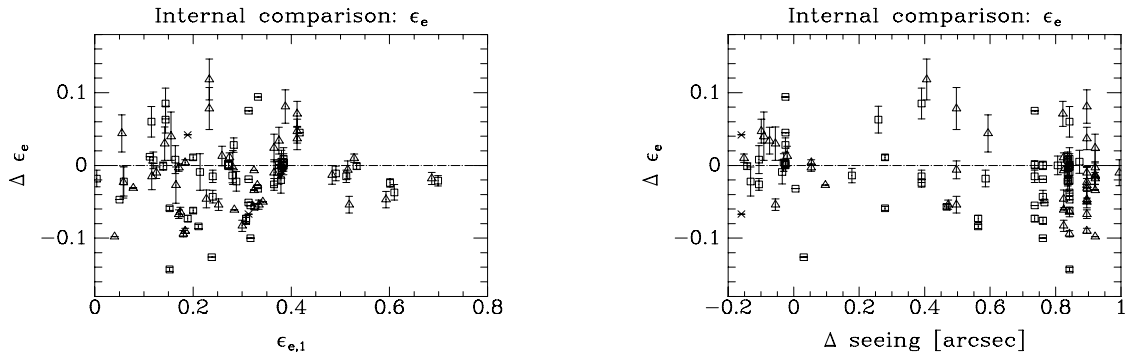

Figure 5.7: Internal comparison, ε_e

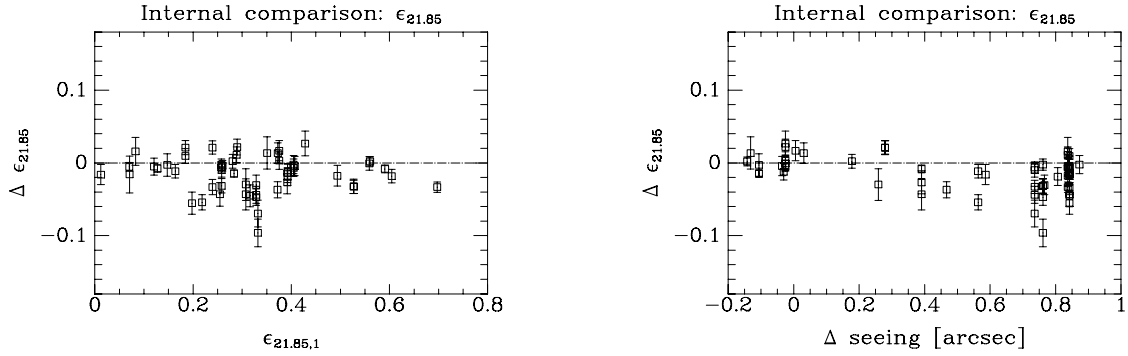

Figure 5.8: Internal comparison, $\varepsilon_{21.85}$

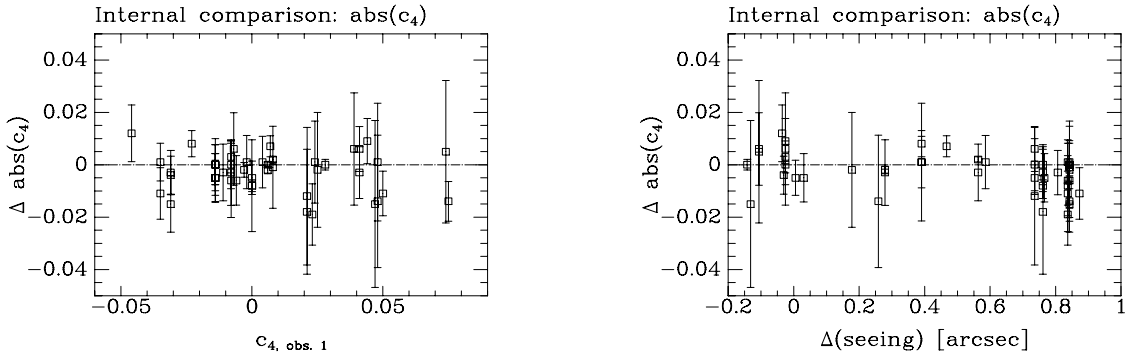

Figure 5.9: Internal comparison, $|c_4|$.

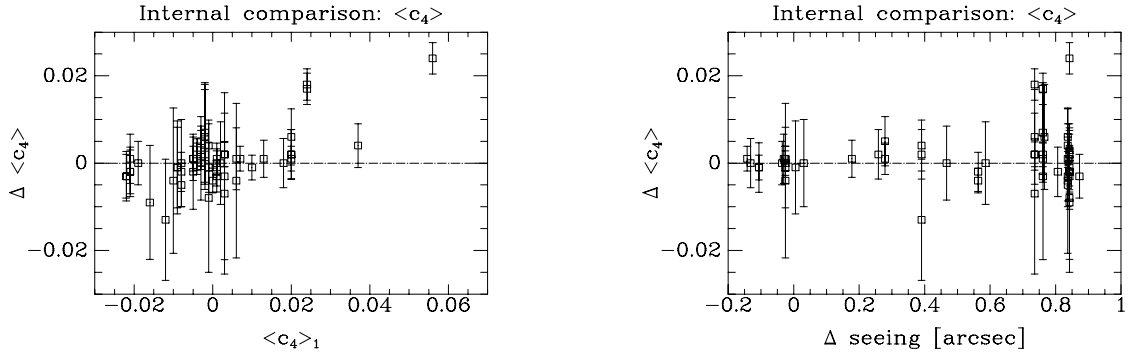

Figure 5.10: Internal comparison, $<c_4>$

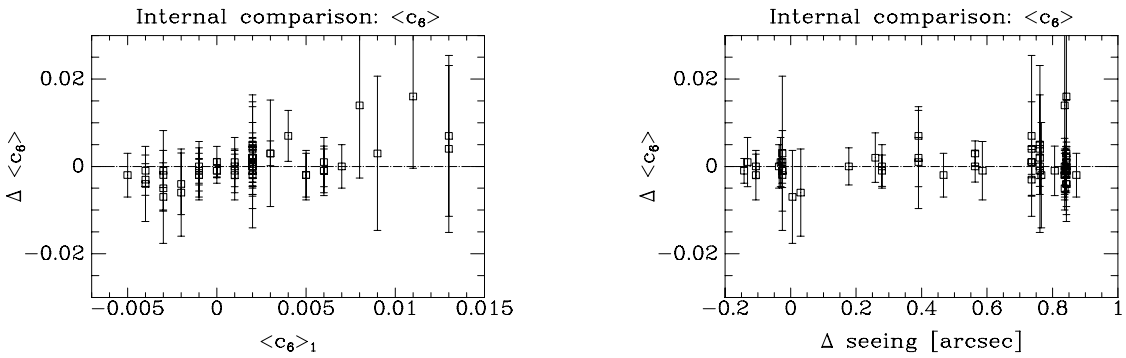

Figure 5.11: Internal comparison, $<c_6>$

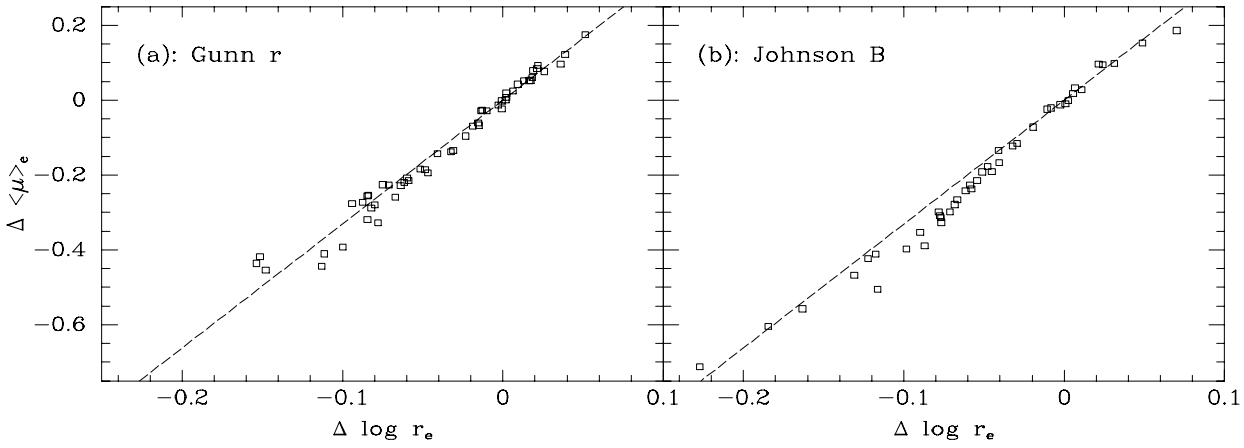

Figure 5.12: Correlation of the errors in $\log r_{\rm e}$ and $<\mu>_{\rm e}$, internal comparison. The dashed line is the expected relation, $\Delta \log r_{\rm e} = 0.302 \Delta <\mu>_{\rm e}$ (JFK95a). It is not clear why the Johnson B data deviate from the expected relation. The linear correlation coefficient r is 0.99 both for the Gunn r data and the Johnson B data.

5.5 External Comparison of Global Photometric Parameters

We compared our global photometric parameters in Gunn r with those from JFK95a. We have 14 galaxies in common, cf. Sect. 4.4 (p. 41). We calculate the differences as "our"−"JFK95a". The result is shown in Table 5.2, and in Fig. 5.14 and 5.15. The agreement is very good for 11 of the 14 galaxies. For R269, R338, and R343 the agreement is less good. These galaxies have been marked in some of the plots. Even for all 14 galaxies, no systematic differences are seen, and the derived typical external uncertainties (rms/$\sqrt{2}$) are low. In other words, our global photometric parameters are of very good quality. Note, however, that JFK95a used the same methods to derive global parameters as we did. We therefore expect a priori that the agreement with JFK95a is better than with authors that use completely different methods.

The correlation of the errors in $\log r_{\rm e}$ and $<\mu>_{\rm e}$ is shown in Fig. 5.13. The linear correlation coefficient is $r = 0.94$.

Table 5.2: External Comparison of Global Photometric Parameters, Gunn r

Source	Parameter	N	mean	rms
JFK95a	$\log r_{\rm e}$	14	0.006 ± 0.010	0.039
JFK95a	$<\mu>_{\rm e}$	14	0.027 ± 0.037	0.137
JFK95a	"FP"	14	-0.003 ± 0.004	0.016
JFK95a	$m_{\rm T}$	14	-0.002 ± 0.022	0.083
JFK95a	$\varepsilon_{\rm e}$	14	0.008 ± 0.006	0.023
JFK95a	$\varepsilon_{21.85}$	14	0.003 ± 0.004	0.016
JFK95a	c_4	14	-0.001 ± 0.002	0.007
JFK95a	$<c_4>$	14	-0.003 ± 0.002	0.008
JFK95a	$<c_6>$	14	-0.001 ± 0.000	0.001

Notes: "FP" $= \log r_{\rm e} - 0.328<\mu>_{\rm e}$.

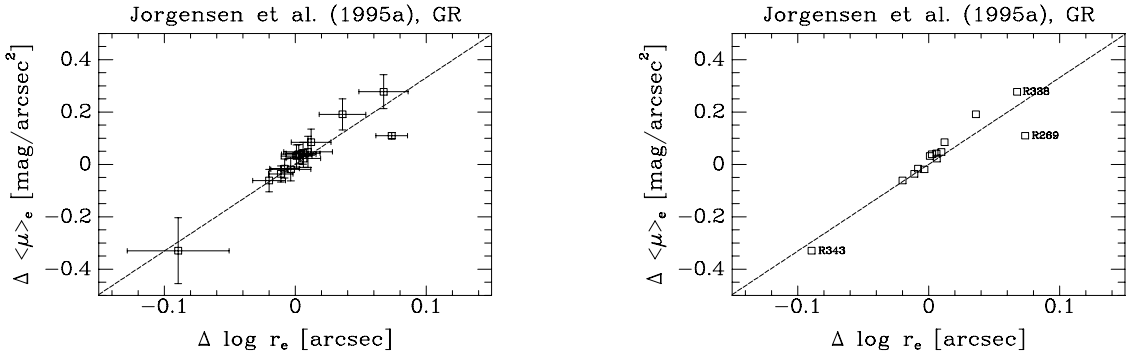

Figure 5.13: Correlation of the errors in $\log r_{\rm e}$ and $<\mu>_{\rm e}$, external comparison. The dashed line is the expected relation, $\Delta \log r_{\rm e} = 0.302\Delta<\mu>_{\rm e}$ (JFK95a). The linear correlation coefficient r is 0.94 for all 14 galaxies, and 0.95 when R269, R338, and R343 are omitted.
Left panel: with errorbars. Right panel: without errorbars.

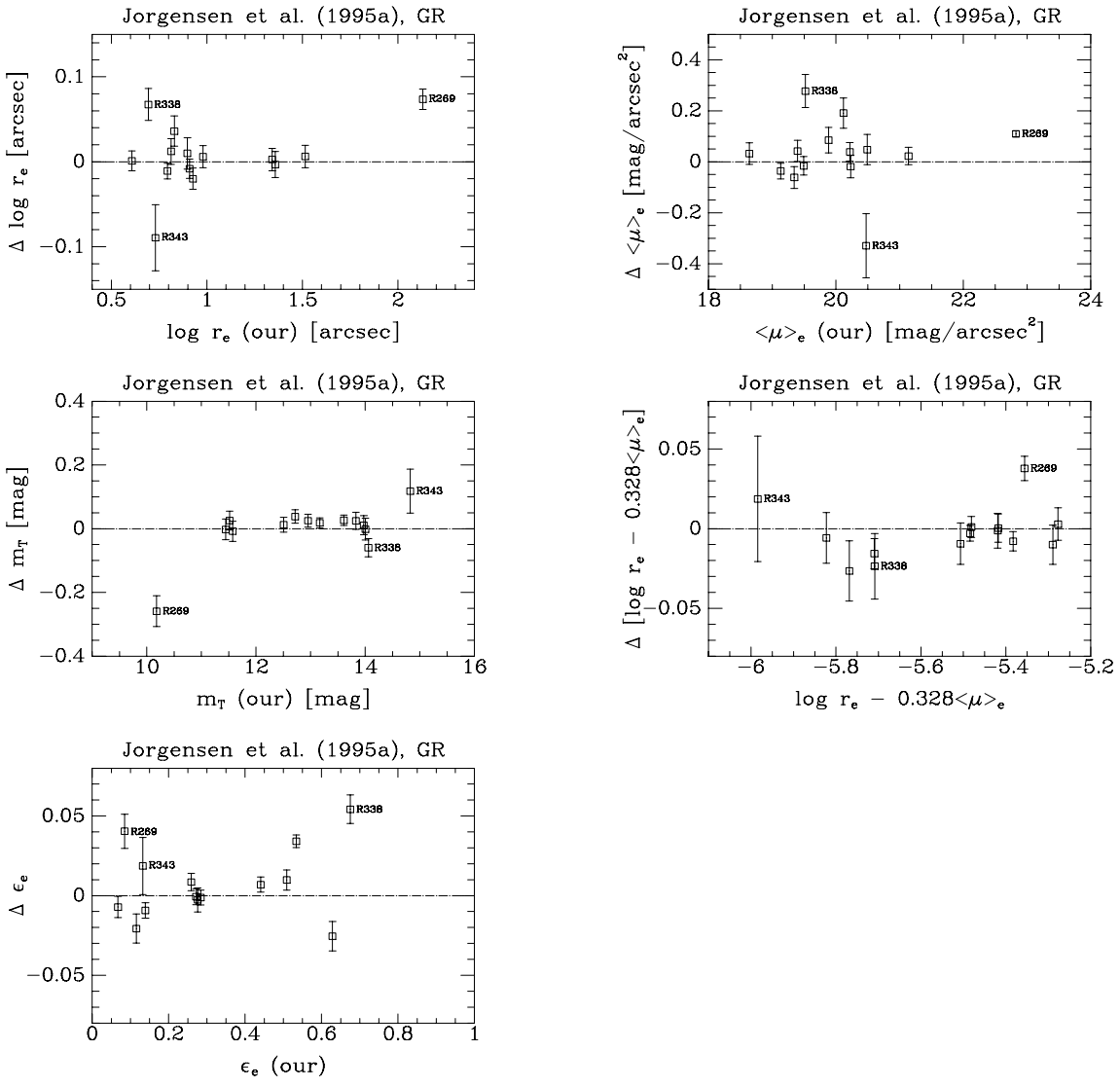

Figure 5.14: External comparison, $\log r_{\rm e}$, $<\mu>_{\rm e}$, $m_{\rm T}$, "FP" $= \log r_{\rm e} - 0.328<\mu>_{\rm e}$, and $\varepsilon_{\rm e}$.

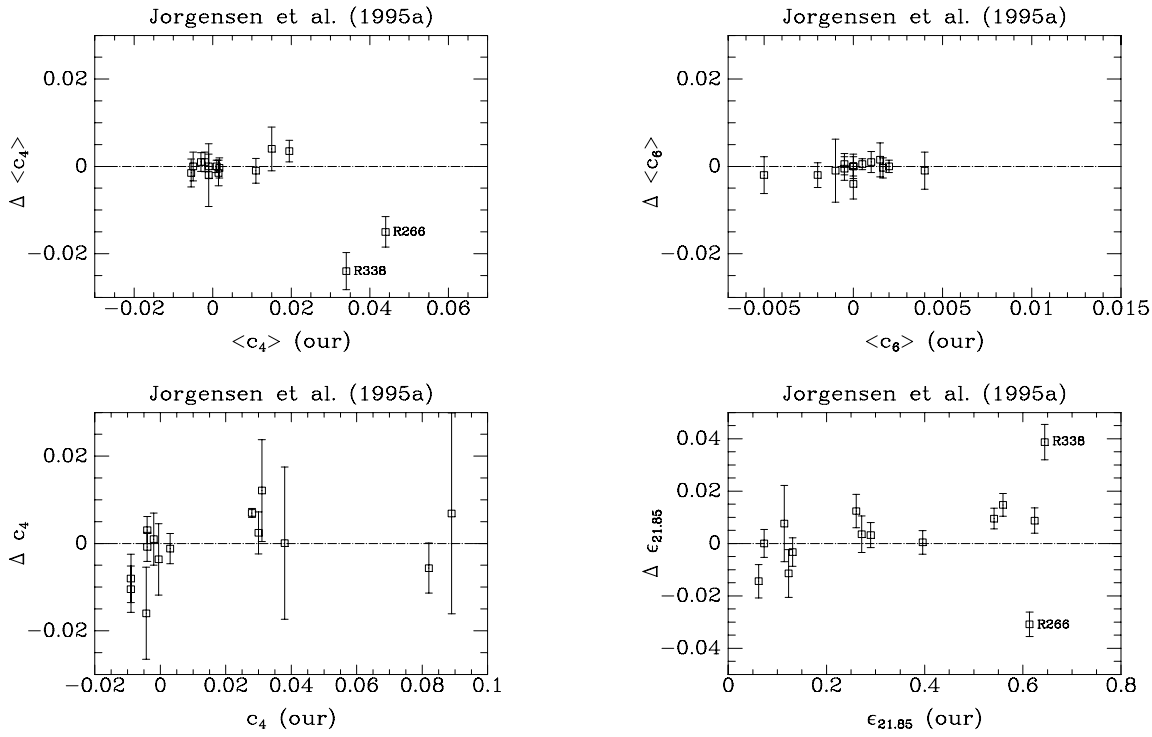

Figure 5.15: External comparison, $<c_4>$, $<c_6>$, $c4$, and $\varepsilon_{21.85}$.

5.6 Corrections to the Magnitudes

5.6.1 Galactic Extinction

We want to correct the galaxy magnitudes and surface brightnesses for galactic extinction (i.e. for the extinction that the Milky Way causes). The galactic extinction in a given filter can be calculated as a constant times the reddening, e.g. $A_B = 4 \cdot E(B-V)$.

Burstein & Heiles (1982) have produced reddening maps for almost the entire sky with $|b| > 10°$. The appropriate section for HydraI is shown in Figure 5.16. As can be seen, there is a strip with no data going right through HydraI. This is more clear in Figure 5.17. Here, the 64 sample galaxies are plotted in galactic coordinates. Overlaied are the values of A_B, calculated from the reddening from Burstein & Heiles (1982) as $4 \cdot E(B-V)$. The actual numbers come from the fortran function `extinction` which D. Burstein has made publicly available via anonymous ftp[1]. The data are given in pixels of size $0.3° \times 0.6°$ in (l, b).

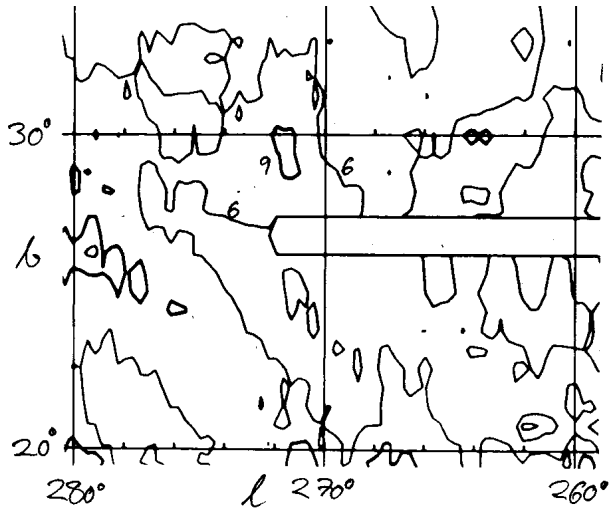

Figure 5.16: Burstein & Heiles (1982) reddening map for the HydraI area, from their Figure 4(b). The contour levels are labeled in units of 0.01 mag in $E(B-V)$ in intervals of 0.03 mag. The rectangle at $b = 26.8°$ is probably due to an absence of HI data within this outlined region. In such a region, no reddening prediction is made. HydraI is centered at $(l, b) = (269.6°, 26.5°)$.

The IRAS 100μ flux did not show a strong correlation with the Burstein & Heiles (1982) A_B values. Therefore, we did not use the IRAS data to determine A_B.

The following scheme was used to determine the extinction for the 64 sample galaxies: For the 30 galaxies located pixels for which Burstein & Heiles (1982) *do* make a reddening prediction, the value in that pixel was used, i.e. no interpolation was done. For the 34 galaxies located pixels for which Burstein & Heiles (1982) do *not* make a reddening prediction, i.e. for the galaxies with $26.494° \leq b < 27.094°$, a linear interpolation between the values just below and above was done:

$$A_B = 4 \cdot E(B-V) = \begin{cases} 0.1965 + x \cdot (0.2445 - 0.1965); & 268.497° < l \leq 268.797° \\ 0.1885 + x \cdot (0.2565 - 0.1885); & 268.797° < l \leq 269.097° \\ 0.1725 + x \cdot (0.2605 - 0.1725); & 269.097° < l \leq 269.397° \\ 0.1645 + x \cdot (0.2685 - 0.1645); & 269.397° < l \leq 269.697° \\ 0.1605 + x \cdot (0.2805 - 0.1605); & 269.697° < l \leq 269.997° \end{cases} \tag{5.4}$$

[1] `ftp://samuri.la.asu.edu/pub/redcats`

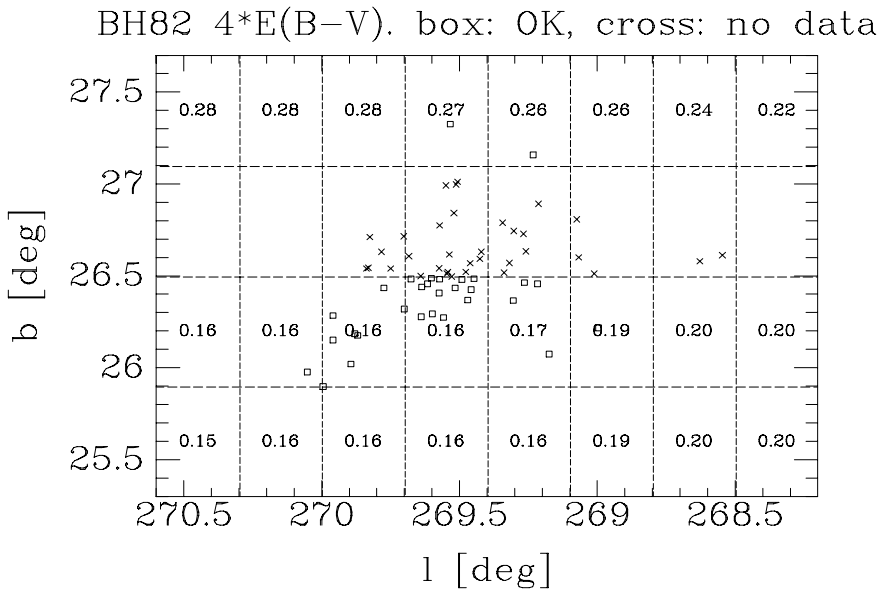

Figure 5.17: The sample galaxies and the Burstein & Heiles extinction values. The 64 sample galaxies are shown as either boxes or crosses. The crosses are the galaxies without a reddening determination from Burstein & Heiles (1982). The overplotted numbers are $A_B = 4 \cdot E(B-V)$, as output from the computer program that corresponds to the Burstein & Heiles (1982) data. Note that there are no data for the pixels with $b = 26.8°$.

where we have used the auxiliary quantity x:

$$x = \frac{b - 26.194°}{1.2°}. \tag{5.5}$$

Which pixel a given value of (l, b) belongs to is calculated by `extinction` as the integer values of $[l/0.3 + 1.01]$ and $[(b - 10.)/0.6 + 1.51]$. From these expressions the limits on l (and b) given in Eq. (5.4) can be derived.

An example of what the interpolation looks like is shown in Figure 5.18. It is unfortunate, that the missing data should appear in a place, where the extinction is changing rapidly.

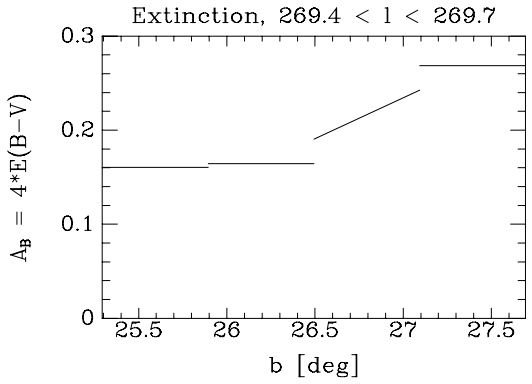

Figure 5.18: An example of the adopted extinction as a function of b. The data are from the fortran function `extinction` that represents the data of Burstein & Heiles (1982). The sloping segment of the curve is given by the 4th branch of the interpolation equation, Eq. (5.4).

Burstein & Heiles (1984) give $A_B = 4 \cdot E(B-V)$ for the galaxies in RC2 (de Vaucouleurs, de Vaucouleurs, & Corwin 1976) and UGC (Nilson 1973), with $E(B-V)$ calculated in almost the same way as in Burstein & Heiles (1982). Of our 34 sample galaxies in the Burstein & Heiles (1982) no data strip, four are in Burstein & Heiles (1984). All four have $A_B = 0.32$ listed, with a note that they are in areas without HI data, and that an interpolation to neighboring HI values have been done. Since the neighboring pixels have $A_B = 0.28$ at most (cf. Fig. 5.17) it is strange how these authors can get $A_B = 0.32$.

Eight galaxies in the no data strip are in common with JFK95a. These authors list $A_B = 0.17$ for all eight galaxies, quoting Burstein & Heiles (1982, 1984).

We conclude that our interpolation scheme is more sensible to do use than either $A_B = 0.17$ or $A_B = 0.32$ for the galaxies in the no data strip.

We calculate the extinction in Gunn r (A_r) and Johnson U (A_U) from A_B following Seaton (1979), see Table 5.3. The extinction values for the HydraI galaxies are given in Table 5.5.

Table 5.3: Galactic Extinction in the Different Filters

Filter	Galactic extinction	Reference
Gunn r	$0.625A_B$	Seaton (1979)
Johnson B	A_B	
Johnson U	$1.183A_B$	Seaton (1979)

5.6.2 k-correction

The magnitudes and surface brightnesses were also k-corrected. For Johnson B and U we used the k-correction given by Pence (1976), see Table 5.4. We used a linear interpolation in $z_{\rm hel}$. All the HydraI galaxies have $z_{\rm hel}$ in the range 0.00–0.02. For Gunn r we used the k-correction $2.5\log(1+z_{\rm hel})$ from JFK92. The value at $z_{\rm hel} = 0.02$ is listed in Table 5.4 for comparison with Johnson B and U. For the 8 galaxies without a measured redshift, the cluster mean of $cz_{\rm hel} = 3718$ km/s (Zabludoff et al. 1990) was used. The k-corrections for the HydraI galaxies are given in Table 5.5.

Table 5.4: k-corrections for E and S0 Galaxies

Filter	k-correction at $z_{\rm hel} = 0.02$	Reference
Gunn r	0.022	JFK92
Johnson B	0.092	Pence (1976)
Johnson U	0.065	Pence (1976)

Notes: The values from Pence (1976) assume a galactic extinction at the galactic poles of zero.

5.6.3 Cosmological Dimming

The surface brightnesses were corrected for cosmological dimming by subtracting $10\log(1+z_{\rm CMB})$, where $z_{\rm CMB}$ is the cluster CMB redshift. HydraI has $cz_{\rm CMB} = 4050$ km/s (Zabludoff et al. 1990).

TABLE 5.5
CORRECTIONS TO THE MAGNITUDES

Galaxy		$cz_{\rm hel}$	Ref.	BH data	Gunn r			Johnson B			Johnson U		
					$A_{\rm r}$	$k_{\rm r}$	$\rm cor_r$	$A_{\rm B}$	$k_{\rm B}$	$\rm cor_B$	$A_{\rm U}$	$k_{\rm U}$	$\rm cor_U$
R112	E501G13	3520	J+D	no	0.13	0.01	0.20	0.21	0.05	0.33	0.25	0.04	0.35
R120	···	3718[a]	···	no	0.13	0.01	0.20	0.21	0.06	0.33	0.25	0.04	0.35
R129	···	3371	R	yes	0.12	0.01	0.19	0.19	0.05	0.30	0.22	0.04	0.32
R138	···	3768	R	yes	0.11	0.01	0.18	0.17	0.06	0.29	0.20	0.04	0.30
R166	E501G20	4353	J+D	no	0.13	0.02	0.20	0.21	0.07	0.33	0.24	0.05	0.35
R185	···	3718[a]	···	no	0.13	0.01	0.20	0.21	0.06	0.33	0.25	0.04	0.35
R188	E501G21	4575	J+D	yes	0.11	0.02	0.18	0.17	0.07	0.30	0.20	0.05	0.31
R193	E501G26	3718[a]	···	yes	0.11	0.01	0.18	0.17	0.06	0.29	0.20	0.04	0.30
R194	···	4424	R	yes	0.11	0.02	0.18	0.17	0.07	0.30	0.20	0.05	0.31
R202	···	2453	R	no	0.14	0.01	0.21	0.22	0.04	0.32	0.26	0.03	0.35
R209	···	4155	S	no	0.12	0.01	0.20	0.20	0.06	0.32	0.23	0.05	0.34
R211	···	3707	S	no	0.13	0.01	0.20	0.20	0.06	0.32	0.24	0.04	0.34
R212	E501G27	3230	J+D	no	0.13	0.01	0.19	0.20	0.05	0.31	0.24	0.04	0.33
R213	···	3583	J+D	yes	0.10	0.01	0.17	0.16	0.05	0.28	0.19	0.04	0.29
R214	···	4069	S	yes	0.10	0.01	0.18	0.16	0.06	0.29	0.19	0.04	0.30
R216	A1033−27	2286	J+D	yes	0.10	0.01	0.17	0.16	0.04	0.26	0.19	0.02	0.28
R217	···	4895	J+D	yes	0.10	0.02	0.18	0.16	0.08	0.30	0.19	0.05	0.31
R218	N3305	3976	J+D	no	0.13	0.01	0.20	0.21	0.06	0.33	0.25	0.04	0.35
R219	···	4188	J+D	yes	0.10	0.02	0.18	0.16	0.06	0.29	0.19	0.05	0.30
R224	N3307	3762	J+D	yes	0.10	0.01	0.17	0.16	0.06	0.28	0.19	0.04	0.29
R225	···	3522	J+D	yes	0.10	0.01	0.17	0.16	0.05	0.28	0.19	0.04	0.29
R226	···	3718[a]	···	yes	0.10	0.01	0.17	0.16	0.06	0.28	0.19	0.04	0.29
R231	···	3685	J+D	no	0.13	0.01	0.20	0.21	0.06	0.33	0.25	0.04	0.35
R234	N3308	3547	J+D	no	0.12	0.01	0.19	0.19	0.05	0.31	0.23	0.04	0.32
R237	···	3006	J+D	no	0.12	0.01	0.19	0.20	0.05	0.30	0.24	0.03	0.33
R238	E501G35	4190	J+D	no	0.14	0.02	0.21	0.22	0.06	0.35	0.26	0.05	0.37
R239	I629	2796	J+D	yes	0.10	0.01	0.17	0.16	0.04	0.27	0.19	0.03	0.28
R241	···	3718[a]	···	no	0.12	0.01	0.19	0.20	0.06	0.31	0.23	0.04	0.33
R243	···	3357	J+D	no	0.13	0.01	0.20	0.20	0.05	0.31	0.24	0.04	0.33
R245	···	4783	J+D	no	0.12	0.02	0.19	0.19	0.07	0.32	0.23	0.05	0.34
R250	E437G08	4392	J+D	yes	0.10	0.02	0.17	0.16	0.07	0.29	0.19	0.05	0.30
R252	E437G09	3681	J+D	yes	0.10	0.01	0.17	0.16	0.06	0.28	0.19	0.04	0.29
R253	···	4686	J+D	no	0.12	0.02	0.20	0.19	0.07	0.32	0.23	0.05	0.34
R254	···	4662	J+D	no	0.14	0.02	0.21	0.22	0.07	0.35	0.26	0.05	0.36
R255	···	3193	LC	no	0.12	0.01	0.19	0.19	0.05	0.30	0.23	0.03	0.32
R256	N3309	4086	J+D	yes	0.10	0.01	0.18	0.16	0.06	0.29	0.19	0.04	0.30
R261	···	3807	J+D	yes	0.10	0.01	0.17	0.16	0.06	0.28	0.19	0.04	0.29
R266	A1034−27A	4759	J+D	yes	0.10	0.02	0.18	0.16	0.07	0.30	0.19	0.05	0.30
R268	···	3640	S	yes	0.10	0.01	0.17	0.16	0.06	0.28	0.19	0.04	0.29
R269	N3311	3868	J+D	yes	0.10	0.01	0.18	0.16	0.06	0.28	0.19	0.04	0.29
R273	···	2731	J+D	no	0.12	0.01	0.19	0.19	0.04	0.29	0.23	0.03	0.32
R278	···	4478	LC	no	0.13	0.02	0.20	0.20	0.07	0.33	0.24	0.05	0.34
R283	E437G11	4897	J+D	yes	0.10	0.02	0.18	0.16	0.08	0.29	0.19	0.05	0.30
R286	···	5626	S	no	0.12	0.02	0.20	0.19	0.09	0.34	0.23	0.06	0.35
R288	E437G13	3561	J+D	yes	0.10	0.01	0.17	0.16	0.05	0.27	0.19	0.04	0.29
R293	···	4482	J+D	yes	0.10	0.02	0.18	0.16	0.07	0.29	0.19	0.05	0.30
R295	E437G15	2725	J+D	yes	0.10	0.01	0.17	0.16	0.04	0.26	0.19	0.03	0.27
R305	···	4033	J+D	yes	0.10	0.01	0.17	0.16	0.06	0.28	0.19	0.04	0.29
R307	···	3924	R	yes	0.16	0.01	0.24	0.26	0.06	0.38	0.31	0.04	0.41
R308	···	4103	J+D	yes	0.10	0.01	0.17	0.16	0.06	0.28	0.19	0.04	0.29
R316	E501G47	4838	J+D	no	0.13	0.02	0.20	0.20	0.07	0.33	0.24	0.05	0.35
R317	N3315	3779	J+D	no	0.14	0.01	0.21	0.22	0.06	0.34	0.26	0.04	0.36
R319	···	4460	J+D	no	0.13	0.02	0.21	0.21	0.07	0.34	0.25	0.05	0.36
R322	E501G49	4063	J+D	no	0.12	0.01	0.19	0.20	0.06	0.32	0.23	0.04	0.33
R327	···	4213	J+D	yes	0.10	0.02	0.17	0.16	0.06	0.28	0.19	0.05	0.29
R334	E501G52	3718[a]	···	no	0.13	0.01	0.20	0.21	0.06	0.33	0.25	0.04	0.35
R336	N3316	3962	J+D	no	0.12	0.01	0.19	0.20	0.06	0.31	0.23	0.04	0.33
R337	···	3718[a]	···	no	0.12	0.01	0.19	0.20	0.06	0.31	0.23	0.04	0.33
R338	···	3075	J+D	no	0.15	0.01	0.22	0.23	0.05	0.34	0.28	0.03	0.37
R340	···	3718[a]	···	no	0.13	0.01	0.20	0.20	0.06	0.32	0.24	0.04	0.34
R343	···	4372	J+D	no	0.15	0.02	0.22	0.24	0.07	0.36	0.28	0.05	0.38
R347	I2597	2983	J+D	no	0.15	0.01	0.22	0.23	0.05	0.34	0.28	0.03	0.37
R359	···	5247	LC	no	0.13	0.02	0.21	0.21	0.08	0.35	0.25	0.06	0.37
R389	···	3432	R	yes	0.17	0.01	0.24	0.27	0.05	0.38	0.32	0.04	0.41

NOTE.— $cz_{\rm hel}$ is in km/s. References for $cz_{\rm hel}$: 'J+D' – variance weighted mean of JFK95b and DFOSC; 'LC' – Lucey & Carter (1988); 'R' – Richter (1989); 'S' – Stein (1996). 'BH data' indicates whether Burstein & Heiles (1982) give a reddening prediction. $A_{\rm x}$, $k_{\rm x}$, and $\rm cor_x$ is the galactic extinction, the k-correction, and the total correction, respectively, in passband 'x'. The total correction includes the cosmological dimming, which for HydraI is 0.06.
[a] – the listed $cz_{\rm hel}$ value is the cluster mean (from Zabludoff et al. 1990).

5.7 The Final HydraI Global Photometric Parameters

The global photometric parameters in Gunn r are given in Table 5.6. The global photometric parameters in Johnson B and Johnson U, including the effective colors, are given in Table 5.7. For galaxies observed more than once, the unweighted mean values are given. Likewise, the unweighted mean values of the uncertainties are given, calculated from the usual propagation of errors formula. Recall, that the internal uncertainties are too low for $\log r_{\rm e}$, $<\mu>_{\rm e}$, and $\varepsilon_{\rm e}$, as shown in the internal comparison, Sect. 5.4 (p. 56).

The total magnitudes are not listed in the tables. They can be calculated as $m_{\rm T} = <\mu>_{\rm e} - 5\log r_{\rm e} - 2.5\log 2\pi$.

TABLE 5.6
GLOBAL PHOTOMETRIC PARAMETERS IN GUNN r

Galaxy		$\log r_e$	$<\mu>_e$	ε_e	$\varepsilon_{21.85}$	c_4	$<c_4>$	$<c_6>$
R112	E501G13	0.93±0.01	19.14±0.03	0.509±0.004	0.541±0.003	0.030	0.011	0.000
R120	···	0.89±0.03	21.57±0.08	0.556±0.000	0.620±0.005	0.033	0.022	0.001
R129	···	0.57±0.01	18.63±0.04	0.475±0.002	0.534±0.004	0.010	0.006	0.003
R138	···	0.73±0.01	19.69±0.05	0.409±0.005	0.474±0.004	0.020	0.001	−0.001
R166	E501G20	1.03±0.01	20.35±0.03	0.287±0.005	0.280±0.005	0.026	0.013	−0.001
R185	···	0.77±0.01	20.29±0.05	0.673±0.004	0.673±0.004	0.066	0.047	−0.007
R188	E501G21	0.96±0.01	19.83±0.03	0.632±0.006	0.704±0.005	0.058	0.006	−0.004
R193	E501G26	1.41±0.02	22.27±0.04	0.577±0.018	0.725±0.003	0.061	0.031	−0.007
R194	···	0.89±0.01	20.24±0.03	0.593±0.005	0.594±0.005	−0.043	−0.008	0.005
R202	···	0.55±0.01	18.72±0.02	0.663±0.004	0.680±0.000	0.038	0.026	−0.001
R209	···	1.23±0.01	22.61±0.03	0.312±0.000	0.359±0.005	−0.015	−0.007	0.000
R211	···	0.75±0.02	21.08±0.06	0.485±0.001	0.521±0.005	−0.002	0.005	0.005
R212	E501G27	1.22±0.02	21.81±0.05	0.497±0.008	0.479±0.005	−0.001	0.005	0.002
R213	···	0.92±0.01	20.64±0.03	0.710±0.003	0.714±0.004	0.056	0.035	0.000
R214	···	0.70±0.01	20.72±0.04	0.613±0.003	0.595±0.003	−0.019	−0.003	0.001
R216	A1033−27	0.90±0.01	20.32±0.03	0.116±0.006	0.123±0.006	−0.009	−0.005	0.002
R217	···	0.58±0.01	18.96±0.02	0.358±0.002	0.549±0.004	0.040	0.012	−0.003
R218	N3305	0.98±0.01	19.19±0.03	0.067±0.004	0.062±0.004	−0.004	−0.002	0.000
R219	···	1.11±0.01	21.58±0.04	0.519±0.005	0.405±0.008	0.004	−0.005	0.001
R224	N3307	1.40±0.01	22.04±0.02	0.497±0.005	0.502±0.007	0.032	0.017	0.002
R225	···	1.03±0.01	21.30±0.02	0.095±0.008	0.332±0.009	0.052	0.019	0.001
R226	···	1.07±0.04	23.17±0.09	0.106±0.000	0.075±0.010	···	−0.008	0.001
R231	···	0.85±0.02	20.97±0.07	0.468±0.013	0.401±0.009	0.027	0.012	0.001
R234	N3308	1.51±0.01	20.95±0.02	0.272±0.002	0.260±0.003	0.031	0.002	0.002
R237	···	0.83±0.01	19.92±0.02	0.259±0.004	0.272±0.004	−0.004	−0.005	0.001
R238	E501G35	1.13±0.01	20.26±0.03	0.526±0.004	0.521±0.004	−0.029	0.000	0.001
R239	I629	1.02±0.01	21.07±0.04	0.299±0.007	0.283±0.006	−0.004	−0.005	−0.000
R241	···	1.31±0.02	23.95±0.04	0.369±0.000	0.387±0.007	···	0.006	0.009
R243	···	0.61±0.00	18.44±0.02	0.534±0.002	0.559±0.003	0.028	0.019	−0.001
R245	···	1.09±0.01	21.07±0.03	0.381±0.005	0.404±0.004	−0.036	−0.020	0.006
R250	E437G08	0.96±0.01	19.86±0.03	0.611±0.009	0.671±0.008	0.087	0.013	−0.001
R252	E437G09	1.02±0.01	20.27±0.03	0.521±0.003	0.519±0.003	0.051	0.014	0.000
R253	···	1.31±0.02	22.29±0.04	0.389±0.009	0.276±0.008	0.023	0.005	0.000
R254	···	1.38±0.02	22.97±0.04	0.336±0.000	0.366±0.008	···	0.005	0.003
R255	···	0.39±0.01	18.85±0.04	0.217±0.002	0.243±0.004	−0.011	−0.006	0.002
R256	N3309	1.34±0.01	20.04±0.02	0.139±0.003	0.131±0.003	−0.004	−0.003	0.001
R261	···	1.39±0.04	22.96±0.09	0.487±0.032	0.366±0.010	−0.010	0.001	0.001
R266	A1034−27A	0.81±0.01	19.71±0.03	0.628±0.005	0.614±0.005	0.082	0.044	0.000
R268	···	1.00±0.03	22.61±0.08	0.374±0.000	0.339±0.007	−0.033	−0.012	0.002
R269	N3311	2.13±0.01	22.65±0.01	0.085±0.011	0.073±0.003	−0.000	0.002	−0.001
R273	···	0.32±0.01	17.45±0.03	0.219±0.001	0.174±0.004	0.007	0.002	0.002
R278	···	0.35±0.03	19.22±0.10	0.070±0.003	0.122±0.006	−0.002	0.001	0.002
R283	E437G11	0.91±0.01	19.32±0.03	0.276±0.005	0.396±0.003	−0.009	−0.001	−0.002
R286	···	1.05±0.03	22.97±0.09	0.074±0.000	0.078±0.013	···	0.003	0.003
R288	E437G13	0.79±0.01	18.96±0.02	0.440±0.004	0.624±0.004	0.038	0.015	0.004
R293	···	0.64±0.02	20.96±0.07	0.218±0.012	0.225±0.008	0.000	−0.004	−0.002
R295	E437G15	0.82±0.01	18.31±0.02	0.486±0.005	0.635±0.007	0.094	0.066	0.002
R305	···	0.93±0.01	20.10±0.03	0.501±0.011	0.467±0.007	0.094	0.015	−0.003
R307	···	1.30±0.02	22.75±0.05	0.142±0.000	0.153±0.012	0.043	0.013	−0.001
R308	···	0.47±0.01	18.77±0.04	0.354±0.001	0.391±0.006	0.004	−0.003	−0.004
R316	E501G47	1.20±0.01	20.69±0.03	0.513±0.003	0.529±0.003	0.015	0.002	−0.001
R317	N3315	1.16±0.01	20.09±0.03	0.013±0.006	0.020±0.007	−0.001	0.002	−0.001
R319	···	0.81±0.02	20.66±0.05	0.513±0.005	0.516±0.005	0.027	0.013	0.000
R322	E501G49	0.90±0.01	20.21±0.04	0.494±0.007	0.500±0.007	−0.006	−0.001	−0.003
R327	···	1.02±0.03	21.17±0.08	0.114±0.025	0.357±0.009	0.059	0.024	0.007
R334	E501G52	1.92±0.01	23.76±0.00	0.588±0.000	0.662±0.011	−0.042	0.002	0.013
R336	N3316	1.12±0.01	19.87±0.03	0.378±0.004	0.290±0.002	0.072	0.010	0.001
R337	···	0.72±0.01	21.01±0.04	0.160±0.010	0.149±0.008	−0.004	−0.001	0.002
R338	···	0.69±0.01	19.30±0.03	0.675±0.005	0.645±0.005	0.089	0.034	−0.005
R340	···	0.70±0.03	20.88±0.08	0.167±0.010	0.160±0.009	0.007	0.001	0.000
R343	···	0.73±0.02	20.25±0.05	0.132±0.013	0.114±0.010	−0.002	−0.001	−0.001
R347	I2597	1.36±0.01	20.01±0.03	0.284±0.003	0.290±0.003	0.003	0.001	0.002
R359	···	0.67±0.01	19.58±0.03	0.430±0.004	0.422±0.005	−0.008	−0.005	−0.002
R389	···	1.19±0.02	22.15±0.05	0.406±0.012	0.451±0.007	−0.002	0.000	0.001

NOTE.— r_e is in arcsec. Typical uncertainties on c_4, $<c_4>$, and $<c_6>$ are 0.006, 0.003, and 0.003, respectively.

TABLE 5.7

GLOBAL PHOTOMETRIC PARAMETERS IN JOHNSON B AND JOHNSON U

Galaxy		Johnson B			Johnson U		
		$\log r_e$	$<\mu>_e$	$(B-r)_e$	$\log r_e$	$<\mu>_e$	$(U-r)_e$
R112	E501G13	0.96±0.01	20.39±0.02	1.13±0.00	... ...	... ...	... ...
R120	...	0.87±0.02	22.47±0.05	0.97±0.02	... ...	... ...	... ...
R129	...	0.56±0.01	19.68±0.02	1.12±0.00	... ...	... ...	... ...
R138	...	0.74±0.01	20.88±0.02	1.13±0.00	... ...	... ...	... ...
R166	E501G20	1.11±0.00	21.81±0.01	1.16±0.00	... ...	... ...	... ...
R185	...	0.73±0.01	21.13±0.03	1.01±0.01	... ...	... ...	... ...
R188	E501G21	1.00±0.00	21.11±0.01	1.13±0.00	... ...	... ...	... ...
R193	E501G26	1.25±0.01	22.91±0.02	1.08±0.05	... ...	... ...	... ...
R194	...	0.89±0.00	21.31±0.01	1.04±0.01	... ...	... ...	... ...
R202	...	0.58±0.00	19.94±0.01	1.10±0.00	... ...	... ...	... ...
R209	...	1.22±0.01	23.65±0.02	1.06±0.03	... ...	... ...	... ...
R211	...	0.74±0.01	22.13±0.03	1.04±0.01	... ...	... ...	... ...
R212	E501G27	1.25±0.01	22.99±0.02	1.03±0.02	... ...	... ...	... ...
R213	...	0.90±0.01	21.73±0.02	1.14±0.01	1.15± 0.01	23.03± 0.00	1.60± 0.02
R214	...	0.63±0.01	21.47±0.02	1.03±0.01	0.79± 0.02	22.38± 0.05	1.38± 0.02
R216	A1033−27	0.86±0.01	21.32±0.02	1.13±0.00	0.99± 0.01	22.19± 0.02	1.54± 0.01
R217	...	0.59±0.00	20.13±0.02	1.15±0.00	0.66± 0.01	20.84± 0.03	1.62± 0.01
R218	N3305	1.00±0.00	20.40±0.02	1.15±0.00	... ...	... ...	... ...
R219	...	1.16±0.01	22.81±0.02	1.06±0.01	1.23± 0.02	23.41± 0.05	1.41± 0.03
R224	N3307	1.43±0.00	23.31±0.01	1.10±0.03	1.61± 0.01	24.17± 0.01	1.44± 0.05
R225	...	0.99±0.01	22.25±0.02	1.09±0.01	1.11± 0.02	23.00± 0.04	1.45± 0.03
R226	...	1.04±0.02	24.06±0.05	0.96±0.06	... ...	... ...	... ...
R231	...	0.85±0.01	22.06±0.03	1.06±0.01	... ...	... ...	... ...
R234	N3308	1.52±0.01	22.13±0.01	1.16±0.01	1.58± 0.01	22.86± 0.03	1.68± 0.02
R237	...	0.82±0.00	21.02±0.02	1.13±0.00	0.94± 0.01	21.91± 0.04	1.60± 0.01
R238	E501G35	1.14±0.00	21.42±0.01	1.09±0.01	... ...	... ...	... ...
R239	I629	0.99±0.01	22.10±0.02	1.14±0.01	1.12± 0.01	22.93± 0.02	1.54± 0.02
R241	...	1.20±0.02	24.66±0.04	0.94±0.16	... ...	... ...	... ...
R243	...	0.65±0.00	19.77±0.01	1.19±0.00	... ...	... ...	... ...
R245	...	1.07±0.00	22.13±0.01	1.09±0.01	1.15± 0.01	22.82± 0.02	1.54± 0.01
R250	E437G08	0.93±0.01	20.92±0.02	1.18±0.00	... ...	... ...	... ...
R252	E437G09	1.06±0.00	21.57±0.01	1.13±0.01	... ...	... ...	... ...
R253	...	1.24±0.01	23.15±0.02	1.07±0.04	1.36± 0.01	23.94± 0.01	1.49± 0.07
R254	...	1.34±0.01	23.80±0.01	0.94±0.07	... ...	... ...	... ...
R255	...	0.38±0.01	19.94±0.02	1.17±0.00	0.58± 0.01	21.21± 0.03	1.68± 0.01
R256	N3309	1.35±0.00	21.28±0.01	1.18±0.00	1.42± 0.01	22.13± 0.02	1.80± 0.01
R261	...	1.36±0.01	23.85±0.03	1.02±0.09	... ...	... ...	... ...
R266	A1034−27A	0.81±0.00	20.83±0.01	1.14±0.00	1.01± 0.01	22.01± 0.02	1.62± 0.01
R268	...	0.98±0.01	23.57±0.04	1.02±0.04	1.06± 0.01	24.12± 0.00	1.33± 0.08
R269	N3311	2.16±0.01	23.91±0.01	1.17±0.08	2.13± 0.01	24.45± 0.01	1.74± 0.15
R273	...	0.38±0.00	18.81±0.02	1.17±0.00	0.44± 0.01	19.56± 0.03	1.64± 0.01
R278	...	0.35±0.02	20.28±0.06	1.15±0.01	... ...	... ...	... ...
R283	E437G11	0.99±0.00	20.83±0.01	1.21±0.00	... ...	... ...	... ...
R286	...	1.02±0.01	23.88±0.02	1.01±0.07	1.60± 0.00	25.78± 0.04	1.16± 0.11
R288	E437G13	0.81±0.00	20.21±0.01	1.19±0.00	... ...	... ...	... ...
R293	...	0.62±0.01	22.04±0.03	1.14±0.01	0.82± 0.02	23.28± 0.03	1.66± 0.03
R295	E437G15	0.85±0.00	19.45±0.01	1.04±0.00	... ...	... ...	... ...
R305	...	0.96±0.01	21.35±0.02	1.13±0.00	... ...	... ...	... ...
R307	...	1.23±0.01	23.49±0.03	0.96±0.05	... ...	... ...	... ...
R308	...	0.52±0.01	20.05±0.02	1.12±0.00	... ...	... ...	... ...
R316	E501G47	1.25±0.01	22.05±0.02	1.16±0.01	1.31± 0.01	22.85± 0.02	1.76± 0.02
R317	N3315	1.24±0.01	21.52±0.02	1.14±0.00	... ...	... ...	... ...
R319	...	0.85±0.01	21.83±0.02	1.05±0.01	... ...	... ...	... ...
R322	E501G49	0.97±0.00	21.53±0.01	1.09±0.01	1.05± 0.01	22.34± 0.02	1.60± 0.01
R327	...	1.06±0.01	22.39±0.03	1.08±0.02	... ...	... ...	... ...
R334	E501G52	2.04±0.00	25.20±0.00	1.00±0.21	... ...	... ...	... ...
R336	N3316	1.19±0.01	21.30±0.02	1.16±0.00	... ...	... ...	... ...
R337	...	0.71±0.01	22.02±0.02	1.06±0.01	... ...	... ...	... ...
R338	...	0.68±0.01	20.38±0.02	1.12±0.00	... ...	... ...	... ...
R340	...	0.77±0.02	22.40±0.05	1.27±0.01	... ...	... ...	... ...
R343	...	0.81±0.01	21.60±0.02	1.07±0.01	... ...	... ...	... ...
R347	I2597	1.42±0.01	21.38±0.01	1.14±0.00	... ...	... ...	... ...
R359	...	0.69±0.00	20.76±0.01	1.12±0.00	... ...	... ...	... ...
R389	...	1.19±0.01	23.13±0.03	0.97±0.03	... ...	... ...	... ...

NOTE.— r_e is in arcsec. The uncertainties on the colors do not include the uncertainty in the transformation to the standard photometric system.

Chapter 6

Spectroscopy

During the April 1994 DFOSC observing run, spectra of 21 E and S0 galaxies in HydraI were obtained. The instrumental setup is described in Table 3.1 (p. 24). The data were subsequently reduced by Inger Jørgensen. This chapter describes these reductions. It also describes how the DFOSC data were supplemented with data from the literature to yield the table of available HydraI spectroscopy, presented in section 6.5.

6.1 The Basic Reductions of the Spectroscopy

Removal of overscan area. The readout window for the spectroscopy was [300:700,1:1028], and since the overscan area is what is outside [19:1042,3:1026] in these untrimmed coordinates, the section to keep (what we refer to as the trim section) was [1:401,3:1026] in the coordinates of the readout window. The trimmed spectroscopy images have the dimensions 401 pixels × 1024 pixels. The spatial direction is x, and the wavelength direction is y.

Subtraction of bias. The bias frame used for the photometry (cf. Section A.1) was also used for the spectroscopy[1].

Correction for fat zero. Like the photometry images, the spectroscopy images were affected by fat zero (cf. Section A.5). The columns affected had the same *relative* numbers as when reading out the entire CCD for the photometry, e.g. column 291, and the effect must therefore originate from the read out register. However, the effect (i.e. fat zero as function of level) was not the same, and it had to be redetermined from the spectroscopy images themselves. A by-eye fit with 1–4 linear functions was used. The fat zero effect in the spectroscopy images was generally smaller than in the photometry images, except for column 291.

Subtraction of dark current. The two dark frames used for the photometry (one for night 0–5, one for night 6–14; cf. Section A.2) were also used for the spectroscopy[1].

Flat field correction for pixel-to-pixel variations. 3 sets of 10 dome flat frames were obtained, with exposure times of 120 sec, 240 sec, and 240 sec, and from night 6, 10, and 13, respectively. After bias and dark subtraction, the images were combined within each set. These 3 flat images were normalized as follows: A 7-piece cubic spline, one per image, was fit to the continuum in the wavelength direction – only the section [40:100,*] was used, in order to avoid edges and low response areas. All columns were then divided by the fit.

[1] More precisely: what was used was the section [282:682,1:1024] of the photometry bias and dark images.

Note, that this normalization is different from that used for the photometry flats – the idea here is to let the flat field image represent only the pixel-to-pixel variations in sensitivity, not the variations in sensitivity with wavelength, and not the spectral energy distribution of the calibration lamp used to illuminate the dome.

The quotients between the 3 normalized flat images were investigated. The quotient between set 1 and set 3 showed a gradient of 1%, and other variations of $\pm 0.5\%$ or less. The quotient between set 2 and set 3 showed no gradient, and other variations of $\pm 0.3\%$.

The slit profile (cf. below) was taken out of nff2 and nff3, and the mean of the resulting images was used as the final flat field image.

Slit correction. In order to find the variations in sensitivity in the spatial direction, a slit profile image was constructed from the two dome flats nff2 and nff3 by averaging over the wavelength direction, and then taking the mean of the two images. The resulting image had the dimensions 401 pixels $\times$ 1 pixel. The variation in this image is a combination of two effects: 1. The pixel-to-pixel variations in the sensitivity of the CCD averaged over the y direction. 2. The variation of light throughput through the spectrograph caused by variations in the width of the slit.

Besides dome flats, also 6 sky flat images were obtained. These were reduced as outlined above, and then divided by the above slit profile image. First it was noted, that the position of the slit with respect to the CCD was *not* the same as for the dome flats – the slit profile image had to be shifted 1.5 pixels to match the 5 steep minima in it (probably caused by 5 grains of dust stuck on the slit)[2]. Second it was noted, that the slit profile extracted from the combined sky flat was *not* flat, despite that the images had been divided by the slit profile derived from the dome flats. This is caused by a difference in the way the slit is illuminated when the telescope is pointed at the illuminated dome, and when the telescope is pointed at the sky. The effect was modeled by fitting a linear function to the profile. After being normalized, the variation was from 0.985 to 1.01.

The final slit profile image was constructed as the product of the slit profile image derived from the dome flats, and the correction derived from the sky flats. The slit correction of the science images was performed by division with the slit profile image, shifted with an offset determined from the thorium lamp exposure taken just after the given science frame.

Removal of signal from remanence. Remanence, i.e. the signal from saturated objects (typically bright stars observed in direct imaging mode) in previous exposures, was also a problem for the spectroscopy images. The remanence signal was removed in the same way as for the photometry images, cf. Section A.7.

Removal of signal from cosmic-ray events. The same method as in JFK95b was used. The spatial profile of the galaxy was modeled from the galaxy spectrum. This model was subtracted from the galaxy spectrum, scaled to the local intensity of the profile. Pixels that deviated more than 7 times the local standard deviation in the resulting residual image were identified as cosmic-ray events. The values in these pixels were replaced by the model values.

Wavelength calibration and geometrical rectification. We want to transform our science spectra, so that the spatial axis is perfectly aligned with the x axis, and the dispersion

[2]Note, that shifting the slit profile image is not strictly correct, since it contains the y-average of the pixel-to-pixel variations intrinsic to the CCD. However, the error is negligible.

axis is perfectly aligned with the y axis. In addition, we want to wavelength calibrate the dispersion axis, and linearize it in $\log(\lambda/\text{Å})$.

During the observations at night, after each science spectrum (of a galaxy or a star), a spectrum of the thorium (Th) calibration lamp was obtained, with the telescope and instrument at the same position. Using a table with wavelengths for the different Th lines (see below), the Th spectra were used to establish the mapping of wavelength in Å as function of position on the CCD, i.e. $\lambda(x, y)$ – this could be done, since the spectral lines are at constant λ, whereas they extend over the entire spatial direction. The galaxy spectra themselves were used to establish the mapping of spatial coordinate as function of position on the CCD (the S-distortion), i.e. $s(x, y)$ – this could be done, since the center of the galaxy is at *one* spatial point, whereas the wavelength varies. The above two mappings were established using the tasks `identify`, `reidentify`, and `fitcoords`. Note, that there is one set of mappings for each science spectrum.

The spectra were then geometrically rectified, wavelength calibrated, and linearized in $\log(\lambda/\text{Å})$ using the task `transform`. The output images were specified to have the wavelength range 4954.2–5612.5 Å, which was the common range for the night time Th exposures, and to have 1024 pixels in the wavelength direction. With these 3 figures specified, the output pixel interval is fixed as $\mathrm{d}\log\lambda = (\log\lambda_2 - \log\lambda_1)/(N-1)$. Note, that the output spectra are still 2-dimensional.

The Th lamp had the advantage of having a high signal, therefore requirering only a short exposure time. It had the disadvantage of having blended lines, so that a line list based on atomic data could not be used. For the helium (He) and neon (Ne) lamps, the opposite was the case. To link Th with He+Ne, high signal-to-noise spectra of all 3 lamps were obtained during the daytime on two occasions. From the He+Ne spectrum the mapping $\lambda(x, y)$ was established using a line list based on atomic data. The rms scatter of this dispersion solution was 0.16 Å. This mapping was used to rectify and wavelength calibrate the two day time high S/N Th spectra. Wavelengths for all the blended Th lines were then determined (rms scatter 0.1–0.15 Å), and the resulting line list was used when identifying lines in the Th spectra obtained at night. The rms scatter of the dispersion solutions for the latter ranged from 0.07 Å to 0.44 Å, with a mean of 0.14 Å = 8.1 km/s [3].

The resolution was determined as σ from a Gaussian fit to the 5577 Å night sky line, in averages of 10 columns. The mean value ($N = 75$) was $\sigma = 1.358$ Å = 79 km/s, with an rms scatter of 0.014 Å = 0.8 km/s. The position of the 5577 Å night sky line had an rms scatter of 0.11 Å = 6.6 km/s, which is a good measure of the accuracy of the wavelength calibration.

Subtraction of the sky background. The sky background spectrum was determined in an area on each side of the galaxy or star at a distance range of typically 77″–91″. The 2D spectrum was rotated 90° so that x became the wavelength direction and y the spatial one – this is the format that the Fourier fitting program requires (cf. Section 6.2). The extracted 1D sky spectrum was kept in row one in the 2D spectrum (with the galaxy spectrum being centered on row 200) to make it possible to calculate the signal-to-noise ratio.

Determination of the velocity dispersion and the radial velocity. See Section 6.2.

Determination of line indices. See Section 6.3. This includes a relative flux calibration.

[3] Throughout this section, if nothing else is stated, the conversion from Å to km/s is done at 5177 Å, the (rest frame) wavelength of the magnesium triplet.

6.2 Determination of Velocity Dispersion and Radial Velocity

We want to determine the velocity dispersion of the galaxies. To do this, we make the following assumptions:

1. The luminosity weighted mean spectrum of the stars in the galaxy (had they been at rest with respect to each other) can be well matched by the spectrum of a *single* template star (e.g. a K giant).

2. The line of sight velocity distribution of the stars in the galaxy (the broadening function) is Gaussian.

Then it is conceptually easy to determine the velocity dispersion:

a. The spectrum of the template star is shifted in wavelength until the absorption lines in it match those in the galaxy spectrum. When knowing the (small) velocity of the template star, this gives the radial velocity of the galaxy.

b. The spectrum of the template star is convolved with a Gaussian broadening function with dispersion σ, and then matched against the galaxy spectrum. The velocity dispersion is determined as the best fitting value of σ. At the same time, the general strength of the absorption lines in the template star spectrum is also varied in order to get a good fit. This general line strength relative to the given template star is not used in our analysis. It is important that the two spectra are observed with the same instrument, since the resolution of the spectrograph then cancels out.

Specifically, we used the Fourier fitting method (Franx, Illingworth, & Heckman 1989a), implemented in a program written by M. Franx. It calculates the Fourier transforms of the galaxy spectrum and the template star spectrum, $\tilde{G}(k)$ and $\tilde{S}(k)$ respectively, using a common rest frame wavelength interval[4]. It then iteratively minimizes

$$\chi^2 = \sum_{k=k_\mathrm{l}}^{k_\mathrm{h}} \left| \tilde{G}(k) - \tilde{B}(k)\tilde{S}(k) \right|^2 \quad , \tag{6.1}$$

where $\tilde{B}(k)$ is the Fourier transform of the Gaussian broadening function. An analytical expression exists for $\tilde{B}(k)$ as function of the velocity dispersion σ, the radial velocity, and the relative line strength, see Sargent et al. (1977). The iteration solves for all these three variables, although the radial velocity is not expected to change much. The Fourier space is used, since a convolution here is a multiplication, which is computationally faster.

The low and high frequencies in Fourier space are filtered out before minimizing χ^2. This is governed by the quantities k_l and k_h in Eq. (6.1) above. We used $k_\mathrm{l} = 7$ [$= 7/N \approx (100$ Å$)^{-1}$] and $k_\mathrm{h} = 330$ [$= 330/N \approx (2$ Å$)^{-1}$], where $N = (1024\,\mathrm{pixels})/(830\,\mathrm{pixels}) \cdot 534\,$Å. JFK95b used the same values of k_l and k_h.

[4]To get a rest frame wavelength interval that is common to the galaxy and the star, their relative radial velocity needs to be known. The program uses the *input guess* on the radial velocity to do this. We computed an accurate such input guess by cross-correlating the two spectra using the task `stsdas.contrib.xcor`.

A common galaxy/star rest frame wavelength interval of the same length was used for all the galaxies. It was defined by always skipping the 130 most blue columns in the galaxy spectrum, and then skipping the number of columns in the template star spectrum required to shift it onto the galaxy spectrum rest frame wise. This latter number depends on the redshift of the galaxy. 830 columns were used for the fitting, skipping 64 columns in the red end of the spectrum to stay clear of the position of the very strong 5577 Å sky line. The resulting wavelength interval was of length 534 Å.

Four K giant template stars were observed a total number of 31 times. The telescope was attempted moved during the exposures in such a way that the star would fill the 2.″5 slit in the same way as the galaxies do. This is needed to get the same resolution for the stars and the galaxies, since the resolution depends in part on the width of the slit, and since the seeing is $\lesssim 2.''5$. However, technical problems made this difficult. Therefore, it was tested which template star observations would give the lowest velocity dispersions, and the three best, one observation of each of the stars HD77236, HD176047, and BD $-43°2527$, were actually used in the Fourier fitting.

From the number of counts in the galaxy spectrum, the number of counts in the sky spectrum, and the CCD read-out noise and conversion factor, the Fourier fitting program calculates $N_{\text{eff. phot.}}$, the number of 'effective photons' for the given spectrum. $N_{\text{eff. phot.}}$ is defined such that the signal-to-noise ratio per Å is

$$S/N = \sqrt{\frac{N_{\text{eff. phot.}}}{\Delta\lambda}} \ , \tag{6.2}$$

where $\Delta\lambda = 534$ Å is the length of the wavelength interval used in the fitting. $N_{\text{eff. phot.}}$ can also be said to be the number of photons required to get the S/N actually obtained, had the sky level and the CCD read-out noise been zero. The 21 HydraI DFOSC observations have S/N in the range 29.0–73.7, with a median value of 40.0.

The derived radial velocities were corrected to the heliocentric frame, cz_{hel}. The final values of cz_{hel} and σ were taken as the mean of the three determinations.

The Fourier fitting was done using an aperture of $2.''5 \times 6.''59$. 2.″5 is the width of the slit, and 6.″59 (13 pixels) is a user specified length in the spatial direction. The area of this rectangular aperture is equivalent to a circular aperture of angular diameter $2r_{\text{aperture}} = 4.''70$ (cf. JFK95b). Since E and S0 galaxies have radial gradients in σ, the size of the aperture within which σ is measured is of importance. Following JFK95b, the measured velocity dispersion, σ_{aperture}, was corrected to an aperture of metric diameter $2r_{\text{norm}} = 1.19\ h^{-1}$ kpc ($H_0 = 100\ h$ km/s/Mpc), corresponding to 3.″4 at the distance of the Coma cluster. The formula used was

$$\log\sigma_{\text{norm}} = \log\sigma_{\text{aperture}} + 0.04\log\left(\frac{r_{\text{aperture}}}{r_{\text{norm}}}\right) \ , \tag{6.3}$$

where σ_{norm} is the corrected velocity dispersion. In practical terms, the calculation was done as

$$\log\sigma_{\text{norm}} = \log\sigma_{\text{aperture}} + 0.04\log\left(\frac{4.''70 \cdot 4050\,\text{km/s}}{3.''4 \ \cdot 7200\,\text{km/s}}\right) \ , \tag{6.4}$$

where 4050 km/s and 7200 km/s is the CMB radial velocity of HydraI and Coma, respectively. The correction was small, only -0.004.

6.3 Determination of Line Indices

The Lick/IDS system (Faber et al. 1985, Worthey et al. 1994) contains twenty-one optical absorption feature indices. All indices measure the strength of a spectral feature (either molecular or atomic) relative to a pseudocontinuum on each side of the feature.

Here only the indices Mg_2, Mgb, Fe5270 and Fe5335 will be considered. Their wavelength definitions are listed in Table 6.1. In the Lick/IDS system, molecular indices (e.g. Mg_2) are expressed in magnitudes, and atomic indices (e.g. Mgb) are expressed in angstroms of equivalent width. We do not use Fe5270 and Fe5335 individually, but only their mean, $< \mathrm{Fe} > \equiv (\mathrm{Fe5270} + \mathrm{Fe5335})/2$.

Table 6.1: Wavelength Definitions for the used Line Indices

Index	Units	Blue continuum	Index passband	Red continuum	Measures
Mg_2	mag	4895.125–4957.625	5154.125–5196.625	5301.125–5366.125	MgH, Mgb, FeI
Mgb	Å	5142.625–5161.375	5160.125–5192.625	5191.375–5206.375	Mgb
Fe5270	Å	5233.150–5248.150	5245.650–5285.650	5285.650–5318.150	FeI, CaI
Fe5335	Å	5304.625–5315.875	5312.125–5352.125	5353.375–5363.375	FeI

Notes: The definitions are from Worthey et al. (1994). The passbands are given in Å.

1-dimensional galaxy spectra were extracted from the 2-dimensional spectra as the central 13 rows. These 1-dimensional spectra were convolved to the Lick/IDS instrumental dispersion of 200 km/s (Gonzáles 1993) and then binned linearly in wavelength. The spectra were flux-calibrated using two spectra of the two spectrophotometric stars LTT7379 and LTT7987. Since not all the spectra had been obtained in photometric weather, the flux-calibration was only relative. Then the line indices Mg_2, Mgb, Fe5270 and Fe5335 were calculated according to the prescription in Worthey et al. (1994).

The indices were corrected to an aperture of metric diameter 1.19 h^{-1} kpc. This was done for Mg_2 following JFK95b as

$$\mathrm{Mg}_{2\mathrm{norm}} = \mathrm{Mg}_{2\mathrm{aperture}} + 0.04 \log \left(\frac{r_{\mathrm{aperture}}}{r_{\mathrm{norm}}} \right) \quad , \tag{6.5}$$

and for Mgb and the iron indices following J97 as

$$\log (\mathrm{index})_{\mathrm{norm}} = \log (\mathrm{index})_{\mathrm{aperture}} + 0.05 \log \left(\frac{r_{\mathrm{aperture}}}{r_{\mathrm{norm}}} \right) \quad . \tag{6.6}$$

All the line indices were corrected for the effect of the velocity dispersion. We used the corrections from JFK95b for Mg_2 and from J97 for $< \mathrm{Fe} >$. The principles in establishing this correction are as follows: The spectra of K giant template stars are first convolved to the Lick/IDS instrumental dispersion and then convolved with Gaussian broadening functions having dispersions in the range 50 to 350 km/s. From these spectra, the various indices at various velocity dispersions are determined. For Mg_2, the difference between the index derived from the unconvolved ($\sigma = 0$ km/s) and convolved ($\sigma = 50, \ldots, 350$ km/s) spectra is fitted with a low-order polynomial, giving the amount to add to the index to correct to zero velocity dispersion. For the other indices, the quotient is used, giving the correction to multiply the given index with. At $\sigma = 200$ km/s, the additive correction for Mg_2 is 0.002, and the multiplicative correction for $< \mathrm{Fe} >$ is 1.15.

6.4 Internal and External Comparison of the Spectroscopy

6.4.1 Internal Comparison

The internal comparisons of the spectroscopy are summarized in Table 6.2 and shown in Figure 6.1 (not Mgb and $<$ Fe $>$). The spectra used for the internal comparison have in general lower S/N than the rest – that is why these galaxies were reobserved. The rms scatter for the line indices is higher than expected due to remanence and signal from cosmic-ray events surviving in the spectra.

Table 6.2: Internal Comparison of the Spectroscopy

Parameter	N	mean	rms
$cz_{\rm hel}$	11	3.2 $\pm$4.3	14.3
$\log\sigma$	11	-0.014 ± 0.011	0.036
$\rm Mg_2$	6	-0.017 ± 0.006	0.015
Mgb	11	-0.110 ± 0.138	0.457
$<$ Fe $>$	11	-0.101 ± 0.113	0.374

Notes: "rms" is the root mean square standard deviation. The uncertainty on the mean has been calculated as rms/$\sqrt{N}$.

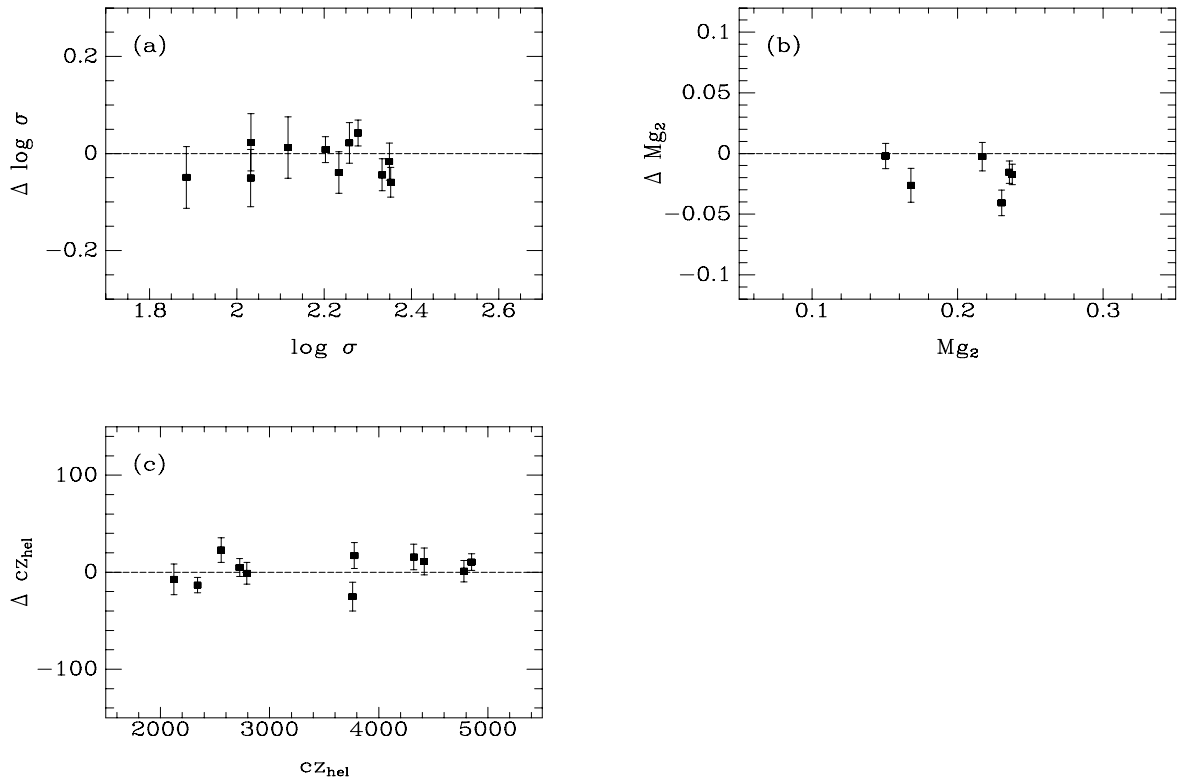

Figure 6.1: Internal comparison, $\log\sigma$, $\rm Mg_2$, and $cz_{\rm hel}$. The quantity on the x-axis is the mean value of the two measurements.

6.4.2 External Comparison and Applied Offsets

The spectroscopic parameters were compared with data from JFK95b, J97, Davies et al. (1987) [D87], Faber (1994) [F94], Lucey & Carter (1988) [LC88], and Richter (1989) [R89]. The comparisons are shown in Fig. 6.2–6.5 and summarized in Table 6.3 (p. 81).

Comparisons of $\log\sigma$ are shown in Figure 6.2. All literature data have been aperture corrected, and the individual values from D87 and F94 have been averaged, cf. JFK95b. The mean differences $\Delta\log\sigma \equiv \log\sigma_{\rm DFOSC} - \log\sigma_{\rm literature}$ are given in Table 6.3. From these, the following offset was adopted to reach the system of JFK95b, which is also the system of D87 (cf. JFK95b):

$$\log\sigma_{\rm JFK95b/D87} = \log\sigma_{\rm DFOSC} - 0.014 \ . \tag{6.7}$$

This gives consistency within 0.010 with D87 and JFK95b. It also gives consistency within 0.010 with LC88 when applying the offset found by JFK95b: $\log\sigma_{\rm JFK95b/D87} = \log\sigma_{\rm LC88} - 0.020$.

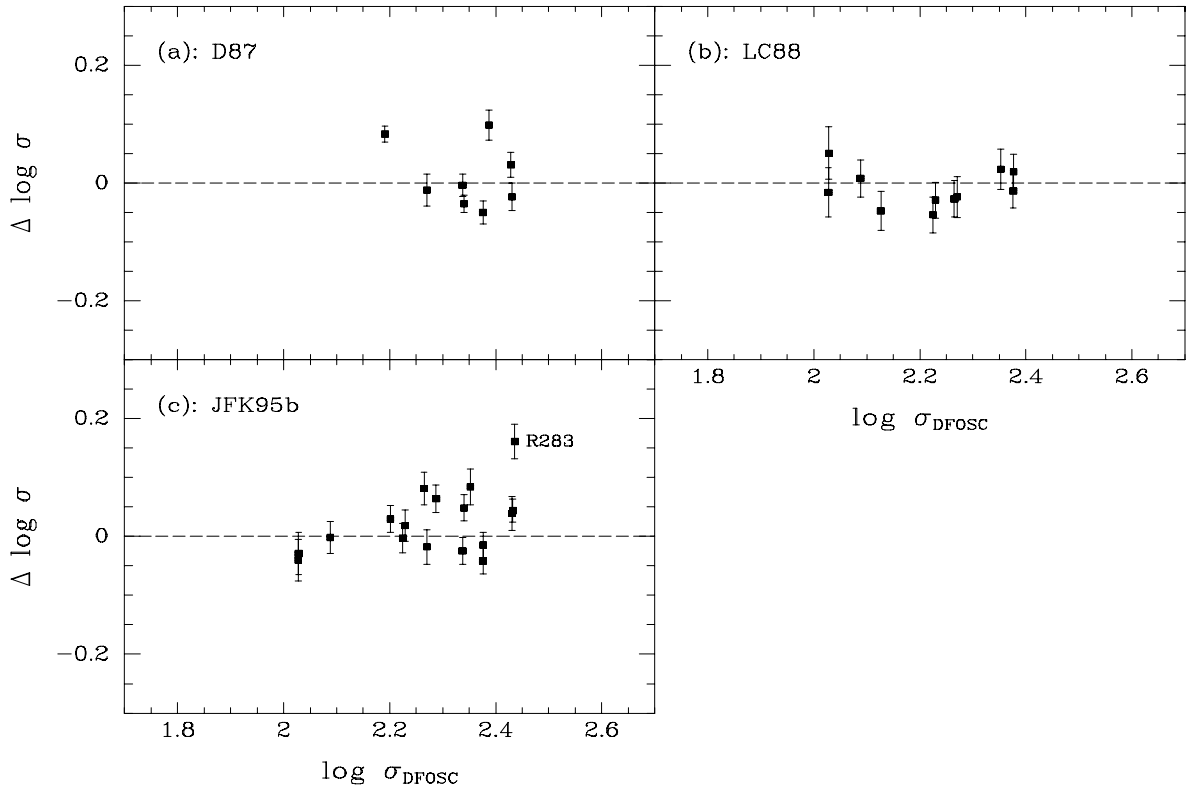

Figure 6.2: External comparison, $\log\sigma$. $\Delta\log\sigma \equiv \log\sigma_{\rm DFOSC} - \log\sigma_{\rm literature}$. All data have been corrected to the same aperture. For panel (a), the errorbars shown represent the error on the DFOSC data, only.

Comparisons of $cz_{\rm hel}$ are shown in Figure 6.3. The consistency is good. In the case of JFK95b, Fig. 6.3(c), we can compute the total error on $\Delta cz_{\rm hel}$ expected from the internal uncertainties on our and their measurements. This error is 17 km/s, which is far less than the observed rms scatter of 48 km/s. Thus, other sources of error, such as the wavelength calibration, dominate. If the observed scatter in the comparison with JFK95b is divided equally on our and their data, the found external accuracy is 34 km/s. JFK95b find their external accuracy to be $\approx$ 35 km/s, in good agreement with this.

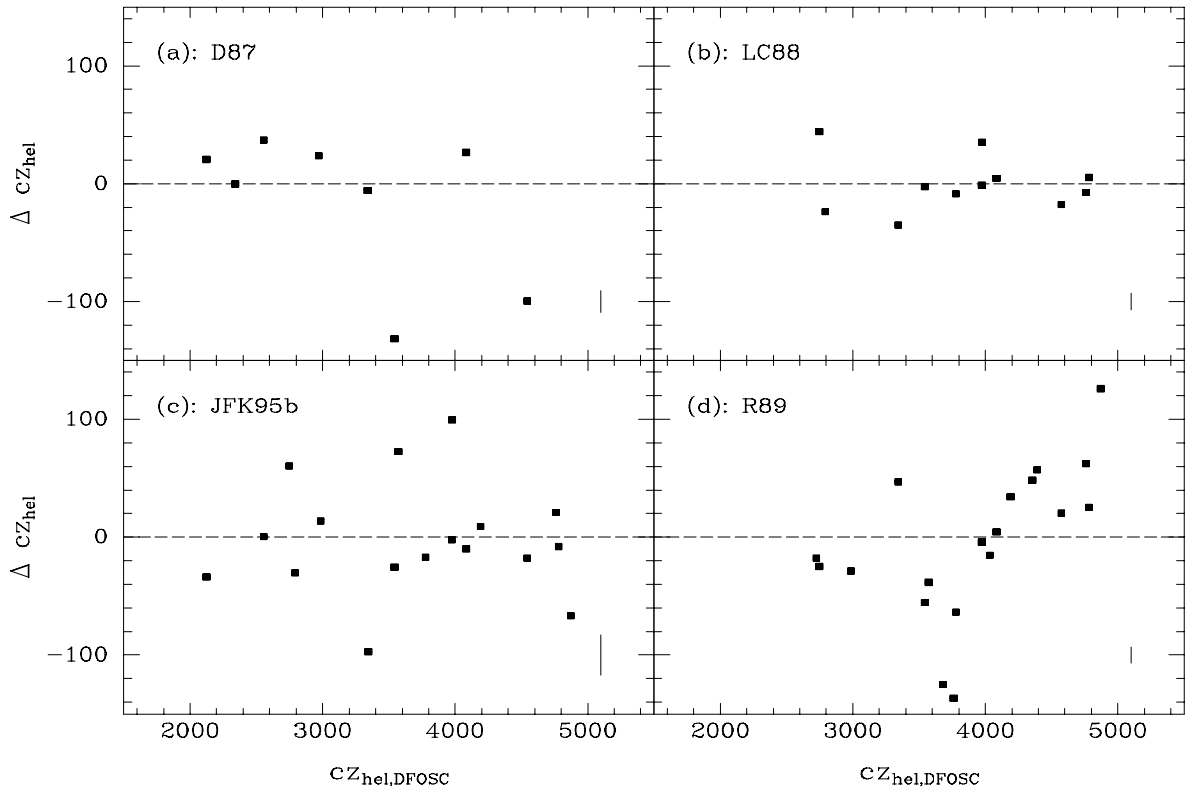

Figure 6.3: External comparison, $cz_{\rm hel}$. $\Delta zc_{\rm hel} \equiv cz_{\rm hel,DFOSC} - cz_{\rm hel,literature}$. For panel (a), (b), and (d), the typical errorbar shown represents the error on the DFOSC data, only.

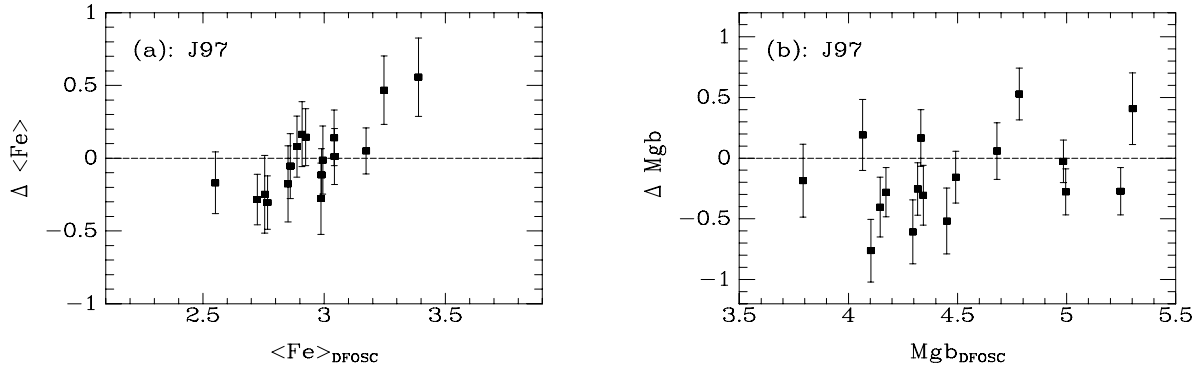

Figure 6.4: External comparison, < Fe > and Mgb. All data have been aperture and velocity dispersion corrected. The differences have been calculated as "DFOSC"−"literature". The apparent correlation seen in panel (a) is most likely due to the fact, that $< {\rm Fe} >_{\rm DFOSC}$ appears on both axes (since $\Delta < {\rm Fe} > = < {\rm Fe} >_{\rm DFOSC} - < {\rm Fe} >_{\rm J97}$) and since the range in $< {\rm Fe} >_{\rm DFOSC}$ is rather small.

J97 presents various line indices calibrated to the Lick/IDS system. Figure 6.4(a) shows the comparison for < Fe >. The mean difference is zero, and therefore the DFOSC < Fe > values are already on the Lick/IDS system,

$$< {\rm Fe} >_{\rm Lick/IDS} = < {\rm Fe} >_{\rm DFOSC} \ . \tag{6.8}$$

Figure 6.4(b) shows the comparison for Mgb. The mean difference is used to transform the DFOSC data to the Lick/IDS system:

$$\mathrm{Mgb}_{\mathrm{Lick/IDS}} = \mathrm{Mgb}_{\mathrm{DFOSC}} + 0.16 \ . \tag{6.9}$$

Mg_2 could not be measured from all the DFOSC spectra since the blue pseudocontinuum of Mg_2 was not fully included in the observed wavelength range for galaxies redshifted less than $cz_{\mathrm{observed}} \approx 3600$ km/s. Therefore, Mgb was used instead for the calibration of Mg_2 to the Lick/IDS system. A transformation from Mgb to Mg_2 has been established by J97 as

$$\begin{array}{rll} \mathrm{Mg}_2 = & 0.638 \log\ \mathrm{Mgb} - 0.133 & \sigma_{\mathrm{fit}} = 0.019 \quad N = 159 \ . \\ & \pm\ 0.044 & \end{array} \tag{6.10}$$

σ_{fit} is the rms scatter and N is the number of galaxies used in the fit. The author reports that the relation has no significant intrinsic scatter. The right hand side of Eq. (6.10) is what we referred to as $\widehat{\mathrm{Mg}_2}$ in Sect. 2.3.

In Figure 6.5, real DFOSC Mg_2 values are compared with fiducial Mg_2 values calculated from Mgb using Eq. (6.10). In panel (a) the Mgb data are from the DFOSC itself (thus being a sort of an internal comparison). The mean difference is $\Delta\mathrm{Mg}_2 = -0.031 \pm 0.004$. In panel (b) the Mgb data are from J97. The mean difference is $\Delta\mathrm{Mg}_2 = -0.024 \pm 0.007$.

The real DFOSC Mg_2 values were also compared with real Mg_2 values from the literature. In comparison with D87, F94, and J97, mean differences $\Delta\mathrm{Mg}_2 \equiv \mathrm{Mg}_{2,\mathrm{DFOSC}} - \mathrm{Mg}_{2,\mathrm{literature}}$ of -0.029, -0.014, and -0.013 were found for 2, 1, and 2 galaxies in common, respectively. It was concluded, that the best transformation to the Lick/IDS system was

$$\mathrm{Mg}_{2\mathrm{Lick/IDS}} = \mathrm{Mg}_{2\mathrm{DFOSC}} + 0.024 \ . \tag{6.11}$$

The uncertainty on the offset was estimated from the consistencies to be 0.010.

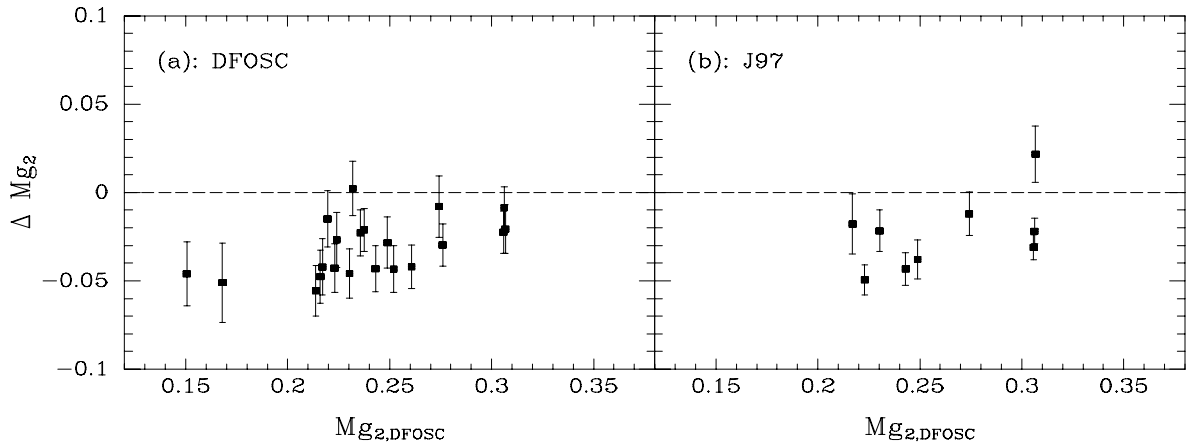

Figure 6.5: Comparison of real Mg_2 with fiducial Mg_2. All data have been aperture and velocity dispersion corrected. The differences have been calculated as $\Delta\mathrm{Mg}_2 \equiv \mathrm{Mg}_{2,\mathrm{DFOSC}} - \mathrm{Mg}_{2,\mathrm{calc}}$, with $\mathrm{Mg}_{2,\mathrm{calc}}$ being calculated from Mgb using Eq. (6.10). (a): Mgb data from the DFOSC. (b): Mgb data from J97.

Table 6.3: External Comparison of the Spectroscopy

Parameter	Source	N	mean	rms	With offset(s)	Comments
$cz_{\rm hel}$	D87	8	$-16.2\pm$ 22.5	63.5		
$cz_{\rm hel}$	LC88	11	$-0.7\pm$ 7.1	23.4		
$cz_{\rm hel}$	JFK95b	17	$-1.8\pm$ 11.6	48.0		
$cz_{\rm hel}$	R89	20	$-4.4\pm$ 14.0	62.6		
$\log\sigma$	D87	8	0.011 ± 0.019	0.055	-0.003 ± 0.019	
$\log\sigma$	LC88	11	-0.010 ± 0.010	0.032	-0.004 ± 0.010	
$\log\sigma$	JFK95b	17	0.023 ± 0.013	0.054	0.009 ± 0.013	
$\log\sigma$	JFK95b	16	0.015 ± 0.011	0.042	0.001 ± 0.011	R283/E437G11 omitted
Mg_2	D87	2	-0.029 ± 0.002	0.002	-0.005 ± 0.002	
Mg_2	F94	1	$-0.014\pm$		0.010	
Mg_2	JFK95b	2	-0.013 ± 0.007	0.010	0.011 ± 0.007	
Mgb	F94	2	-0.037 ± 0.034	0.049	0.123 ± 0.034	
Mgb	J97	17	-0.159 ± 0.084	0.346	0.001 ± 0.084	
$<$ Fe $>$	F94	2	-0.147 ± 0.212	0.300		
$<$ Fe $>$	J97	17	-0.002 ± 0.060	0.249		

Notes: All differences have been calculated as "DFOSC" − "literature". "rms" is the root mean square standard deviation. The uncertainty on the mean has been calculated as rms/$\sqrt{N}$. The column "With offset(s)" gives the mean difference after the following offsets have been applied to the DFOSC data
$\log\sigma_{\rm JFK95b/D87} = \log\sigma_{\rm DFOSC} - 0.014$
$\rm Mg_{2Lick/IDS} = Mg_{2DFOSC} + 0.024$
$\rm Mgb_{Lick/IDS} = Mgb_{DFOSC} + 0.16$
$< \rm Fe >_{Lick/IDS} = < Fe >_{DFOSC}$
and the following offset has been applied to the LC88 data (cf. JFK95b)
$\log\sigma_{\rm JFK95b/D87} = \log\sigma_{\rm LC88} - 0.020$.

6.5 The Available HydraI Spectroscopy

Variance-weighted mean values for $cz_{\rm hel}$, $\log\sigma$, Mgb, $\rm Mg_2$, and $<\rm Fe>$ were calculated from the DFOSC data and the data from JFK95b and J97[5]. Where no $\rm Mg_2$ data existed, a fiducial value was calculated from Mgb, cf. the last section. For 3 additional galaxies not observed by DFOSC and JFK95b, $cz_{\rm hel}$ and $\log\sigma$ were taken from LC88, with $\log\sigma$ offset by -0.020 to match the system of JFK95b, cf. JFK95b. The data (except for Mgb) are presented in Table 6.4.

To sum up, $\log\sigma$, $\rm Mg_2$, and $<\rm Fe>$ refer to an aperture of metric diameter 1.19 h^{-1} kpc. $\log\sigma$ is on the system defined by JFK95b. $\rm Mg_2$ and $<\rm Fe>$ have been corrected for the effect of the velocity dispersion, and are on the Lick/IDS system.

[5]The JFK95b and J97 data for the galaxies R338/RMH48 and R343/RMH50 were switched, cf. the caption to Table 3.2, p. 27.

TABLE 6.4
THE HYDRAI SPECTROSCOPY

Galaxy		$cz_{\rm hel}$	$\log\sigma$	Mg_2	$<$ Fe $>$	S/N	Spec[a]	Mg_2[b]
R066	E501G03	4199	2.323±0.018	0.285±0.008	2.87± 0.24	26.8	J	J
R112	E501G13	3520	2.352±0.021	0.306±0.009	2.78± 0.27	24.2	J	J
R166	E501G20	4354	2.143±0.018	0.297±0.005	3.02± 0.16	40.6	D	D
R167	E436G44	3165	2.213±0.024	0.258±0.009	2.78± 0.29	22.4	J	J
R171	E436G45	3402	2.279±0.028	0.268±0.010	2.19± 0.30	22.2	J	J
R188	E501G21	4574	2.112±0.023	0.253±0.005	2.63± 0.16	41.1	D	D
R212	E501G27	3230	1.739±0.072	0.133±0.036[c]	2.89± 0.29	22.2	J	
R213	···	3583	1.997±0.017	0.279±0.011[c]	3.30± 0.16	40.5	J	
R216	···	2286	2.024±0.019	0.241±0.014[c]	2.51± 0.17	38.9	J	
R217	···	4895	2.076±0.014	0.250±0.010	2.68± 0.13	49.9	J	J
R218	N3305	3974	2.386±0.009	0.328±0.005	3.14± 0.07	100.0	D J	D
R219	···	4188	2.023±0.022	0.260±0.014[c]	2.89± 0.19	33.9	J	
R224	N3307	3761	2.057±0.023	0.189±0.007	2.98± 0.15	42.5	D J	D
R225	···	3522	1.937±0.031	0.247±0.019[c]	3.03± 0.24	27.5	J	
R231	···	3685	1.942±0.031	0.226±0.019[c]	2.73± 0.22	29.7	J	
R234	N3308	3549	2.284±0.010	0.303±0.011	2.85± 0.10	68.2	D J	J
R237	···	3006	2.148±0.020	0.273±0.011	3.18± 0.21	30.6	J	J
R238	E501G35	4189	2.175±0.009	0.244±0.005	3.00± 0.08	83.6	D J	D
R239	I0629	2796	2.044±0.017	0.238±0.011[c]	2.91± 0.13	49.2	D J	
R243	···	3362	2.210±0.014	0.266±0.008[c]	2.78± 0.11	58.9	D J	
R245	···	4782	2.051±0.016	0.238±0.006	2.96± 0.13	49.9	D J	D
R250	E437G08	4390	2.192±0.020	0.282±0.005	2.69± 0.16	40.1	D	D
R252	E437G09	3682	2.078±0.024	0.237±0.006	3.31± 0.17	37.2	D	D
R253	···	4686	1.904±0.034	0.221±0.021[c]	3.16± 0.24	26.8	J	
R254	···	4662	1.661±0.098	0.223±0.029[c]	2.53± 0.34	19.2	J	
R255	···	3193	2.074±0.030	··· ···	··· ···	24.5		
R256	N3309	4086	2.407±0.008	0.330±0.005	3.08± 0.07	94.5	D J	D J
R261	···	3807	1.816±0.079	0.198±0.033[c]	2.78± 0.35	18.7	J	
R266	···	4758	2.085±0.013	0.270±0.006	2.90± 0.11	60.9	D J	D
R269	N3311	3868	2.291±0.015	0.332±0.012	3.20± 0.16	40.5	J	J
R273	···	2727	2.285±0.013	0.278±0.007[c]	2.60± 0.09	69.5	D J	
R278	···	4478	1.930±0.049	··· ···	··· ···	15.1		
R283	E437G11	4897	2.315±0.013	0.297±0.006	2.99± 0.12	56.0	D J	D
R288	E437G13	3559	2.238±0.010	0.266±0.006[c]	2.87± 0.09	74.5	D J	
R293	···	4482	1.643±0.124	0.273±0.034[c]	2.49± 0.49	13.4	J	
R295	E437G15	2725	2.259±0.013	0.149±0.010[c]	2.48± 0.09	73.7	D	
R303	···	2758	1.967±0.037	0.203±0.021[c]	2.60± 0.22	29.7	J	
R305	···	4033	2.053±0.021	0.234±0.005	2.63± 0.17	37.7	D	D
R308	···	4103	2.086±0.027	0.277±0.014[c]	2.47± 0.20	33.3	J	
R316	E501G47	4838	2.135±0.015	0.287±0.010[c]	2.78± 0.14	45.7	J	
R317	N3315	3779	2.213±0.012	0.251±0.005	2.82± 0.10	64.3	D J	D
R319	···	4460	1.865±0.050	0.208±0.026[c]	2.67± 0.28	23.1	J	
R322	E501G49	4063	2.036±0.022	0.237±0.016[c]	3.07± 0.20	33.0	J	
R327	···	4213	1.966±0.045	0.263±0.022[c]	2.26± 0.30	21.7	J	
R336	N3316	3960	2.224±0.011	0.264±0.005	3.04± 0.09	73.9	D J	D
R338	···	3075	1.963±0.022	0.244±0.013[c]	2.60± 0.16	40.7	J	
R343	···	4372	1.750±0.074	0.233±0.026[c]	2.39± 0.32	20.7	J	
R347	I2597	2983	2.402±0.009	0.318±0.007	3.11± 0.08	85.1	D J	J
R359	···	5247	2.012±0.024	··· ···	··· ···	31.2		
R369	E437G21	3931	2.248±0.019	0.283±0.008	3.08± 0.25	26.5	J	J
R498	E437G45	3757	2.103±0.031	0.279±0.014	3.03± 0.42	15.5	J	J

NOTE.— $cz_{\rm hel}$ is in km/s. S/N is the signal-to-noise ratio per Å.
[a] Reference for $\log\sigma$, Mgb, and $<$ Fe $>$. Reference codes: D = DFOSC; J = JFK95b (for $\log\sigma$ and Mg_2) and J97 (for $<$ Fe $>$). If no reference code is given, $\log\sigma$ is from LC88. [b] Reference for true Mg_2.
[c] Mg_2 has been calculated from Mgb. More notes are found in the text.

Chapter 7

Analysis

7.1 The Cluster and Sample Properties of HydraI and Coma

The analysis presented in this chapter is based on data for 159 E and S0 galaxies in the two clusters HydraI (Abell 1060) and Coma (Abell 1656). The properties of the two *samples* used are briefly discussed in Sect. 7.1.1 and summarized in Table 7.1. The properties of the two *clusters* are discussed in Sect. 7.1.2 and summarized in Table 7.2.

7.1.1 Data Overview

The HydraI data have already been described in detail in the previous chapters. In summary, the photometry (Chapter 3–5) is based on observations made in April 1994 with the Danish 1.5 meter telescope at ESO, La Silla, equipped with the DFOSC instrument. Global photometric parameters for 64 galaxies in Gunn r and Johnson B and 22 galaxies in Johnson U are listed in Table 5.6 (p. 68) for Gunn r, and Table 5.7 (p. 69) for Johnson B and U. The spectroscopy (Chapter 6) is in part from the above-mentioned observing run, and in part from JFK95b and J97. In addition data from Lucey & Carter (1988) were used for three galaxies. Global spectroscopic parameters for 51 galaxies are listed in Table 6.4 (p. 83). The number of galaxies with both photometry and spectroscopy is 45; for details see Table 7.1 (p. 87). The photometry is estimated to be complete to $m_{\mathrm{r_T}} = 14\overset{\mathrm{m}}{.}5$, corresponding to $M_{\mathrm{r_T}} = -20\overset{\mathrm{m}}{.}1$. (The calculation of distance dependent quantities is explained below.) Of these galaxies, 80% have spectroscopy. The sample covers the central part of the cluster, with a maximum center distance of $57'$, corresponding to 1.3 Mpc. *This sample is larger than any other complete sample of HydraI galaxies used for investigations of the FP.*

The Coma sample consists of 116 galaxies. The data are given in Appendix D (p. 207). Of the 116 galaxies, D120 and D121 are omitted from the analysis, as their photometric parameters are highly uncertain, due to the small angular distance between the galaxies. The photometry is from JF94. We use the seeing corrected values that are given in JFK95a. Velocity dispersions and $\mathrm{Mg_2}$ values are from the literature (Davies et al. 1987; Dressler 1987; Lucey et al. 1991b; Guzmán et al. 1992) as compiled into a consistent system by JFK95b, and from Jørgensen (1997b, in prep.). $<\mathrm{Fe}>$ indices are available for a subsample of 44 of the galaxies (Jørgensen 1997b, in prep.) – this subsample is not magnitude limited. The photometry is estimated to be complete to $m_{\mathrm{r_T}} = 15\overset{\mathrm{m}}{.}05$ corresponding to $M_{\mathrm{r_T}} = -20\overset{\mathrm{m}}{.}75$. Of these galaxies, 93% have a measured σ and $\mathrm{Mg_2}$. The sample covers the central $64' \times 70'$ of the cluster, with a maximum center distance of $47'$, corresponding to 1.7 Mpc. *This sample is larger than any other complete sample of Coma galaxies used for investigations of the FP.* For comparison, the Coma sample used in JFK96 has 79 galaxies. Their Coma sample is a subsample of the Coma sample used in this study.

Table 7.1 also list typical measurement errors for the different quantities. These are all based on external comparisons. The exception is $\log <\mathrm{Fe}>$, where the typical uncertainties are based on comparisons between data from different observing runs using different instruments, but not from other authors. The HydraI and Coma samples do not have enough galaxies in common with e.g. Faber (1994) to enable an actual external comparison. The errors in $\log r_\mathrm{e}$ and $\log <I>_\mathrm{e}$ are highly anti-correlated, with a linear correlation coefficient r of about -0.95. The uncertainty on a function $f = f(\log r_\mathrm{e}, \log <I>_\mathrm{e})$ is calculated as

$$\begin{aligned} \sigma_f &= \left[\left(\frac{\partial f}{\partial \log r_\mathrm{e}} \right)^2 \sigma^2_{\log r_\mathrm{e}} + \left(\frac{\partial f}{\partial \log <I>_\mathrm{e}} \right)^2 \sigma^2_{\log <I>_\mathrm{e}} \right. \\ &\quad \left. + 2r\sigma_{\log r_\mathrm{e}} \sigma_{\log <I>_\mathrm{e}} \left(\frac{\partial f}{\partial \log r_\mathrm{e}} \right) \left(\frac{\partial f}{\partial \log <I>_\mathrm{e}} \right) \right]^{1/2} , \end{aligned} \tag{7.1}$$

which is the usual propagation of errors formula with the covariance term included (e.g. Bevington & Robinson 1992), since $\mathrm{Cov}(\log r_\mathrm{e}, \log <I>_\mathrm{e}) = r\sigma_{\log r_\mathrm{e}} \sigma_{\log <I>_\mathrm{e}}$ (e.g. Press et al. 1992). As an important example, the combination $(\log r_\mathrm{e} - \beta \log <I>_\mathrm{e}) \approx (\log r_\mathrm{e} + 0.82 \log <I>_\mathrm{e})$ enters the FP, and as can be seen from Table 7.1, this combination has a much smaller uncertainty than $\log r_\mathrm{e}$ and $\log <I>_\mathrm{e}$ individually have. Where nothing else is stated, the typical error bars shown on the figures in this chapter are based on the values listed in Table 7.1.

The distance dependent quantities (absolute magnitudes, r_e in kpc, and cluster center distances in Mpc) were calculated as follows. Coma was assumed to be at rest with respect to the CMB frame at $cz = 7200\,\mathrm{km\,s^{-1}}$, and the distance to HydraI relative to Coma was calculated from the FP zero point difference $\Delta\gamma = 0.232$ (Eq. 7.6). $H_0 = 50\,\mathrm{km\,s^{-1}\,Mpc^{-1}}$ and $q_0 = 0.5$ was assumed. The formulas used are given in Sect. 2.2.6 (p. 16). The derived redshift for HydraI (Eq. 2.32) is $cz = 4143\,\mathrm{km\,s^{-1}}$. For comparison, the CMB redshift is $cz = 4050\,\mathrm{km\,s^{-1}}$. The distance moduli for Coma and HydraI are

$$(m-M)_\mathrm{Coma} = 35\overset{\mathrm{m}}{.}80\,; \quad (m-M)_\mathrm{HydraI} = 34\overset{\mathrm{m}}{.}60 \ . \tag{7.2}$$

The conversion of r_e from arcsec to kpc (Eq. 2.33, p. 17) is

$$\log r_\mathrm{e,kpc} = \log r_\mathrm{e,arcsec} - \begin{cases} 0.174 & \text{for Coma} \\ 0.407 & \text{for HydraI} \end{cases} \ . \tag{7.3}$$

Cluster center distances in Mpc can be calculated using a similar expression. Note that the assumed value of H_0 does not affect the comparison of the two clusters, since their relative distance is determined from the FP. The dependence on q_0 is negligible.

Table 7.1: Properties of the HydraI and Coma Samples

Galaxies with photometry in Gunn r

	HydraI	Coma
Number of galaxies with σ	45	114
Number of galaxies with Mg_2	42	113
Number of galaxies with $<$ Fe $>$	42	44
Maximum distance from cluster center[a]	$57' = 1.3$ Mpc	$47' = 1.9$ Mpc
Median distance from cluster center[a]	$13' = 0.3$ Mpc	$14' = 0.6$ Mpc
Completeness	80% to $m_{r_T} = 14\overset{m}{.}5$ i.e. $M_{r_T} = -20\overset{m}{.}1$	93% to $m_{r_T} = 15\overset{m}{.}05$ i.e. $M_{r_T} = -20\overset{m}{.}75$
Number of galaxies[a] fainter than completeness	6	9
Number of galaxies[a] fainter than Coma limit[b]	17	9

Typical Measurement Errors[c]

	HydraI	Coma
Uncertainty on $\log r_e$	0.028	0.045
Uncertainty on $\log <I>_e$	0.039	0.064
Correlation[d] between $\Delta \log r_e$ and $\Delta \log <I>_e$	-0.94	-0.94
Uncertainty on $(\log r_e + 0.82 \log <I>_e)$[e]	0.011	0.020
Uncertainty on $\log \sigma$	0.036	0.031
Uncertainty on Mg_2	0.013	0.013
Uncertainty on $\log <$ Fe $>$	0.030	0.037

Galaxies with photometry in Johnson B

	HydraI	
Number of galaxies with σ	45	
Number of galaxies with Mg_2	42	
Number of galaxies with $<$ Fe $>$	42	
Maximum distance from cluster center[a]	$57' = 1.3$ Mpc	
Median distance from cluster center[a]	$13' = 0.3$ Mpc	

Galaxies with photometry in Johnson U

	HydraI	
Number of galaxies with σ	19	
Number of galaxies with Mg_2	18	
Number of galaxies with $<$ Fe $>$	18	
Maximum distance from cluster center[a]	$13' = 0.3$ Mpc	
Median distance from cluster center[a]	$6' = 0.1$ Mpc	

Notes: All galaxies are classified as E or S0. The distance dependent quantities are based on $H_0 = 50\,\mathrm{km\,s^{-1}\,Mpc^{-1}}$; further explanation is given in the text.
[a] This refers to galaxies with a measured σ. [b] The galaxies fainter than the Coma completeness limit ($M_{r_T} = -20\overset{m}{.}75$) are plotted as open symbols throughout this chapter. [c] The typical measurement errors are estimated from external comparisons, except for $\log <$ Fe $>$, where comparisons between different observing runs using different instruments are used. The uncertainties on the photometric parameters refer to Gunn r, but we assume that they are also representative for Johnson B and U. [d] The number given is the linear correlation coefficient (Pearson's r). [e] This is the combination that enters the FP. It has a low uncertainty because the errors in r_e and $<I>_e$ are highly anti-correlated.

7.1.2 The Cluster Properties of HydraI and Coma

Table 7.2 lists key cluster properties of HydraI and Coma, namely the Abell richness, the cluster velocity dispersion, the intracluster gas temperature, and the mean projected galaxy density. They all indicate that Coma is substantially (a factor 2–3) more massive than HydraI. In addition the table gives the fraction of spiral galaxies. Hydra has more spiral galaxies than Coma, which is in agreement with Coma being more massive than HydraI – this is the so-called morphology-density relation (Dressler 1980a, Postman & Geller 1984).

Given the above differences, it is interesting to investigate whether there is a difference in the global scaling relations (e.g. the FP and the Mg_2–σ relation) between the two clusters.

The mean projected galaxy densities $<\mu_{\rm gal}>$ given in Table 7.2 have been calculated as follows. For the Coma cluster, Kent & Gunn (1982) have counted the number of galaxies brighter than $V = 16\overset{\rm m}{.}5$ and within $33\arcmin.6$ from the cluster center. They find this number to be 221 galaxies. This is after subtracting an estimated number of 5 background galaxies. They use a background galaxy density from the literature of 10 galaxies/deg^2. The above-mentioned projected radius corresponds to 1.35 Mpc at the Coma distance. The above-mentioned magnitude limit (i.e. $V = 16\overset{\rm m}{.}5$) corresponds to $M_{\rm r_T} = -19\overset{\rm m}{.}5$, where we have used a typical E/S0 galaxy color of $(r - V) = -0\overset{\rm m}{.}2$.

For HydraI, $M_{\rm r_T} = -19\overset{\rm m}{.}5$ corresponds to $m_{\rm r_T} = 15\overset{\rm m}{.}1$. For the 64 E and S0 galaxies in our HydraI photometry sample, we find the relation $m_{\rm r_T} = V_{25} - 0.75$ (rms = 0.32) when comparing with the V_{25} isophotal magnitudes given in the catalog of Richter (1989). The above magnitude limit therefore corresponds to $V_{25} = 15\overset{\rm m}{.}85$. Note, that this is just a bit fainter than the completeness limit of the Richter catalog, which is $V_{25} = 15\overset{\rm m}{.}65$. The metric projected center distance of 1.35 Mpc corresponds to $57\arcmin.4$ at the distance of HydraI. Within this radius, the Richter catalog has 114 galaxies brighter than $V_{25} = 15\overset{\rm m}{.}85$. Richter estimates the fraction of background galaxies to be 0.15 for galaxies brighter than $V_{25} = 15\overset{\rm m}{.}85$. This is based on the galaxies that has spectroscopy. It is not clear what a representative outer radius for this spectroscopy sample is, but if we use $57\arcmin.4$, the implied background galaxy density is 6 galaxies/deg^2 for $V_{25} \leq 15\overset{\rm m}{.}85$. When simply subtracting $0.15 \cdot 114$ as the estimated number of background galaxies, we are left with 97 galaxies.

The mean projected galaxy density for $r \leq 1.35$ Mpc and $M_{\rm r_T} \leq -19\overset{\rm m}{.}5$ comes out to 39 galaxies/Mpc^2 for Coma and 17 galaxies/Mpc^2 for HydraI.

The fraction of spiral galaxies given in Table 7.2 has been calculated as follows. In the Coma catalog of Dressler (1980b) there are 25 spiral galaxies within the area that our Coma sample covers and to the completeness limit of our Coma sample, $M_{\rm r_T} = -20\overset{\rm m}{.}75$. Since we have 105 E+S0 galaxies in our 93% complete Coma sample brighter than $M_{\rm r_T} = -20\overset{\rm m}{.}75$, the spiral fraction is 25/(25+113) = 18%. In the HydraI catalog of Richter (1989) there are 20 spiral galaxies and 49 E+S0 galaxies within $1\arcdeg.5$ from the center and brighter than $M_{\rm r_T} = -20\overset{\rm m}{.}75$. This gives a spiral fraction of 20/(20+49) = 29%. Note, that the galaxies in the two catalogs are classified by two different persons, and might therefore not be quite comparable.

Table 7.2: Cluster Properties of HydraI and Coma

	HydraI	Coma	References
Abell richness[a]	39	106	Abell, Corwin, & Olowin (1989)
$\sigma_{\rm cl}$ [km/s][b]	608^{+58}_{-39}	1010^{+51}_{-44}	Zabludoff et al. (1990)
$T_{\rm gas}$ [keV][c]	3.9 ± 0.2	8.3 ± 0.6	David et al. (1993)
$<\mu_{\rm gal}>$ [galaxies/Mpc^2][d]	17	39	Richter (1989); Kent & Gunn (1982)
Spiral fraction[e]	29%	18%	Richter (1989); Dressler (1980b)

Notes:
[a] Abell richness is the number of galaxies in the magnitude range m_3 to $m_3 + 2$, where m_3 is the magnitude of the third brightest galaxy in the cluster. The numbers from Abell et al. (1989) have been corrected for background galaxies on a statistical basis.
[b] $\sigma_{\rm cl}$ is the line-of-sight velocity dispersion of the cluster, in the rest frame of the cluster.
[c] $T_{\rm gas}$ is the intracluster gas temperature derived from X-ray observations.
[d] $<\mu_{\rm gal}>$ is the mean projected galaxy density for galaxies brighter than $M_{\rm r_T} = -19\overset{\rm m}{.}5$ and within a projected radius of 1.35 Mpc from the cluster center, cf. the text. Here and below $H_0 = 50\,{\rm km\,s^{-1}\,Mpc^{-1}}$ is assumed. The densities have been corrected for background galaxies on a statistical basis.
[e] The spiral fraction is the fraction of spiral galaxies. The numbers given refer to galaxies brighter than $M_{\rm r_T} = -20\overset{\rm m}{.}75$ and within ≈ 1.9 Mpc from the cluster center, cf. the text.

7.2 The Fundamental Plane in Gunn r

We fitted a plane to the distribution of galaxies in $(\log r_{\rm e}, \log\sigma, \log <I>_{\rm e})$. This was done as an "orthogonal fit"; we seek the vector normal to the plane, $\vec{n} = (-1, \alpha, \beta)$, that minimizes the sum of the absolute residuals perpendicular to the plane. The equivalent equation for the FP is

$$\log r_{\rm e} = \alpha \log\sigma + \beta \log <I>_{\rm e} + \gamma_{\rm cl} \ . \tag{7.4}$$

$r_{\rm e}$ is in arcsec. $\gamma_{\rm cl}$ was taken as the median value. For photometry in Gunn r we find

$$\begin{array}{lrrrrrr} \text{HydraI} : & \log r_{\rm e} = & 1.52\log\sigma & - 0.79\log <I>_{\rm e} + \gamma_{\rm cl} & \sigma_{\rm fit} = 0.109 & N = 45 \\ & & \pm\ 0.16 & \pm\ 0.05 & & \\ \text{Coma} \ : & \log r_{\rm e} = & 1.28\log\sigma & - 0.83\log <I>_{\rm e} + \gamma_{\rm cl} & \sigma_{\rm fit} = 0.095 & N = 114 \\ & & \pm\ 0.06 & \pm\ 0.03 & & \end{array} \tag{7.5}$$

$\sigma_{\rm fit}$ is the rms scatter in the $\log r_{\rm e}$ direction and N is the number of galaxies involved in the fit. The numerical values of $\gamma_{\rm cl}$ have been omitted since they are only of interest when the two clusters are fitted with the same coefficients α and β. The uncertainties on α and β were derived using the bootstrap method (Efron 1979; see also Efron & Tibshirani 1986, 1993).

The above-mentioned fitting method treats the variables symmetrically, which is preferred when we want to establish the physical relation between them, as opposed to when we want to predict one variable from the other variable(s). The fact that we minimize the sum of the absolute residuals and not the sum of the square of the residuals makes the determination more robust against a few galaxies with large deviations from the relation, as does the use of median zero points instead of mean zero points. This fitting method has been used in the literature by e.g. JFK96, Baggley (1996), and Mohr & Wegner (1997). Unless otherwise stated, all fits presented in the following are of this type.

Figure 7.1 shows the FP edge-on. The coefficients of the two FPs are not significantly different, from Eq. (7.5) we find $\Delta\alpha = 0.24 \pm 0.17$ and $\Delta\beta = 0.04 \pm 0.06$. If we fix β at the value -0.82 and only fit α, we find $\alpha_{\rm HydraI} = 1.66 \pm 0.16$ and $\alpha_{\rm Coma} = 1.32 \pm 0.05$. The difference, $\Delta\alpha = 0.34 \pm 0.17$, is significant at the 2 sigma level.

The difference becomes non-significant if we impose the same limiting magnitude of $M_{\rm r_T} = -20\overset{\rm m}{.}75$ (the Coma completeness limit) on the two samples, reducing the number of galaxies as $N_{\rm HydraI}$: 45 → 28 and $N_{\rm Coma}$: 114 → 105. We find $\alpha_{\rm HydraI} = 1.51 \pm 0.24$ and $\alpha_{\rm Coma} = 1.38 \pm 0.08$ (still for $\beta \equiv -0.82$). The difference is non-significant, $\Delta\alpha = 0.13 \pm 0.25$.

However, we do not find any significant evidence that the FP coefficients depend on the limiting magnitude. If we fit HydraI alone and only galaxies brighter than $M_{\rm r_T} = -20\overset{\rm m}{.}75$, we find $\alpha = 1.42 \pm 0.24$ and $\beta = -0.79 \pm 0.08$ (with $\sigma_{\rm fit} = 0.097$), which is not significantly different from the fit to the full HydraI sample, see Eq. (7.5). If we fit Coma alone and only galaxies brighter than $M_{\rm r_T} = -21\overset{\rm m}{.}58$ (the point that split the sample in half, $N = 57$), we find $\alpha = 1.32 \pm 0.10$ and $\beta = -0.83 \pm 0.05$ (with $\sigma_{\rm fit} = 0.093$), which is not significantly different from the fit to the full Coma sample, see Eq. (7.5).

We conclude, that no significant differences in the coefficients for the FP for the HydraI and Coma samples can be detected. Differences in α on the 10% level cannot be ruled out. A common fit to the full HydraI and Coma samples gives

$$\begin{array}{lrrrrrr} \text{HydraI} : & \log r_{\rm e} = & 1.35\log\sigma & - 0.83\log <I>_{\rm e} + 0.189 & \sigma_{\rm fit} = 0.104 & N = 45 \\ \text{Coma} \ : & \log r_{\rm e} = & 1.35\log\sigma & - 0.83\log <I>_{\rm e} - 0.044 & \sigma_{\rm fit} = 0.099 & N = 114 \\ & & \pm\ 0.07 & \pm\ 0.03 & & \end{array} \tag{7.6}$$

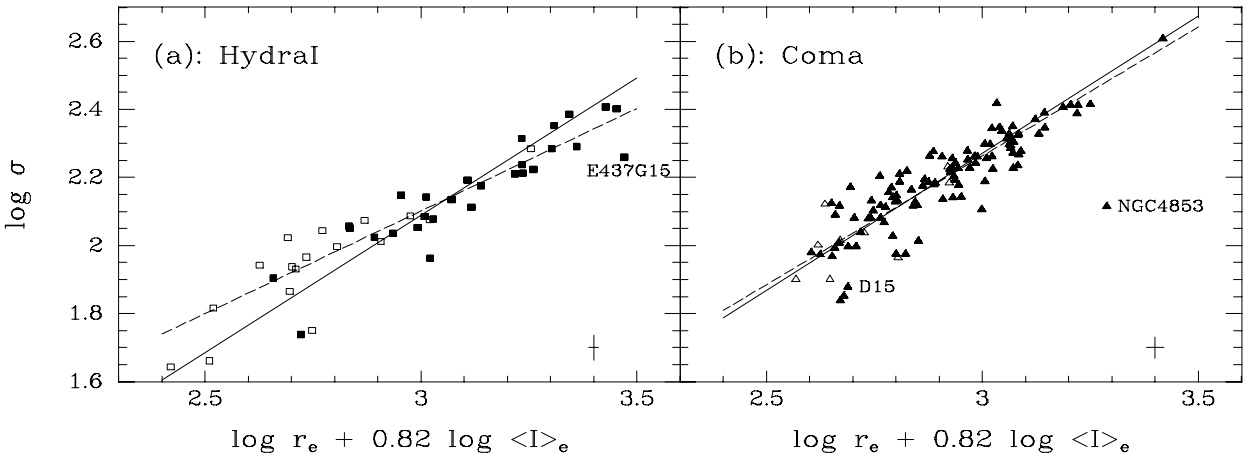

Figure 7.1: The FP in Gunn r seen edge-on. $r_{\rm e}$ is in arcsec. Solid line: $\alpha = 1.24$ (JFK96). Dashed lines: (a) $\alpha = 1.66$, (b) $\alpha = 1.32$. R295/E437G15, D15 and NGC4853 deviate strongly from the Mg_2–σ relation, Fig. 7.6. D15 and NGC4853 also deviate strongly from the $<\mathrm{Fe}>$–σ relation, Fig. 7.7.
Data symbols: Boxes/triangles – HydraI/Coma galaxies. Filled/open symbols – galaxies brighter/fainter than $M_{\rm r_T} = -20\overset{\rm m}{.}75$. Typical error bars are given on the panels, cf. Sect. 7.1.1.

This is not significantly different from the coefficients found by JFK96, $\alpha = 1.24 \pm 0.07$, $\beta = -0.82 \pm 0.02$, based on 226 E and S0 galaxies in 10 clusters.

In the following we adopt the values of α and β from Eq. (7.6). At this point, we determine the peculiar velocity implied by the FP. The peculiar velocity for a given cluster is given by $v_{\rm pec} \approx cz_{\rm CMB} - cz$ to first order in z, where z is the expected redshift in the CMB frame in the absence of peculiar velocities. Since we do not have an accurate calibration of the intrinsic FP zero point, we use the observed FP zero point difference to calculate the *relative* distance between HydraI and Coma. We assume Coma to have no peculiar velocity. From the FP zero points, $\gamma_{\rm HydraI} = 0.189 \pm 0.0155$ and $\gamma_{\rm Coma} = -0.044 \pm 0.0092$, we then find the peculiar velocities $v_{\rm pec,HydraI} = -93 \pm 152\,{\rm km\,s^{-1}}$ and $v_{\rm pec,Coma} = 0 \pm 160\,{\rm km\,s^{-1}}$. The peculiar velocity for HydraI is non-significant.

For the JFK96 FP, we get the same peculiar velocity for HydraI within the uncertainties. We find FP zero points $\gamma_{\rm HydraI} = 0.410 \pm 0.0153$ and $\gamma_{\rm Coma} = 0.184 \pm 0.0086$, and peculiar velocities $v_{\rm pec,HydraI} = -157 \pm 152\,{\rm km\,s^{-1}}$ and $v_{\rm pec,Coma} = 0 \pm 149\,{\rm km\,s^{-1}}$.

We have calculated the uncertainty on γ, which is a median value, as $\sigma_{\rm fit}/\sqrt{N}$ (where $\sigma_{\rm fit}$ is the rms scatter, cf. above). It is known from the statistical literature (e.g. Stuart & Ord 1987) that the uncertainty on the mean is $\mathrm{rms}/\sqrt{N}$ regardless of the probability distribution that the data points are drawn from, whereas the uncertainty on the median depends on the distribution. For the special case of a normal distribution, the uncertainty on the median is $\sqrt{\pi/2} \cdot \mathrm{rms}/\sqrt{N} \approx 1.25\,\mathrm{rms}/\sqrt{N}$. For distributions with increasingly larger tails than the normal distribution, the uncertainty on the median becomes increasingly less than the uncertainty on the mean. Mohr & Wegner (1997) used the bootstrap method to calculate the uncertainty on the FP zero point difference, and found the value $\mathrm{rms}/\sqrt{N}$ to be a conservative estimate on the uncertainties on the individual FP zero points. Throughout this work we calculate the uncertainty on the median as $\mathrm{rms}/\sqrt{N}$.

We now calculate $r_{\rm e}$ in kpc using Eq. (7.3). The FP, Eq. (7.6), then becomes

$$\begin{array}{rcccl} \log r_{\rm e} = & 1.35 \log\sigma & - 0.83 \log <I>_{\rm e} - 0.218 & \sigma_{\rm fit} = 0.099 & (r_{\rm e}\ \text{in kpc}) \\ & \pm\ 0.07 & \pm\ 0.03 & & \end{array} \tag{7.7}$$

In order to plot the FP face-on, we define a new 3-space (x, y, z) by

$$\begin{aligned} x &= [(\alpha^2+\beta^2)\log r_{\rm e} + \alpha\log\sigma + \beta\log<I>_{\rm e}] \;/\; \left(\alpha^2+\beta^2+(\alpha^2+\beta^2)^2\right)^{0.5} \\ y &= [-\beta\log\sigma + \alpha\log<I>_{\rm e}] \;/\; (\alpha^2+\beta^2)^{0.5} \\ z &= [-\log r_{\rm e} + \alpha\log\sigma + \beta\log<I>_{\rm e}] \;/\; (1+\alpha^2+\beta^2)^{0.5} \end{aligned} \tag{7.8}$$

This is an orthonormal transformation of the original 3-space $(\log r_{\rm e}, \log\sigma, \log<I>_{\rm e})$. The (x, y) projection shows the FP face-on, since z is constant for the FP. Furthermore, x is proportional to $\log r_{\rm e}$ for the FP. For our values of α and β we get

$$\begin{aligned} x &= [2.51\log r_{\rm e} + 1.35\log\sigma - 0.83\log<I>_{\rm e}] \;/\; 2.97 \\ y &= [0.83\log\sigma + 1.35\log<I>_{\rm e}] \;/\; 1.58 \\ z &= [-\log r_{\rm e} + 1.35\log\sigma - 0.83\log<I>_{\rm e}] \;/\; 1.87 \end{aligned} \tag{7.9}$$

Figure 7.2 shows the FP face-on for the two samples. The dashed line marks $M_{\rm r_T} = -20\overset{\rm m}{.}75$, the completeness limit of the Coma data. The equation for the plane in 3-space of constant absolute magnitude $M_{\rm r_T}$ is given by $0.4(M_\odot - M_{\rm r_T}) = \log<I>_{\rm e} + 2\log r_{\rm e} + \log(2\pi) + 6$ (with $<I>_{\rm e}$ in $L_\odot/{\rm pc}^2$ and $r_{\rm e}$ in kpc, as noted earlier). The intersection with the (x, y) plane can be found using the equation for the FP and the equations for x and y by eliminating $\log r_{\rm e}$, $\log\sigma$, and $\log<I>_{\rm e}$. The galaxies brighter and fainter than $M_{\rm r_T} = -20\overset{\rm m}{.}75$ are shown in Fig. 7.2 as filled and open symbols, respectively. The fact that a few of the points are on the wrong side of the line marking $M_{\rm r_T} = -20\overset{\rm m}{.}75$ is because the plane of constant $M_{\rm r_T}$ intersects the FP at an angle of 132°, not 90°. This is most easily seen in $(\log r_{\rm e}, \log\sigma, \log<I>_{\rm e})$ space where the FP and the plane of constant $M_{\rm r_T}$ have normal vectors $(-1, \alpha, \beta)$ and $(2, 0, 1)$, respectively. Since the galaxies scatter somewhat perpendicular to the plane, the projection onto the plane might render them on the "wrong" side.

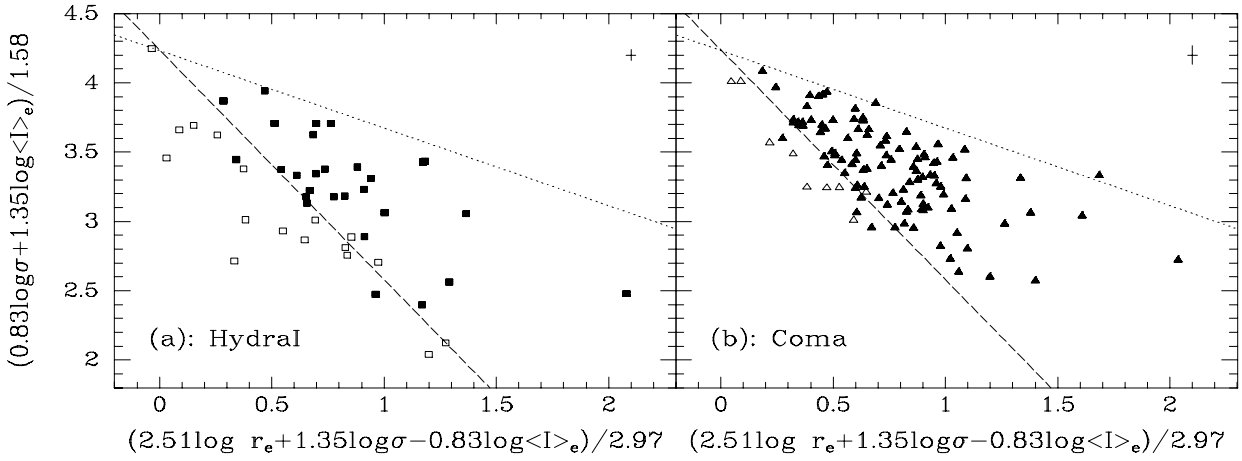

Figure 7.2: The Fundamental Plane in Gunn r, Eq. (7.7), seen face-on. $r_{\rm e}$ is in kpc. The dashed line marks $M_{\rm r_T} = -20\overset{\rm m}{.}75$, the completeness limit of the Coma data. The upper boundary (dotted line), given by $y \approx -0.56x + 4.23$, is not caused by selection effects. This line demarcates the so-called exclusion zone noted by Bender et al. (1992) and Burstein et al. (1992). The distribution within the FP is similar for the two samples when imposing the same absolute magnitude limit. Data symbols as in Fig. 7.1.

Bender et al. (1992) noted, that the region occupied within the FP by luminous ellipticals was

delimited by the line $y \approx -0.56x + 4.13$[1], which is shown as the dotted line in Fig. 7.2. The region beyond this line was coined the *exclusion zone* by Burstein, Bender, & Faber (1992), and recently the *zone of exclusion (ZOE)* by Burstein et al. (1997).

The existence of the exclusion zone is not caused by selection effects. Rather, it is a physical constraint in addition to the FP, corresponding to $r_{\rm e}\,\sigma^{7.46}{<}I{>}_{\rm e}^{2.73} \lesssim$ constant (note, that the sign of the $<I>_{\rm e}$ exponent is wrong in Bender et al. 1992 and Burstein et al. 1992).

As can be seen from Fig. 7.2, the distribution within the FP is similar for the HydraI and Coma samples when imposing the same absolute magnitude limit. This can be quantified by means of the 2-dimensional 2-sample Kolmogorov-Smirnov test (Fasano & Franceschini 1987; as implemented by Press el al. 1992). This test gives the probability $P_{\rm same\ distr.}$ that the two samples are drawn from the same distribution. We find $P_{\rm same\ distr.} = 25\%$ for HydraI vs. Coma for galaxies brighter than $M_{\rm r_T} = -20\overset{\rm m}{.}75$. This test is not invariant under a rotation of the coordinate system. In our case, we might as well have used another coordinate system (x', y') that was rotated by an angle θ with respect to (x, y) to describe the distribution of galaxies within the FP. If we perform the above-mentioned test using coordinates rotated by $\theta = 0.0°, 0.1°, 0.2°, \ldots, 89.9°$, we obtain values of $P_{\rm same\ distr.}$ in the range 14%–67%, with a mean value of 31%. Fortunately, all the values agree in the sense that they all indicate a non-significant difference. For comparison, for a normal distribution, a two sigma deviation has a probability of 4.6%, so in that sense the differences we find are not significant at the two sigma level.

Figure 7.3 shows the FP *edge-on* along $\log r_{\rm e}$. Since the galaxies span a larger range in $\log r_{\rm e}$ than in $\log\sigma$, 1.8 and 1.0, respectively, the scatter *looks* smaller along $\log r_{\rm e}$ (Fig. 7.3) than along $\log\sigma$ (Fig. 7.1). Nevertheless, the scatter (in the $\log r_{\rm e}$ direction) of the two FPs is somewhat higher than found earlier, though the difference in the scatter is not statistically significant. For the Coma sample we find $\sigma_{\rm fit} = 0.095 \pm 0.009$. JFK96 found $\sigma_{\rm fit} = 0.079 \pm 0.009$ for a sample of 79 galaxies in the Coma cluster (their sample is a subset of ours). The two values of $\sigma_{\rm fit}$ are not significantly different. If galaxies with $\log\sigma < 2.0$ are omitted from our two samples, we get $\sigma_{\rm fit} = 0.090$ for HydraI and 0.088 for Coma. We note, that of the 8 Coma galaxies with residuals > 0.19, 4 have been observed by Caldwell et al. (1993), and two of these, NGC4853 and D15, were classified as peculiar (starburst or post-starburst). NGC4853 has an FP residual more than twice as large as any of the other galaxies, see Fig. 7.1(b) and 7.3(b). NGC4853 and D15 also have large residuals from the $\rm Mg_2$–σ relation, Fig. 7.6(b), and the $<$ Fe $>$–σ relation, Fig. 7.7(b). The high residuals are most likely caused by the presence of young stars in these two galaxies.

The FP has significant intrinsic scatter ($\sigma_{\rm int}$). We estimate $\sigma_{\rm int}$ by subtracting the typical measurement errors in quadrature from $\sigma_{\rm fit}$, taking into account the correlation between the errors in $\log r_{\rm e}$ and $\log{<}I{>}_{\rm e}$. We do this as $\sigma_{\rm int} = ({\sigma_{\rm fit}}^2 - [\sigma^2_{(\log r_{\rm e} - \beta \log <I>_{\rm e})} + (\alpha\sigma_{\log\sigma})^2])^{1/2}$. When we insert $\sigma_{(\log r_{\rm e} - \beta \log <I>_{\rm e})} = 0.017$ and $\sigma_{\log\sigma} = 0.032$ (Table 7.1, p. 87; weighted mean values for HydraI and Coma), and $\sigma_{\rm fit} = 0.099$ and $\alpha = 1.35$ (Eq. 7.7), we get $\sigma_{\rm int} = 0.087$. JFK96 found an intrinsic scatter of 0.070, which is lower than our value at the 2 sigma level.

Unless our estimates of the measurement errors are a factor of two too low, which seems unlikely, there is significant intrinsic scatter in the FP. We will search for the source of this scatter in Sect. 7.6, where we investigate correlations between the FP residuals and a number of available parameters.

[1]This corresponds to the line $\kappa_1 + \kappa_2 = 8.0$, which is what is shown in Fig. 2b in Bender et al. (1992). These authors define a new 3-space $(\kappa_1, \kappa_2, \kappa_3)$ in which the (κ_1, κ_2) projection shows the FP nearly face-on. Note, that in the text of Bender et al., the line is given as $\kappa_1 + \kappa_2 = 7.8$, a line that fall just *inside* the the distribution of galaxies, not at the edge. The relation $\kappa_1 + \kappa_2 = 8.0$ is also what is used recently by Burstein et al. (1997).

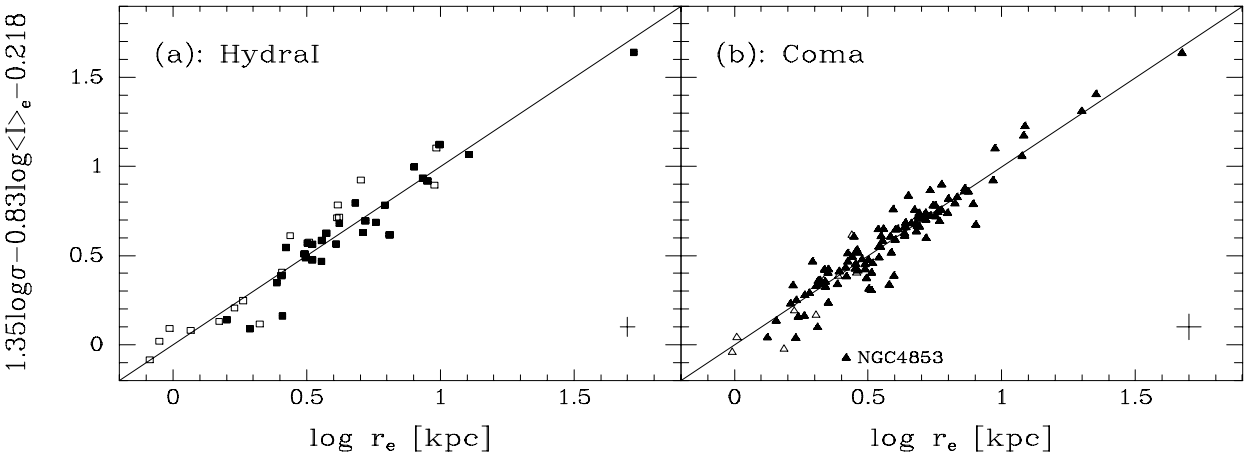

Figure 7.3: The Fundamental Plane in Gunn r, Eq. (7.7), seen edge-on. r_e is in kpc. Data symbols as in Fig. 7.1.

Do galaxies classified as E and S0 follow the same FP? JFK96 found, that E and S0 galaxies had similar FP zero points. This is also the case for the samples studied here, we find an FP zero point difference of 0.000 ± 0.015. In Fig. 7.4 we plot the FP face on with E and S0 galaxies in separate panels. The dot-dashed line on the figure marks $M_{r_T} = -23\overset{m}{.}1$. JF94 found no S0 galaxies brighter than this magnitude in their Coma sample. Their Coma sample is the one we use here. The visual impression from Fig. 7.4 might be that E and S0 galaxies are *not* distributed in the same way within the FP. However, a statistical test gives the opposite result. When we select galaxies with M_{r_T} between $-20\overset{m}{.}75$ and $-23\overset{m}{.}1$ to get a complete sample and to take into account the effect found by JF94, a 2D K-S test gives $P_{\text{same distr.}}$ in the range 13%–44%, with a mean value of 26%, indicating a non-significant difference.

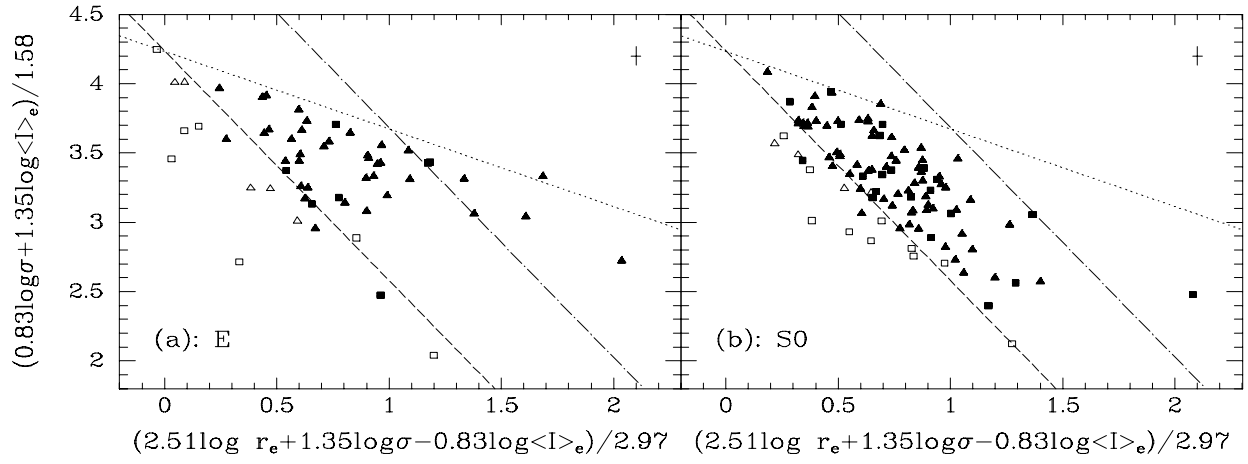

Figure 7.4: The Fundamental Plane in Gunn r, Eq. (7.7), seen face-on. r_e is in kpc. (a): E galaxies. (b): S0 galaxies. HydraI and Coma are plotted together. Dashed line: $M_{r_T} = -20\overset{m}{.}75$. Dot-dashed line: $M_{r_T} = -23\overset{m}{.}1$. Dotted line: exclusion zone. Data symbols as in Fig. 7.1.

7.3 The Fundamental Plane in Other Passbands

For the HydraI sample of 45 galaxies photometry is also available in Johnson B, and for a subsample of 19 galaxies also in Johnson U. A fit to the Johnson B data gives (r_e in kpc)

$$\text{HydraI, JB}: \quad \log r_e = \underset{\pm\ 0.14}{1.46}\log\sigma \underset{\pm\ 0.04}{-\ 0.80}\log <I>_e - 0.701 \quad \sigma_{\rm fit} = 0.110 \quad N = 45 \tag{7.10}$$

The scatter is the same as in Gunn r (Eq. 7.5).
A fit to the Johnson U data gives (r_e in kpc)

$$\text{HydraI, JU}: \quad \log r_e = \underset{\pm\ 0.21}{1.38}\log\sigma \underset{\pm\ 0.07}{-\ 0.82}\log <I>_e - 0.623 \quad \sigma_{\rm fit} = 0.066 \quad N = 19 \tag{7.11}$$

For the same 19 galaxies, the result in Gunn r is

$$\text{HydraI, GR}: \quad \log r_e = \underset{\pm\ 0.29}{1.61}\log\sigma \underset{\pm\ 0.06}{-\ 0.83}\log <I>_e + \gamma_{\rm cl} \quad \sigma_{\rm fit} = 0.087 \quad N = 19 \tag{7.12}$$

The scatter in those two passbands is also not significantly different. Figure 7.5 shows the Fundamental Plane seen edge-on in Johnson B and Johnson U.

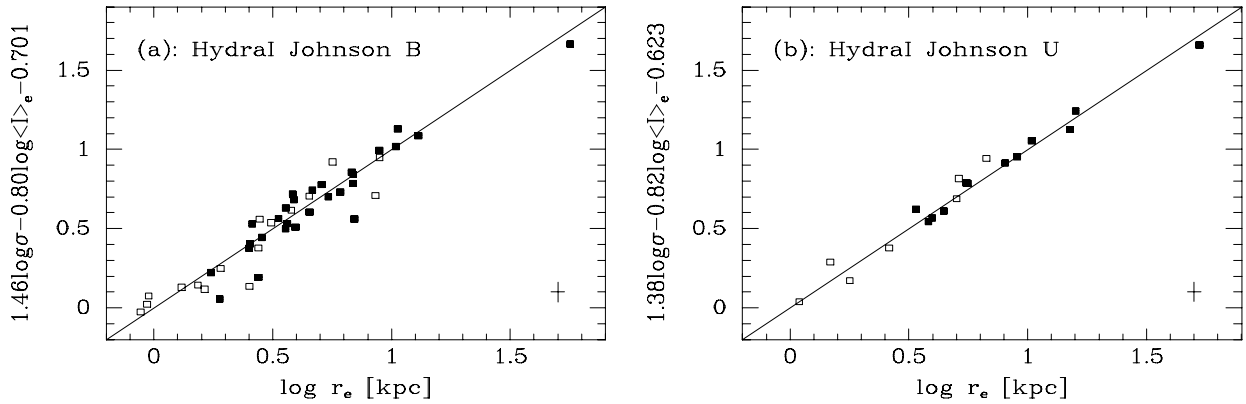

Figure 7.5: The Fundamental Plane for HydraI seen edge-on. r_e is in kpc. (a): Johnson B, Eq. (7.10). (b): Johnson U, Eq. (7.11). The equivalent plot for Gunn r is Fig. 7.3(a). Data symbols as in Fig. 7.1.

We assume that the contribution to the scatter from the measurement errors is the same in the different passbands. This is supported by the internal comparison of the photometry: we found an rms scatter of $0\overset{\rm m}{.}012$ for Gunn r and $0\overset{\rm m}{.}011$ for Johnson B (Table 4.1, p. 42). This implies that the intrinsic scatter in the three passbands is approximately the same. This is also what JFK96 found for the passbands Gunn r, Gunn g, Johnson B, and Johnson U. As JFK96 noted, one consequence of this is that intrinsic dust absorption in the galaxies cannot be a major source of the intrinsic FP scatter, since dust absorption depends on wavelength.

Another consequence is related to the question whether the intrinsic FP scatter is produced by an age scatter or a metallicity scatter. If the galaxies have similar structure, we can translate the FP scatter into a scatter in the $(M/L) \propto M^b$ relation (cf. Sect. 2.2.3), where b can be calculated from α as $b = (2-\alpha)/(2+\alpha)$. The scatter in the quantity $[\log(M/L) - b\log(M)]$ (i.e. the zero point in the $(M/L) \propto M^b$ relation) is 0.127 dex in Gunn r and Johnson B, 0.075 dex in Johnson U,

and 0.103 dex in Gunn r selected as Johnson U. This includes scatter from the measurement errors. The typical measurement error on $\log(M/L)$ is 0.074 for the 45 HydraI galaxies with Gunn r and Johnson B photometry, and 0.068 for the 19 HydraI galaxies with Johnson U photometry. This is based on the values in Table 7.1, p. 87, and corrected for the fact that the 19 galaxies have lower $\log\sigma$ uncertainties than all the 45 galaxies. As an approximation, we estimate the intrinsic scatter in the $(M/L) \propto M^b$ relation by subtracting in quadrature the typical measurement error on $\log(M/L)$ only. We get 0.103 dex (24%) in Gunn r and Johnson B, 0.020 dex (5%) in Johnson U, and 0.078 dex (18%) in Gunn r selected as Johnson U. By means of stellar population models, we can translate the scatter in (M/L) into a scatter in age or metallicity. Specifically, the models by Vazdekis et al. (1996) with a bi-modal IMF with high mass slope $\mu = 1.35$ can for ages > 5 Gyr be well approximated by

$$\log(M/L_{\rm r}) \approx 0.63\log\text{age} + 0.26\,[\text{M/H}] - 0.16 \quad (7.13)$$

$$\log(M/L_{\rm B}) \approx 0.78\log\text{age} + 0.41\,[\text{M/H}] - 0.05 \quad (7.14)$$

$$\log(M/L_{\rm U}) \approx 0.97\log\text{age} + 0.58\,[\text{M/H}] - 0.07 \quad (7.15)$$

If we consider Gunn r, the scatter in $\log(M/L_{\rm r})$ of 0.10 dex (i.e. 24% in $(M/L_{\rm r})$) can be translated into a scatter in $\log$ age of 0.16 dex (38% in age) or a scatter in [M/H] of 0.40 dex (90% in Z). However, since the scatter is approximately constant for the three passbands (when comparing the same galaxies), and since neither the $\log$ age coefficients nor the [M/H] coefficients are the same, variations in *both* age and metallicity are needed. We revisit this issue in Sect. 7.5.2 (p. 111) in the light of the age–metallicity–sigma relation.

7.4 Line Indices, Colors and Velocity Dispersions

7.4.1 The Mg_2–σ Relation

The existence of a tight correlation between Mg_2 and $\log\sigma$ is well established (e.g. Burstein et al. 1988, Bender et al. 1993). It is remarkable that the stellar population (Mg_2) is so closely connected with the structural properties (σ).

For our samples, Mg_2 has been measured for 42 of the HydraI galaxies and 113 of the Coma galaxies. We test if the two samples follow the same Mg_2–σ relation as follows. First we fit the two samples individually. We compare the slopes and find a non-significant difference of $\Delta(\text{slope}) = 0.009 \pm 0.043$. Second we fit the two samples together, with the zero point for each sample left free. We find a non-significant difference of $\Delta(\text{zero point}) = -0.002 \pm 0.006$. We conclude that the galaxies in the central parts of the HydraI cluster and the Coma cluster follow the same Mg_2–σ relation. We then fit the two samples together and get

$$\text{HydraI} + \text{Coma}: \quad Mg_2 = \underset{\pm\ 0.014}{0.189}\log\sigma - 0.139 \quad \sigma_{\text{fit}} = 0.028 \quad N = 155 \tag{7.16}$$

Mg_2 versus $\log\sigma$ is shown in Figure 7.6.

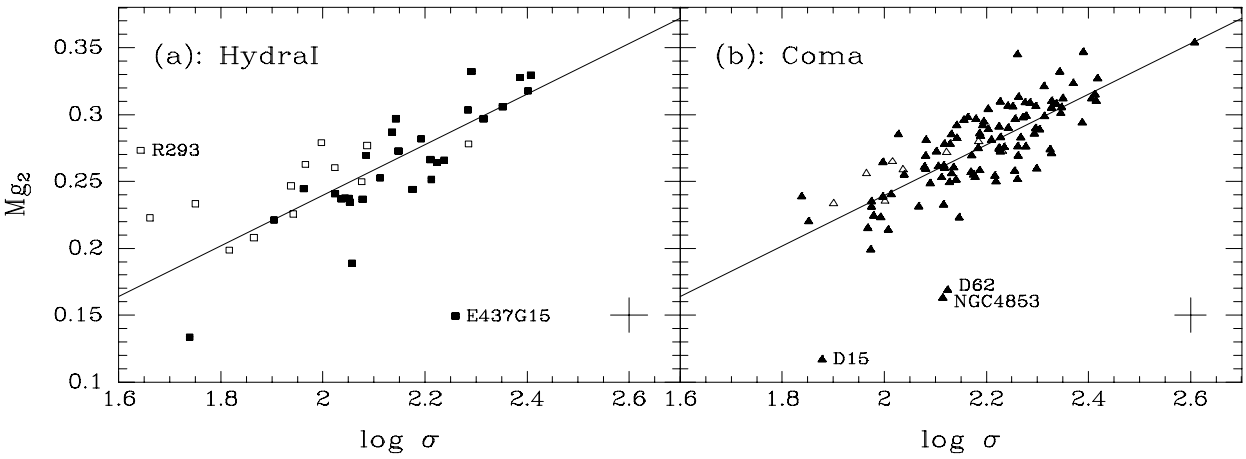

Figure 7.6: The Mg_2–σ relation, Eq. (7.16). The spectrum of R293 has very low S/N. R295/E437G15 has a strong disk and $v_{\text{rot}}>150\,\text{km}\,\text{s}^{-1}$. The spectra of D15/MRK55 and D43/NGC4853, but *not* D62, show signs of recent star formation or nuclear activity (Caldwell et al. 1993). Data symbols as in Fig. 7.1.

The slope that we find, 0.189 ± 0.014, is in agreement with other studies in the literature: 0.175 (Burstein et al. 1988), 0.20 (Bender et al. 1993), 0.196 ± 0.016 (JFK96), and 0.196 ± 0.009 (J97). Note that the Bender et al. value is for all types of 'dynamically hot galaxies' (DHGs), from dwarf spheroidals to giant ellipticals, with M_{B_T} in the impressive range -8 to -24 mag. For comparison, our 155 galaxies fall in the categories 'giant ellipticals' ($M_{B_T} \leq -20\overset{\text{m}}{.}5$; 66 galaxies), 'intermediate ellipticals' ($-20\overset{\text{m}}{.}5 < M_{B_T} \leq -18\overset{\text{m}}{.}5$; 88 galaxies), and 'bright dwarf ellipticals' ($M_{B_T} > -18\overset{\text{m}}{.}5$; 1 galaxy) in the classification scheme of Bender et al. A typical E/S0 color of $(B-r) = 1\overset{\text{m}}{.}15$ was used.

We estimate the intrinsic scatter σ_{int} by subtracting the uncertainties on Mg_2 and $\log\sigma$ (see Table 7.1) in quadrature from σ_{fit}. We find $\sigma_{\text{int}} = (0.028^2 - [(0.189 \cdot 0.032)^2 + 0.013^2])^{1/2} = 0.024$. A large part of the scatter is caused by the five very deviating galaxies, which are marked in Fig. 7.6. For all but D62, we have a possible explanation why they deviate, cf. the caption to

the figure. If these five galaxies are omitted, the scatter $\sigma_{\rm fit}$ decreases from 0.028 to 0.020. The latter value corresponds to $\sigma_{\rm int} = 0.014$. Bender et al. (1993) found $\sigma_{\rm int} = 0.018$ for their DHG sample. Mg_2 depends on both age and metallicity. For the Vazdekis et al. (1996) models with a bi-modal IMF with high mass slope $\mu = 1.35$, the predictions can be approximated by $Mg_2 = 0.12 \log \text{age} + 0.19\,[\text{M/H}] + 0.14$ (J97; Eq. 2.34) for ages > 5 Gyr. If the intrinsic scatter ($\sigma_{\rm int} = 0.024$) in the Mg_2–σ relation is due to scatter in age alone, the scatter in log age at a given $\log\sigma$ is 0.20 dex (46% in age). If it is due to scatter in metallicity alone, the scatter in [M/H] is 0.13 dex (30% in Z). These considerations are revisited in Sect. 7.5.2 (p. 111) in the light of the age–metallicity–sigma relation. Bender et al. (1993) found the allowed scatter in age or Z to be 15% for both. This value was based on their $\sigma_{\rm int} = 0.018$ and different population synthesis models than the ones we use.

7.4.2 The $<$ Fe $>$–σ Relation

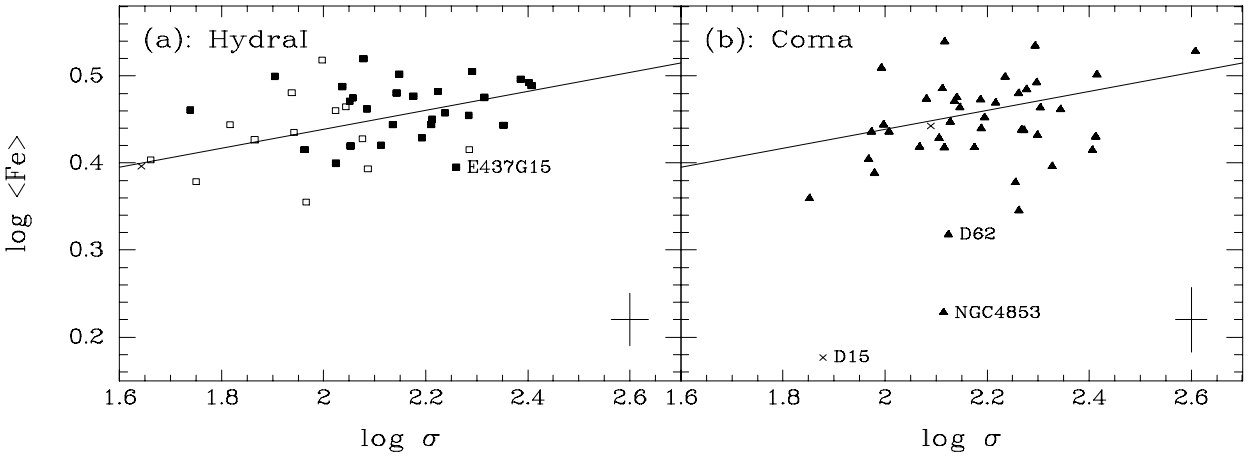

Figure 7.7: The $<$ Fe $>$–σ relation, Eq. (7.17). R295/E437G15 has a strong disk and $v_{\rm rot}$>150 km s^{-1}. The spectra of D15/MRK55 and D43/NGC4853, but *not* D62, show signs of recent star formation or nuclear activity (Caldwell et al. 1993).
Data symbols: Boxes/triangles – HydraI/Coma galaxies. Filled/open symbols – galaxies brighter/fainter than $M_{\rm r_T} = -20\overset{\rm m}{.}75$. Crosses – galaxies with $\sigma_{\log <\rm Fe>} > 0.065$, these were excluded from the fits. Note, that there are no Coma galaxies fainter than $M_{\rm r_T} = -20\overset{\rm m}{.}75$ with a measured $<$ Fe $>$.

$\log <$ Fe $>$ is also known to correlate with $\log\sigma$ (J97), although the scatter compared to the slope is much larger than for the Mg_2–σ relation. For our data, $<$ Fe $>$ has been measured for 42 of the HydraI galaxies and 44 of the Coma galaxies. Since our fitting method does not take into account the uncertainties on the individual data points, we exclude galaxies with an uncertainty on $\log <$ Fe $>$ larger than 0.065, corresponding to a relative uncertainty on $<$ Fe $>$ of 15%. 3 galaxies are excluded by this: R293 in HydraI, and D15 and D110 in Coma.

We test if the $<$ Fe $>$ indices and the velocity dispersions are significantly correlated by means of Spearman rank order tests. For our HydraI, Coma, and HydraI+Coma samples we find $P_{\rm no\ corr.} =$ 8.6%, 16.0%, and 3.6%, respectively. $P_{\rm no\ corr.}$ is the probability of *no* correlation. J97 found $P_{\rm no\ corr.}$ = 0.18%. Thus, it is clear that there is actually a $<$ Fe $>$–σ relation. However, J97 found that it was driven by galaxies with low and high σ. Specifically, she found that when excluding galaxies with $\log\sigma$ outside the range 2.0–2.4, there was no significant correlation between $\log <$ Fe $>$ and $\log\sigma$. For our HydraI+Coma sample we find the same to be the case: $P_{\rm no\ corr.}$ increases from 3.6% to 42% when we omit the 24 galaxies with $\log\sigma$ outside 2.0–2.4.

We test if the two samples follow the same $<\mathrm{Fe}>$–σ relation in the same way as done above for the $\mathrm{Mg_2}$–σ relation. For the HydraI and Coma samples we find $\Delta(\mathrm{slope}) = -0.032 \pm 0.083$ and $\Delta(\mathrm{zero\ point}) = 0.019 \pm 0.011$. The differences are not significant. When we fit the two samples together we get

$$\mathrm{HydraI + Coma}: \quad \log <\mathrm{Fe}> = \begin{array}{l} 0.109 \log \sigma + 0.222 \\ \pm\ 0.041 \end{array} \quad \sigma_{\mathrm{fit}} = 0.050 \quad N = 83 \tag{7.17}$$

J97 found a slope of 0.075 ± 0.025 for 187 E and S0 galaxies mainly in clusters, consistent with our value. We note, that had we excluded the very deviating galaxy NGC4853 we would have got a slope of 0.095 ± 0.043, still in agreement with J97. The $<\mathrm{Fe}>$–σ relation is shown in Figure 7.7.

7.4.3 $<\mathrm{Fe}>$ versus $\mathrm{Mg_2}$

The strong $\mathrm{Mg_2}$–σ relation and the weak $<\mathrm{Fe}>$–σ relation indicate that there is no strong correlation between $\log <\mathrm{Fe}>$ and $\mathrm{Mg_2}$. This can be seen in Fig. 7.8. Overplotted as dashed lines are the model predictions from the single-age single metallicity stellar population models from Vazdekis et al. (1996). It is seen that no variation of age or metallicity can reproduce the shallow slope of the $\log <\mathrm{Fe}>$–$\mathrm{Mg_2}$ relation in the interval in $\mathrm{Mg_2}$ spanned by the data. The Vazdekis et al. models have solar abundance ratios, including $[\mathrm{Mg/Fe}] = 0$. Also overplotted on the figure are predictions from the Weiss et al. (1995) models. These have $[\mathrm{Mg/Fe}] = 0.45$, and they are able to reproduce the shallow slope of the $\log <\mathrm{Fe}>$–$\mathrm{Mg_2}$ relation (by varying only the age). Based on these arguments, several authors (e.g. Worthey et al. 1992, J97) have concluded that at least some E and S0 galaxies must have $[\mathrm{Mg/Fe}] > 0$. Already O'Connell (1976) concluded, that Mg I exhibited a distinct enhancement in giant E nuclei with respect to the Fe-peak elements. J97 further noted, that since $\log <\mathrm{Fe}>$ and $\mathrm{Mg_2}$ depend in the same way on the mean age of the stellar population (at least in the Vazdekis et al. models), the different slope of the $\mathrm{Mg_2}$–σ and the $<\mathrm{Fe}>$–σ relations imply that [Mg/Fe] is correlated with σ. We determine [Mg/Fe] in a more direct way in the next section (Sect. 7.5).

7.4.4 Color Relations

σ, $\mathrm{Mg_2}$, and $<\mathrm{Fe}>$ are all measured in the *central* part of the galaxy. Specifically, the HydraI spectroscopical parameters, which originates from four different observing runs, were measured within apertures of equivalent radius $1\farcs3$–$2\farcs35$, corresponding to 0.5–0.9 kpc (here and below we assume $H_0 = 50\,\mathrm{km\,s^{-1}\,Mpc^{-1}}$). The measurements were aperture corrected to an aperture of radius 1.19 kpc, i.e. the standard JFK95b aperture of *diameter* 1.19 h^{-1} kpc (note the h^{-1} factor), cf. Sect. 6.2 and 6.3. The HydraI *effective* colors $(B-r)_{\mathrm{e}}$, $(U-r)_{\mathrm{e}}$, and $(U-B)_{\mathrm{e}}$ on the other hand, are measured within a radius of 0.8–53 kpc, typically 3.6 kpc. The fact that tight correlations exist between e.g. central velocity dispersion and global color has been interpreted by Burstein et al. (1988), Franx & Illingworth (1990), and Bender et al. (1993) as an indication that the galaxy to galaxy variations in radial gradients in colors and line indices are small. However, if the size of the gradient is correlated with the central value, this conclusion does not necessarily hold. Since the relative uncertainties on the radial gradients currently available in the literature are quite large, it is not yet clear whether the radial gradients are correlated with e.g. central velocity dispersion or global color.

For the 45 galaxies in the HydraI sample we have the color $(B-r)_{\mathrm{e}}$, and for 19 of these galaxies we also have the colors $(U-r)_{\mathrm{e}}$ and $(U-B)_{\mathrm{e}}$. All the colors correlate strongly with $\log \sigma$. We find

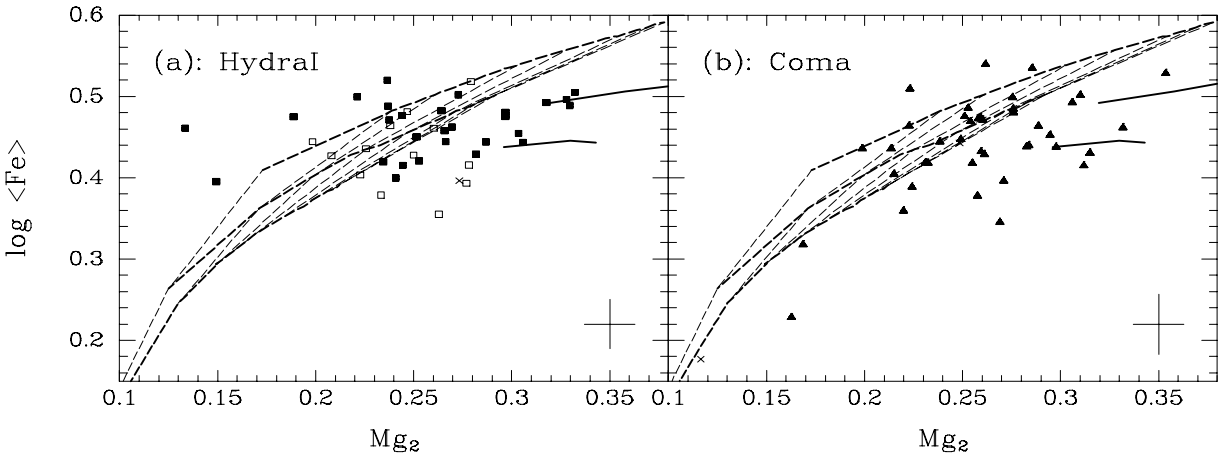

Figure 7.8: $\log <\mathrm{Fe}>$ versus Mg_2. Overplotted are predictions from single-age single-metallicity stellar population models. Dashed lines – Vazdekis et al. (1996), (bi-modal IMF with high mass slope $\mu = 1.35$), with [Mg/Fe] = 0. The thin dashed lines are at constant age, from left to right 1, 2, 3, 5, 8, 12, 15, and 17 Gyr (approximately). The thick dashed lines are at constant metallicity $[\mathrm{M/H}] \equiv \log(Z/Z_\odot)$, from bottom to top −0.4, 0.0, and 0.4. Solid lines – Weiss et al. (1995), with [Mg/Fe] = 0.45. The two lines shown are at constant (total) metallicity [M/H], from bottom to top 0.0 and 0.4. The ages vary from left to right from 12 to 18 Gyr, with the 18 Gyr point being outside the plot for [M/H] = 0.4. The models have been offset to enable a comparison with the Vazdekis et al. models, cf. Sect. 2.3 (p. 18). Data symbols as in Fig. 7.7.

the following color–σ relations

$$\begin{aligned}
&\text{HydraI}: \quad (B-r)_\mathrm{e} = 0.268\log\sigma + 0.562 \pm 0.049 \quad \sigma_\mathrm{fit} = 0.039 \quad N = 44 \\
&\text{HydraI}: \quad (U-r)_\mathrm{e} = 0.655\log\sigma + 0.220 \pm 0.407 \quad \sigma_\mathrm{fit} = 0.076 \quad N = 18 \\
&\text{HydraI}: \quad (U-B)_\mathrm{e} = 0.461\log\sigma - 0.498 \pm 0.126 \quad \sigma_\mathrm{fit} = 0.062 \quad N = 18
\end{aligned} \tag{7.18}$$

We have excluded the galaxy R293, since the spectrum of this galaxy has very low S/N (only 13 per Å; cf. Table 6.4, p. 83), and since it deviates strongly from the relation defined by the other galaxies. The galaxy R295/E437G15, which also deviates substantially, was not excluded – however, the fit is not sensitive to this. The color–σ relations are shown in Fig. 7.9(a–c).

Franx & Illingworth (1990) found the relations $(B-R) = (0.70\pm0.3)\log\sigma + 0.22$, and $(U-R) = (1.42\pm0.3)\log\sigma - 0.92$. It is not specified which photometric system the R-magnitudes are on. By comparing with our data, we find that it could well be Johnson R and most likely not Kron-Cousins R. The difference between the two is $R_\mathrm{J} - R_\mathrm{C} = -0\overset{\mathrm{m}}{.}25$, based on $R_\mathrm{J} - R_\mathrm{C} = -0.12(B-R_\mathrm{C}) - 0.07$ (Davis et al. 1985) and a typical E/S0 color of $(B-R_\mathrm{C}) = 1\overset{\mathrm{m}}{.}5$. It is seen from Fig. 7.9(a–b) that the dot-dashed lines matches our data reasonably well, while a line $\approx 0\overset{\mathrm{m}}{.}25$ above would match our data less well, especially for $(B-r)$. We conclude that the R-magnitudes that Franx & Illingworth used for their color–σ relations are probably close to Johnson R, but that the zero point could be a bit off.

Under the assumption that the color–σ relations from Franx & Illingworth refer to Johnson R, we can transform their $(B-R)$ relation by means of Eq. (4.10, p. 48) to the relation $(B-r) = (0.63\pm$

$0.27)\log\sigma - 0.22$. This relation is shown as the dot-dashed line in Fig. 7.9(a). To transform their $(U-R)$ relation, we combine the relation $(U-R_{\rm J}) = 1.07(U-R_{\rm C})+0.08$ from Davis et al. (1985) and the relation $r-R_{\rm C} = 0.354$ from Jørgensen (1994) to give the relation $(U-R_{\rm J}) = 1.07(U-r)+0.46$. Then the Franx & Illingworth $(U-R)$–σ relation becomes $(U-r) = (1.33\pm0.28)\log\sigma - 1.29$. This relation is shown as the dot-dashed line in Fig. 7.9(b). Finally, we subtract their two color–σ relations to give $(U-B) = 0.72\log\sigma - 1.14$. This relation is shown as the dot-dashed line in Fig. 7.9(c).

The $\log\sigma$ coefficients in the Franx & Illingworth color–σ relations are determined as the geometrical mean of the coefficients from two least squares fits, one in each direction. When we fit our data in the same way, we get $(B-r)_{\rm e} = (0.30\pm0.07)\log\sigma + {\rm const}$, and $(U-r)_{\rm e} = (0.83\pm0.28)\log\sigma + {\rm const}$. These slopes do not differ much from the slopes obtained from our normal fitting method, cf. Eq. (7.18). The slopes from Franx & Illingworth are in rough agreement with the slopes that we find. The slope differences ('our'−'their') are -0.33 ± 0.28 for $(B-r)$ and -0.50 ± 0.40 for $(U-r)$.

Bender et al. (1993) established the relation ${\rm Mg}_2 = 0.20\log\sigma - 0.166$ for their DHG sample. They found that the relation $(B-V) = 1.12{\rm Mg}_2 + 0.615$ matched their DHG sample well. This relation was established by Burstein et al. (1988) for 276 bright ellipticals. Bender et al. combined the two relations to $(B-V) = 0.224\log\sigma + 0.429$. By means of the relation $(B-V) = 0.673(B-r)+0.184$ from Jørgensen (1994), this can be transformed to $(B-r) = 0.333\log\sigma+0.364$. This is shown as the dotted line in Fig. 7.9(a). The slope is in agreement with our data, but not the zero point, we find a mean difference of $0\overset{\rm m}{.}064\pm0\overset{\rm m}{.}007$ (with the differences calculated as $\Delta = (B-r)_{\rm e} - 0.333\log\sigma - 0.364$).

The colors are also well correlated with ${\rm Mg}_2$. We find the following relations

$$\begin{aligned}
&{\rm HydraI}: \quad (B-r)_{\rm e} = \ 1.32{\rm Mg}_2 + 0.777 \quad \sigma_{\rm fit} = 0.044 \quad N = 42\\
&\qquad\qquad\qquad\qquad \pm\ 0.74\\
&{\rm HydraI}: \quad (U-r)_{\rm e} = \ 2.84{\rm Mg}_2 + 0.861 \quad \sigma_{\rm fit} = 0.071 \quad N = 18\\
&\qquad\qquad\qquad\qquad \pm\ 1.95\\
&{\rm HydraI}: \quad (U-B)_{\rm e} = \ 2.21{\rm Mg}_2 - 0.118 \quad \sigma_{\rm fit} = 0.058 \quad N = 18\\
&\qquad\qquad\qquad\qquad \pm\ 1.41
\end{aligned} \tag{7.19}$$

No galaxies were excluded from the fits. R293 does not deviate from the color–${\rm Mg}_2$ relations, and excluding it has very little effect. The effect of omitting R295/E437G15 is larger, but still not significant, the slope of the $(B-r)_{\rm e}$–${\rm Mg}_2$ relations changes from 1.32 ± 0.74 to 1.45 ± 0.65. The color–${\rm Mg}_2$ relations are shown in Fig. 7.9(d–f).

Burstein et al. (1988) established the relation $(B-V) = 1.12{\rm Mg}_2 + 0.615$ for 276 bright ellipticals, as mentioned above. This can be transformed into $(B-r) = 1.66{\rm Mg}_2 + 0.640$. This is shown as the dotted line in Fig. 7.9(d). The slope is in agreement with the slope that we find. The zero point is not in agreement with our data, we find a mean residual from their relation of $0\overset{\rm m}{.}054\pm0\overset{\rm m}{.}008$.

We would like to use stellar population models to estimate the variation in age and metallicity needed to reproduce the three observed color–${\rm Mg}_2$ relations. Unfortunately, the Vazdekis et al. (1996) models (with a bi-modal IMF with high mass slope $\mu = 1.35$) are not able to reproduce any of them – galaxies with large ${\rm Mg}_2$ values (say ~ 0.3) are predicted to have much redder colors than what is actually observed. The failure to reproduce the color–${\rm Mg}_2$ relations could be due to problems reproducing the colors and/or problems reproducing ${\rm Mg}_2$. Several models cannot reproduce the ${\rm Mg}_2$–Mgb relation, which could indicate a problem in reproducing ${\rm Mg}_2$. Some models do not get the colors right. Worthey (1994) noted that his $(B-V)$ colors were too red

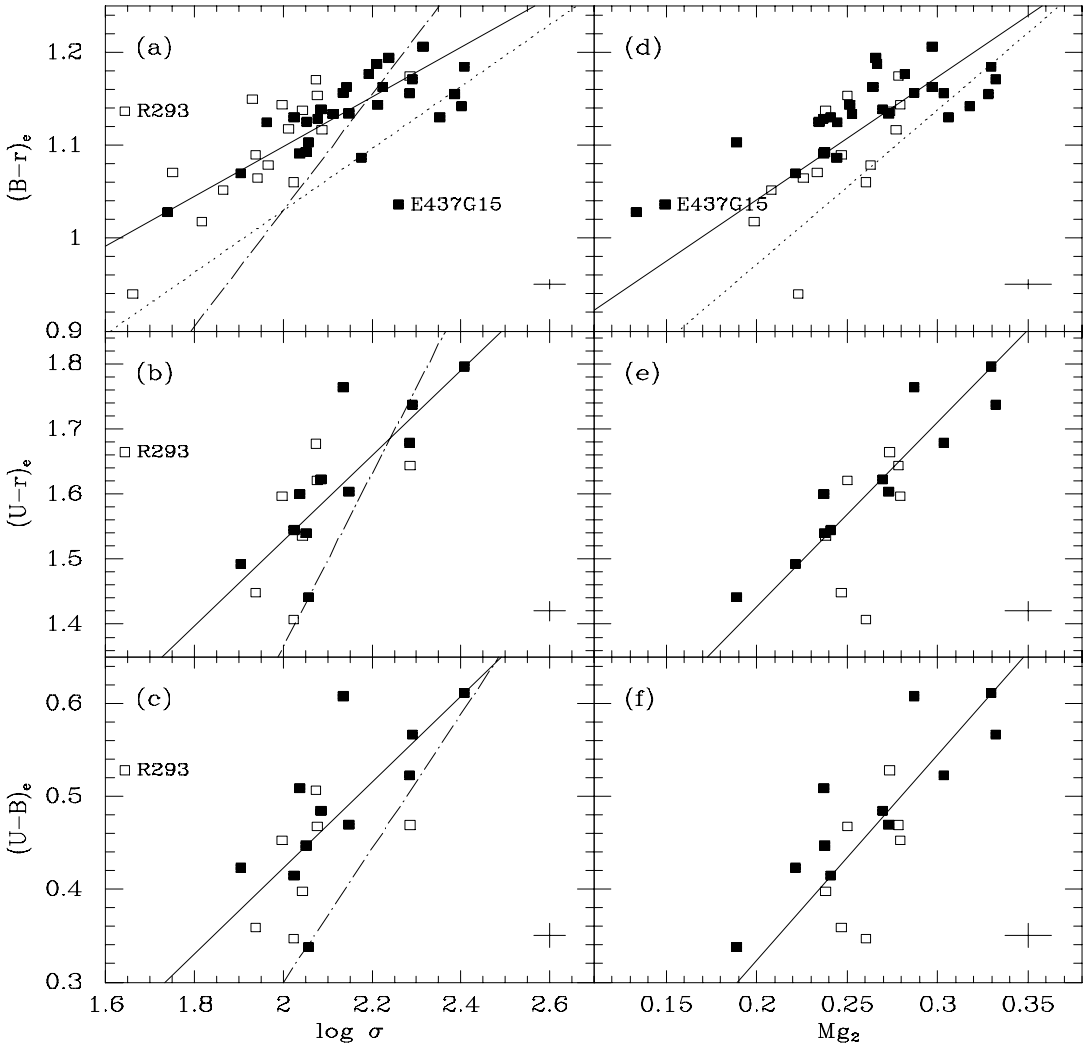

Figure 7.9: Panel (a)–(c): The color–σ relations. Panel (d)–(f): The color–Mg_2 relations. Solid lines: our fits, Eq. (7.18) and (7.19). Dotted lines: Burstein et al. (1988) or Bender et al. (1993), cf. the text. Dot-dashed lines: Franx & Illingworth (1990), for (a) and (b) under the assumption that their R is Johnson R.
R295/E437G15 has a strong disk and $v_{\rm rot}$>150 km s^{-1} (it does not have photometry in Johnson U). The spectrum of R293 has very low S/N, and this galaxy was not included in the color–σ fits. Data symbols as in Fig. 7.1. The typical error bars shown for the colors are the median internal errors.

by $0\overset{\rm m}{.}05$ when compared to globular clusters. This might be related to the problems we observe with the Vazdekis et al. models. However, we also observe problems for the $(U-r)$ color, which is independent of B. Systematic differences between the different models are known to exist. For example, Borges et al. (1995) find that their $(B-V)$ colors are $0\overset{\rm m}{.}1$–$0\overset{\rm m}{.}03$ more blue than those of Worthey (1994).

Finally, we note that $\log <$ Fe $>$ is also weakly correlated with the $(B-r)_{\rm e}$, as expected from the weak correlations with $\log\sigma$ and Mg_2. For the HydraI sample we find $P_{\rm no\ corr.} = 7.0\%$. No significant correlations can be seen with $(U-r)_{\rm e}$ and $(U-B)_{\rm e}$, but this is most likely due to the small sample size ($N = 17$).

7.5 Ages, Metallicities, and Abundance Ratios

In this section we use the single-age single-metallicity stellar population models from Vazdekis et al. (1996) to infer luminosity weighted mean ages, metallicities, and abundance ratios from the data. We use the models with a bi-modal IMF with high mass slope $\mu = 1.35$.

It is not surprising that from a single observational quantity, such as $(B-r)$, it is not possible to determine both age and metallicity (e.g. Worthey 1994). For example, a color of $(B-r) = 1\overset{\mathrm{m}}{.}15$, which is typical for E and S0 galaxies, can be matched by both a low age and high metallicity, say 3 Gyr and $Z = 0.05$, an intermediate age and solar metallicity, say 8 Gyr and $Z = 0.02$, and a high age and low metallicity, say 13–17 Gyr and $Z = 0.008$. The numbers quoted are from the Vazdekis et al. models.

Given two observational quantities we could hope to determine both the age and metallicity. Unfortunately, for a number of such color–color, color–index, and index–index diagrams the effects of age and metallicity are nearly degenerate (e.g. Worthey 1994, Faber et al. 1995).

It turns out, that in the two-dimensional Mg_2–$\log(M/L)$ and $\log <\mathrm{Fe}>$–$\log(M/L)$ diagrams the effects of age and metallicity are not degenerate. This was mentioned by Faber et al. (1995).

We assume homology and are then able to calculate $\log(M/L_\mathrm{r})$ from the data (Eq. 2.26; cf. Sect. 2.2.3, p. 12). Our data are plotted in the Mg_2–$\log(M/L_\mathrm{r})$ and $\log <\mathrm{Fe}>$–$\log(M/L_\mathrm{r})$ diagrams in Fig. 7.10. Overplotted are the predictions from the Vazdekis et al. models. The first thing to note is that the models span the data quite well, the measurement errors taken into account. We are free to shift the values of $\log(M/L)$ up and down since they depend on the two unknown quantities H_0 and the fraction of dark matter. The used values of $H_0 = 50\,\mathrm{km\,s^{-1}\,Mpc^{-1}}$ and $M_\mathrm{total} = 10 M_\mathrm{luminous}$ give a good match to the data, and we do not apply any offset.

The Vazdekis et al. models predict $\log(M/L)$, Mg_2, and $<\mathrm{Fe}>$ for a grid of 45 (age,[M/H]) points, with the 15 age values ranging from 1.00 to 17.38 Gyr, and the three [M/H] values being -0.4, 0.0, and 0.4. Recall that $[\mathrm{M/H}] \equiv \log(Z/Z_\odot)$, with $Z_\odot = 0.02$. Note, that not all the age values are shown on Fig. 7.10. The *inverse problem*, i.e. given observed values of $\log(M/L)$ and Mg_2 (or $\log(M/L)$ and $<\mathrm{Fe}>$) determine the corresponding age and metallicity, is a question of interpolation in an irregular grid. That the grid is irregular is apparent in Fig. 7.10.

We did this irregular interpolation in three steps. First, a Delaunay triangulation of the irregular grid points was established. Second, a large (say 1000×1000) regular grid of interpolated *or extrapolated* values of both log age and [M/H] was calculated, with the grid being chosen to span the data. The interpolation and extrapolation was done using the Akima's quintic polynomials. Third, a standard bilinear interpolation was used to get the final values of log age and [M/H]. These calculations were done using IDL (Interactive Data Language). For details, see the help pages for `triangulate` and `trigrid`. Estimates of uncertainties on log age and [M/H] were obtained by in turn keeping $\log(M/L)$ and Mg_2 (or $<\mathrm{Fe}>$) constant while varying the other by plus/minus the observational error, calculating log age and [M/H] for those four points, and taking half the min-max variation as the estimate of uncertainty. For the interpolation in the $\log <\mathrm{Fe}>$–$\log(M/L_\mathrm{r})$ diagram, we omitted the three galaxies with an uncertainty on $\log <\mathrm{Fe}>$ larger than 0.065.

To discuss the results from the interpolation in the Mg_2–$\log(M/L_\mathrm{r})$ and $\log <\mathrm{Fe}>$–$\log(M/L_\mathrm{r})$ diagrams, we introduce the following notation

$$[\mathrm{Mg/H}] \equiv [\mathrm{M/H}] \text{ inferred from } \mathrm{Mg}_2\text{–}\log(M/L) \text{ diagram} \tag{7.20}$$

$$\log \mathrm{age}_\mathrm{Mg} \equiv \log \mathrm{age} \text{ inferred from } \mathrm{Mg}_2\text{–}\log(M/L) \text{ diagram} \tag{7.21}$$

$$[\mathrm{Fe/H}] \equiv [\mathrm{M/H}] \text{ inferred from } \log <\mathrm{Fe}>\text{–}\log(M/L) \text{ diagram} \tag{7.22}$$

$$\log \mathrm{age}_\mathrm{Fe} \equiv \log \mathrm{age} \text{ inferred from } \log <\mathrm{Fe}>\text{–}\log(M/L) \text{ diagram} \tag{7.23}$$

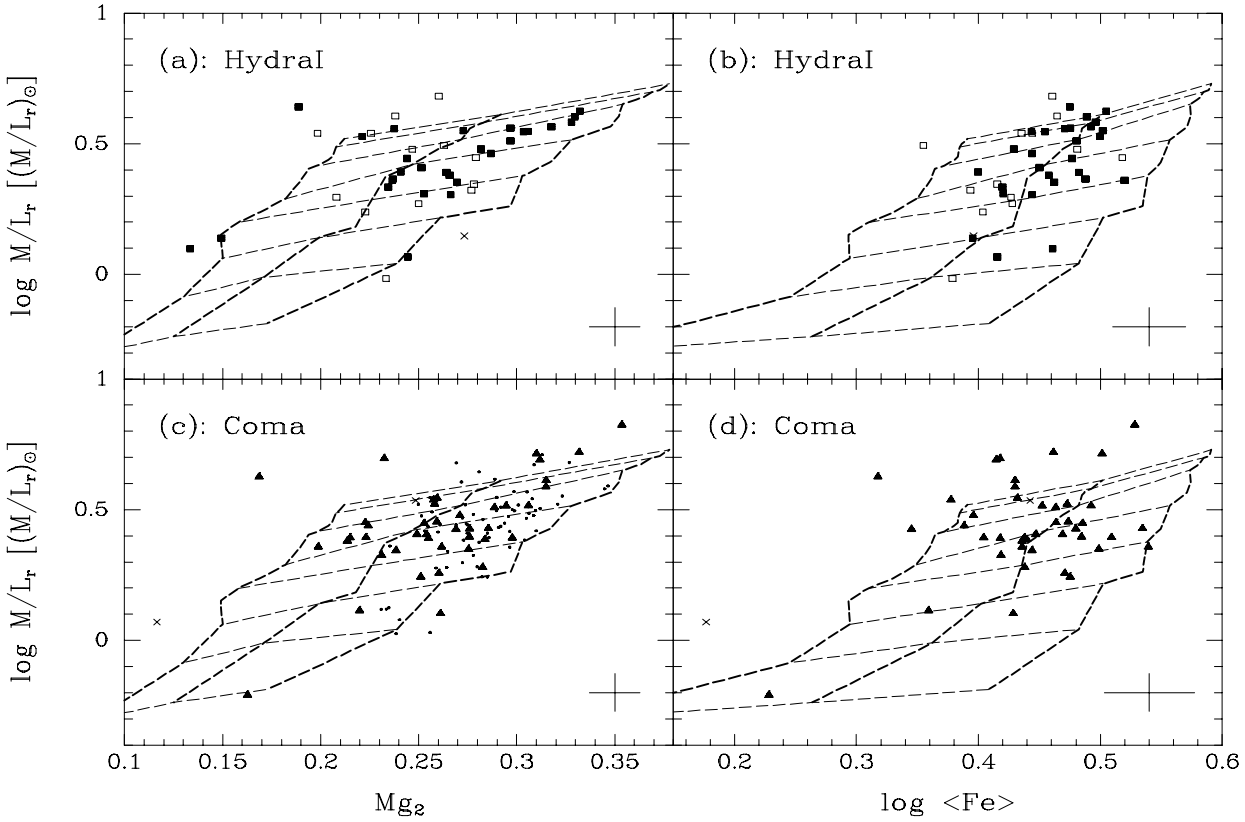

Figure 7.10: $\log(M/L_{\rm r})$ versus Mg_2 and $\log <\mathrm{Fe}>$. The overplotted grids are the predictions from the static single-age single-metallicity models from Vazdekis et al. (1996), using a bi-modal IMF with high mass slope $\mu = 1.35$. The thin dashed lines are at constant age, from bottom to top 1, 2, 3, 5, 8, 12, 15, and 17 Gyr (approximately). The thick dashed lines are at constant metallicity $[\mathrm{M/H}] \equiv \log(Z/Z_\odot)$, from left to right -0.4, 0.0, and 0.4 dex.
Data symbols: Boxes/triangles – HydraI/Coma galaxies. Filled/open symbols – galaxies brighter/fainter than $M_{\mathrm{r_T}} = -20\overset{\mathrm{m}}{.}75$. Crosses – galaxies with $\sigma_{\log <\mathrm{Fe}>} > 0.065$, these were excluded from the analysis. Small dots – galaxies without $<\mathrm{Fe}>$ data.

We also define the two differential quantities

$$[\mathrm{Mg/Fe}] \equiv [\mathrm{Mg/H}] - [\mathrm{Fe/H}] \tag{7.24}$$

$$\Delta \log \mathrm{age}_{\mathrm{Mg/Fe}} \equiv \log \mathrm{age}_{\mathrm{Mg}} - \log \mathrm{age}_{\mathrm{Fe}} \tag{7.25}$$

The uncertainties on [Mg/Fe] and $\Delta \log \mathrm{age}_{\mathrm{Mg/Fe}}$ were calculated in the same way as for [Mg/H], $\log \mathrm{age}_{\mathrm{Mg}}$, [Fe/H], and $\log \mathrm{age}_{\mathrm{Fe}}$, i.e. by half the min-max variation over the four points described above. This takes into account the correlation between the errors caused by the fact that $\log(M/L)$ appears in both diagrams.

The above notation indicates our first order assumptions: we assume that the metallicity inferred from Mg_2 gives the magnesium abundance [Mg/H], and that the metallicity inferred from $<\mathrm{Fe}>$ gives the iron abundance [Fe/H]. This is despite the fact that the Vazdekis et al. models have solar abundance ratios, including $[\mathrm{Mg/Fe}] = 0$. That these are reasonable approximations is supported by the work of Tripicco & Bell (1995), and Weiss et al. (1995), as described in Sect. 2.3 (p. 18). In summary, Tripicco & Bell (1995) found that the Mg_2 index depended strongly on the

magnesium abundance, and that the $<\mathrm{Fe}>$ index depended strongly on the iron abundance, although is was just as sensitive to changes in the total metallicity. Weiss et al. (1995) found from isochrones with [Mg/Fe] $\neq 0$ that the effect on e.g. the luminosity of changing the abundance ratios while keeping the total metallicity constant was small.

If the models provided an adequate description of the data, the metallicity difference [Mg/Fe] and the age difference $\Delta \log \mathrm{age}_{\mathrm{Mg/Fe}}$ should be zero within their errors caused by the observational errors. However, this is not the case, and we already suspected this discrepancy from the $\log <\mathrm{Fe}>$–Mg_2 diagram, Fig. 7.8 (p. 100). The metallicity difference [Mg/Fe] is large compared with the two metallicities, typically 70%, while the age difference $\Delta \log \mathrm{age}_{\mathrm{Mg/Fe}}$ is *small* compared with the two ages, typically only 5%. We regard the differences in ages as an indication of the limitations in the method, and use our [Mg/Fe] as an estimate of the true [Mg/Fe]. Note, that $\Delta \log \mathrm{age}_{\mathrm{Mg/Fe}}$ has to be non-zero since [Mg/Fe] is non-zero, because $\log(M/L)$ appears in both diagrams. The Vazdekis et al. models for ages > 5 Gyr can be approximated by $\log(M/L_{\mathrm{r}}) = 0.63 \log \mathrm{age} + 0.26\,[\mathrm{M/H}] - 0.16$ (J97; Eq. 2.36). Applying this to the two diagrams, we get $0 = 0.63\,\Delta \log \mathrm{age}_{\mathrm{Mg/Fe}} + 0.26\,[\mathrm{Mg/Fe}]$, or $[\mathrm{Mg/Fe}] = -2.42\,\Delta \log \mathrm{age}_{\mathrm{Mg/Fe}}$. A fit to the combined HydraI+Coma sample ($N = 83$) gives $[\mathrm{Mg/Fe}] = (-2.48 \pm 0.09)\,\Delta \log \mathrm{age}_{\mathrm{Mg/Fe}} + 0.00$, in agreement with this. The scatter is small, $\sigma_{\mathrm{fit}} = 0.09$.

Note, that since [Mg/H], [Fe/H], and the ages all depend on $\log(M/L)$, and since we can only determine $\log(M/L)$ to within an offset (cf. above), these four quantities are also only determined to within an offset. For [Mg/Fe], on the other hand, the effect of this unknown offset cancels out, at least to some extend.

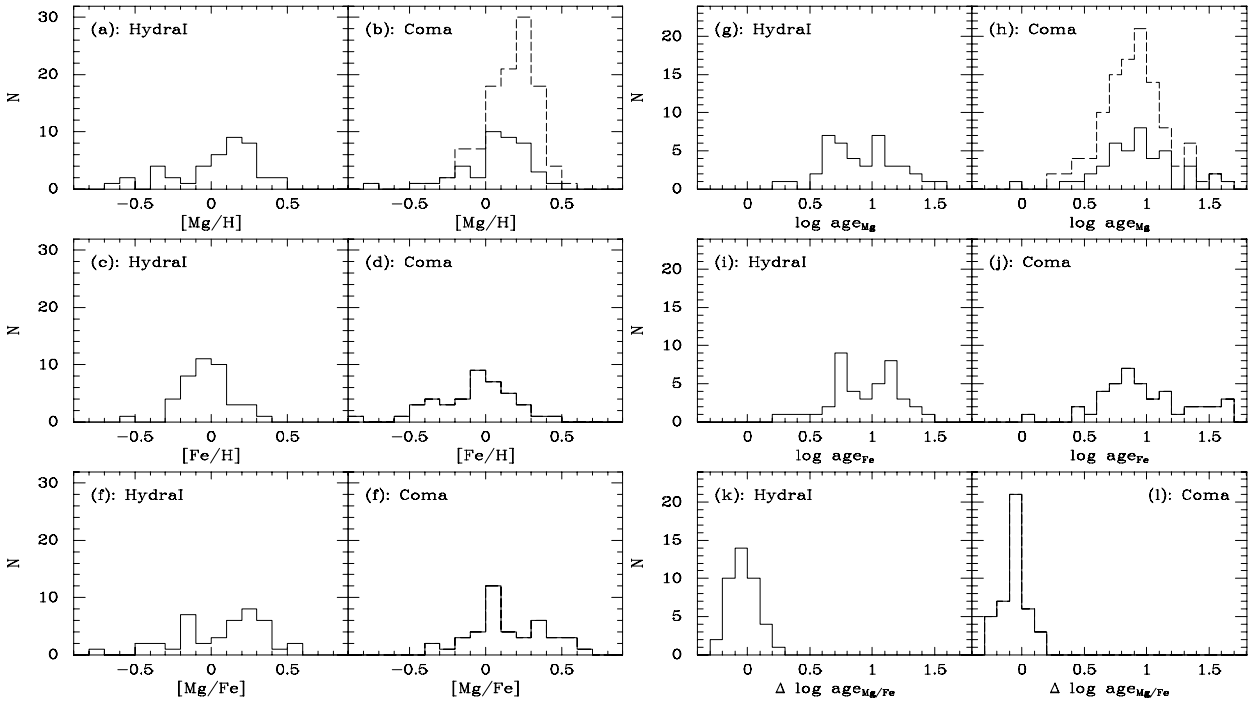

Figure 7.11: Histograms over [Mg/H], [Fe/H], [Mg/Fe], $\log \mathrm{age}_{\mathrm{Mg}}$, $\log \mathrm{age}_{\mathrm{Fe}}$, and $\Delta \log \mathrm{age}_{\mathrm{Mg/Fe}}$. Solid histograms – galaxies with both Mg_2 and $<\mathrm{Fe}>$ data. Dashed histograms – galaxies with Mg_2 data.

In Figure 7.11 we show histograms over the distribution of [Mg/H], [Fe/H], [Mg/Fe], $\log \mathrm{age}_{\mathrm{Mg}}$, $\log \mathrm{age}_{\mathrm{Fe}}$, and $\Delta \log \mathrm{age}_{\mathrm{Mg/Fe}}$. $\Delta \log \mathrm{age}_{\mathrm{Mg/Fe}}$ is included just to show that also the *absolute* range

in in this quantity is rather small.

We tested the HydraI and the Coma data against each other by means of Kolmogorov-Smirnov tests. This test gives the probability $P_{\text{same distr.}}$ that the two samples are drawn from the same underlying distribution. For the HydraI sample ($N = 41$) and the Coma sample with $<$ Fe $>$ data ($N = 42$) we find $P_{\text{same distr.}}$ in the range 26%–98% for the above six quantities. In other words, we do not find any significant differences between the HydraI and the Coma samples. For the HydraI sample and the full Coma sample ($N = 111$) we find $P_{\text{same distr.}} = 15\%$ for [Mg/H] and 41% for $\log \text{age}_{\text{Mg}}$; again we find no significant differences between the HydraI and the Coma samples.

7.5.1 [Mg/H], [Fe/H], [Mg/Fe], and ages versus σ and Mass

In Figure 7.12 we plot [Mg/H], [Fe/H], and [Mg/Fe] versus $\log \sigma$. For the HydraI sample, the following trends are seen: [Mg/H] increases with $\log \sigma$, [Fe/H] is independent of $\log \sigma$, and therefore [Mg/Fe] increases with $\log \sigma$. The Coma sample is compatible with the same pattern, although the trends for [Mg/H] and [Fe/H] are somewhat less clear. But still [Mg/Fe] is highly correlated with $\log \sigma$. It should be recalled, that the part of the Coma sample that has $<$ Fe $>$ data is not magnitude limited.

$\log \sigma$ did not directly enter the calculation of [Mg/H] and [Fe/H]. However, $\log(M/L)$ depends on $\log \sigma$ as $\log(M/L_{\text{r}}) = 2 \log \sigma - \log <I>_{\text{e}} - \log r_{\text{e}} - 0.733$ (Eq. 2.26). The Vazdekis et al. models can be approximated by $\log(M/L_{\text{r}}) = 0.63 \log \text{age} + 0.26\,[\text{M/H}] - 0.16$ (J97; Eq. 2.36). Measurement errors in $\log \sigma$ can therefore cause a slope in the [M/H]–$\log \sigma$ diagrams of $\Delta[\text{M/H}]/\Delta \log \sigma = 7.7$. However, since the measurement errors in $\log \sigma$ are small compared to the range in $\log \sigma$, the effect should be small. Further, [Mg/Fe] is not affected since the effect cancels out.

For the combined HydraI+Coma sample ($N = 83$), the correlation between [Mg/Fe] and $\log \sigma$ is very significant, a Spearman rank order test gives $P_{\text{no corr.}} < 0.01\%$. A fit to the HydraI+Coma sample with the sum of the absolute residuals in [Mg/Fe] minimized gives the relation

$$\text{HydraI} + \text{Coma}: \quad [\text{Mg/Fe}] = \begin{array}{c} 0.74 \log \sigma - 1.50 \\ \pm\ 0.23 \end{array} \quad \sigma_{\text{fit}} = 0.25 \quad N = 83 \tag{7.26}$$

(A least squares fit gives almost the same, $[\text{Mg/Fe}] = (0.67 \pm 0.20) - 1.34$.) We choose to minimize the residuals in [Mg/Fe] since we want to predict [Mg/Fe] from $\log \sigma$. We find, that when $\log \sigma$ increases by 0.4 dex (e.g. from $\sigma = 100\,\text{km s}^{-1}$ to $\sigma \approx 250\,\text{km s}^{-1}$), [Mg/Fe] increases by 0.3 dex. This is in agreement with J97, who found a 0.3–0.4 dex increase for the same $\log \sigma$ interval. This was based on the different slopes of the Mg_2–σ and the $<$ Fe $>$–σ relations and the analytical approximations to the predictions from the Vazdekis et al. models.

In Figure 7.13 we plot [Mg/H], [Fe/H], and [Mg/Fe] versus log(Mass). The relations are more noisy than for $\log \sigma$. Still, for the combined HydraI+Coma sample, the correlation between [Mg/Fe] and log(Mass) is significant at the 2 sigma level, we find $P_{\text{no corr.}} = 5.5\%$. It seems that the most massive galaxies (Mass $\gtrsim 3 \cdot 10^{11} M_{\odot}$, or log(Mass) $\gtrsim 11.5$) have a smaller variation in [Mg/H], [Fe/H], and [Mg/Fe] than galaxies with lower mass, but this could be due to the small number of objects. Also galaxies with high velocity dispersion (say $\log \sigma > 2.3$) have a smaller scatter than galaxies with lower velocity dispersion, but the division is not as pronounced as for the mass.

What are the implications of [Mg/Fe] > 0? Worthey, Faber, & Gonzáles (1992) found that [Mg/Fe] was larger than zero in giant ellipticals, and that [Mg/Fe] reached 0.2–0.3 dex for the average strongest-lined galaxies. They reached this conclusion by comparing data with models in the $<$ Fe $>$–Mg_2 diagram. These authors discussed the following possible explanations for [Mg/Fe] > 0. Magnesium and iron are preferably produced in supernovae (SNe) of type II and Ia, respectively. Therefore, a change in the fraction (SN II)/(SN Ia) will give a change in [Mg/Fe]. The following

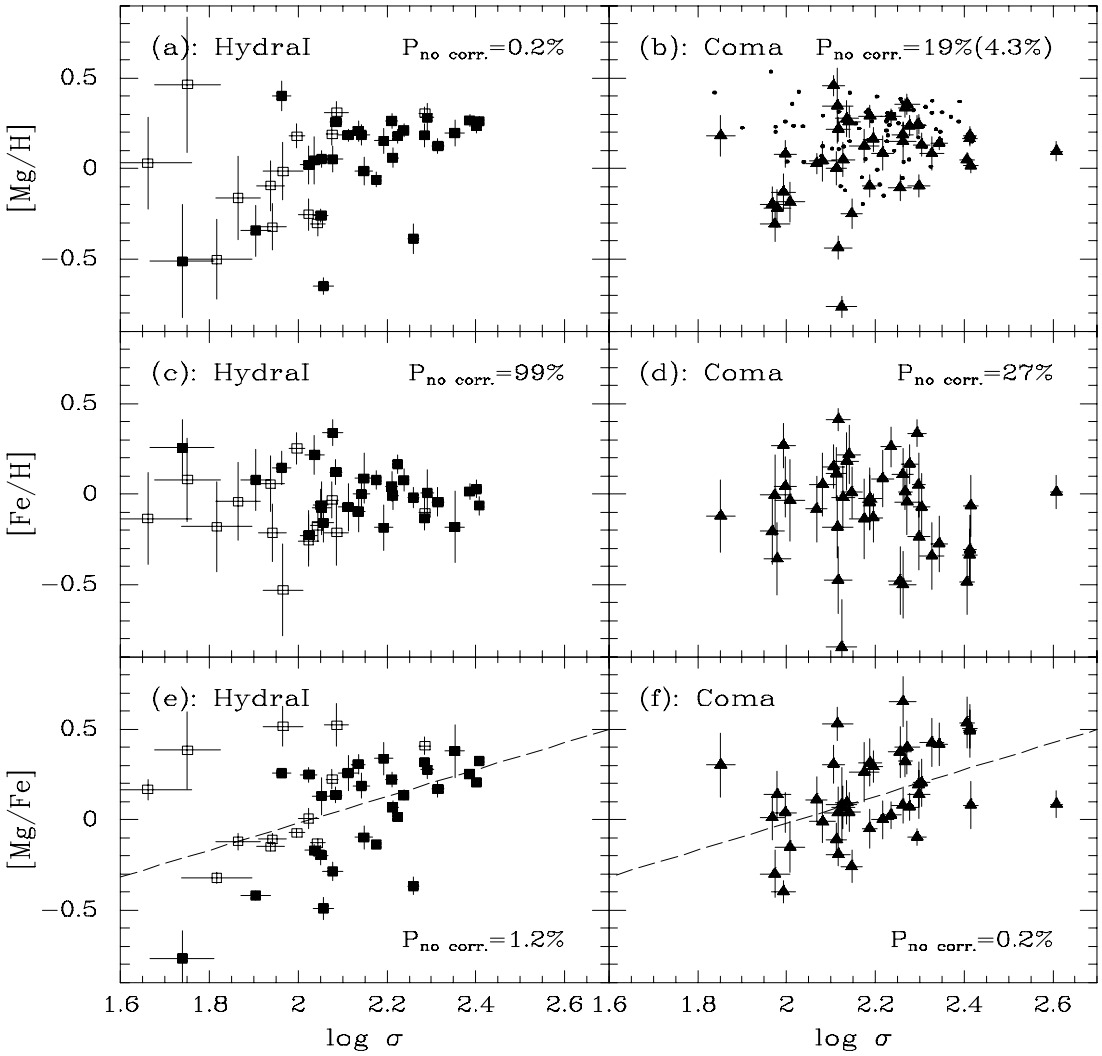

Figure 7.12: [Mg/H], [Fe/H], and [Mg/Fe] versus $\log \sigma$. For definitions see Eq. (7.20), (7.22), and (7.24). '$P_{\rm no\ corr.}$' is the Spearman rank order probability that the parameters are *not* correlated. For panel (b), the number in parenthesis refers to the galaxies with $<$ Fe $>$ data (triangles), only. The dashed line in panel (e) and (f) is Eq. (7.26).
Data symbols as in Fig. 7.10, except that the three galaxies with $\sigma_{\log <\rm Fe>} > 0.065$ are not shown in any of the panels. The individual error bars for [Mg/H], [Fe/H], and [Mg/Fe] are based on the individual error bars for $\log(M/L_{\rm r})$, $\rm Mg_2$, and $<$ Fe $>$, cf. the text. The error bars for the galaxies without $<$ Fe $>$ data (small dots) are omitted for clarity – they are similar in size to the error bars for the other Coma data.

three scenarios can give [Mg/Fe] > 0.
1. Different time scales for star formation. The progenitor stars of type II SNe are more massive and short-lived than those of type Ia SNe. Therefore, if star formation is fast, a large fraction of the total amount of gas available for star formation will have been processed by type II SNe and locked up in long-lived stars before the first generation of type Ia SNe after ~ 1 Gyr will enrich the interstellar medium (ISM) with iron. At this point, only a small fraction of gas is left for new long-lived stars to be formed out of this iron enriched material.

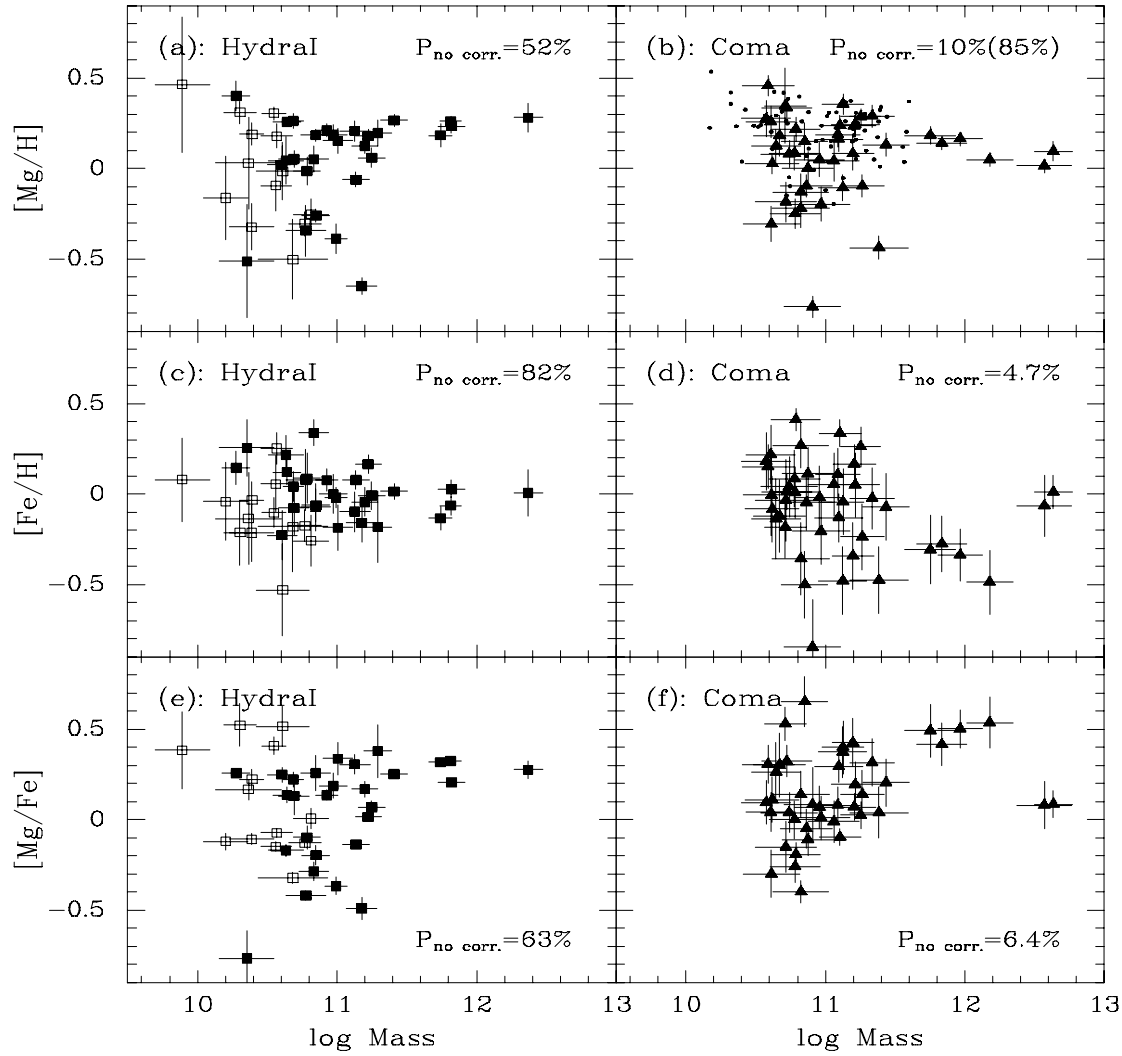

Figure 7.13: [Mg/H], [Fe/H], and [Mg/Fe] versus log(Mass). This figure is similar to Fig. 7.12, except here log(Mass) rather than $\log\sigma$ is used. Mass refers to the luminous mass and is calculated as Mass $= 5.0\,\sigma^2 r_{\rm e}/G$ (Eq. 2.25).

2. A variable IMF slope. A smaller IMF slope μ (i.e. a more flat IMF) results in the formation of more massive stars, which give rise to more type II SNe.
3. Selective loss mechanisms. If for some reason a galactic wind of some sort would retain magnesium with greater efficiency than iron, then it is also possible to get [Mg/Fe] > 0. In the standard picture of SN-driven winds, the outcome is [Mg/Fe] < 0, in contradiction to the observations.

Any viable theory for star formation in elliptical galaxies should be able to explain not only [Mg/Fe] > 0 *per se*, but also the correlation between [Mg/Fe] and velocity dispersion (or mass).

Also the ages are correlated with $\log\sigma$ and log(Mass), see Fig. 7.14 and 7.15. For the combined HydraI+Coma sample, Spearman rank order tests give $P_{\rm no\ corr.} < 0.01\%$ for $\log {\rm age}_{\rm Mg}$ vs. $\log\sigma$, $P_{\rm no\ corr.} = 0.04\%$ for $\log {\rm age}_{\rm Fe}$ vs. $\log\sigma$, $P_{\rm no\ corr.} < 0.01\%$ for $\log {\rm age}_{\rm Mg}$ vs. log(Mass), and $P_{\rm no\ corr.} < 0.01\%$ for $\log {\rm age}_{\rm Fe}$ vs. log(Mass). Also for the ages we find that the scatter is smaller for the most massive galaxies (Mass $\gtrsim 3 \cdot 10^{11} M_\odot$, or log(Mass) $\gtrsim 11.5$).

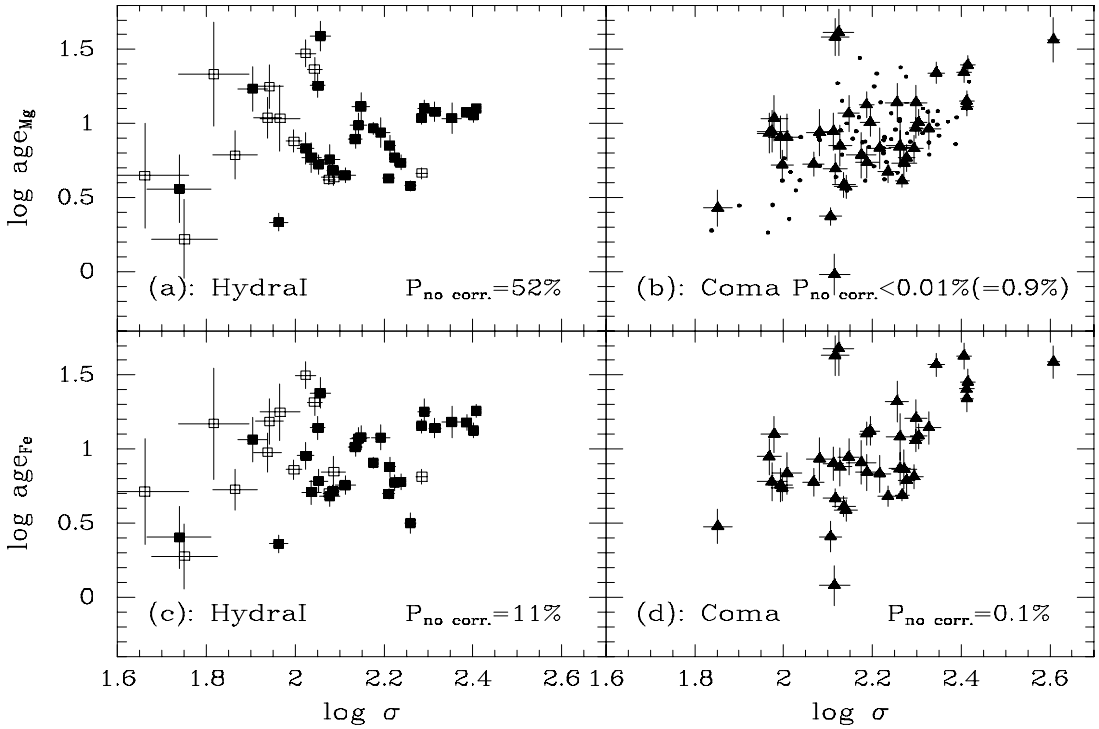

Figure 7.14: $\log \mathrm{age}_{\mathrm{Mg}}$ and $\log \mathrm{age}_{\mathrm{Fe}}$ versus $\log \sigma$. This figure is similar to Fig. 7.12, except here the ages rather than the metallicity quantities are plotted on the y-axes.

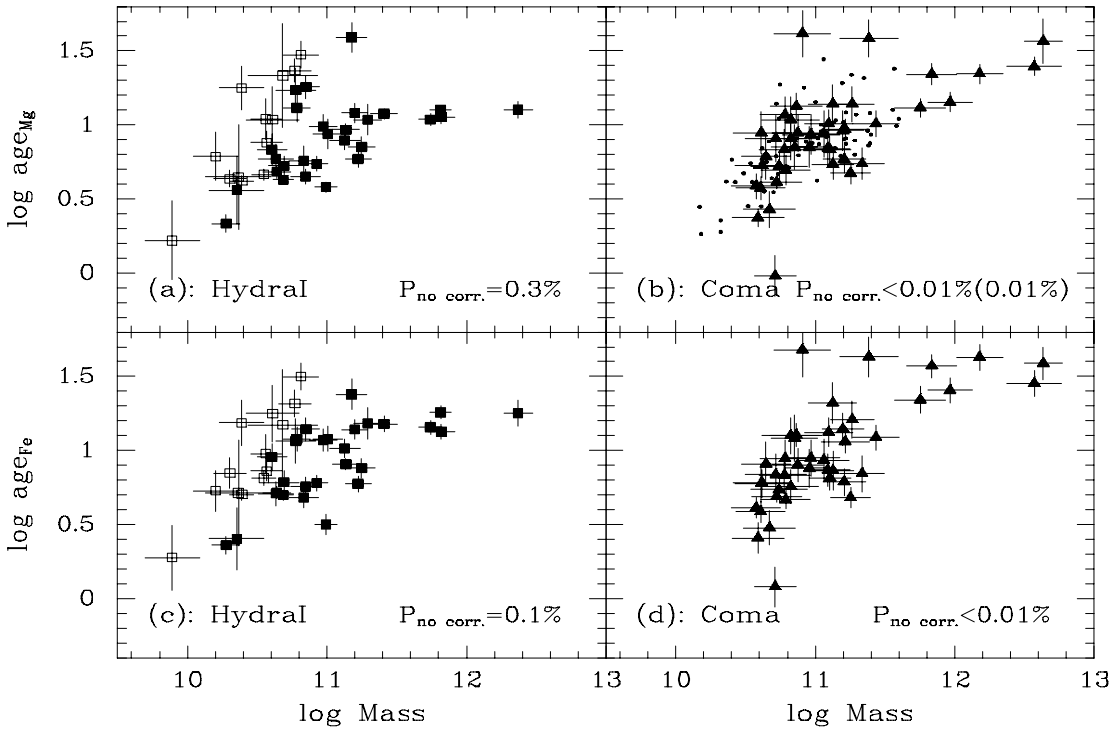

Figure 7.15: $\log \mathrm{age}_{\mathrm{Mg}}$ and $\log \mathrm{age}_{\mathrm{Fe}}$ versus log(Mass). This figure is similar to Fig. 7.14, except here log(Mass) rather than $\log \sigma$ is used. Mass refers to the luminous mass and is calculated as $\mathrm{Mass} = 5.0\,\sigma^2 r_{\mathrm{e}}/G$ (Eq. 2.25).

In Fig. 7.16 we plot [Mg/H], [Fe/H], [Mg/Fe], $\log \mathrm{age}_{\mathrm{Mg}}$, and $\log \mathrm{age}_{\mathrm{Fe}}$ versus total absolute magnitude in Gunn r, $M_{\mathrm{r_T}}$. Shown on the figure is the line $M_{\mathrm{r_T}} = -23\overset{\mathrm{m}}{.}1$. JF94 found this line to demarcate two classes of E and S0 galaxies. The E and S0 galaxies fainter than this limit were best fitted by a model with 10% of the galaxies being diskless, and 90% of the galaxies being drawn from a uniform distribution of relative disk luminosity $L_{\mathrm{D}}/L_{\mathrm{tot}}$. The E (no S0 galaxies found!) brighter than this limit were all diskless.

It is seen from Fig. 7.16 that also for the five quantities studied here, there is a striking difference in properties for galaxies fainter and brighter than approximately $M_{\mathrm{r_T}} = -23\overset{\mathrm{m}}{.}1$. The brighter galaxies show a smaller scatter than the fainter galaxies. The brighter galaxies have an old stellar population, with [Mg/H] a bit above average, [Fe/H] a bit below average, and thus [Mg/Fe] somewhat above average.

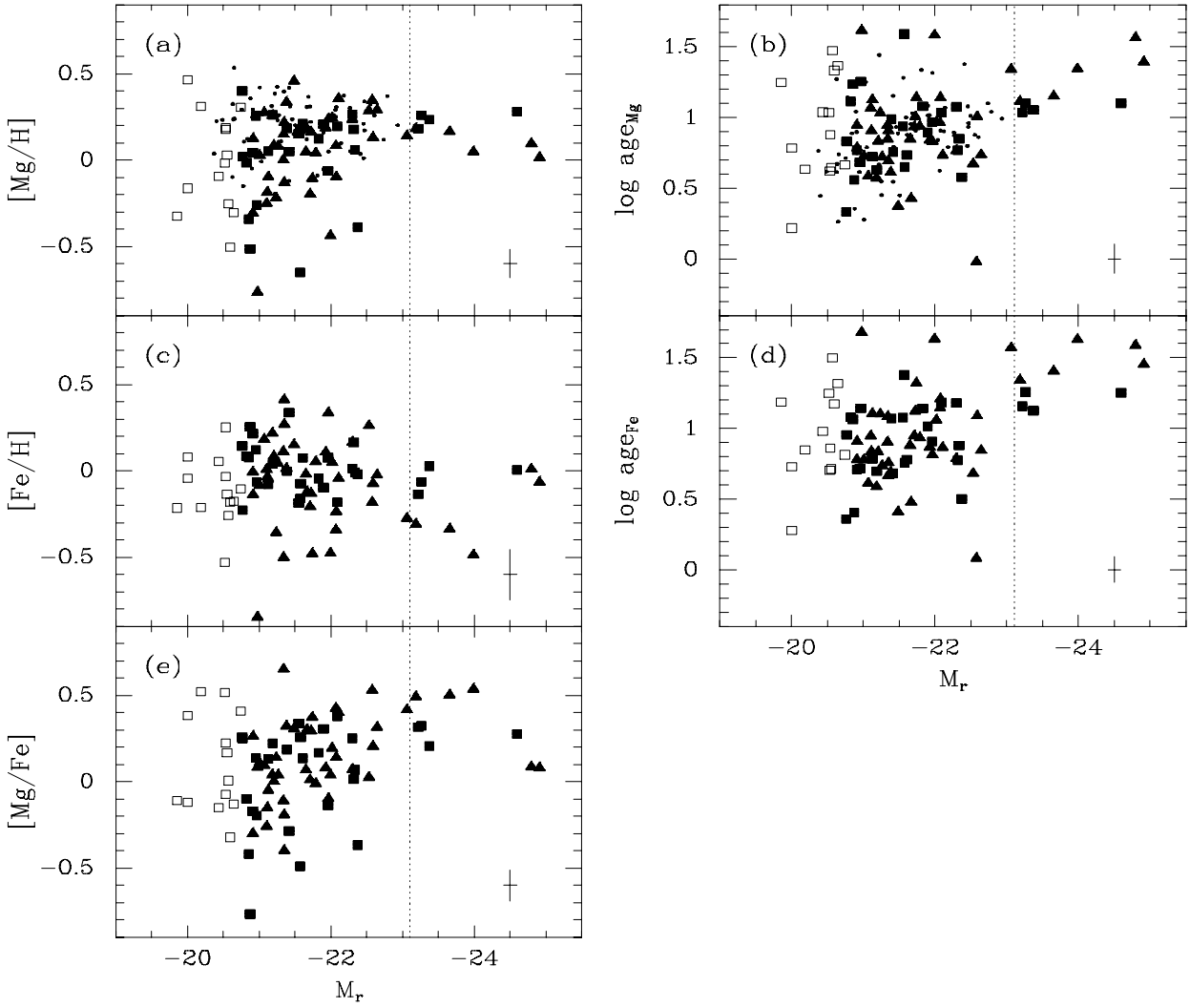

Figure 7.16: [Mg/H], [Fe/H], [Mg/Fe], $\log \mathrm{age}_{\mathrm{Mg}}$, and $\log \mathrm{age}_{\mathrm{Fe}}$ versus total absolute magnitude in Gunn r, $M_{\mathrm{r_T}}$. HydraI and Coma are plotted together. The dotted line is at $M_{\mathrm{r_T}} = -23\overset{\mathrm{m}}{.}1$, corresponding to $M_{\mathrm{B_T}} \approx -22\overset{\mathrm{m}}{.}0$. JF94 found E and S0 below and above this magnitude to have different properties, and this is also the case for the five quantities plotted here. Data symbols as in Fig. 7.12.

7.5.2 The Galaxian Age-Metallicity Relation

In Figure 7.17 we plot [Mg/H], [Fe/H], and [Mg/Fe] versus $\log \mathrm{age}_{\mathrm{Mg}}$. Both [Mg/H] and [Fe/H] are highly (anti-)correlated with $\log \mathrm{age}_{\mathrm{Mg}}$. Part of the age–metallicity relation may be due to measurement errors. This is because the lines of constant age and metallicity are not quite perpendicular to each other in the Mg_2–$\log(M/L)$ and $\log <\mathrm{Fe}>$–$\log(M/L)$ diagrams (see Fig. 7.10). To quantify this effect, Monte-Carlo simulations are needed. This is planned for a future extension of this work.

[Mg/Fe] is not significantly correlated with $\log \mathrm{age}_{\mathrm{Mg}}$. For the combined HydraI+Coma sample, we find $P_{\mathrm{no\ corr.}} = 26\%$.

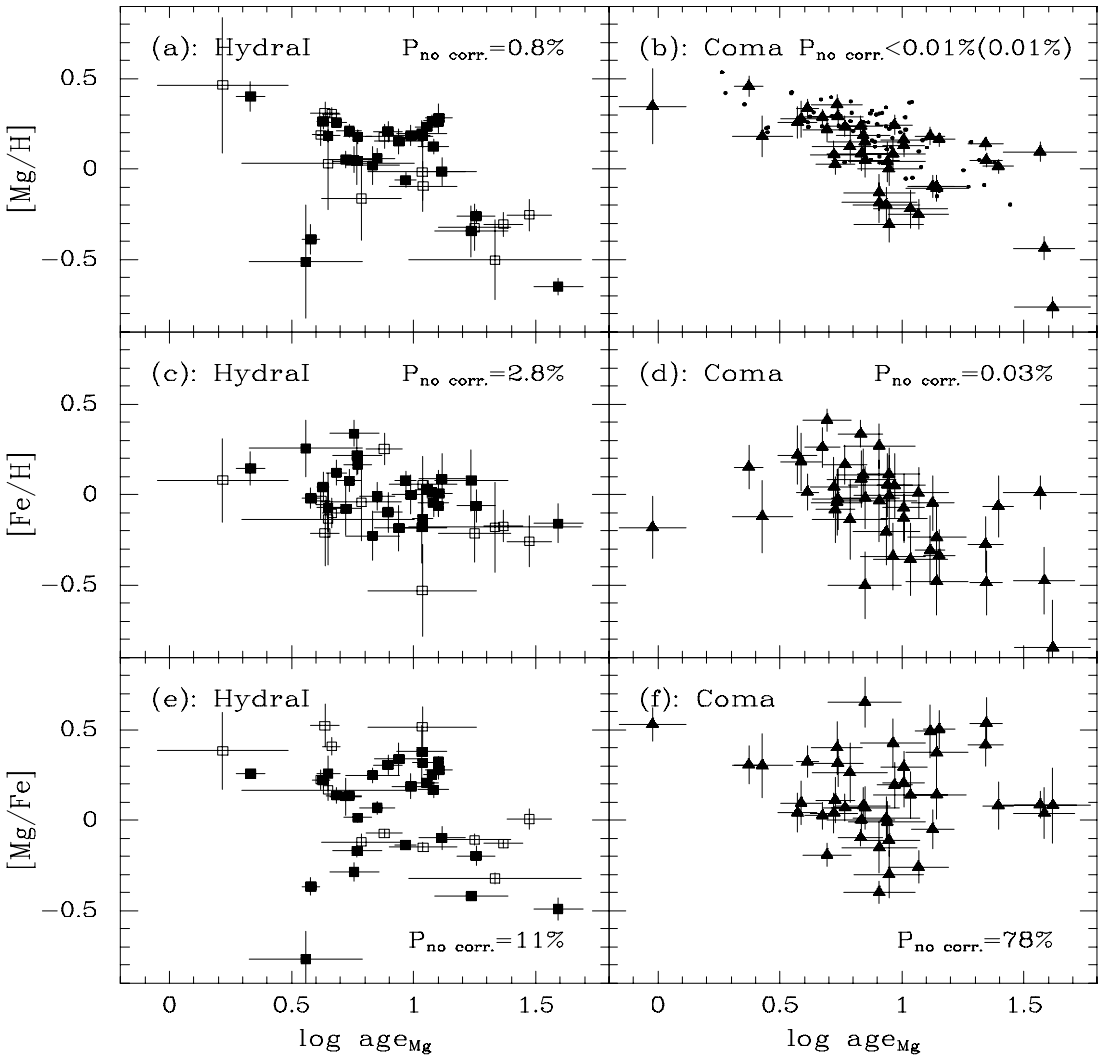

Figure 7.17: [Mg/H], [Fe/H], and [Mg/Fe] versus $\log \mathrm{age}_{\mathrm{Mg}}$. This figure is similar to Fig. 7.12, except here $\log \mathrm{age}_{\mathrm{Mg}}$ rather than $\log \sigma$ is used.

A fit to the Mg and Fe age–metallicity relations for the combined HydraI+Coma sample gives

$$\begin{aligned}[\mathrm{Mg/H}] = &-0.67 \log \mathrm{age}_{\mathrm{Mg}} + 0.74 \quad \sigma_{\mathrm{fit}} = 0.19 \quad N = 152 \\ &\pm 0.10\end{aligned} \tag{7.27}$$

and

$$[\mathrm{Fe/H}] = \underset{\pm\ 0.14}{-\ 0.64} \log \mathrm{age}_{\mathrm{Fe}} + 0.57 \quad \sigma_{\mathrm{fit}} = 0.19 \quad N = 83 \tag{7.28}$$

The 'mixed' relation with [Fe/H] and $\log \mathrm{age}_{\mathrm{Mg}}$, which is what is plotted in Fig. 7.17(c–d), gives

$$[\mathrm{Fe/H}] = \underset{\pm\ 0.20}{-\ 0.35} \log \mathrm{age}_{\mathrm{Mg}} + 0.28 \quad \sigma_{\mathrm{fit}} = 0.19 \quad N = 152 \tag{7.29}$$

We also tried to include a $\log \sigma$ term in the age–metallicity relations. Still for the combined HydraI+Coma sample, a fit gives

$$[\mathrm{Mg/H}] = \underset{\pm\ 0.11}{1.15} \log \sigma \underset{\pm\ 0.07}{-\ 0.78} \log \mathrm{age}_{\mathrm{Mg}} - 1.69 \quad \sigma_{\mathrm{fit}} = 0.14 \quad N = 152 \tag{7.30}$$

and

$$[\mathrm{Fe/H}] = \underset{\pm\ 0.27}{1.25} \log \sigma \underset{\pm\ 0.14}{-\ 0.95} \log \mathrm{age}_{\mathrm{Fe}} - 1.84 \quad \sigma_{\mathrm{fit}} = 0.24 \quad N = 83 \tag{7.31}$$

The $\log \sigma$ terms are highly significant. The two relations look similar, but there is the important difference, that while [Mg/H] is correlated with $\log \sigma$ ($P_{\text{no corr.}} = 0.22\%$), [Fe/H] is not significantly correlated with $\log \sigma$ ($P_{\text{no corr.}} = 36\%$). Both $\log \mathrm{age}_{\mathrm{Mg}}$ and $\log \mathrm{age}_{\mathrm{Fe}}$ are correlated with $\log \sigma$ ($P_{\text{no corr.}} < 0.01\%$ and $P_{\text{no corr.}} = 0.04\%$, respectively). There is also the difference, that for the Mg relation the scatter decreases when we add a $\log \sigma$ term, while it *increases* for the Fe relation. We also fitted the 'mixed' relation with [Fe/H] and $\log \mathrm{age}_{\mathrm{Mg}}$. The result is $[\mathrm{Fe/H}] = (1.66 \pm 30\,000) \log \sigma - (0.99 \pm 1.9) \log \mathrm{age}_{\mathrm{Mg}} - 2.78$, with $\sigma_{\mathrm{fit}} = 0.36$. As can be seen from the bootstrap uncertainties, the relation is not well defined.

The above restates the result from Worthey, Trager, & Faber (1995), that (a) there is an age–metallicity relation with a large span in age, and (b) galaxies of higher velocity dispersion follow an age–metallicity relation at higher metallicity (or older age). These authors used the index $\mathrm{C_2}4668$ and several Balmer line indices (probably H_β, $\mathrm{H}_{\gamma_\mathrm{A}}$, and $\mathrm{H}_{\gamma_\mathrm{F}}$) to derive mean metallicities and ages, not Mg_2 and $\log(M/L_\mathrm{r})$ (or $< \mathrm{Fe} >$ and $\log(M/L_\mathrm{r})$) as we did. It is therefore encouraging that our result is in qualitative agreement with their result.

Worthey et al. report that they were not able to establish the slope nor the zero point of this age–metallicity–sigma relation. No doubt they could have made a fit to their data, so what they mean is probably that the different indices give different ages and metallicities. For example, they find that an Mg index gives a significantly different age than an Fe index. While we also find our two ages to be significantly different, the size of this difference is small. In accordance with this, the coefficients for 'log age' in Eq. (7.30) and (7.31) are not significantly different. We are not able to establish the true zero point.

We can now revisit two problems raised earlier, namely the interpretation of (a) the intrinsic scatter in the Mg_2–σ relation, and (b) the similar intrinsic scatter in the FP in Gunn r, Johnson B, and Johnson U.

If we take the Mg-version of the age–metallicity–sigma relation (Eq. 7.30) *at face value* and insert it in the analytical approximation to the predictions from the Vazdekis et al. models for Mg_2 (J97; Eq. 2.34), we can eliminate either [Mg/H] or $\log \mathrm{age}_{\mathrm{Mg}}$. We get

$$\mathrm{Mg}_2 = \underset{\pm\ 0.01}{-\ 0.03} \log \mathrm{age}_{\mathrm{Mg}} + c\,; \quad \mathrm{Mg}_2 = \underset{\pm\ 0.01}{0.04}\, [\mathrm{Mg/H}] + d \tag{7.32}$$

where the constants c and d depend on $\log \sigma$. This means that due to the relation between age and metallicity for a given sigma the Mg_2 index changes very little as either age or metallicity changes.

Using these relations, the intrinsic scatter in the Mg_2–σ relation of 0.024 translates into a log age variation of 0.8 dex or a [M/H] variation of 0.6 dex, both at a given $\log\sigma$. This is much larger than the estimates obtained without the age–metallicity–sigma relation taken into account, 0.2 dex and 0.13 dex. Worthey et al. (1995) also reached the conclusion that when taking into account the age–metallicity relation, the intrinsic scatter in the Mg_2–σ relation allowed for a larger variation in age than 15%. If we had excluded the 5 (out of 155) galaxies that have very large residuals from the Mg_2–σ relation, the intrinsic scatter would be 0.014, which translates into either 0.45 dex in log age or 0.35 dex in [M/H]. The corresponding numbers without taking into account the age–metallicity–sigma relation are 0.13 dex and 0.08 dex, respectively.

In a similar manner, we insert the Mg-version of the age–metallicity–sigma relation (Eq. 7.30) into the analytical approximations to the predictions from the Vazdekis et al. models for $\log(M/L)$ (Eq. 7.13–7.15). When eliminating either [Mg/H] or $\log\mathrm{age}_{\mathrm{Mg}}$, the result is

$$\begin{aligned}
\log(M/L_{\mathrm{r}}) &= 0.43\log\mathrm{age}_{\mathrm{Mg}} + c_1\,; \quad \log(M/L_{\mathrm{r}}) = -0.55\,[\mathrm{Mg/H}] + d_1\\
&\pm\ 0.02 \qquad\qquad\qquad\qquad\quad \pm\ 0.07\\
\log(M/L_{\mathrm{B}}) &= 0.46\log\mathrm{age}_{\mathrm{Mg}} + c_2\,; \quad \log(M/L_{\mathrm{B}}) = -0.59\,[\mathrm{Mg/H}] + d_2\\
&\pm\ 0.03 \qquad\qquad\qquad\qquad\quad \pm\ 0.09\\
\log(M/L_{\mathrm{U}}) &= 0.52\log\mathrm{age}_{\mathrm{Mg}} + c_3\,; \quad \log(M/L_{\mathrm{U}}) = -0.66\,[\mathrm{Mg/H}] + d_3\\
&\pm\ 0.04 \qquad\qquad\qquad\qquad\quad \pm\ 0.11
\end{aligned} \tag{7.33}$$

where the constants c_i and d_i depend on $\log\sigma$. It is seen that the coefficients for $\log\mathrm{age}_{\mathrm{Mg}}$ and [Mg/H] vary much less with passband than when the age–metallicity–sigma relation is not taken into account, see Eq. (7.13)–(7.15), p. 96. Therefore, if we explain the intrinsic scatter in the FP (interpreted as the $(M/L) \propto M^b$ relation) by either an age variation at a given sigma and metallicity, or a metallicity variation at a given sigma and age, the scatter in $\log(M/L)$ is not expected to be very different in the different passbands, in agreement with the observations.

The intrinsic scatter in the $(M/L) \propto M^b$ relation is 0.103 dex in Gunn r. This translates into a variation in log age of 0.24 dex, or a variation in [M/H] of 0.19 dex. This is substantially less than the variation needed to explain the intrinsic scatter in the Mg_2–σ relation in the same way. Since we do not have a detailed understanding of the origin of these two relations, it might well be, that galaxy formation and evolution made Mg_2 be less well determined from σ than (M/L) from mass.

7.6 Correlations with the FP Residuals

As mentioned above (p. 93), the FP has significant intrinsic scatter. The identification of the source of this intrinsic scatter could provide new insight into the physics of a galaxies, and give more reliable or even more precise distance determinations. We search for this source by searching for correlations between the FP residuals and a number of available parameters.

For the given galaxy we define the residual from the Gunn r FP (Eq. 7.7) as

$$\Delta\mathrm{FP} \equiv \log r_\mathrm{e} - 1.35\log\sigma + 0.83\log <I>_\mathrm{e} + 0.218 \quad (r_\mathrm{e} \text{ in kpc}) \ . \tag{7.34}$$

We tested for correlations between ΔFP and a number of other parameters by means of either Spearman rank order tests, or for small sample sizes ($N \leq 30$) Kendall's tau rank order tests. The results are given in Table 7.3 ('significant' correlations) and Table 7.4 ('non-significant' correlations). Here 'significant' is defined as $P_{\text{no corr.}} < 4.6\%$, which corresponds to 2 sigma for a normal distribution. In the case of a significant correlation, the sign of the Spearman rank order coefficient r_S indicates the direction of the correlation (e.g. $r_\mathrm{S} > 0$: ΔFP *increases* with the given parameter).

Table 7.3: 'Significant' Correlations with the FP Residuals

	HydraI			Coma			HydraI+Coma		
Parameter	N	r_S	$P_{\text{no corr.}}$	N	r_S	$P_{\text{no corr.}}$	N	r_S	$P_{\text{no corr.}}$
$\log\sigma$	45	0.154	31.00%	114	−0.298	**0.15%**	159	−0.147	6.50%
$\log <I>_\mathrm{e}$	45	0.255	9.00%	114	0.130	17.00%	159	0.174	**2.80%**
M_{r_T}	45	−0.342	**2.30%**	114	−0.058	54.00%	159	−0.153	5.40%
log(Mass)	45	0.042	78.00%	114	−0.299	**0.15%**	159	−0.180	**2.40%**
Mg_2	42	−0.056	72.00%	113	−0.263	**0.53%**	155	−0.200	**1.30%**
$\log(M/L_\mathrm{r})$	45	−0.644	**<0.01%**	114	−0.789	**<0.01%**	159	−0.751	**<0.01%**
$\log \mathrm{age}_{\mathrm{Mg}}$	42	−0.776	**<0.01%**	113	−0.793	**<0.01%**	155	−0.795	**<0.01%**
[Mg/H]	42	0.421	**0.71%**	113	0.469	**<0.01%**	155	0.461	**<0.01%**
[Fe/H]	41[a]	0.434	**0.60%**	42[a]	0.472	**0.25%**	83	0.419	**0.01%**
$<c_4>$	45	0.296	4.90%	114	0.136	15.00%	159	0.174	**2.90%**
$<c_6>$	45	−0.260	8.50%	114	−0.135	15.00%	159	−0.165	**3.70%**
c_4	44	0.327	**3.20%**	114	0.072	45.00%	158	0.133	9.60%
$(U-r)_\mathrm{e}$	19	0.716	**0.15%**						
$(U-B)_\mathrm{e}$	19	0.712	**0.23%**						
$(B-r)_\mathrm{e}$	19[b]	0.526	**3.30%**						
$\log R_\mathrm{cl}$	45	0.291	5.30%	113[c]	0.205	**3.00%**	158	0.227	**0.45%**
$\log \rho_\mathrm{cl}$	45	−0.291	5.30%	113[c]	−0.205	**3.00%**	158	−0.205	**1.00%**

Notes: This table shows results from Spearman / Kendall's tau rank order tests between the listed parameters and the Gunn r FP residuals (defined by Eq. 7.34). Tests were performed for the HydraI, Coma, and HydraI+Coma samples. Parameters for which $P_{\text{no corr.}} < 4.6\%$ for at least one of the three samples are included in this table, with the remaining results being given in Table 7.4. $P_{\text{no corr.}} = 4.6\%$ corresponds to 2 sigma for a normal distribution. Values of $P_{\text{no corr.}} < 4.6\%$ are shown in boldface. Unless otherwise noted, the number of galaxies N was set simply by the the number of galaxies for which ΔFP and the given parameter were available.
[a] Galaxies with $\sigma_{\log <\mathrm{Fe}>} > 0.065$ excluded. [b] Only galaxies with Johnson U photometry selected.
[c] D43/NGC4853 excluded.

Table 7.4: 'Non-Significant' Correlations with the FP Residuals

	HydraI			Coma			HydraI+Coma		
Parameter	N	r_S	$P_{\text{no corr.}}$	N	r_S	$P_{\text{no corr.}}$	N	r_S	$P_{\text{no corr.}}$
$\log r_e$	45	−0.038	80.00%	114	−0.052	58.00%	159	−0.057	47.00%
$\Delta(\text{Mg}_2\text{–}\sigma)$	42	−0.144	36.00%	113	−0.070	46.00%	155	−0.098	22.00%
$\log <\text{Fe}>$	41	−0.245	12.00%	42	0.087	58.00%	83	−0.108	33.00%
$\Delta(<\text{Fe}>\text{–}\sigma)$	41	−0.306	5.30%	42	0.131	40.00%	83	−0.113	31.00%
[Mg/Fe]	41	0.199	21.00%	42	0.034	83.00%	83	0.150	17.00%
$<c_3>$	45	−0.272	7.10%	114	0.020	83.00%	159	−0.037	64.00%
$<c_5>$	45	0.150	32.00%	114	0.095	31.00%	159	0.097	22.00%
$<s_3>$	45	0.027	86.00%	114	−0.097	30.00%	159	−0.082	30.00%
$<s_4>$	45	−0.080	59.00%	114	−0.056	55.00%	159	−0.056	49.00%
$<s_5>$	45	0.125	41.00%	114	−0.056	56.00%	159	−0.013	87.00%
$<s_6>$	45	−0.141	35.00%	114	−0.039	67.00%	159	−0.076	34.00%
ε_e	45	0.133	38.00%	114	0.161	8.80%	159	0.152	5.70%
$\varepsilon_{21.85}$	45	0.179	24.00%	114	0.156	9.70%	159	0.158	4.70%
$(B-r)_e$	45	0.070	64.00%						

Notes: See the notes to Table 7.3. $\Delta(\text{Mg}_2\text{–}\sigma)$ and $\Delta(<\text{Fe}>\text{–}\sigma)$ are the residuals from the Mg_2–σ relation (Eq. 7.16) and the $<\text{Fe}>$–σ relation (Eq. 7.17), respectively.

From Table 7.3 it is seen that the FP residuals are significantly correlated with a number of parameters. We will discuss these in the following five groups: (1): Structural parameters ($\log\sigma$ and $\log <I>_e$) and related issues. (2): Mass-to-light ratios, ages, and metallicities. (3): Geometrical parameters ($<c_4>$, $<c_6>$, c_4, and ellipticities). (4): Colors. (5): Environment (projected cluster center distances R_{cl} and projected cluster mass densities ρ_{cl}).

(1): Structural parameters and related issues. From Table 7.3 it is seen that for the Coma sample there is a significant correlation with $\log\sigma$ ($P_{\text{no corr.}} = 0.15\%$). If we use the residuals from the Coma FP (Eq. 7.5) rather than the Hydra+Coma FP, we find $P_{\text{no corr.}} = 7.0\%$ for $\log\sigma$ (and $P_{\text{no corr.}} = 5.8\%$ for $\log <I>_e$). For the combined HydraI+Coma sample there may be a correlation with $\log <I>_e$ ($P_{\text{no corr.}} = 2.8\%$). The above may indicate, that *the samples* deviate from the fitted models (for one cluster a plane, for two clusters two parallel planes). However, to assess whether this also pertains to *the underlying distribution* from which the samples were drawn, Monte Carlo simulations that take into account selection effects and measurement errors are needed.

ΔFP may be correlated with M_{r_T} ($P_{\text{no corr.}} = 5.4\%$). JFK96 found that the residuals from their FP was not significantly correlated M_{r_T} (for their data). We find, that for our data there *is* a significant correlation between the JFK96 FP residuals and M_{r_T}, $P_{\text{no corr.}} = 0.01\%$ (and $P_{\text{no corr.}} = 0.21\%$ for galaxies brighter than $M_{r_T} = -20\overset{\text{m}}{.}75$). If the samples are selected in M_{r_T}, this will cause a systematic effect on the derived distances.

For the Coma [and the combined] sample, ΔFP is correlated with $\log(\text{Mass}) = 2\log\sigma + \log r_e +$ const ($P_{\text{no corr.}} = 0.15\%$) and with Mg_2 ($P_{\text{no corr.}} = 0.53\%$). Part of this may be 'left over' correlation with $\log\sigma$, as JFK96 noted – for $\log(\text{Mass})$ since $\log\sigma$ enters the calculation directly, and for Mg_2 through the Mg_2–σ relation. In addition, $\log(\text{Mass})$ also has the parameter $\log r_e$ in common with ΔFP. Common parameters are discussed further in point (2) below. For the Coma sample, if we use the Coma FP (where the ΔFP–$\log\sigma$ correlation is less significant), we find for ΔFP versus $\log(\text{Mass})$ and Mg_2 $P_{\text{no corr.}} = 3.1\%$ and 8.1%, respectively. These values are indeed larger, but

still leaves it as an open question whether the ΔFP–log(Mass) and ΔFP–Mg_2 correlations are due to 'left over' correlation with $\log\sigma$ *only*. The values of $P_{\rm no\ corr.}$ for the HydraI sample do not seem to agree with those for the Coma sample; however, this could be due just to the small sample size.

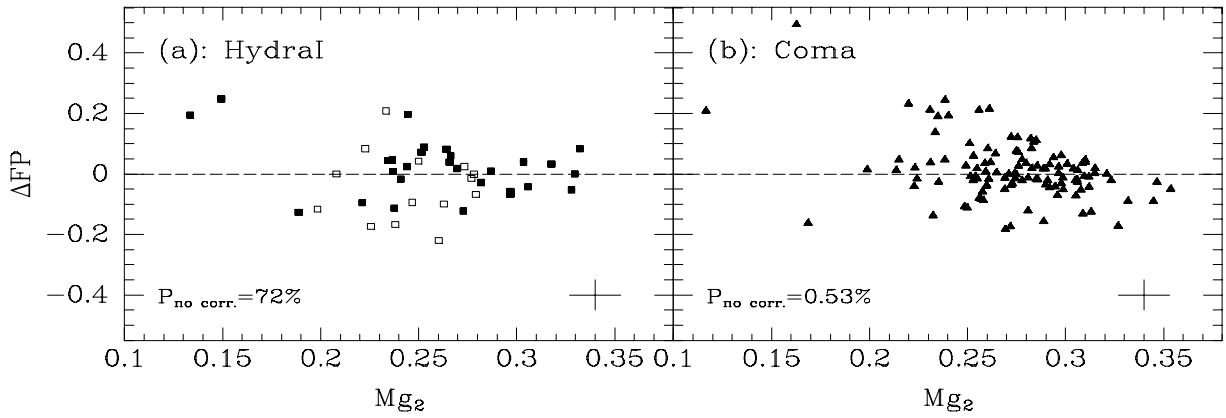

Figure 7.18: FP residuals versus Mg_2. Data symbols as in Fig. 7.1.

(2): Mass-to-light ratios, ages, and metallicities. In Fig. 7.19 we show ΔFP versus $\log(M/L_{\rm r})$, $\log {\rm age}_{\rm Mg}$, [Mg/H], and [Fe/H]. Highly significant correlations are found for all four quantities, both for the HydraI and Coma samples individually and for the combined sample (cf. Table 7.3). The problem is to determine to what extend these correlations reflect *intrinsic* correlations.

Let us first consider the ΔFP–$\log(M/L_{\rm r})$ correlation. Recall the definitions of these two quantities, $\Delta{\rm FP} = \log r_{\rm e} - 1.35\log\sigma + 0.83\log <I>_{\rm e} + 0.218$, and $\log(M/L_{\rm r}) = -\log r_{\rm e} + 2\log\sigma - \log <I>_{\rm e} - 0.733$. ΔFP and $\log(M/L_{\rm r})$ have three common parameters (and nothing but that), and these are combined in a to some extend similar way. Another way of saying this is that the angle between the FP and the plane of $\log(M/L_{\rm r}) = {\rm const}$ is only 9°. This alone will cause ΔFP and $\log(M/L_{\rm r})$ to be correlated. To assess whether the ΔFP–$\log(M/L_{\rm r})$ correlation that we find is due *solely* to this, some kind of Monte Carlo simulations are needed. Note, that common parameters per se do not necessarily give a correlation. For example, ΔFP is not significantly correlated with x and y (Eq. 7.9, p. 92). Of course, the planes of constant x and y are both at right angles to the FP.

Since $\log {\rm age}_{\rm Mg}$, [Mg/H], and [Fe/H] are based in part on $\log(M/L)$, simulations are also needed to assess to what extend the correlations between these three parameters and ΔFP are spurious. However, there is the important difference, that unlike $\log(M/L)$, ages and metallicities could have been estimated using e.g. H_β and thus independently of the three FP parameters. (Note that we do not have H_β measurements for our samples.) And since the age–metallicity–sigma relation found by Worthey et al. (1995) without using $\log(M/L)$ is in qualitative agreement with the relation that we find using $\log(M/L)$, it seems likely that the correlations between ΔFP and $\log {\rm age}_{\rm Mg}$, [Mg/H], and [Fe/H] are real.

Unlike for [Mg/H] and [Fe/H], we find that [Mg/Fe] is not significantly correlated with ΔFP, see Fig. 7.20. For the HydraI, Coma, and HydraI+Coma samples we find $P_{\rm no\ corr.} = 21\%$, 93%, and 17%, respectively.

The direct tests between the FP residuals on the one hand and ages, metallicities, and abundance ratios on the other hand have not previously been discussed in the literature.

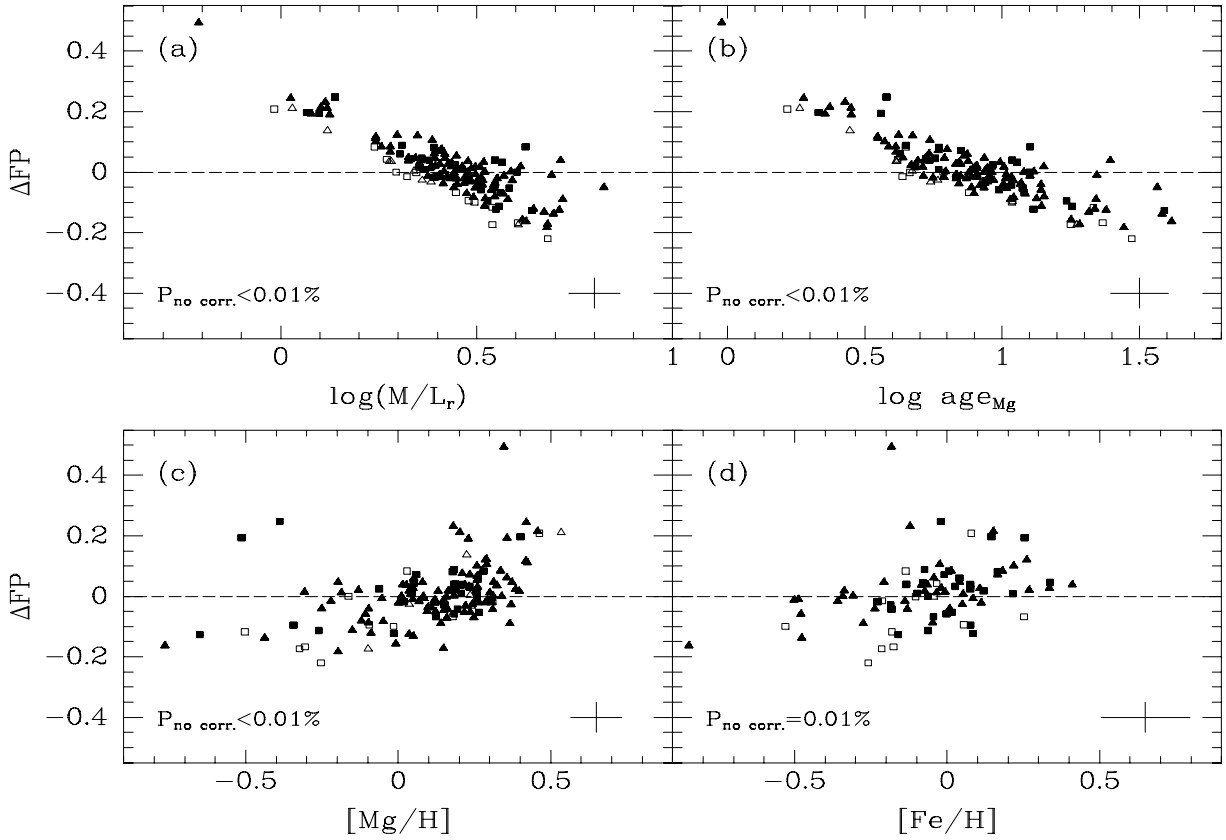

Figure 7.19: FP residuals versus $\log(M/L_{\rm r})$, $\log {\rm age}_{\rm Mg}$, [Mg/H], and [Fe/H]. HydraI and Coma are plotted together – there are no apparent differences between the two for the shown relations. Data symbols as in Fig. 7.1.

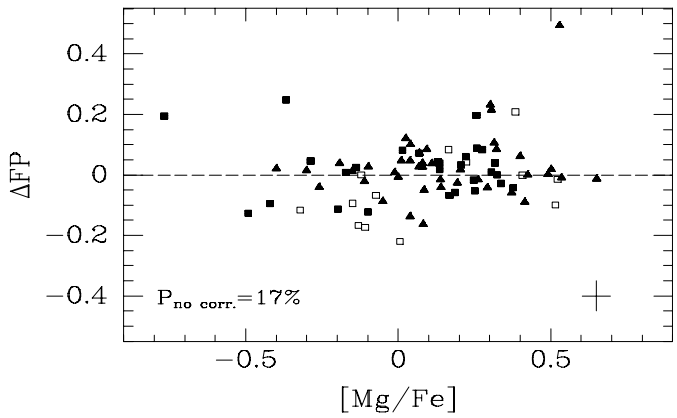

Figure 7.20: FP residuals versus [Mg/Fe]. HydraI and Coma are plotted together. No significant correlations are found. Data symbols as in Fig. 7.1.

(3): Geometrical parameters. In Fig. 7.21 we plot ΔFP versus the geometrical parameters $<c_4>$, $<c_6>$, c_4, and $\varepsilon_{21.85}$. The correlations are marginally significant, with $P_{\text{no corr.}} = 2.9\%$, 3.7%, 9.6%, and 4.7%, respectively. ΔFP increases with $<c_4>$, c_4, and $\varepsilon_{21.85}$, and decreases with $<c_6>$. As JFK96 also found, all the correlations are caused by the 15 galaxies with $\varepsilon_{21.85} > 0.6$.

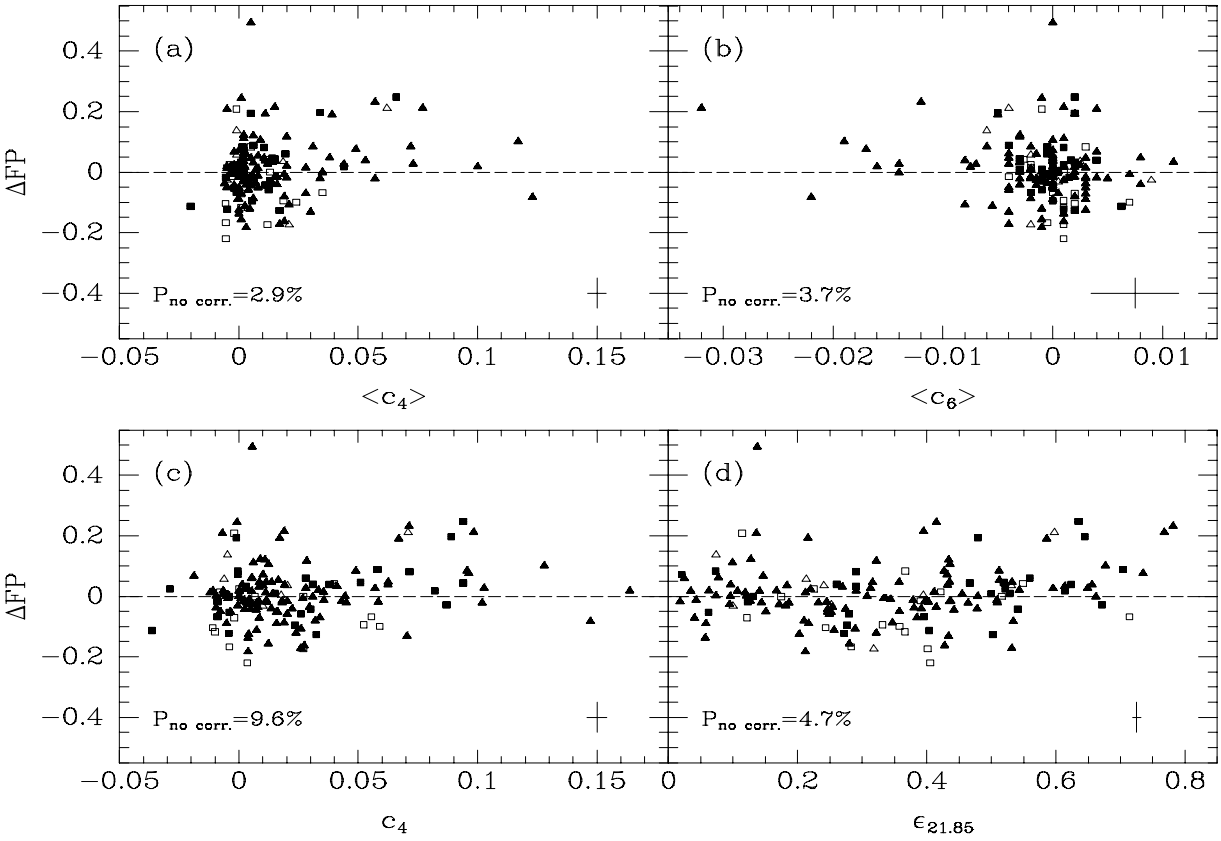

Figure 7.21: FP residuals versus the geometrical parameters $<c_4>$, $<c_6>$, c_4, and $\varepsilon_{21.85}$. HydraI and Coma are plotted together. Data symbols as in Fig. 7.1.

The correlations between ΔFP and the geometrical parameters could be caused by the presence of a disk *per se*, i.e. without assuming the disk to have a different stellar population than the spheroid/bulge. JFK96 studied this by constructing simple axisymmetric galaxy models consisting of a disk with an exponential profile and a bulge with an $r^{1/4}$ profile. The intrinsic ellipticities of the disk and bulge were 0.85 and 0.3, respectively, and the two components were assumed to be oblate. The kinematical part of the models assumed the distribution function to be a function of energy and angular momentum around the z-axis, only. The models predict ΔFP to increase with $<c_4>$ and $\varepsilon_{21.85}$, in agreement with the data. However, JFK96 found that their data did *not* show a significant correlation between ΔFP and the relative disk luminosity $L_{\text{D}}/L_{\text{tot}}$ as their models predicted. (We have not derived estimates of $L_{\text{D}}/L_{\text{tot}}$ for the HydraI data. To do this, new pseudo-photometry that matches the typical seeing should be produced; see JF94. This has yet to be done.)

It would be interesting to include the possible effects of stellar population differences between the disk and the bulge in the models. It could be, that it is not the presence of a disk per se that is causing the FP residuals, but that the stellar population in the disk differs from the stellar population in the bulge. In Fig. 7.22 we plot $\log \text{age}_{\text{Mg}}$ versus $<c_4>$ and $\varepsilon_{21.85}$. It is seen that galaxies with high ellipticities and large values of $<c_4>$ have lower mean ages than the rest of the

galaxies. Since lower mean ages are found to give positive values of ΔFP (Fig 7.19b), at least part of the ΔFP–$<c_4>$ and ΔFP–$\varepsilon_{21.85}$ correlations could be explained by this. An elaborate analysis of these matters is beyond the limits of this work.

As mentioned before, E and S0 galaxies have similar FP residuals, with the median difference being 0.000 ± 0.015.

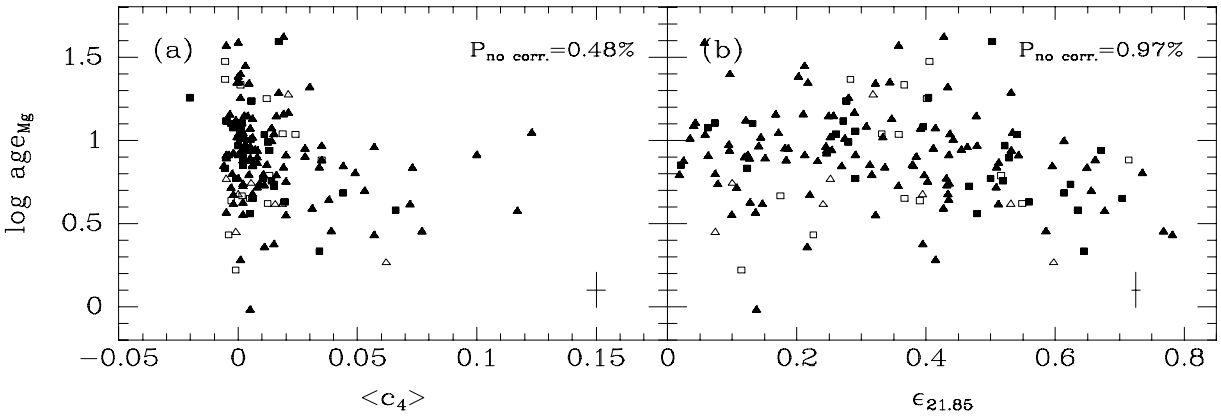

Figure 7.22: $\log \mathrm{age}_{\mathrm{Mg}}$ versus $<c_4>$ and $\varepsilon_{21.85}$. HydraI and Coma are plotted together. Data symbols as in Fig. 7.1.

(4): Colors. For the HydraI sample, the color $(B-r)_{\mathrm{e}}$ is available for the full sample ($N = 45$), and the colors $(U-r)_{\mathrm{e}}$ and $(U-B)_{\mathrm{e}}$ are available for a subsample ($N = 19$). The FP residuals are significantly correlated with $(U-r)_{\mathrm{e}}$ and $(U-B)_{\mathrm{e}}$, with $P_{\mathrm{no\ corr.}} = 0.15\%$ and 0.23%, respectively. See Fig. 7.23.

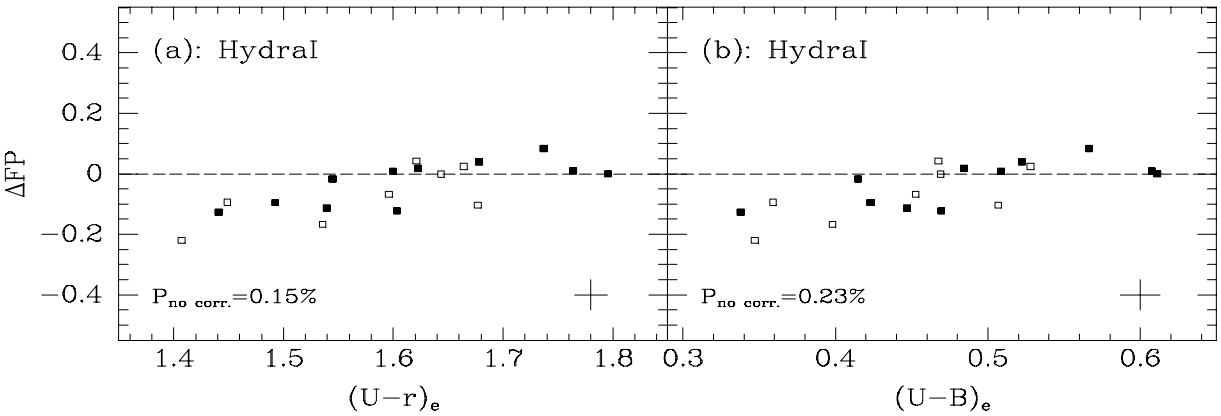

Figure 7.23: FP residuals versus $(U-r)_{\mathrm{e}}$ and $(U-B)_{\mathrm{e}}$. Data symbols as in Fig. 7.1.

ΔFP is not correlated with $(B-r)_{\mathrm{e}}$ for the full sample ($P_{\mathrm{no\ corr.}} = 64\%$), and the hint of a correlation for the subsample ($P_{\mathrm{no\ corr.}} = 3.3\%$) could be spurious. An interesting result appears if we test for correlations between the colors one the one hand and either metallicity or age on the other hand. Specifically, let us on the one hand consider the following four quantities: $(U-r)_{\mathrm{e}}$, $(U-B)_{\mathrm{e}}$, $(B-r)_{\mathrm{e}}$ for the full sample, and $(B-r)_{\mathrm{e}}$ for the subsample. If we test for correlations between these four quantities and [Mg/H], we get $P_{\mathrm{no\ corr.}} = 0.01\%$, 0.04%, 0.01%, and 0.13%, respectively (all with $r_{\mathrm{S}} > 0$). If we test for correlations between these four quantities and $\log \mathrm{age}_{\mathrm{Mg}}$, we get $P_{\mathrm{no\ corr.}} = 2.1\%$, 4.5%, 97%, and 16%, respectively (all with $r_{\mathrm{S}} < 0$). It seems that all three colors are correlated with [Mg/H], but that only $(U-r)_{\mathrm{e}}$ and $(U-B)_{\mathrm{e}}$ are correlated with $\log \mathrm{age}_{\mathrm{Mg}}$. These correlations should be understood in the light of the age–metallicity[–sigma] relation that we

have found the galaxies to follow. Note the sign of the $(U-r)_{\rm e}$–$\log {\rm age}_{\rm Mg}$ and $(U-B)_{\rm e}$–$\log {\rm age}_{\rm Mg}$ correlations: the galaxies get more *blue* for larger mean ages! See Fig. 7.24. This must be due to the counter-trend in metallicity more than balances the age-trend for these colors. In summary, the correlations between ΔFP and some colors but not others are likely caused by the fact that galaxies follow an age–metallicity[–sigma] relation and that the different colors have different sensitivities to age and metallicity.

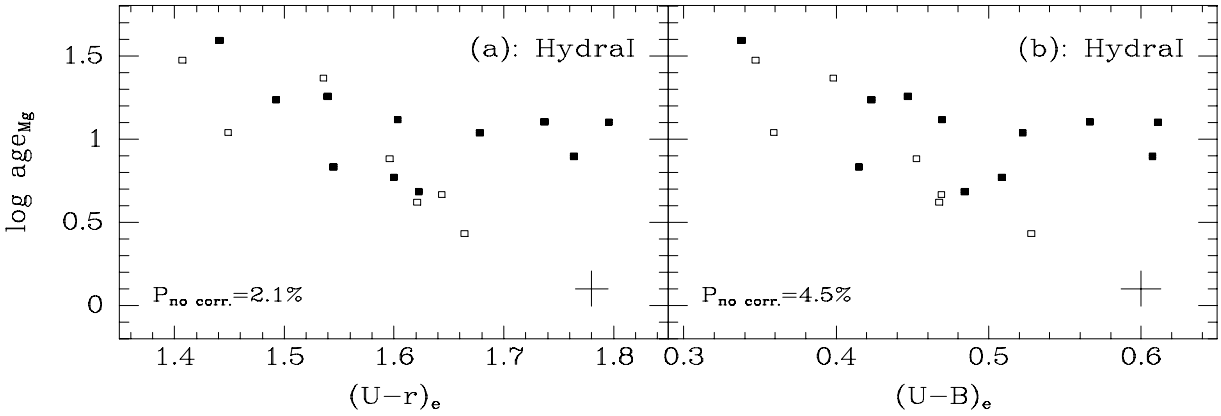

Figure 7.24: $\log {\rm age}_{\rm Mg}$ versus versus $(U-r)_{\rm e}$ and $(U-B)_{\rm e}$. In these colors, galaxies get more *blue* for larger mean ages. This is due to the age–metallicity[–sigma] relation. Data symbols as in Fig. 7.1.

(5): Environment. Figure 7.25 shows ΔFP versus $\log R_{\rm cl}$ and $\log \rho_{\rm cl}$. $R_{\rm cl}$ is the projected cluster center distance in Mpc, where the center of HydraI is defined as the position of the brightest galaxy R269/NGC3311, and the center of Coma is defined as the mean position of the two brightest galaxies D129/NGC4874 and D148/NGC4889. R269, which has $R_{\rm cl}=0$, has been assigned the value $\log R_{\rm cl}=-1.5$. $\rho_{\rm cl}$ is the estimated projected cluster mass density, derived from

$$\rho_{\rm cl} \propto {\rm Mass}/R_{\rm cl}^2 \propto \sigma_{\rm cl}^2/R_{\rm cl} \ , \tag{7.35}$$

as done by JFK96. $\sigma_{\rm cl}$ is the cluster velocity dispersion in $\rm km\,s^{-1}$ (from Table 7.2, p. 89). Our results indicate, that ΔFP is correlated with environment. For the combined HydraI+Coma sample, we find $P_{\rm no\ corr.}=1.0\%$ for ΔFP versus $\log \rho_{\rm cl}$. This result also holds for the JFK96 FP coefficients, where we find $P_{\rm no\ corr.}=0.57\%$. JFK96 did not find a significant correlation between ΔFP and $\log \rho_{\rm cl}$. Note, however, that JFK96 had ten clusters, and the FP zero point was a free parameter for each of them. This could hide a possible correlation between ΔFP and $\log \rho_{\rm cl}$.

Figure 7.25(d) could indicate, that galaxies with large values of $\log \rho_{\rm cl}$, say $\log \rho_{\rm cl} > 6.75$, do not follow the same ΔFP–$\log \rho_{\rm cl}$ relation as the rest of the galaxies. However, the number of galaxies with $\log \rho_{\rm cl} > 6.75$ is only about 15.

Figure 7.26 shows ΔFP versus $\log R_{\rm cl}$ for the HydraI Johnson B and U FPs. It is seen that the behavior in Johnson B resembles that in Gunn r, so the effect does not seem to be very wavelength dependent. This rules out the hypothesis that the ΔFP–$\log \rho_{\rm cl}$ correlation is caused by an intra-cluster *dust*, since the dust extinction in Gunn r is expected to be only 0.63 times that in Johnson B (Seaton 1979), at least for the kind of dust found in the Milky Way. This hypothesis is also unlikely for other reasons: any dust present in the intra-cluster medium would probably be destroyed by the hot ($T_{\rm gas}$ = 4–8 keV) intra-cluster gas on a fairly short time scale. The Johnson U data only span a small range in $R_{\rm cl}$, and even though no correlation between ΔFP and $\log R_{\rm cl}$ is found, this is not in contradiction to the results in Gunn r and Johnson B.

Is the ΔFP–log $\rho_{\rm cl}$ correlation caused by the ΔFP–age and ΔFP–metallicity correlations? We find log $\rho_{\rm cl}$ *not* to be significantly correlated with log age$_{\rm Mg}$, [Mg/H], and [Fe/H] ($P_{\rm no\ corr.}$ = 21%, 13%, and 63%, respectively). However, this could be due to a somewhat limited range in log $\rho_{\rm cl}$ – our data only go to log $\rho_{\rm cl}$ = 5.5. J97 had data out to very low densities, log $\rho_{\rm cl}$ = 4, and found significant Mg$_2$–log $\rho_{\rm cl}$ and log < Fe >–log $\rho_{\rm cl}$ correlations. These imply that metallicity and/or age is correlated with log $\rho_{\rm cl}$. Therefore, it is possible that the ΔFP–log $\rho_{\rm cl}$ correlation is caused by the ΔFP–age and ΔFP–metallicity correlations.

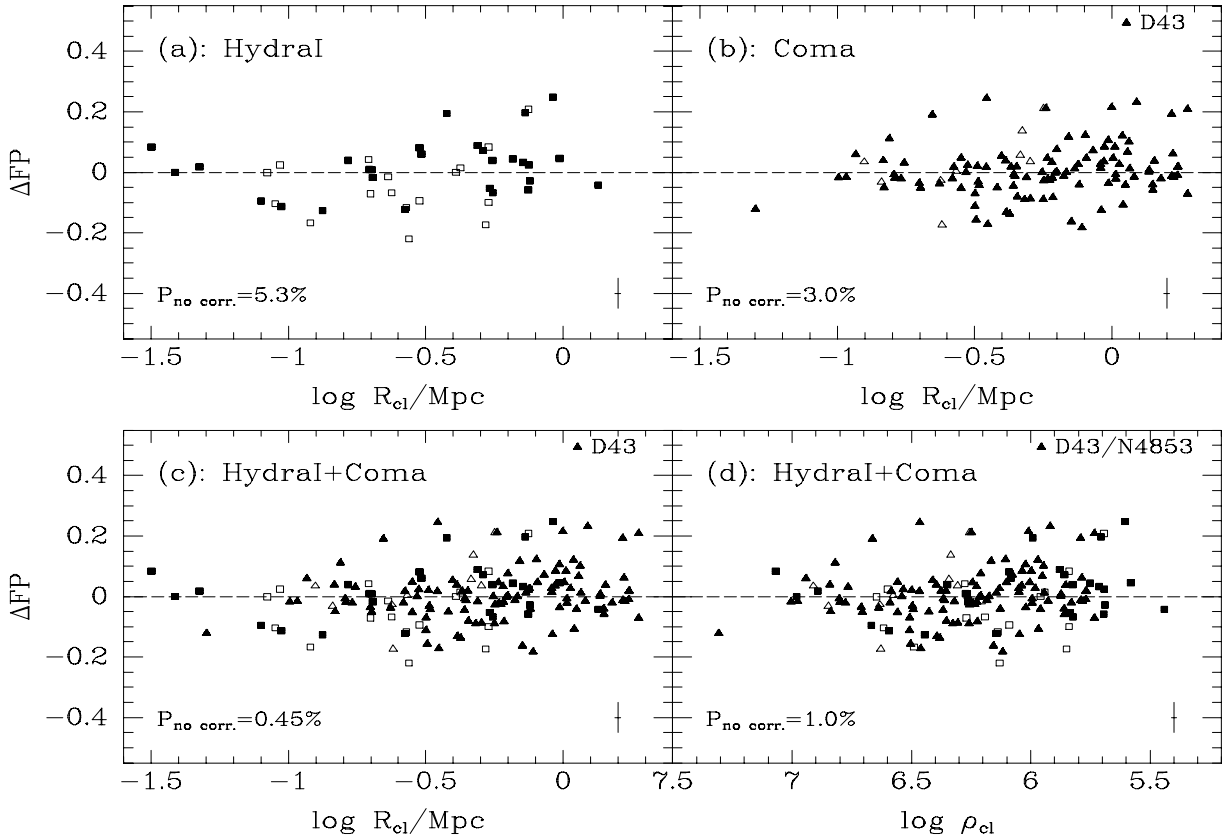

Figure 7.25: FP residuals versus log $R_{\rm cl}$ (panel a, b, and c), and also versus log $\rho_{\rm cl}$ (panel d). $R_{\rm cl}$ is the projected cluster center distance, and $\rho_{\rm cl} \equiv \sigma_{\rm cl}^2/R_{\rm cl}$ is the estimated projected cluster mass density. The cluster center is to the left in all four panels, since the log $\rho_{\rm cl}$ axis in panel d has been inverted. D43/NGC4853 was excluded from the Spearman tests – if it is included, the $P_{\rm no\ corr.}$ values for panel b, c, and d decreases to 2.0%, 0.29%, and 0.78%, respectively. Data symbols as in Fig. 7.1.

Finally, and not in the context of correlations with ΔFP, we investigate whether [Mg/Fe] is correlated with log $\rho_{\rm cl}$. J97 found [Mg/Fe] to decrease about 0.1 dex between log $\rho_{\rm cl}$ = 4.5 and 7. In Fig. 7.27 we plot [Mg/Fe] versus log $R_{\rm cl}$ and log $\rho_{\rm cl}$. Our HydraI sample does not show a [Mg/Fe]–log $\rho_{\rm cl}$ correlation, while there is some evidence of it from the Coma sample. However, there are selection effects that are not well understood for the subsample of the Coma sample that has < Fe >-data, for example there are few galaxies close to the center. Again, it is important to note that J97 had data out to very low densities, and that the effect found by J97 is large for log $\rho_{\rm cl}$ < 5.0. From our data alone, we cannot claim a firm detection of a [Mg/Fe]–log $\rho_{\rm cl}$ correlation, but this is not in contradiction to the correlation found by J97.

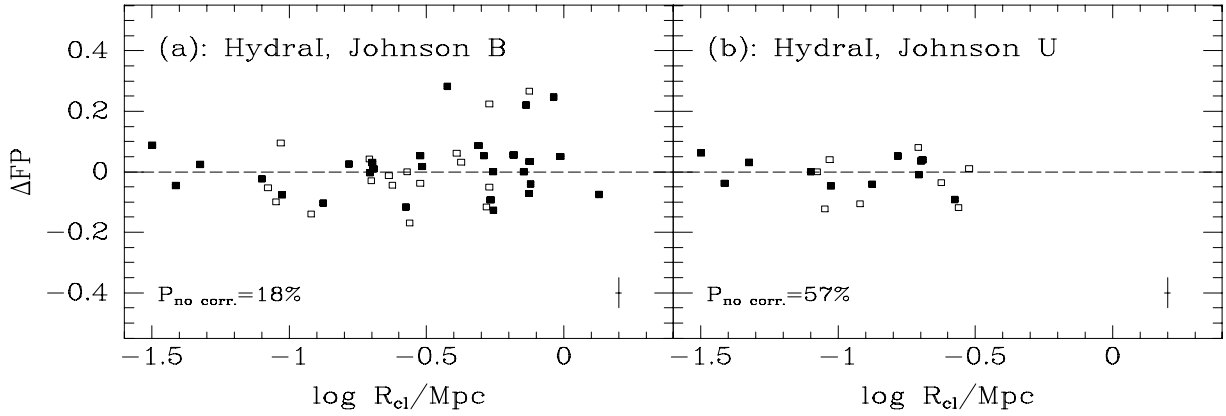

Figure 7.26: FP residuals versus $\log R_{\rm cl}$ for HydraI Johnson B (Eq. 7.10) and Johnson U (Eq. 7.11). Data symbols as in Fig. 7.1.

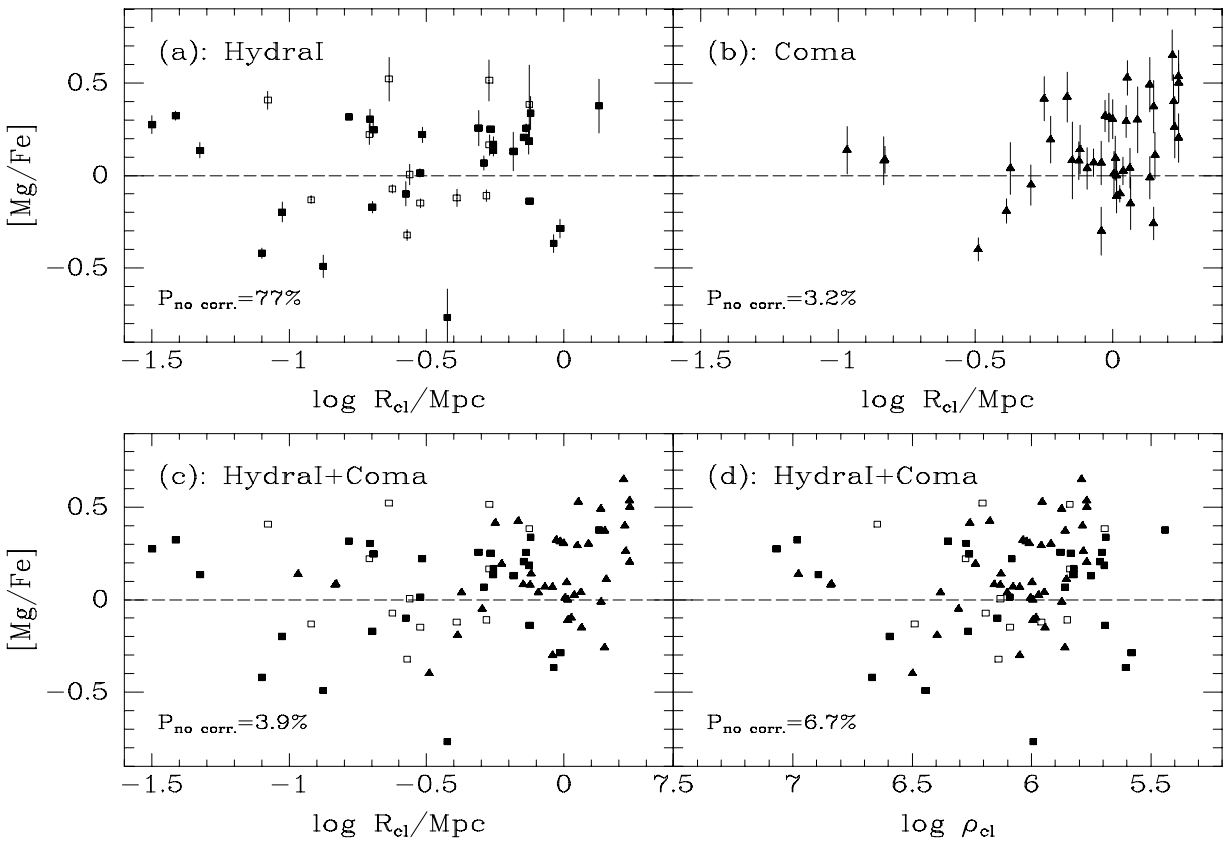

Figure 7.27: [Mg/Fe] versus $\log R_{\rm cl}$ (panel a, b, and c), and also versus $\log \rho_{\rm cl}$ (panel d). In panel a and b, the individual [Mg/Fe] error bars are shown. Data symbols as in Fig. 7.1.

Chapter 8

Conclusions

We have investigated properties of E and S0 galaxies in the central parts of the clusters HydraI (Abell 1060) and Coma (Abell 1656) using large magnitude limited samples. The investigations serve the following main purposes: (1) They add pieces to our knowledge about galaxy formation and evolution, including the formation and evolution of the stellar populations of the galaxies. (2) They help establish a good reference point at $z \approx 0$ needed for the similar studies of high redshift galaxies. (3) They help identify possible limitations in the use of the Fundamental Plane (FP) as a distance determinator.

For the HydraI cluster we have presented CCD surface photometry for 64 E and S0 galaxies. The galaxies have been observed in Gunn r and Johnson B, and for a subset of 22 galaxies also in Johnson U. The observations were made with the Danish 1.5 meter telescope at La Silla, equipped with the DFOSC instrument. The surface photometry was done by fitting ellipses to the images. This gave the radial profiles of surface brightness, ellipticity, and position angle, as well as the deviations from elliptical isophotes described by Fourier coefficients. In addition, the color profiles were derived. From the surface photometry we have derived effective radius, mean surface brightness, and total magnitude by fitting an $r^{1/4}$ growth curve. We take the seeing into account. We have also derived global Fourier coefficients. From external comparisons we find the following typical uncertainties: $\log r_{\rm e}$: ± 0.028; $\log <I>_{\rm e}$: ± 0.039. For the combination that enters the FP we find: $(\log r_{\rm e} + 0.82 \log <I>_{\rm e})$: ± 0.011.

For the HydraI cluster, the spectroscopical parameters σ, Mg_2, and $<\mathrm{Fe}>$ for 21 E and S0 galaxies have been presented. These data are also from the Danish 1.5 meter telescope and the DFOSC instrument. Together with data from the literature, spectroscopy is available for 51 E and S0 galaxies in HydraI, of which 45 are part of our magnitude limited photometric sample. From external comparisons we find the following typical uncertainties: $\log \sigma$: ± 0.036; Mg_2: ± 0.013; $\log <\mathrm{Fe}>$: ± 0.030.

From the literature and from work not yet published we have compiled a magnitude limited sample of 114 E and S0 galaxies in the central part of the Coma cluster. All the galaxies have photometry in Gunn r and spectroscopy.

From the analysis of the HydraI and Coma samples we draw the following conclusions:

The FP in Gunn r is not significantly different for the two samples, although differences in the $\log \sigma$ coefficient α on the 10% level cannot be ruled out. For the combined sample, we find the FP to be $\log r_{\rm e} = 1.35 \log \sigma - 0.83 \log <I>_{\rm e} + \gamma$. This is in agreement with most previous studies, e.g. JFK96. The distribution within the FP is not significantly different for the two samples. Based on typical measurement errors derived from external comparisons we find that the FP has an intrinsic scatter of 0.087 in $\log r_{\rm e}$. The FP zero points imply a non-significant peculiar velocity for HydraI relative to Coma. When we assume Coma to have zero peculiar velocity, we

find $v_{\rm pec,HydraI} = -93 \pm 152\,{\rm km\,s^{-1}}$ and $v_{\rm pec,Coma} = 0 \pm 160\,{\rm km\,s^{-1}}$. E and S0 galaxies are found to have FP zero points that are not significantly different (as also found by JFK96), and also the distribution within the FP is not significantly different when taking into account the fact that few (if any) S0 galaxies exist brighter than $M_{\rm r_T} = -23\overset{\rm m}{.}1$ (JF94).

For the HydraI sample we find that the intrinsic scatter is not significantly different in Gunn r, Johnson B, and Johnson U. This is in agreement with the findings of JFK96. This implies that the scatter cannot be caused by variations in only the age or only the metallicity. Changes in the age must be balanced to some extent by changes in the metallicity. This is compatible with the age–metallicity–sigma relation that we find (cf. below).

We find that the $\rm Mg_2$–σ relation is not significantly different for the HydraI and Coma samples. The $\rm Mg_2$–σ relation for the combined sample is in agreement with previous determinations by Burstein et al. (1988), Bender et al. (1993), JFK96, and J97. The iron index $<{\rm Fe}>$ is also correlated with velocity dispersion (at the two sigma level for the HydraI+Coma sample). The $<{\rm Fe}>$–σ relation is not significantly different for the HydraI and Coma samples. For the combined sample, the $<{\rm Fe}>$–σ relation is in agreement with J97. As pointed out by J97, the different slopes of the $\rm Mg_2$–σ and $<{\rm Fe}>$–σ relations combined with predictions from stellar population models imply that the abundance ratio [Mg/Fe] increases with velocity dispersion.

For the HydraI sample, we find tight relations between effective colors (measured within a radius of 0.8–53 kpc, typically 3.6 kpc) and $\rm Mg_2$ and $\log\sigma$ (measured within a radius of 0.5–0.9 kpc and corrected to a radius of 1.2 kpc). This could mean that the variations in radial gradients in colors and line indices from galaxy to galaxy are small (e.g. Burstein et al. 1988, Franx & Illingworth 1990, Bender et al. 1993). However, these tight relations could also be due to the gradients being correlated with e.g. the central values.

We have used the $\rm Mg_2$–$\log(M/L)$ and $\log<{\rm Fe}>$–$\log(M/L)$ diagrams in combination with predictions from the stellar population models of Vazdekis et al. (1996) to derive estimates of the metal abundances [Mg/H] and [Fe/H], the abundance ratio [Mg/Fe], and ages. These quantities should be understood as luminosity weighted mean values.

The derived abundance ratio [Mg/Fe] increases with the velocity dispersion. This is mainly due to an increase in [Mg/H], with [Fe/H] being constant or slightly decreasing. For high velocity dispersion galaxies [Mg/Fe] is larger than solar and can reach values of 0.3 dex or more. This can be explained by an increase in the fraction of type II supernovae over type Ia supernovae with velocity dispersion. This could for example be caused by a variation in IMF slope or in the time scale for star formation (e.g. Worthey et al. 1992).

Both [Mg/H], [Fe/H], [Mg/Fe], and age show a much smaller scatter for galaxies brighter than $M_{\rm r_T} \approx -23\overset{\rm m}{.}1$ (corresponding to $M_{\rm B_T} \approx -22\overset{\rm m}{.}0$) than for galaxies fainter than this magnitude. The galaxies brighter than $M_{\rm r_T} \approx -23\overset{\rm m}{.}1$ have an old stellar population, with [Mg/H] a bit above average, [Fe/H] a bit below average, and thus [Mg/Fe] somewhat above average. Interestingly, JF94 found $M_{\rm r_T} \approx -23\overset{\rm m}{.}1$ to demarcate two classes of galaxies, with the brighter ones showing no signs of disks, and with the fainter ones having a broad distribution of relative disk luminosities.

We find that the ages and metallicities are related, with the metallicity increasing with decreasing age. Further, galaxies of higher velocity dispersion follow an age–metallicity relation at higher metallicity (or older age). The 'Mg-version' of this relation is $[{\rm Mg/H}] = 1.15\log\sigma - 0.78\log{\rm age_{Mg}} + c$. Our results are in qualitative agreement with the ones from Worthey et al. (1995). It is important to note that these authors did not use mass-to-light ratios and $\rm Mg_2$ (or $<{\rm Fe}>$) to derive ages and metallicities, but rather Balmer lines indices and the $\rm C_2 4668$ index. One consequence of the age–metallicity–sigma relation is that it allows for a large variation in age and metallicity while still keeping e.g. the FP and the $\rm Mg_2$–σ relation thin. This was also the conclusion of Worthey et al. (1995). Another consequence is that the FP scatter independent of passband is compatible with

the models, which otherwise would not be the case.

To search for the source of the intrinsic scatter in the FP we have tested for correlations between the FP residuals (ΔFP) and a number of available parameters. Highly significant correlations are found with [Mg/H], [Fe/H], and age (but not [Mg/Fe]). Therefore, age or metallicity differences can cause systematic errors in the distances determined by the FP. Caution should be exercised when interpreting these correlations, since [Mg/H], [Fe/H], and age in part are calculated from (M/L), which in turn have common parameters with the FP. However, since Worthey et al. (1995) find an age–metallicity–sigma relation in qualitative agreement with our relation *without* using (M/L), it seems likely that the found correlations reflect intrinsic relations. It would be valuable to quantify these matters by means of Monte Carlo simulations. And it would be very valuable to get e.g. H_β data for our samples, since from the $\log H_\beta$–Mg_2 and $\log H_\beta$–$\log <Fe>$ diagrams it would be possible to derive ages and metallicities independent of the FP parameters.

We also find weaker ΔFP-correlations with geometrical parameters ($<c_4>$, $<c_6>$, c_4, and ellipticities) and the colors $(U-r)_e$ and $(U-B)_e$. These correlations are at least in part related to the correlations with age and metallicity. In addition we find weak ΔFP-correlation with the projected cluster mass density $\rho_{cl} \equiv \sigma_{cl}^2/R_{cl}$ (where σ_{cl} is the cluster velocity dispersion and R_{cl} is the projected cluster center distance). This was not seen in the study by JFK96. We do not find that $\log \rho_{cl}$ is significantly correlated with age or metallicity. However, the results from J97 indicate that age and/or metallicity are correlated with $\log \rho_{cl}$. The reason that we do not find these correlations could be the limited interval in $\log \rho_{cl}$ that our data cover. Thus, it is possible that also the ΔFP–$\log \rho_{cl}$ correlation is related to the ΔFP-correlations with age and metallicity.

For none of the relations studied do we find any significant differences between HydraI and Coma. This is despite the fact that Coma is 2–3 times more massive than HydraI and has a smaller fraction of spiral galaxies. This suggests that the environmental differences between rich and less rich clusters have only a small effect on the properties of the E and S0 galaxies found in clusters as rich as HydraI and Coma.

References

Abell, G. O., Corwin Jr., H. G., & Olowin, R. P. 1989, "A Catalog of Rich Clusters of Galaxies", ApJS, 70, 1

Baggley, G. 1996, "Peculiar Velocities of Clusters Determined from Early-Type Galaxies", D. Phil. Thesis, St John's College, Oxford

Bender, R., Burstein, D., & Faber, S. M. 1992, "Dynamically Hot Galaxies. I. Structural Properties", ApJ, 399, 462

Bender, R., Burstein, D., & Faber, S. M. 1993, "Dynamically Hot Galaxies. II. Global Stellar Populations", ApJ, 411, 153

Bender, R., Surma, P., Döbereiner, S., Möllenhoff, D., & Madejsky, R. 1989, "Isophote shapes of elliptical galaxies. II. Correlations with global optical, radio and X-ray properties", A&A, 217, 35

Bertelli, G., Bressan, A., Chiosi, C., Fagotto, F., & Nasi, E. 1994, "Theoretical isochrones from models with new radiative opacities", A&AS, 106, 275

Bevington, P. R., & Robinson, D. K. 1992, "Data Reduction and Error Analysis for the Physical Sciences", 2nd edition, New York: McGraw-Hill

Borges, A. C., Idiart, T. P., de Freitas Pacheco, J. A., & Thévenin, F. 1995, "Age and Abundance Effects in Single-Stellar Populations", AJ, 110, 2408

Burkert, A. 1993, "Do elliptical galaxies have $r^{1/4}$ brightness profiles?", A&A, 278, 23

Burstein, D., Bender, R., & Faber, S. M. 1992, "The Structural Properties of Dynamically Hot Galaxies", in Structure, Dynamics and Chemical Evolution of Elliptical Galaxies, eds. Danziger, I. J., Zeilinger, W. W., & Kjär, K., (Garching: ESO), p. 59

Burstein, D., Bender, R., Faber, S. M., & Nolthenius, R. 1997, "Global Relationships Among the Physical Properties of Stellar Systems", AJ, to appear (astro-ph/9707037)

Burstein, D., Davies, R. L., Dressler, A., Faber, S. M., Stone, R. P. S., Lynden-Bell, D., Terlevich, R. J., & Wegner, G. 1987, "Spectroscopy and Photometry of Elliptical Galaxies. III. *UBV* Aperture Photometry, CCD Photometry, and Magnitude-related Parameters", ApJS, 64, 601

Burstein, D., Davies, R. L., Dressler, A., Faber, S. M., Lynden-Bell, D., Terlevich, R. J., Wegner, G. 1988, "Global Stellar Populations of Elliptical Galaxies: A. Optical Properties", in Towards Understanding Galaxies at Large Redshifts, eds. Kron, R. G., Renzini, A., (Dordrecht: Kluwer), p. 17

Burstein, D., & Heiles, C. 1982, "Reddening Derived from HI and Galaxy Counts: Accuracy and Maps", AJ, 87, 1165

Burstein, D., & Heiles, C. 1984, "Reddening Estimates for Galaxies in the Second Reference Catalog and the Uppsala General Catalog", ApJS, 54, 33

Caldwell, N., Rose, J. A., Sharples, R. M., Ellis, R. S., & Bower, R. G. 1993, "Star Formation in Early-type Galaxies in the Coma Cluster", AJ, 106, 473

Caon, N., Capaccioli, M., & D'Onofrio, M. 1993, "On the shape of the light profiles of early-type galaxies", MNRAS, 265, 1013

Capaccioli, M., Held, E. V., Lorenz, H., & Vietri, M. 1990, "Photographic and CCD Surface Photometry of the Standard Elliptical Galaxy NGC 3379", AJ, 99, 1813

Carter, D. 1987, "Weak Disks in Rapidly Rotating Elliptical Galaxies", ApJ, 312, 514

Ciotti, L., Lanzoni, B., & Renzini, A. 1996, "The tilt of the fundamental plane of elliptical galaxies – I. Exploring dynamical and structural effects", MNRAS, 282, 1

David, L. P., Slyz, A., Jones, C., Forman, W., Vrtilek, S. D., & Arnaud, K. A. 1993, "A Catalog of Intracluster Gas Temperatures", ApJ, 412, 479

Davies, R. L., Burstein, D., Dressler, A., Faber, S. M., Lynden-Bell, D., Terlevich, R. J., & Wegner, G. 1987, "Spectroscopy and Photometry of Elliptical Galaxies. II. The Spectroscopic Parameters", ApJs, 64, 581

Davis, L. E., Cawson, M., Davies, R. L., & Illingworth, G. 1985, "CCD Surface Photometry of Galaxies with Dynamical Data. I. NGC 3379, M87, and NGC 1052", AJ, 90, 169

de Carvalho, R. R., & Djorgovski, S. 1992, "Systematic Differences Between the Field and Cluster Elliptical Galaxies", ApJ, 389, L49

de Vaucouleurs, G. 1948, "Recherches sur les Nébuleuses Extragalactiques", Ann. d'Ap., 11, 247

de Vaucouleurs, G., & Capaccioli, M. 1979, "Luminosity Distribution in Galaxies. I. The Elliptical Galaxy NGC 3379 as a Luminosity Distribution Standard", ApJS, 40, 699

de Vaucouleurs, G., de Vaucouleurs, A., & Corwin, H. G. 1976, "The Second Reference Catalogue of Bright Galaxies", Austin: University of Texas Press

Djorgovski, S. 1985, "Calibration of the Lick red CCD bandpasses", PASP, 97, 1119

Djorgovski, S. 1995, "The Fundamental Plane Correlations for Globular Clusters", ApJ, 438, L29

Djorgovski, S., & Davis, M. 1987, "Fundamental Properties of Elliptical Galaxies", ApJ, 313, 59

Djorgovski, S., de Carvalho, R., & Han, M.-S. 1988, "The Universality(?) of Distance-indicator Relations", in The Extragalactic Distance Scale, eds. van den Bergh, S., & Prichet, C. J., ASP Conf. Ser. Vol. 4, (Provo: ASP), p. 329

Djorgovski, S., & Santiago, B. X. 1993, "The Meaning and the Implications of the Fundamental Plane", in Structure, Dynamics and Chemical Evolution of Elliptical Galaxies, eds. Danziger, I. J., Zeilinger, W. W., & Kjär, K., (Garching: ESO), p. 59

Dressler, A. 1980a, "Galaxy Morphology in Rich Clusters: Implications for the Formation and Evolution of Galaxies", ApJ, 236, 351

Dressler, A. 1980b, "A Catalog of Morphological Types in 55 Rich Clusters of Galaxies", ApJS, 42, 565

Dressler, A. 1987, "The $D_{\rm n}$–σ relation for Bulges of Disk Galaxies: A New, Independent Measure of the Hubble Constant", ApJ, 317, 1

Dressler, A., Faber, S. M., Burstein, D., Davies, R. L., Lynden-Bell, D., Terlevich, R. J., & Wegner, G. 1987a, "Spectroscopy and Photometry of Elliptical Galaxies: A Large-Scale Streaming Motion in the Local Universe", ApJ, 313, L37

Dressler, A., Lynden-Bell, D., Burstein, D., Davies, R. L., Faber, S. M., Terlevich, R. J., & Wegner, G. 1987b, "Spectroscopy and Photometry of Elliptical Galaxies. I. A New Distance Estimator", ApJ, 313, 42

Efron, B. 1979, "Bootstrap methods: another look at the jackknife", Annals Statist., 7, 1

Efron, B. & Tibshirani, R. J. 1986, "Bootstrap measures for standard errors, confidence intervals, and other measures of statistical accuracy", Statist. Science, 1, 54

Efron, B. & Tibshirani, R. J. 1993, "An Introduction to the Bootstrap", New York: Chapman & Hall

Eggen & Sandage 1964, "New Photoelectric Observations of Stars in the Old Galactic Cluster M67", ApJ, 140, 130

Faber, S. M. 1994, private communication with I. Jørgensen

Faber, S. M., & Burstein, D. 1988, "Motions of Galaxies in the Neighborhood of the Local Group", in Large-Scale Motions in the Universe. A Vatican Study Week, eds. Rubin, V. C., & Coyne, G. V., (Princeton: Princeton University Press), p. 115

Faber, S. M., Dressler, A., Davies, R. L., Burstein, D., Lynden-Bell, D., Terlevich, R. J., Wegner, G. 1987, "Global Scaling Relations for Elliptical Galaxies and Implications for Formation", in Nearly Normal Galaxies, ed. Faber, S. M., (New York: Springer), p. 175

Faber, S. M., Friel, E. D., Burstein, D., & Gaskell, C. M. 1985, "Old Stellar Populations. II. An Analysis of K-giant Spectra", ApJS, 57, 711

Faber, S. M., Trager, S. C., Gonzáles, J. J., & Worthey, G. 1995, "The Stellar Ages of Elliptical Galaxies", in Stellar Populations, IAU Symp. 164, eds. van der Kruit, P. C., & Gilmore, G., (Dordrecht: Kluwer), p. 249

Faber, S. M., Wegner, G., Burstein, D., Davies, R. L., Dressler, A., Lynden-Bell, D., & Terlevich, R. J. 1989, "Spectroscopy and Photometry of Elliptical Galaxies. VI. Sample Selection and Data Summary", ApJS, 69, 763

Fasano, G., & Franceschini, A. 1987, "A multidimensionel version of the Kolmogorov-Smirnov test", MNRAS, 225, 155

Franx, M., & Illingworth, G. 1990, "Color Gradients in Elliptical Galaxies", ApJ, 359, L41

Franx, M., Illingworth, G., & Heckman, T. 1989a, "Major and Minor Axis Kinematics of 22 Ellipticals", ApJ, 344, 613

Franx, M., Illingworth, G., & Heckman, T. 1989b, "Multicolor Surface Photometry of 17 Ellipticals", AJ, 98, 538

Gonzáles, J. J. 1993, Ph.D. Thesis, Univ. California, Santa Cruz

Gregg, M. D. 1992, "Stellar Population-induced Peculiar Velocities of Elliptical Galaxies", ApJ, 384, 43

Guzmán, R., Lucey, J. R., & Bower, R. G. 1993, "The fundamental relations of elliptical galaxies", MNRAS, 265, 731

Guzmán, R., Lucey, J. R., Carter, D., & Terlevich, R. J. 1992, "The environmental dependence of the Mg_2 correlations for elliptical galaxies", MNRAS, 257, 187

Hjorth, J., & Madsen, J. 1995, "Small Deviations from the $R^{1/4}$ Law, the Fundamental Plane, and Phase Densities of Elliptical Galaxies", ApJ, 445, 55

Hjorth, J., & Tanvir, N. R. 1997, "Calibration of the fundamental plane zero-point in the Leo-I group and an estimate of the Hubble constant", ApJ, to appear (astro-ph/9701025)

Idiart, T. P., de Freitas Pacheco, J. A., & Costa, R. D. D. 1996, "Metallicity Indices For Multipopulation Models. I. The Galactic Bulge", AJ, 111, 1169

Jedrzejewski, R. I. 1987, "CCD Surface Photometry of Elliptical Galaxies – I. Observations, Reductions and Results", MNRAS, 226, 747

Johnson, H. L., & Sandage, A. R. 1955, "The Galactic Cluster M67 and its Significance for Stellar Evolution", ApJ, 121, 616

Jørgensen, I. 1994, "Secondary Photometric Standard Stars for the Thuan-Gunn and Johnson-Kron-Cousins System", PASP, 106, 967

Jørgensen, I. 1997a, "Stellar populations of cluster E and S0 galaxies", MNRAS, in press (astro-ph/9702076) (J97)

Jørgensen, I. 1997b, in prep.

Jørgensen, I. 1997c, "The Fundamental Plane and the choice of photometric parameters", to appear in the proceedings of the 3rd ESO-VLT Workshop: Galaxy Scaling Relations, eds. da Costa et al., (Springer)

Jørgensen, I., & Franx, M. 1994, "The Nature of E and S0 Galaxies: A Study of a Magnitude-limited Sample of Galaxies in the Coma Cluster", ApJ, 433, 553 (JF94)

Jørgensen, I., Franx, M., & Kjærgaard, P. 1992, "CCD Surface Photometry for E and S0 Galaxies in the Coma Cluster", A&AS, 95, 489 (JFK92)

Jørgensen, I., Franx, M., & Kjærgaard, P. 1993, "Sources of Scatter in the Fundamental Plane and the $D_{\rm n}$–σ Relation", ApJ, 411, 34 (JFK93)

Jørgensen, I., Franx, M., & Kjærgaard, P. 1995a, "Multicolour CCD Surface Photometry for E and S0 Galaxies in 10 Clusters", MNRAS, 273, 1097 (JFK95a)

Jørgensen, I., Franx, M., & Kjærgaard, P. 1995b, "Spectroscopy for E and S0 Galaxies in Nine Clusters", MNRAS, 276, 1341 (JFK95b)

Jørgensen, I., Franx, M., & Kjærgaard, P. 1996, "The Fundamental Plane for Cluster E and S0 Galaxies", MNRAS, 280, 167 (JFK96)

Kent, S. M., & Gunn, J. E. 1982, "The Dynamics of Rich Clusters of Galaxies. I. The Coma Cluster", AJ, 87, 945

Landolt, A. U. 1992, "*UBVRI* Photometric Standard Stars in the Magnitude Range $11.5 < V < 16.0$ Around the Celestial Equator", AJ, 104, 340

Lucey, J. R., Bower, R. G., & Ellis, R. S. 1991a, "The fundamental plane of cluster ellipticals", MNRAS, 249, 755

Lucey, J. R., & Carter, D. 1988, "Distances to Five Nearby Southern Galaxy Clusters and the Absolute Motion of the Local Group", MNRAS, 235, 1177

Lucey, J. R., Guzmán, R., Carter, D., & Terlevich, R. J. 1991b, "New $D - \sigma$ results for Coma cluster ellipticals", MNRAS, 253, 584

Lynden-Bell, D., Faber, S. M., Burstein, D., Davies, R. L., Dressler, A., Terlevich, R. J., & Wegner, G. 1988, "Spectroscopy and Photometry of Elliptical Galaxies. V. Galaxy Streaming Toward the New Supergalactic Center", ApJ, 326, 19

Makino, J., Akiyama, K., & Sugimote, D. 1990, "On the Apparent Universality of the $r^{1/4}$ Law for Brightness Distribution in Galaxies", PASJ, 42, 205

Montgomery, K. A., Marschall, L. A., & Janes, K. A. 1993, "CCD Photometry of the Old Open Cluster M67", AJ, 106, 181

Mohr, J. J., & Wegner, G. 1997, "Using the Fundamental Plane Distance to Estimate the Total Binding Mass in Abell 2626", AJ, in press (astro-ph/9704202)

Nieto, J.-L., Bender, R., Davoust, E., & Prugniel, P. 1990, "The low-mass extension of the fundamental plane of elliptical galaxies", A&A, 230, L17

Nilson, P. 1973, "Uppsala General Catalogue of Galaxies", Vol. 6, Uppsala: Uppsala Obs. Ann.

O'Connell, R. W. 1976, "Galaxy Spectral Synthesis. I. Stellar Populations in the Nuclei of Giant Ellipticals", ApJ, 206, 370

Peletier, R. F., Davies, R. L., Illingworth, G. D., Davis, L. E., & Cawson, M. 1990, "CCD Surface Photometry of Galaxies with Dynamical Data. II. *UBR* Photometry of 39 Elliptical Galaxies", AJ, 100, 1091

Pence, W. 1976, "*K*-corrections for Galaxies of Different Morphological Types", ApJ, 203, 39

Petrosian, V. 1976, "Surface Brightness and Evolution of Galaxies", ApJ, 209, L1

Phillipps, S. 1988, "On the D_n–σ relation for elliptical galaxies", MNRAS, 233, 561

Postman, M., & Geller, M. J. 1984, "The Morphology-Density Relation: The Group Connection", ApJ, 281, 95

Poulain, P., & Nieto, J.-L. 1994, "*UBVRI* Photoelectric Photometry of Bright Southern Early-type Galaxies", A&AS, 103, 573

Press, W. H., Teukolsky, S. A., Vetterling, W. T., & Flannery, B. P. 1992, "Numerical Recipes", 2nd edition, Cambridge: Cambridge University Press

Prugniel, P., & Simien, F. 1996, "The fundamental plane of early-type galaxies: stellar populations and mass-to-light ratio", A&A, 309, 749

Recillas-Cruz, E., Carrasco, L., Serrano, P. G., & Cruz-Gonzáles, I. 1990, "The manifold of early-type galaxies from IR photometry: the Coma cluster", A&A, 229, 64

Renzini, A., & Ciotti, L. 1993, "Transverse Dissections of the Fundamental Planes of Elliptical Galaxies and Clusters of Galaxies", ApJ, 416, L49

Rich, R. M. 1988, "Spectroscopy and Abundances of 88 K Giants in Baade's Window", AJ, 95, 828

Richter, O.-G. 1989, "The Hydra I Cluster of Galaxies. V. A catalogue of galaxies in the cluster area", ApJS, 77, 237

Saglia, R. P., Bertschinger, E., Baggley, G., Burstein, D., Colless, M., Davies, R. L., McMahan Jr., R. K., & Wegner, G., 1993, "The effects of seeing on the photometric properties of elliptical galaxies", MNRAS, 264, 961

Salpeter, E. E. 1955, "The Luminosity Function and Stellar Evolution", ApJ, 121, 161

Sandage, A. 1975, "The Redshift-distance Relation. VIII. Magnitudes and Redshifts of Southern Galaxies in Groups: A Further Mapping of the Local Velocity Field and an Estimate of q_0", ApJ, 202, 563

Sargent, W. L. W., Schechter, P. L., Boksenberg, A., & Shortridge, K. 1977, "Velocity Dispersions for 13 Galaxies", ApJ, 212, 326

Scalo, J. M. 1986, "The Stellar Initial Mass Function", Fundam. Cosmic Phys., 11, 1

Schild 1983, "CCD Photometry of M67 Stars Useful as BVRI Standards", PASP, 95, 1021

Schweizer, F., Seitzer, P., Faber, S. M., Burstein, D., Dalle Ore, C. M., Gonzáles, J. J. 1990, "Correlation Between Line Strengths and Fine Structure in Elliptical Galaxies", ApJ, 364, L33

Seaton, M. J. 1979, "Interstellar Extinction in the UV", MNRAS, 187, 73p

Smyth, R. J. 1980, Ph. D. Thesis, University of Edingburgh

Stein, P. 1996, "Structure and Kinematics of Galaxy Clusters. I. The Redshift Catalogue", A&AS, 116, 203

Stetson, P. B. 1989, "Some Factors Affecting the Accuracy of Stellar Photometry with CCDs (And Some Ways of Dealing with them)", in Highlights of Astronomy, 8, 635, ed. D. McNally

Stetson, P. B. 1990, "On the Growth-Curve Method for Calibrating Stellar Photometry with CCDs", PASP, 102, 932

Stuart, A., & Ord, J. K. 1987, "Kendall's Advanced Theory of Statistics", 5th ed., vol. 1, London: Charles Griffin & Company

Tripicco, M. J., & Bell, R. A. 1995, "Modeling the Lick/IDS Spectral Feature Indices Using Synthetic Spectra", AJ, 110, 3035

van den Bergh, S. 1977, "Photometric Observations of Galaxies in the Hydra I Cluster", ApJ, 212, 317

van der Marel, R. P. 1991, "The velocity dispersion anisotropy and mass-to-light ratio of elliptical galaxies", MNRAS, 253, 710

Vazdekis, A., Casuso, E., Peletier, R. F., Beckman, & J. E. 1996, "A New Chemo-evolutionary Population Synthesis Model for Early-type Galaxies. I. Theoretical Basis", ApJS, 106, 307

Weedman, D. W. 1976, "The Hubble Diagram for Nuclear Magnitudes of Cluster Galaxies", ApJ, 203, 6

Weinberg, S. 1972, "Gravitation and Cosmology", New York: John Wiley & Sons

Weiss, A., Peletier, R. F., & Matteucci, F. 1995, "Synthetic metal line indices for elliptical galaxies from super metal-rich α-enhanced stellar models", A&A, 296, 73

Wolf, N. J. 1982, "High Resolution Imaging from the Ground", ARA&A, 20, 367

Worthey, G. 1994, "Comprehensive Stellar Population Models and the Disentanglement of Age and Metallicity Effects", ApJS, 95, 107

Worthey, G., Faber, S. M., & Gonzáles, J. J. 1992, "Mg and Fe Absorption Features in Elliptical Galaxies", ApJ, 398, 69

Worthey, G., Faber, S. M., Gonzáles, J., & Burstein, D. 1994, "Old Stellar Populations. V. Absorption Feature Indices for the Complete Lick/IDS Sample of Stars", ApJS, 94, 687

Worthey, G., Trager, S. C., & Faber, S. M. 1995, "The Galaxian Age-Metallicity Relation", in Fresh Views of Elliptical Galaxies, eds. Buzzoni, A., Renzini, A., & Serrano, A., ASP Conf. Ser. Vol. 86, (Provo: ASP), p. 203

Zabludoff, A. I., Huchra, J. P., & Geller, M. J. 1990, "The Kinematics of Abell Clusters", ApJS, 74, 1

Appendix A

Details of the Basic Reductions of the Photometry

A.1 Bias

There are 55 bias exposures, taken on 6 different nights, as listed in Table A.1.

Table A.1: The Bias Exposures

set #	night	#frames	dfsc #
1	2	10	1514–1526 (not: 1516 & 1518)
2	5	10	1909–1918
3	6	5	1921–1925
4	8	10	2192–2201
5	10	10	2499–2508
6	12	10	2558–2567

Notes: The names of the raw images from the DFOSC are in the form `dfsc`*nnnn*.

The frames within each set were combined. In this process, values in pixels affected by cosmic-ray-events were excluded. The bias level is around 124.2 ADU, but it is not the same in the 6 sets, it varies within ±0.5 ADU. There is a positive gradient in the y-direction, but the slope is not the same for the 6 sets, it ranges from 0 to 0.5 ADU over the length of the chip (1024 pixels). There is no simple relation between the change of level and gradient, and time. These two phenomena are illustrated in Figure A.1.

As can also be seen in Figure A.1 (left), there are some stripes which run along y (i.e., across x). They are the same in the 6 frames, and are part of the bias image.

All the 6 frames were combined into one (weighting by the number of frames they had been made from). No further processing was done. We would have liked to smooth the image to remove the pixel-to-pixel noise, but since we believe the stripes to be part of the bias image, we could not do that. The mean bias level is 124.2 ADU/pixel. The standard deviation on the final bias image in areas between the vertical stripes is 0.31 ADU/pixel.

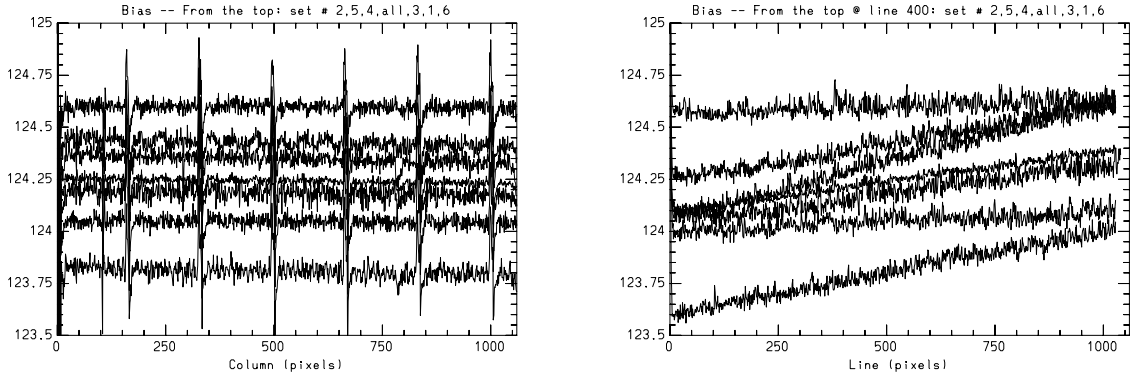

Figure A.1: The bias images from the 6 nights, and the mean bias image. Left: Along x (columns). Right: Along y (Lines). From the top (at $y = 400$): set 2, 5, 4, mean, 3, 1, and 6, corresponding to night 5, 10, 8, mean, 6, 2, and 12. All the images all have dimension 1060×1028, except the set 3 image (from night 6), which have dimension 1080×1040 (this image is extended only at large x and y, so that when trimming using the same section as for the rest of the images, one gets the same physical part of the CCD).

A.2 Dark

There are 22 dark exposures, all with exposure time 1 hour, taken on 7 different nights, as listed in Table A.2.

Table A.2: The Dark Exposures

image #	dfsc #	night	level
1	1511	2	5.09
2	1512	2	5.70
3	1513	2	7.51
4	1642	3	4.58
5	1643	3	5.04
6	1644	3	5.76
7	2057	6	16.13
8	2058	6	17.07
9	2059	6	23.15
10	2189	7	17.89
11	2190	7	25.09
12	2191	7	40.16
13	2353	8	23.83
14	2354	8	20.96
15	2355	8	22.77
16	2415	9	16.63
17	2416	9	17.90
18	2417	9	22.47
19	2418	9	32.98
20	2509	10	21.68
21	2510	10	31.07
22	2511	10	47.11

Notes: "level" is the median value (after bias subtraction). The median is approximated by `midpt` from `imstat`, using an upper cut of 200 to avoid most of the cosmic-ray-events.

The level histograms of the 22 images is shown in Figure A.2.

As is evident from Table A.2 and Figure A.2, the levels in the 22 images are *not* the same. Two effects are seen:

1. There is a big difference of the levels before and after the change of CCD temperature, which happened between night 5 and 6.

2. Within each night, there is a tendency towards higher levels for later times. Since the dark exposures were made in the morning, this indicates a light leak in the camera.

From this it was decided to make two dark frames, one for night 1–5, and one for night 6–14. The following frames were considered not affected by the light-leak, and therefore usable for constructing the two final dark images: 1, 2 (night 1), 4, 5, 6 (night 2), which were combined to the image dark1; and 7, 8 (night 6), 16, 17 (night 9), which were combined to the image dark2. The combination was done using a 2 sigma clipping (avsigclip) with a grow radius of 1. The images from night 8

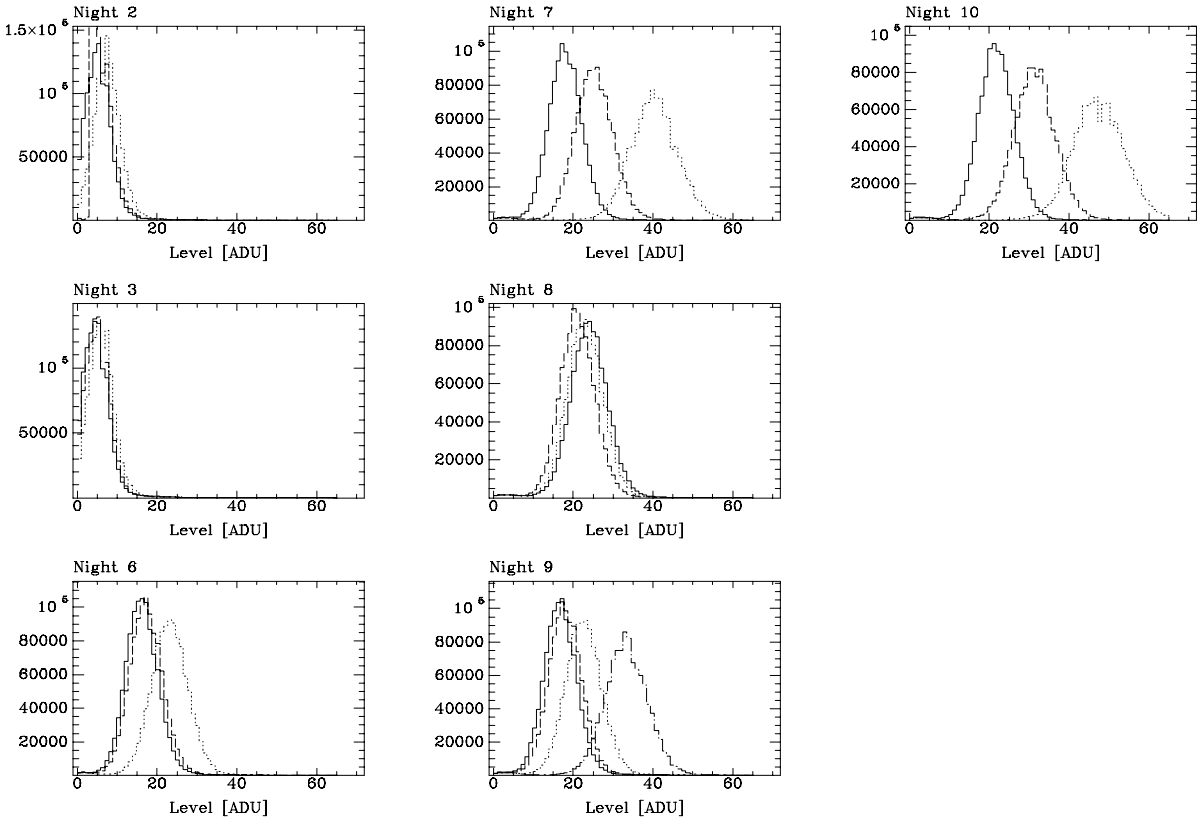

Figure A.2: The histograms for the 22 raw dark images. Within each night, the time order of the 3 or 4 frames are marked as solid, dashed, dotted, and dot-dashed.

was not used, since they all had a higher level, even though they did not show the time evolution the other did.

To get rid of the cosmic-ray-events, the values in the tails of the two combined images (dark1 and dark2) were replaced (using `imreplace`) by the median value, using the following values: dark1: values outside [INDEF,20.] replaced by 5.457, dark2: values outside [7.,27.] replaced by 17.14.

The two images (especially dark1) had a number of columns with higher or lower levels (the lower ones being fat zero, the higher ones probably being remanence), which were removed by linear interpolation of the unaffected neighboring pixels (using `fixpix`).

The dark images had now two kinds of structure left: some smooth variations, and a discontinuity between $y = 512$ and 513 (in the coordinates of the final 1024×1024 trimmed image). The two images, dark1 and dark2, where cut in halves according to the discontinuity, and to each of these 4 pieces a Legendre polynomial of third order in x and y with cross terms was fitted. Afterwards, the corresponding halves were joined. It was tested that these two new dark1 and dark2 images did not have any residuals or large scale gradients with respect to the "unsmoothed" ones. The two final dark images are shown in Figure A.3.

The two images do not exactly scale, the relative standard deviation on the quotient of the two is 2%. Given the low absolute counts, this is a small difference.

The mean dark levels the final two dark images are: dark1: 5.6 ADU/hour, dark2: 17.3 ADU/hour. The low frequency pattern, characterized by the standard deviation of the two images, is 0.12 (dark1) and 0.24 (dark2). Since they are smooth legendre polynomials, there is no

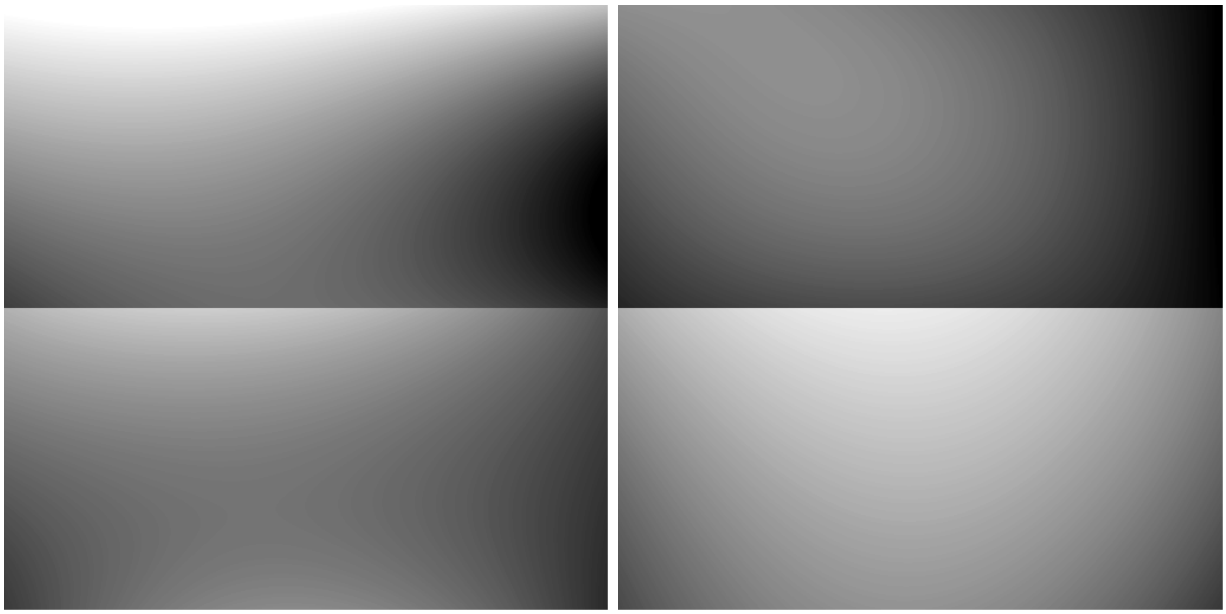

Figure A.3: The two final dark images. Left: dark1 (nights 1–5). Right: dark2 (nights 6–14). The display cuts for both images are ±2.5 standard deviations around the mean. The values from low to high are color coded as white to black.

pixel-to-pixel noise in them.

A.3 Shutter

If we ask the data acquisition system to make an exposure of time t, and it instead makes one of time $t + \delta$ (with $\delta \neq 0$), we have to make a *shutter correction*, where we multiply the image with $t/(t + \delta)$. δ can be a scalar (i.e. be the same for all the pixels), or it can an image (i.e. vary across the CCD), depending on what kind of shutter the system has.

δ can be determined from two images with different "apparent" exposure time t_1 and t_2, as follows: Since the CCD is a linear detector, when it is exposed to the intensity I in the time t_{real}, the level we read out N for a given pixel is proportional to the product of the two,

$$N_1 \propto I_1 \cdot t_{real,1} \tag{A.1}$$

$$N_2 \propto I_2 \cdot t_{real,2} \tag{A.2}$$

If we keep the intensity constant, and since we have $t_{real} = t + \delta$, we get

$$\frac{N_1}{N_2} = \frac{t_1 + \delta}{t_2 + \delta}, \quad t_1 \neq t_2, \tag{A.3}$$

from which we can determine δ.

One can use more images to get a better determination. We used the temporal sequence of one 10 sec, ten 1 sec, and one 10 sec exposure. If we let N_1' denote the sum of the levels in the ten 1 sec exposures, and N_2' the sum of the levels of the two 10 sec exposures, we get

$$\frac{N_1'}{N_2'} = \frac{10 \cdot (1 \text{ sec} + \delta)}{2 \cdot (10 \text{ sec} + \delta)} \tag{A.4}$$

which yields

$$\delta = \frac{10(2N_1'/N_2' - 1)}{10 - 2N_1'/N_2'} \text{ sec} \tag{A.5}$$

For the determination of the shutter correction, a number of dome flats were taken, using the same lamp with constant voltage, thereby hoping to get a constant intensity. The images are listed in Table A.3.

The images in Table A.3 were corrected for bias and dark. The delta image was then computed using equation A.5 for each of the four (1×10 sec, 10×1 sec, 1×10 sec) sequences. The mean of the four was also calculated. The results are in Table A.4.

A visual inspection of the four delta images showed, that they were all almost flat, as the low standard deviations also suggest. There was, however, a small gradient in the x direction of about 0.001 sec, but since it was much lower than our estimated uncertainty of 0.02 sec (see below), we decided to neglect it.

Therefore, we decided to use a *scalar* delta value instead of a delta image. We set this delta value to the (scalar) mean of the mean delta image, which amounts to 0.41 sec. We estimate the uncertainty on this value to be half of the maximum difference between the four individual determinations, i.e. 0.02 sec.

The differences between the four is probably due to the light not being constant. The symmetric sequence (1×10 sec, 10×1 sec, 1×10 sec) makes the determination insensitive to a light variation which is linear in time, so the light variations was probably more ill-behaved than that.

A cl-script `b_dcorr` was written to implement the scalar shutter correction.

Table A.3: The Images Used to Determine the Shutter Correction

dfsc #	#frames	exp. time [sec]
2233	1	10
2234	1	10
2235–2244	10	1
2245	1	10
2246	1	10
2247–2256	10	1
2257	1	10
2258	1	10
2259–2268	10	1
2269	1	10
2270	1	10
2271–2280	10	1
2281	1	10
2282	1	10

Notes: All images are from night 8. The first and the last image in the table were not used.

Table A.4: Statistics of the four Individual Delta Images and the Mean Delta Image

image	mean	median	stddev
1	0.3999	0.3997	0.01101
2	0.4093	0.4090	0.01051
3	0.4004	0.4004	0.01065
4	0.4325	0.4323	0.01073
mean	0.4105	0.4105	0.00682

Notes: "median" is the `midpt` from `imstat`.

A.4 Linearity Test

We want to test, whether our CCD is linear, i.e. whether the level we read out (when bias has been subtracted, of course), N, is proportional to the integration time, t, times the intensity of the light reaching the CCD, I.

We envisioned that we could do two tests of the linearity of the CCD. An *indirect* test where we would test whether the conversion factor was constant with level, and a *direct* test where we would test whether the level per unit time was constant with level. Results from these two test are reported in Sect. A.4.1 and A.4.2 below.

For both purposes, 68 dome flats were taken, with an attempted constant light source. 2 filters were used: Johnson B (JB) and Gunn r (GR). Only the section `[1:1060,300:700]` (in untrimmed coordinates) was read out (this should not affect the results). All the images were taken in pairs with equal exposure time. The exposure time was varied in on order to span the full range of the CCD (0 – 65535 ADU). In between every one or two pairs of exposures with varying exposure time, a pair of exposures with exposure time 10 sec was taken. The sequence of exposure times is shown in Table A.5.

Table A.5: Exposure Times for the 34 Pairs of Images used for the Linearity Test

Johnson B:	10, 1, 2, 10, 4, 7, 10, 15, 20, 10, 30, 45, 10, 60, 10, 80, 10, 100, 10, 120, 10
Gunn r:	10, 2, 4, 7, 10, 15, 20, 10, 30, 45, 10, 55, 10

Notes: The exposure times are in seconds. The images are dfsc2284–2325 (JB) and dfsc2327–2352 (GR).

A.4.1 Conversion factor vs. level

`findgain` was used to determine the conversion factor (CF) and the read-out noise (RON) for the 34 pairs of images. The bias images dfsc1922 and 1925 (using the same section: `[1:1060,300:700]`) were used. These are from night 6 (whereas the dome flats used were from night 8). The bias images from night 6 are the ones which resembles the mean bias image the most.

`findgain` was used at the section `[480:0600,160:280]` (center of CCD) and `[910:1030,080:200]` (right hand side of CCD). It was suspected, that the CCD would behave strange in the right hand side. The result is shown in Figure A.4. It it seen that apparently CF increases with level. However, this can not be the case since the CCD found to be linear in the direct test, cf. Sect. A.4.2 below. More probable a malfunction in the read-out electronics caused RON to vary with the exposure level.

A direct way to calculate the RON in ADU is the fact, that the standard deviation on a bias image is the RON in ADU. The standard deviation of 5 raw bias images (dfsc1921–1925) was found to be 2.25 ADU (using `imstat` with an upper limit of 150 to cut cosmic-ray-events).

If we use only flat field images with levels above 1000 ADU and without severe cosmic-ray-events, we get CF = 1.95 e^-/ADU and RON = 2.25 ADU. These are the values that have been used hereafter.

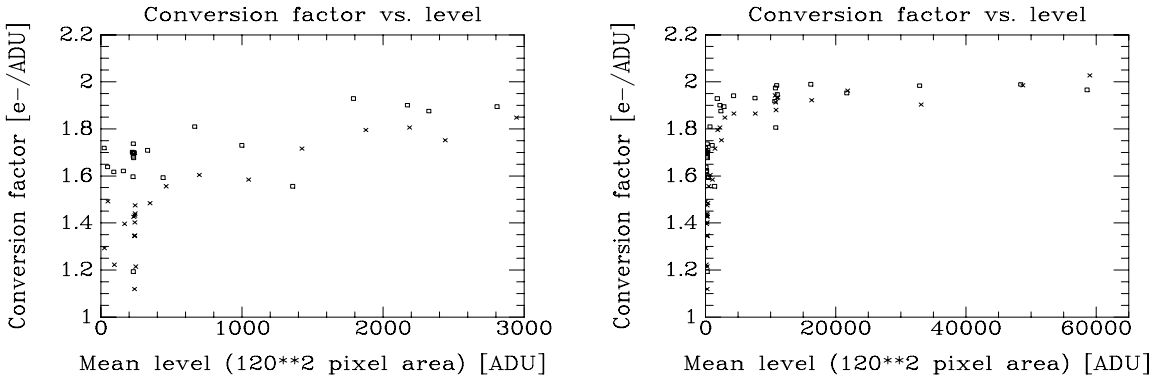

Figure A.4: Conversion factor versus level. Boxes: center of CCD, crosses: right hand side of CCD. Left: levels from 0 to 3000 ADU. Right: levels from 0 to 65000 ADU.

A.4.2 The direct test

A direct way of checking the linearity of the CCD is to plot level pr. unit time versus level, since if we have $N \propto I \cdot t$, and I is constant, then N/t is constant.

The level used before (e.g. in Figure A.4) was computed using `imstat` with a suitable upper cut to avoid cosmic-ray-events. To get more precise level, `fitsky` was used. This task fits a Gaussian to the histogram of the sky values and determines the mean level from the fit. The center area was defined as $(x, y) = (500, 200)$, and the right hand side area as $(x, y) = (995, 300)$, both with an inner radius (`annulus`) of 2.5 pixels and an outer radius (`dannulus`) of 40.0 pixels.

Since we have a number of images with the same exposure time (10 sec, see Table A.5), we can check whether the intensity really was constant by plotting the level versus the (clock) time. This is shown in Fig. A.5. It is seen that the illumination level was *not* constant.

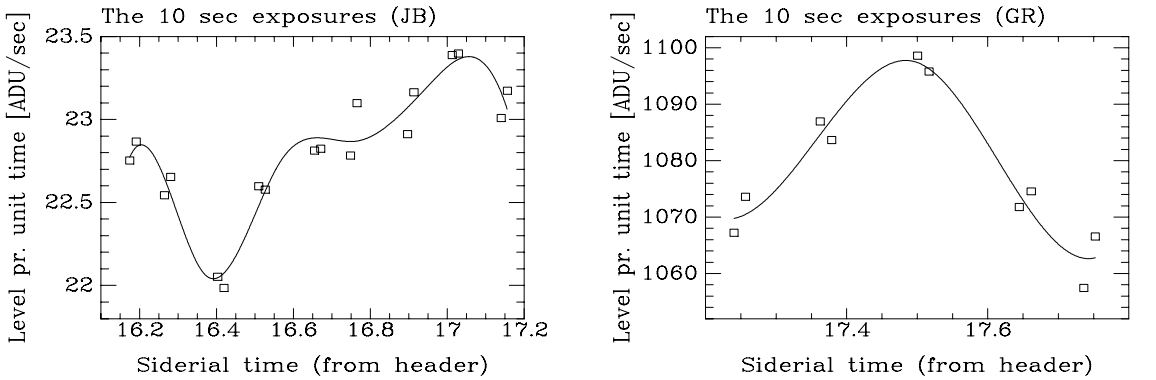

Figure A.5: The light variation with time. Left: Johnson B, the first sequence. Right: Gunn r, the second sequence. The levels shown are the ones in the center area; the right hand side area levels are different, but by a constant factor.

The points shown in Figure A.5 were fitted with a 5 piece (JB) / 2 piece (GR) cubic spline using `gfit1d`, as also shown in the figure.

All the N/t values for the 68 images were now divided by the fit to the time variation. Now N/t vs. t could be plotted, as shown in Figure A.6.

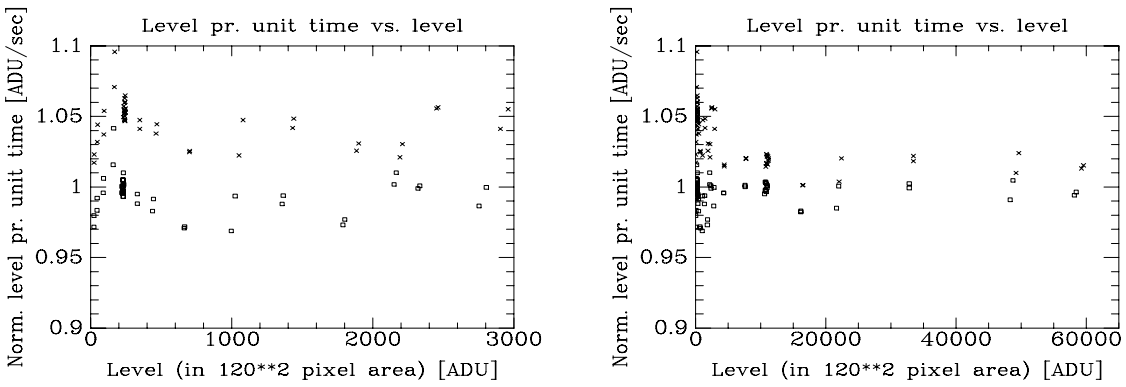

Figure A.6: The level pr. unit time normalized by the lamp time variation, versus the level. Boxes: center of CCD, crosses: right hand side of CCD. Note, that the center and right hand side values are normalized by the same function. The time dependence is the same in the two areas, but since the levels are not the same, there is an offset between the two in this graph. Left: levels from 0 to 3000 ADU. Right: levels from 0 to 65000 ADU.

As Figure A.6 shows, the CCD is in fact linear up to the very highest levels.

The rms standard deviation of all the data with levels > 100 ADU is 1.1%. The rms for the first sequence (JB) and the second sequence (GR) separately, is 1.4% and 0.7%, respectively. The reason for the difference is probably the more ill-behaved lamp variation for the first sequence, as seen in Figure A.5. We conclude, that the CCD is linear within 0.7%.

A.5 Fat Zero

Though the CCD on the overall is linear, it nevertheless turned out, that 20 of the 1024 columns were *not* linear – they were affected by the so-called fat zero effect.

The fat zero affected columns can be seen in the 2 dimensional images images as vertical stripes with (usually) lower level than the background.

This phenomenon was investigated using the dome flats used for the linearity test (with levels in the range 22 – 58437 ADU) and an extra sequence of dome flats with very low levels (with levels in the range 1 – 48 ADU). The very low level dome flats are dfsc2597–2616, from night 13 (filter: Johnson B). These were also corrected for bias, dark current, and shutter effect.

We have the following 3 sequences of images:

1. The very low level images, with exposure times 1, 2, 4, 7, 10, 13, 16, 20, 25, 30 sec, and levels in the range 1 – 48 ADU (filter: JB).

2. The low level images from the linearity test, with exposure times 1, 2, 4, 7, 10, 15, 20, 30, 45, 60, 80, 100, 120 sec, and levels in the range 22 – 2700 ADU (filter: JB).

3. The high level images from the linearity test, with exposure times 2, 4, 7, 10, 15, 20, 30, 45, 55 sec, and levels in the range 2100 – 58000 (filter: GR).

Within each of the 3 sequences, all the images with the same exposure time (usually this number is 2, except for the 10 sec images in the 2 last sequences, which were more numerous) and thus same level, were combined. That yielded 32 $(10 + 13 + 9)$ images.

These 32 images were now made 1 dimensional by averaging in the y-dimension using `blkavg`. This is because the fat zero effect only varies from column to column (x), not from line to line (y).

To find the columns affected by fat zero, the following was done: All the exposures in sequence 1 and all the non 10 sec exposures in sequence 2 was divided by the 10 sec exposure from sequence 2, and all the non 10 sec exposures in sequence 3 was divided by the 10 sec exposure from sequence 3. Since the 10 sec exposure from sequence 2 were made from 18 images, and the one from sequence 3 from 10 images, they both had better signal-to-noise (S/N) than the other ones.

If we did not have any fat zero columns, the plot of the quotients should be flat (within the noise and cosmic-ray-events), since the flat field pattern (which also is seen even in the 1 dimensional images) is divided out. By inspecting the 30 $(10 + 12 + 8)$ quotient plots, 44 fat zero column candidates were noted. The columns were in 6 "locations", with each location having a number of fat zero columns next to each other.

The fat zero effect as function of the level in the non-affected neighbor column was now measured as follows: In a 25 pixel wide area on each side of the given fat zero location the median value was calculated, and the mean of these 2 medians was defined as the background level. The level in each of the suspected fat zero columns together with the level in a test column on each side was measured, and the difference between the background level and the level in the given column calculated. This procedure is implemented in the cl-script `calc_fatzero`.

If the images had been flat fielded, the plot of a non fat zero column would be flat and zero (diff = 0·background). When not flat fielded, one gets a straight line (diff = k·background).

In the case of a fat zero column, one does not get a straight line, but a more complicated non-linear behavior. If the image has not been flat fielded, there might be a flat field effect of the form diff = k·background superimposed, which will show up at high levels. Two examples are shown in Figure A.7.

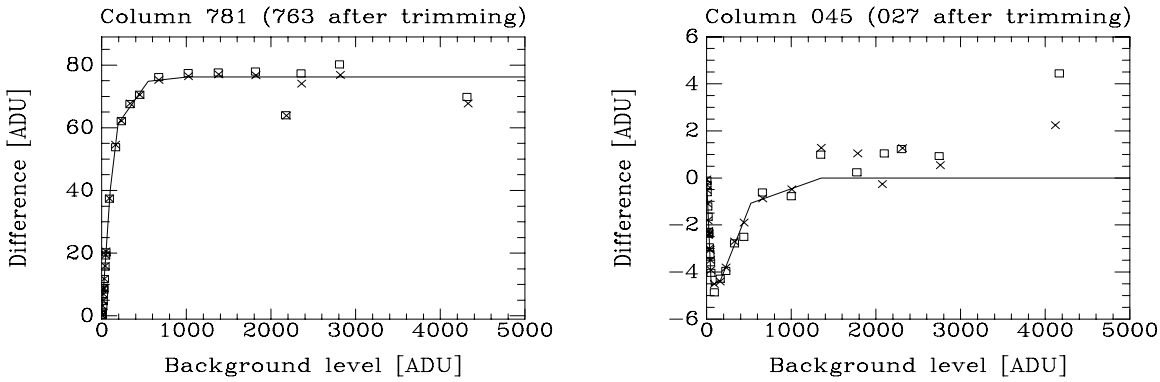

Figure A.7: 2 of the 20 fat zero columns. Boxes: before flat fielding, using a 2×25 pixel background area. Crosses: after flat fielding, using a 2×2 pixel background area. The fit to the flat fielded points is overplotted.

Table A.6: The 20 Fat Zero Columns

044, 045, 046; 098; 176, 177; 290, 291, 292; 781, 782, 783, 784, 785, 786, 787, 788; 949, 950, 951

Notes: The column numbers are in the untrimmed frame, after trimming subtract 18 pixels.

The plot similar to the ones shown in Figure A.7 were investigated for the 44 fat zero column candidates. Of these, 20 were actually fat zero columns with an effect > 1 ADU. The 20 columns are listed in Table A.6.

It was not possible to find any simple analytical function that fitted the fat zero effect as function of the background level, so it was decided to use the following piecewise linear function

$$f(x) = \begin{cases} (y_1 - 0)/(x_1 - 0) \cdot (x - 0) + 0 & ; \quad 0 \le x < x_1 \\ (y_2 - y_1)/(x_2 - x_1) \cdot (x - x_1) + y_1 & ; \quad x_1 \le x < x_2 \\ (y_3 - y_2)/(x_3 - x_2) \cdot (x - x_2) + y_2 & ; \quad x_2 \le x < x_3 \\ (y_4 - y_3)/(x_4 - x_3) \cdot (x - x_3) + y_3 & ; \quad x_3 \le x < x_4 \\ y_4 & ; \quad x_4 \le x \end{cases} \tag{A.6}$$

where f is the difference and x is the background level. This is just a straight line between the following points: $(0, 0)$, (x_1, y_1), (x_2, y_2), (x_3, y_3), (x_4, y_4), and (∞, y_4). The function has 8 free parameters: (x_i, y_i), $i = 1, \ldots, 4$. Two examples of the 8 fitted parameters are shown in Table A.7

Table A.7: Two examples of fat zero fit parameters.

Column	(x_1, y_1)	(x_2, y_2)	(x_3, y_3)	(x_4, y_4)
045 (027 after trimming)	(53.7,−4.57)	(160,−4.39)	(523,−1.07)	(1353,0)
781 (763 after trimming)	(100,40.4)	(193,61.3)	(548,74.8)	(1013,76.2)

The actual fitting was done using the task `nfit1d`, which uses least squares fitting implemented by a downhill simplex minimization algorithm ("amoeba").

In some cases we decided, that the asymptotic level should be zero (i.e. $y_4 = 0$), even though when fit y_4 might not turn out to be zero. An example is column 045, shown in Figure A.7.

The method requires an initial guess on the free parameters (x_i, y_i). The problem is not very well constrained, and is therefore quite sensitive to the initial conditions. Nevertheless, it produces a quite good fit, with lower residuals than the initial guess.

A cl-script `b_fatzero` was written. This procedure corrects a 2 dimensional image for the fat zero effect in the 20 columns, using equation (A.6) and the corresponding 20×8 coefficients. The background level is determined locally, i.e. it is not the same for the entire column.

We wanted to have our images flat fielded before we determined the fat zero correction. However, we could not make any flat fields as long as we were not able to correct for fat zero. Therefore, the above determination of the fat zero effect on the non flat fielded images is only a first approximation. We can now use this to make fat zero corrected flat fields, which we can then use to flat field our images, after which we can get a second approximation to the fat zero effect.

The 10 JB dome flats dfsc1670–1679 (night 4) and the 10 GR dome flats dfsc1808–1817 (night 5) were corrected for bias, dark, shutter, and fat zero as determined from the first iteration as mentioned above, and then combined. The two 2 dimensional images (using the same section as the fat zero images) were made 1 dimensional, and the 32 1 dimensional fat zero images were then flat fielded.

Now the measuring of the fat zero effect using `calc_fatzero` could be repeated, this time using areas for background level determination only 2 pixels wide (this is the width we want to use for the science images).

Hereafter, the fat zero functions could be fitted again. As seen in Figure A.7, the change from no flat fielding and 25 pixel background areas to flat fielding and 2 pixel background areas is not that big on small levels (< 5000 ADU). On larger levels (up to 65000 ADU), a bigger difference can be seen, with the flat fielded images indeed being more flat that the non flat fielded images.

`b_fatzero` was updated to use the new coefficients. The maximum correction for the 20 columns ranges from 1 to 76 ADU).

A.5.1 The Extra Correction

When all the science images (from night 1, 2, 3, 4, 6, & 9) were reduced using the fat correction mentioned above, it turned out, that it did not remove the fat zero stripes for the images from night 1–4. The fat zero effect had changed with the CCD temperature change between night 5 and 6, and since the images used to determine the fat zero effect were from night 8 and 13 (i.e. both after the temperature change), the established correction worked only for night 6–14.

Since we did not have the same type of calibration images taken before the temperature change, the extra correction needed to remove the fat zero effect from the night 1–5 images needed to be modeled from the science images.

The approach was the following: For all the science images from night 1–4: for all the 20 fat zero columns, and for the 6 background areas, the level (one number) representing the sky background (not the objects, such as galaxies and stars, which happens to be in that column somewhere) was calculated. This was done by a 3 step process: First guess, N_1, was `midpt` from `imstat` using no cuts. Second guess, N_2, was `midpt` using cuts $\pm 5\sigma$, with σ being the theoretical standard deviation corresponding to that level, $\sigma = (N/\mathrm{CF} + \mathrm{RON}^2_{\mathrm{ADU}})^{1/2}$, with $N = N_1$ in this step. Third and final guess, N_3, was `midpt` using cuts $\pm 3\sigma$, with σ being calculated using $N = N_2$. When having the level in the background and in the fat zero column, the difference can be calculated. This process was implemented in the cl-script `extra_fat`.

An example of the extra fat effect can be seen in Figure A.8.

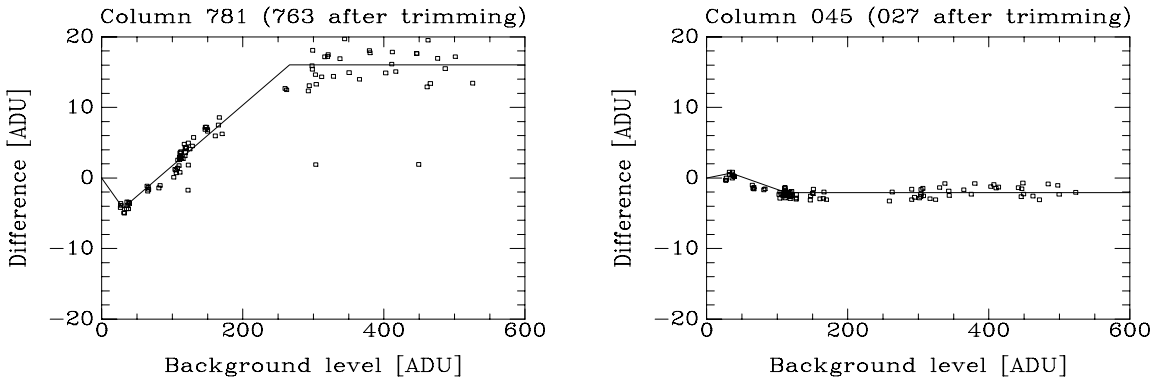

Figure A.8: The extra fat zero effect for the nights before the CCD temperature change, shown for 2 of the 20 fat zero columns. "Difference" is background level minus value in the given fat zero column. Also the 3 piece linear by eye fit is shown.

The data were fit by eye with a 3 piece linear function (example of fit also shown in Figure A.8). 13 out of the 20 fat column had a significant (> 2 ADU) extra effect. `b_fatzero.cl` was modified to be able to make the extra correction.

A.6 Flat Fields

A number of sky and dome flats had been taken, as listed in Table A.8. Additional data, such as exposure time and level, can be found in Table A.9, A.10, and A.11, although the ordering of the images in the JB and JU tables is not chronological, i.e. the dfsc numbers can not be inferred from them.

Table A.8: The Available Photometry Flat Fields

Type	Filter	#frames	dfsc numbers	night(s)
Sky flat	Gunn r	14	1362–1364, 1498–1501, 2175–2181	1, 2, 7
Sky flat	Johnson B	14	1365–1366, 1502–1505, 2048–2052, 2182–2184	1, 2, 6, 7
Sky flat	Johnson U	16	1367–1369, 1506–1510, 2053–2056, 2185–2188	1, 2, 6, 7
Sky flat	Johnson V	0		
Dome flat	Gunn r	10	1808–1817	5
Dome flat	Johnson B	10	1670–1679	4
Dome flat	Johnson U	20	1649–1668	4
Dome flat	Johnson V	14	2515–2528	11

The 44 sky flats were corrected for bias, dark, shutter, and fat zero. The images from before the CCD temperature change (i.e. the flat fields from night 1 and 2) did *not* get the extra fat zero correction, since it was not known at that time.

A thorough comparison of the flat fields from the different nights showed, that they were not the same, there were gradients in their quotients. While the flats within night 2+ (i.e. night 2, 6, and 7) agreed well (within 0.2% in GR and $< 0.1\%$ in JB and JU), the agreement between night 2+ and night 1 was not good, 0.4% in GR and 0.15% in JB and JU. Therefore it was decided to make one set (GR, JB, JU) of flats for night 1, and one set for night 2+.

In each of the 3 filters, the images from night 1 and 2+ were combined separately (weighting by the level in the images, and using a 2 sigma clipping) into a night 1 and 2+ flat, respectively. Care was taken that objects (stars) did not make it to the combined flat.

Since the night 1 flats are made from only 2 or 3 images, the noise in them are too big. Therefore we do the following: we assume, that the pixel-to-pixel variation does not change from night 1 to 2+, but only the large-scale variation. We therefore make the 3 quotients between the night 1 and the night 2+ flats, and fit the large-scale pattern in this using a many piece (6 in x and 10 in y) cubic spline. This fit is then multiplied with the flat from night 2+, thereby getting flats with the pixel-to-pixel variation from night 2+, and the large-scale variation from night 1.

A.6.1 The Uncertainty on the Flat Fields

We would like to calculate how well we are able to flat field our science images, i.e. what the uncertainty (or noise) on the flat fields are.

Given the read out noise in ADU, $\mathrm{RON_{ADU}}$, the conversion factor in $\mathrm{e^-/ADU}$, CF, and the number of counts, $\mathrm{N_{ADU}}$, the uncertainty on $\mathrm{N_{ADU}}$ is given by

$$\sigma_{N_{\mathrm{ADU}}} = \left(\frac{N_{\mathrm{ADU}}}{\mathrm{CF}} + \mathrm{RON}^2_{\mathrm{ADU}} \right)^{1/2} . \tag{A.7}$$

If we make an unweighted average of n images with individual uncertainties σ_i, the uncertainty on

the combined image is

$$\sigma = \frac{1}{n}\left(\sigma_{x_1}^2 + \ldots + \sigma_{x_n}^2\right)^{1/2} . \tag{A.8}$$

The Gunn r night 2+ flats (of which there are 11), where combined in one round. The combination was made using `combine` with the following parameters different from the default: `lsigma` = 2, `hsigma` = 2, `scale` = `mean`, `weight` = `mean`, `nkeep` = 1, `grow` = 2. *The intention* with scaling was, that the different flats, which have different levels, should be scaled to a common level, so that sigma rejection can be used, after which they should be scaled back, and then made into a weighted average. Unfortunately, it seems that `combine` does *not* scale back, leading to the output being just an unweighted mean. The uncertainty should not be much higher due to this, since the individual flat field images have similar levels (within a factor of less than 4 at worst). It also means, that the uncertainty on the combined image is very easy to calculate.

Table A.9 lists the levels in ADU, N_i, and the uncertainties on the individual flats, σ_i, with σ_i is calculated from Eq. (A.7) (using $N = N_i$). They also lists the scale factors, s_i, and the weights, a_i, but these quantities do not enter the uncertainty equations.

Table A.9: The levels and uncertainties on the individual Gunn r night 2+ flat fields.

i	exptime	N_i	s_i	a_i	σ_i
1	30	2896.5	1.289	0.071	38.6
2	25	4046.9	0.922	0.099	45.6
3	20	5307.4	0.703	0.129	52.2
4	10	4127.3	0.905	0.101	46.1
5	60	3029.7	1.232	0.074	39.5
6	45	4004.2	0.932	0.098	45.4
7	25	3737.3	0.999	0.091	43.8
8	15	3447.3	1.083	0.084	42.1
9	10	3388.5	1.102	0.083	41.7
10	7	3500.6	1.066	0.085	42.4
11	5	3579.7	1.043	0.087	42.9

Notes: exptime is in seconds. N_i, s_i, and a_i, are the level (mean) in ADU, the scale factor, and weight, respectively, as reported from `combine`. σ_i was calculated from Eq. (A.7) using CF = 1.95 e^-/ADU and RON = 2.25 ADU.

To calculate the uncertainty on the combined GR flat, we apply Eq. (A.8) to the individual uncertainties, σ_i (calculated from Eq. A.7), which yields

$$\sigma_{\rm GR} = 13.21\,{\rm ADU} \ . \tag{A.9}$$

What we really want is the relative uncertainty, σ/N, and since the Gunn r combined flat had a level before normalization of 3723 ADU, we get

$$\left(\frac{\sigma}{N}\right)_{\rm GR} = \frac{13.21\,{\rm ADU}}{3723\,{\rm ADU}} = 0.35\% \ . \tag{A.10}$$

The Johnson B and U night 2+ flats (of which there are 12 and 13, respectively), were combined in two rounds: first in 3 groups of 4 or 5 images, and then these 3 images were combined. The combination on both levels were made with `combine` using the same parameters as for Gunn r (the

so-called scaled weighted mean). The two-level combination was used to make sure that no objects (stars) would make it to the final flat field, since there was not applied any offset of the telescope between the individual flats from night 6 (where only JB and JU flats were taken). Table A.10 and Table A.11 lists the levels in ADU, N_{ij}, and the uncertainties on the individual flats, σ_{ij}, with σ_{ij} calculated from Eq. (A.7) (using $N = N_{ij}$). They also lists the scale factors, t_{ij}, and the weights, b_{ij}, but these quantities do not enter the uncertainty equations.

Table A.10: The levels and uncertainties on the individual Johnson B night 2+ flat fields.

i	j	exptime	N_{ij}	t_{ij}	b_{ij}	σ_{ij}
1	1	15	5665.3	0.844	0.296	53.9
1	2	30	4348.0	1.099	0.227	47.3
1	3	5	4840.9	0.987	0.253	49.9
1	4	17	4264.5	1.121	0.223	46.8
2	1	7	5064.0	0.871	0.287	51.0
2	2	30	2305.3	1.914	0.131	34.5
2	3	20	5632.8	0.783	0.319	53.8
2	4	10	4649.1	0.949	0.263	48.9
3	1	20	2174.1	2.271	0.110	33.5
3	2	20	3982.4	1.240	0.202	45.2
3	3	15	7823.4	0.631	0.396	63.4
3	4	7	5767.3	0.856	0.292	54.4

Notes: exptime is in seconds. N_{ij}, t_{ij}, and b_{ij}, are the level (mean) in ADU, the scale factor, and weight, respectively, as reported from `combine`. σ_{ij} was calculated from Eq. (A.7) using CF = 1.95 e^-/ADU and RON = 2.25 ADU.

To calculate the uncertainty the combined JB flat, we apply Eq. (A.8) to the individual uncertainties, σ_{ij}, in each of the 3 groups, which yields

$$\sigma_{\mathrm{JB},1} = 24.8\,\mathrm{ADU} \quad (A.11)$$

$$\sigma_{\mathrm{JB},2} = 23.8\,\mathrm{ADU} \quad (A.12)$$

$$\sigma_{\mathrm{JB},3} = 25.2\,\mathrm{ADU} \quad (A.13)$$

Using Eq. (A.8) one more time, we get

$$\sigma_{\mathrm{JB}} = \frac{1}{3}\left(\sigma^2_{\mathrm{JB},1} + \sigma^2_{\mathrm{JB},2} + \sigma^2_{\mathrm{JB},3}\right)^{1/2} = 14.20\,\mathrm{ADU}\ . \quad (A.14)$$

The relative uncertainty is:

$$\left(\frac{\sigma}{N}\right)_{\mathrm{JB}} = \frac{14.20\,\mathrm{ADU}}{4645\,\mathrm{ADU}} = 0.31\%\ . \quad (A.15)$$

To calculate the uncertainty the combined JU flat, we follow the same procedure as for JB:

$$\sigma_{\mathrm{JU},1} = 25.0\,\mathrm{ADU} \quad (A.16)$$

$$\sigma_{\mathrm{JU},2} = 25.1\,\mathrm{ADU} \quad (A.17)$$

$$\sigma_{\mathrm{JU},3} = 20.2\,\mathrm{ADU} \quad (A.18)$$

and

$$\sigma_{\mathrm{JU}} = \frac{1}{3}\left(\sigma^2_{\mathrm{JU},1} + \sigma^2_{\mathrm{JU},2} + \sigma^2_{\mathrm{JU},3}\right)^{1/2} = 13.61\,\mathrm{ADU}\ . \quad (A.19)$$

Table A.11: The levels and uncertainties on the individual Johnson U night 2+ flat fields.

i	j	exptime	N_{ij}	t_{ij}	b_{ij}	σ_{ij}
1	1	25	4645.9	1.047	0.239	48.9
1	2	15	5130.9	0.948	0.264	51.3
1	3	18	4618.8	1.053	0.237	48.7
1	4	7	5065.0	0.961	0.260	51.0
2	1	8	4833.0	1.018	0.246	49.8
2	2	5	4935.4	0.997	0.251	50.4
2	3	9	4014.5	1.226	0.204	45.4
2	4	14	5898.6	0.834	0.300	55.0
3	1	3	4685.0	0.851	0.235	49.1
3	2	5	3731.4	1.068	0.187	43.8
3	3	3	3544.5	1.125	0.178	42.7
3	4	20	4546.8	0.877	0.228	48.3
3	5	3	3426.9	1.163	0.172	42.0

Notes: exptime is in seconds. N_{ij}, t_{ij}, and b_{ij}, are the level (mean) in ADU, the scale factor, and weight, respectively, as reported from `combine`. σ_{ij} was calculated from Eq. (A.7) using CF = 1.95 e^-/ADU and RON = 2.25 ADU.

The relative uncertainty is:

$$\left(\frac{\sigma}{N}\right)_{\rm JU} = \frac{13.61\,{\rm ADU}}{4384\,{\rm ADU}} = 0.31\% \ . \tag{A.20}$$

The levels used to calculate the relative uncertainties (Eq. A.10, A.15, and A.20), are the levels in the section `[25:800,25:925]`. This section is in some sense "normal", as opposed to the right and upper edge, which is more sensitive in the blue than the rest of the chip. The levels in the entire frames are 3733 ADU (GR), 4710 ADU (JB), and 4591 ADU (JU). If these values are used for calculating the relative uncertainty, we get 0.35% (GR), 0.30% (JB), and 0.30% (JU), so there is only a small difference.

Even though the chip is more blue-sensitive in the right and upper side, it is still linear in that area. This was checked using 10 JU dome flats with levels of $\sim$ 13000 ADU (dfsc1649–1658, exptime 10 sec), and 10 with levels of $\sim$ 6000 ADU (dfsc1659–1663, exptime 5 sec; dfsc1664–1668, exptime 7 sec). The high and the low level images were separately combined, and the quotient of the 2 resulting images was made. This quotient images had a gradient in the x-direction of $<$ 0.05%, and in the y-direction of $<$ 0.1%, which is very small. The quoted numbers are (maximum – minimum)/2.

The relative uncertainties are summarized in Table 3.6 (p. 32).

A.6.2 Illumination Correction

Even though we use (twilight) *sky* flats, there still seems to be a large-scale difference between the (sky) flat field and the sky background in the science frames. Since the color of the morning sky (where the sky flats are taken) and of the night sky is different, a large-scale gradient in the quotient of the flat field at different wavelengths (colors) will give an effect that behaves like the above mentioned illumination effect. The problem might be accentuated by a red leak in the Gunn r filter that we used, see Stetson (1989) for a discussion of read leaks.

To determine the illumination correction, one could observe parts of the sky without (or with few) objects. Indeed, two such *empty fields* were observed; the field SPKS04 was observed in GR and JB (dfsc2413 and 2414), and SPKS10 was observed in GR (dfsc2487). Unfortunately (and surprisingly), these images were not useful since a) the large-scale variation in the two GR empty fields did *not* match (relative difference on their quotient was up to $\pm$ 1.5%), and b) the large-scale variation in the empty fields did not match that in the science frames. It was checked that the moon was not up when these images were taken (the moon *could* have caused scattered light problems).

Instead it was tried to determine the illumination correction directly from the science images. A number (48 out of 118) of the GR and JB science images were read from tape and corrected for bias, fat zero, dark, shutter, and flat field (the sky flat fields without any illumination correction were used). The images with few bright objects were found; which was images of the following fields: 214, 21 (two exposures), 22, 36, and 44.

The objects (stars and galaxies) in the images were now removed in the following two step procedure: First all values outside $\pm 5\sigma$ from the median were replaced by the median value, with σ calculated from equation (A.7). The median was estimated as the `midpt` from `imstat` in two steps, first with no cuts, and then with cuts $\pm 5\sigma$, calculating σ from the first `midpt`. Second, `imsurfit` was used to fit a legendre polynomial in x and y (with cross terms) of order 4 in x and 3 in y (using the IRAF definition of *order*), and applying a sigma rejection with a lower sigma of 3 and an upper sigma of 2, using 3 iterations.

The agreement between the large-scale sky background variation in the above mentioned 6 science frames was not that good. In some cases objects had not been totally removed, and in some cases there was no straightforward explanation.

It was decided to use the derived large-scale sky background variation in the two field 21 frames and the field 44 frame (i.e. the mean of the 3) as the illumination correction. These two illumination images (one in GR and one in JB) were normalized using the same section as for the sky flats, `[25:800,25:925]`.

The size of the illumination can be characterized as follows (values for the entire frame): (min,max) is (0.9807,1.013) for GR and (0.9869,1.012) for JB. The standard deviation is 0.62% for GR and 0.47% for JB.

How well the illumination correction is determined is hard to say. If we look at the abovementioned 7 or 8 images (that is, 6 science frames with all objects removed, and 2 (for JB 1) empty field(s)), and we exclude the field 36 science frame because there is an unremoved object in it, and the SPKS10 (GR only) empty field because it is just strange, we can get an estimate of how well we do. The mean standard deviation of the 6 individual GR large-scale patterns is 0.62%. When making the quotient with the decided final illumination correction mentioned above (which is the mean of 3 of the 6 images), the mean standard deviation of the 6 quotients is 0.42%. For JB the numbers are 0.50% and 0.34%

So far, no remaining large-scale pattern has been noticed in the science frames reduced with the abovementioned illumination correction.

For JU, where we only have 5 science frames and no empty fields (though they did not prove useful for GR and JB), no illumination correction could be established, since the 5 frames were full of objects, and the background levels were low.

A.6.3 The Final Photometry Flats

To make the final flats, the illumination correction was multiplied to the flats. To summarize in a hopefully understandable notation:

$$\text{flat(GR,1)} = \text{sky\_flat(GR,2+)} * \text{ill.\_corr.(GR)} * \text{smooth}\left(\frac{\text{sky\_flat(GR,1)}}{\text{sky\_flat(GR,2+)}}\right) \quad \text{(A.21)}$$

$$\text{flat(GR,2+)} = \text{sky\_flat(GR,2+)} * \text{ill.\_corr.(GR)} \quad \text{(A.22)}$$

$$\text{flat(JB,1)} = \text{sky\_flat(JB,2+)} * \text{ill.\_corr.(JB)} * \text{smooth}\left(\frac{\text{sky\_flat(JB,1)}}{\text{sky\_flat(JB,2+)}}\right) \quad \text{(A.23)}$$

$$\text{flat(JB,2+))} = \text{sky\_flat(JB,2+)} * \text{ill.\_corr.(JB)} \quad \text{(A.24)}$$

$$\text{flat(JU,1)} = \text{sky\_flat(JU,2+)} * \text{smooth}\left(\frac{\text{sky\_flat(JU,1)}}{\text{sky\_flat(JU,2+)}}\right) \quad \text{(A.25)}$$

$$\text{flat(JU,2+))} = \text{sky\_flat(JU,2+)} \quad \text{(A.26)}$$

A.7 Overflow and Remanence

When there is a very bright object (star) in the frame, there will be so much charge build up in the corresponding pixels, that the potential well can not hold on to it, and it overflows. For this CCD, it flows upwards (i.e. towards higher y's) along the column(s) (typically 1-5 columns, but it can be even more). To have such an overflow stripe is in itself a problem.

But the real problem comes in the following frames, where one can now see a *remanence* stripe going downwards from where the star was in the last frame (say, we are now looking at another field without any star at the point where the bright star was in the last frame). In approximately 20 frames (not including a similar number of frames used only for pointing the telescope) after the exposure of the bright star, this remanence stripe can be seen, only fading slowly. The strength of the remanence stripe increases with exposure time. We do not fully understand the physical processes involved with this phenomenon.

It is possible to measure how much extra signal there is in an overflow or remanence affected column compared to the background. For the remanence effect, this signal is (to a good approximation) a linear function of y, although sometimes 2 (or more) linear pieces are needed, with an abrupt jump usually at $y = 512$. The overflow signal falls off much faster than a linear function in y, but it is not easily approximated by a simple function. A many-piece cubic spline works satisfactory.

The remanence and overflow stripes were removed using the cl-script `remanence`, written by IJ. It works like this: On the displayed image, the user marks the position of all the stripes and their widths in pixels (only the interval 1–9 is supported, since the width is marked just by pressing one of the keys 1 to 9). Thereafter, for each stripe, the program plots the level along the stripe (i.e. along y). The user then marks a number of intervals in y where a correction needs to be applied. The choices are fitting a linear function, `l`, or a many-piece cubic spline, `s`. The appropriate key is pressed at the endpoints of the interval. The program then fits the appropriate function to the stripe, and fits the background on each side of the stripe using a linear function. After this, the difference between the stripe fit and the sky fit can be subtracted from the original image (if this difference is less than zero, no action is taken), and one has the cleaned image.

As the above might indicate, the process involves a lot of manual work, and is rather time consuming. However, it works remarkably well in most cases.

114 of the 123 images were corrected for one or (usually) more remanence and/or overflow stripes. No of the 5 JU images needed correction. 6 of the images had also horizontal stripes (very strong overflow), and this was removed by rotating the images 90 degrees, running `remanence` on it, and rotating them back again.

A.8 Removal of Spectroscopy Calibration Lamp Signature

The DFOSC spectroscopy calibration lamp was accidentally left on while taking 8 of the photometry science images, i.e. with the DFOSC in imaging mode. These images are listed in Table A.12.

Table A.12: Images affected by the spectroscopy calibration lamp.

Image	Filter	Field
d1549	GR	00
d1550	JB	00
d1552	GR	14
d1553	JB	14
d1555	GR	15
d1556	JB	15
d1558	GR	13
d1559	GR	13

It was not possible to see the lamp signature in the Johnson B images – the lamp must have been very red – so only the 5 Gunn r images needed to have the lamp signature removed.

By coincidence, an image, dfsc1205, had been taken earlier, also with the lamp on. This image was binned 4×4. This image was expanded to full size using `blkavg`, had bias subtracted, had some cosmic-ray-events removed, and was trimmed. It is shown in Figure A.9 (left).

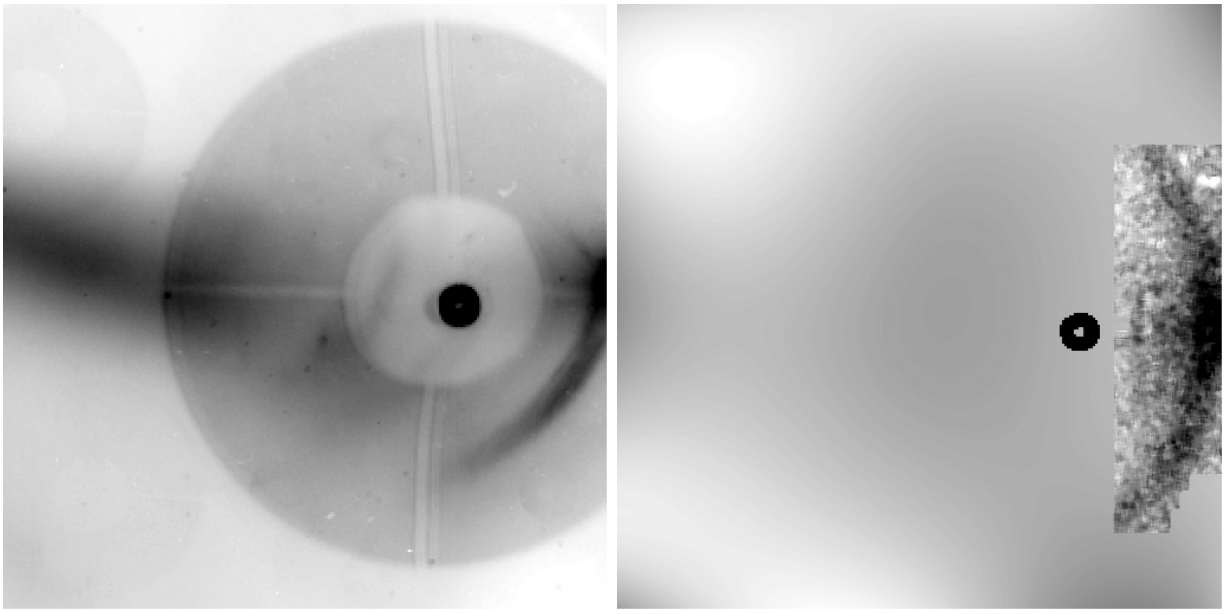

Figure A.9: The spectroscopy lamp signature. Left: the image `d1205` (see text). Right: the image `lamp_5mGR`, which is the applied correction for the lamp signature. The values from low to high are color coded as white to black.

However, the lamp signature in the science images did not look exactly like d1205. The bright small ring in the middle right hand side of the image matched well if it was shifted, but the arcs in the right hand side was symmetric in the science images, whereas it was asymmetric in d1205.

The lamp correction image was constructed as follows:

- The ring was cut out of d1205, and shifted in x and y, and scaled in intensity.
- The symmetric arc was taken from the science image d1555 of field 15, where the arc is free of galaxies in the image. Unfortunately, field 15 is next to the central field, field 00, so at the position of the arc, there was a contribution from (especially) the very bright galaxy R256/NGC3309 A model of this was made by simply taking the corresponding part from the field 00 image d1278 (since the fields overlap), translating it to the corresponding location in d1555, and subtracting the d1278 background level to get only the galaxy contribution. The shift was computed using 3 stars in common to the two images.

  The arc could now be cut out of d1555. The d1555 background was subtracted to get only the arc contribution. A number (~ 50) of weak objects was removed by replacing the affected pixels by a linear interpolation of the neighbor values, using `fixpix`. The image was then median filtered using a 11×11 box, using the task `median`.
- The low frequency variation was fitted to d1555 with the ring and the arc subtracted, using `imsurfit`. The objects (stars and galaxies) in d1555 was excluded from the fit by specifying the parts of the image not affected by galaxies, and by doing a sigma-rejection for the rest (setting `low`=3, `up`=2, and `niter`=3). The function used was a 2×2 piece cubic spline.

The three parts were put together to the image `lamp_5mGR`, which is shown in Figure A.9 (right). This image has a maximum value of 46 and a minimum value of -7. It was subtracted from the 5 affected Gunn r science images mentioned in Table A.12 – no scaling was necessary. The correction worked remarkably well.

A.9 Astrometry

Astrometry was done on all 68 focused standard star images (cf. Table C.1, p. 181 further on), using tasks in the package `finder`. The main purpose was to determine the CCD pixel scale, since that had not been determined before with sufficient accuracy.

First, the task `tfinder` was run on the images. It is given the epoch and the center coordinates of the image, the intended orientation of the CCD (in our case north at the bottom, and east to the right), and a good guess on the CCD ("plate") scale (in our case 0.51 ″/pixel). It then uses the Hubble Guide Star Catalog (GSC; on CD-ROM) to find the GSC stars present in the given CCD image. The GSC stars are drawn as rings on top of the image, which is displayed in SAOimage. The user does the coarse centering, after which the task does the real centering, and outputs a catalog *image*`.tab`, in which the following columns are of particular interest: `RA_DEG`, `DEC_DEG`, `X_CENTER`, and `Y_CENTER`.

A note should be made about the two coordinate systems involved. (x, y) are the *ideal plate coordinates*, in radians. They are given in the columns `RA_DEG` and `DEC_DEG`, with a conversion from degrees to radians. The x-axis points towards east, and the y-axis points towards north, making it a left-handed system. (x', y') are the CCD coordinates, in pixels. They are given in the columns `X_CENTER` and `Y_CENTER`. In our case, the x'-axis points approximately towards east, and the y'-axis points approximately towards south, making it a usual right-handed system. See Figure A.10.

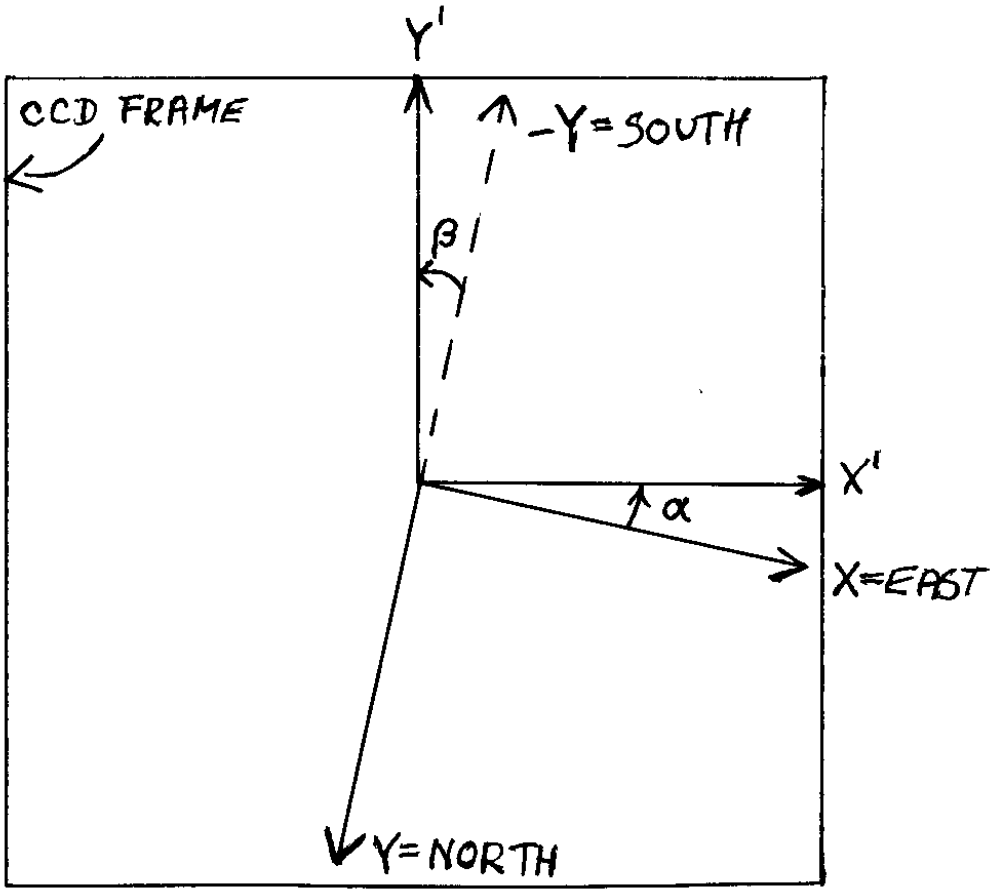

Figure A.10: Coordinate systems. Note, that for simplicity, the two coordinate systems are shown to have coinciding origins, i.e. with the offset vector $\mathbf{b} = \mathbf{0}$ (cf. Eq. A.27).

The task `tastrom` takes the catalog *image*`.tab` produced by `tfinder` and computes a 6 coefficient co-called plate solution of the form

$$\begin{pmatrix} x \\ y \end{pmatrix} = \begin{pmatrix} a_{11} & a_{12} \\ a_{21} & a_{22} \end{pmatrix} \begin{pmatrix} x' \\ y' \end{pmatrix} + \begin{pmatrix} b_1 \\ b_2 \end{pmatrix}. \tag{A.27}$$

These 6 coefficients, a_{ij} and b_i, are written to the ASCII file *image*`.ast`, along with a number of other informations. An example of the lines giving the 6 coefficients from `d1318.ast` is:

```
1PLATE SOLUTION - EMPIRICAL, 6-COEFF
 --------------   ------------------

     X,Y = IDEAL PLATE COORDINATES (RADIANS)

     X =   -0.001269                          Y =    0.001301
       +   0.2458474E-05 * XMEAS                +  -0.2458925E-05 * YMEAS
       +  -0.1837236E-07 * YMEAS                +  -0.1840916E-07 * XMEAS
```

We identify a_{ij} and b_i as

$$\begin{array}{rclcrcl} x & = & b_1 & & y & = & b_2 \\ & + & a_{11} \cdot x' & & & + & a_{22} \cdot y' \\ & + & a_{12} \cdot y' & & & + & a_{21} \cdot x' \end{array} \tag{A.28}$$

The transformation matrix $\mathbf{A}$ can be written in terms of the following geometrical quantities

1. α: The angle from the x-axis (east) to the x'-axis (CCD abscissa), measured counterclockwise
2. β: The angle from the $-y$-axis (south) to the y'-axis (CCD ordinate), measured counterclockwise
3. $s_{x'}$: The CCD scale in the x' direction
4. $s_{y'}$: The CCD scale in the y' direction

as

$$\mathbf{A} = \begin{pmatrix} s_{x'} \cos\alpha & -s_{y'} \sin\beta \\ -s_{x'} \sin\alpha & -s_{y'} \cos\beta \end{pmatrix}, \tag{A.29}$$

where the minus signs on a_{21} and a_{22} are due to the fact that we have a usual right-handed coordinate system being rotated with respect to a *left-handed* coordinate system, cf. Figure A.10.

A.9.1 CCD Orientation

The angles α and β were calculated from the extracted elements of $\mathbf{A}$ as

$$\tan\alpha = -\frac{a_{21}}{a_{11}} \tag{A.30}$$

and

$$\tan\beta = +\frac{a_{12}}{a_{22}}. \tag{A.31}$$

Figure A.11 shows the values of α and β as function of a chronological image serial number for the 68 images. Vertical dashed lines demarcates the different nights. The observations come in

sets of 4 images, one in each filter. These sets are labeled with the field name, with "PG" being PG1633+099, and "SA" being SA110–503.

The observation history is, that on night 1 there was no encoder on the rotator. After images with serial numbers 1 to 8 had been observed, the rotator was turned, and therefore it is expected that images with serial number 9 to 12 have a different orientation than the above. On night 2, an encoder was available.

It is seen, that for all the PG images, α and β agree well. $\alpha = \beta$ is expected, since it means that the CCD is right-angled. However, for all the SA image, there is a systematic difference between α and β of about 0.1°. This is probably due to the fact, that the 18 GSC stars in the SA field comes from two different Schmidt plates, with 9 stars from plate 0192, and 9 stars from plate 050T. For the PG field, all 12 stars come from one plate, 006K. This can be seen from the `PLATE_ID` column in the *image*`.tab` tables. The hardcopy documentation for `finder` actually warns against using data from more than one plate at the time, so it seems justified to exclude the SA data.

The PG data only is plotted in Figure A.12. The horizontal dotted-dashed line shows the mean of these data of +0.29°. The data points scatter around this value within ±0.3° (min-max). The step size of the encoder is 0.2°, which almost explains the scatter.

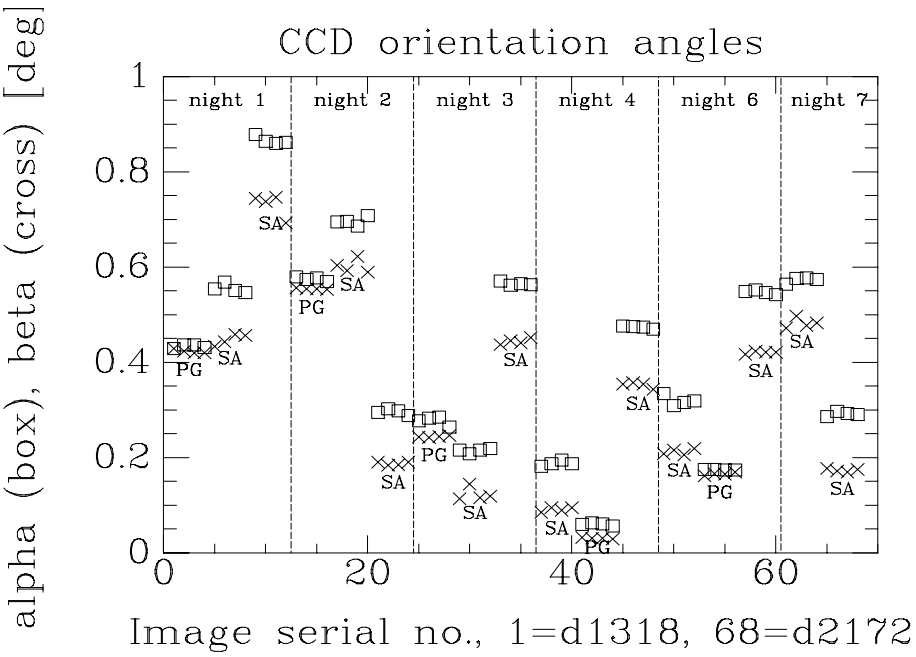

Figure A.11: CCD orientation angles. Each set of four observations is labeled by the field name.

A.9.2 CCD Scale

`tastrom` directly outputs the CCD scales in the x and y direction, $s_{x'}$ and $s_{y'}$, in the *image*`.ast` file, with 4 decimal places. A manual calculation using the found values of α and β and equation (A.29) gives the same result. The scales are shown in Figure A.13. There seems to be a small difference between the x scale and the y scale. This is small enough to be ignored.

The horizontal dotted-dashed line shows the adopted value of the CCD scale of 0.5073 ″/pixel. This is actually not a mean of all the data, but only of 6 images on which astrometry was done at an earlier point. However, this value is very representative for all the data, as the figure shows.

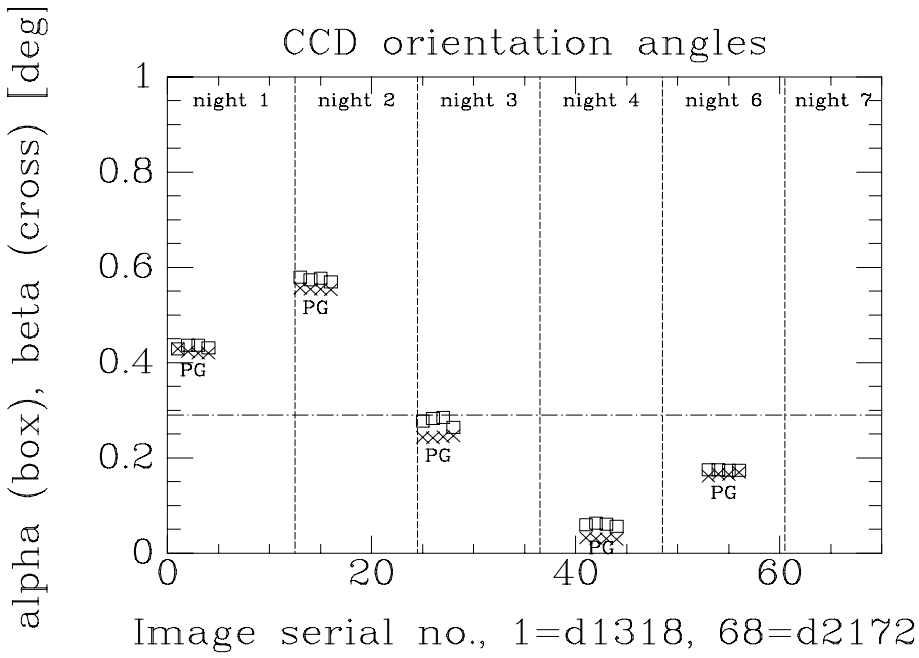

Figure A.12: CCD orientation angles, PG images only. The horizontal dotted-dashed line is at $+0.29°$.

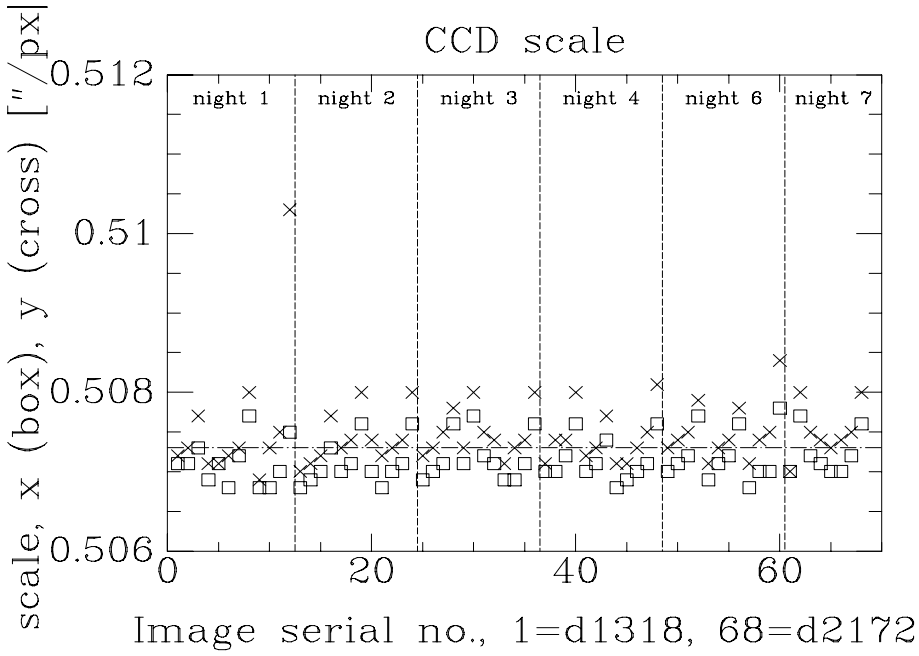

Figure A.13: CCD scale in the x and y direction. The horizontal dotted-dashed line is at 0.5073 $''$/pixel.

Appendix B

Details of the Surface Photometry

B.1 Details on How to Fit Ellipses

This section gives a more detailed description of the things that is needed to consider when fitting ellipses using the current implementation of GALPHOT. Since the description in the main text (Sect. 4.1, p. 35) was kept in general terms, we start by introducing the terminology specific to GALPHOT and its implementation. In the following '*galaxy*' is a generic name for a galaxy observation. An example is `r214_GR_1`, which is a Gunn r (GR) observation of the galaxy R214. Since this galaxy has been observed more than once in Gunn r, it is given a serial number, in this case 1.

`classify` is the task that does the classification of objects into 'stars' and cosmic-ray-events. It outputs the positions and flagging radii of the two types of objects in the two files *galaxy*`.star` and *galaxy*`.cosmic`. In addition, the center coordinates of the program galaxy is put in the file *galaxy*`.gal`.

`harmfit` is the task that does the harmonic expansion along concentric circles. It outputs the radial profiles of the Fourier coefficients from the expansion and their uncertainties in the STSDAS table *galaxy*`.har.tab`, and also produces a residual image called *galaxy*`.resh.imh`.

`deviate` is the task that flags the pixels that deviate by more than (say) 5 sigma in the above residual image. The output is a list of additional pixels to be flagged called *galaxy*`.pos.del`.

`ellipfit` is the task that does the ellipse fitting. The radial profiles are output in the STSDAS table *galaxy*`.prf.tab`, and the residual image is called *galaxy*`.res.imh`. `ellipfit` has some parameters that sometimes need to be fine tune. `errcen` and `errshap` are the uncertainties that the first and second order coefficients from `harmfit` needs to be below to keep the center and shape as free parameters, respectively. As default values for both we used 0.02 for Gunn r and Johnson B, and 0.04 for Johnson U. `rcen` and `rshap` can be used to explicitly set $r_{\mathrm{free-center}}$ and $r_{\mathrm{free-shape}}$ and thus overriding the automatic determination using `errcen` and `errshap`. The parameters `dposmax`, `dellmax`, and `dangmax` control how much the center position, the ellipticity, and the position angle, respectively, are allowed to change at a given radius per iteration step. These need to be increased when the initial guess on the profiles computed from the `harmfit` output are far from the actual values for some reason.

`model` is a task that can construct a model image from the ellipse fit.

Finally, the task `galfit` is an 'umbrella task' that basically calls the three tasks `harmfit`, `deviate`, and `ellipfit`.

We are now ready to fit an isolated galaxy (Sect. B.1.1) or two overlapping galaxies (Sect. B.1.2).

B.1.1 Fitting a Single Galaxy

By single galaxy, we mean a galaxy, which has a large angular separation from other galaxies, i.e., no other galaxies overlap with the galaxy in question.

First, we run `galfit` on all the single galaxies using the default parameters. Most of the galaxies are so relatively small, that it is not necessary to use the entire 1024 pixel × 1024 pixel image to fit them. Usually, a 400 pixel × 400 pixel section will do. When possible, the section should be centered on the galaxy. A typical call to `galfit` is:

```
galfit d1293[096:495,517:916] infiles=r214_GR_1 output=r214_GR_1
```

where the name of the galaxy image in the example is `d1293`.

Besides the galaxy image, the input files to `galfit` are *galaxy*`.gal`, *galaxy*`.star`, and *galaxy*`.cosmic`, and the output files are *galaxy*`.har.tab`, *galaxy*`.resh.imh`, *galaxy*`.pos.del`, *galaxy*`.prf.tab`, and *galaxy*`.res.imh`.

The two images are examined to see whether the obtained fit is good. It is mostly the `ellipfit` residual image (i.e. *galaxy*`.res.imh`) that is interesting. Two typical types of problems are:

- $r_{\rm free}$ is wrong and/or there are overlapping ellipses. Since the center and shape parameters of the galaxy actually change with r, we want to have $r_{\rm free}$ as large as possible. However, when the signal to noise becomes too low, the fit is poorly constrained, and one can get overlapping ellipses, which is undesirable. In a number of cases, it is necessary to manually intervene to get the best fit:
  - If $r_{\rm free}$ is too low, i.e. if one can see from the `ellipfit` residual image that e.g. the ellipticity is still rising beyond $r_{\rm free}$, one can try to increase `errcen` and `errshap`, or set `rcen` and `rshap` to something suitable.
  - If $r_{\rm free}$ is too high and one gets overlapping ellipses, one can try to set `rcen` and `rshap` to the radius just before the overlap occurs.
  - If a galaxy has a sharp isophote twist, and has been observed in good seeing, it is not possible to just decrease $r_{\rm free}$ to avoid the overlapping ellipses, because then the outer parts beyond the sharp isophote twist are not fitted correctly. This can be solved by making sure $r_{\rm free}$ is large enough to fit the entire galaxy, and then manually remove the radius/radii from *galaxy*`.prf.tab` at which the ellipses overlap (this is reported by `galfit` as e.g. 'MODELINIT: WARNING: ellipses overlapping at $r = 24.05$'). One can construct a residual image corresponding to this new profile using `model` with `residual=yes`. From this image it should be checked, that the model is well behaved in the flagged pixels, where the model values will be used when calculating aperture magnitudes. One can do that by blinking the above `cmodel` residual image with an image that has the flagged pixels marked, e.g. the residual image from `galfit`. The above procedure was done for 1 of the 147 observations that I (BMJ) fitted (`r253_JB_2`).
- Problems with flagging other objects.
  - Even though `classify` is quite good at assigning radii to the extended objects, there will still be some objects where the radius is not correct, being either too large or too small. This is particularly a problem close to the center of the galaxy, both because the non-flat background confuses `classify`, and because the flagging is more critical here. Correction of the assigned radii is done by editing *galaxy*`.star`.

- Some extended objects might not have been detected, typically faint galaxies, so they need to be added to *galaxy*`.star`.
- Some cosmic-ray-events might not have been detected, so they need to be added to *galaxy*`.cosmic`.
- In a few cases, there are cosmic-ray-events very close to the center. Flagging them using *galaxy*`.cosmic` or letting `deviate` do the job might not work, because the interpolation routine used by `ellipfit` cannot handle having such a large fraction of the ellipse flagged. One has to replace the affected pixels by the values in their symmetric counterparts, assuming symmetry around the center of the galaxy. This was done for 3 of the 147 observations which were fitted by me.

B.1.2 Fitting Overlapping Galaxies

By overlapping galaxies, we mean two (or more) galaxies, which have a small angular separation, so that it is not possible just flag the other galaxy. Therefore, the galaxies have to be fitted iteratively. GALPHOT does not support this per se, so one has to do it in a manual fashion. In the following, *image* is the original image, *gal1* is the brightest of the two overlapping galaxies, and *gal2* is the faintest.

1. (a) Using *image*, *gal1* is fitted with *gal2* flagged with a large radius. A model image based on the fit is subtracted from *image* to get *image_mod*. The background level in *image* is added to *image_mod*, so that the two has the same background levels, keeping photon statistics unaltered.

   (b) Using *image_mod*, *gal2* is fitted with *gal1* flagged with a large radius. A model image based on the fit is subtracted from *image* to get *image_gal1* – the notation is, that *gal1* is the galaxy *left* in the image *image_gal1*. The background level in *image* is added to *image_gal1*.

2. (a) Using *image_gal1*, *gal1* is fitted with *gal2* flagged with a small radius. A model image based on the fit is subtracted from *image* to get *image_gal2*. The background level in *image* is added to *image_gal2*.

   (b) Using *image_gal2*, *gal2* is fitted with *gal1* flagged with a small radius.

We found that the above 2 steps were enough. Otherwise the procedure could be continued further.

The iterative procedure were also used on galaxies with bright stars very close to the center. This gave a much better fit than if we had just flagged the star. This kind of star subtraction was done for 2 of the 34 galaxies fitted by me. Note the notation: we have 64 *galaxies* and 227 galaxy *observations*.

B.2 Corrections to the PA-profiles

Note: in this section, we will use primes to denote the CCD coordinate system, to keep the notation consistent with that of the astrometry section (Sect. A.9, p. 156). For example, we will use the term "the CCD x'-axis", or just "the x'-axis", to denote what would otherwise just be called "the CCD x-axis". Unprimed quantities will refer to the ideal plate coordinate system.

B.2.1 Transformation to the Standard System

The ellipse fitting task (`galfit`) measures the position angle from the CCD x'-axis and counterclockwise. The standard way of measuring position angles is "from north through east". The task that calculates instrumental magnitudes (`galmag`) also attempts to transform the position angles to the standard system.

In our case, the CCD x'-axis points (approximately; see Sect. B.2.2 below) towards east, and the CCD y'-axis points (approximately) towards south, so "from north through east" still means counterclockwise. However, instead of starting from the CCD x'-axis, we need to start from *minus* the CCD y'-axis. Therefore, in our case, `galmag` does the following transformation:

1. $\mathrm{PA}_{\texttt{galmag}} = \mathrm{PA}_{\texttt{galfit}} + 90^\circ$
2. If $\mathrm{PA}_{\texttt{galmag}} > 180^\circ$ then $\mathrm{PA}_{\texttt{galmag}} = \mathrm{PA}_{\texttt{galmag}} - 180^\circ$

$\mathrm{PA}_{\texttt{galfit}}$ denotes the position angles calculated by `galfit` (found in *galaxy*`.prf.tab`), and $\mathrm{PA}_{\texttt{galmag}}$ denotes the position angles calculated by `galmag` (found in *galaxy*`.mags.tab`).

B.2.2 Correction for the Slight CCD Misalignment

We found in the astrometry section (Sect. A.9, p. 156), that the CCD coordinate system was turned $+0.29^\circ$ with respect to the ideal plate coordinates. Let us denote this angle by γ, i.e. $\gamma = +0.29^\circ$. Because of this misalignment, `galmag` did not quite get us to the standard system, we are still 0.29° off.

Figure B.1 shows the setup. On the figure, an angle θ' is shown. θ' is measured from minus the CCD y'-axis counterclockwise, i.e. just as the position angles that `galmag` outputs. It can readily be seen, that the angle θ, measured from the true north axis and also counterclockwise, can be calculated as

$$\theta = \theta' + \gamma \ . \tag{B.1}$$

Therefore, all the PA-profiles of the galaxies from all nights where corrected for this mean $+0.29^\circ$ CCD misalignment as

$$\mathrm{PA}_{\mathrm{corr}} = \mathrm{PA}_{\texttt{galmag}} + 0.29^\circ \ . \tag{B.2}$$

B.2.3 PA-profiles that Cross 0° or 180°

The position angles determined from `galmag` are in the range 0°–180°. They do not go all the way to 360°, since the major axis of a galaxy does not have a positive and a negative direction, as opposed to for example a coordinate axis.

If a galaxy has an isophote twist, i.e. the position angle changes with the radius r, the position angle might cross the upper or lower limit of 180° or 0°, respectively, and thereby appearing discontinuous. This is in a way a cosmetical problem. Since the position angle is only determined to within a factor of 180°, we can add or subtract 180° at certain radii to make the profile look continuous. This was done using the task `pa1shift`. An example of this is shown in Figure B.2.

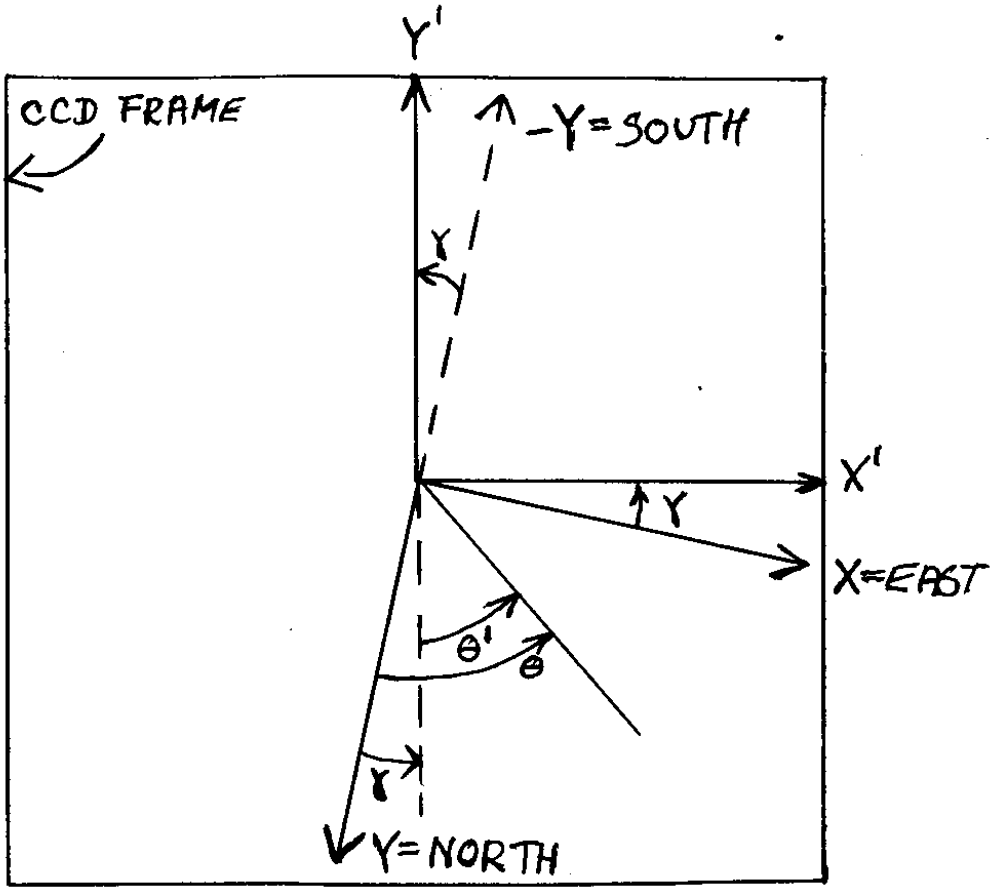

Figure B.1: Correction for the CCD orientation

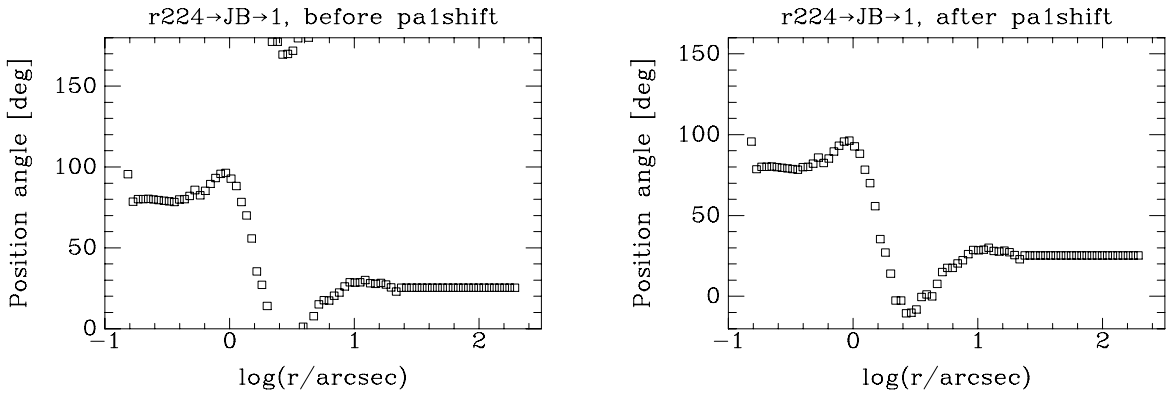

Figure B.2: Example of a PA-profile that crosses 0°/180°, and which was cosmetically changed to look continuous. The isophote twist of R224 is visible in the image on p. 219. Note that 'isophote twist' just means that the position angle is changing significantly with radius, not necessarily that it crosses 0° or 180°. The seeing for the shown observation is 1.8 arcsec, i.e. $\log(r/\mathrm{arcsec}) = 0.25$.

B.3 Corrections to Non-Photometric Observations

Unfortunately, not all the images have been taken in photometric weather. We need to identify these, and then compute offsets that will bring these images to the same system as the images observed under photometric conditions.

The observations log is shown in Table B.1. It clearly states, that the weather was non-photometric when observing field 210 on night 4, that the weather might not have been photometric when observing fields 427, 215, 28, and 33 just after this, and that there might be problems with the 5 JU fields on night 9.

One check of the photometric consistency comes from the program galaxies that have been observed more than once in a given filter. All possible pairs of such observations were formed, giving 53 pairs in GR, 42 pairs in JB, and 2 pairs in JU. The order of the two observations within the pairs was chosen to be chronological. About half of the observations are tested in this way see the "Pair" column in Table B.2 (p. 172). The number of pairs can be calculated from the numbers in Table 3.4 (p. 29) as $N_{\rm pair} = N_2 + 3N_3 + 6N_4$, where N_2, N_3, and N_4 is the number of galaxies observed twice, three times, and four times, respectively. Note, that the one pair that can be formed from a galaxy observed exactly twice can be uniquely referred to by the name of the galaxy (and the filter).

From the raw magnitudes (cf. Sect. 4.2, p. 39) instrumental magnitudes were calculated as

$$m_{\rm inst} = m_{\rm raw} - kX + n, \tag{B.3}$$

where $-kX$ is the extinction correction and $+n$ is the night shift. (This equation is described briefly in Sect. 4.3, p. 40, and in more detail in Ap. C, p. 179.) For each pair of observations, the (instrumental) magnitude difference within a circular aperture, $\Delta m_{\rm circ}(r) \equiv m_{\rm circ,1}(r) - m_{\rm circ,2}(r)$, was calculated at aperture radii $6.26''$ and $10.08''$.

Magnitude difference at these two apertures for the three filters are plotted in Figure B.3. Most magnitude differences are within $0\overset{\rm m}{.}02$. Only two galaxies, R336 and R337, have large magnitude differences of around $0\overset{\rm m}{.}1$. These two pairs are due to R336 and R337 being located in the overlap region between field 210 and 28. Field 210 is the one for which the observations log clearly states that the weather was non-photometric. Field 28 was observed later on night 4, where the log says that is should be checked whether the weather was photometric.

The only other pairs that have large deviations are R317 and R308. The R317 pair is due to field 33 being observed twice, on night 1 and 4. The R308 pair is due to field 16 being observed twice, on night 1 and 6.

We note that for the $6.26''$ aperture there is a small systematic offset of $\sim 0\overset{\rm m}{.}01$. This is most likely a seeing effect, as is shown in Sect. 4.4 (p. 41). It is not important for the determination of the non-photometric offsets. First of all it is a small effect, and second, the $10.08''$ aperture, which was also used, is not significantly affected.

From the above we have identified 5 field complexes that need to be checked:

Field complex	Filter	Indication of problems	
		Observations log	Galaxy $\Delta(m)$
210/28/16	GR+JB	210: yes; 28: maybe; 16: no	210/28: yes; 16: maybe
427	GR+JB	maybe	n/a
215	GR+JB	maybe	n/a
33	GR+JB	maybe	maybe
00/13/14/15/18	JU	maybe	maybe

Table B.1: The Notes in the Observations Log about the Weather

Night	Page	Weather	Galaxy fields observed
1	1	Photometric – to be checked	–
1	2	Photometric	–
1	3	Photometric	00, 16, 13, 25, 37
1	4	Photometric	37c, 18, 12, 21, 33, 45
1	5	Photometric	–
1	6	Photometric	–
1	7	Photometric	–
2	8	Photometric	214, 320
2	9	Photometric	428, 632, 29, 419, 519
2	10	Photometric	15
2	11	Photometric	–
2	12	Photometric	–
2	13	Photometric	–
3	14	[nothing written]	–
3	15	Photometric	00, 14, 15, 13
3	16	Photometric	27, 23, 43, 18, 321, 535
3	17	Photometric	535c, 35
3	17	May not be photometric right now, check this	–
3	18	Photometric (?)	–
3	19	Photometric	–
4	20	Photometric	–
4	21	Photometric	46
4	22	Photometric	47, 34, 22, 26, 24
4	22	NON-photometric	210
4	23	Photometric? check this	427, 215, 28, 33
4	24	Photometric	–
4	25	Photometric	–
4	26	Photometric	–
6	25	Photometric	–
6	26	Photometric	213, 39, 36, 44
6	27	Photometric	45, 32, 64, 66, 615, 16
6	28	Photometric	21
6	29	Photometric (?)	–
6	30	Photometric (?)	–
9	42	Photometric – but clouds may come later	–
9	43	Photometric – but clouds on their way!	00, 14, 15, 13, 18
9	44	Non-photometric!	–

Notes: The weather was noted on top of each page of the log book, except for page 17 and 22, where it was also noted further down. On night 5, the first page number was set to 21 instead of 27 as it should have been, therefore the strange page numbers for night 6. A "c" after the field number means that the observations of the given field were noted over two pages of the log.

For each field complex, aperture photometry using the task `phot` was performed on all suitable stars in the overlap regions within the complex and with at least one other field that had been observed under photometric conditions according to the observations log. From the raw magnitudes, instrumental magnitudes were calculated in the same way as for the galaxy magnitudes, i.e. using Eq. (B.3). For each overlap region, the magnitude difference for the stars, $m_1 - m_2$, was plotted

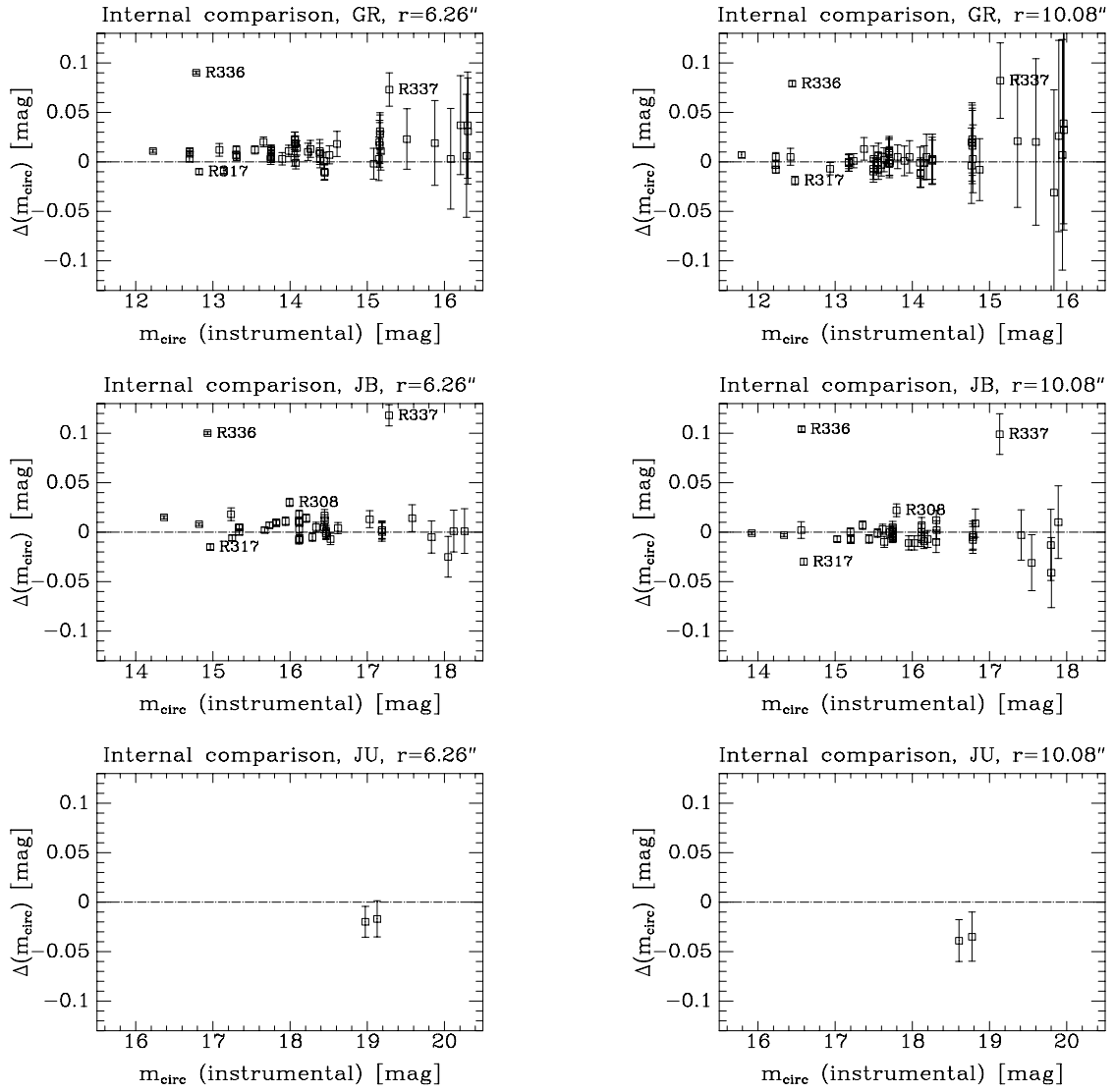

Figure B.3: Comparison of instrumental aperture magnitudes for galaxies observed more than once. From top to bottom the filters are GR, JB, and JU. The left three panels are for an aperture of 6.26″, the right three panels are for an aperture of 10.08″. The galaxies R317, R336 and R337 have been marked, and for JB also R308. The systemtic offset of $\sim 0\overset{\mathrm{m}}{.}01$ seen for the 6.26″ aperture is a seeing effect, cf. the text.

against m_1, using open boxes as the plotting symbol. These plots are referred to as *offset plots*. The first offset plots appear in Fig. B.4 (p. 173). The title of each of these plots are of the form "Overlap: *image1* (*field1*) – *image2* (*field2*)", where m_1 corresponds to *image1*, and m_2 corresponds to *image2*. The aperture radius (usually 9 pixels = 4.6″) is noted in the label of the x-axis. If there were any program galaxies in the overlap region, the magnitude differences for these at apertures 6.26″ and 10.08″ (12 and 20 pixels) were also plotted as filled triangles and boxes, respectively. The horizontal dashed line indicates the derived offset.

The offset plots for a given field complex are summarized in what is termed an *offset diagram*. The first offset diagrams appear in Fig. B.6 (p. 175). In these, each observation of a field is shown

as a box, and the overlaps are indicated by arrows. Each arrow is labeled by the derived offset. The direction of the arrow indicates how the offset was calculated: if the arrow goes from field 2 to field 1 the offset was calculated as $\langle m_1 - m_2 \rangle$. The idea is, that to go in the direction of the arrow, one has to *add* the given offset.

How the fields are positioned on the sky relative to each other can be seen from Fig. 3.1 (p. 25) for GR and JB, and Fig. B.14 (p. 177; left panel) for JU.

We now summarize the overlaps studied within the 5 field complexes that we found above needed to be checked. After that, we give the conclusions.

Field 210, 28, and 16

Offset plots: Figure B.4 (GR) and B.5 (JB). Offset diagrams: Figure B.6. 8 overlaps involving 6 images pr. filter were studied:

- field 210 night 4 – field 16 night 1
- field 210 night 4 – field 16 night 6
- field 16 night 1 – field 16 night 6
- field 210 night 4 – field 28 night 4
- field 16 night 1 – field 14 night 3
- field 16 night 6 – field 14 night 3
- field 14 night 3 – field 28 night 4
- field 26 night 4 – field 28 night 4

Note, that the field 14, night 3 GR image, d1552, has scattered light, which may cause extra scatter.

Field 427

Offset plots: Figure B.7. Offset diagrams: Figure B.8. 1 overlap was studied: field 428 night 2 – field 427 night 4.

Field 215

Offset plots: Figure B.9. Offset diagrams: Figure B.10. 1 overlap was studied: field 18 night 1 – field 215 night 4.

Field 33

Offset plots: Figure B.11. Offset diagrams: Figure B.12. 1 overlap was studied: field 33 night 1 – field 33 night 4.

A strange phenomenon can be observed in the JB offset plot: $m_1 - m_2$ is not constant with m_1, it decreases with increasing m_1. If the y-axis had been extended, this would be even more clear. The sky determination in both images was checked and was found to be OK. The phenomenon may either be related to fat zero at low levels (both images have low background levels), or related to the 2 images being stacked from several (2 or 4) shorter exposures. In any case, the bright stars are believed to not be significantly influenced by this.

The 5 JU fields

Offset plots: Figure B.13. Offset diagrams: Figure B.14 (right). 4 overlaps involving 4 images all from night 9 were studied:

- field 00 – field 13
- field 00 – field 14
- field 00 – field 15
- field 13 – field 15

Note, that field 18 does not overlap with any of the other JU images.

Conclusions

Two problem areas were identified, namely the last part of night 4, and night 9. Conclusions:

Night 4

- Clearly, field 210 in both GR and JB are non-photometric.
- The offsets between field 33 night 1 and field 33 night 4 of -0.01 in GR and -0.02 in JB are well determined. Field 33 night 1 were taken to be photometric, and field 33 night 4 were taken to be non-photometric by the above amounts.
- The rest of the night 4 checked fields, 26, 24[1], 427, 215, and 28, have nominal offsets no larger than 0.02. These offsets are not determined better than that, so they were all taken to be zero.

  That the accuracy of these offsets are 0.01–0.02 can be seen from the field 210 complex offsets diagrams, Figure B.6. Different paths from one field to another give results that differ by up to 0.03.
- The adopted value of the offset for field 210 were taken as a suitable mean to be -0.10 in GR and -0.11 in JB.

Night 9

- Field 00 was taken to be the reference image, since it was the one most likely to be photometric, because it had been observed first.
- The offsets for field 14, 15, and 13 were taken to be the derived offset with field 00, namely $+0.03$, -0.04, and -0.06, respectively. The derived offset between field 13 and 15 is very consistent with these other offsets, the difference is only 0.01, which is less than the uncertainty of the offsets.
- That the field 00 – field 14 offset is positive means that field 14 is a better photometric reference than field 00. However, since no standard stars were observed on night 9 and hence no night coefficient is available, we will need to determine the zero point using comparison with external references anyway.

[1]No overlap photometry on stars using `phot` was done involving field 24, but for the galaxy R243 located in the overlap between field 24 night 4 and field 23 night 3, an offset $\Delta m_{\rm circ}$ is available. At the $10.08''$ aperture, it is -0.007 ± 0.006 in GR and -0.007 ± 0.003 in JB.

- Field 18, observed just after field 15, did not overlap with any of the other 4 fields. Since it was believed that it was observed under non-photometric conditions, it was assigned an offset equal to that of field 15, namely -0.06.

Other nights

- Field 16 night 1 and field 16 night 6 were both believed to be photometric. The nevertheless non-zero offsets between them of 0.01 in GR and 0.02 in JB[2] were taken to be the typical internal photometric uncertainties. No offsets should be applied to either of these images.

The correcting offsets derived above are listed in Table B.2. These offsets (where non-zero) were added to the 4 magnitude quantities, $m_{\rm ell}(r)$, $m_{\rm circ}(r)$, $\mu(r)$, and $<\mu>(r)$.

[2]To these magnitude differences at a finite aperture r, $\Delta m(r)$, should be added the difference in aperture correction induced by the difference in seeing, Δapcor(r), to get the intrinsic magnitude difference, $\Delta m_{\rm T}$; i.e. $\Delta m_{\rm T} = \Delta m(r) + \Delta$apcor$(r)$. Δapcor(r) for those particular images and the used 9 pixel aperture is -0.002 for GR and -0.003 for JB, and thus negligible. For reference, the seeing values are listed in Table 3.5 (p. 30), the aperture correction vs. seeing is plotted in Fig. C.2 (p. 184) and C.3 (p. 184), and the pixel scale is 0.5073 $''$/pixel.

Table B.2: List of Non-photometric Corrections

Night	Offset		Field	Pair	Program galaxies
	GR	JB			
1			00	x	R245, R253, R255, R256, R266, R268, R269, R273, R286, R293
1	0.00	0.00	16	x	R308
1			13	x	R209, R217, R234, R237, R241
1			25		–
1			37	x	R166, R185
1	0.00	0.00	18	x	R214, R219, R225
1			12	x	R255, R273, R278
1			21		–
1	0.00	0.00	33	x	R317
1			45		–
2			214		R261
2			320		R327
2	0.00	0.00	428		R250
2			632		–
2			29		R193
2			419		R138
2			519		R129
2			15	x	R213, R216, R224, R226, R239, R245
3			00	x	R245, R253, R255, R256, R266, R268, R269, R273, R286, R293
3	0.00	0.00	14		R316, R322
3			15	x	R213, R216, R224, R226, R239, R245
3			13	x	R209, R217, R234, R237, R241
3			27	x	R188, R194, R209
3			23	x	R243
3			43		R338, R343, R347
3			18	x	R214, R219, R225
3			321		R283, R288
3			535		R252, R295
3			35		R218, R231
4			46		R238
4			47		R202
4			34		R254
4			22		R319
4	0.00	0.00	26		R334, R359
4			24	x	R211, R212, R243
4	−0.10	−0.11	210	x	R336, R337
4	0.00	0.00	427		R305
4	0.00	0.00	215	x	R225
4	0.00	0.00	28	x	R336, R337, R340
4	−0.01	−0.02	33	x	R317
6			213		–
6			39	x	R166
6			36		–
6			44		–
6			45		–
6			32		–
6			64		R389
6			66		R307
6			615		R112, R120
6	0.00	0.00	16	x	R308
6			21		–
	JU				
9	0.00		00	x	R239, R245, R253, R255, R256, R266, R268, R269, R273, R286, R293
9	+0.03		14		R316, R322
9	−0.04		15	x	R213, R216, R224, R239, R245
9	−0.06		13		R217, R234, R237
9	−0.06		18		R214, R219, R225

Notes: The list is in chronological order. Exactly those images that appear in the offset plots in this section has a listed offset (with the exception of field 18 JU; see the text). "Pair" means that the given entry has one or more galaxies that have been observed more than once. The 64 galaxies in this table are the ones in the HydraI surface photometry sample, cf. Table 3.3 (p. 28).

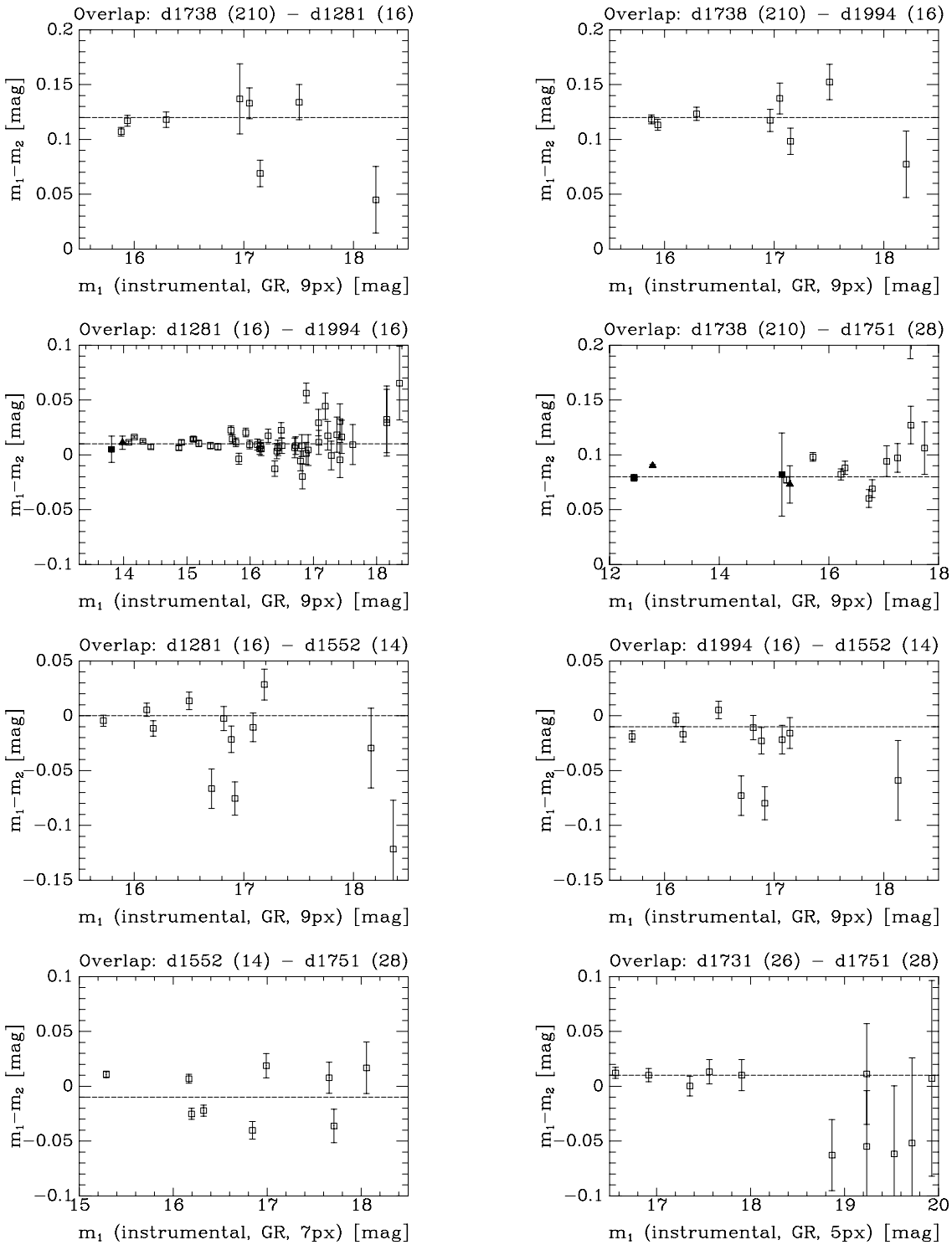

Figure B.4: Offset plots, field 210 and 28, GR. The galaxies in the overlap between field 210 and 28 are R336 (bright) and R337 (faint). The galaxy in the overlap between field 16 and 16 (sic!) is R308. Note, that the image d1552 has scattered light, which may cause extra scatter.

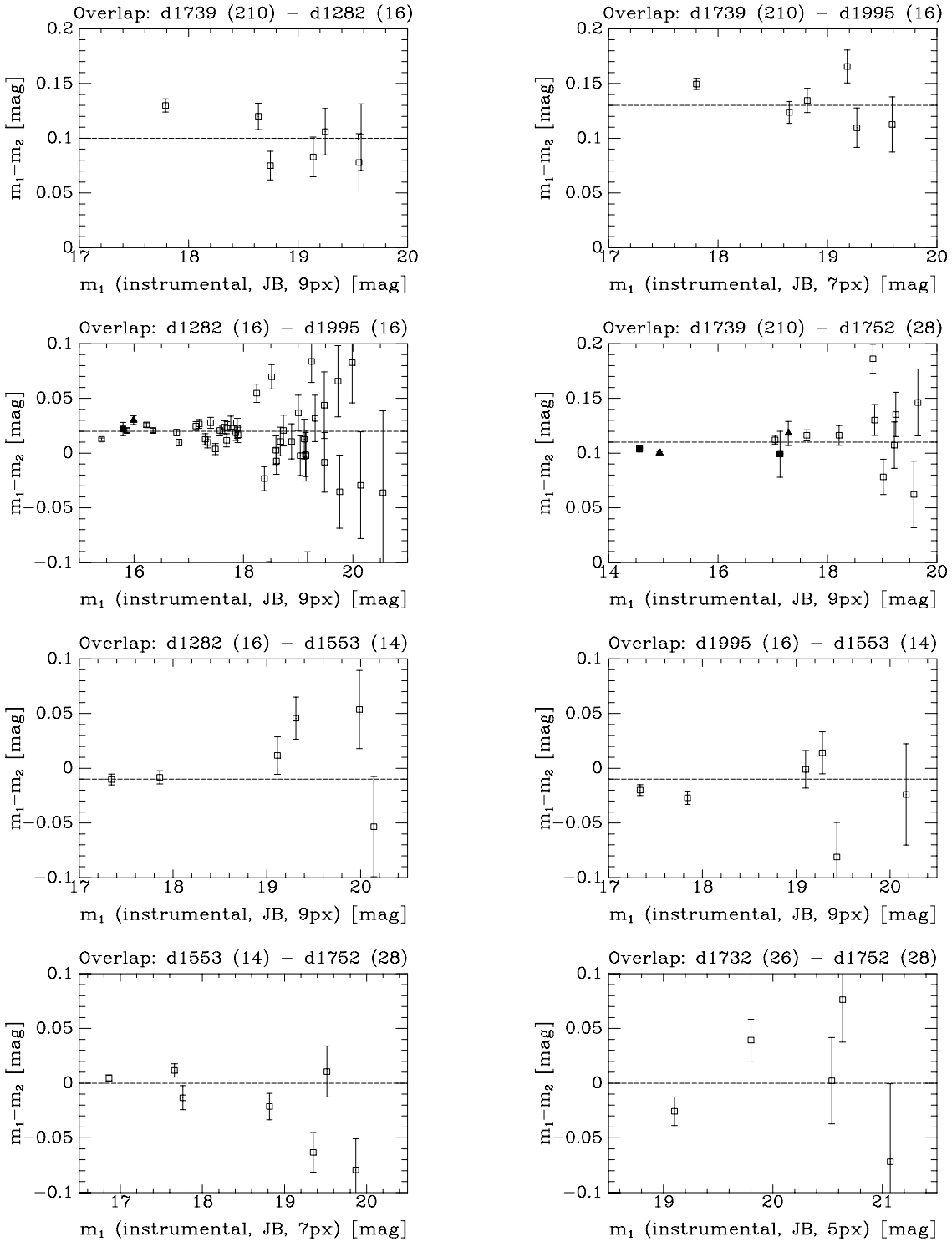

Figure B.5: Offset plots, field 210 and 28, JB. The galaxies in the overlap between field 210 and 28 are R336 (bright) and R337 (faint). The galaxy in the overlap between field 16 and 16 (sic!) is R308.

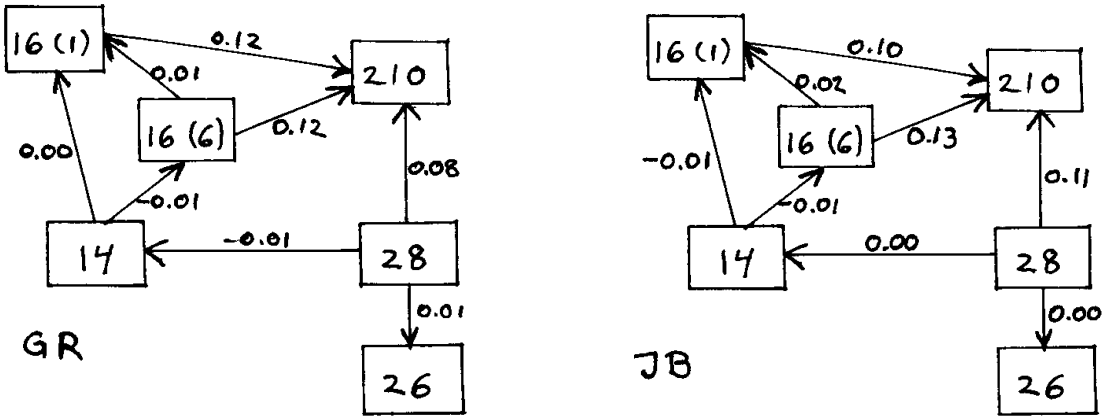

Figure B.6: Offset diagrams, field 210 and 28.

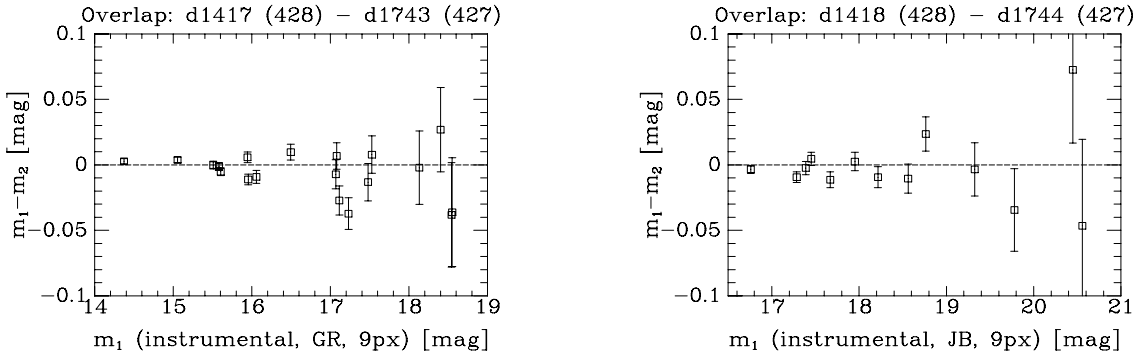

Figure B.7: Offset plots, field 427.

Figure B.8: Offset diagrams, field 427.

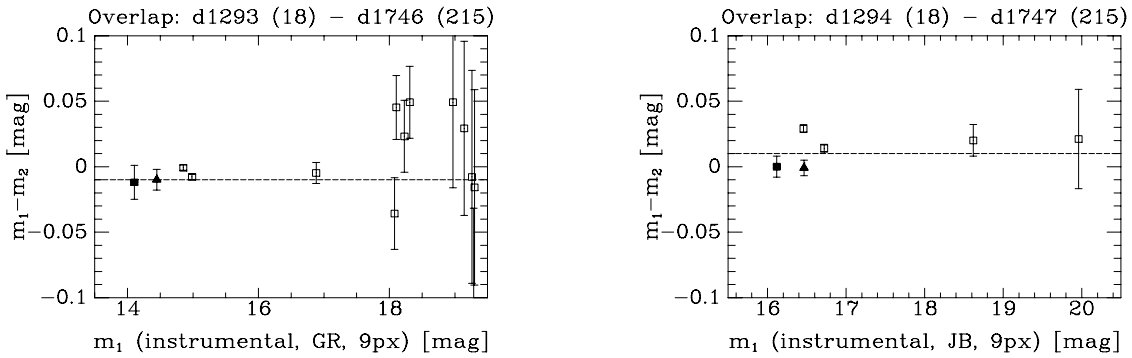

Figure B.9: Offset plots, field 215. The galaxy is R225.

Figure B.10: Offset diagrams, field 215.

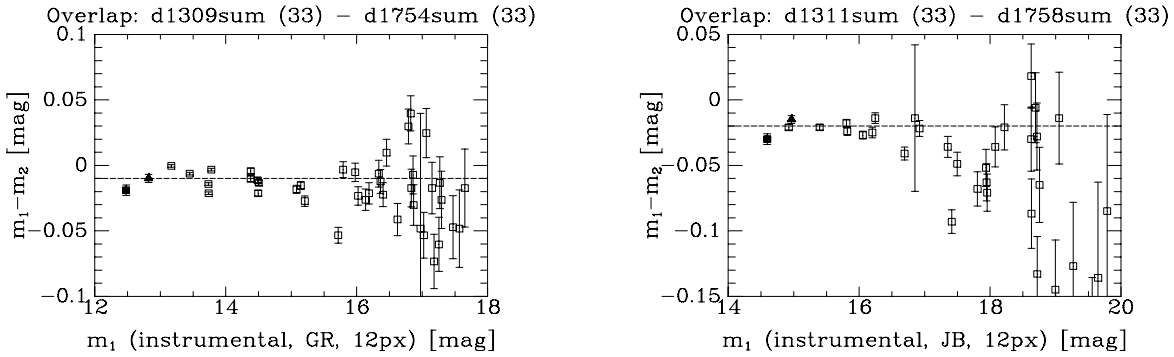

Figure B.11: Offset plots, field 33. The galaxy (seen to the very left) is R317.

Figure B.12: Offset diagrams, field 33.

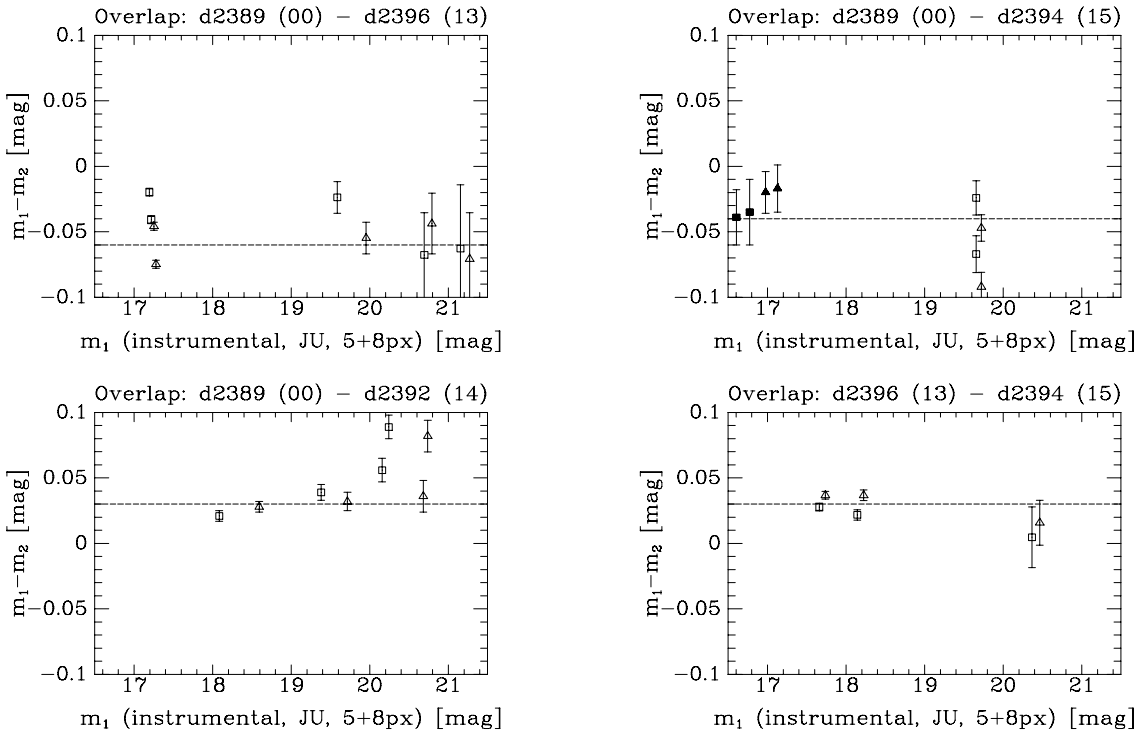

Figure B.13: Offset plots, the JU fields. The galaxies in the overlap between field 00 and 15 are R239 (faint) and R245 (bright). Here, two `phot` apertures are shown: open triangle: 5 pixels; open box: 8 pixels. The `galmag` points are as in the other offset plots: filled triangle: 6.26″; filled box: 10.08″.

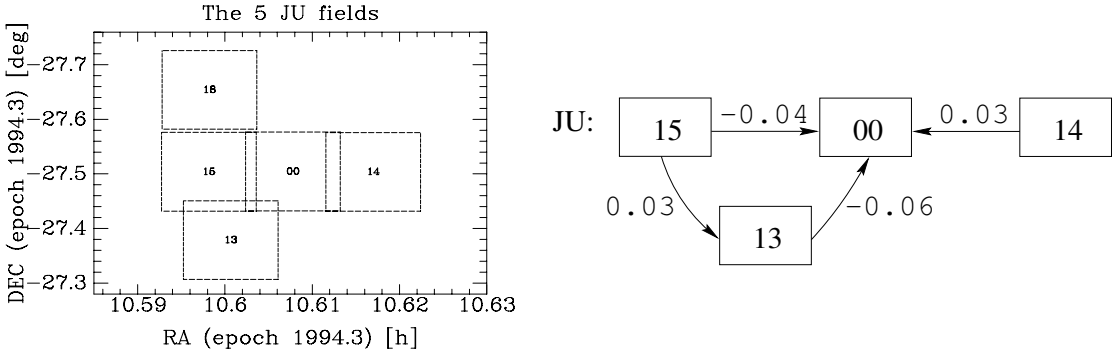

Figure B.14: Left: The position of the JU fields on the sky. Right: Offset diagrams, the JU fields.

Appendix C

The Standard Calibration

C.1 Standard Star Observations

Three standard star fields were observed: M67, PG1633+099, and SA110 centered on star 503 (hereafter SA110–503). The M67 field was observed with the telescope defocused, since the stars in that field are very bright; the other two fields were observed with the telescope focused. Examples of the visual appearance of a defocused and a focused star are shown in Figure C.1. four passbands were used: Gunn r, and Johnson V, B, and U. Standard stars were observed on all the nights that the Hydra galaxies were observed in Gunn r and Johnson B (night 1, 2, 3, 4, & 6), but not the night that the Hydra galaxies were observed in Johnson U (night 9). In addition, standard stars were observed on night 7. Details of the standard star observations are in Table C.1 and C.2.

Two naming schemes exist for the stars in the M67 field: The F numbers (e.g. F108), and the quadrant numbers (e.g. II20). They are almost, but not completely, disjoint. A finding chart for the F numbered stars is in Johnson & Sandage (1955). A finding chart for the quadrant numbered stars is in Eggen & Sandage (1964). Four stars (of interest to this study) with F numbers, are not marked on the map of Johnson & Sandage (1955), and have also been assigned quadrant numbers by Eggen & Sandage (1964). These are: F93=I12, F106=I11, F128=I198, and F129=I199. The finding chart of Schild 1983, which covers a smaller area than that of Johnson & Sandage (1955), has these 4 stars on it with the F numbers. Also note, that *two* stars are labeled 124 (i.e. F124) in the map of Johnson & Sandage (1955). The bright one (the one most to the east) is F124, the other one is I10.

Finding charts for the PG1633+099 and the SA110 field are in Landolt (1992).

The standard star images were reduced in the same way as the galaxy images, i.e. trim, bias, fat zero, dark, shutter, and flat field, with the exception, that the height of the fat zero background box (`boxh`) was set to 3 pixels instead of 21 pixels. This worked better for the stars close to the fat zero columns. The flat field used for the Johnson V images was a dome flat – no sky flats were taken in this filter.

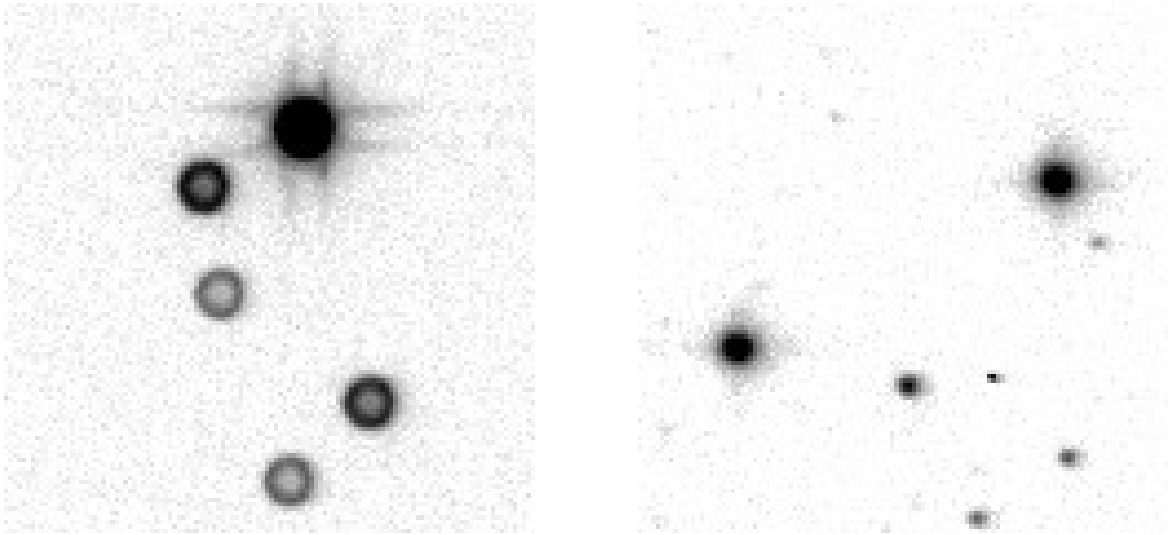

Figure C.1: Examples of defocused and focused star images. Both images are 120 pixels × 120 pixels ($61'' \times 61''$) sections, in the Gunn r filter, displayed logarithmically, and have north down and east to the right. Left: Part of the M67 field, image d1534, display cuts: z1=0, z2=1500. The bright star is F108 (r = 9.3 mag), and the semi-bright star to the (lower) right is F111 (r = 12.7 mag). Right: Part of the SA110–503 field, image d1603, display cuts: z1=0, z2=1200. The bright star to the left is 499 (r = 11.5 mag), the one to the right is 502 (r = 11.4 mag).

Table C.1: Standard star observations, by night

Night	Field	Airmass	Exposure time [sec]				Image name (dfsc #)			
			GR	JV	JB	JU	GR	JV	JB	JU
1	M67	1.33	5	10	20	120	d1263	d1262	d1264	d1266
1	PG1633+099	1.43	10	20	120	300	d1322	d1318	d1320	d1321
1	SA110–503	1.67	4	7	20	240	d1325	d1326	d1327	d1329
1	SA110–503	1.16	3	6	20	90	d1349	d1350	d1351	d1352
2	M67	1.34	5	10	20	120	d1388	d1389	d1390	d1391
2	PG1633+099	1.38	7	20	120	300	d1464	d1465	d1466	d1467
2	SA110–503	1.67	4	7	20	120	d1472	d1469	d1470	d1471
2	SA110–503	1.15	4	7	20	120	d1494	d1495	d1496	d1497
3	M67	1.34	5	10	20	120	d1534	d1535	d1536	d1537
3	PG1633+099	1.42	10	20	120	300	d1597	d1598	d1599	d1600
3	SA110–503	1.68	4	7	20	120	d1603	d1606	d1605	d1604
3	SA110–503	1.15	4	6	20	120	d1632	d1633	d1634	d1635
4	M67	1.34	5	10	20	120	d1689	d1690	d1691	d1692
4	SA110–503	1.60	4	10	20	120	d1771	d1772	d1773	d1774
4	PG1633+099	1.29	10	20	120	300	d1785	d1781	d1782	d1783
4	SA110–503	1.15	4	7	20	120	d1797	d1798	d1799	d1800
6	M67	1.35	5	10	20	120	d1948	d1949	d1950	d1951
6	SA110–503	1.44	4	10	20	120	d2016	d2018	d2021	d2022
6	PG1633+099	1.29	10	20	120	300	d2023	d2024	d2026	d2027
6	SA110–503	1.16	4	7	20	60	d2044	d2045	d2046	d2047
7	M67	1.33	5	10	20	120	d2092	d2093	d2094	d2095
7	SA110–503	1.64	4	7	20	120	d2145	d2148	d2147	d2146
7	SA110–503	1.15	4	7	20	120	d2169	d2170	d2171	d2172

Notes: Only the images used to fit the parameters of the transformation equations are shown (i.e. the images in the output from `mkimsets`). Airmass is an approximate average for the 4 exposures. In the actual calculations, the exact airmass for the individual images has been used. The M67 images were defocused, the PG1633+099 and SA110–503 were focused. GR, JV, JB, and JU are the 4 used passbands: Gunn r, and Johnson V, B, and U.

Table C.2: Standard star observations, by field

Night	Field	Airmass	Exposure time [sec]				Image name (dfsc #)			
			GR	JV	JB	JU	GR	JV	JB	JU
1	M67	1.33	5	10	20	120	d1263	d1262	d1264	d1266
2	M67	1.34	5	10	20	120	d1388	d1389	d1390	d1391
3	M67	1.34	5	10	20	120	d1534	d1535	d1536	d1537
4	M67	1.34	5	10	20	120	d1689	d1690	d1691	d1692
6	M67	1.35	5	10	20	120	d1948	d1949	d1950	d1951
7	M67	1.33	5	10	20	120	d2092	d2093	d2094	d2095
1	PG1633+099	1.43	10	20	120	300	d1322	d1318	d1320	d1321
2	PG1633+099	1.38	7	20	120	300	d1464	d1465	d1466	d1467
3	PG1633+099	1.42	10	20	120	300	d1597	d1598	d1599	d1600
4	PG1633+099	1.29	10	20	120	300	d1785	d1781	d1782	d1783
6	PG1633+099	1.29	10	20	120	300	d2023	d2024	d2026	d2027
1	SA110–503	1.67	4	7	20	240	d1325	d1326	d1327	d1329
1	SA110–503	1.16	3	6	20	90	d1349	d1350	d1351	d1352
2	SA110–503	1.67	4	7	20	120	d1472	d1469	d1470	d1471
2	SA110–503	1.15	4	7	20	120	d1494	d1495	d1496	d1497
3	SA110–503	1.68	4	7	20	120	d1603	d1606	d1605	d1604
3	SA110–503	1.15	4	6	20	120	d1632	d1633	d1634	d1635
4	SA110–503	1.60	4	10	20	120	d1771	d1772	d1773	d1774
4	SA110–503	1.15	4	7	20	120	d1797	d1798	d1799	d1800
6	SA110–503	1.44	4	10	20	120	d2016	d2018	d2021	d2022
6	SA110–503	1.16	4	7	20	60	d2044	d2045	d2046	d2047
7	SA110–503	1.64	4	7	20	120	d2145	d2148	d2147	d2146
7	SA110–503	1.15	4	7	20	120	d2169	d2170	d2171	d2172

Notes: Same data as in Table C.1.

C.2 Aperture Photometry

To establish the transformation between instrumental magnitudes and standard magnitudes, we need to do photometry on the standard stars. Since the galaxy surface photometry is done as aperture photometry, we also need to do aperture photometry on the standard stars, as opposed to for example point spread function fitting.

The larger the aperture, the more of the flux from the star is within the aperture. But the larger the aperture, the larger is the error from the sky subtraction, and the more cosmic ray events will be within the aperture. Thus, the optimal aperture is one which is large enough to enclose most of the flux, but otherwise is as small as possible.

The correction for the finite size of the aperture is called the aperture correction. It is computed from a growth curve, i.e. a plot of magnitude within a given aperture versus aperture size. The aperture correction is simply the magnitude difference between the asymptotic magnitude and the magnitude at the given aperture.

The most straightforward way to determine the aperture correction is to measure it directly from a number of growth curves. A more advanced method is the DAOgrow algorithm (Stetson 1990), implemented in the task `mkapfile` in `digiphotx.photcalx`. It fits a five parameter (with usually only 3 of them free) stellar profile model to the growth curves for one or more stars in one or more images. It then computes the aperture correction from a given aperture to the largest aperture.

One of the five parameters in the model, R_i, represent the seeing radius for the individual images. The other four parameters are global for all the images. For more details, see Stetson (1990).

C.2.1 The Focused Images

Aperture photometry using the task `phot` (in `digiphotx.apphotx`) was done on the 5 standard stars in the PG1633+099 images and the 8 standard stars in the SA110–503 images (cf. Table C.11). As previously mentioned, these two fields were observed with the telescope focused. The apertures used were $2, 3, \ldots, 30$ pixels (1 pixel = $0.5073''$). The crucial sky fitting algorithm parameters (`fitskypars`) were set as follows: `salgorithm`=gauss, `annulus`=30.0 pixels, and `dannulus`=10.0 pixels, giving a background region of 30–40 pixels, or 15.22–$20.29''$. The length of the box within which the star is centered, `centerpars.cbox`, was set to 10 pixels.

`mkapfile` was used to determine the aperture correction from a number of apertures, $7, 8, \ldots, 14$ pixels to "infinity" (taken as the largest aperture, 30 pixels). The resulting aperture corrections versus the seeing is shown in Figure C.2.

The figure shows, as expected, that the size of the aperture correction decreases with increasing aperture size. It also shows, that the aperture correction (for most of the apertures used) is significantly seeing dependent.

It was decided, that an aperture of 9 pixels ($4.57''$) was optimal. The aperture correction versus seeing for this aperture only is shown in Figure C.3.

As can be seen, the dependence of aperture correction on seeing is very smooth. This is not totally surprising, since the seeing is calculated by `mkapfile` itself, and is one of the parameters it uses in the stellar profile model.

To further reduce the scatter, a 3rd order (`order`=4) Legendre polynomial was fitted to the points using `gfit1d`. The fit was very good, with residual no larger than 0.0008 mag, and typically 0.0002 mag. The final aperture corrections for the focused stars were calculated from the fit. The errors from `mkapfile` were used.

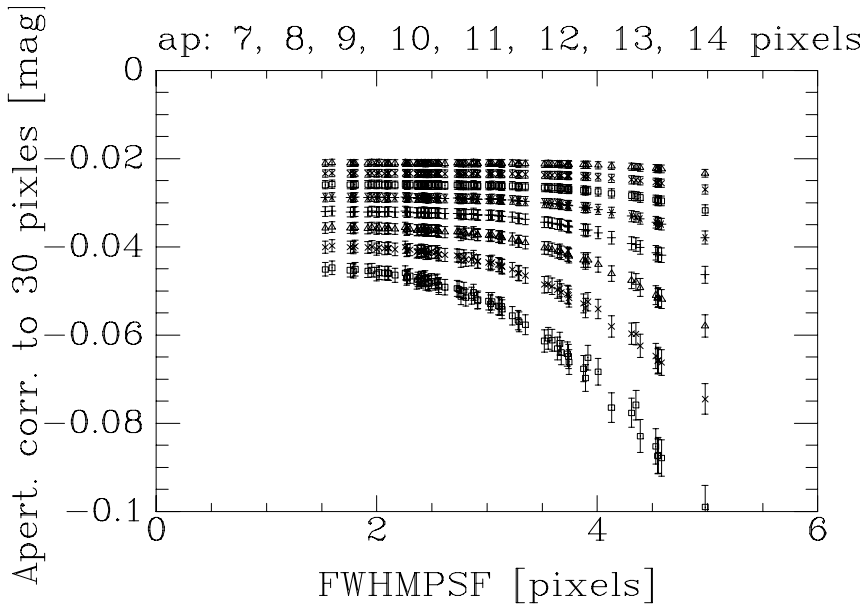

Figure C.2: Aperture corrections for different sized apertures, from 14 pixels (top) to 7 pixels (bottom). FWHMPSF is calculated as 2.355 times the seeing radius from `mkapfile`. For a Gaussian profile, 2.355 is the ratio between the FWHM and the standard deviation.

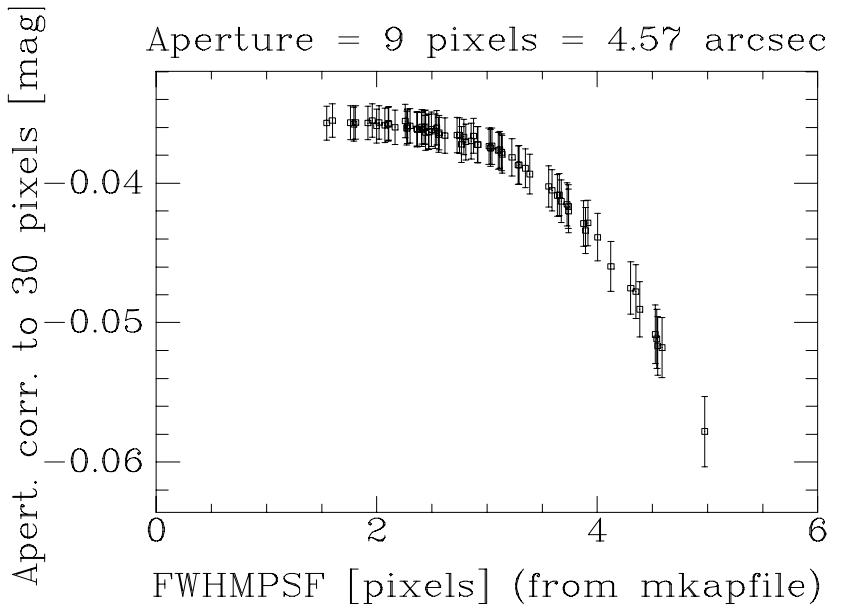

Figure C.3: Aperture corrections for the 9 pixels aperture. FWHMPSF is calculated as 2.355 times the seeing radius from `mkapfile`.

Seeing versus night is plotted in Figure C.4, right panel. The corresponding aperture correction variation with night is shown in Figure C.4, left panel.

Finally, `phot` was run again, this time with only one aperture: 9 pixels.

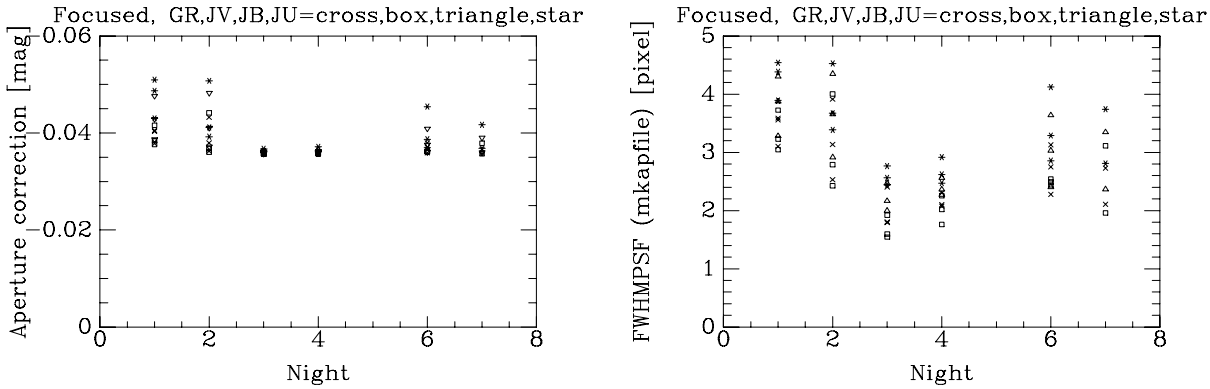

Figure C.4: Aperture correction and seeing versus night, same data as in Figure C.3. Left: Aperture correction versus night. Right: Seeing (FWHMPSF) versus night. FWHMPSF is calculated as 2.355 times the seeing radius from `mkapfile`.

C.2.2 The Defocused Images

`phot` was run on 4 well isolated stars (F81, F153, F170, & I27) in the defocused images, with apertures $5, 6, \ldots, 42$ pixels, and with `salgorithm`=gauss, `annulus`=42.0 pixels, and `dannulus`=14.0 pixels. Even though the defocused stars did not have a peak to define their centers, they were centered well using a somewhat large box, `centerpars.cbox`=15 pixels, which still was small enough to exclude the neighboring stars.

A large effort went into trying to get `mkapfile` to fit the profiles of the defocused stars, and compute the aperture correction. This did not succeed.

Instead, aperture corrections at 12 and 15 pixels were manually read from the growth curves that `mkapfile` produced. These growth curves, one for each image, were based on the above 4 stars. An example of such a curve is shown in Figure C.5. The resulting aperture corrections are shown in Table C.3, and plotted in Figure C.6, the two left panels. In the top right panel, the difference between the two is shown.

From the plots it can readily be seen, that the aperture correction is not the same for the 4 filters, and that it is not the same from night to night. Further, the difference between the aperture corrections at the two apertures is not the same for the 4 filters and from night to night.

The M67 field of this study had 23 stars in common with the standard stars of Jørgensen (1994). Besides of these standard stars, 36 stars were selected as "program" stars on the following three criteria: they should be somewhat bright (we required a peak > 500 ADU in the GR image d1262), they should not be too close to other stars, and they should have a unique name. The reason for including these program stars was: 1) the derived magnitudes for these stars could be useful in another context (they could perhaps serve as tertiary standard stars), and 2) the more stars, the better statistics for the test of the aperture correction, see below.

`phot` was run on these 59 stars, using two apertures: 12 and 15 pixels. `cbox` was increased to 20 pixels. The reason for using two apertures was to test the aperture corrections determined above at these two apertures. Since per definition

$$m(\text{total}) = m(12\text{px}) + \text{apcor}(12\text{px}) \quad \text{(C.1)}$$

$$= m(15\text{px}) + \text{apcor}(15\text{px}), \quad \text{(C.2)}$$

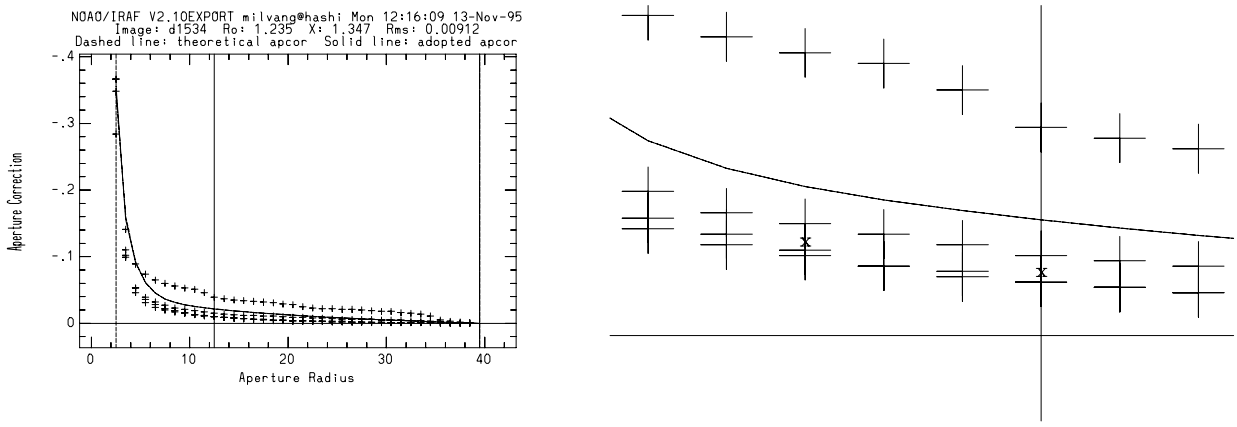

Figure C.5: Example of a growth curve (or *aperture correction curve*) made by `mkapfile`. The image is d1534, which is in Gunn r and from night 3.
Left: The entire curve. The x-axis is aperture radius minus 2.5 pixels. The y-axis is aperture correction with respect to the magnitude at 42 pixels. The dotted vertical line is at 5 pixels, the left solid vertical line is at 15 pixels, and the right solid vertical line is at 42 pixels. The curve is the fit, which was not used.
Right: A zoom around apertures 12 and 15 pixels. The "x"-s show approximately the values read by the user as the aperture correction to be used. As can be seen, the top point has been regarded as erroneous and omitted from the eye fit. The 15 pixels aperture is at the vertical solid line, the 12 pixels aperture is 4 "steps" to the left. The 3 "good" values at 12 pixels are -0.0150, -0.0160, -0.0210, with the eye fit mean of -0.0173. The arithmetical mean is also -0.0173. The estimated uncertainty on this is 0.002.

it follows that

$$m(12\text{px}) - m(15\text{px}) = -\left[\text{apcor}(12\text{px}) - \text{apcor}(15\text{px})\right]. \tag{C.3}$$

This only holds in the absence of contributions from neighboring stars and cosmic ray events. $m(12\text{px}) - m(15\text{px})$ for the above 59 stars for each image (with one image per night per filter) is shown in Figure C.7 for Gunn r and Johnson V, and Figure C.8 for Johnson B and U. The median value of $m(12\text{px}) - m(15\text{px})$ for each of the 24 images is shown in Figure C.6, bottom right panel. In the top right panel of the same figure is shown $-\left[\text{apcor}(12\text{px}) - \text{apcor}(15\text{px})\right]$.

As can be seen, the form of the "curves" is qualitatively the same, but there is a small offset. This offset is probably due to contributions from neighboring stars for the sample of 59 stars. This contribution is much less in the sample of 4 stars, since they were selected from being isolated. This can be checked by inspecting these 4 stars in Figure C.7 and C.8. They are almost always in the lower range of the 59 points. The mapping between names and serial ID number for these 4 stars is F81=ID1, F153=ID26, F170=ID28, and I27=ID38. F81 with and ID of 1 is particularly easy to locate. The conclusion is, that the manually determined aperture corrections pass the test of equation (C.3).

The M67 field is quite crowded. For example, F128/I198 and F129/I199 are 25 pixels ($13''$) apart, F129/I199 and F130 are 23 pixels ($12''$) apart, and F106/I11 and its fainter neighbor I10 are only 16 pixels ($8''$) apart. This also shows up in the magnitude difference plots in Figure C.7 and C.8. The mapping between names and serial ID number for these 4 stars is F128/I198=ID15, F129/I199=ID16, F130=ID17, and F106/I11=ID7. Especially F106/I11 is very contaminated. The above speaks in favor of a small aperture

Also, the images are quite defocused. Inspection of screen dumps of the images used in Jørgensen

Table C.3: The manually measured aperture corrections, by night

night	filter	image	apcor12	apcor15	delta
1	GR	d1263	–0.032	–0.018	0.015
1	JV	d1262	–0.027	–0.014	0.012
1	JB	d1264	–0.034	–0.019	0.014
1	JU	d1266	–0.048	–0.023	0.025
2	GR	d1388	–0.025	–0.017	0.009
2	JV	d1389	–0.020	–0.012	0.007
2	JB	d1390	–0.032	–0.020	0.012
2	JU	d1391	–0.044	–0.026	0.018
3	GR	d1534	–0.017	–0.012	0.006
3	JV	d1535	–0.015	–0.010	0.005
3	JB	d1536	–0.021	–0.016	0.006
3	JU	d1537	–0.043	–0.030	0.013
4	GR	d1689	–0.021	–0.014	0.007
4	JV	d1690	–0.017	–0.013	0.004
4	JB	d1691	–0.024	–0.015	0.009
4	JU	d1692	–0.040	–0.027	0.013
6	GR	d1948	–0.022	–0.017	0.005
6	JV	d1949	–0.017	–0.012	0.005
6	JB	d1950	–0.023	–0.015	0.008
6	JU	d1951	–0.038	–0.024	0.013
7	GR	d2092	–0.021	–0.015	0.006
7	JV	d2093	–0.016	–0.010	0.005
7	JB	d2094	–0.021	–0.014	0.008
7	JU	d2095	–0.038	–0.027	0.011

Notes: apcor12 and apcor15 are the aperture corrections for the defocused images at an aperture of 12 pixels and 15 pixels, respectively, in magnitudes. delta is minus the difference between the two, i.e. delta = –(apcor12–apcor15). The aperture corrections were manually measured from growth curves based on the 4 stars F81, F153, F170, and I27. Uncertainties were estimated from the scatter of the used individual points. Typical values are: GR: 0.002 mag, JV: 0.001 mag, JB: 0.002 mag, JU: 0.006 mag. When doing the eye fit, the JU values from night 4 was noted as uncertain, and a more realistic uncertainty for these values is probably 0.010–0.015 mag.

(1994) shows, that that these images were less defocused than the images of this study, despite that both used a defocusing of +200 encoder steps. This is probably because the filters are now placed in the DFOSC, instead in the instrument adapter as they previously were.

Jørgensen (1994) used two apertures for her defocused images, 7.52″ and 9.40″.

It was decided to use an aperture of 12 pixels (6.09″), and to use the corresponding aperture corrections listed in Table C.3. As previously mentioned, the background region was 42–56 pixels, i.e. 21.31–28.41″.

Finally, we can compare the aperture corrections for the focused and the defocused images. This in done in Figure C.9. The variation with night is quite similar for the focused and defocused images.

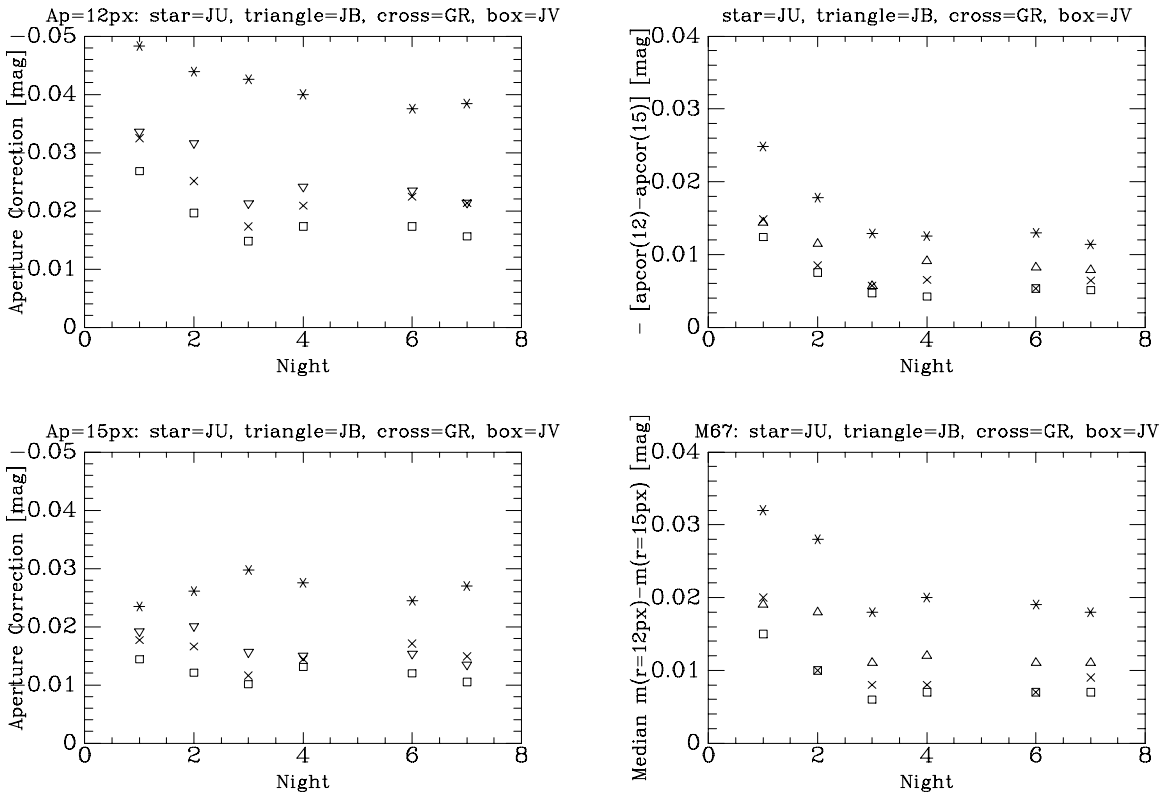

Figure C.6: The manually measured aperture corrections for the defocused images. Symbol legend: star: Johnson U, triangle: Johnson B, cross: Gunn r, box: Johnson V. Top left: aperture correction at 12 pixels. Bottom left: aperture correction at 15 pixels. Top right: difference between the aperture corrections at 12 and 15 pixels. Typical uncertainties on the manually measured aperture corrections are: GR: 0.002 mag, JV: 0.001 mag, JB: 0.002 mag, JU: 0.006 mag (night 4: 0.010 mag). Bottom right: difference between the magnitudes within 12 and 15 pixels (median value of 59 stars, cf. Figure C.7 and C.8).

Table C.4: Mapping between star names and ID numbers

ID	Name	Type	ID	Name	Type	ID	Name	Type
1	M67–F81	standard	21	M67–F141	standard	41	M67–I56	program
2	M67–F83	program	22	M67–F143	program	42	M67–I60	program
3	M67–F93/I12	standard	23	M67–F145	program	43	M67–II20	program
4	M67–F94	program	24	M67–F147	program	44	M67–II22	standard
5	M67–F95	standard	25	M67–F149	program	45	M67–II30	program
6	M67–F105	standard	26	M67–F153	standard	46	M67–III1	program
7	M67–F106/I11	standard	27	M67–F164	program	47	M67–III2	program
8	M67–F108	standard	28	M67–F170	program	48	M67–III7	program
9	M67–F111	standard	29	M67–I1	program	49	M67–III12	program
10	M67–F115	program	30	M67–I5	program	50	M67–IV2	program
11	M67–F117	standard	31	M67–I9	program	51	M67–IV3	program
12	M67–F119	program	32	M67–I14	program	52	M67–IV4	program
13	M67–F124	standard	33	M67–I15	standard	53	M67–IV6	program
14	M67–F127	standard	34	M67–I17	program	54	M67–IV12	program
15	M67–F128/I198	standard	35	M67–I20	standard	55	M67–IV13	program
16	M67–F129/I199	standard	36	M67–I24	program	56	M67–IV21	program
17	M67–F130	standard	37	M67–I25	standard	57	M67–IV34	program
18	M67–F132	program	38	M67–I27	standard	58	M67–IV35	program
19	M67–F134	standard	39	M67–I31	program	59	M67–IV59	program
20	M67–F135	standard	40	M67–I49	standard			

Notes: ID is the identification serial number which `phot` uses internally. It is also the number used in Figure C.7 and C.8.

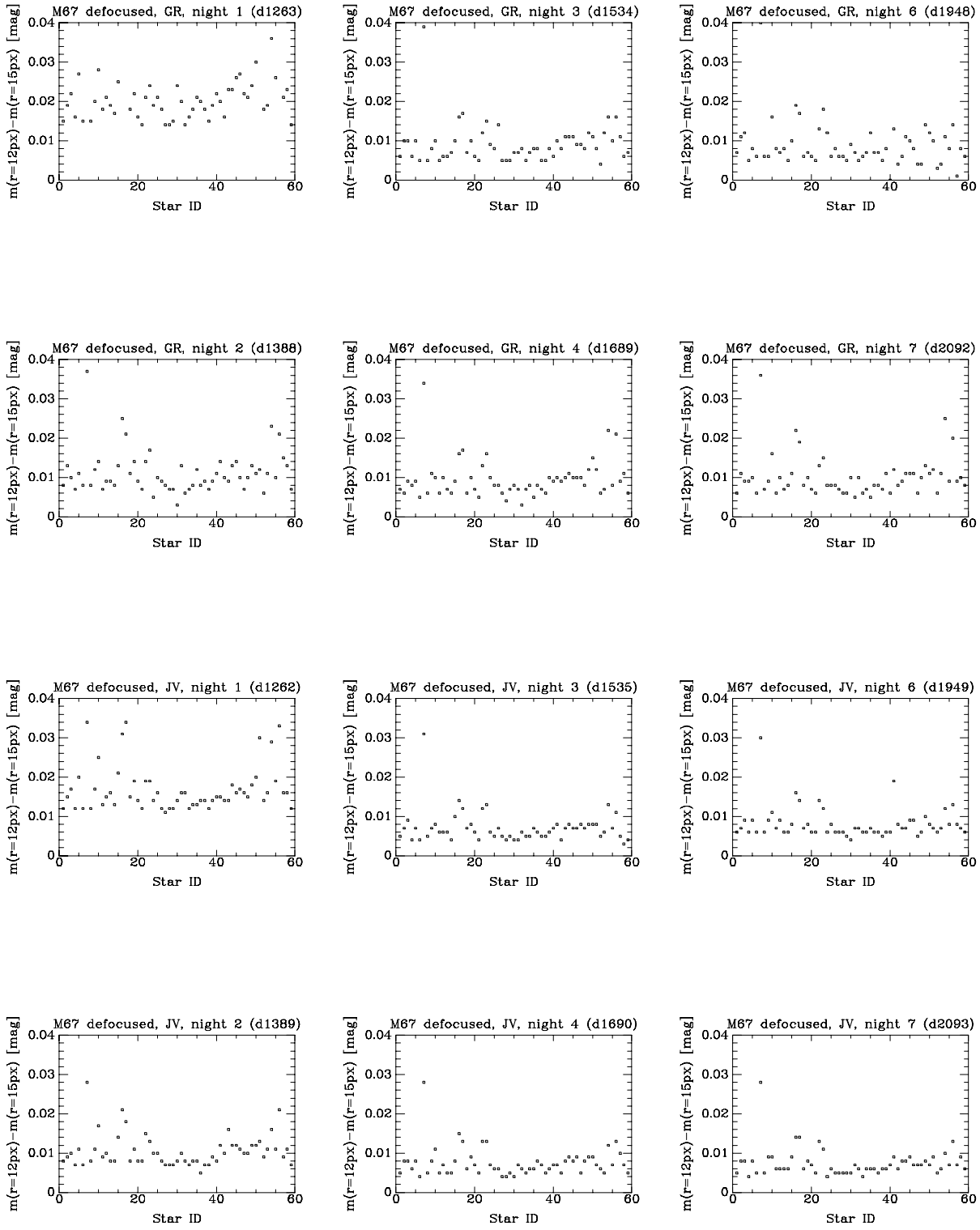

Figure C.7: Magnitude difference between apertures of 12 and 15 pixels. Top 6 panels: Gunn r. Bottom 6 panels: Johnson V. Along the x-axis is star ID number; mapping between this and star name can be found in Table C.4.

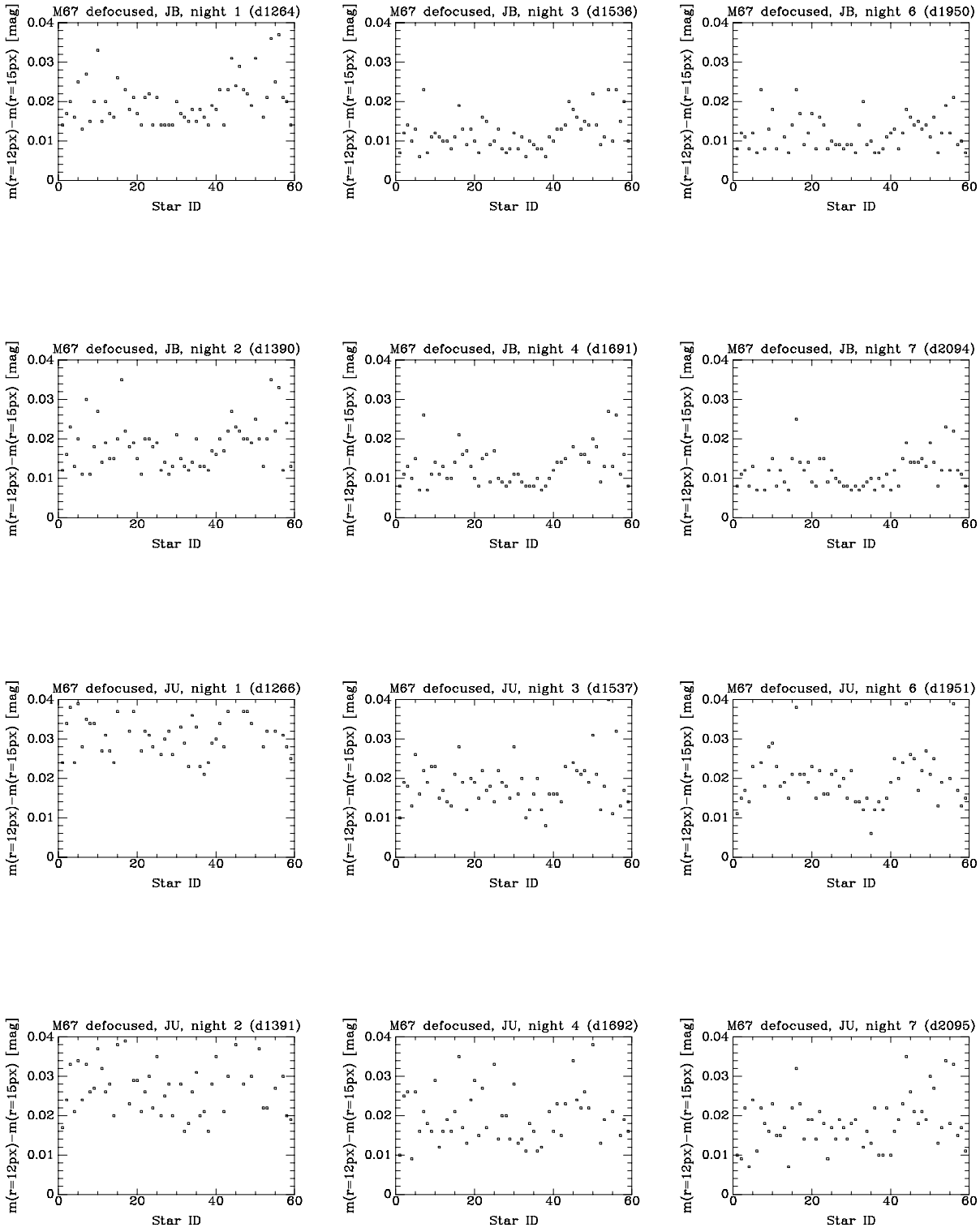

Figure C.8: Magnitude difference between apertures of 12 and 15 pixels. Top 6 panels: Johnson B. Bottom 6 panels: Johnson U. Along the x-axis is star ID number; mapping between this and star name can be found in Table C.4.

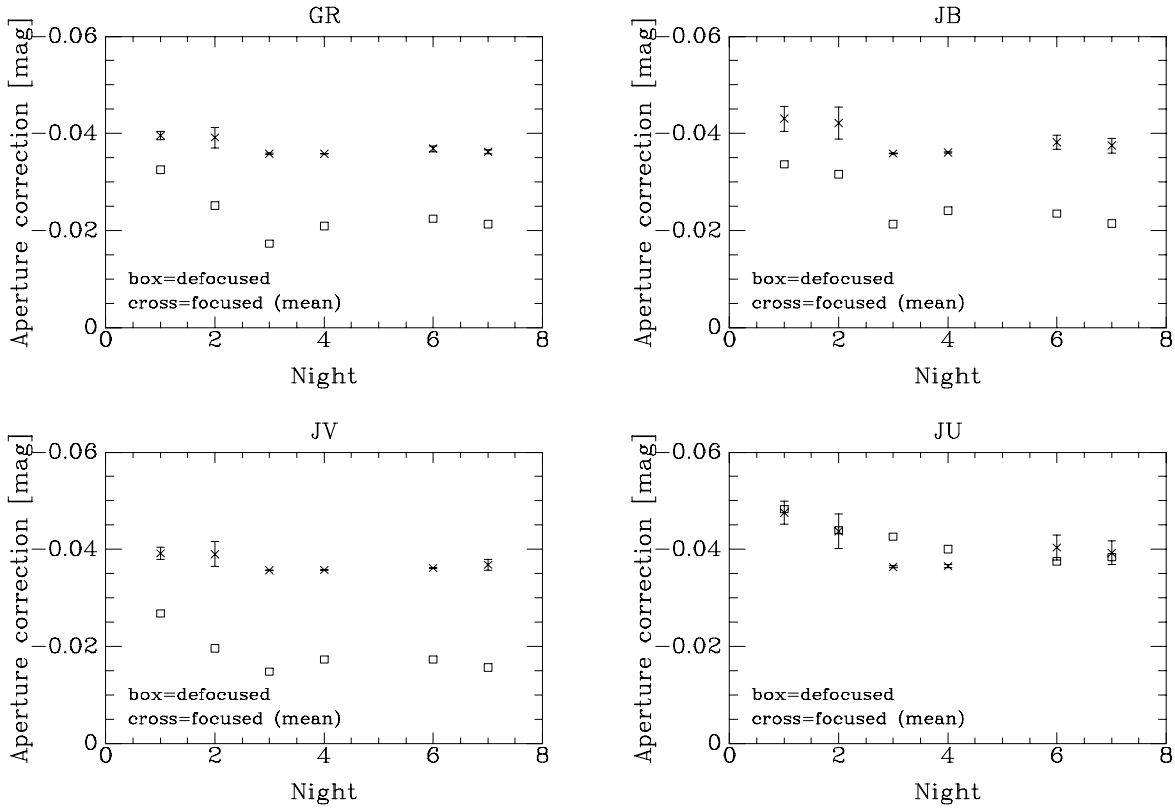

Figure C.9: Aperture corrections for the focused and defocused images. The focused data are the mean of the usually 3 images (2 SA110–503, and 1 PG1633+099) per night per filter, and are based on the data in Figure C.4, left panel. The aperture is 9 pixels (4.57″). The defocused data are the same as in Figure C.6, upper left panel. The aperture is 12 pixels (6.09″). Typical uncertainties on the aperture corrections for the defocused images are: GR: 0.002 mag, JV: 0.001 mag, JB: 0.002 mag, JU: 0.006 mag (night 4: 0.010 mag).

C.3 Extinction and Night Coefficients

As Table C.2 shows, the SA110–503 field was observed twice every night at different airmasses, typically 1.65 and 1.15. The extinction coefficient, k, can now be determined by fitting the relation $m = m_0 + kX$ to the two $(X, m(X))$ points for each night and filter. m is the observed magnitude, X is the airmass, and m_0 is the magnitude of the star outside the atmosphere. By the *observed magnitude* we mean the magnitude that `phot` outputs, m_{phot}, which in turn is given by

$$m_{phot} = \texttt{zmag} - 2.5 \log \left(\frac{I_{star+sky} - I_{sky}}{t_{exp}} \right). \tag{C.4}$$

`zmag` is the arbitrary zero point of the magnitude scale, $I_{star+sky}$ is the total number of counts (in ADU) from the star and the sky background within the aperture, I_{sky} is the equivalent number of counts (in ADU) from the sky background alone within the aperture, and t_{exp} is the exposure time (in seconds, say). `zmag` = 22 mag was used.

Since there are 8 stars in the SA110–503 field, we get 8 determinations of k for each image. The final k can then be calculated as the mean, with the possibility of rejecting points. This procedure is implemented in the task `stars.calext`. The package `stars` is written by IJ.

First, `mkimsets` was used to create an image set file for each night for the SA110–503 images.

Second, `mknobsfile` was used to create an observations file for each night for the SA110–503 images. `mknobsfile` inputs the APPHOT databases (the *image*`.mag.1` files) and the image set file, and outputs the observations file[1]. In the process of compiling the data of the multiple APPHOT databases into one file, it also does the aperture correction.

`calext` is given an observations file and a fields file. The first column of the latter contains the star names to be used. Optionally, in the second column it contains a color, e.g. (B–V). One can either fit k as a constant, or as a function of star color, $k = k((B-V)) = c_1 + c_2 \cdot (B-V)$, still for the same given filter.

`calext` was first run without a color term. The stars which seemed to deviate too much were deleted. The deleted stars are shown in Table C.5. No more than 3 of the 8 stars were deleted. Some of the deleted stars were inspected in the images; in some cases, there were cosmic ray events within the aperture, whereas in other cases, noting unusual could be seen. It should be noted, that the star SA110–502, which was deleted in 4 out of 6 cases in Johnson U, is very faint in that filter, U = 17.0 mag (cf. Table C.11).

Table C.5: Deleted Stars When Determining the Extinction

Night	GR	JV	JB	JU
1	–	496	502, 504	502
2	–	–	–	502
3	–	504	–	504
4	–	496	504	497, 504
6	497, 504	497	496	502, 497, 504
7	–	506	504	502

Notes: All stars are from the SA110 field. Magnitudes of the stars can be found in Table C.11.

[1]It should be noted, that the output from the `mknobsfile` in `digiphotx.photcalx` and from the `mknobsfile` in `digiphot.photcal` is not in the same format: the x version has eight columns with OTIME as the third, the non-x version has only seven columns, and does not have OTIME. Here, the x version was used.

The resulting nightly extinctions coefficients are shown in Figure C.10 and Table C.6. It can be seen, that there are variations from night to night. These variations are qualitatively the same in all the filters.

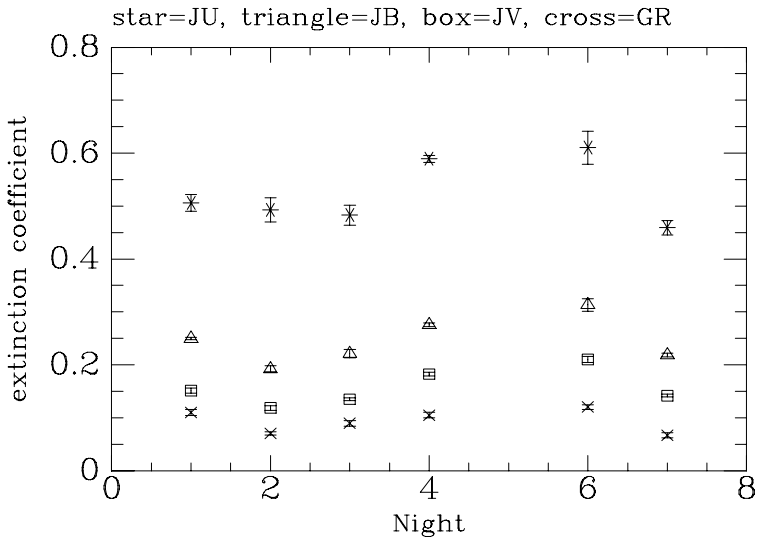

Figure C.10: The nightly extinction coefficients.

Table C.6: The Nightly Extinction Coefficients

Night	GR	JV	JB	JU
1	0.110	0.151	0.250	0.506
2	0.070	0.118	0.192	0.493
3	0.089	0.135	0.221	0.483
4	0.105	0.182	0.276	0.589
6	0.120	0.210	0.313	0.610
7	0.067	0.142	0.219	0.459

`calext` was also run fitting k as a function af (B–V), $k = c_1 + c_2 \cdot (B - V)$, with (B–V) taken from Landolt (1992). The stars which were deleted were the same as when fitting k without a color term, with three exceptions (night 1, JB: star 502 & 504 *not* deleted, night 2, JU: star 502 *not* deleted), and they were not very clear. The resulting color term coefficients, c_2, averaged over the 6 nights, were -0.007 ± 0.003, -0.001 ± 0.003, -0.012 ± 0.009, and -0.104 ± 0.043, for GR, JV, JB, and JU, respectively. At face value, these are different from zero at the 2.0, 0.5, 1.4, & 2.4 sigma level, respectively. For JU it was noted when doing the fit of $c_1 + c_2 \cdot (B - V)$ to the 8 values of k per night, that the scatter was very high, and that the mean c_2 for the given night was very sensitive to which stars were included in the fit, which in turn was not easy to decide. The 6 mean values of c_2 scatter a lot, too, from 0.00 to -0.27, with the latter value being for night 2 where the star 502 *was* included.

It was concluded, that if there was any color dependence it was small, and that it therefore was appropriate to use the color independent fit of k.

Now having determined the nightly extinction coefficients, we were ready to apply these to all the stars. `mkimsets` and `mknobsfile` (including aperture correction) were run on all the stars in the 3 fields, and the names were corrected to what they were in the standard catalog. All the magnitudes were then corrected for extinction (Table C.6) using the task `stars.magcorrect`. `magcorrect` can also apply night coefficients, but that function was not used at this step, the parameter `nitecoef` was set to `""`. The above was done separately for the focused and defocused images, and separately for the 6 nights.

Having corrected the magnitudes for extinction, they should in principle be consistent from night to night. However, this is usually not the case, so one brings them to the same relative system by *adding* so-called night coefficients. The night coefficient for night i with respect to night *ref* is given by

$$n(\text{night } i) = \langle m(\text{night } ref, \text{star } j) - m(\text{night } i, \text{star } j) \rangle, \tag{C.5}$$

where the mean is taken over all stars j observed on both of the nights. If a star has been observed more than once on a given night, $m(\text{night } i, \text{star } j)$ can be taken to be the mean value. Typically, night coefficients are of the order of a few hundredths of a magnitude.

Since night coefficients are relative, it is arbitrary which night is chosen as reference night. One might as well chose the night that would seem to be the most reliable one, e.g. the night with the most observations, or the night with the lowest extinction. Here, night 2 was chosen.

Calculations of night coefficients can be done by the task `stars.calnitecoef`. It calculates mean magnitudes using the task `stars.meanphot` (or, alternative, the user can do that directly first, and tell `calnitecoef` to use these mean magnitude files). The user can do the fitting of the mean of the individual night coefficients (one for each star in common) interactively.

Night coefficients with respect to night 2 were determined for the 6 nights, separately for the focused and the defocused images, using `calnitecoef`. The result is shown in Figure C.11.

As can be seen, the night coefficients are very large, indicating that something is wrong. It is also striking, that the variation of the night coefficients from night to night (Figure C.11) is qualitatively the same as the variation of the *nightly extinction coefficients* from night to night (Figure C.10). This suggests, that the nightly extinction coefficients are uncorrect.

The weather needs to be photometric in order to be able to determine the extinction coefficient. If the weather is not photometric, the stars will appear too faint.

If it is photometric when observing at low airmass, but not photometric when observing at high airmass, the determined extinction coefficient will be higher than the true value. If it is the other way round, the determined extinction coefficient will be lower than the true value. If it is not photometric neither at low nor at high airmass, anything can happen.

Notes about the weather was written by the observer usually on top of each page of the observations log, see Table C.7. These are the only notes about the weather in the log for the days in question. Only once it was stated, that the weather was not photometric for sure. A few places it was stated, that the weather might not be photometric.

If we assume, that the weather in fact was *not* photometric where it was stated that it *might* not be, we would expect, that the extinction coefficients were too high for night 3, and too low for night 6. In Figure C.10 one sees, that the night 3 extinction coefficients are not high compared to the values from the other nights, so it does not seem likely, that the night 3 values are actually *too* high. One also sees, that the night 6 extinction coefficients are high compared to the values from the other nights, so it does not seem likely, that the night 6 values are actually too *low*, either.

However, the above assumption might not be correct. It is difficult *per se* to precisely determine whether the weather is photometric, and since the observer is busy observing, he/she cannot spend all the time monitoring the weather. We will conclude, that it was not photometric all the time, but that we cannot say precisely *when*.

In any case, the night coefficients based on the nightly extinction coefficients are very large, and the variation does resemble that of the nightly extinction coefficients, so something with the latter must be wrong.

It was concluded, that the nightly extinction coefficients for night 4 and 6 were too high. It was decided to use the mean value of the nightly extinction coefficients for night 1, 2, 3, and 7 as *the* extinction coefficient for the given filter. Those 4 final extinction coefficients are shown in Table C.8. Also shown are the La Silla mean extinction coefficients. For JV, JB, & JU, the adopted values are 4–10% higher than the La Silla mean values. For GR, the adopted value is 30% higher than the La Silla mean value. However, the adopted value agrees very well ($< 4\%$) with the values of run 1–3 of Jørgensen (1994), in which the very same filter (ESO #460) was used. These comparisons give confidence that the adopted values of the extinction coefficients are reasonable.

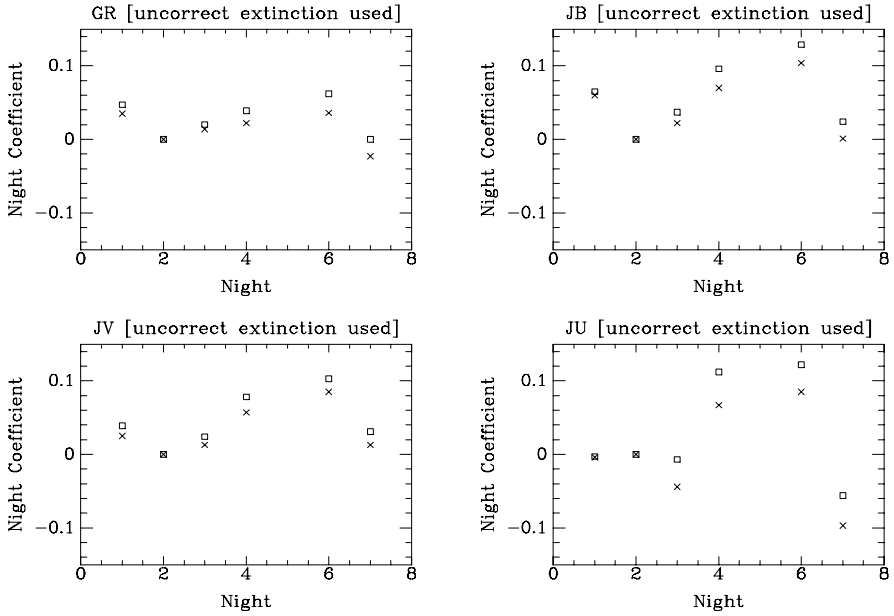

Figure C.11: The night coefficients based on the nightly extinction coefficients (Table C.6 and Figure C.10). The night coefficients are with respect to night 2. Legend: Boxes: defocused images. Crosses: focused images.

The observations were extinction corrected using the new extinction coefficients, and the night coefficients were determined again, still with respect to night 2. The result is shown in Figure C.12.

Now the night coefficients were of a more reasonable size, although still somewhat large. What is striking is, that the focused and defocused stars do not have the same night coefficients, except for the reference night, night 2, where they per definition are 0. This indicates, that night 2 is not representative – if another night had been chosen as reference night, this offset would have been smaller for more of the nights (and of course for night 2, it would be large and with opposite sign).

It was decided to proceed and to calculate night coefficients for the combined sample of focused and defocused stars. In doing this, the defocused stars were weighted more than the focused, as 59 stars to 13 stars. When fitting, it was sometimes obvious, that there was an offset between the focused and defocused individual night coefficients. Nevertheless, the mean was calculated more or less blindly, only throwing away points which seemed to deviate for other reasons. The result is shown in Figure C.12 and Table C.9.

Finally, the night coefficients were applied to the already aperture and extinction corrected

Table C.7: The Notes in the Observations Log About the Weather

Night	Page	Weather	Standard fields observed
1	1	Photometric – to be checked	
1	2	Photometric	M67
1	3	Photometric	
1	4	Photometric	
1	5	Photometric	PG1633+099, SA110 (high airmass)
1	6	Photometric	SA110 (low airmass)
1	7	Photometric	
2	8	Photometric	M67
2	9	Photometric	
2	10	Photometric	
2	11	Photometric	PG1633+099, SA110 (high airmass)
2	12	Photometric	SA110 (low airmass)
2	13	Photometric	SA110 (low airmass) continued
3	14	[nothing written]	
3	15	Photometric	M67
3	16	Photometric	
3	17	Photometric	
3	17	May not be photometric right now, check this	PG1633+099
3	18	Photometric (?)	SA110 (high airmass)
3	19	Photometric	SA110 (low airmass)
4	20	Photometric	
4	21	Photometric	M67
4	22	Photometric	
4	22	NON-photometric	
4	23	Photometric? check this	
4	24	Photometric	SA110 (high airmass)
4	25	Photometric	PG1633+099
4	26	Photometric	SA110 (low airmass)
6	25	Photometric	
6	26	Photometric	M67
6	27	Photometric	
6	28	Photometric	SA110 (high airmass)
6	29	Photometric (?)	PG1633+099, SA110 (low airmass)
6	30	Photometric (?)	
7	31	Photometric	M67
7	32	Photometric	
7	33	Photometric	SA110 (high airmass)
7	34	Photometric	SA110 (low airmass)
7	35	Photometric	

Notes: The weather was noted on top of each page of the log book, except for page 17 and 22, where it was also noted further down. On night 5, the first page number was set to 21 instead of 27 as it should have been, therefore the strange page numbers for night 6 and 7.

observations files using `magcorrect` again, this time setting `extcoef=""`. These magnitudes are called *instrumental magnitudes*. In short, they are given by

$$m_{inst} = m_{phot} + \text{apcor} - kX + n, \tag{C.6}$$

where k is the extinction coefficients for the given filter, X is the airmass for the given observation,

Table C.8: The Final Extinction Coefficients

Filter	GR	JV	JB	JU
Adopted ext. coeff.	0.084	0.137	0.220	0.485
La Silla mean ext. coeff.	0.065	0.125	0.212	0.459

Notes: The adopted extinction coefficient for a given filter is the mean of the nightly extinction coefficients for night 1, 2, 3, and 7 (cf. Table C.6 and Figure C.10). The La Silla mean values are taken from Jørgensen (1994). This author used the exact same filters as in this study, viz. ESO # 460, 451, 450, & 632, respectively.

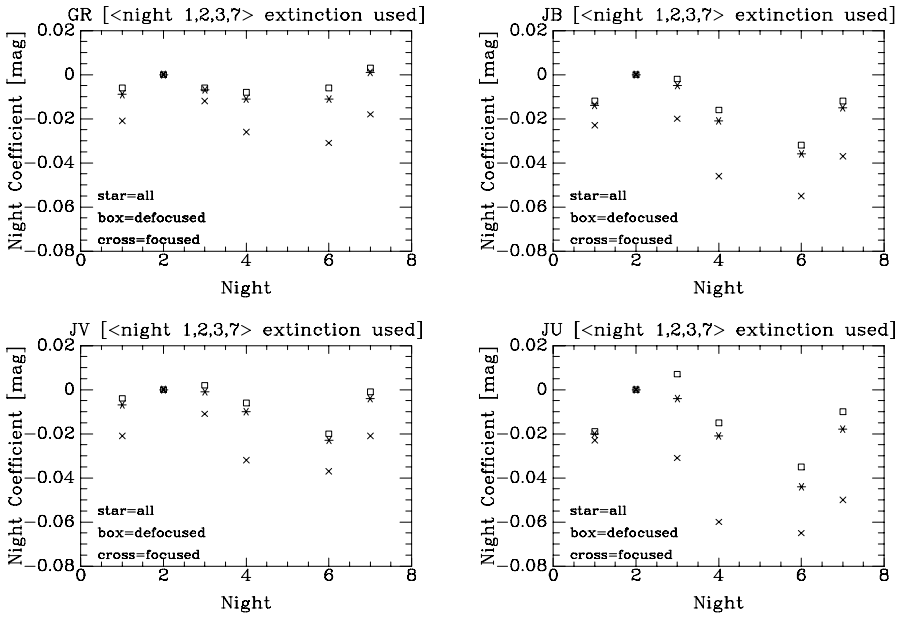

Figure C.12: The night coefficients based on the final extinction coefficients (Table C.8). The night coefficients are with respect to night 2. Legend: Boxes: defocused images fit alone. Crosses: focused images fit alone. Stars: defocused and focused images fit together.

and n is the night coefficient for the given filter and night. m_{phot} and apcor should correspond to the same aperture.

Table C.9: The Night Coefficients Based on the Final Extinction Coefficients

Night	GR	JV	JB	JU
1	–0.009	–0.007	–0.014	–0.020
2	0.0	0.0	0.0	0.0
3	–0.007	–0.001	–0.005	–0.004
4	–0.011	–0.010	–0.021	–0.021
6	–0.011	–0.023	–0.036	–0.044
7	0.001	–0.004	–0.015	–0.018

C.4 The Standard Catalog

A catalog of standard magnitudes was compiled as follows: For the SA110–503 field and the PG1633+099 field, Johnson V, B, & U magnitudes were taken from Landolt (1992). B and U were calculated from the listed (B–V) and (U–B) as follows:

$$B = V + (B - V) \quad \text{(C.7)}$$
$$\sigma(B) = \max\{\sigma(V), \sigma((B - V))\} \quad \text{(C.8)}$$
$$U = V + (B - V) + (U - B) \quad \text{(C.9)}$$
$$\sigma(U) = \max\{\sigma(V), \sigma((B - V)), \sigma((U - B))\} \quad \text{(C.10)}$$

Gunn r magnitudes were taken from Jørgensen (1994).

For the M67 field, Johnson V & B, and Gunn r magnitudes were taken from Jørgensen (1994). B was calculated from the listed (B–V) in the same way as for the Landolt stars, Eq. (C.7) and (C.8). U magnitudes were taken from Montgomery et al. (1993) for the 13 stars in common. U was calculated from the listed (B–V) and (U–B) in the same way as for the Landolt stars, Eq. (C.9), whereas the errors were somewhat arbitrarily set to 0.01 mag, since these authors do not list any errors. The stars were identified from Figure 7 in Montgomery et al. (1993), since these authors do not use the F or quadrant numbers. The established correspondence is shown in Table C.10.

The final catalog (called `DFC_std.dat`) is shown in Table C.11.

Table C.10: Identification for Stars in Montgomery et al. (1993)

Star	Fig ID
M67–F141	14
M67–F105	15
M67–F95	18
M67–F93/I12	19
M67–F124	20
M67–F127	21
M67–F130	22
M67–F129/I199	23
M67–F128/I198	24
M67–F111	25
M67–F108	28
M67–F81	29
M67–I20	30

Notes: Fig ID refers to Table 7 and Figure 7 in Montgomery et al. (1993).

Table C.11: Catalog of standard star magnitudes

Star	GR	σ(GR)	JV	σ(JV)	JB	σ(JB)	JU	σ(JU)
SA110–496	12.763	0.007	13.004	0.003	14.044	0.006	14.781	0.023
SA110–497	13.889	0.007	14.196	0.005	15.248	0.006	15.628	0.014
SA110–499	11.497	0.007	11.737	0.003	12.724	0.003	13.363	0.007
SA110–502	11.440	0.008	12.330	0.003	14.656	0.005	16.982	0.023
SA110–503	11.756	0.007	11.773	0.003	12.444	0.003	12.950	0.005
SA110–504	13.629	0.007	14.022	0.001	15.270	0.006	16.593	0.027
SA110–506	11.349	0.007	11.312	0.002	11.880	0.002	11.939	0.006
SA110–507	12.208	0.007	12.440	0.005	13.581	0.006	14.411	0.006
PG1633+099	14.799	0.018	14.397	0.002	14.205	0.002	13.231	0.005
PG1633+099A	15.104	0.018	15.256	0.004	16.129	0.005	16.449	0.009
PG1633+099B	12.772	0.017	12.969	0.002	14.050	0.002	15.057	0.007
PG1633+099C	13.004	0.017	13.229	0.003	14.363	0.003	15.501	0.004
PG1633+099D	13.711	0.017	13.691	0.002	14.226	0.002	14.201	0.005
M67–F81	10.392	0.006	10.030	0.008	9.947	0.008	9.556	0.010
M67–F93/I12	12.837	0.003	12.833	0.007	13.383	0.007	13.468	0.010
M67–F95	12.721	0.003	12.678	0.006	13.169	0.006	13.232	0.010
M67–F105	9.982	0.004	10.267	0.010	11.510	0.010	12.889	0.010
M67–F106/I11	13.064	0.003	13.062	0.005	13.625	0.005	–	–
M67–F108	9.310	0.003	9.662	0.006	11.024	0.006	12.623	0.010
M67–F111	12.736	0.003	12.741	0.006	13.297	0.006	13.357	0.010
M67–F117	12.517	0.003	12.632	0.005	13.411	0.005	–	–
M67–F124	12.184	0.003	12.129	0.007	12.584	0.007	12.605	0.010
M67–F127	12.789	0.003	12.785	0.007	13.338	0.007	13.365	0.010
M67–F128/I198	13.155	0.004	13.158	0.022	13.734	0.022	13.777	0.010
M67–F129/I199	13.169	0.003	13.174	0.010	13.761	0.010	13.831	0.010
M67–F130	12.954	0.004	12.895	0.022	13.349	0.022	13.356	0.010
M67–F134	12.254	0.003	12.265	0.008	12.832	0.008	–	–
M67–F135	11.216	0.003	11.428	0.008	12.480	0.008	–	–
M67–F141	10.245	0.004	10.442	0.011	11.527	0.011	12.586	0.010
M67–F153	11.559	0.011	11.280	0.015	11.385	0.015	–	–
M67–I15	11.635	0.007	11.563	0.010	11.961	0.010	–	–
M67–I20	13.440	0.007	13.444	0.010	13.996	0.010	14.038	0.010
M67–I25	12.643	0.007	12.669	0.010	13.273	0.010	–	–
M67–I27	11.492	0.007	11.333	0.010	11.614	0.010	–	–
M67–I49	13.447	0.005	13.465	0.007	14.046	0.007	–	–
M67–II22	12.766	0.011	12.911	0.015	13.809	0.015	–	–

C.5 The Transformation Equations

The following transformation equations were used:

$$r_{std} = r_{inst} + r_1 + r_2(B-r)_{inst} \quad \text{(C.11)}$$
$$V_{std} = V_{inst} + v_1 + v_2(B-V)_{inst} \quad \text{(C.12)}$$
$$B_{std} = B_{inst} + b_1 + b_2(B-r)_{inst} \quad \text{(C.13)}$$
$$U_{std} = U_{inst} + u_1 + u_2(U-B)_{inst} \quad \text{(C.14)}$$

"std" denotes standard magnitudes, and "inst" denotes instrumental magnitudes.

The fitting of the variables in the transformation equations to the data was done using the task `fitparams` (in `digiphotx.photcalx`).

At the very first it was tried to use transformation equations without a color term (i.e. with the subscript 2 variables set to zero). The rms scatter was so large, that it was concluded that a color term was needed. As will be seen in the following, the resulting color coefficients are indeed significantly different from zero at the 3 sigma level.

`fitparams` was run 3 times for the 4 filters:

1. On all the stars, focused and defocused, with the color term coefficient as a free variable. Plots showing $m_{std} - m_{inst}$ vs. instrumental color for the data points and the resulting fit are in Figure C.13–C.16. Note, that the aspect ratio of the 4 figures is the same, $\Delta y/\Delta x = 2/15$, so the color dependence can easily be compared.

2. On the focused stars only, with the color term coefficient fixed to the value from fit 1.

3. On the defocused stars only, with the color term coefficient fixed to the value from fit 1.

In all 3 fitting series, a number of stars were deleted (i.e. excluded from the fit) all together, that is, all the observations of the given star were deleted. These stars are listed in Table C.12. They were deleted for a number of different reasons:

- 3 stars (PG1633+099, M67–F81, & SA110–502) were deleted because they were either very blue ((B–V)$_{std} \sim -0.1$ mag) or red ((B–V)$_{std} \sim 2.3$ mag). Since we only need a transformation which is valid for the color range of E/S0 galaxies, say (B–V)$_{std} = 0.75$–1.1 mag (Jørgensen, private communication), this is perfectly justifiable. The remaining stars still span a sufficient range in (B–V)$_{std}$, from 0.1 (M67–F153) to 1.2 (SA110–504).

- 1 star (M67–F117) was deleted (in the Gunn r and Johnson V fits only) because it had a large scatter, i.e. the individual observations of this star were very scattered. This can be seen in Figure C.13 for Gunn r, and Figure C.14 for Johnson V. The reason for this was not further investigated.

- 3 stars (M67–F108, M67–F105, & M67–F141) were deleted (in the Gunn r and Johnson V fits only) because they deviated systematically from the fit. This can be seen in Figure C.13 for Gunn r, and Figure C.14 for Johnson V. These stars were the reddest and brightest of the defocused stars. The important question is, whether it is only these reddest and brightest defocused stars that behave differently, or if they are just the most extreme cases of a general trend that the focused and the defocused stars do not behave in the same way.

In addition, individual observations with uncertainties larger than 0.1 mag were deleted. This was only the case for Johnson U, for 9 data points, of which 4 belonged to SA110–502, which would

Table C.12: Deleted stars

Star	Deleted in				(B–r)	(B–V)	(U–B)	(B–V)	r	V	Reason for deletion
	GR	JV	JB	JU	instrumental, [mag]			standard, [mag]			
PG1633+099	x	x	x	x	0.24	0.87	1.26	–0.2	14.8	14.4	Very blue
M67–F81	x	x	x	x	0.41	0.95	1.88	–0.1	10.4	10.0	Very blue
SA110–502	x	x	x	x	3.96	3.02	4.86	2.3	11.4	12.3	Very red
M67–F117	x	x			1.69	1.69		0.8	12.5	12.6	Large scatter
M67–F108	x	x			2.44	2.16		1.4	9.3	9.7	Large res., bright
M67–F105	x	x			2.28	2.07		1.2	10.0	10.3	Large res., bright
M67–F141	x	x			2.05	1.94		1.1	10.2	10.4	Large res., bright

Notes: The instrumental colors are mean values for the individual observations of the given star. The standard color and magnitudes are taken from Table C.11. The instrumental colors are useful for locating the stars in the $m_{std} - m_{inst}$ vs. instrumental color plots, Figure C.13–C.16.
The above stars were deleted in the same way in the 3 fitting series: all stars with free color term, focused stars with fixed color term, and defocused stars with fixed color term.

have been deleted anyway. Also individual deviating observations were deleted. This also was only the case for Johnson U, for 3 data points.

The result from the 3 series of fit are shown in Table C.13.

Table C.13: Transformation equation coefficients

Type	Zero point [mag]	Color term	Scatter [mag]
all	$r_1 = +0.7718 \pm 0.0049$	$r_2 = 0.1244 \pm 0.0029$	rms = 0.0185
foc	$r_1 = +0.7816 \pm 0.0012$	$r_2 = 0.1244$ (fixed)	rms = 0.0124
def	$r_1 = +0.7624 \pm 0.0018$	$r_2 = 0.1244$ (fixed)	rms = 0.0187
all	$v_1 = +0.9380 \pm 0.0065$	$v_2 = 0.0861 \pm 0.0038$	rms = 0.0144
foc	$v_1 = +0.9406 \pm 0.0016$	$v_2 = 0.0861$ (fixed)	rms = 0.0164
def	$v_1 = +0.9353 \pm 0.0011$	$v_2 = 0.0861$ (fixed)	rms = 0.0117
all	$b_1 = -0.0523 \pm 0.0055$	$b_2 = 0.1253 \pm 0.0031$	rms = 0.0219
foc	$b_1 = -0.0518 \pm 0.0029$	$b_2 = 0.1253$ (fixed)	rms = 0.0291
def	$b_1 = -0.0526 \pm 0.0012$	$b_2 = 0.1253$ (fixed)	rms = 0.0139
all	$u_1 = -2.2369 \pm 0.0168$	$u_2 = 0.0187 \pm 0.0058$	rms = 0.0390
foc	$u_1 = -2.2404 \pm 0.0047$	$u_2 = 0.0187$ (fixed)	rms = 0.0461
def	$u_1 = -2.2320 \pm 0.0031$	$u_2 = 0.0187$ (fixed)	rms = 0.0256

Notes: "all": all stars fitted, color term free. "foc": only focused stars fitted, color term fixed. "def": only defocused stars fitted, color term fixed. The "all" coefficients are the final ones, i.e. the ones used to standard calibrate the surface photometry.

The reason for fitting the focused and defocused stars separately with forced same color dependence, was to be able to compare their zero points. These zero point differences are shown in Table C.14. There is a zero point difference in Gunn r at the 9 sigma level, and a zero point difference in Johnson V at the 3 sigma level.

That the focused and defocused stars behave differently in Gunn r and Johnson V can be seen

Table C.14: Zero point differences

Zero point def [mag]	Zero point foc [mag]	Zero point difference [mag]
$r_1 = +0.7624 \pm 0.0018$	$r_1 = +0.7816 \pm 0.0012$	$\Delta = -0.0192 \pm 0.0022$ (8.7σ)
$v_1 = +0.9353 \pm 0.0011$	$v_1 = +0.9406 \pm 0.0016$	$\Delta = -0.0053 \pm 0.0019$ (2.8σ)
$b_1 = -0.0526 \pm 0.0012$	$b_1 = -0.0518 \pm 0.0029$	$\Delta = -0.0008 \pm 0.0031$ (0.3σ)
$u_1 = -2.2320 \pm 0.0031$	$u_1 = -2.2404 \pm 0.0047$	$\Delta = +0.0084 \pm 0.0056$ (1.5σ)

Notes: "def" denotes the defocused stars, "foc" denotes the focused stars. "Zero point difference" is defined as "Zero point def" minus "Zero point foc".

in Figure C.13 and and Figure C.14. The question is what kind of difference it is. The figures could indicate, that it is not only a zero point difference, but also a difference in color dependence.

However, the rms scatter when fitting all the stars together (with the deletions previously mentioned) is still sufficiently low, less than 0.02 mag in both Gunn r and Johnson V. The conclusion is, therefore, to accept the result of the fit of all the stars together (Table C.15), and then to watch out for small differences in the derived galaxy magnitudes when compared with literature values.

Table C.15: Adopted transformation equation coefficients

Zero point [mag]	Color term	Scatter [mag]
$r_1 = +0.7718 \pm 0.0049$	$r_2 = 0.1244 \pm 0.0029$	rms = 0.0185
$v_1 = +0.9380 \pm 0.0065$	$v_2 = 0.0861 \pm 0.0038$	rms = 0.0144
$b_1 = -0.0523 \pm 0.0055$	$b_2 = 0.1253 \pm 0.0031$	rms = 0.0219
$u_1 = -2.2369 \pm 0.0168$	$u_2 = 0.0187 \pm 0.0058$	rms = 0.0390

Notes: These are the "all" coefficients from Table C.13, listed here alone for convenience.

Finally, we can check if the stars from night 4 and 6 have larger residuals than the stars from the other nights. Figure C.17 shows mean absolute residual for the 3 fields, with the SA110 field split up into the low and the high airmass observations. No such difference is seen, except for the SA110 high airmass observations in Johnson U, but it might not be significant due to the large random scatter of the data in this filter. Otherwise, these plots do not show any correlations with night and field/airmass, except that the night 2 and 3 residual in Gunn r are somewhat higher. The conclusion is still that the standard transformation we have arrived at is acceptable.

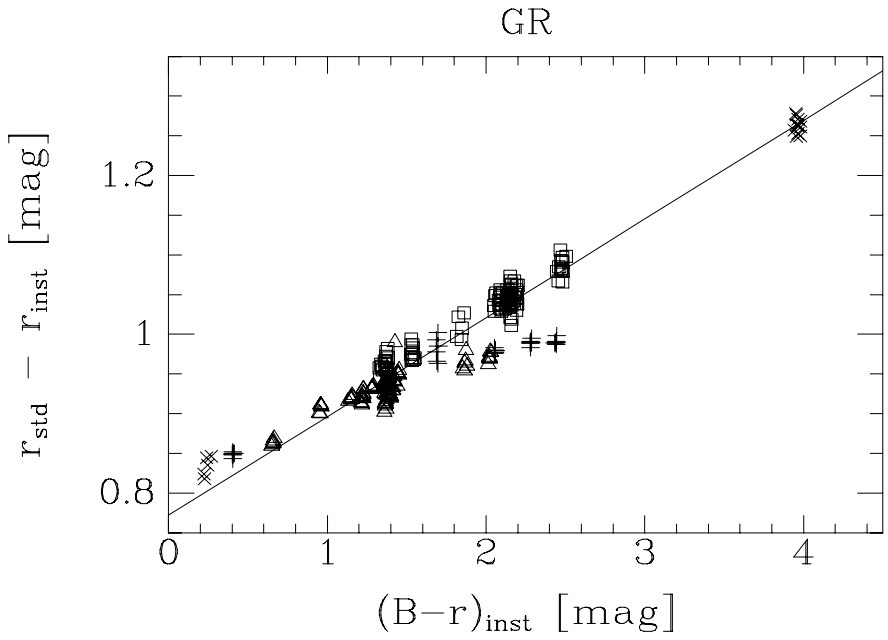

Figure C.13: $m_{std} - m_{inst}$ vs. instrumental color, Gunn r. Legend: box: focused & not deleted, triangle: defocused & not deleted, cross: focused & deleted, plus: defocused & deleted.

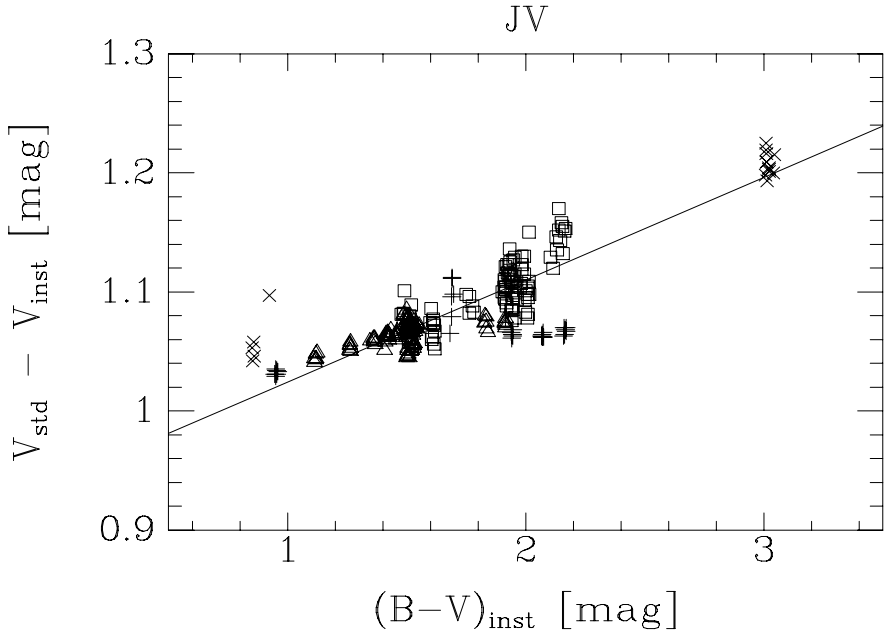

Figure C.14: $m_{std} - m_{inst}$ vs. instrumental color, Johnson V. Legend: box: focused & not deleted, triangle: defocused & not deleted, cross: focused & deleted, plus: defocused & deleted.

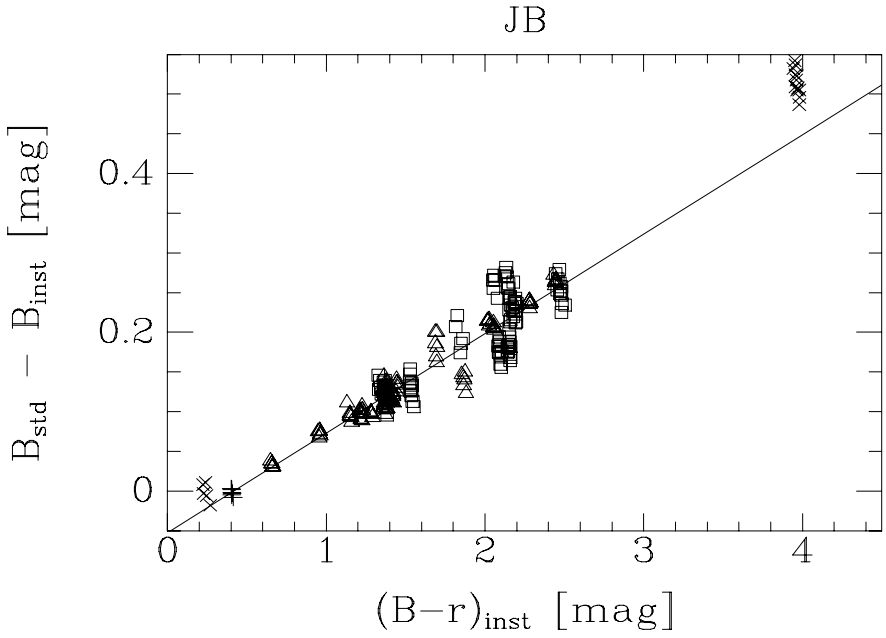

Figure C.15: $m_{std} - m_{inst}$ vs. instrumental color, Johnson B. Legend: box: focused & not deleted, triangle: defocused & not deleted, cross: focused & deleted, plus: defocused & deleted.

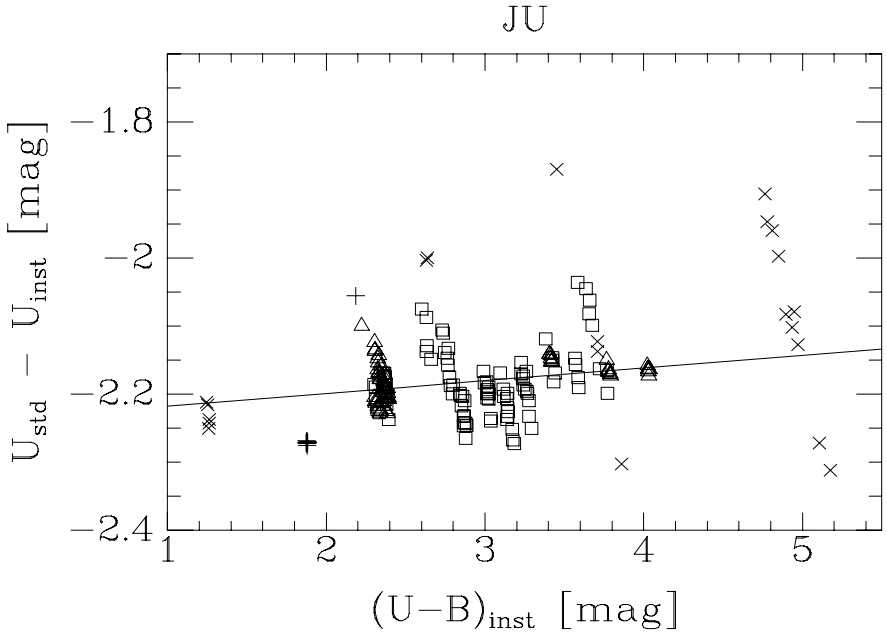

Figure C.16: $m_{std} - m_{inst}$ vs. instrumental color, Johnson U. Legend: box: focused & not deleted, triangle: defocused & not deleted, cross: focused & deleted, plus: defocused & deleted.

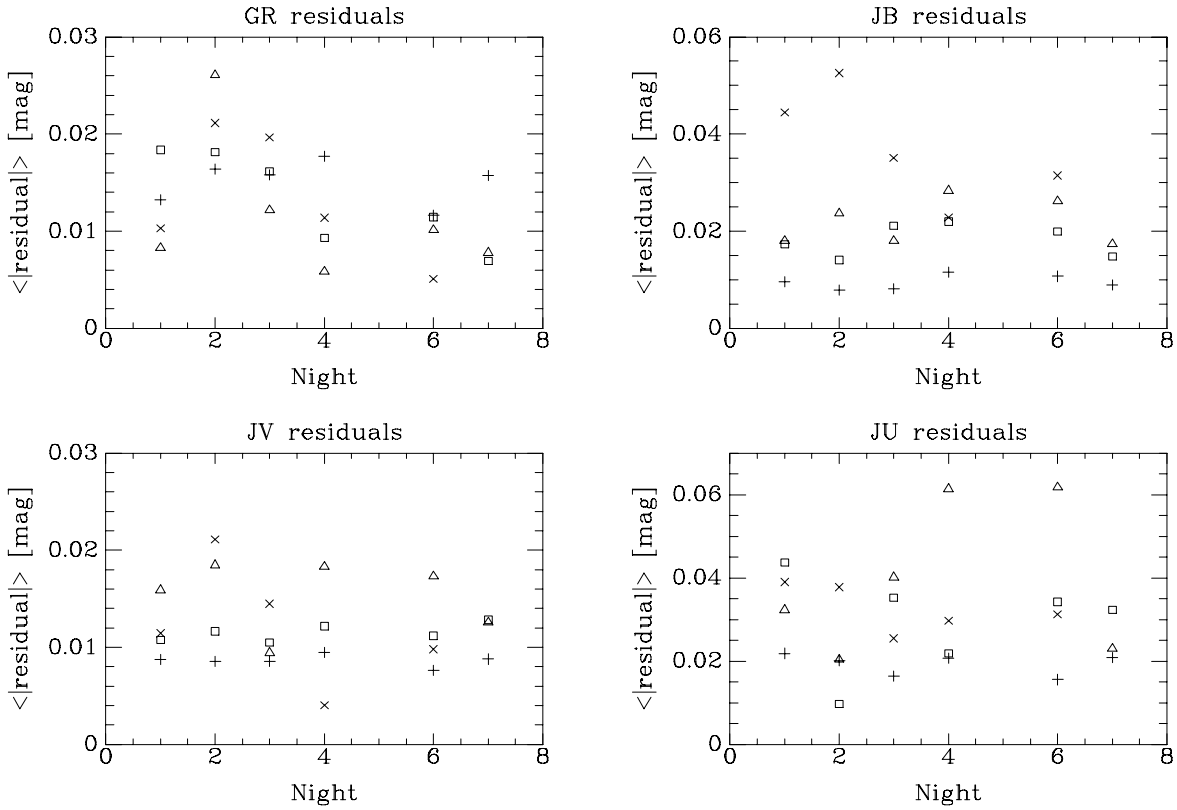

Figure C.17: Mean absolute residuals with respect to the final transformation equation fit. The mean is calculated for 4 disjoint groups: SA110 low airmass ($N = 7$), SA110 high airmass ($N = 7$), PG1633+099 ($N = 4$), and M67 ($N = 12$–22). Only points which were included in the transformation equation fit were used in this calculation. The typical numbers of points, N, is shown above; it can be deduced from Table C.11 (the standard catalog) and Table C.12 (the list of deleted stars). Legend: box: SA110 low airmass, triangle: SA110 high airmass, cross: PG1633+099, plus: M67.

Appendix D

Data for the Coma Cluster

The Coma data used for this work are given in Table D.1 (photometry) and Table D.2 (spectroscopy) below. Both tables have the same 116 galaxies.

The Coma data are described in Sect. 7.1.1 (p. 85).

TABLE D.1

COMA GLOBAL PHOTOMETRIC PARAMETERS, GUNN r

Galaxy		$\log r_e$	$<\mu>_e$	ε_e	$\varepsilon_{21.85}$	c_4	$<c_4>$	$<c_6>$
D 13	···	0.72±0.03	19.67±0.10	0.30	0.249	0.020	0.004	−0.004
D 15	···	0.69±0.03	20.30±0.10	0.15	0.136	−0.007	−0.005	0.004
D 20	···	0.59±0.04	19.76±0.13	0.41	0.432	0.019	0.011	0.000
D 23	NGC4842B	0.41±0.03	18.91±0.10	0.23	0.397	0.020	0.016	0.002
D 24	···	0.63±0.02	19.06±0.08	0.14	0.040	0.009	0.001	0.003
D 27	···	0.66±0.04	20.17±0.14	0.16	0.147	−0.019	−0.002	0.004
D 30	NGC4842A	0.69±0.02	19.15±0.07	0.09	0.077	0.005	0.002	−0.004
D 31	NGC4839	1.47±0.03	21.18±0.07	0.42	0.344	0.004	0.001	0.000
D 33	···	0.44±0.02	18.64±0.09	0.25	0.379	0.011	0.006	−0.001
D 39	···	0.76±0.03	20.25±0.11	0.19	0.186	0.003	0.003	0.005
D 42	···	0.41±0.03	18.79±0.11	0.32	0.427	0.049	0.031	−0.002
D 43	NGC4853	0.59±0.02	18.18±0.06	0.18	0.137	0.006	0.005	0.000
D 46	NGC4840	0.81±0.02	19.35±0.07	0.18	0.144	0.008	0.006	0.003
D 49	NGC4926	1.04±0.03	19.79±0.10	0.13	0.121	−0.009	−0.001	−0.001
D 57	···	0.94±0.02	20.05±0.06	0.71	0.735	0.096	0.049	−0.017
D 58	NGC4854	1.15±0.03	21.13±0.09	0.27	0.202	0.004	0.000	0.003
D 62	···	0.77±0.04	20.66±0.12	0.43	0.428	0.027	0.019	0.001
D 65	···	0.82±0.03	20.55±0.11	0.45	0.435	0.008	0.000	0.003
D 67	···	0.38±0.03	18.81±0.12	0.20	0.403	0.058	0.020	0.004
D 68	IC3963	0.89±0.03	20.58±0.09	0.47	0.464	0.102	0.057	−0.003
D 69	IC3959	0.73±0.03	19.42±0.10	0.13	0.095	0.005	0.003	−0.002
D 70	IC3957	0.63±0.04	19.51±0.13	0.08	0.073	−0.004	−0.002	0.001
D 72	IC3947	0.52±0.03	19.00±0.11	0.28	0.322	0.028	0.020	−0.003
D 75	···	1.08±0.03	21.52±0.09	0.79	0.781	0.071	0.057	−0.012
D 78	NGC4923	0.93±0.02	19.88±0.08	0.17	0.183	0.010	0.002	0.000
D 79	NGC4919	0.76±0.02	19.30±0.08	0.31	0.431	0.010	0.000	0.000
D 80	···	0.85±0.04	20.81±0.13	0.25	0.357	0.009	0.002	0.003
D 81	···	0.82±0.04	20.70±0.13	0.21	0.212	0.004	0.003	−0.001
D 84	···	0.66±0.03	19.77±0.10	0.63	0.656	0.062	0.053	−0.008
D 87	···	0.48±0.04	19.79±0.16	0.07	0.074	−0.005	−0.001	−0.006
D 88	IC3976	0.47±0.03	18.58±0.10	0.41	0.532	0.026	0.017	−0.004
D 91	IC3946	0.65±0.02	18.98±0.07	0.31	0.479	0.044	0.035	−0.003
D 92	···	0.45±0.03	18.86±0.12	0.34	0.336	0.027	0.019	0.007
D 93	···	0.44±0.03	18.79±0.11	0.43	0.677	0.128	0.117	−0.019
D 98	···	0.72±0.02	19.78±0.08	0.62	0.662	0.031	0.035	−0.014
D101	···	0.56±0.03	19.42±0.11	0.30	0.435	0.063	0.038	0.008
D103	IC3973	0.64±0.03	19.06±0.10	0.23	0.252	0.016	0.000	0.000
D104	NGC4875	0.52±0.03	18.96±0.10	0.17	0.246	0.016	0.008	0.003
D105	NGC4869	0.88±0.02	19.74±0.08	0.13	0.096	−0.000	0.002	0.000
D106	···	0.39±0.04	18.99±0.13	0.05	0.256	0.007	0.002	−0.005
D107	···	0.75±0.04	20.55±0.14	0.41	0.415	−0.001	0.001	−0.001
D108	···	0.51±0.04	19.61±0.13	0.43	0.508	0.036	0.008	0.000
D109	IC3960	0.73±0.02	19.77±0.08	0.04	0.058	0.016	0.000	0.003
D110	···	0.71±0.04	20.46±0.13	0.29	0.289	0.026	0.021	−0.008
D111	···	0.81±0.03	20.15±0.09	0.25	0.274	0.005	0.003	−0.003
D116	···	0.85±0.03	20.62±0.10	0.16	0.210	0.032	0.019	0.002
D118	NGC4906	0.87±0.03	20.09±0.10	0.12	0.124	−0.005	−0.004	0.000
D119	···	0.62±0.03	19.87±0.11	0.17	0.280	0.012	0.001	−0.001
D120	NGC4898B	0.77±0.02	19.22±0.06	0.28	0.277	0.015	0.007	−0.001
D121	NGC4898A	0.30±0.02	18.39±0.08	0.06	0.116	−0.007	−0.003	−0.001
D122	NGC4894	0.68±0.03	19.93±0.11	0.53	0.586	0.067	0.039	−0.005
D123	···	0.97±0.04	21.43±0.12	0.32	0.437	0.043	0.015	0.000
D124	NGC4876	0.71±0.03	19.47±0.09	0.29	0.333	0.001	−0.001	−0.001
D125	···	0.18±0.04	18.06±0.14	0.05	0.100	0.010	0.005	0.001
D128	···	0.40±0.05	19.30±0.19	0.37	0.531	0.041	0.019	−0.003
D129	NGC4874	1.85±0.04	22.13±0.09	0.16	0.096	0.001	0.001	0.000
D130	NGC4872	0.48±0.03	18.53±0.11	0.06	0.232	0.018	0.006	−0.002
D131	NGC4871	0.92±0.04	20.24±0.12	0.43	0.414	0.030	0.014	−0.001
D132	···	0.61±0.04	20.24±0.14	0.30	0.318	0.026	0.021	−0.002
D133	NGC4867	0.49±0.03	18.53±0.10	0.25	0.246	0.002	−0.002	−0.002
D135	···	0.63±0.05	20.50±0.15	0.21	0.213	−0.006	−0.001	−0.002
D136	···	0.17±0.03	17.99±0.13	0.15	0.241	0.020	0.015	0.002
D137	NGC4850	0.67±0.03	19.07±0.09	0.21	0.127	0.009	0.002	−0.003
D143	IC4051	1.26±0.03	21.02±0.09	0.26	0.217	−0.005	−0.000	0.000
D144	IC4042	0.86±0.02	19.96±0.08	0.06	0.063	−0.011	−0.005	0.001
D145	IC4041	0.87±0.03	20.52±0.09	0.45	0.442	0.007	0.005	0.000
D146	···	1.05±0.03	21.31±0.10	0.29	0.291	0.164	0.100	−0.016
D147	···	0.95±0.04	21.19±0.11	0.54	0.543	0.033	0.020	0.001
D148	NGC4889	1.53±0.02	20.64±0.05	0.36	0.358	−0.008	−0.005	0.000
D150	IC4011	0.69±0.04	19.98±0.12	0.09	0.099	0.006	0.002	0.001
D151	NGC4886	0.97±0.03	20.38±0.09	0.02	0.024	0.005	0.003	−0.002
D152	IC3998	0.95±0.02	20.73±0.07	0.33	0.322	0.024	0.005	−0.001
D153	···	0.57±0.02	19.58±0.10	0.01	0.018	0.002	0.004	0.000

TABLE D.1—*Continued*

Galaxy		$\log r_e$	$<\mu>_e$	ε_e	$\varepsilon_{21.85}$	c_4	$<c_4>$	$<c_6>$
D155	NGC4873	0.87±0.02	20.09±0.08	0.25	0.269	0.008	0.006	−0.003
D156	···	0.51±0.05	19.96±0.16	0.21	0.252	0.006	−0.005	0.009
D157	···	0.49±0.03	19.48±0.12	0.24	0.380	−0.010	−0.006	0.003
D159	NGC4864	0.89±0.02	19.78±0.08	0.15	0.141	0.000	0.002	−0.007
D160	IC3955	0.91±0.03	20.36±0.08	0.44	0.434	0.070	0.030	−0.004
D161	···	0.91±0.03	20.07±0.09	0.12	0.119	0.011	0.008	−0.002
D167	NGC4908	0.85±0.02	19.60±0.08	0.31	0.308	−0.005	−0.002	0.002
D168	IC4045	0.64±0.03	18.79±0.10	0.33	0.316	0.014	0.011	0.000
D170	IC4026	0.86±0.03	20.38±0.09	0.18	0.181	−0.000	0.002	−0.001
D172	IC4021	0.51±0.03	19.02±0.10	0.10	0.107	0.000	−0.003	0.002
D173	···	0.53±0.05	19.52±0.19	0.26	0.385	0.034	0.028	0.001
D174	IC4012	0.33±0.04	18.23±0.14	0.16	0.220	0.002	−0.002	0.002
D175	NGC4883	0.84±0.02	19.91±0.08	0.20	0.245	0.012	0.005	−0.002
D176	···	0.49±0.03	18.98±0.11	0.43	0.509	0.045	0.034	−0.002
D177	···	0.56±0.04	19.98±0.13	0.34	0.394	0.018	0.000	−0.003
D179	NGC4865	0.71±0.02	18.77±0.06	0.41	0.512	0.016	0.008	0.000
D180	···	1.26±0.04	22.11±0.11	0.06	0.057	0.004	0.000	0.001
D181	···	0.51±0.03	19.45±0.13	0.24	0.534	0.147	0.123	−0.022
D190	···	0.63±0.02	18.96±0.08	0.52	0.649	0.103	0.073	−0.014
D191	···	0.36±0.04	18.95±0.14	0.41	0.598	0.071	0.062	−0.004
D192	···	0.77±0.03	20.15±0.12	0.74	0.768	0.098	0.077	−0.032
D193	···	0.62±0.03	20.04±0.12	0.17	0.151	−0.004	−0.005	−0.004
D194	NGC4860	0.93±0.02	19.64±0.07	0.15	0.171	0.004	0.002	0.001
D197	IC3943	0.67±0.02	19.24±0.08	0.48	0.595	0.057	0.044	−0.007
D198	···	0.78±0.04	20.76±0.12	0.40	0.411	0.035	0.028	0.003
D199	NGC4851	0.81±0.03	20.20±0.10	0.32	0.313	0.028	0.012	−0.004
D200	···	0.30±0.03	17.90±0.13	0.36	0.512	0.096	0.072	−0.006
D204	···	0.78±0.04	20.42±0.15	0.22	0.254	0.008	0.007	0.000
D206	NGC4895	1.00±0.02	19.86±0.06	0.58	0.614	0.041	0.014	0.011
D207	···	0.60±0.03	19.66±0.12	0.29	0.347	0.019	0.006	−0.002
D209	···	1.14±0.04	21.80±0.11	0.56	0.532	0.011	0.005	−0.004
D210	···	0.59±0.03	19.26±0.11	0.22	0.126	0.018	0.005	−0.002
D212	···	1.01±0.03	21.04±0.09	0.50	0.455	0.014	0.007	−0.002
D217	NGC4881	1.04±0.03	20.24±0.11	0.04	0.043	0.002	0.002	−0.001
D218	···	0.78±0.02	19.61±0.08	0.41	0.478	0.022	0.016	−0.003
D229	···	0.81±0.04	20.73±0.14	0.21	0.212	−0.012	−0.005	0.000
D230	···	0.89±0.02	19.72±0.06	0.40	0.434	0.011	0.006	−0.003
D231	···	0.49±0.03	18.74±0.12	0.39	0.395	0.019	0.015	0.001
D232	NGC4896	1.07±0.02	20.49±0.07	0.44	0.436	0.012	0.009	0.000
D238	···	0.40±0.03	18.94±0.11	0.20	0.216	0.017	0.011	0.002
D239	NGC4841B	0.93±0.03	19.88±0.09	0.04	0.035	0.005	0.001	0.001
D240	NGC4841A	1.25±0.02	20.39±0.07	0.16	0.167	−0.007	−0.004	0.000
D242	···	0.60±0.03	19.69±0.11	0.34	0.391	0.014	0.005	0.008

NOTE.— Galaxy IDs from Dressler (1980b). All data from JF94. $\log r_e$, $<\mu>_e$, and ε_e are the seeing corrected values given by JFK95a. r_e is in arcsec. Typical uncertainties on ε_e, $\varepsilon_{21.85}$, c_4, $<c_4>$, and $<c_6>$ are 0.006, 0.007, 0.004, 0.004, and 0.004, respectively; see also JF94.

TABLE D.2
COMA GLOBAL SPECTROSCOPIC PARAMETERS

Galaxy		$cz_{\rm hel}$	$\log\sigma$	Mg_2	$<$ Fe $>$
D 13	···	5699	2.255±0.025	0.258±0.007	2.39± 0.23
D 15	···	4859	1.878±0.048	0.117±0.008	1.50± 0.28
D 20	···	7051	2.068±0.024	0.231±0.007	2.62± 0.22
D 23	NGC4842B	7261	2.175±0.034	0.255±0.009	2.62± 0.28
D 24	···	7455	2.347±0.033	0.305±0.013	··· ···
D 27	···	7825	1.997±0.022	0.264±0.013	··· ···
D 30	NGC4842A	7322	2.272±0.029	0.298±0.008	2.74± 0.24
D 31	NGC4839	7454	2.406±0.017	0.312±0.006	2.60± 0.22
D 33	···	5579	2.262±0.030	0.269±0.007	2.21± 0.23
D 39	···	5907	2.112±0.024	0.253±0.007	3.06± 0.23
D 42	···	6031	2.136±0.026	0.260±0.008	2.96± 0.24
D 43	NGC4853	7718	2.115±0.035	0.163±0.006	1.69± 0.21
D 46	NGC4840	5996	2.370±0.033	0.323±0.013	··· ···
D 49	NGC4926	7834	2.413±0.015	0.315±0.007	2.69± 0.27
D 57	···	8375	2.225±0.036	0.275±0.013	··· ···
D 58	NGC4854	8062	2.263±0.021	0.313±0.013	··· ···
D 62	···	8341	2.124±0.035	0.169±0.008	2.08± 0.27
D 65	···	6172	2.079±0.036	0.261±0.013	··· ···
D 67	···	6033	2.187±0.036	0.286±0.013	··· ···
D 68	IC3963	6812	2.129±0.036	0.278±0.013	··· ···
D 69	IC3959	7059	2.297±0.015	0.306±0.007	3.11± 0.25
D 70	IC3957	6364	2.180±0.025	0.296±0.013	··· ···
D 72	IC3947	5677	2.142±0.022	0.282±0.013	··· ···
D 75	···	6168	1.852±0.032	0.220±0.008	2.29± 0.26
D 78	NGC4923	5446	2.286±0.017	0.309±0.013	··· ···
D 79	NGC4919	7341	2.277±0.019	0.276±0.006	3.05± 0.18
D 80	···	6708	1.997±0.026	0.238±0.007	2.78± 0.23
D 81	···	5976	2.171±0.022	0.269±0.013	··· ···
D 84	···	6562	2.117±0.027	0.262±0.009	3.46± 0.27
D 87	···	7748	1.901±0.025	0.234±0.013	··· ···
D 88	IC3976	6838	2.418±0.036	0.327±0.013	··· ···
D 91	IC3946	5923	2.327±0.027	0.271±0.008	2.49± 0.24
D 92	···	7149	2.217±0.026	0.254±0.007	2.94± 0.23
D 93	···	6063	2.140±0.025	0.251±0.007	2.99± 0.22
D 98	···	6846	2.184±0.036	0.275±0.013	··· ···
D101	···	8062	2.118±0.036	0.278±0.013	··· ···
D103	IC3973	4717	2.337±0.036	0.308±0.013	··· ···
D104	NGC4875	8016	2.278±0.036	0.299±0.013	··· ···
D105	NGC4869	6787	2.313±0.025	0.321±0.013	··· ···
D106	···	5114	2.219±0.036	0.250±0.013	··· ···
D107	···	6429	1.838±0.025	0.238±0.013	··· ···
D108	···	6406	2.082±0.036	0.281±0.013	··· ···
D109	IC3960	6559	2.261±0.036	0.345±0.013	··· ···
D110	···	6969	2.090±0.044	0.249±0.014	2.77± 0.42
D111	···	5885	2.195±0.021	0.295±0.007	2.83± 0.20
D116	···	8414	2.132±0.036	0.256±0.013	··· ···
D118	NGC4906	7486	2.227±0.025	0.310±0.013	··· ···
D119	···	6965	2.204±0.036	0.289±0.013	··· ···
D120	NGC4898B	6371	2.151±0.025	0.264±0.013	··· ···
D121	NGC4898A	6869	2.308±0.025	0.275±0.013	··· ···
D122	NGC4894	4623	1.975±0.036	0.235±0.013	··· ···
D123	···	7728	1.979±0.030	0.224±0.008	2.45± 0.26
D124	NGC4876	6658	2.261±0.025	0.251±0.013	··· ···
D125	···	6898	2.231±0.025	0.273±0.013	··· ···
D128	···	8001	2.037±0.036	0.259±0.013	··· ···
D129	NGC4874	7206	2.415±0.016	0.310±0.007	3.17± 0.23
D130	NGC4872	7204	2.328±0.025	0.305±0.013	··· ···
D131	NGC4871	6757	2.243±0.036	0.290±0.013	··· ···
D132	···	7683	2.122±0.036	0.272±0.013	··· ···
D133	NGC4867	4807	2.350±0.025	0.312±0.013	··· ···
D135	···	8320	1.901±0.033	··· ···	··· ···
D136	···	5653	2.184±0.017	0.280±0.013	··· ···
D137	NGC4850	5995	2.227±0.022	0.272±0.013	··· ···
D143	IC4051	4981	2.344±0.018	0.332±0.006	2.89± 0.20
D144	IC4042	6363	2.228±0.036	0.283±0.013	··· ···
D145	IC4041	7070	2.142±0.036	0.292±0.013	··· ···
D146	···	7585	2.039±0.036	0.255±0.013	··· ···
D147	···	7728	1.993±0.028	0.223±0.007	3.23± 0.23
D148	NGC4889	6458	2.608±0.014	0.354±0.005	3.37± 0.17
D150	IC4011	7234	2.027±0.025	0.285±0.013	··· ···
D151	NGC4886	6349	2.178±0.017	0.253±0.013	··· ···
D152	IC3998	9403	2.210±0.036	0.281±0.013	··· ···
D153	···	6665	2.132±0.025	0.285±0.013	··· ···

TABLE D.2—*Continued*

Galaxy		$cz_{\rm hel}$	$\log\sigma$	Mg_2	$<$ Fe $>$
D155	NGC4873	5798	2.193±0.036	0.292±0.013	··· ···
D156	···	6665	2.001±0.022	0.235±0.013	··· ···
D157	···	6082	2.118±0.036	0.260±0.013	··· ···
D159	NGC4864	6812	2.297±0.025	0.290±0.013	··· ···
D160	IC3955	7642	2.276±0.036	0.309±0.013	··· ···
D161	···	7254	2.242±0.022	0.306±0.013	··· ···
D167	NGC4908	8712	2.325±0.036	0.274±0.013	··· ···
D168	IC4045	6944	2.328±0.025	0.310±0.013	··· ···
D170	IC4026	8152	2.164±0.036	0.298±0.013	··· ···
D172	IC4021	5717	2.204±0.025	0.304±0.013	··· ···
D173	···	7504	2.156±0.036	0.296±0.013	··· ···
D174	IC4012	7225	2.257±0.025	0.296±0.013	··· ···
D175	NGC4883	8132	2.252±0.036	0.306±0.013	··· ···
D176	···	6902	2.225±0.036	0.291±0.013	··· ···
D177	···	5619	2.016±0.036	0.265±0.013	··· ···
D179	NGC4865	4589	2.388±0.036	0.294±0.013	··· ···
D180	···	7834	2.116±0.031	0.232±0.007	2.62± 0.23
D181	···	6059	2.170±0.036	0.257±0.013	··· ···
D190	···	5821	2.294±0.021	0.286±0.007	3.42± 0.20
D191	···	6612	1.965±0.036	0.256±0.013	··· ···
D192	···	5423	1.975±0.036	0.231±0.013	··· ···
D193	···	7541	2.081±0.025	0.269±0.013	··· ···
D194	NGC4860	7934	2.390±0.017	0.347±0.013	··· ···
D197	IC3943	6821	2.262±0.023	0.276±0.007	3.02± 0.22
D198	···	6707	1.973±0.034	0.199±0.009	2.73± 0.29
D199	NGC4851	7895	2.128±0.026	0.249±0.007	2.80± 0.23
D200	···	7495	2.267±0.016	0.283±0.004	2.74± 0.13
D204	···	7667	2.102±0.033	0.272±0.013	··· ···
D206	NGC4895	8525	2.346±0.036	0.301±0.013	··· ···
D207	···	6764	2.187±0.017	0.258±0.006	2.97± 0.22
D209	···	7202	1.968±0.027	0.215±0.007	2.54± 0.23
D210	···	7245	2.225±0.033	0.274±0.013	··· ···
D212	···	8211	2.081±0.029	0.259±0.008	2.98± 0.26
D217	NGC4881	6705	2.314±0.017	0.299±0.013	··· ···
D218	···	8048	2.298±0.025	0.259±0.008	2.70± 0.25
D229	···	6941	2.008±0.033	0.214±0.009	2.73± 0.29
D230	···	7672	2.235±0.023	0.276±0.007	3.15± 0.21
D231	···	7928	2.106±0.025	0.261±0.007	2.68± 0.22
D232	NGC4896	5986	2.188±0.026	0.284±0.007	2.75± 0.22
D238	···	7339	2.013±0.022	0.240±0.013	··· ···
D239	NGC4841B	6527	2.304±0.019	0.289±0.007	2.91± 0.27
D240	NGC4841A	6765	2.412±0.017	0.315±0.006	2.69± 0.20
D242	···	7622	2.147±0.025	0.223±0.006	2.91± 0.20

NOTE.— Galaxy IDs from Dressler (1980b). $\log\sigma$ and Mg_2 from Davies et al. (1987), Dressler (1987), Lucey et al. (1991b), and Guzmán et al. (1992) as compiled into a consistent system by JFK95b, and from Jørgensen (1997b, in prep.). $<$ Fe $>$ from Jørgensen (1997b, in prep.). The uncertainties on $\log\sigma$ and Mg_2 for the data *not* from JFK95b and Jørgensen (1997b, in prep.) are based on the mean uncertainties quoted by the respective references.

Appendix E

The HydraI Galaxy Images

In this appendix we show Gunn r images for the 35 HydraI fields that contain the 64 photometry program galaxies. All the images have north down and east to the right, and are of size $8.7' \times 8.7'$. Where a field have been observed several times in Gunn r, the image with best seeing is shown. The images are displayed with logarithmic intensity, with a low cut calculated by `display` algorithm (in the range 210–460 ADU), and with a fixed high cut of 4000 ADU.

Table E.1 can be used to look up the field number(s) for a given galaxy. Figure 3.1 (p. 25) shows the positions of the fields on the sky. More details about the observations are given in Section 3.2 (p. 25).

Table E.1: Mapping From Rnum to Field Number(s)

Rnum	Name	Type	Field(s)	Rnum	Name	Type	Field(s)
R112	E501G13	S0(4)	615	R253		S(rs)0(1)	00
R120		S0/a	615	R254		E3	34
R129		S0(5)	519	R255		E3	00, 12
R138		S0(5)	419	R256	N3309	E1	00
R166	E501G20	SB0(2)	37, 39	R261		S0	214
R185		S0	37	R266	A1034-27A	E7/S0	00
R188	E501G21	S0(6)pec	27	R268		S0	00
R193	E501G26	S0(6)	29	R269	N3311	S0(2)	00
R194		S0/a(r)	27	R273		E1	00, 12
R202		S0	47	R278		E1	12
R209		E3/S0(3)	13, 27	R283	E437G11	S0(4)	321
R211		S0	24	R286		E	00
R212	E501G27	E6/S0	24	R288	E437G13	S0(5)pec	321
R213		S0(6)	15	R293		E2	00
R214		S0	18	R295	E437G15	S0(7)	535
R216	A1033-27	E2	15	R305		SB(r)0(1)	427
R217		S0(6)	13	R307		E2	66
R218	N3305	E1	35	R308		E3/S0	16
R219		S0(4)	18	R316	E501G47	S0(5)	14
R224	N3307	S0(5)/a(rs)	15	R317	N3315	SB0(0)	33
R225		SB(r)0(1)	18, 215	R319		S0	22
R226		E	15	R322	E501G49	SB(s)0(6)	14
R231		S0	35	R327		SB(r)0(3)	320
R234	N3308	SB0(2)	13	R334	E501G52	S0(5)/a	26
R237		S0(3)	13	R336	N3316	SB0(1)	210, 28
R238	E501G35	S0(6)/a	46	R337		E/S0	210, 28
R239	I629	E2/S0	15	R338		S0(5)	43
R241		S0	13	R340		E	28
R243		S0(4)	23, 24	R343		S0(2)	43
R245		SB(rs)0(0)	00, 15	R347	I2597	E3/S0	43
R250	E437G08	S0(6)	428	R359		SB(r)0(5)	26
R252	E437G09	E4/S0	535	R389		S0(5)	64

Notes: Rnum, Name, and Type are from Richter (1989); see references therein.

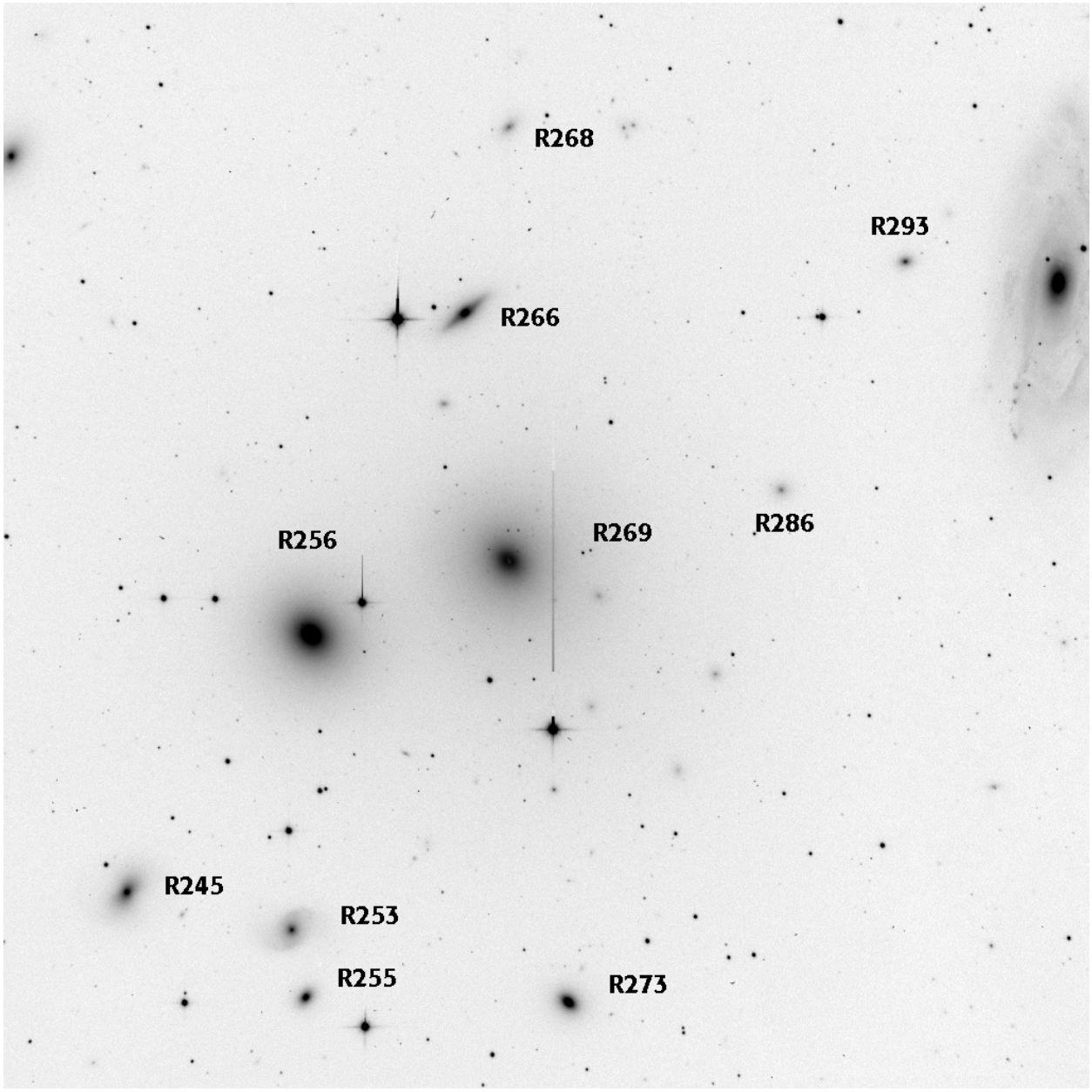

Field 00. Image: `d1549`. Seeing: 0.81″.

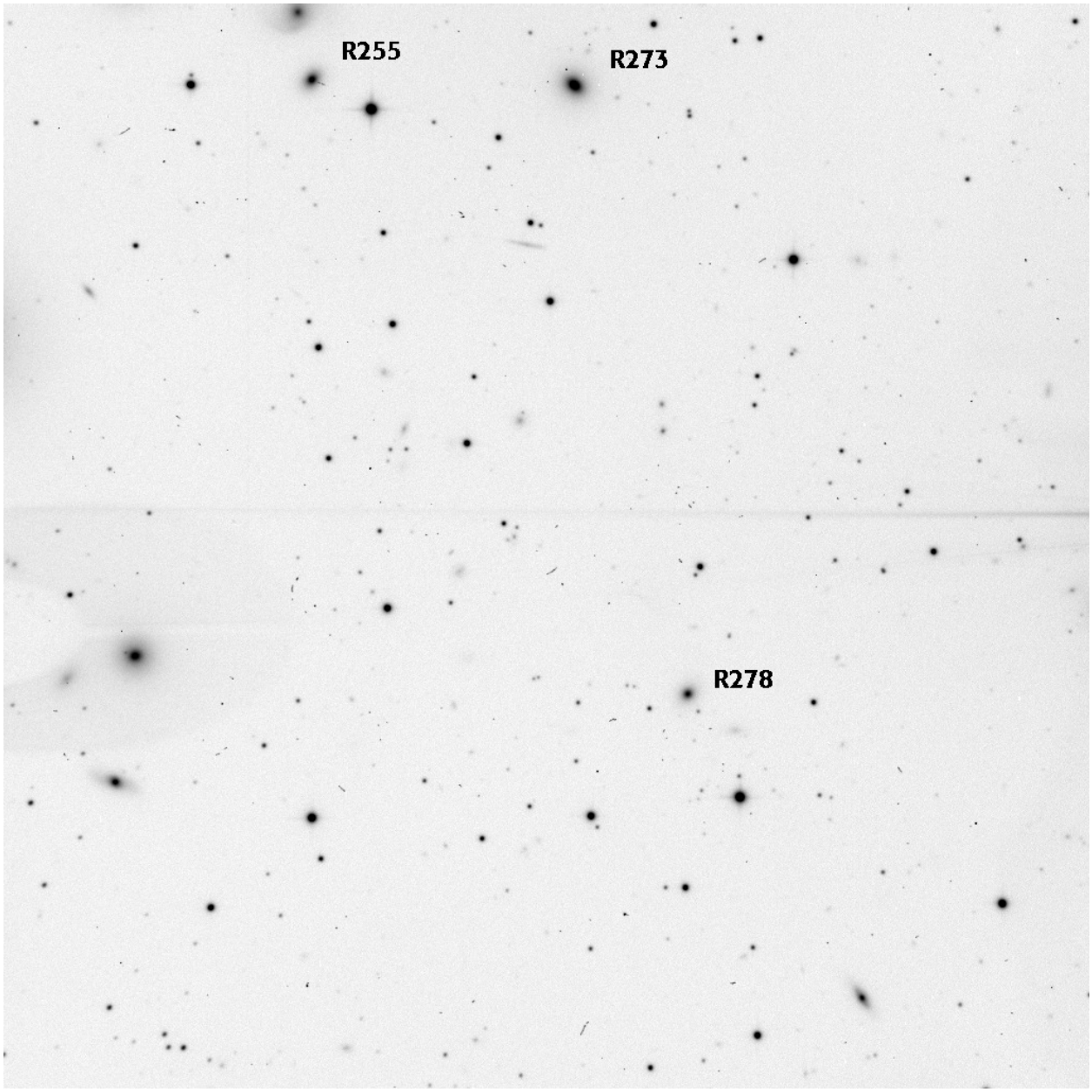

Field 12. Image: `d1300`. Seeing: 1.37″.

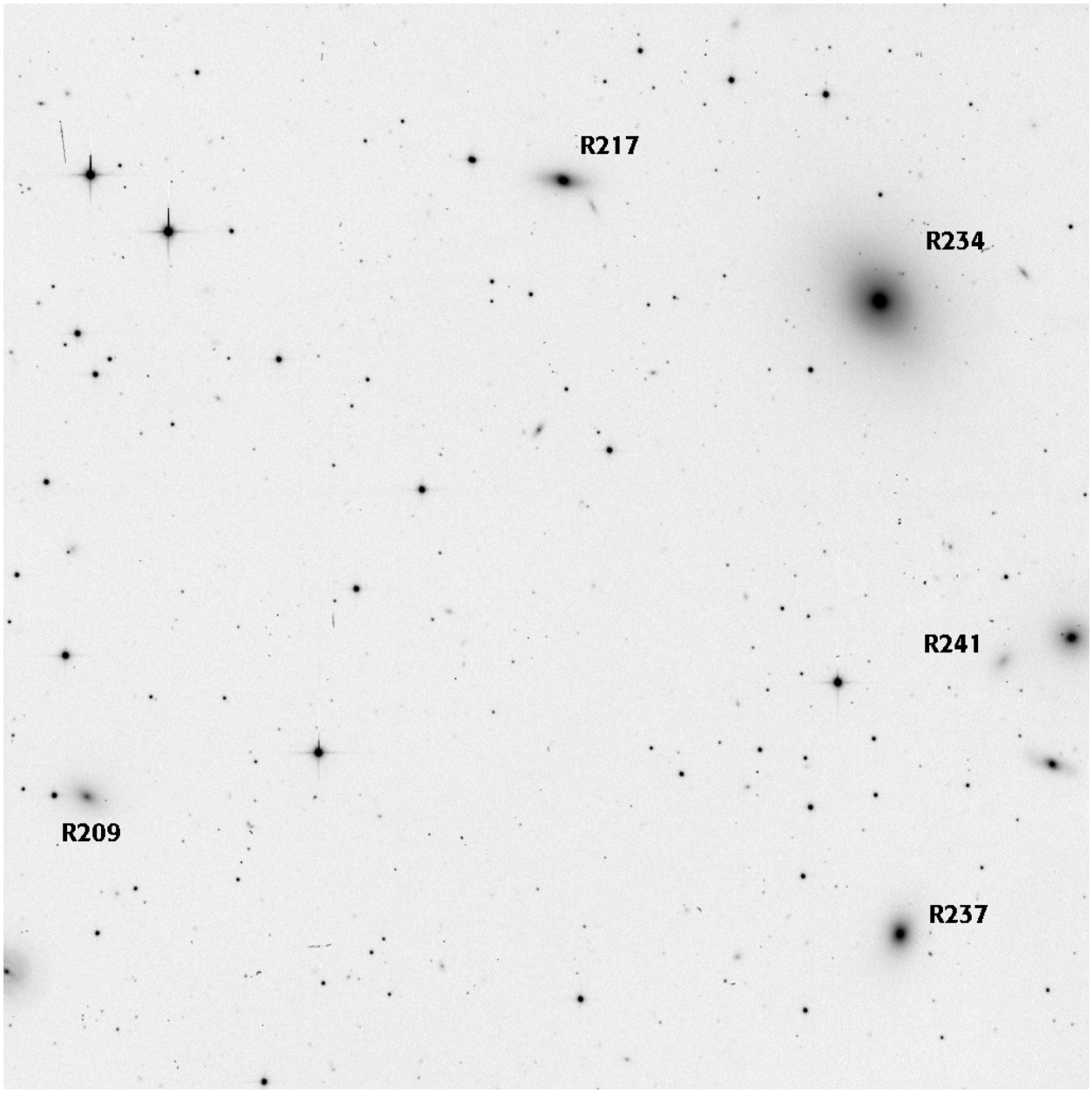

Field 13. Image: `d1559`. Seeing: 0.89″.

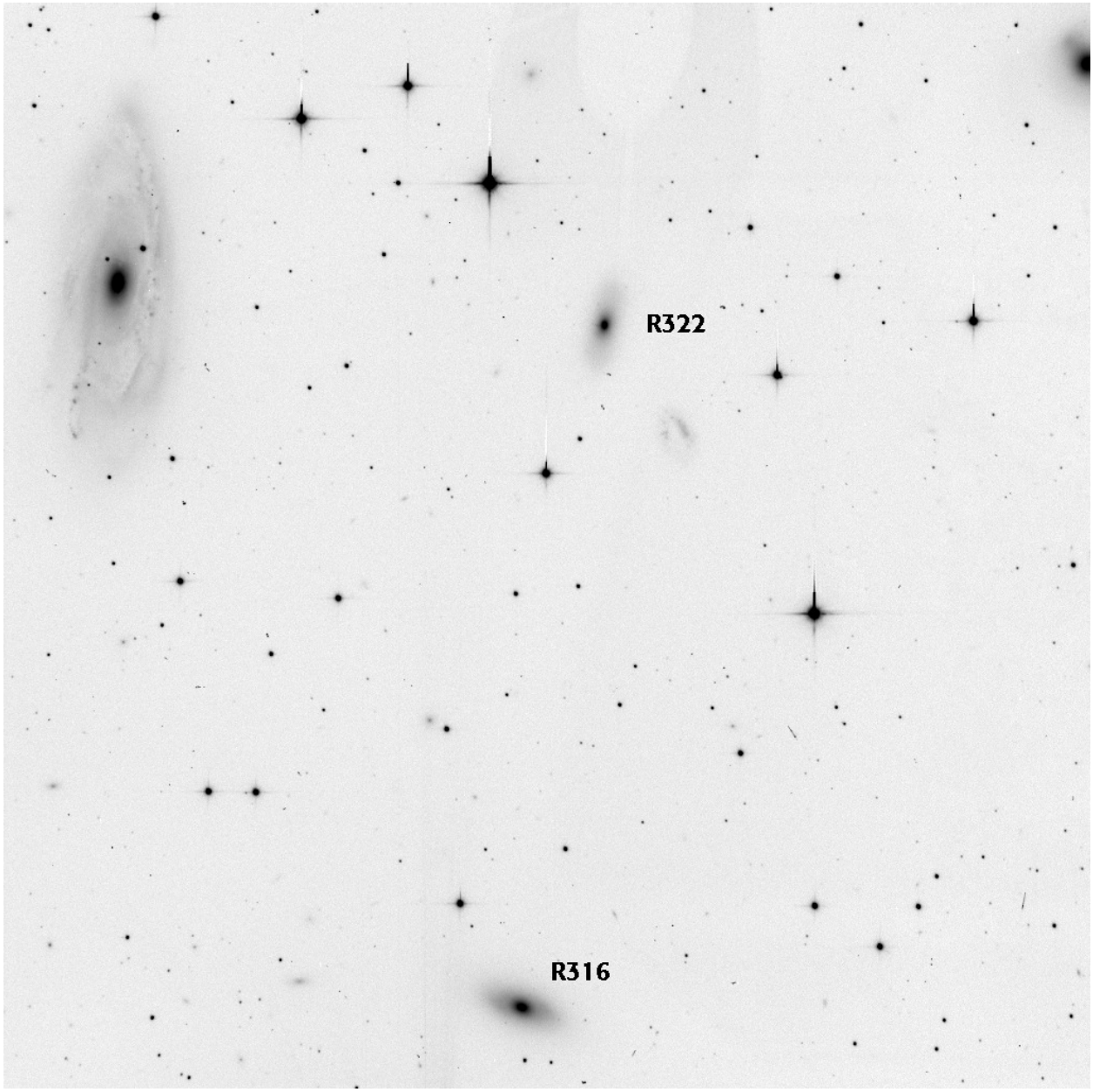

Field 14. Image: `d1552`. Seeing: 0.86″.

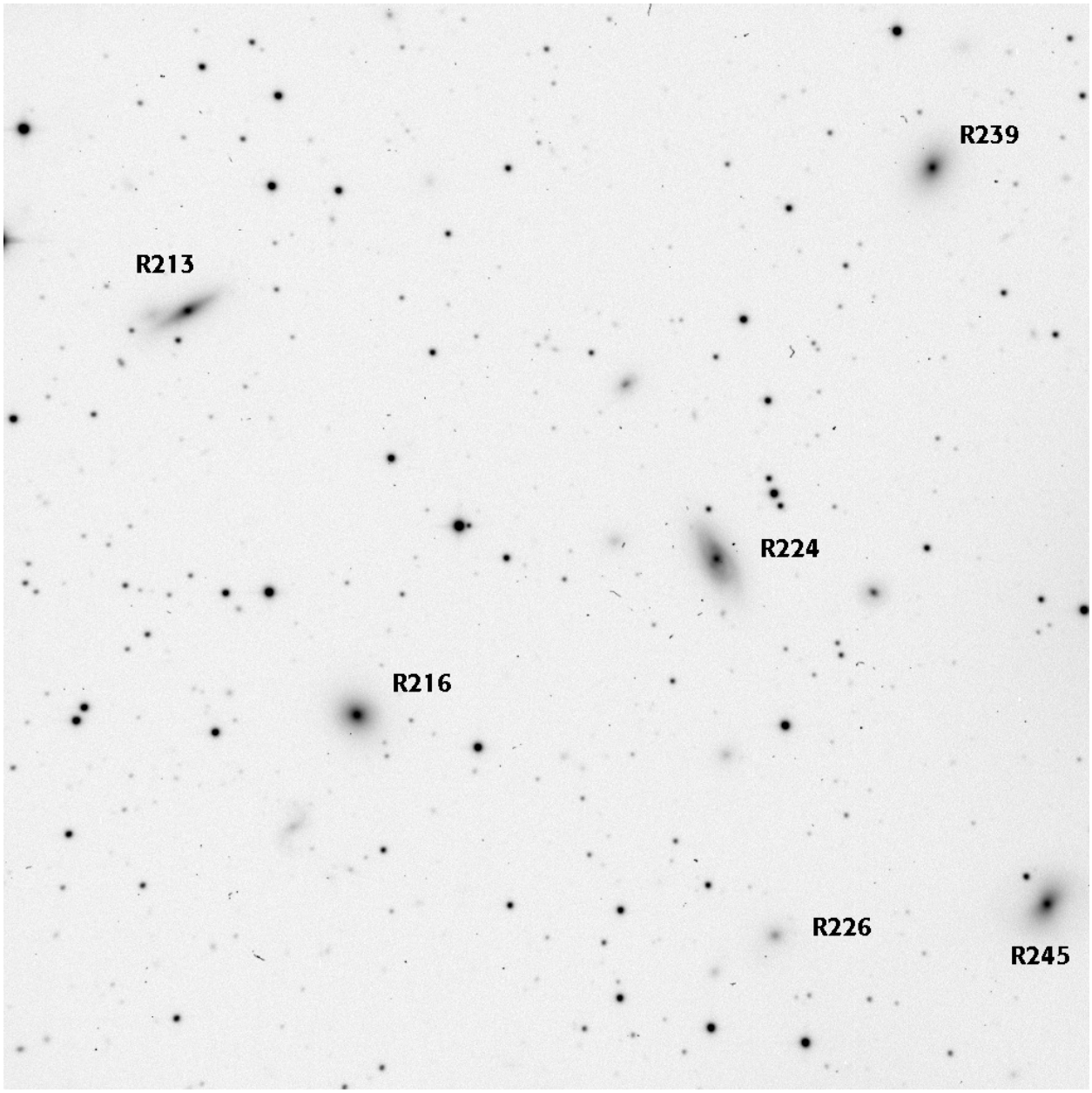

Field 15. Image: d1445. Seeing: 1.68″.

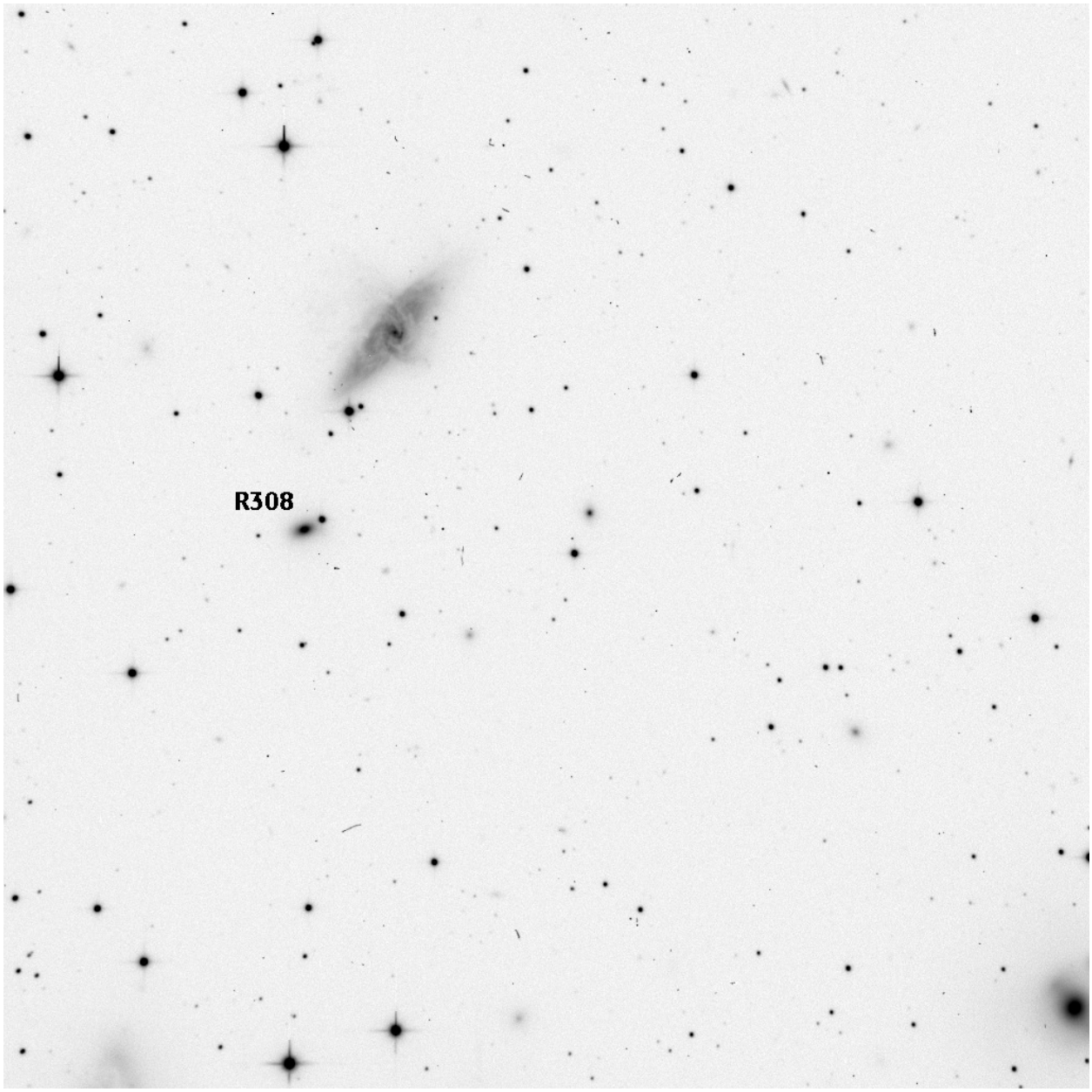

Field 16. Image: `d1994`. Seeing: 1.13″.

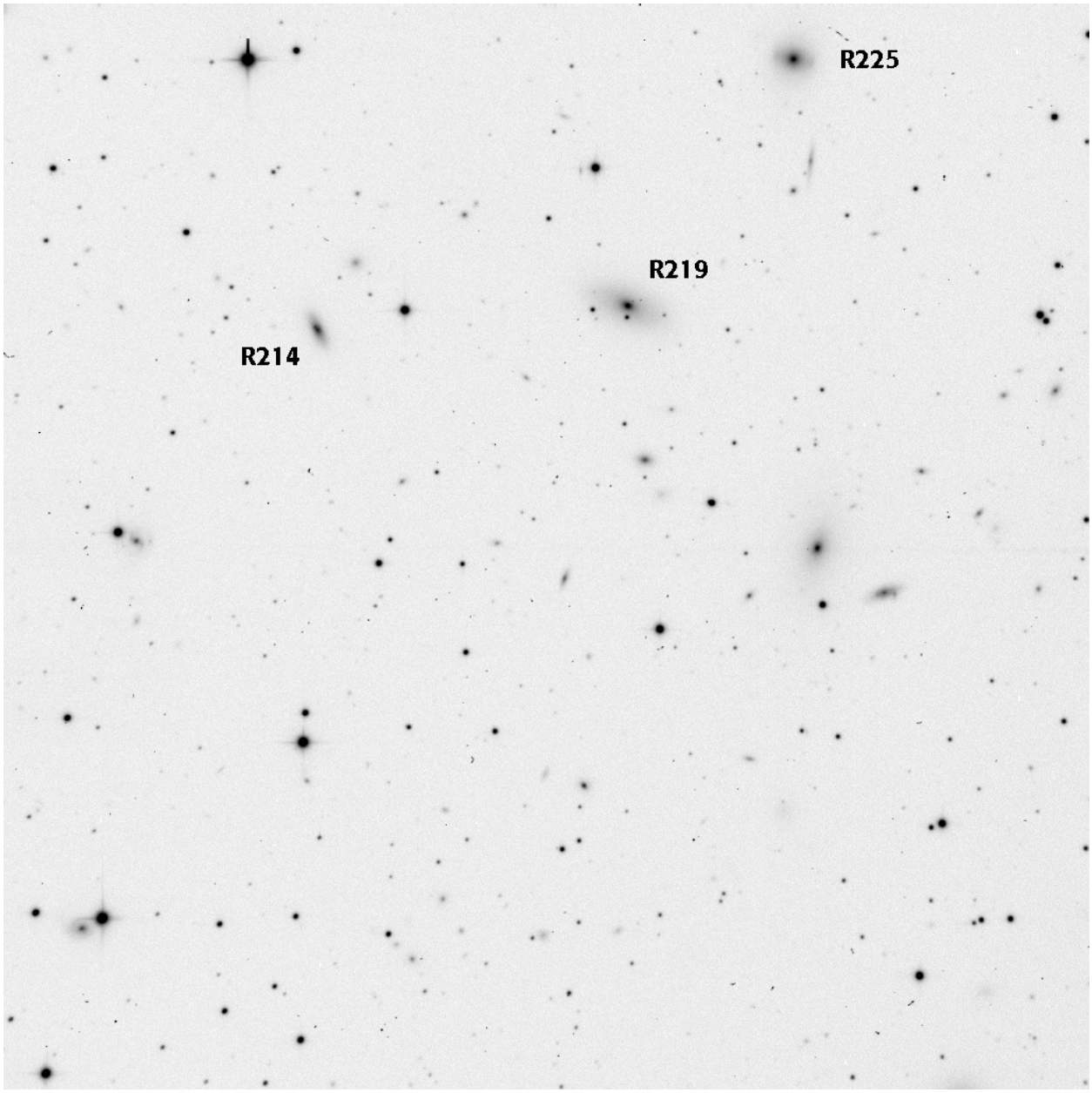

Field 18. Image: `d1293`. Seeing: 1.29″.

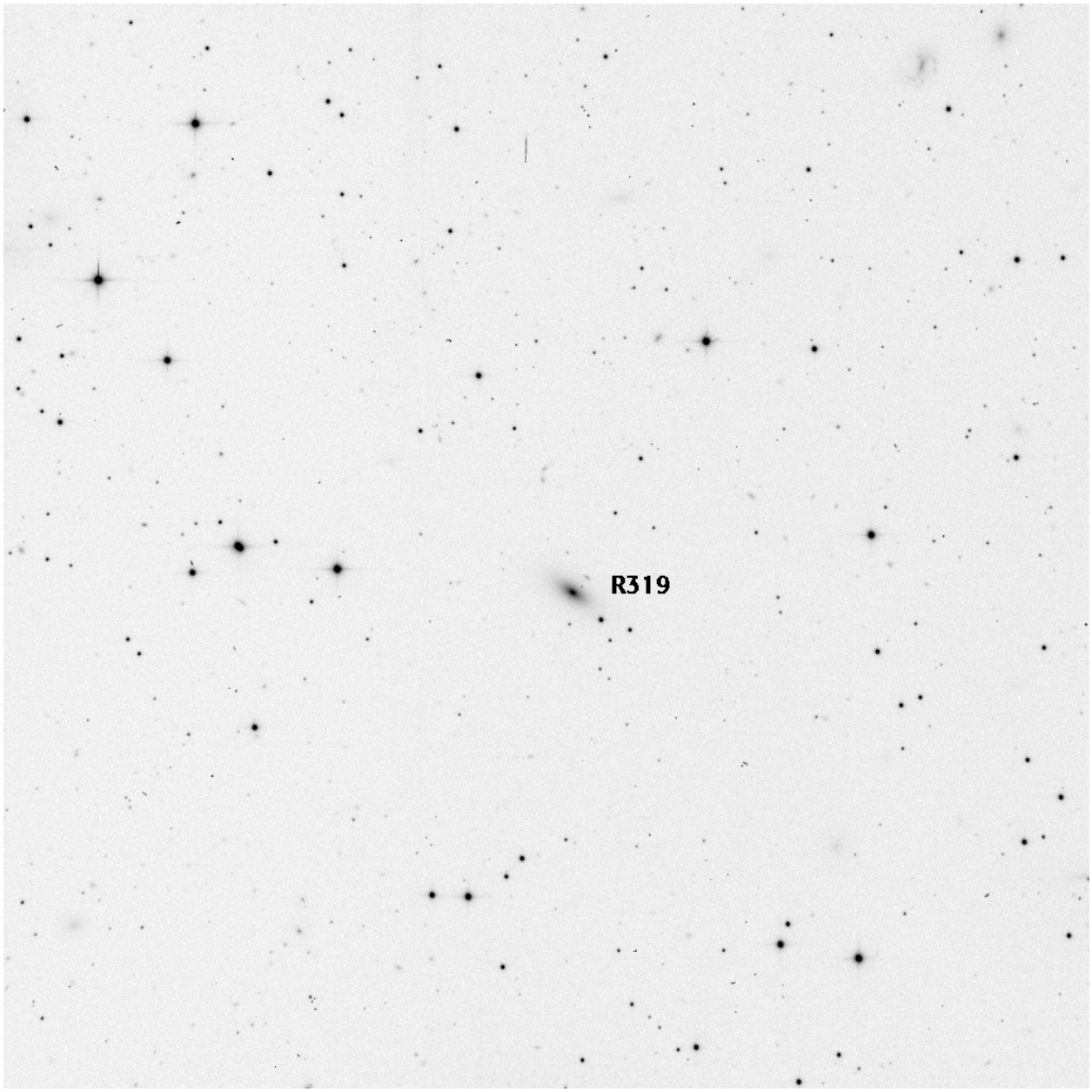

Field 22. Image: `d1728`. Seeing: 0.90″.

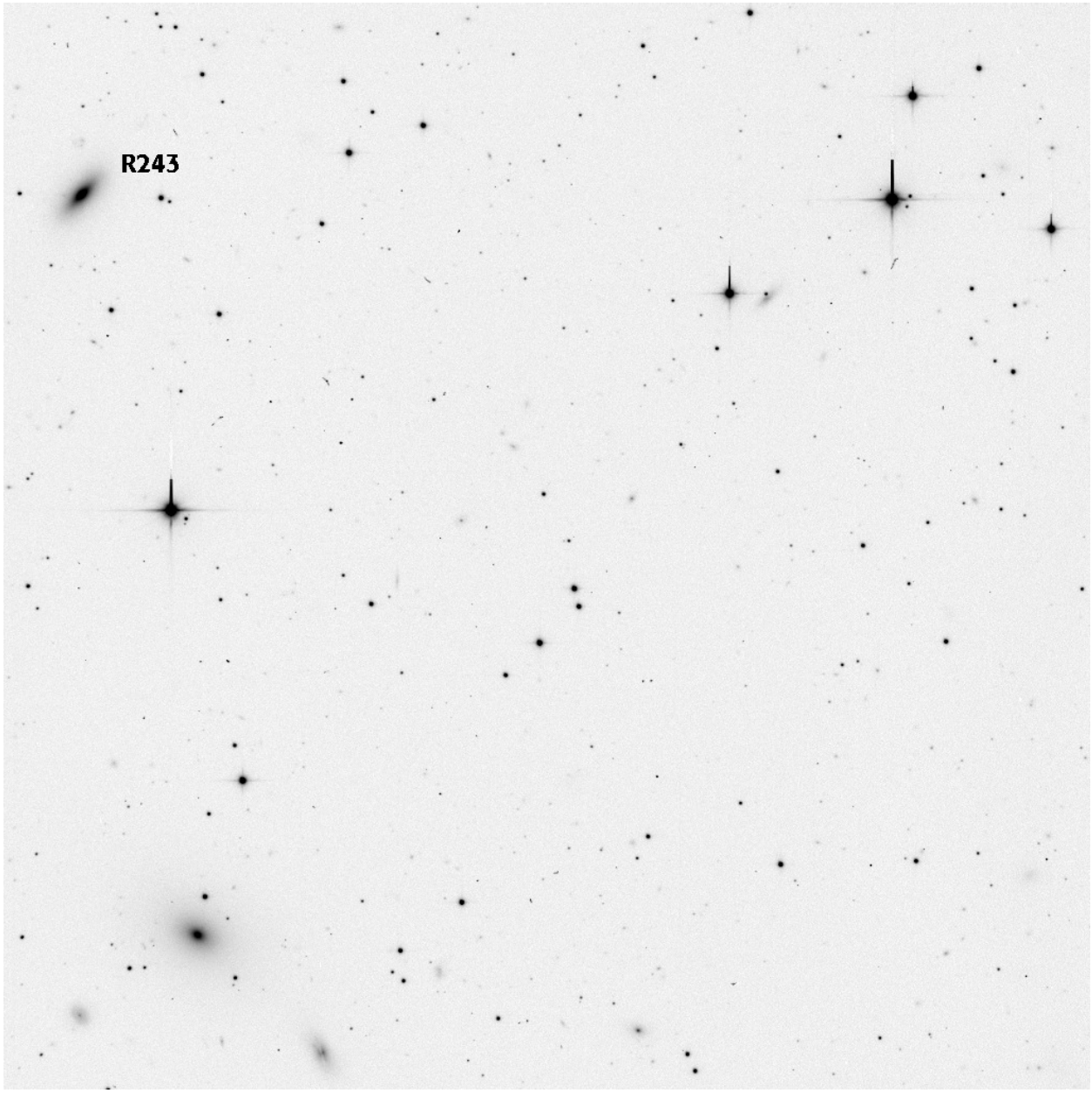

Field 23. Image: d1566. Seeing: 0.86″.

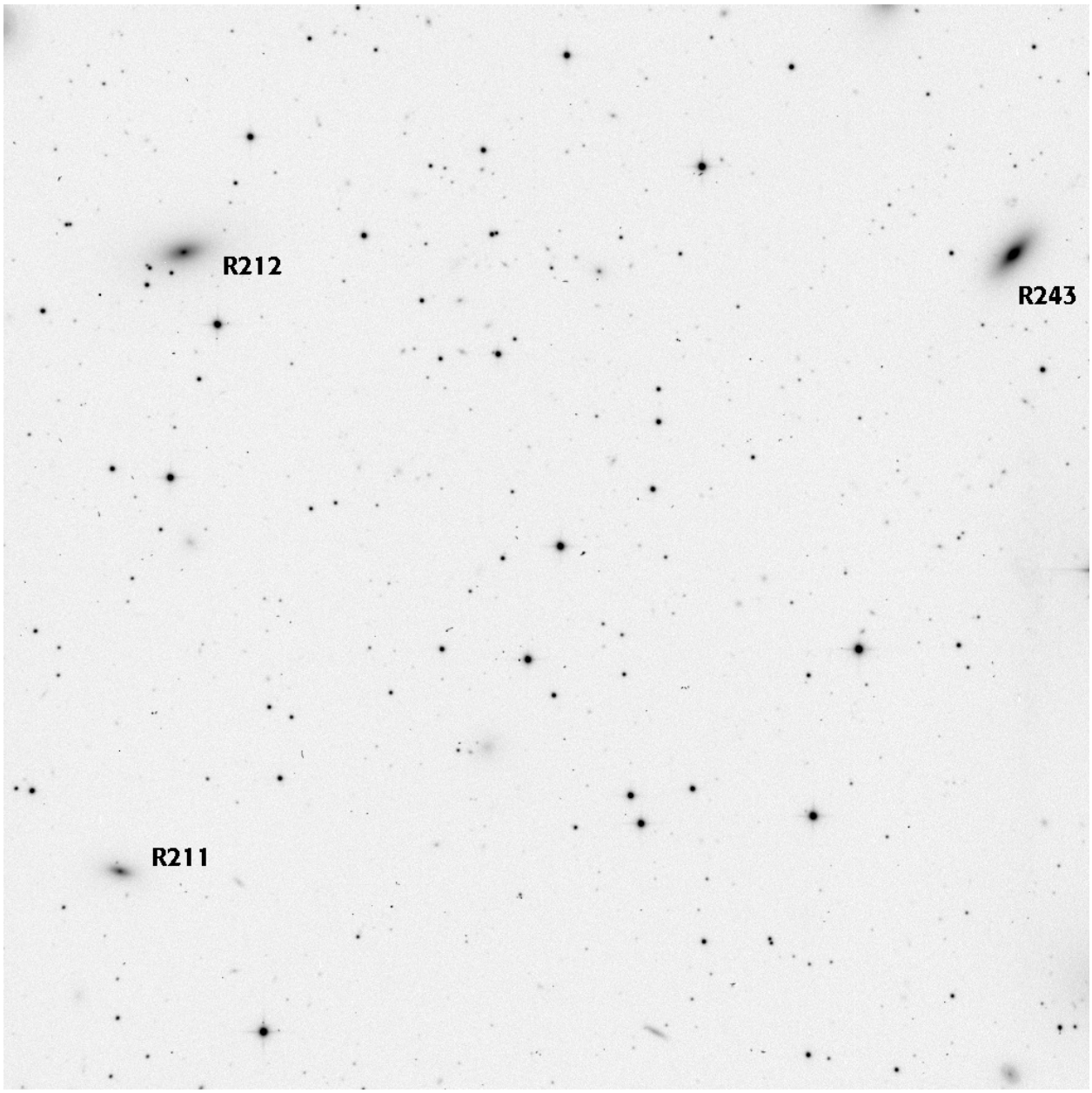

Field 24. Image: `d1734`. Seeing: 1.00″.

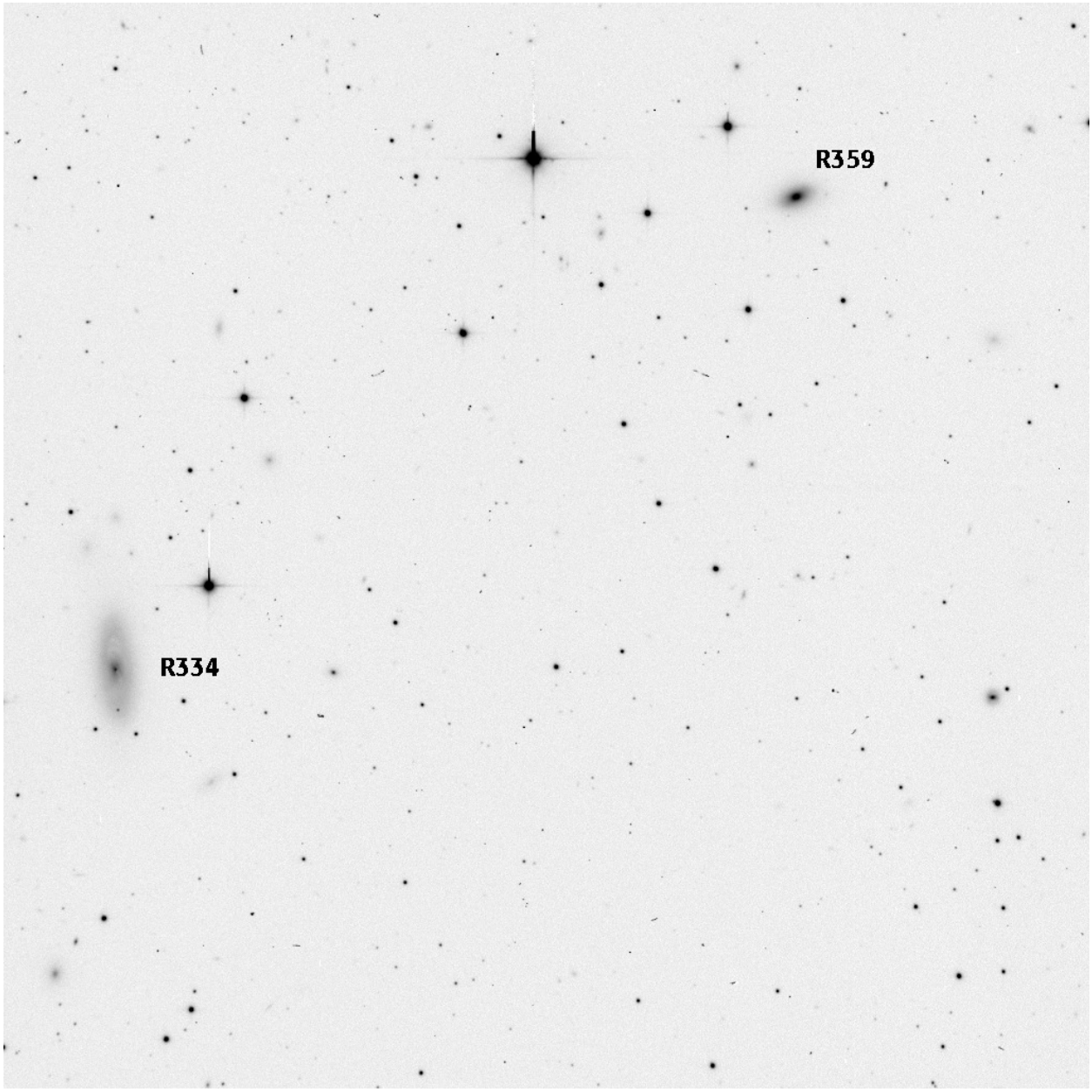

Field 26. Image: `d1731`. Seeing: 0.94″.

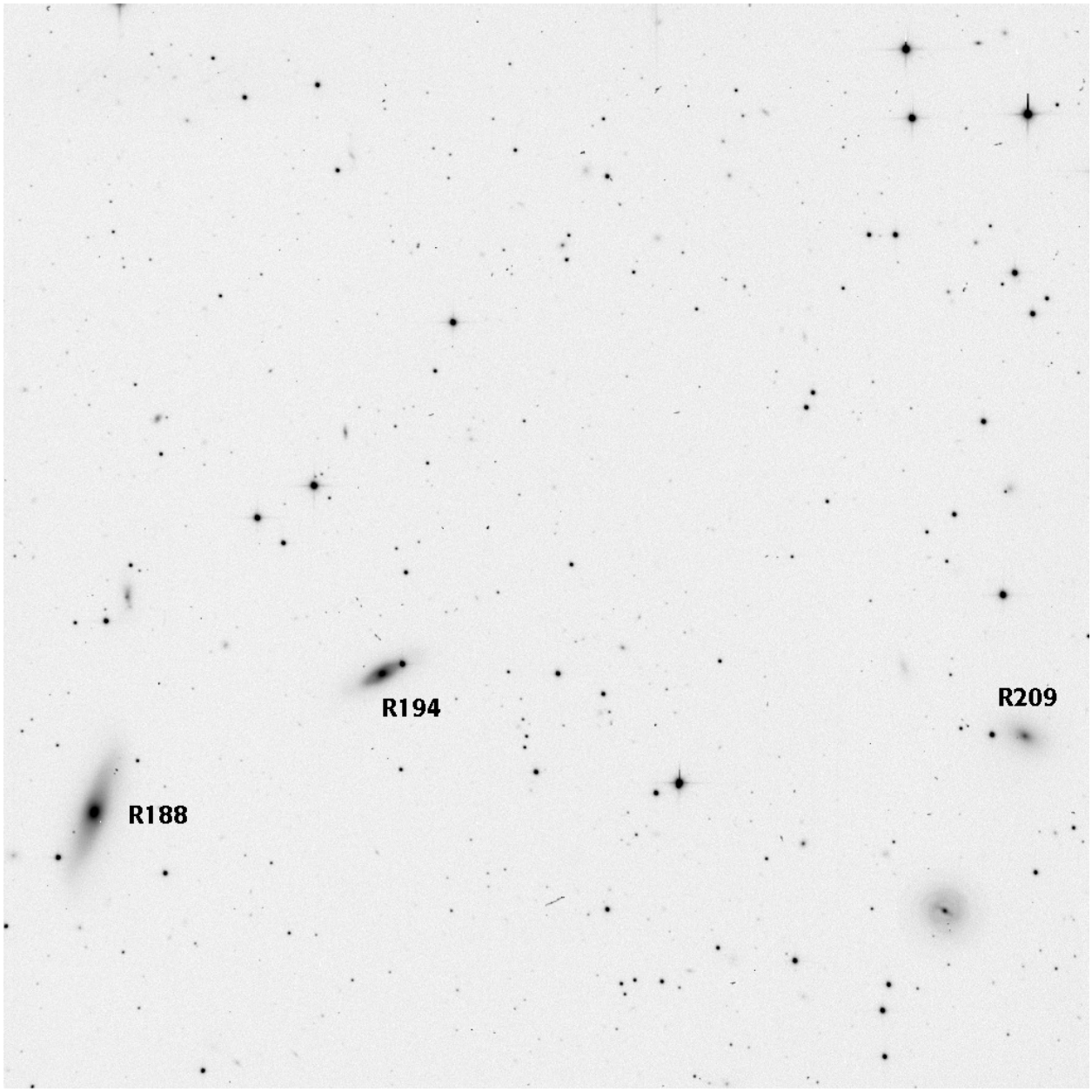

Field 27. Image: `d1563`. Seeing: 0.86″.

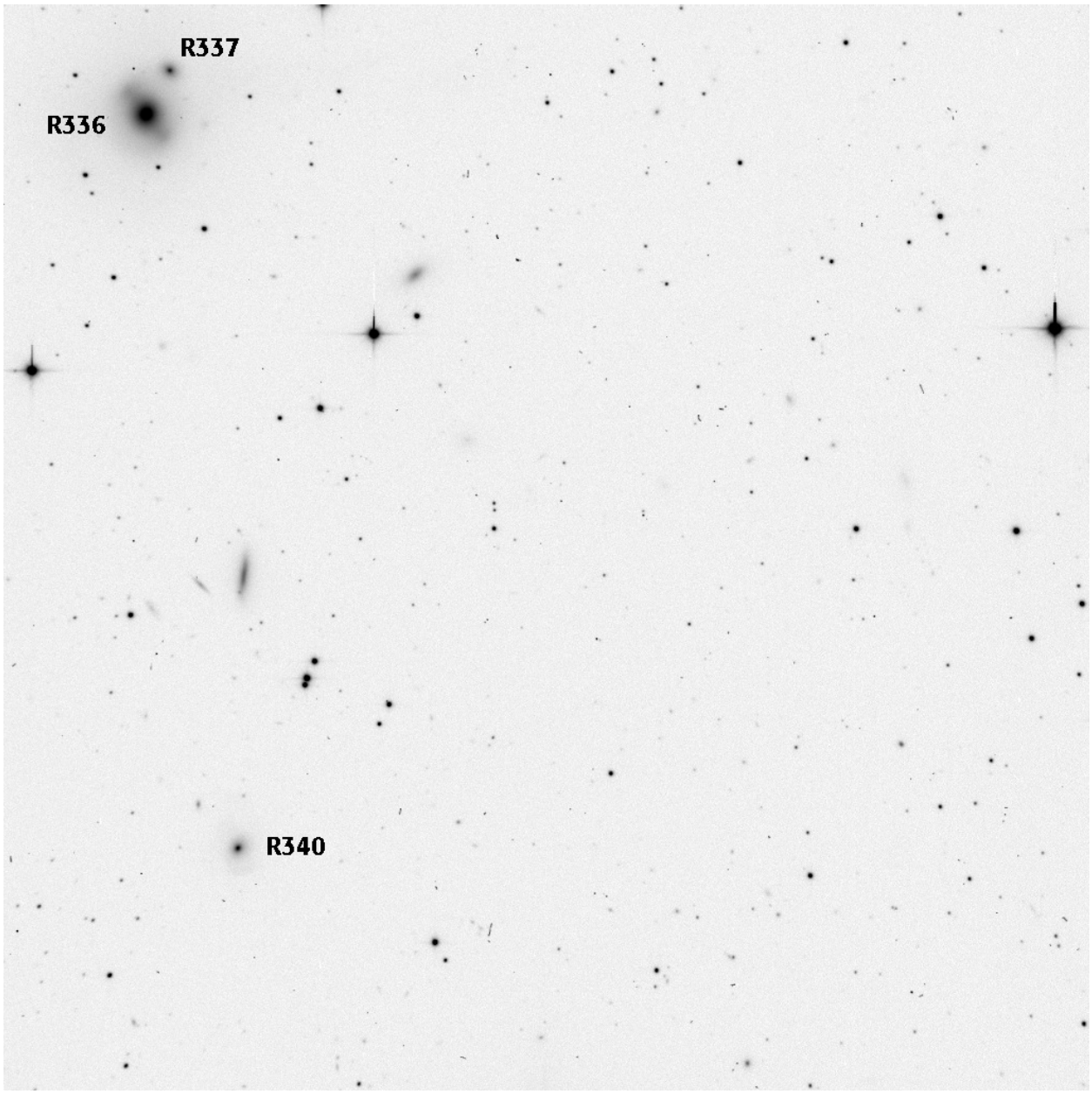

Field 28. Image: `d1751`. Seeing: 1.04″.

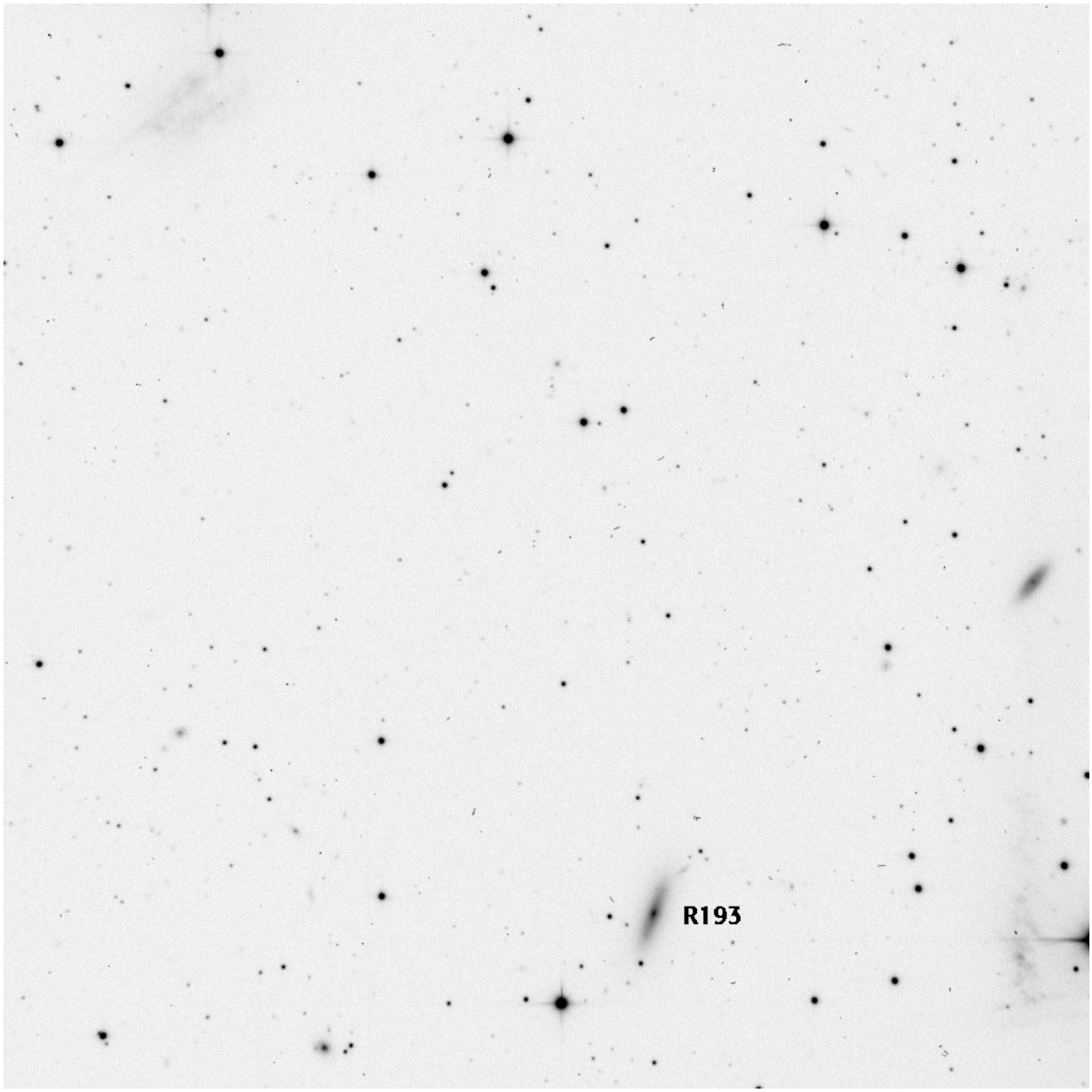

Field 29. Image: d1426. Seeing: 1.15″.

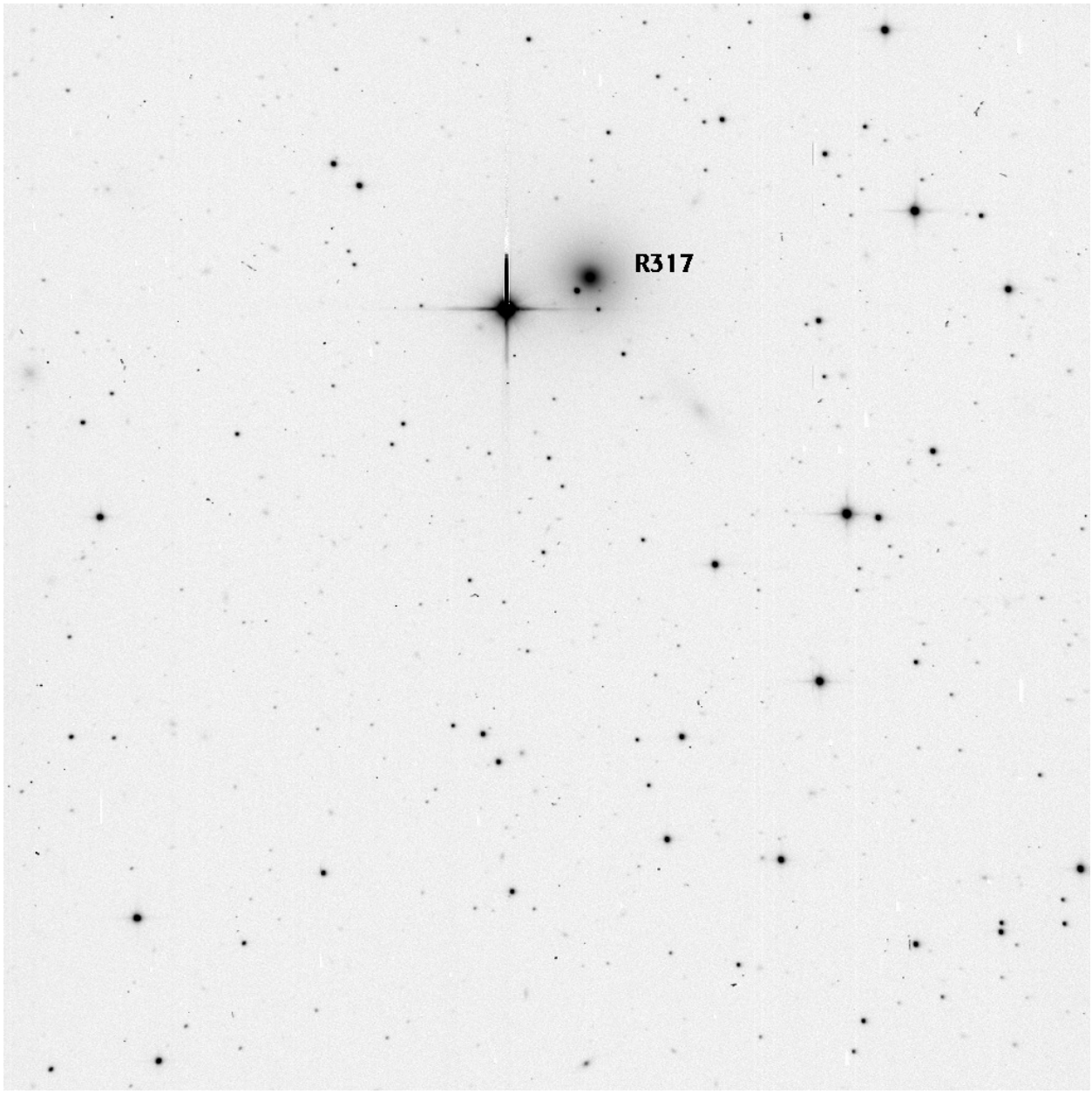

Field 33. Image: `d1754sum`. Seeing: 1.09″.

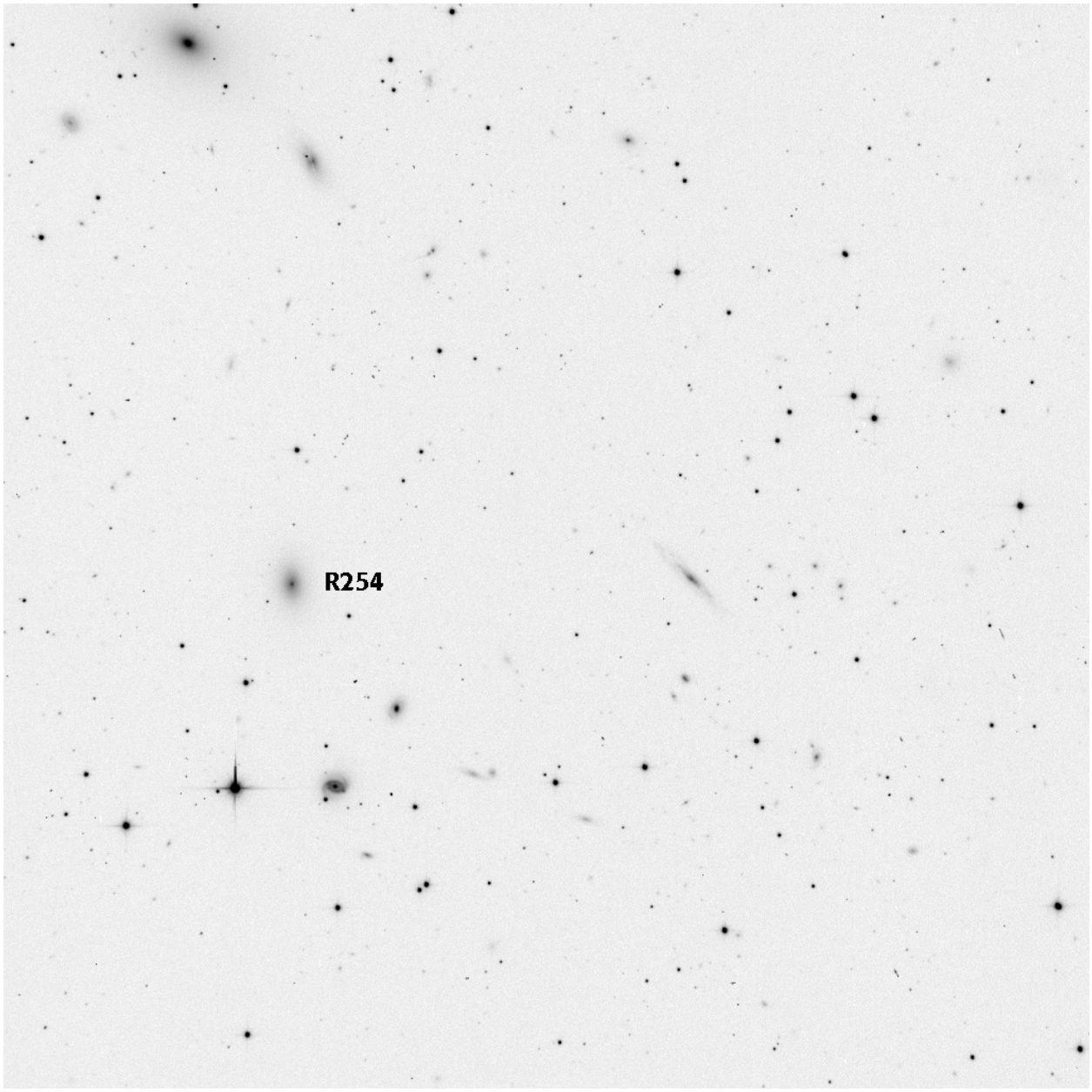

Field 34. Image: `d1725`. Seeing: 0.77″.

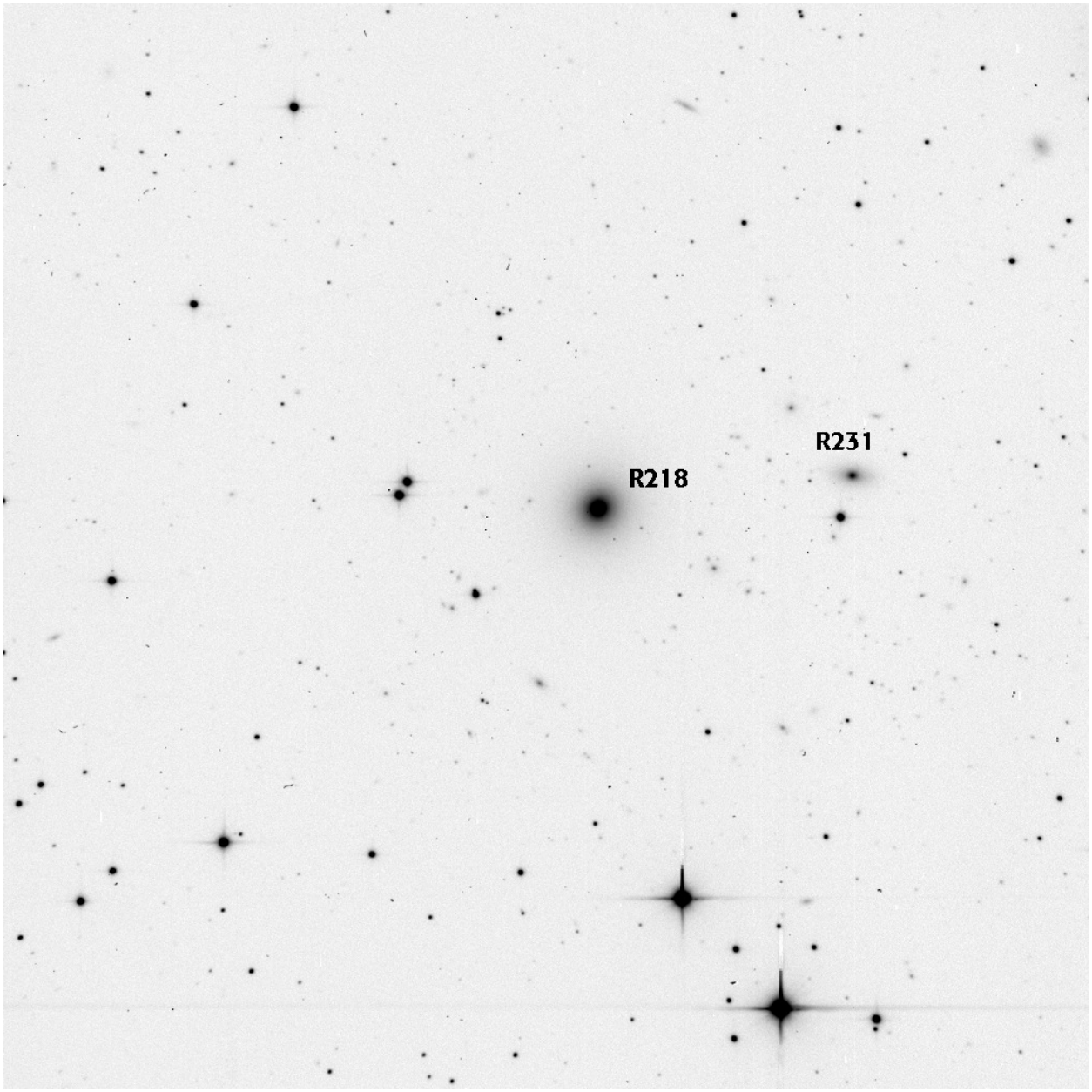

Field 35. Image: `d1591sum`. Seeing: 1.17″.

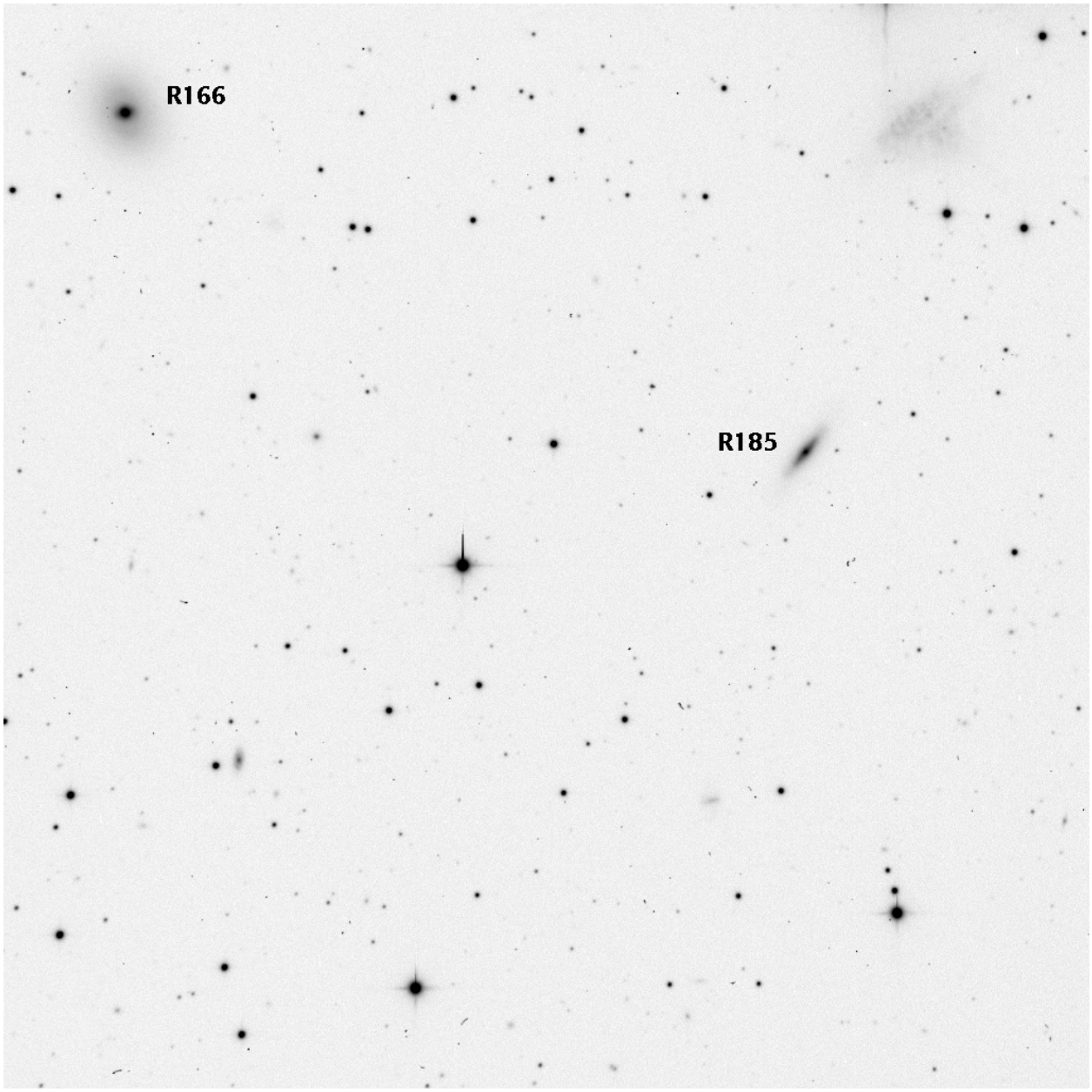

Field 37. Image: `d1290`. Seeing: 1.26″.

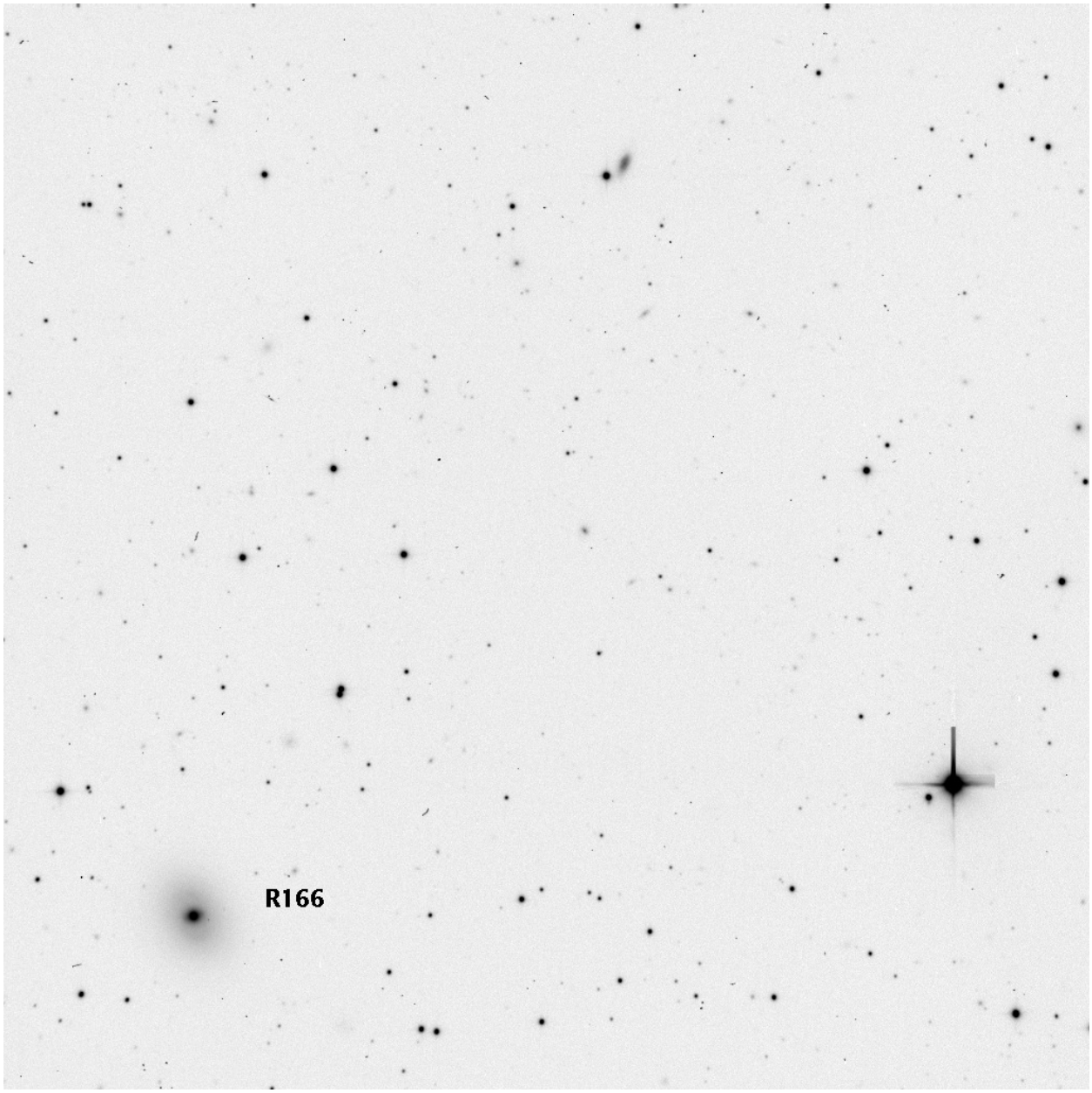

Field 39. Image: d1967. Seeing: 1.08″.

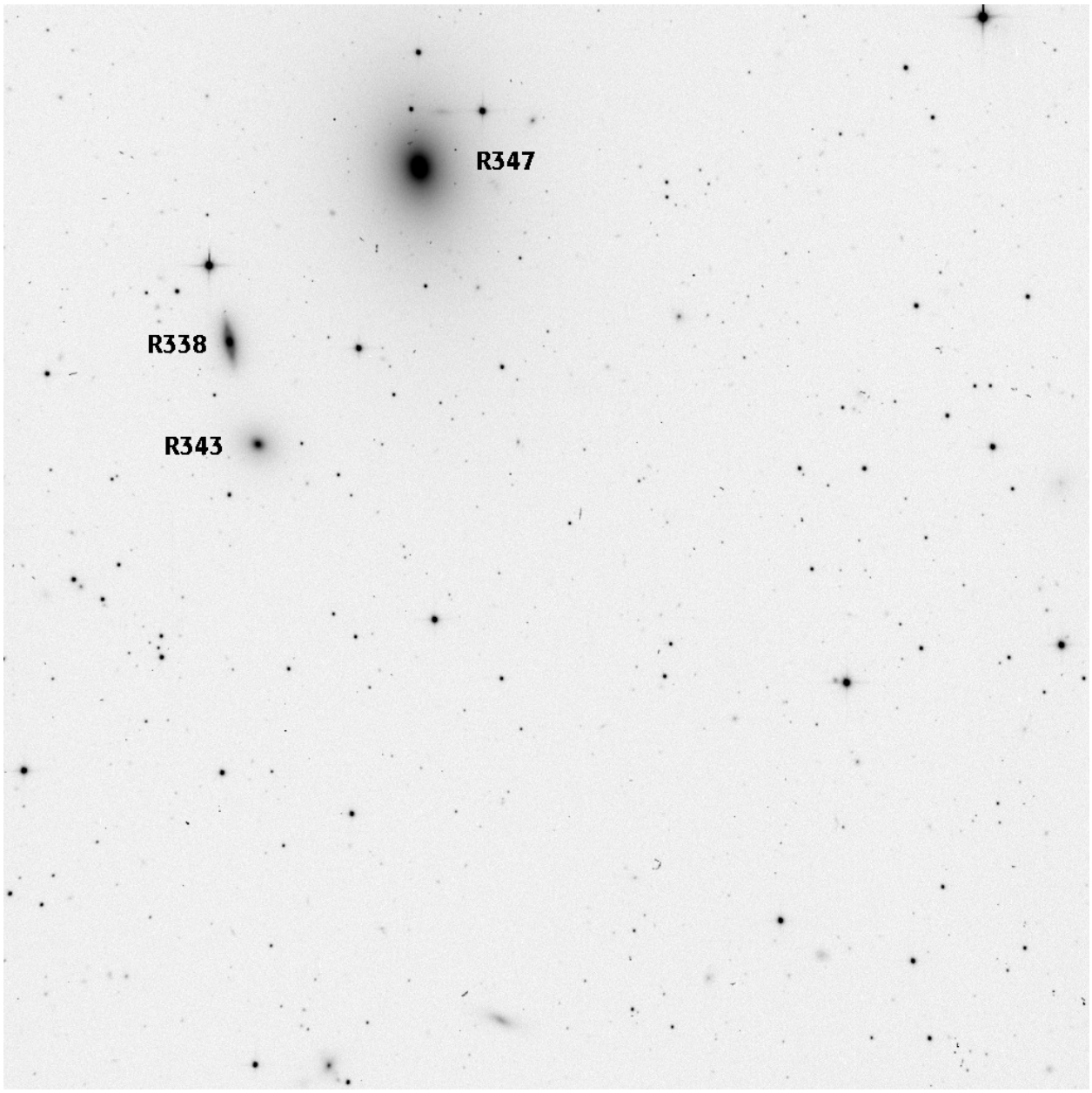

Field 43. Image: `d1571`. Seeing: 0.85″.

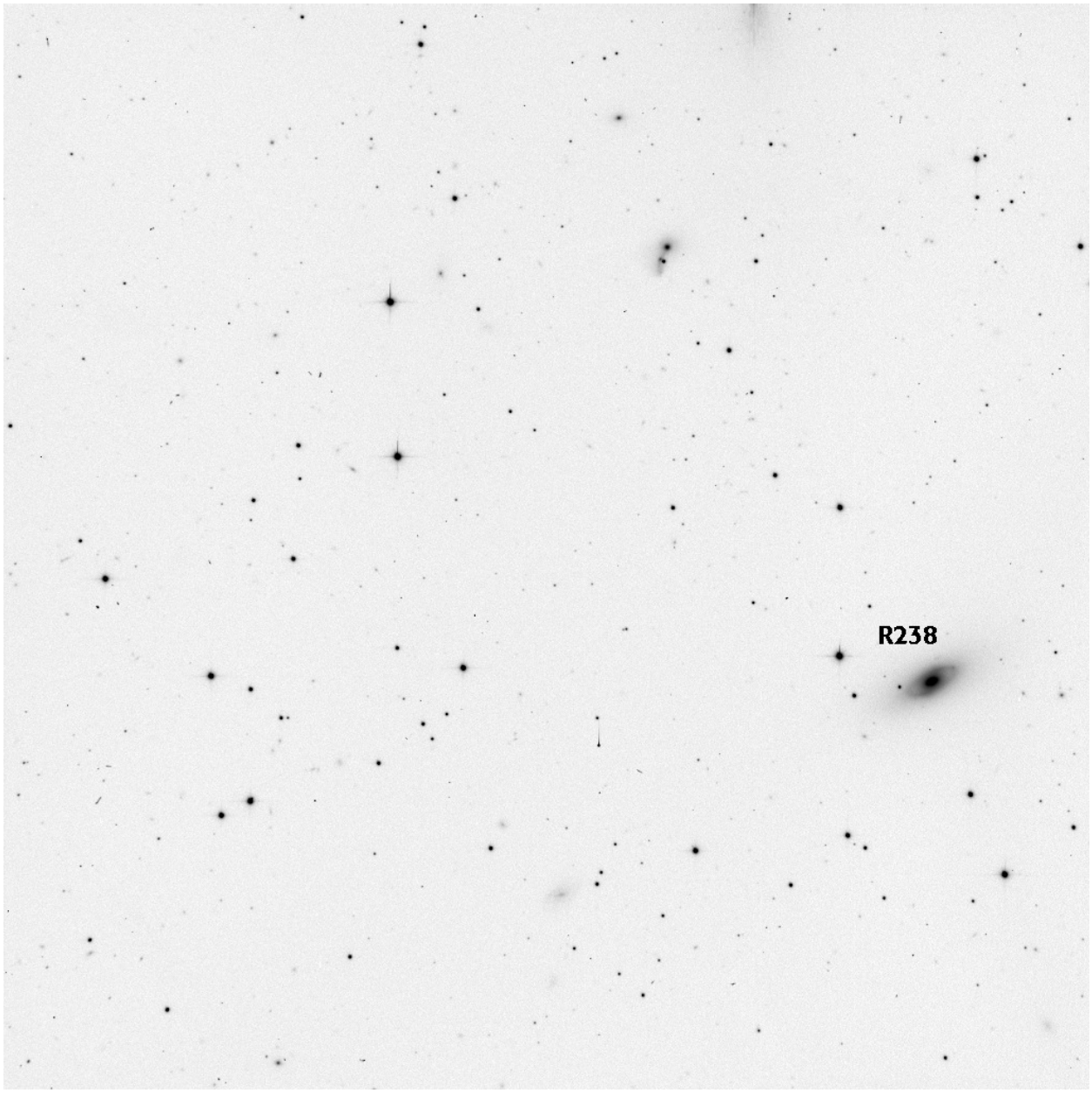

Field 46. Image: `d1719`. Seeing: 0.81″.

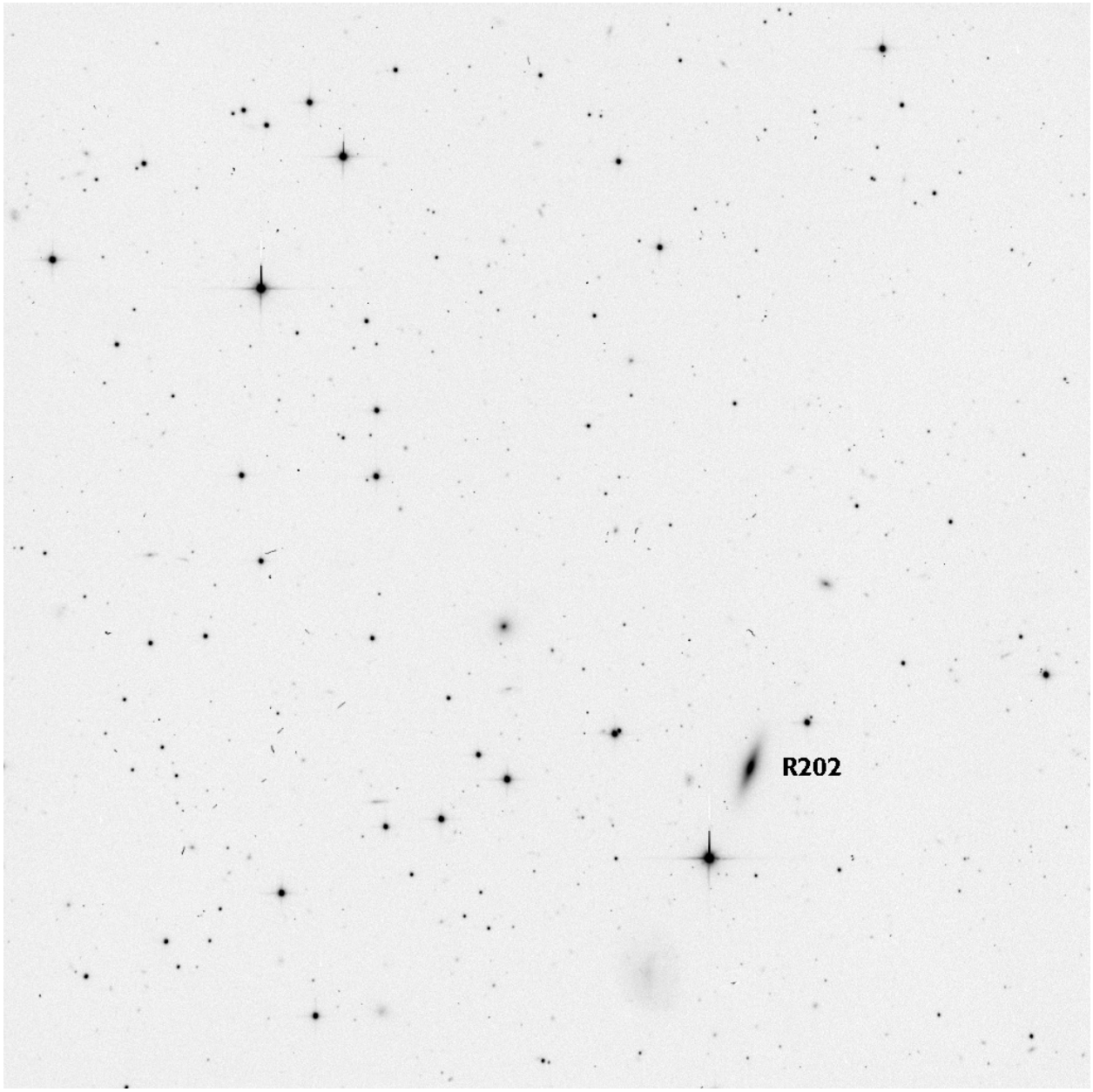

Field 47. Image: d1722. Seeing: 0.84″.

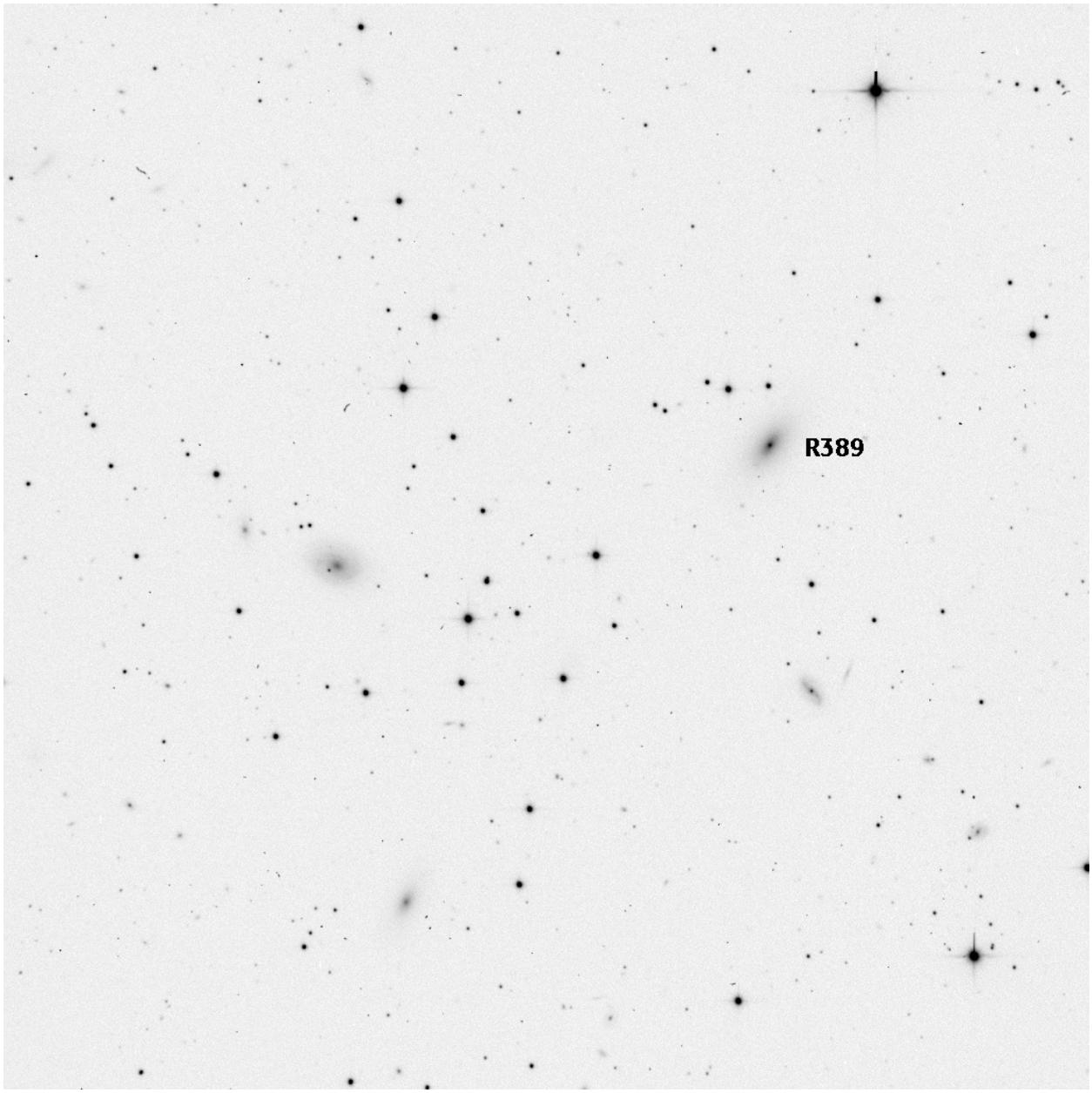

Field 64. Image: `d1985`. Seeing: 0.96″.

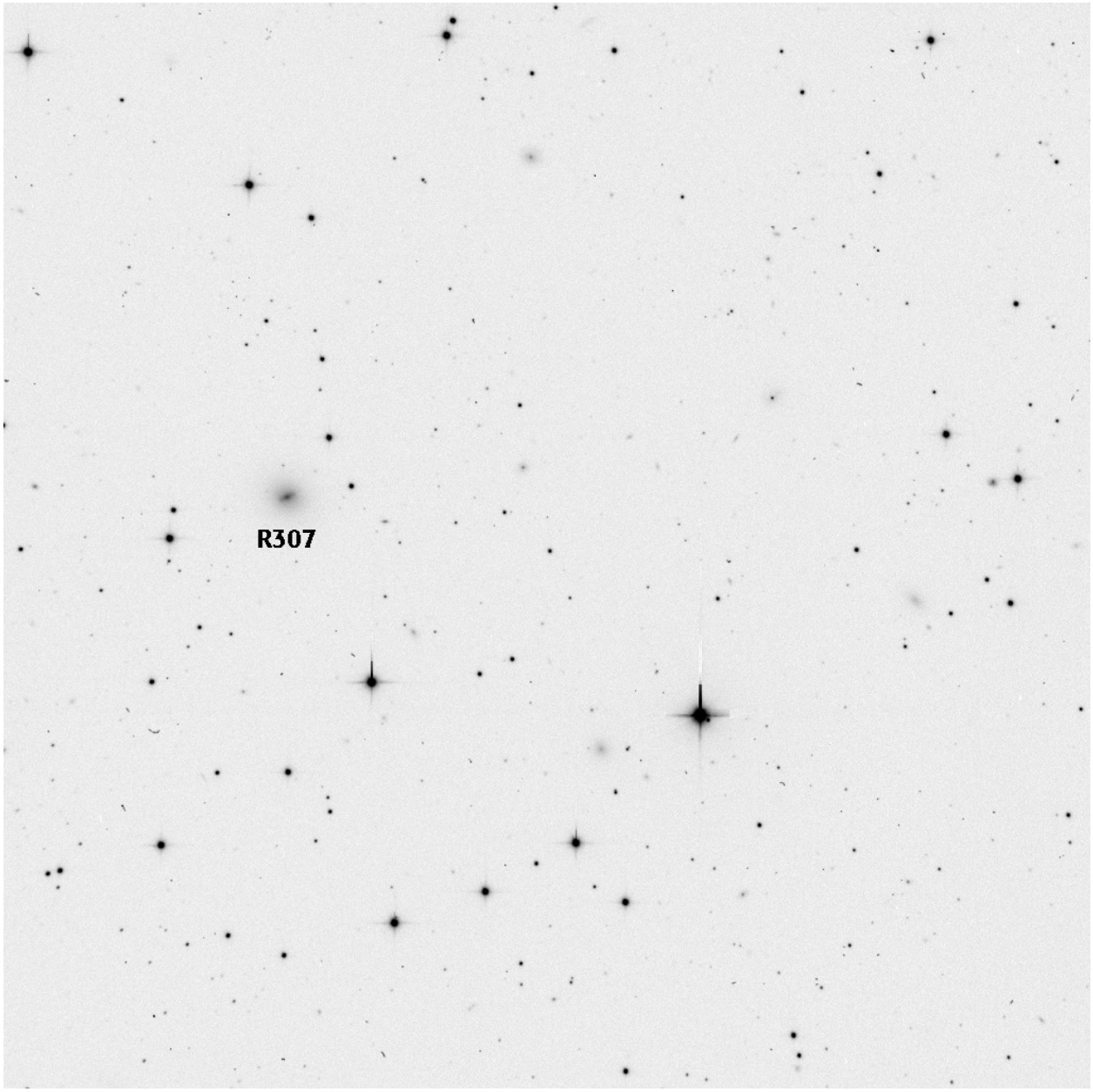

Field 66. Image: `d1988`. Seeing: 0.89″.

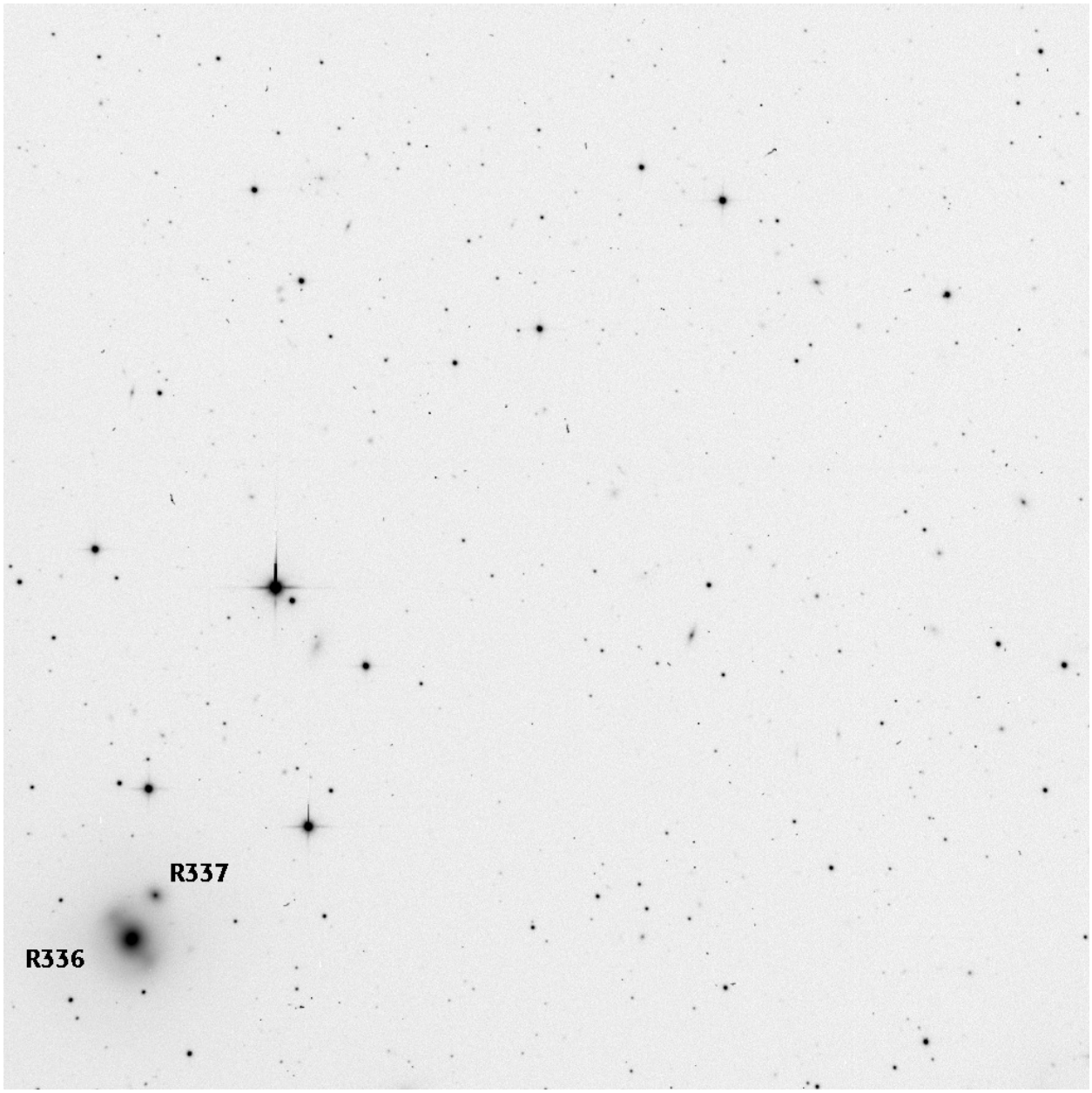

Field 210. Image: d1738. Seeing: 0.93″.

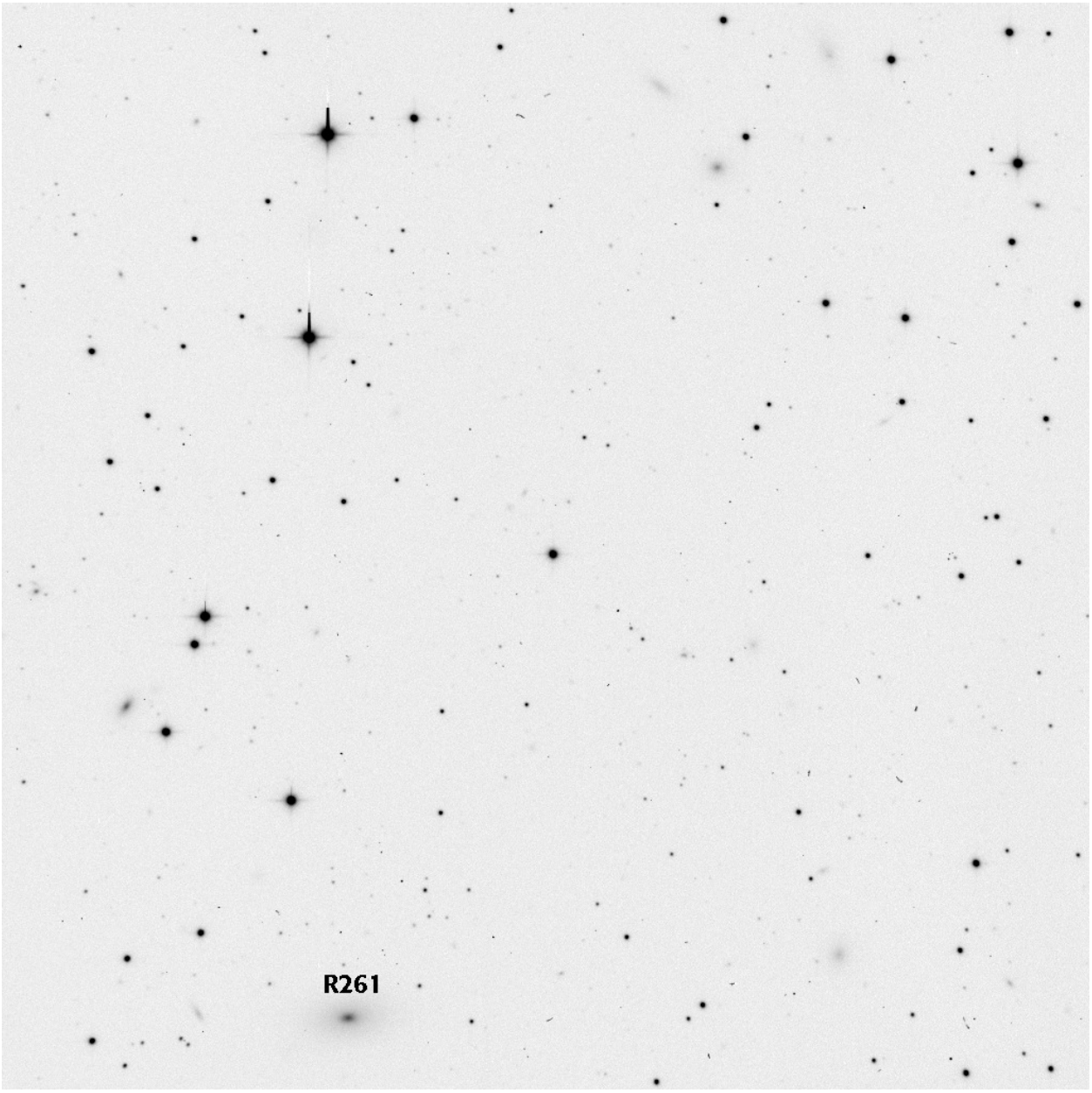

Field 214. Image: `d1407`. Seeing: 1.13″.

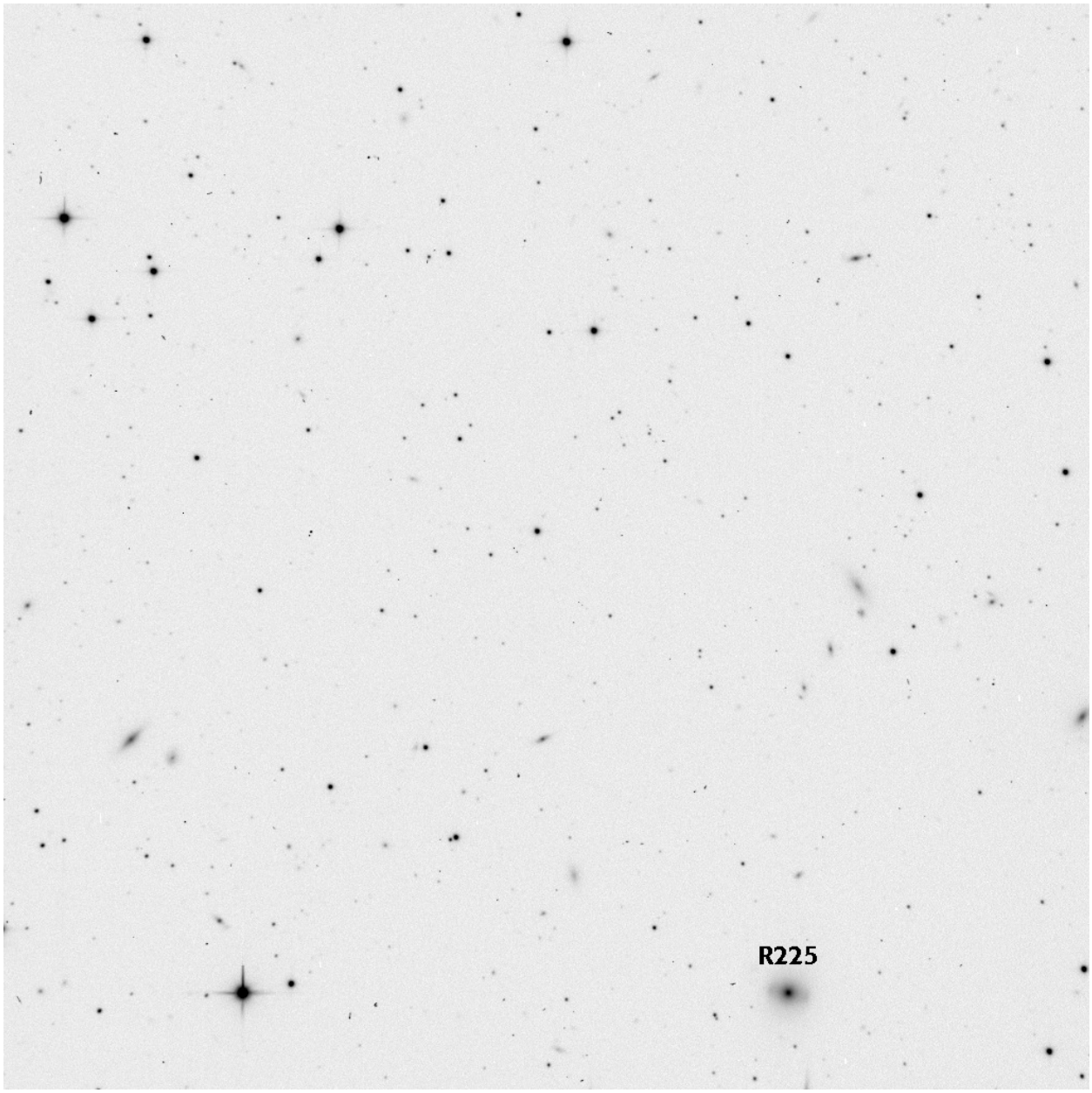

Field 215. Image: d1746. Seeing: 1.03″.

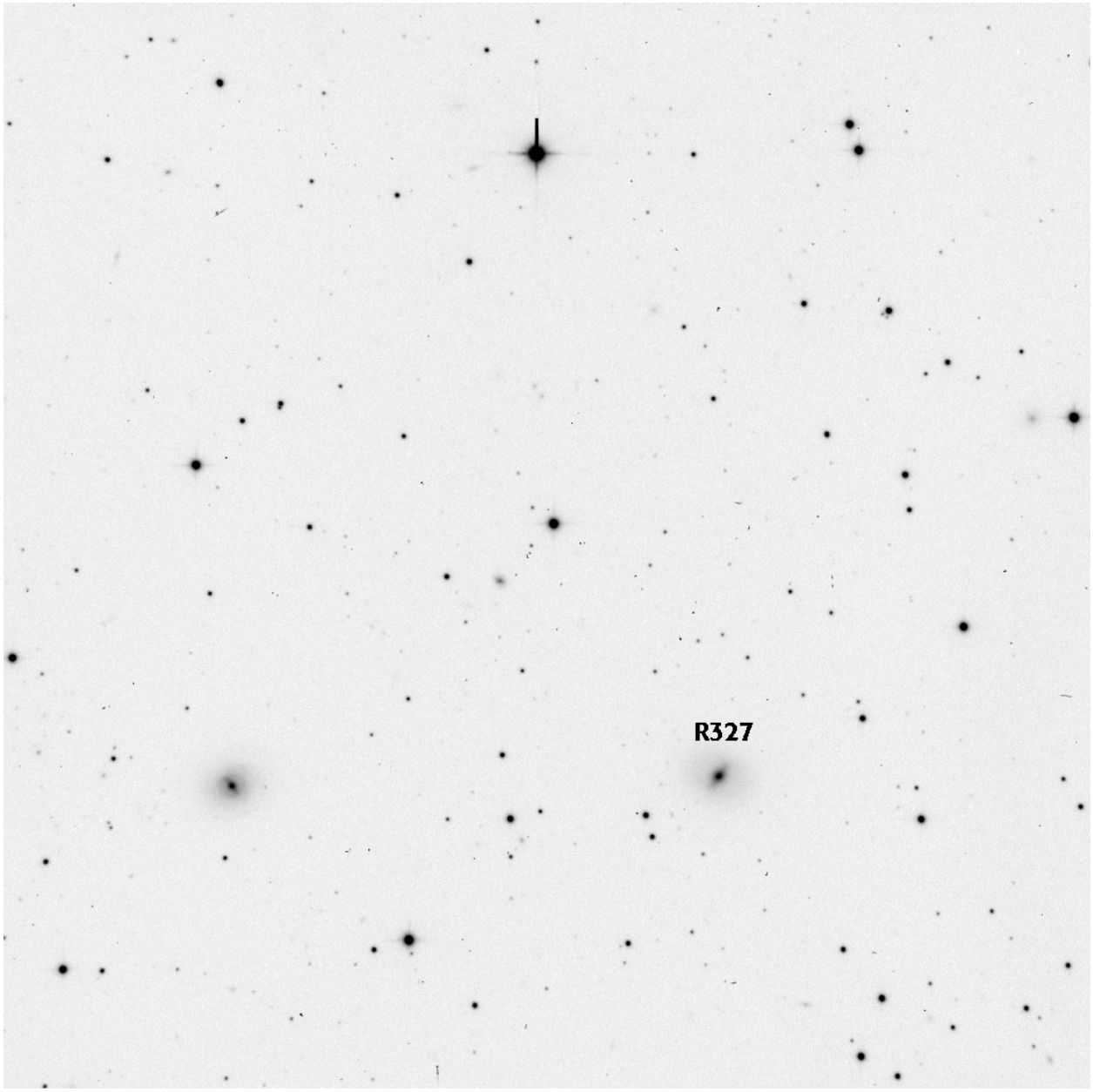

Field 320. Image: `d1410`. Seeing: 1.20″.

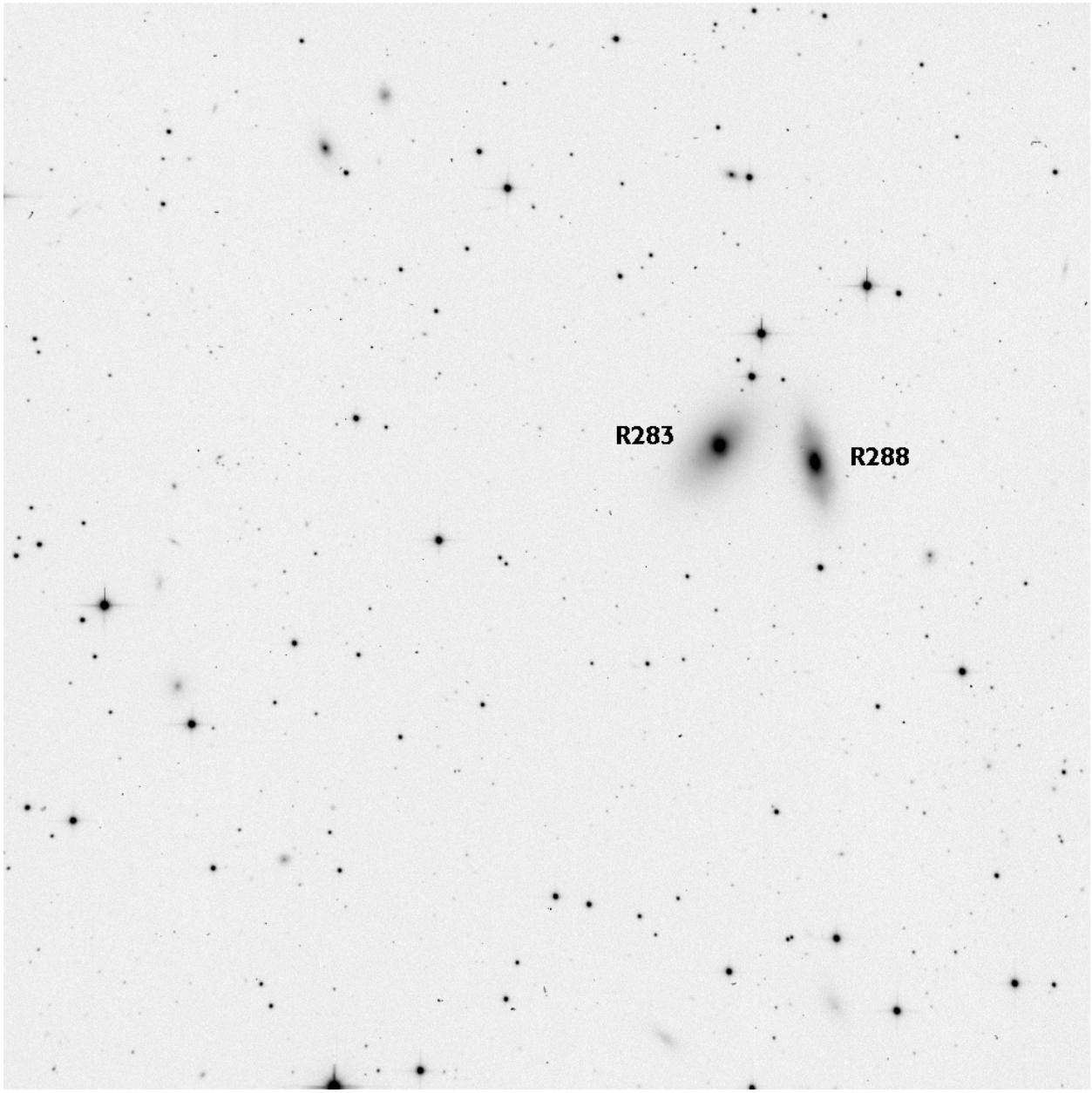

Field 321. Image: `d1579`. Seeing: 0.94″.

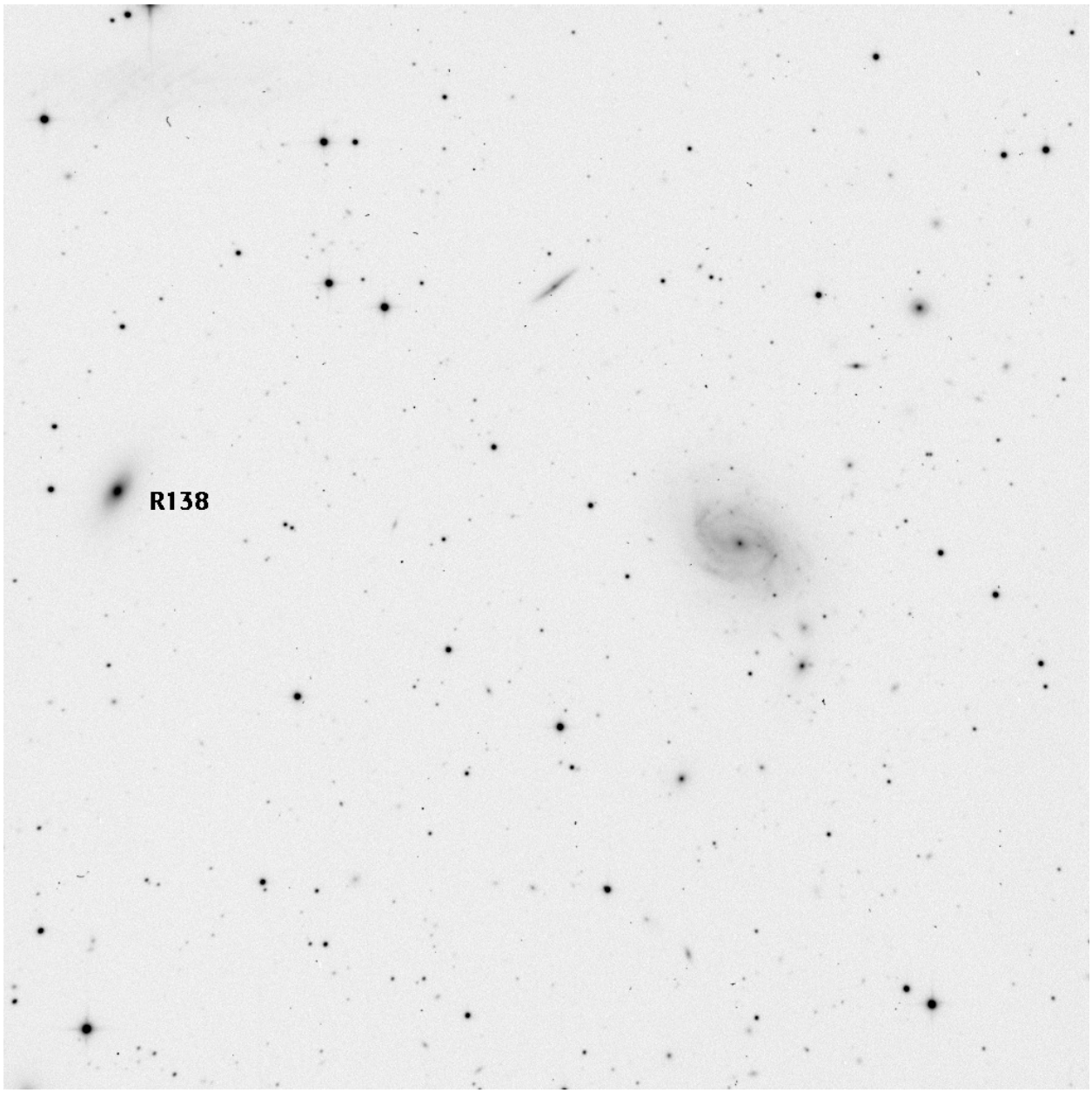

Field 419. Image: `d1431`. Seeing: 1.14″.

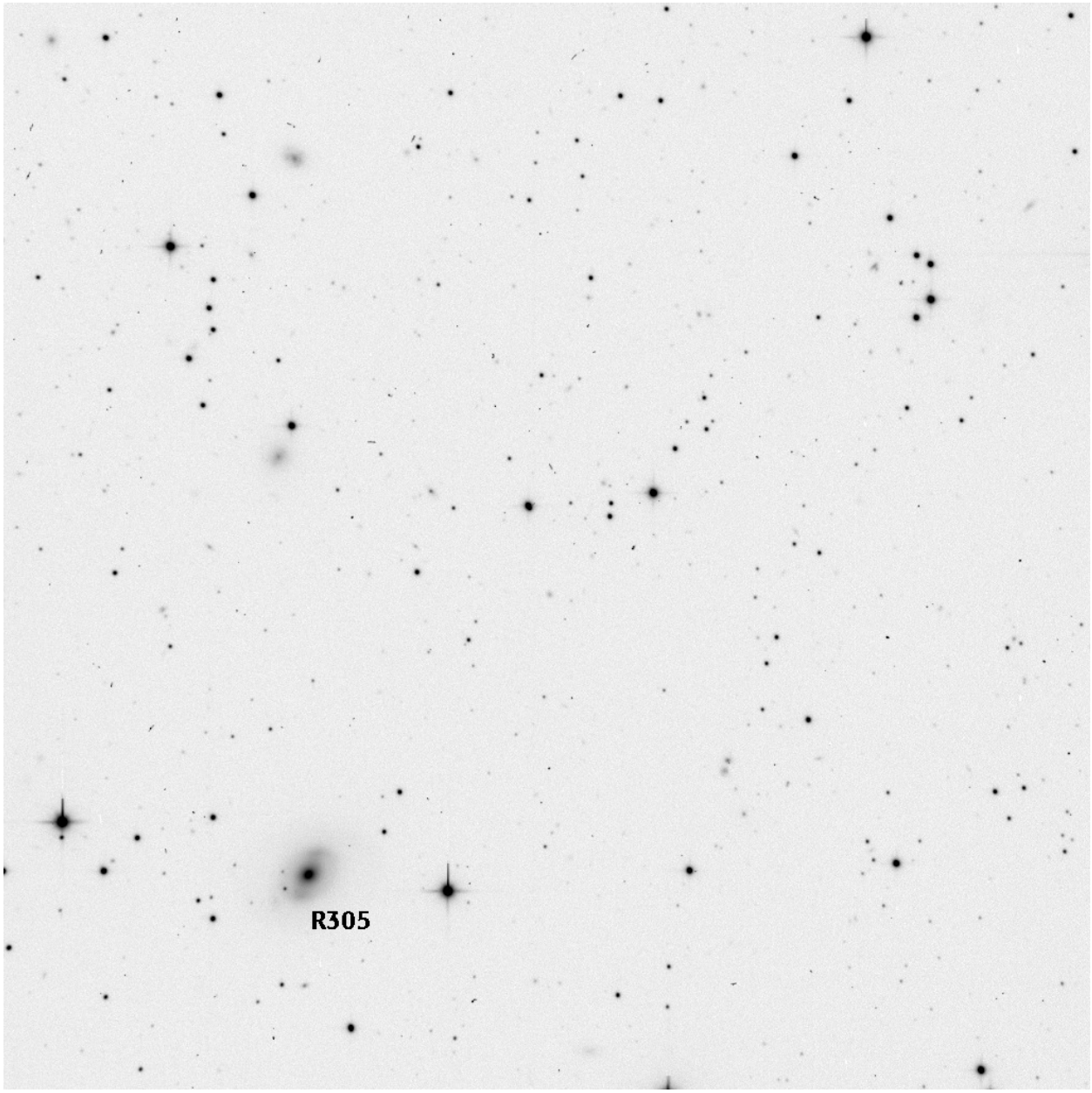

Field 427. Image: d1743. Seeing: 1.09″.

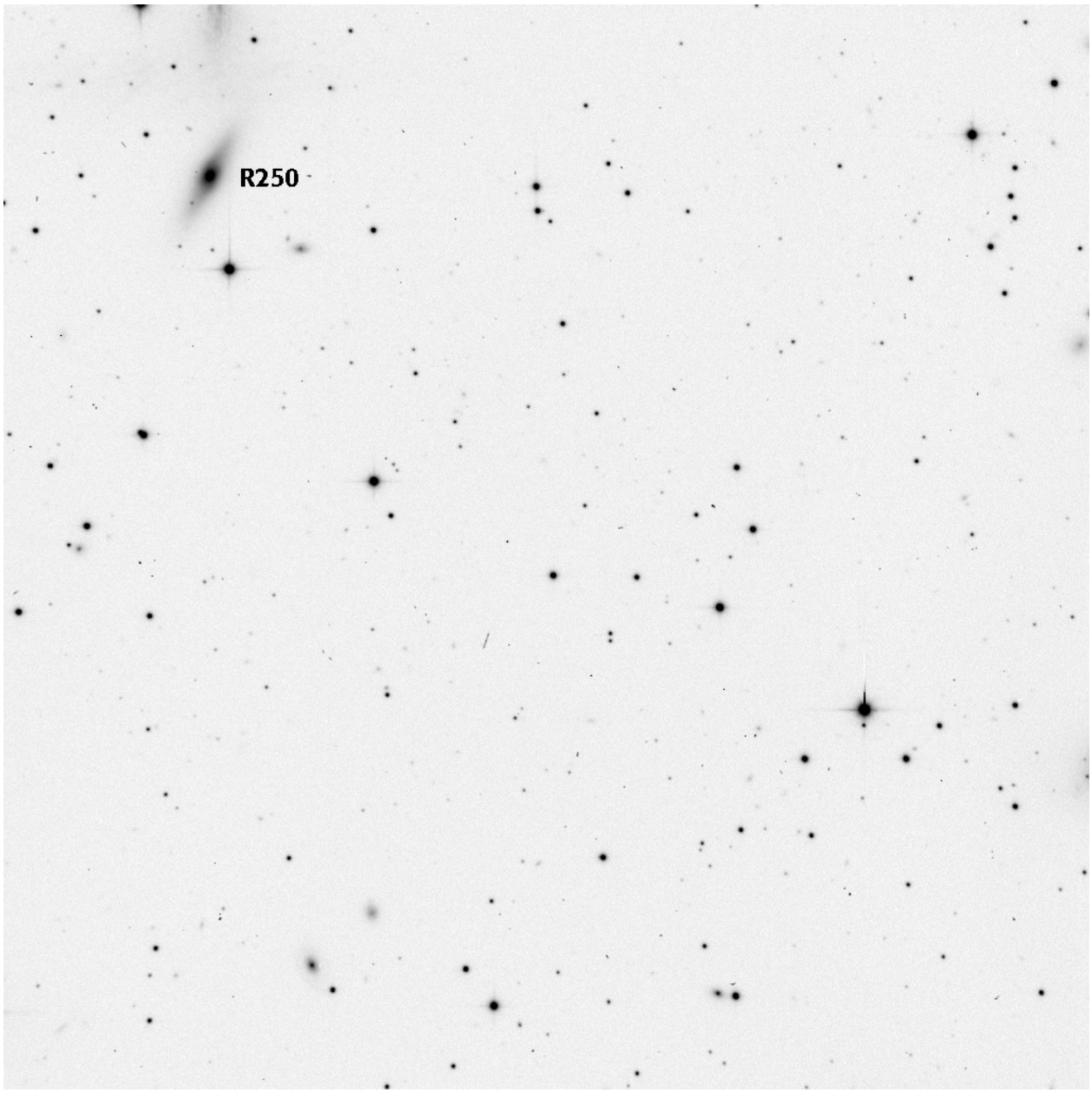

Field 428. Image: `d1417`. Seeing: 1.13″.

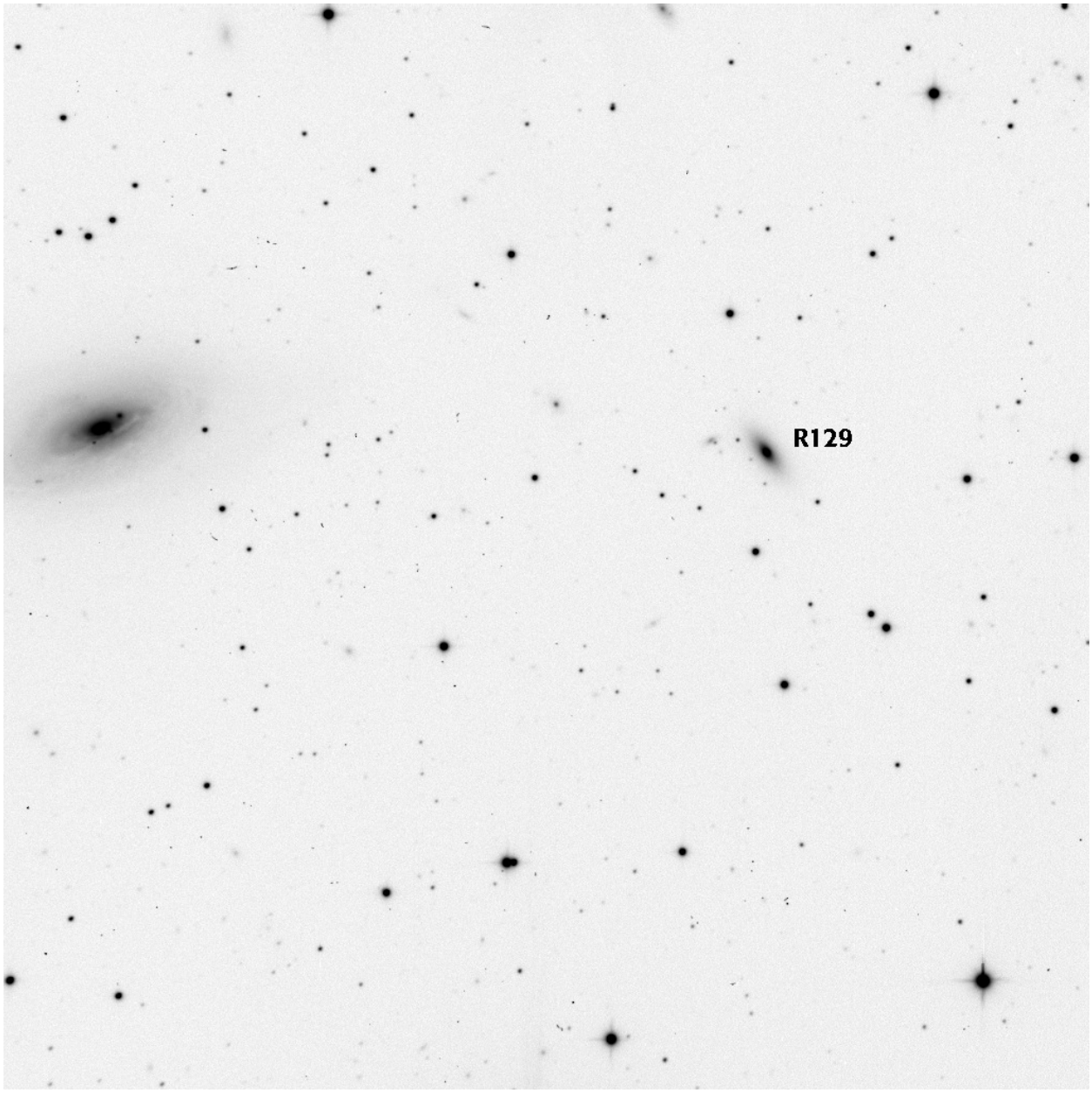

Field 519. Image: `d1439`. Seeing: 1.35″.

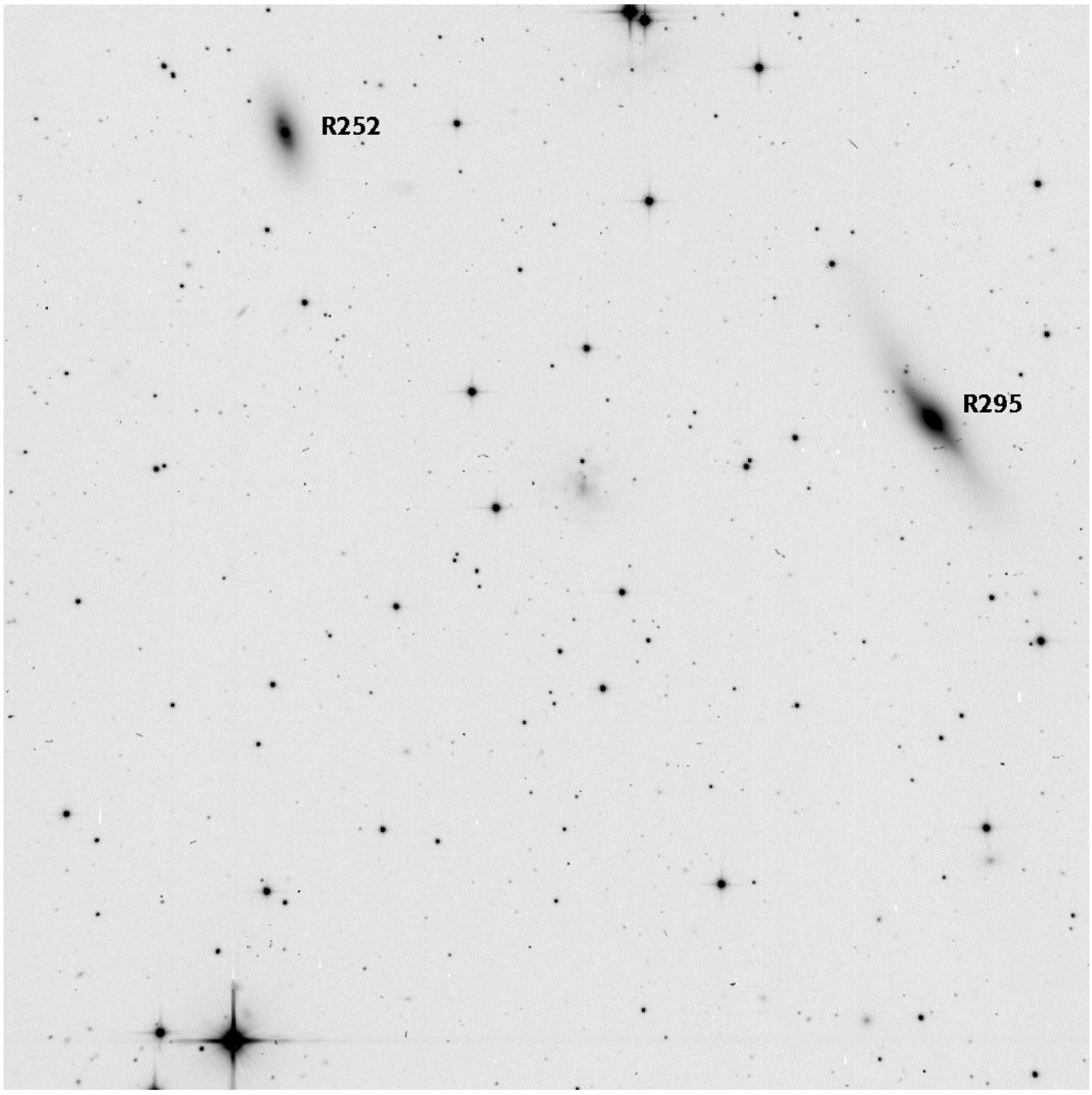

Field 535. Image: `d1584sum`. Seeing: 0.96″.

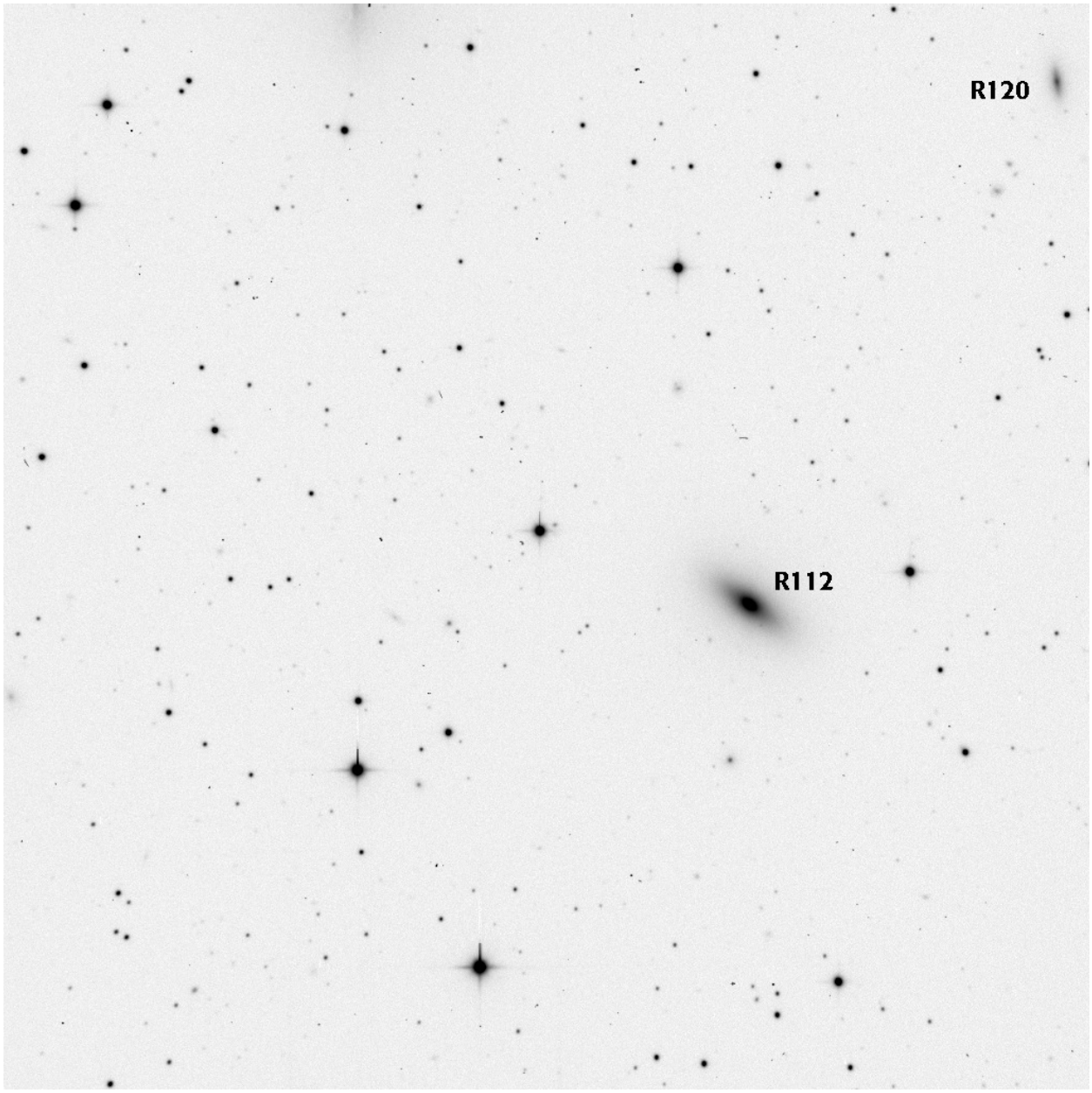

Field 615. Image: `d1991`. Seeing: 1.27″.

Appendix F

The HydraI Multi-Color Surface Photometry

On the following pages (pp. 252–267) we show the surface photometry for the 64 galaxies in the HydraI photometric sample (Table 3.3, p. 28). We plot the surface brightness μ (in $^{\rm m}/\mathrm{arcsec}^2$); from top to bottom on the panels the passband is Gunn r (squares), Johnson B (crosses), and Johnson U (triangles). We plot the colors $(B-r)$ (crosses) and $(U-r)$ (triangles). Note that Johnson U photometry is only available for 22 of the 64 galaxies (cf. Table 3.5, p. 30). We plot the ellipticity, the position angle, and the Fourier coefficients c_3, s_3, c_4, and s_3 for Gunn r only.

All the plots have the same axis intervals. This makes a galaxy-to-galaxy comparison easy. An axis interval for the Fourier coefficients as large as ± 0.13 is needed to accommodate the 'semi-spiral' galaxy R224 (p. 256) and the very disky galaxy R338 (p. 266). Other very disky galaxies include R250 (p. 259), R266 (p. 261), and R295 (p. 263). Only the interval for the position angle is shifted in the cases where the position angle profile crosses 0° or 180°.

The interval on the $\log(r/\mathrm{arcsec})$-axis is 0.0–1.9, corresponding to a range in r of $1''$–$79''$. The surface brightnesses μ are plotted from $1''$ to the radius where the uncertainty on μ exceeds $0.2^{\rm m}/\mathrm{arcsec}^2$. The colors are plotted from $2''$ to the radius where the uncertainty on the color exceeds $\sqrt{2}\cdot 0\overset{\rm m}{.}2$. The other quantities are plotted from $2''$ to either the radius where the ellipticity and the position angle are no longer free parameters in the fit (cf. Sect. 4.1, p. 35), or the maximum radius for the μ plot, whichever is the smallest.

Given in the title for each plot is the galaxy ID from Richter (1989) (e.g. R269), the common galaxy name if available (e.g. N3311), and the morphological type listed by Richter.

The surface brightnesses and the colors are on the standard photometric system (cf. Sect. 4.3, p. 40), but no offsets for galactic extinction, k-correction, or cosmological dimming have been applied. This is the standard way of presenting surface photometry. The errorbars for the surface brightnesses and the colors include a conservative estimate of the uncertainty on the background subtraction of 1% for Gunn r and 0.5% for Johnson B and U.

For the galaxies that have been observed more than once the best seeing observation was chosen (cf. Table 3.5, p. 30). The only exception to this is the Johnson B observation of R166, where an observation with a marginally ($0.02''$) worse seeing was chosen. By doing so it was achieved that all 64 pairs of Gunn r and Johnson B observations shown here were observed just after each other (within ~ 10 minutes).

The seeing for the shown observations is in the range $0.77''$–$1.37''$ for Gunn r, $0.81''$–$1.70''$ for Johnson B, and $1.01''$–$1.57''$ for Johnson U. The mean values are $0.95''$, $1.04''$, and $1.20''$, respectively. For Gunn r, the seeing range corresponds to a range in $\log(r/'')$ of -0.11 to $+0.14$.

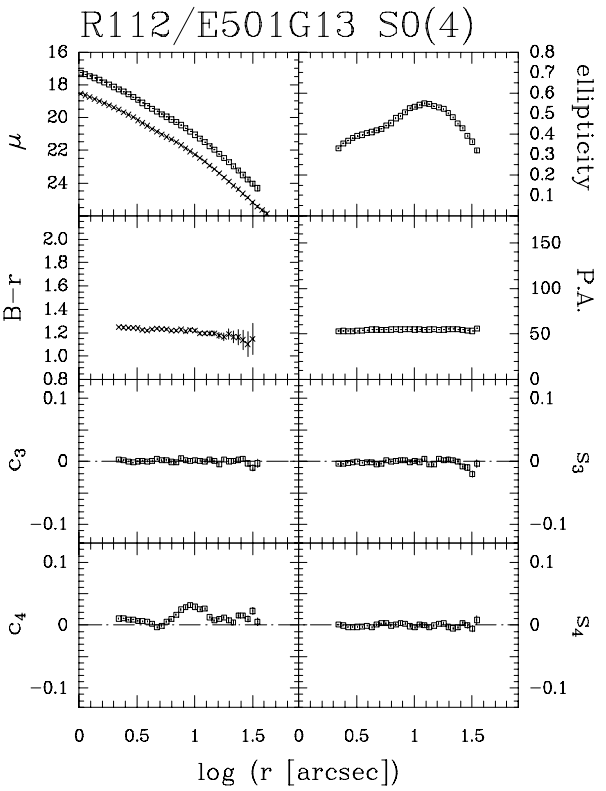
R112/E501G13 S0(4)
μ
ellipticity
B−r
P.A.
c3
s3
c4
s4
log (r [arcsec])

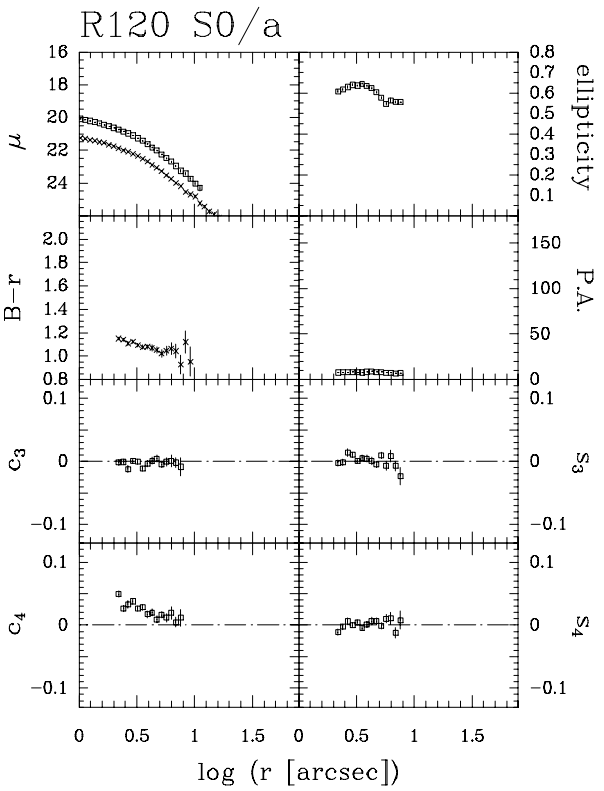
R120 S0/a
μ
ellipticity
B−r
P.A.
c3
s3
c4
s4
log (r [arcsec])

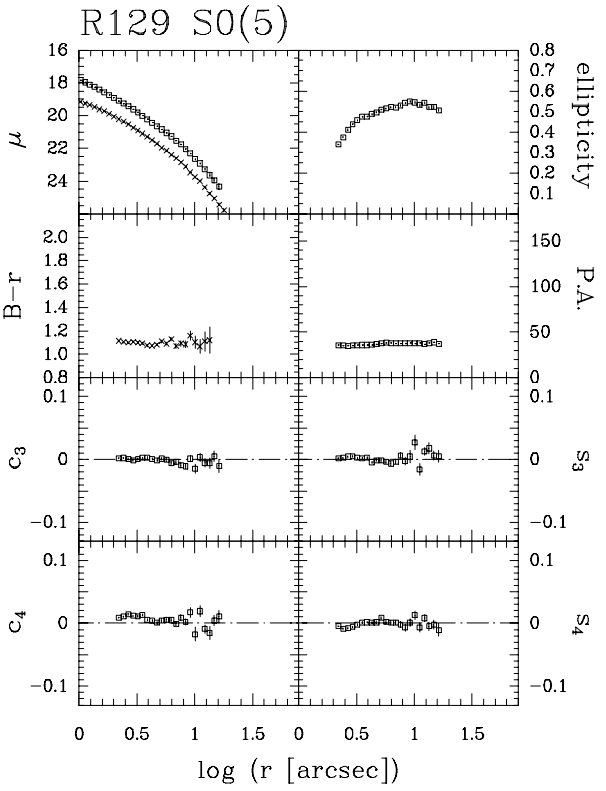
R129 S0(5)
μ
ellipticity
B−r
P.A.
c3
s3
c4
s4
log (r [arcsec])

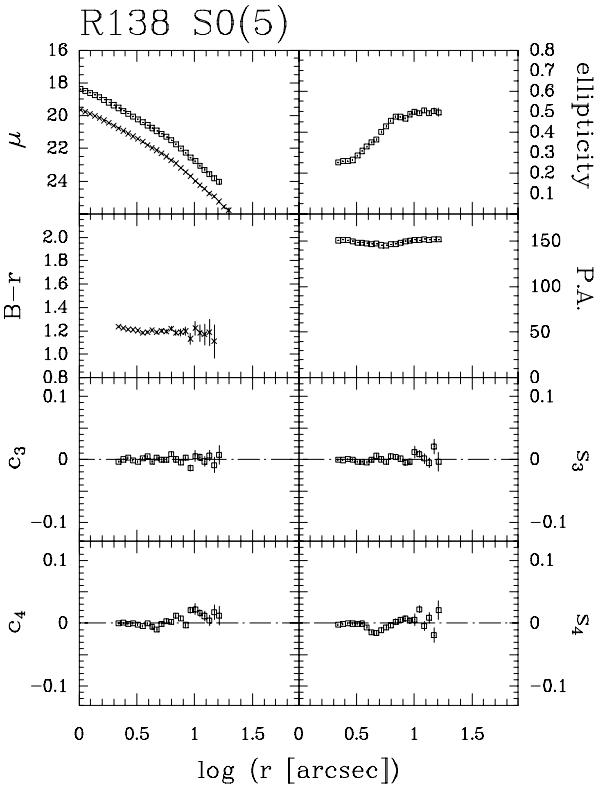
R138 S0(5)
μ
ellipticity
B−r
P.A.
c3
s3
c4
s4
log (r [arcsec])

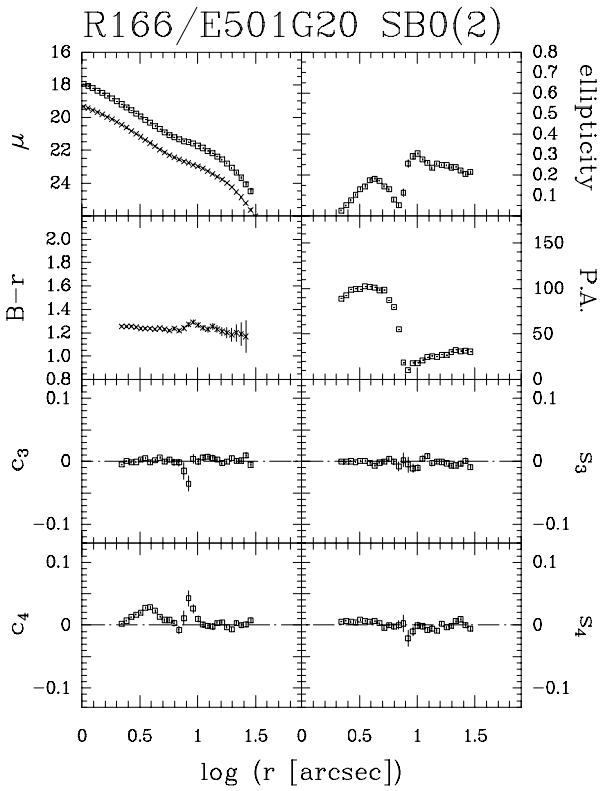
R166/E501G20 SB0(2)
μ
B−r
c3
c4
ellipticity
P.A.
S3
S4
log (r [arcsec])

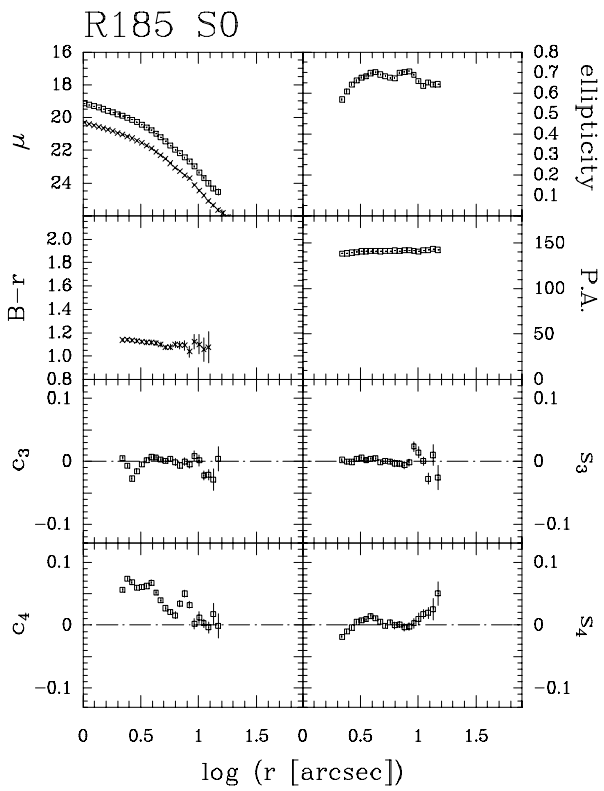
R185 S0
μ
B−r
c3
c4
ellipticity
P.A.
S3
S4
log (r [arcsec])

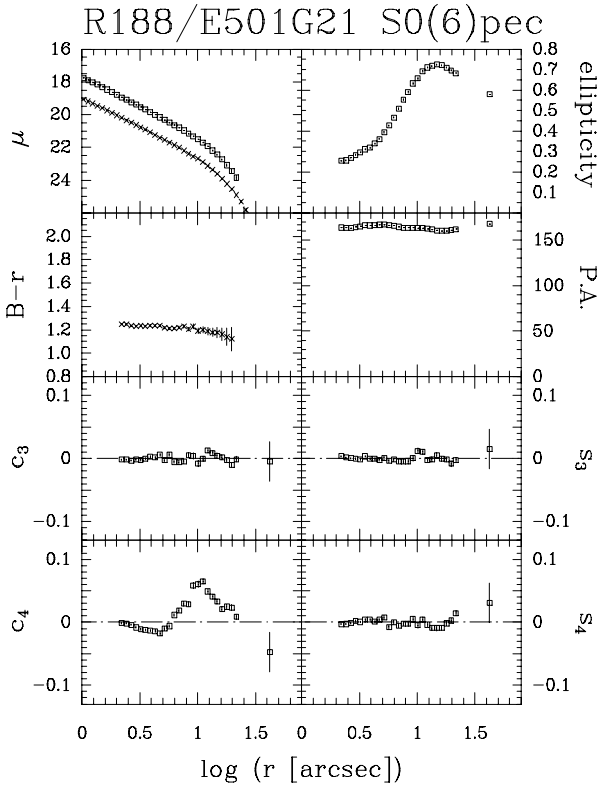
R188/E501G21 S0(6)pec
μ
B−r
c3
c4
ellipticity
P.A.
S3
S4
log (r [arcsec])

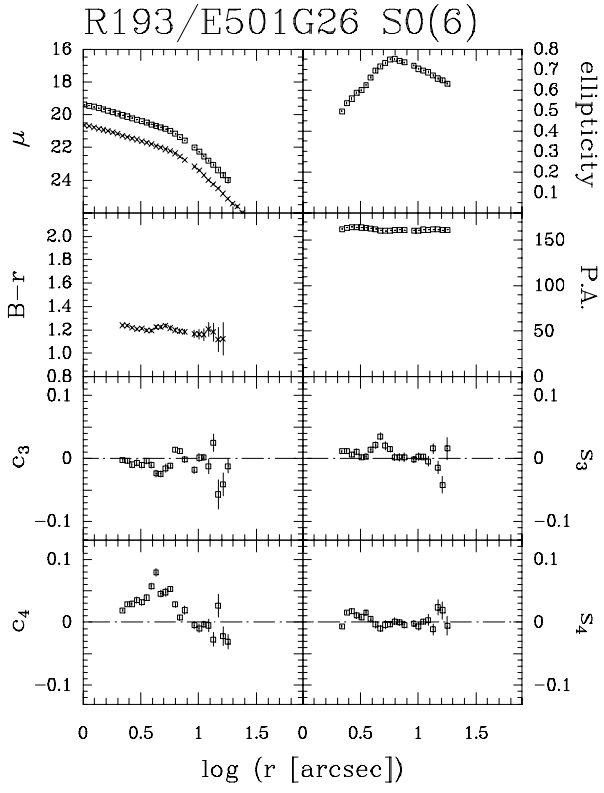
R193/E501G26 S0(6)
μ
B−r
c3
c4
ellipticity
P.A.
S3
S4
log (r [arcsec])

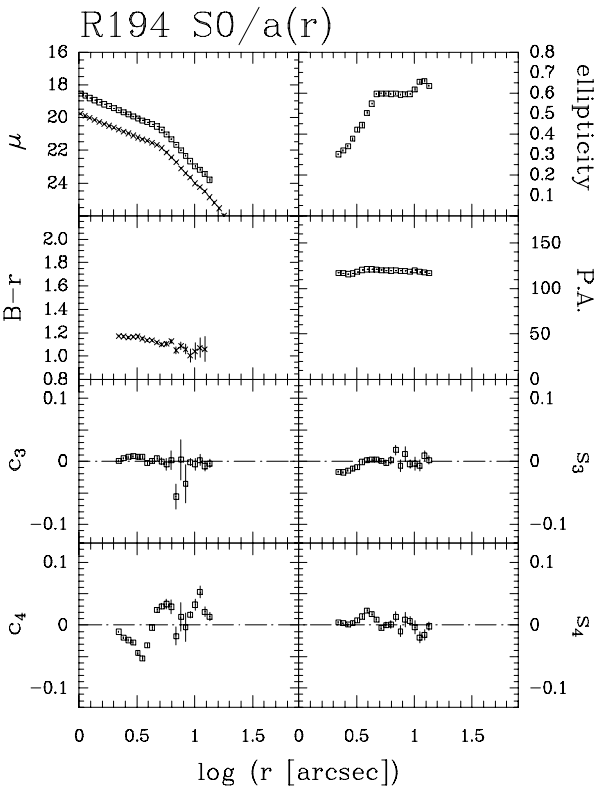
R194 S0/a(r)
μ
ellipticity
B−r
P.A.
c3
s3
c4
s4
log (r [arcsec])

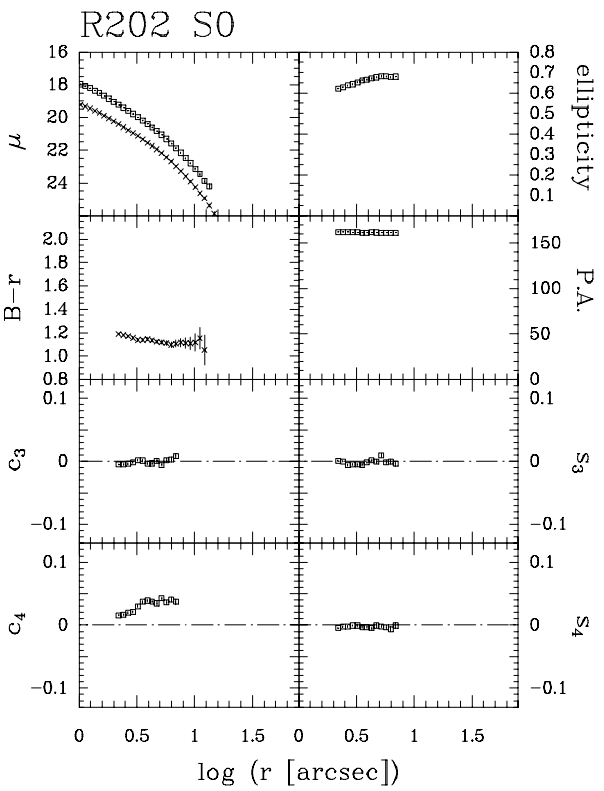
R202 S0
μ
ellipticity
B−r
P.A.
c3
s3
c4
s4
log (r [arcsec])

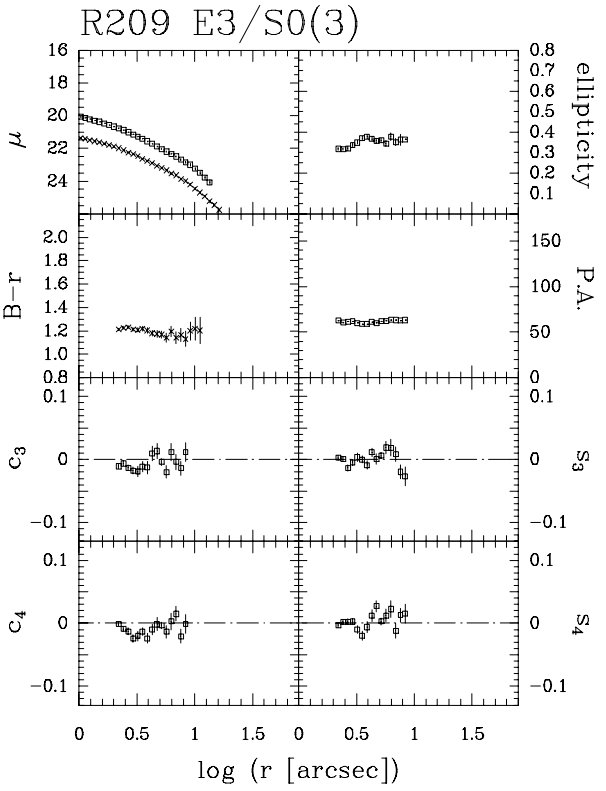
R209 E3/S0(3)
μ
ellipticity
B−r
P.A.
c3
s3
c4
s4
log (r [arcsec])

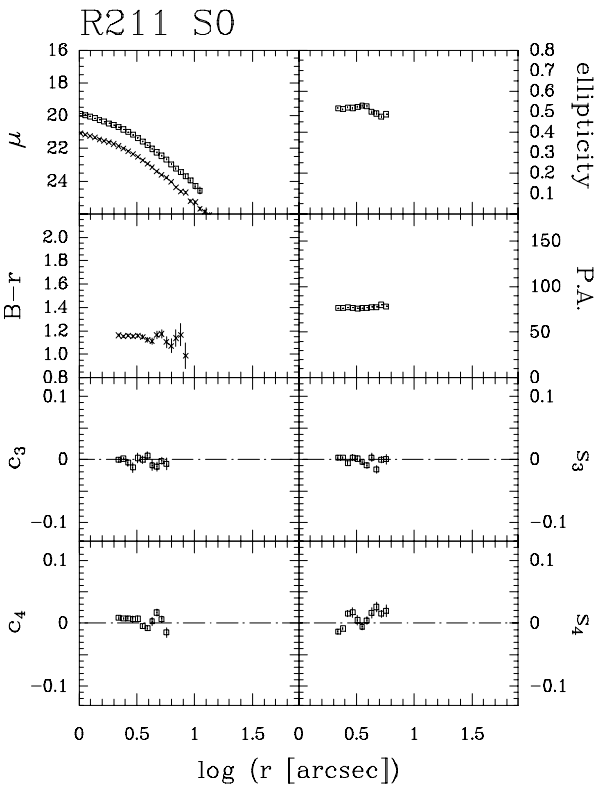
R211 S0
μ
ellipticity
B−r
P.A.
c3
s3
c4
s4
log (r [arcsec])

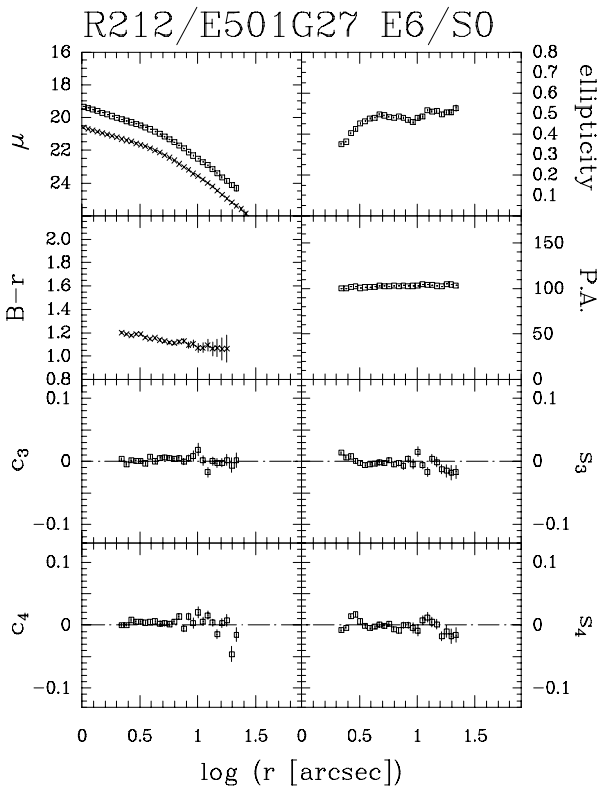
R212/E501G27 E6/S0
μ
B−r
c3
c4
ellipticity
P.A.
S3
S4
log (r [arcsec])

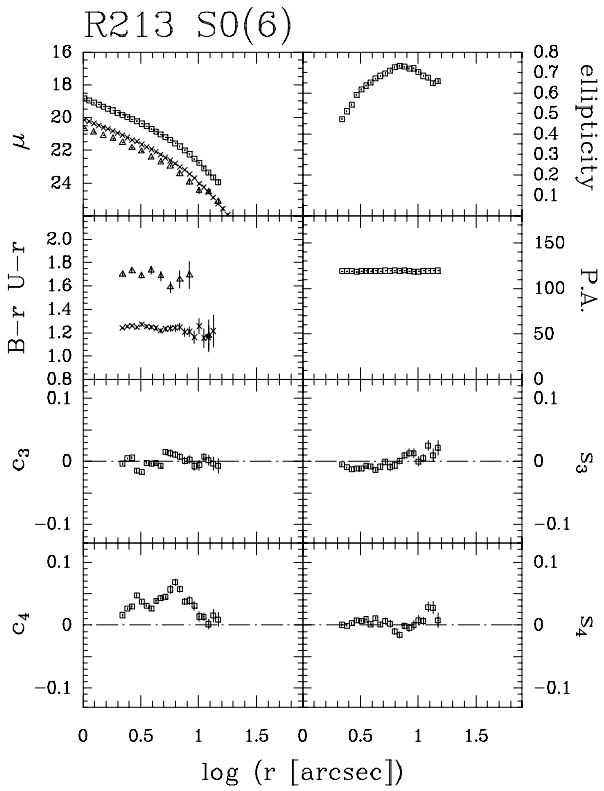
R213 S0(6)
μ
B−r U−r
c3
c4
ellipticity
P.A.
S3
S4
log (r [arcsec])

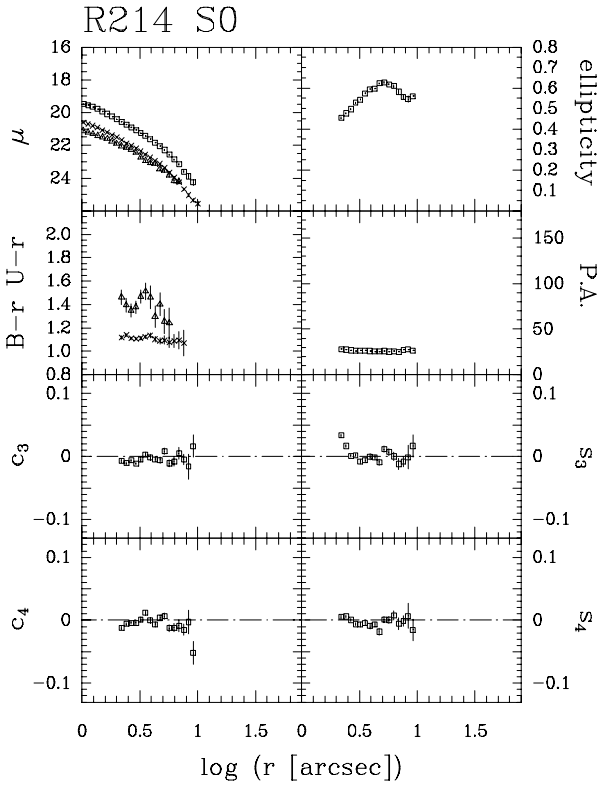
R214 S0
μ
B−r U−r
c3
c4
ellipticity
P.A.
S3
S4
log (r [arcsec])

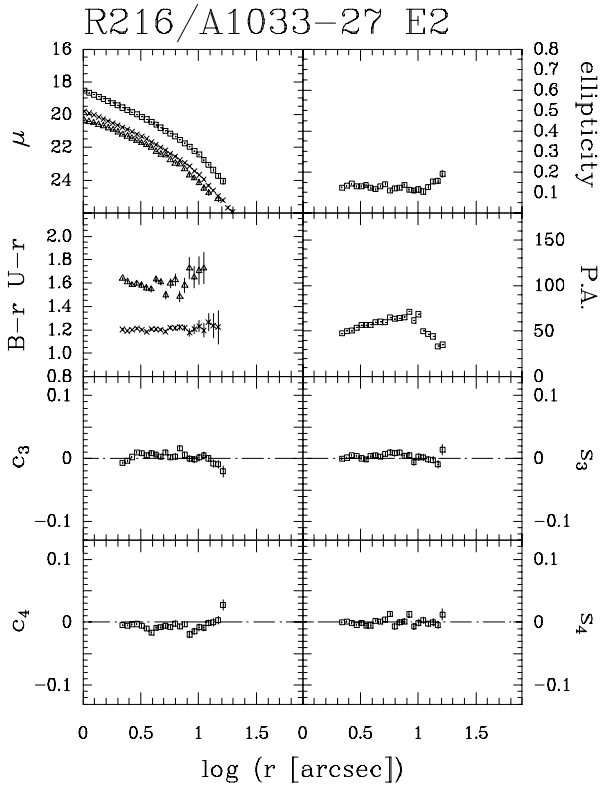
R216/A1033−27 E2
μ
B−r U−r
c3
c4
ellipticity
P.A.
S3
S4
log (r [arcsec])

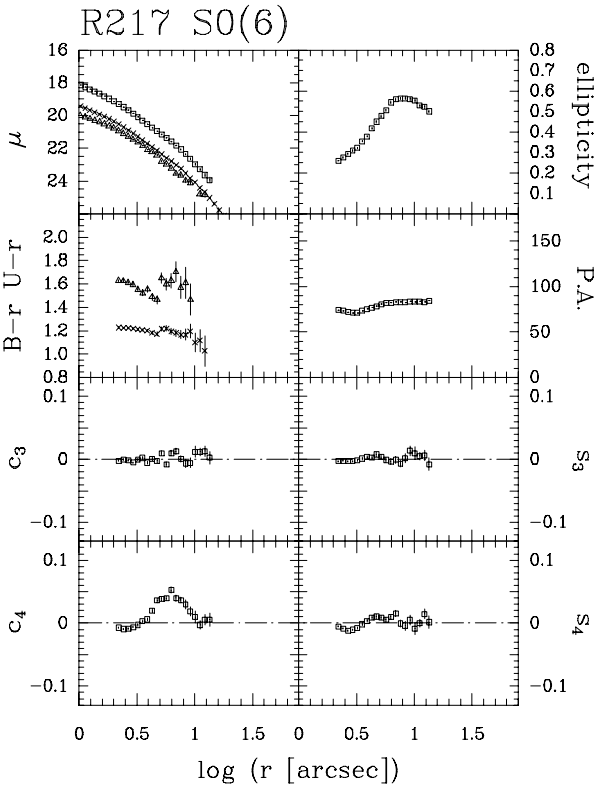
R217 S0(6)
μ
ellipticity
B−r U−r
P.A.
c3
s3
c4
s4
log (r [arcsec])

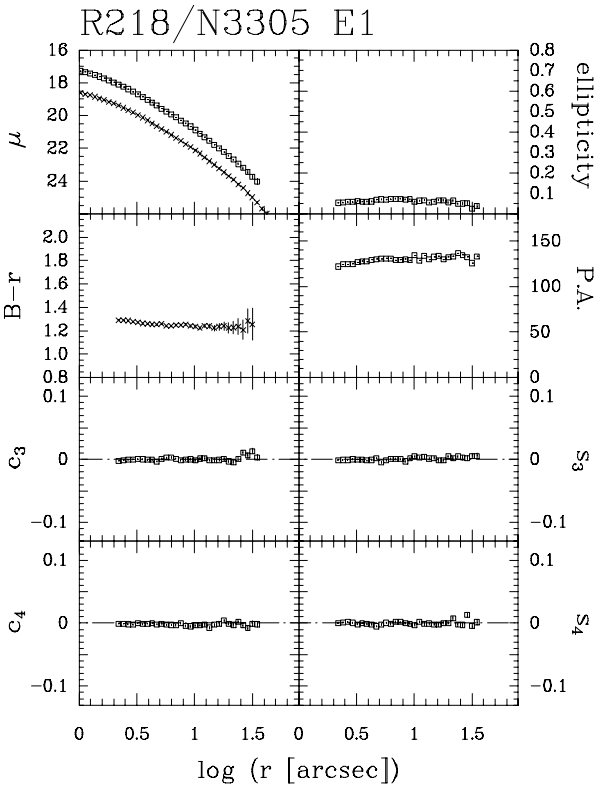
R218/N3305 E1
μ
ellipticity
B−r
P.A.
c3
s3
c4
s4
log (r [arcsec])

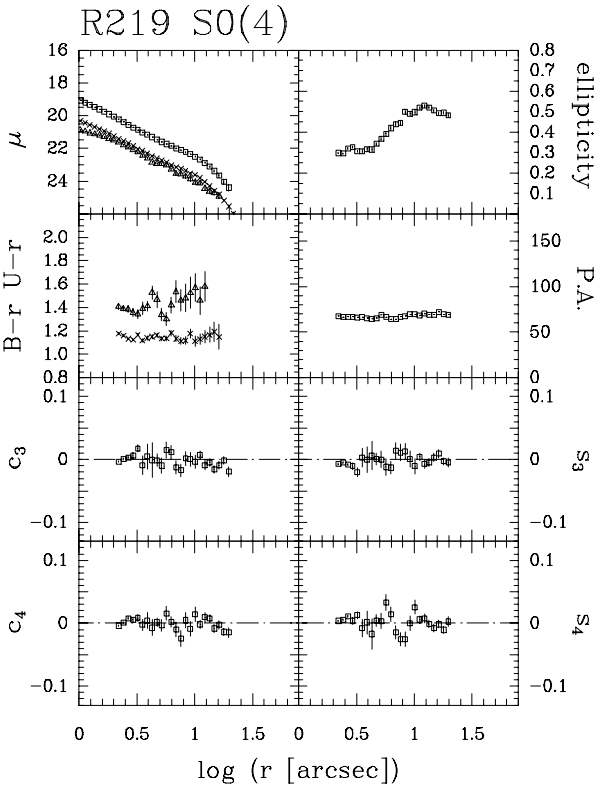
R219 S0(4)
μ
ellipticity
B−r U−r
P.A.
c3
s3
c4
s4
log (r [arcsec])

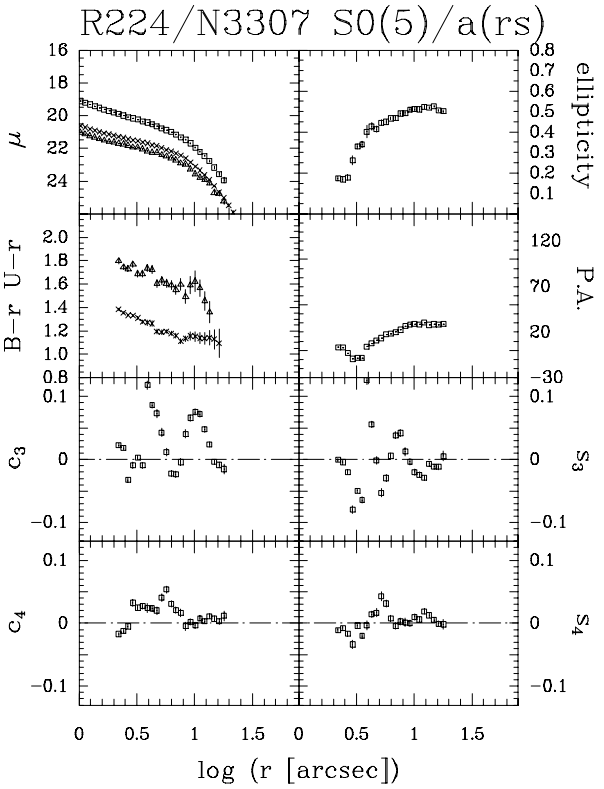
R224/N3307 S0(5)/a(rs)
μ
ellipticity
B−r U−r
P.A.
c3
s3
c4
s4
log (r [arcsec])

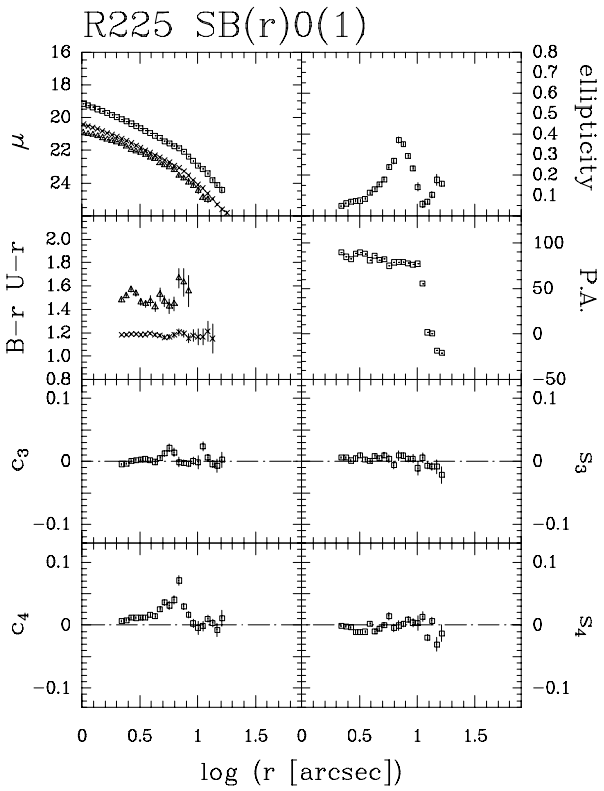
R225 SB(r)0(1)
μ
ellipticity
B−r U−r
P.A.
c3
s3
c4
s4
log (r [arcsec])

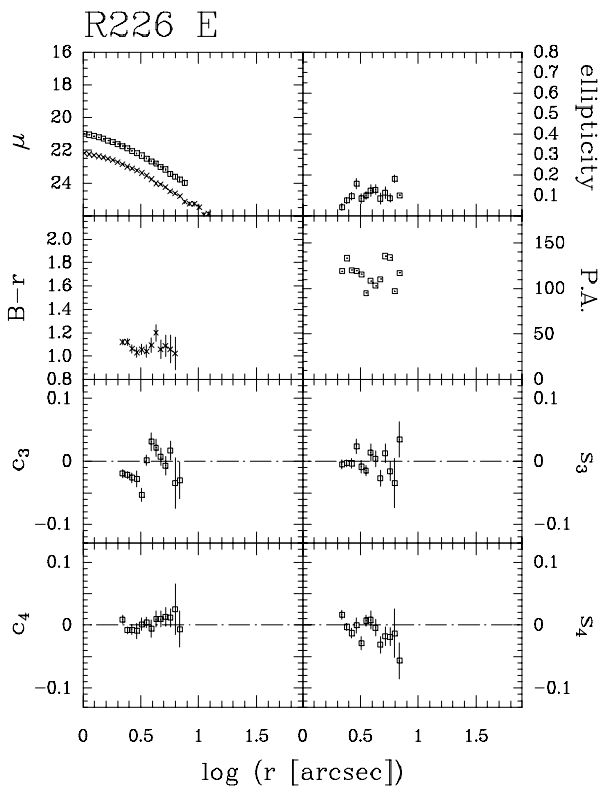
R226 E
μ
ellipticity
B−r
P.A.
c3
s3
c4
s4
log (r [arcsec])

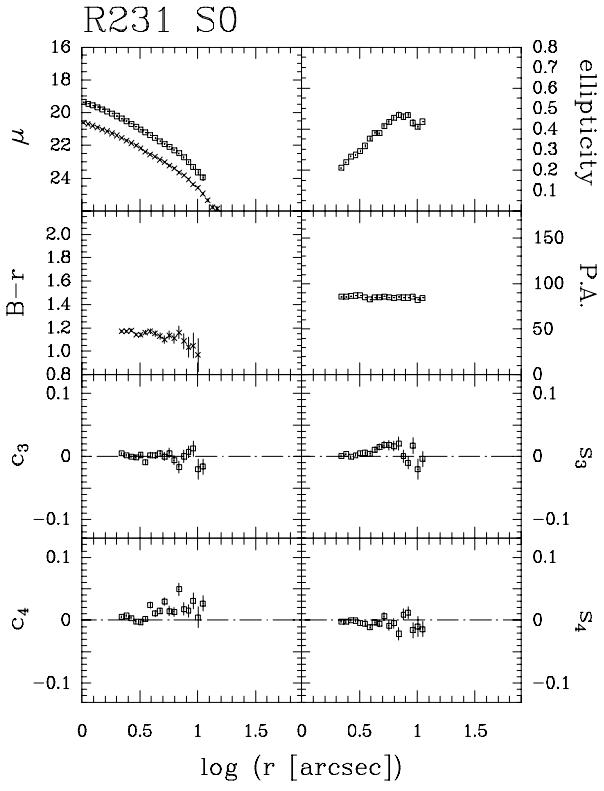
R231 S0
μ
ellipticity
B−r
P.A.
c3
s3
c4
s4
log (r [arcsec])

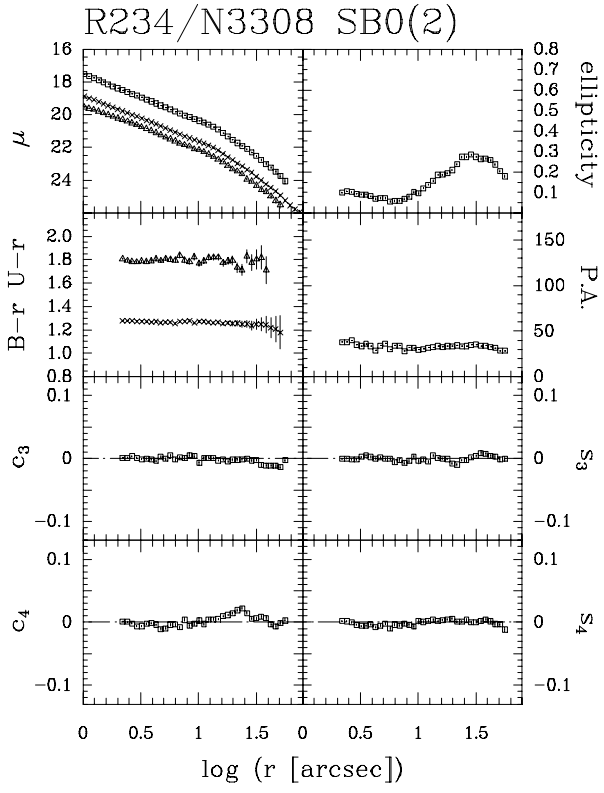
R234/N3308 SB0(2)
μ
ellipticity
B−r U−r
P.A.
c3
s3
c4
s4
log (r [arcsec])

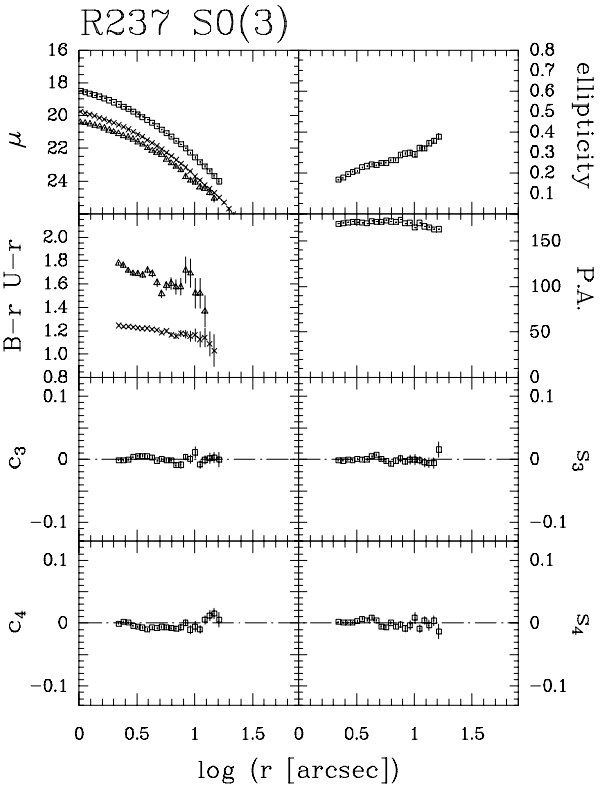
R237 S0(3)
μ
B−r U−r
c3
c4
ellipticity
P.A.
s3
s4
log (r [arcsec])

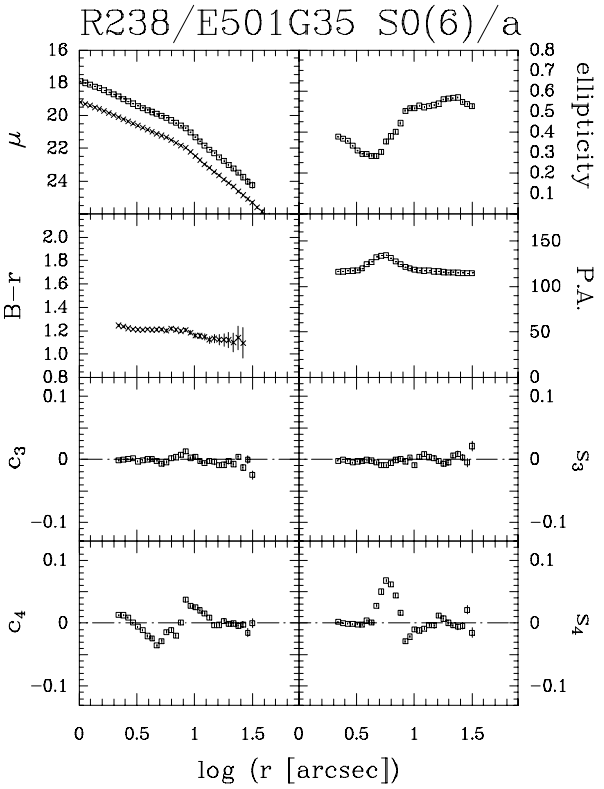
R238/E501G35 S0(6)/a
μ
B−r
c3
c4
ellipticity
P.A.
s3
s4
log (r [arcsec])

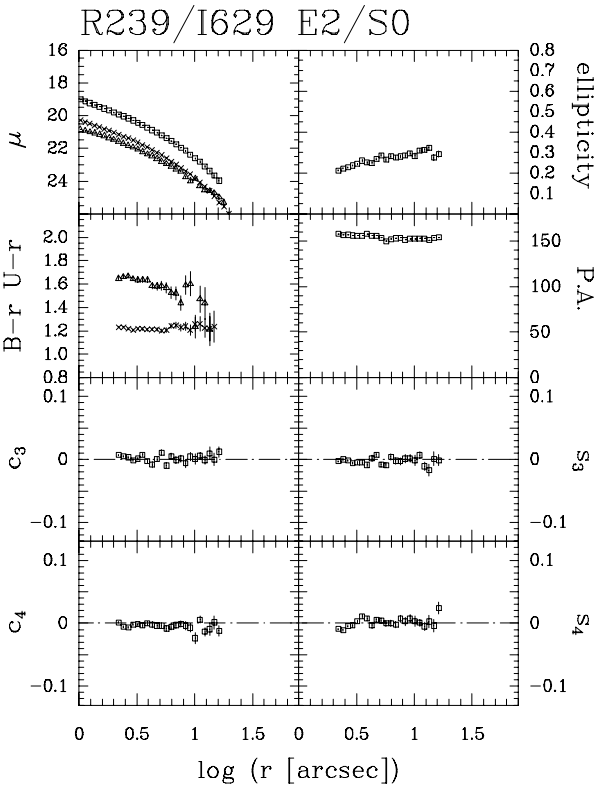
R239/I629 E2/S0
μ
B−r U−r
c3
c4
ellipticity
P.A.
s3
s4
log (r [arcsec])

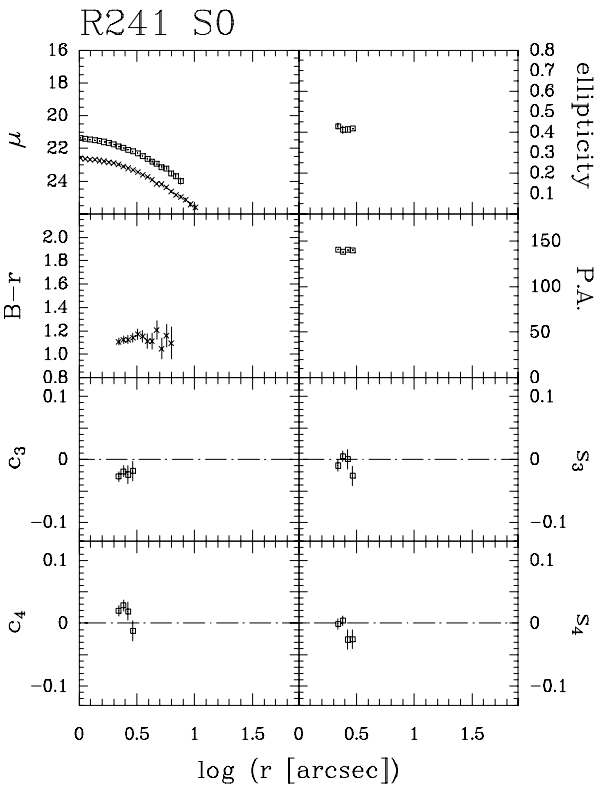
R241 S0
μ
B−r
c3
c4
ellipticity
P.A.
s3
s4
log (r [arcsec])

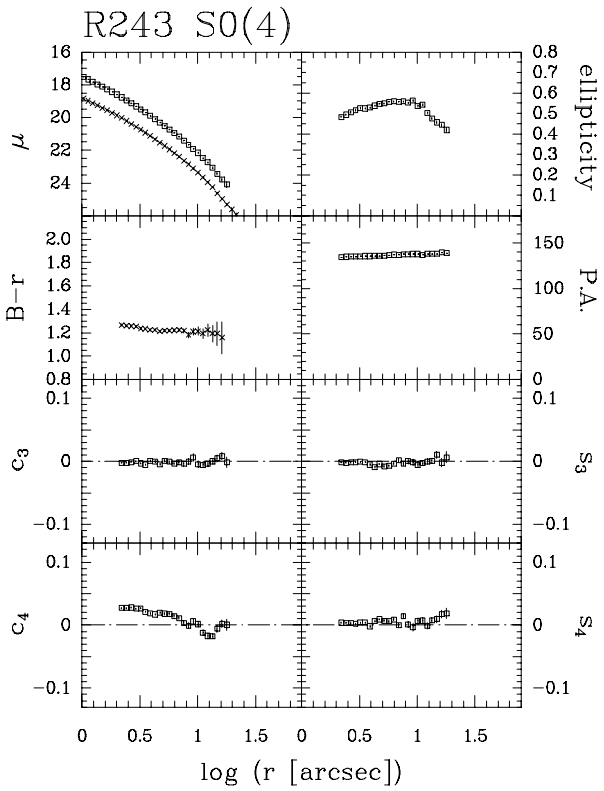
R243 S0(4)
μ
ellipticity
B−r
P.A.
c3
S3
c4
S4
log (r [arcsec])

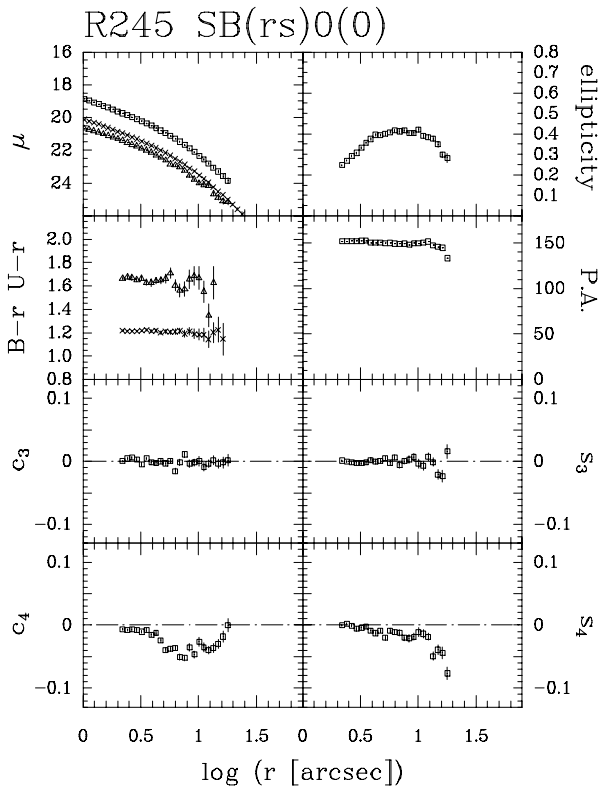
R245 SB(rs)0(0)
μ
ellipticity
B−r U−r
P.A.
c3
S3
c4
S4
log (r [arcsec])

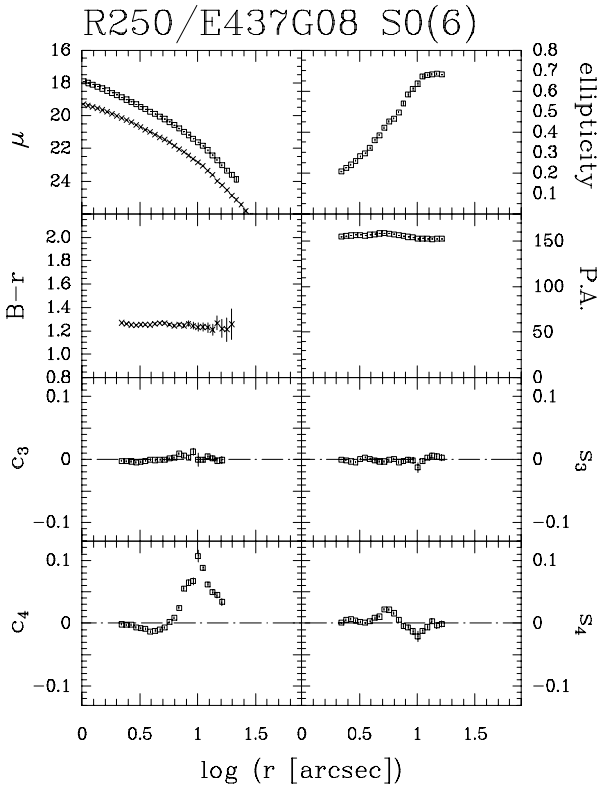
R250/E437G08 S0(6)
μ
ellipticity
B−r
P.A.
c3
S3
c4
S4
log (r [arcsec])

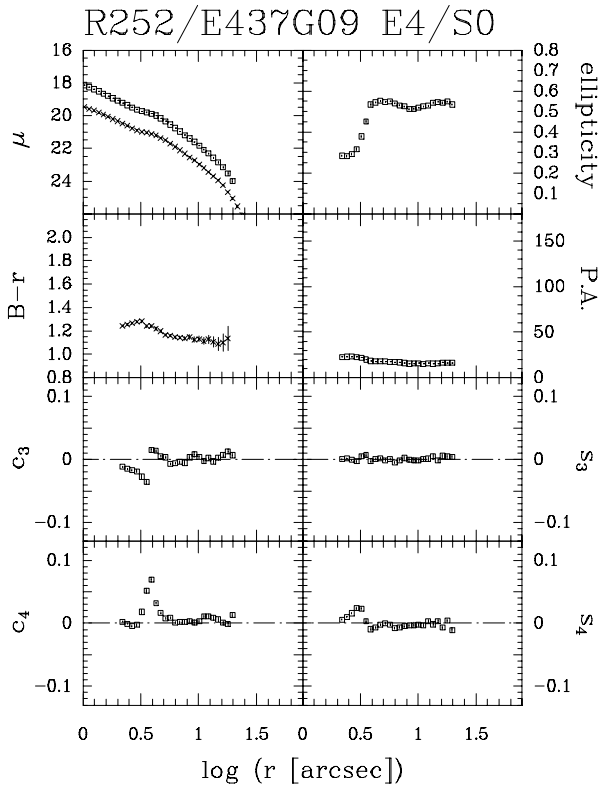
R252/E437G09 E4/S0
μ
ellipticity
B−r
P.A.
c3
S3
c4
S4
log (r [arcsec])

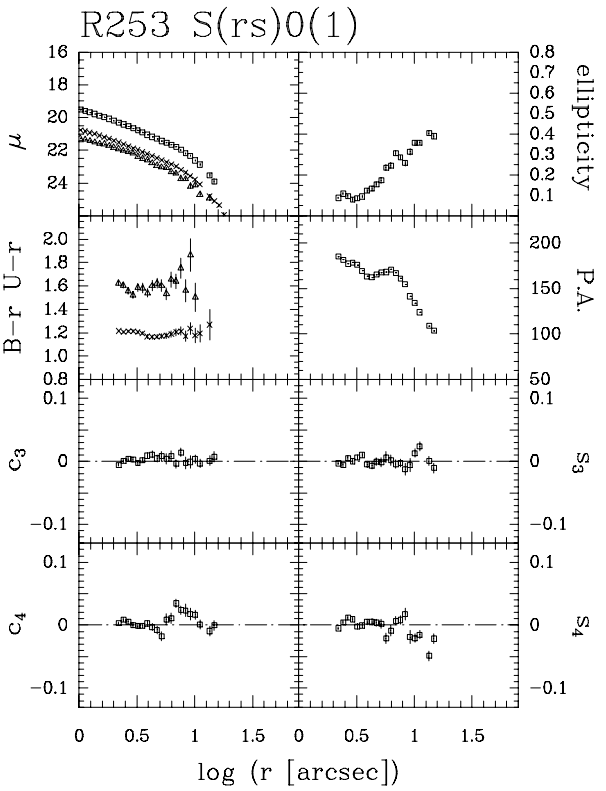
R253 S(rs)0(1)
μ
B−r U−r
ellipticity
P.A.
c3
s3
c4
s4
log (r [arcsec])

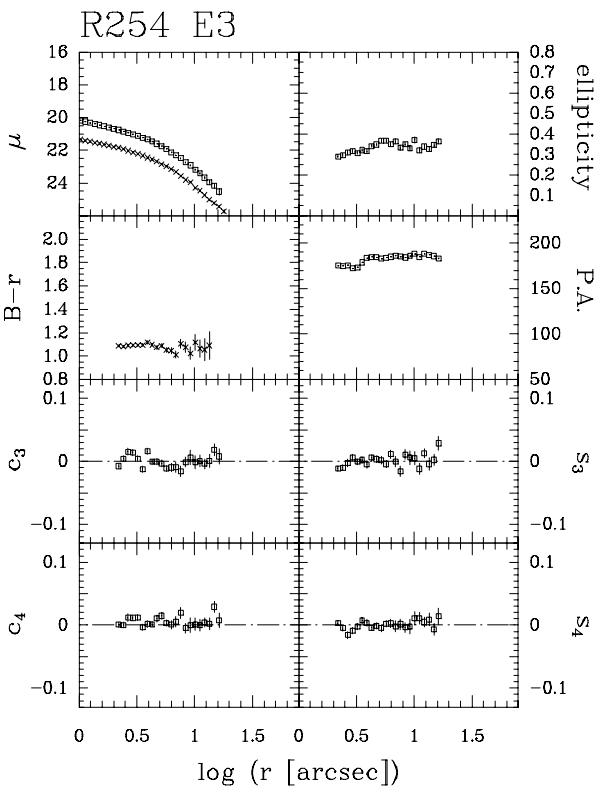
R254 E3
μ
B−r
ellipticity
P.A.
c3
s3
c4
s4
log (r [arcsec])

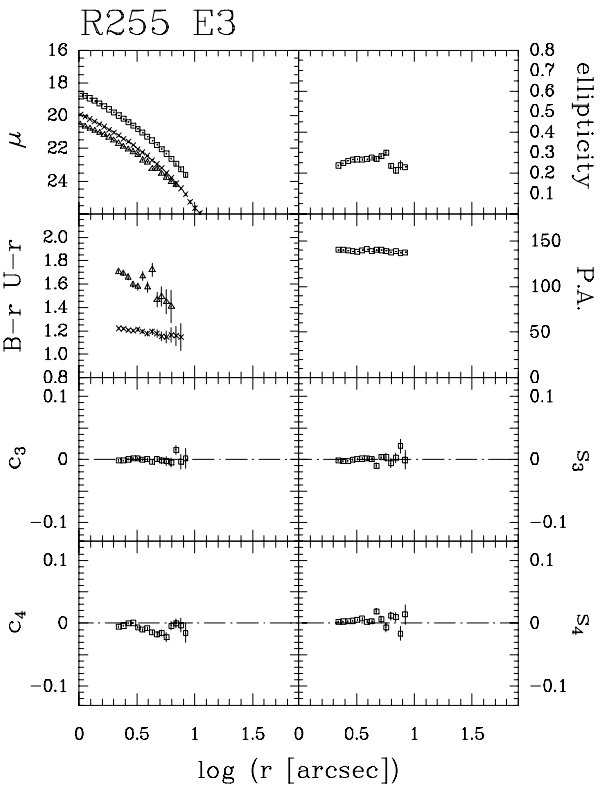
R255 E3
μ
B−r U−r
ellipticity
P.A.
c3
s3
c4
s4
log (r [arcsec])

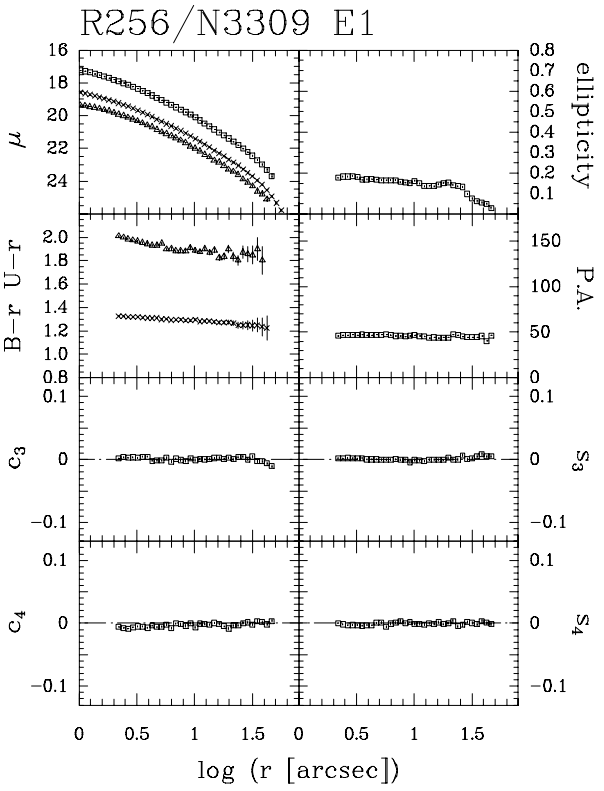
R256/N3309 E1
μ
B−r U−r
ellipticity
P.A.
c3
s3
c4
s4
log (r [arcsec])

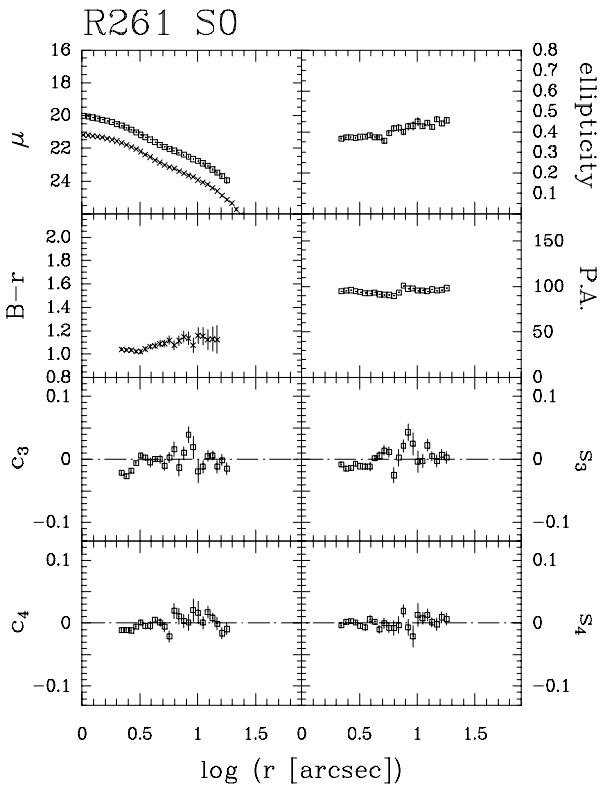
R261 S0
μ
B−r
c3
c4
ellipticity
P.A.
S3
S4
log (r [arcsec])

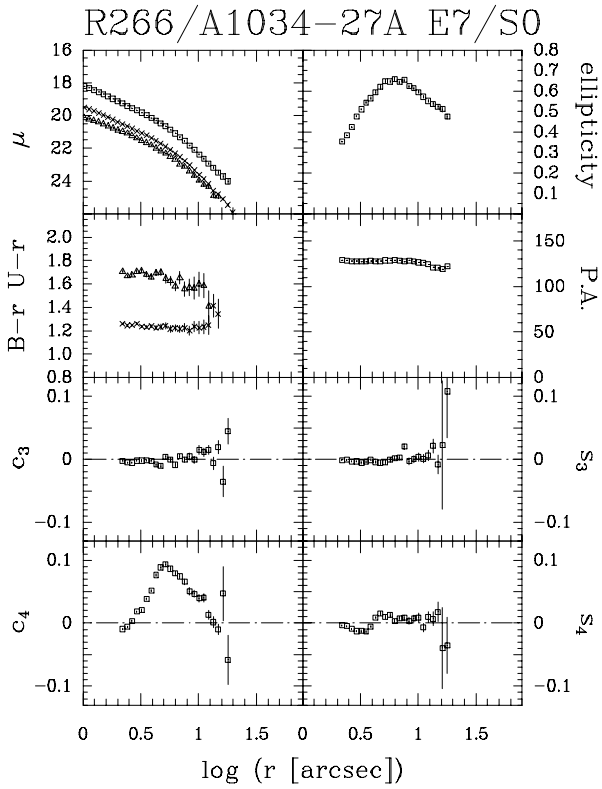
R266/A1034−27A E7/S0
μ
B−r U−r
c3
c4
ellipticity
P.A.
S3
S4
log (r [arcsec])

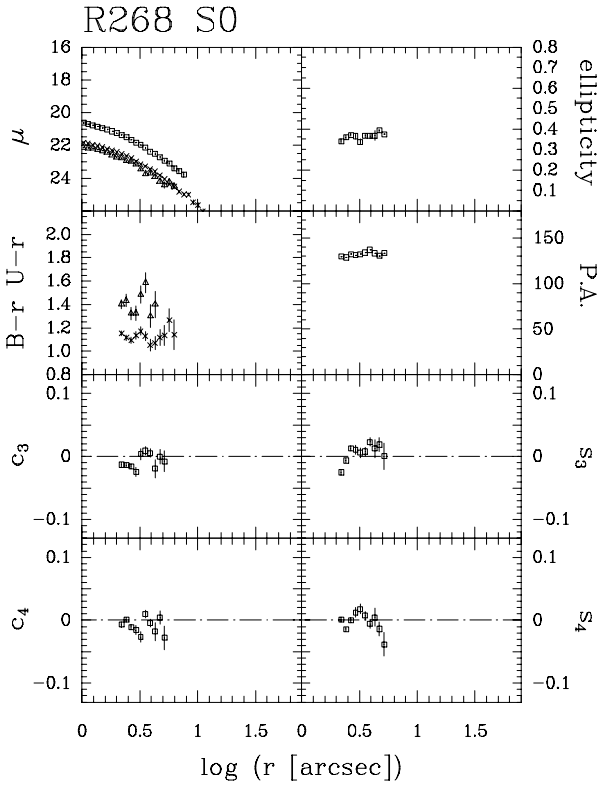
R268 S0
μ
B−r U−r
c3
c4
ellipticity
P.A.
S3
S4
log (r [arcsec])

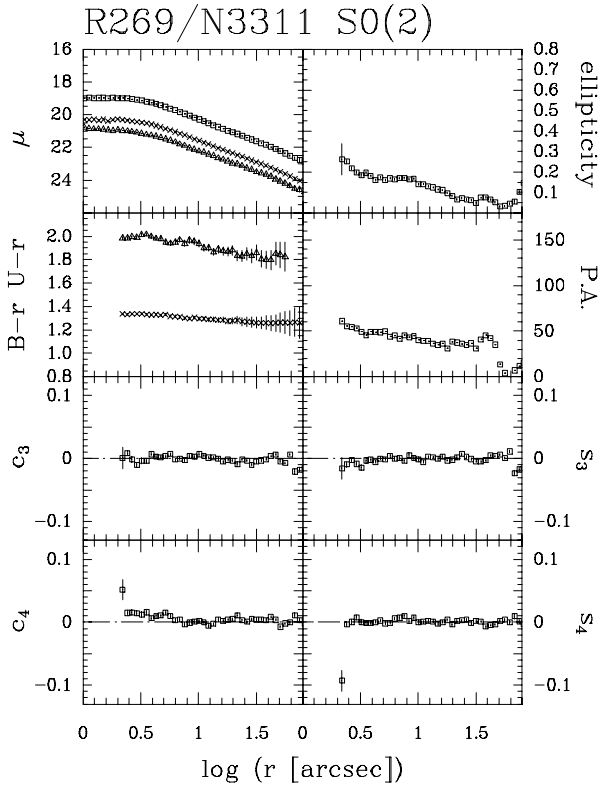
R269/N3311 S0(2)
μ
B−r U−r
c3
c4
ellipticity
P.A.
S3
S4
log (r [arcsec])

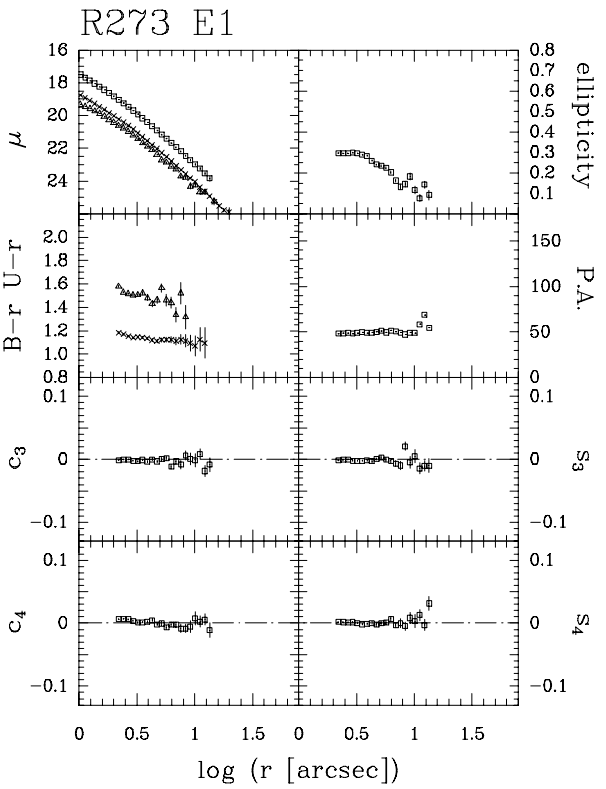
R273 E1
μ
B−r U−r
ellipticity
P.A.
c3
s3
c4
s4
log (r [arcsec])

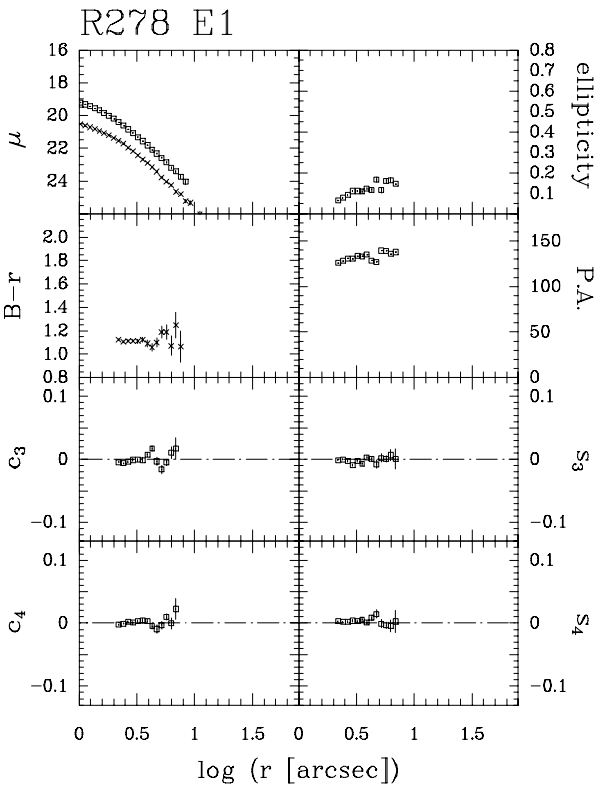
R278 E1
μ
B−r
ellipticity
P.A.
c3
s3
c4
s4
log (r [arcsec])

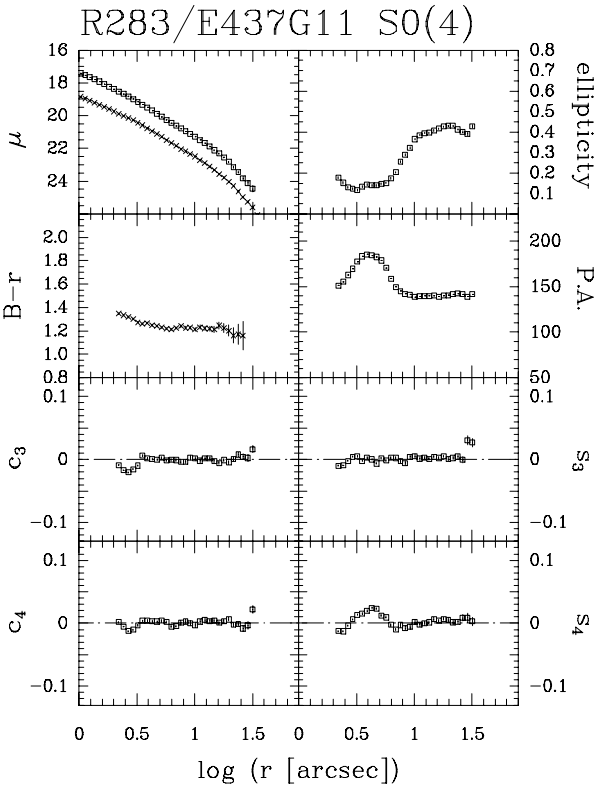
R283/E437G11 S0(4)
μ
B−r
ellipticity
P.A.
c3
s3
c4
s4
log (r [arcsec])

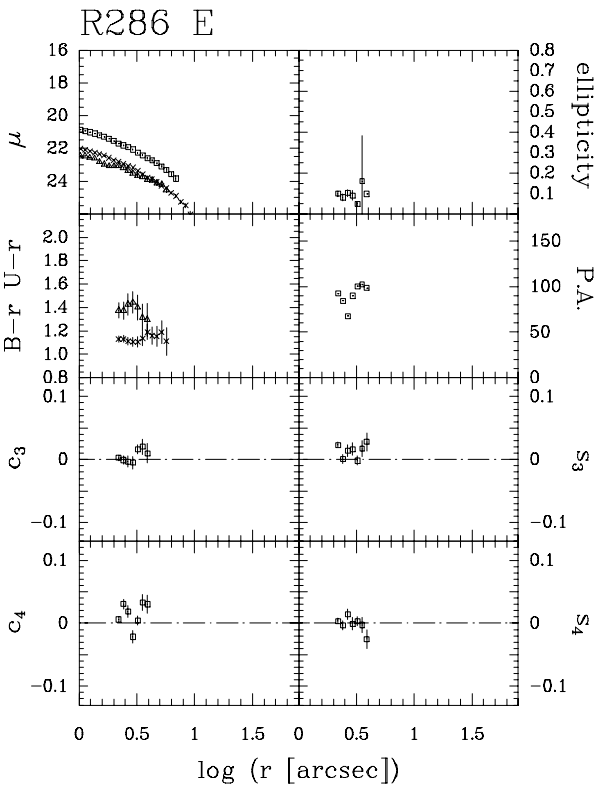
R286 E
μ
B−r U−r
ellipticity
P.A.
c3
s3
c4
s4
log (r [arcsec])

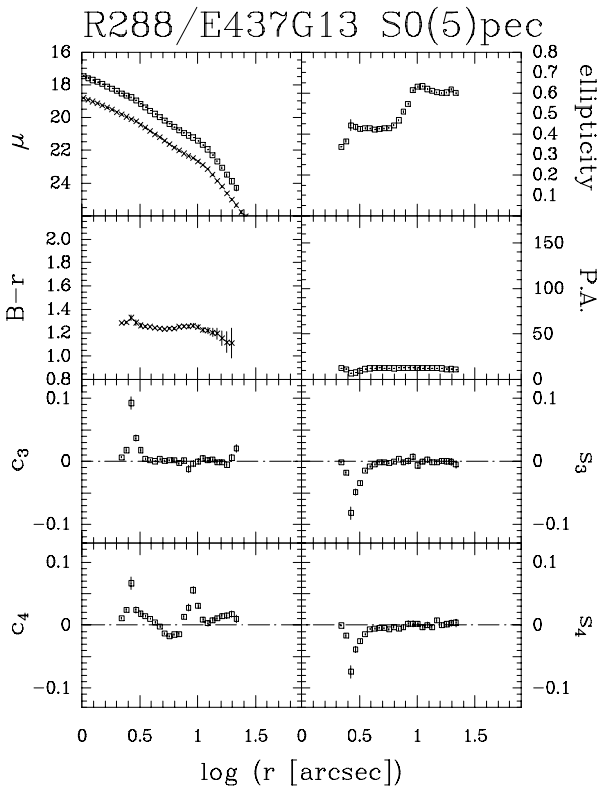
R288/E437G13 S0(5)pec
μ
ellipticity
B−r
P.A.
c3
S3
c4
S4
log (r [arcsec])

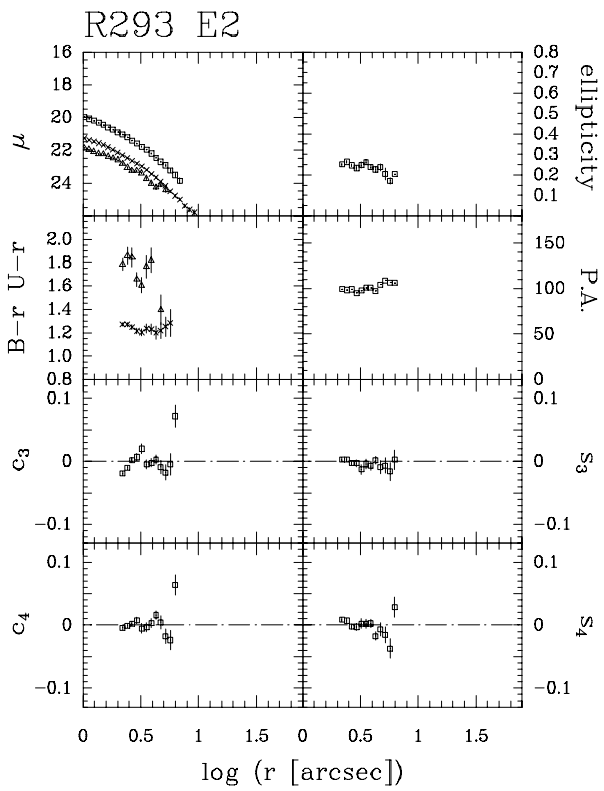
R293 E2
μ
ellipticity
B−r U−r
P.A.
c3
S3
c4
S4
log (r [arcsec])

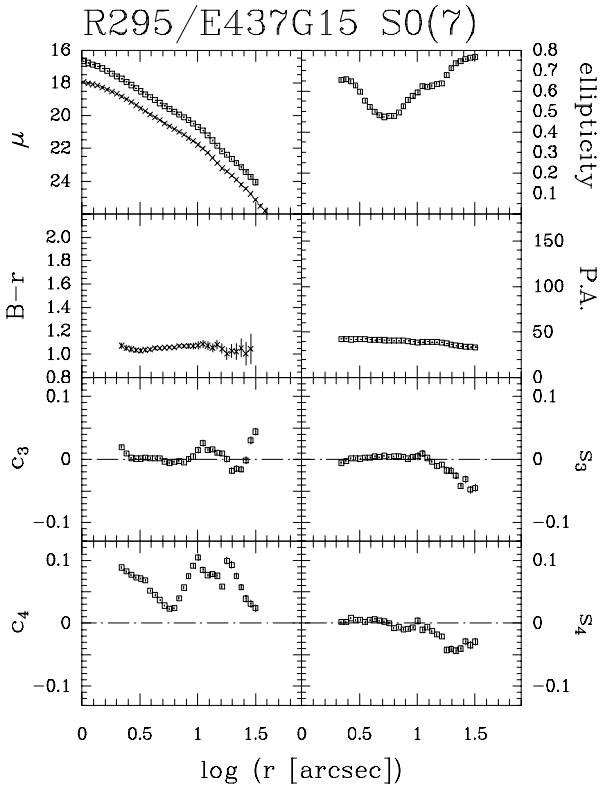
R295/E437G15 S0(7)
μ
ellipticity
B−r
P.A.
c3
S3
c4
S4
log (r [arcsec])

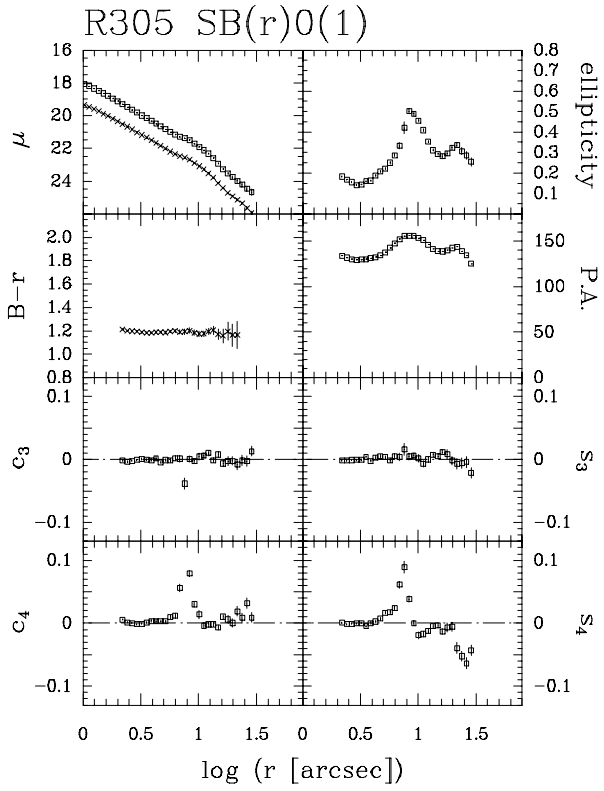
R305 SB(r)0(1)
μ
ellipticity
B−r
P.A.
c3
S3
c4
S4
log (r [arcsec])

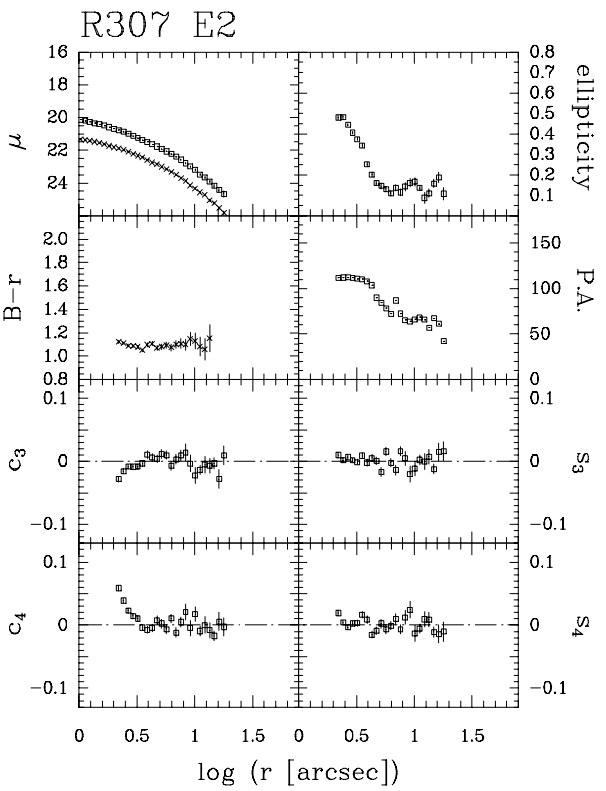
R307 E2
μ
B−r
c3
c4
ellipticity
P.A.
s3
s4
log (r [arcsec])

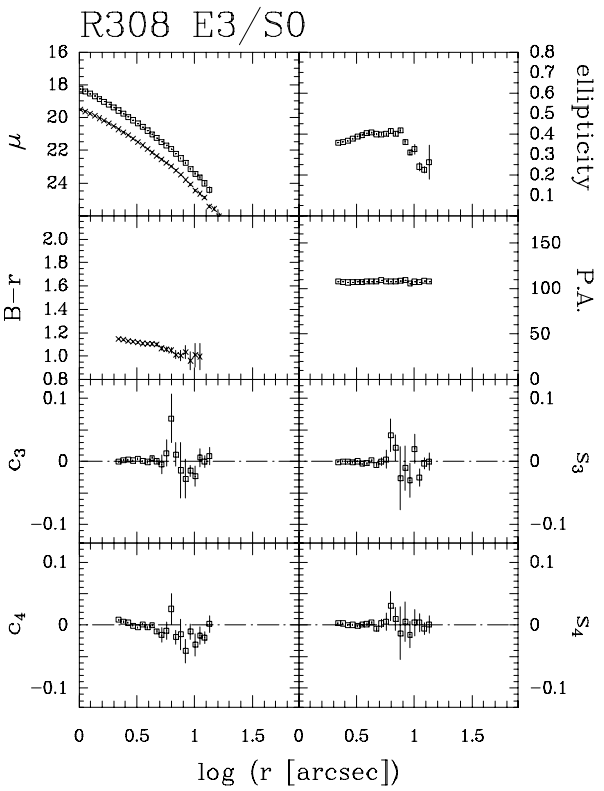
R308 E3/S0
μ
B−r
c3
c4
ellipticity
P.A.
s3
s4
log (r [arcsec])

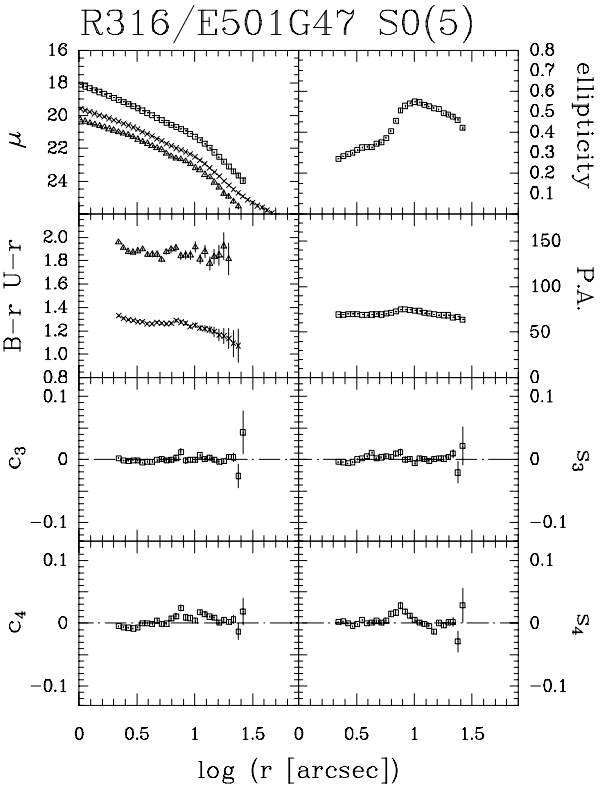
R316/E501G47 S0(5)
μ
B−r U−r
c3
c4
ellipticity
P.A.
s3
s4
log (r [arcsec])

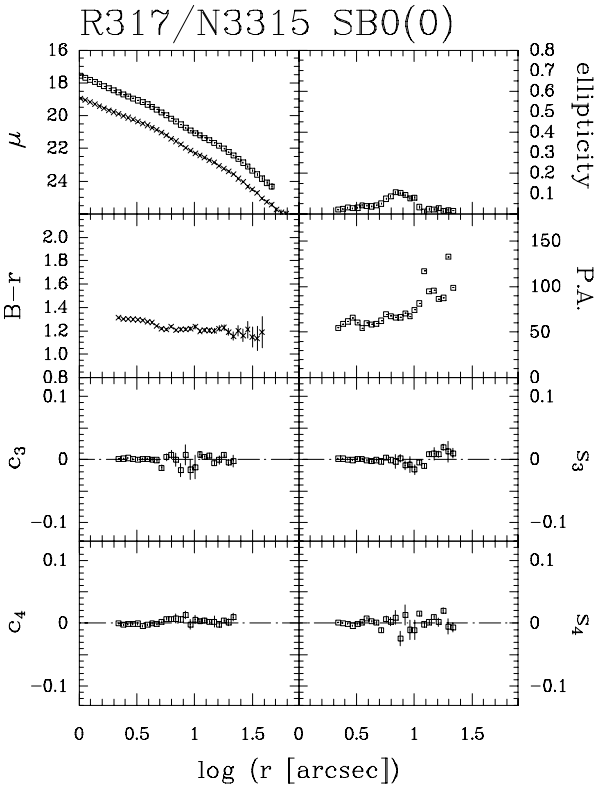
R317/N3315 SB0(0)
μ
B−r
c3
c4
ellipticity
P.A.
s3
s4
log (r [arcsec])

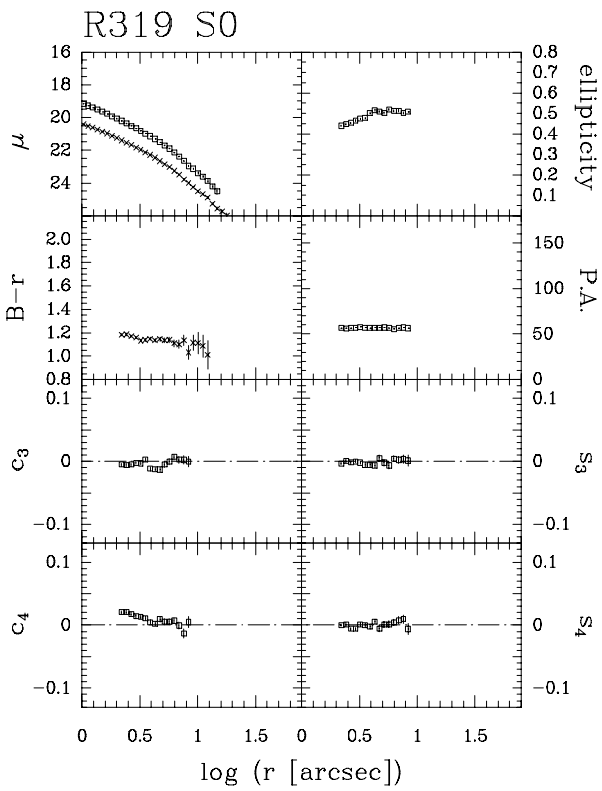
R319 S0
μ
B−r
c3
c4
ellipticity
P.A.
s3
s4
log (r [arcsec])

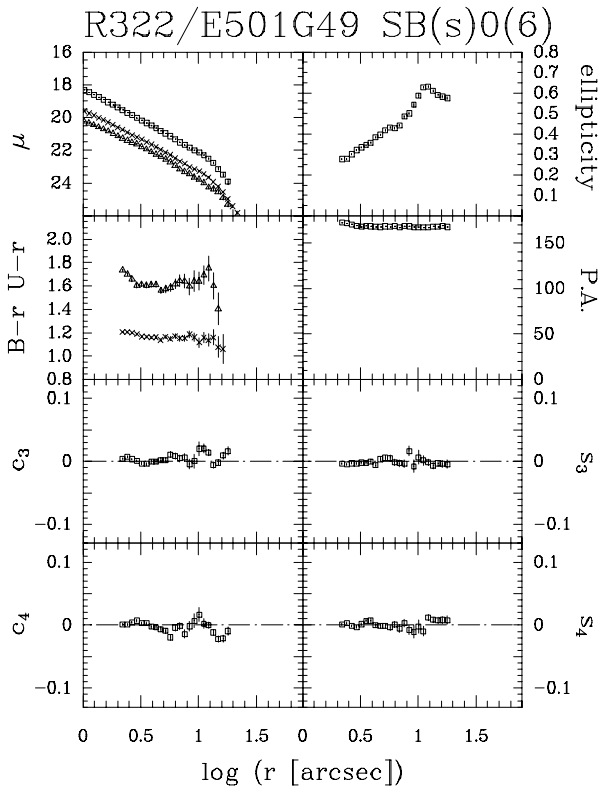
R322/E501G49 SB(s)0(6)
μ
B−r U−r
c3
c4
ellipticity
P.A.
s3
s4
log (r [arcsec])

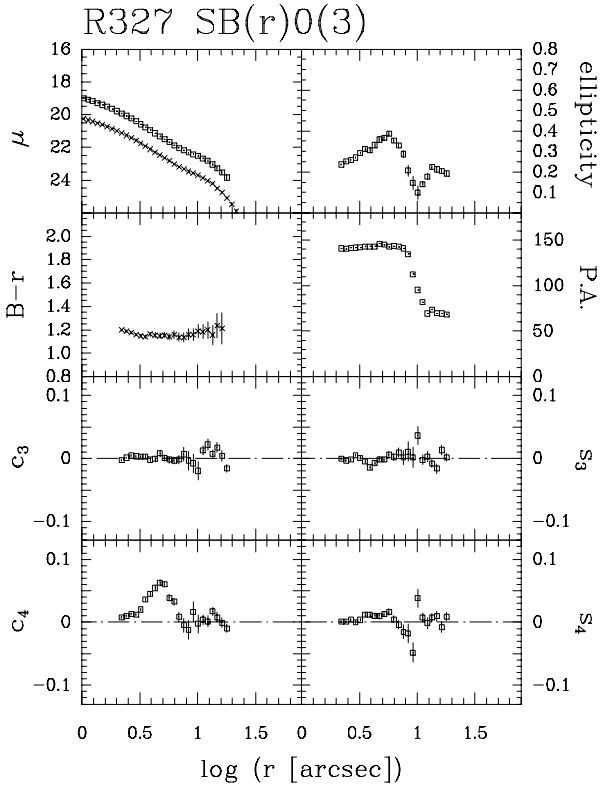
R327 SB(r)0(3)
μ
B−r
c3
c4
ellipticity
P.A.
s3
s4
log (r [arcsec])

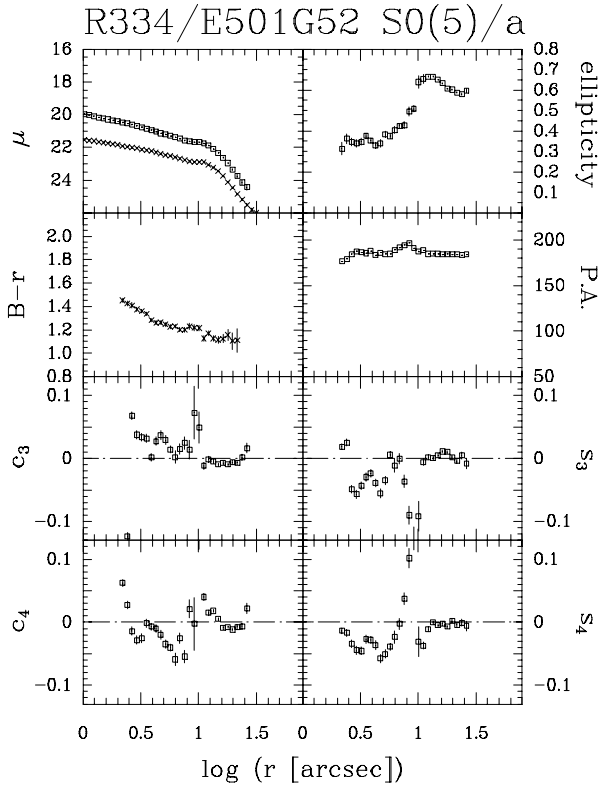
R334/E501G52 S0(5)/a
μ
B−r
c3
c4
ellipticity
P.A.
s3
s4
log (r [arcsec])

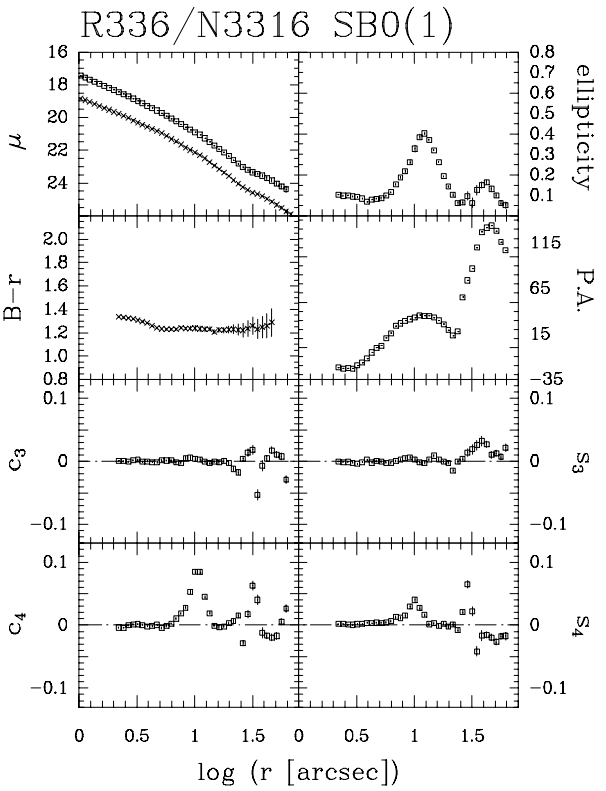
R336/N3316 SB0(1)
μ
ellipticity
B−r
P.A.
c3
s3
c4
s4
log (r [arcsec])

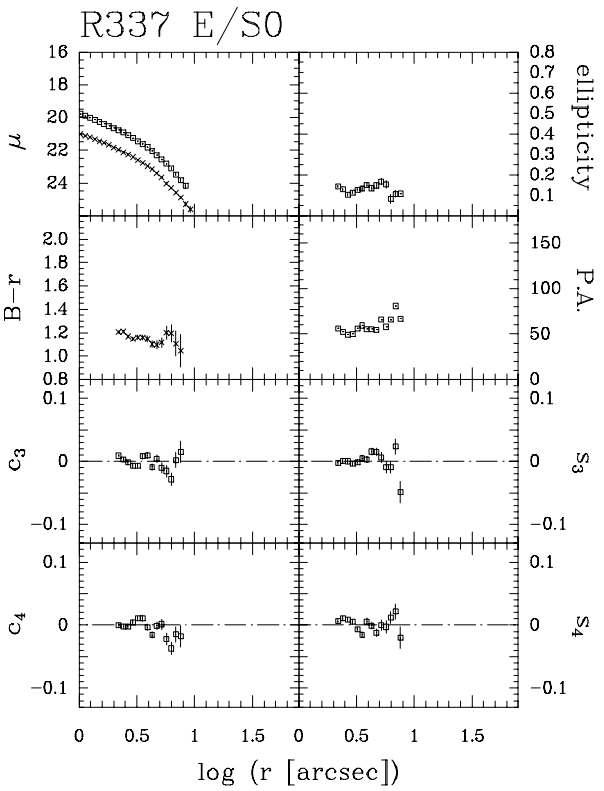
R337 E/S0
r'
ellipticity
B−r
P.A.
c3
s3
c4
s4
log (r [arcsec])

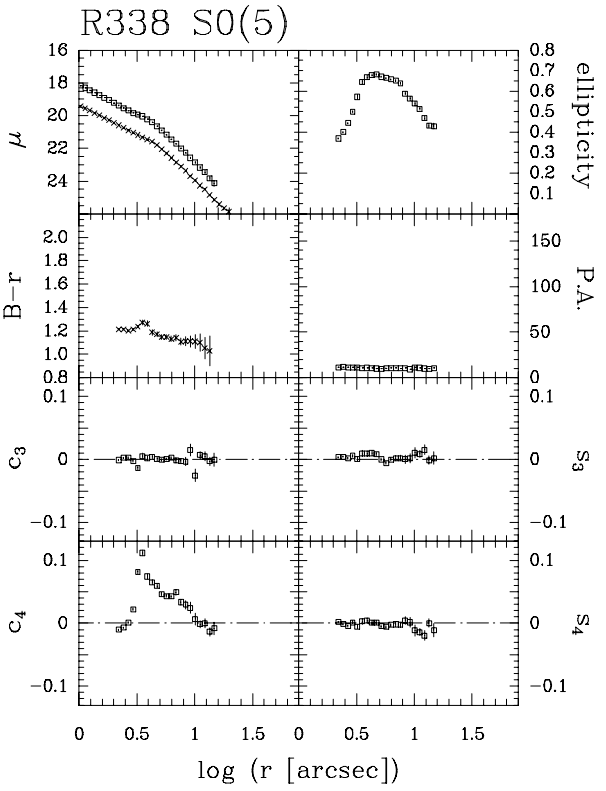
R338 S0(5)
μ
ellipticity
B−r
P.A.
c3
s3
c4
s4
log (r [arcsec])

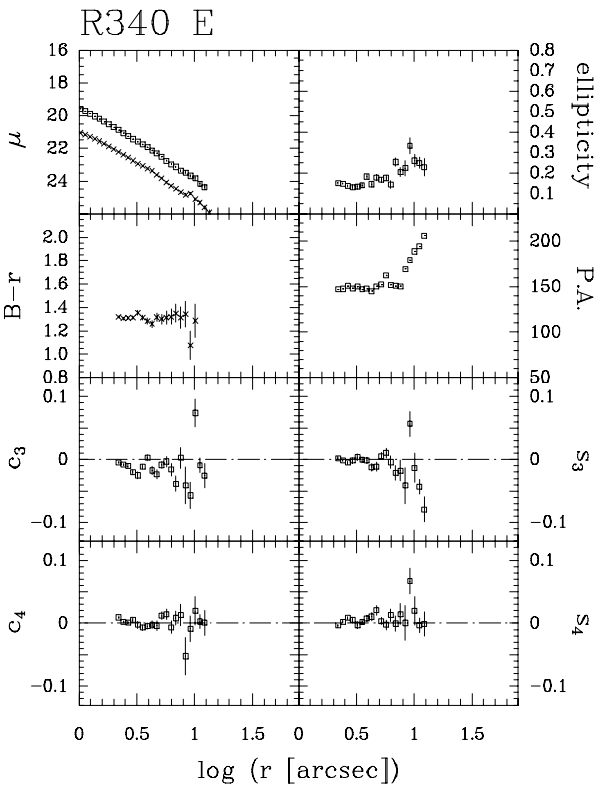
R340 E
r'
ellipticity
B−r
P.A.
c3
s3
c4
s4
log (r [arcsec])

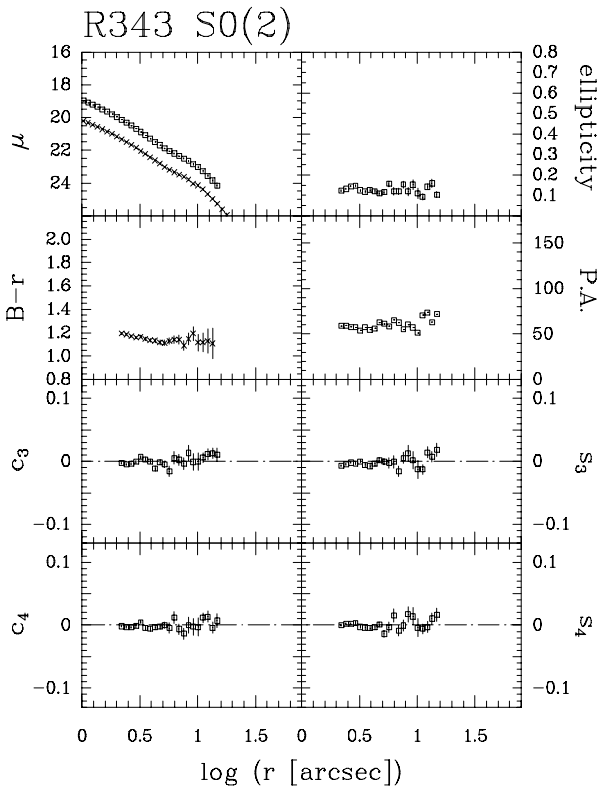
R343 S0(2)
μ
ellipticity
B−r
P.A.
c3
s3
c4
s4
log (r [arcsec])

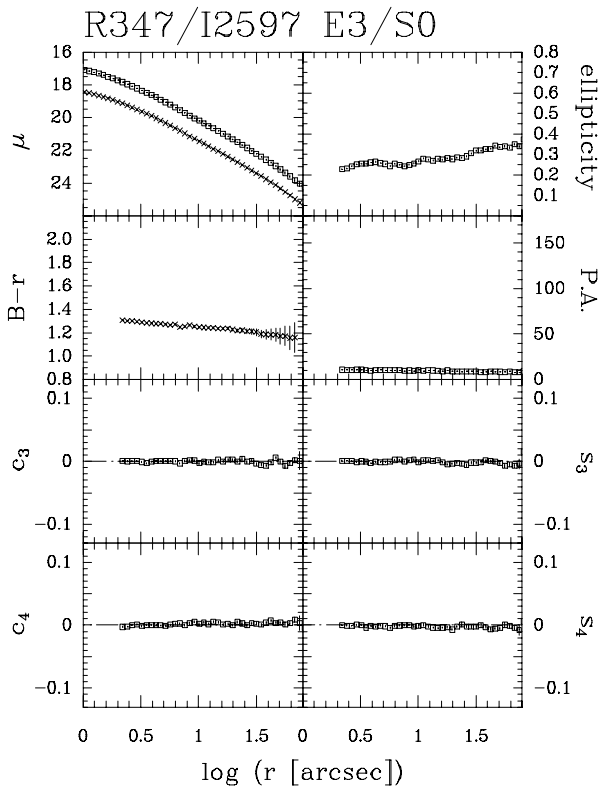
R347/I2597 E3/S0
μ
ellipticity
B−r
P.A.
c3
s3
c4
s4
log (r [arcsec])

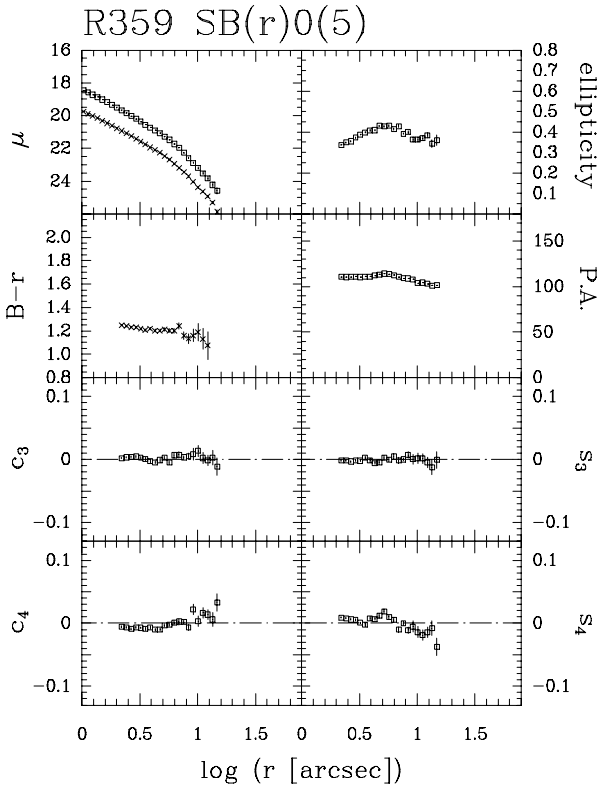
R359 SB(r)0(5)
μ
ellipticity
B−r
P.A.
c3
s3
c4
s4
log (r [arcsec])

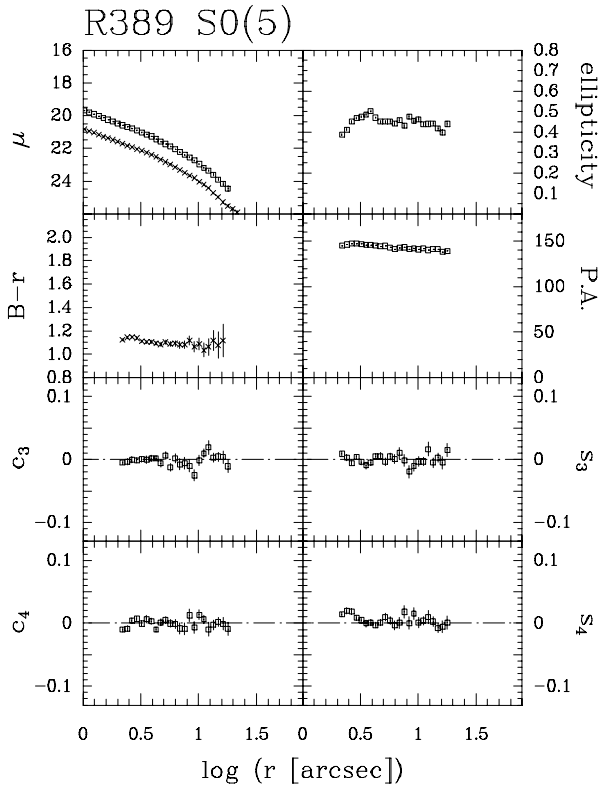
R389 S0(5)
μ
ellipticity
B−r
P.A.
c3
s3
c4
s4
log (r [arcsec])